THERAPEUTIC EFFECTS OF HERBAL MEDICINES: HOW CAN WE BEST INVESTIGATE BIOACTIVE METABOLITES?

EDITED BY: Shuai Ji, Wenzhi Yang, Bin Chen, Xionghao Lin, Wei Song and Marcello Locatelli

PUBLISHED IN: Frontiers in Pharmacology

frontiers Research Topics

ISSN 1664-8714
ISBN 978-2-88974-958-4
DOI 10.3389/978-2-88974-958-4

About Frontiers

Frontiers is more than just an open-access publisher of scholarly articles: it is a pioneering approach to the world of academia, radically improving the way scholarly research is managed. The grand vision of Frontiers is a world where all people have an equal opportunity to seek, share and generate knowledge. Frontiers provides immediate and permanent online open access to all its publications, but this alone is not enough to realize our grand goals.

Frontiers Journal Series

The Frontiers Journal Series is a multi-tier and interdisciplinary set of open-access, online journals, promising a paradigm shift from the current review, selection and dissemination processes in academic publishing. All Frontiers journals are driven by researchers for researchers; therefore, they constitute a service to the scholarly community. At the same time, the Frontiers Journal Series operates on a revolutionary invention, the tiered publishing system, initially addressing specific communities of scholars, and gradually climbing up to broader public understanding, thus serving the interests of the lay society, too.

Dedication to Quality

Each Frontiers article is a landmark of the highest quality, thanks to genuinely collaborative interactions between authors and review editors, who include some of the world's best academicians. Research must be certified by peers before entering a stream of knowledge that may eventually reach the public - and shape society; therefore, Frontiers only applies the most rigorous and unbiased reviews.
Frontiers revolutionizes research publishing by freely delivering the most outstanding research, evaluated with no bias from both the academic and social point of view. By applying the most advanced information technologies, Frontiers is catapulting scholarly publishing into a new generation.

What are Frontiers Research Topics?

Frontiers Research Topics are very popular trademarks of the Frontiers Journals Series: they are collections of at least ten articles, all centered on a particular subject. With their unique mix of varied contributions from Original Research to Review Articles, Frontiers Research Topics unify the most influential researchers, the latest key findings and historical advances in a hot research area! Find out more on how to host your own Frontiers Research Topic or contribute to one as an author by contacting the Frontiers Editorial Office: frontiersin.org/about/contact

THERAPEUTIC EFFECTS OF HERBAL MEDICINES: HOW CAN WE BEST INVESTIGATE BIOACTIVE METABOLITES?

Topic Editors:
Shuai Ji, Xuzhou Medical University, China
Wenzhi Yang, Tianjin University of Traditional Chinese Medicine, China
Bin Chen, Nanjing University of Chinese Medicine, China
Xionghao Lin, Howard University, United States
Wei Song, Peking Union Medical College Hospital (CAMS), China
Marcello Locatelli, University of Studies G. d'Annunzio Chieti and Pescara, Italy

Citation: Ji, S., Yang, W., Chen, B., Lin, X., Song, W., Locatelli, M., eds. (2022). Therapeutic Effects of Herbal Medicines: How Can We Best Investigate Bioactive Metabolites? Lausanne: Frontiers Media SA. doi: 10.3389/978-2-88974-958-4

Table of Contents

frontiers in Pharmacology

EDITORIAL
published: 29 March 2022
doi: 10.3389/fphar.2022.878789

Editorial: Therapeutic Effects of Herbal Medicines: How Can We Best Investigate Bioactive Metabolites?

Shuai Ji[1], *Wenzhi Yang*[2], *Bin Chen*[3], *Xionghao Lin*[4], *Wei Song*[5] *and Marcello Locatelli*[6]*

[1]Department of Pharmaceutical Analysis, Xuzhou Medical University, Xuzhou, China, [2]Tianjin State Key Laboratory of Modern Chinese Medicine, Tianjin University of Traditional Chinese Medicine, Tianjin, China, [3]Affiliated Hospital of Integrated Traditional Chinese and Western Medicine, Nanjing University of Chinese Medicine, Nanjing, China, [4]College of Medicine, Howard University, Washington, DC, United States, [5]Peking Union Medical College Hospital (CAMS), Beijing, China, [6]University of Studies G. d'Annunzio Chieti and Pescara, Chieti, Italy

Keywords: herbal medicines, pharmacodynamics, pharmacological effects, pharmacokinetics, bioactive compounds, bioactive metabolites

Editorial on the Research Topic

Therapeutic Effects of Herbal Medicines: How Can We Best Investigate Bioactive Metabolites?

Since ancient times, natural products have always been used as remedies for more or less serious pathologies. The great advantage of traditional medicine lies above all in the wealth of experience obtained "in the field" by experimenting with different natural products and different preparations to deal with specific diseases.

Only recently, starting from the information of traditional medicine, an attempt has been made to apply a more "scientific" approach, trying to actually evaluate which molecules present in the natural preparation have the therapeutic effect.

The awareness of being able to "take a cue" from the natural world in the process of developing new drugs has also developed from this approach, especially as these compounds are generally well tolerated and with reduced (or no) side effects.

In this context, therefore, traditional medicine plays a predominant role in the discovery of new drugs based on natural products, leading to the continuous need to study new herbal matrices for pharmaceutical and nutraceutical purposes, coupled with a continuous progress of the techniques applied to the characterization of natural matrices and to the evaluation of the observed biological activities, in order to better identify the bioactive compounds.

Herbal medicines contain hundreds or even thousands of primary and secondary metabolites, and it is a vital task for pharmacologists to explore which components contribute to the therapeutic effects of herbal medicines and which compounds do not. The complexity and low content of the chemical constituents of these metabolites in herbal medicines pose complex challenges. Up to now, the active components of most herbal medicines remain obscure, which hinders further pharmacological study and development of herbal medicines. In this scenario, the possibility of evaluating and characterizing herbal medicines is of great importance in order to obtain a product that is safe for human health, standardized, whose effects have been studied and evaluated from all points of view.

In general, the absorption of these metabolites needs to be understood in order to evaluate their potential therapeutic effects. Up to now, pharmacologists have tried many methods and techniques to explore the pharmacodynamics of herbal medicines. This includes the *in vivo* characterization of metabolites by pharmaco-metabonomics techniques or *ex vivo* models focusing on the delivery, for example, in the gastrointestinal tract.

In this Research Topic, the main goal aims to attract innovative original contributions in the interdisciplinary area in order to understand the relative impact of different compounds/compound

Edited by:
Javier Echeverria, University of Santiago, Chile

Reviewed by:
Andrei Mocan, Iuliu Haţieganu University of Medicine and Pharmacy, Romania

***Correspondence:**
Marcello Locatelli
m.locatelli@unich.it

Specialty section:
This article was submitted to Ethnopharmacology, a section of the journal Frontiers in Pharmacology

Received: *18 February 2022*
Accepted: *14 March 2022*
Published: *29 March 2022*

Citation:
Ji S, Yang W, Chen B, Lin X, Song W and Locatelli M (2022) Editorial: Therapeutic Effects of Herbal Medicines: How Can We Best Investigate Bioactive Metabolites? Front. Pharmacol. 13:878789. doi: 10.3389/fphar.2022.878789

classes to reported pharmacological effects, but also to highlight the state of the art on profiling of metabolites' pharmacokinetics *in vivo*, on new unreported biological activities or biological targets, and on new bioactive compounds as leads for the pharmaceutical industry.

This result can be achieved through a multidisciplinary approach that involves not only pharmacology and botany, but also disciplines such as analytical chemistry (which guarantees the quality and reproducibility of data), pharmaceutical chemistry, physiology, and biochemistry.

Through an integration of these disciplines and knowledge, it is possible to describe and characterize most of the observed.

In the papers accepted after peer review in this Research Topic, it is also highlighted that in recent years the search for products of natural origin that can be used as they are or as lead compounds for the pharmaceutical development of new drugs is increasingly a central element of scientific research.

What we have seen so far has foundations in the traditional use of many products of plant origin, as highlighted by Zeng et al., Fan et al., and Wang et al. Today these uses are being rediscovered, however, trying to follow a more scientific and systematic approach, associating what has been traditionally observed with chemical characterization and innovative techniques for evaluating biological activity in order to find a possible correlation. Han et al., Wan et al., Zheng Li et al., and Xu et al., which report approaches to proteomics, metabolomics and new strategies, respectively, amply highlight this.

Other authors such as He et al., Gao et al., and Yang et al., focus their attention on specific markers of some native products and try to evaluate their targets and their respective biological effects.

Jing et al., Gao et al., Hui-Yu Li et al., and Zixuan Li et al., instead closely evaluate traditional uses with respect to specific pathways involved in various pathologies.

Nan et al., Xuerui Wang et al., and Su et al., instead evaluate how pills and capsules containing natural products can show therapeutic and/or preventive effects against human pathologies. Interesting the work of Pan et al., which reports how metabolomics studies carried out by hyphenated analytical approaches of LC-MS allow to evaluate and correlate the effects of EGCG on A549 cells.

AUTHOR CONTRIBUTIONS

All authors listed have made a substantial, direct, and intellectual contribution to the work and approved it for publication.

Conflict of Interest: The authors declare that the research was conducted in the absence of any commercial or financial relationships that could be construed as a potential conflict of interest.

The reviewer AM declared a past co-authorship with the author ML to the handling editor.

Publisher's Note: All claims expressed in this article are solely those of the authors and do not necessarily represent those of their affiliated organizations, or those of the publisher, the editors and the reviewers. Any product that may be evaluated in this article, or claim that may be made by its manufacturer, is not guaranteed or endorsed by the publisher.

frontiers in Pharmacology

REVIEW
published: 22 April 2021
doi: 10.3389/fphar.2021.652926

The Traditional Uses, Phytochemistry and Pharmacology of *Sarcandra glabra* (Thunb.) Nakai, a Chinese Herb With Potential for Development: Review

Yuanlian Zeng[1], *Junyu Liu*[1], *Qiang Zhang*[2], *Xuhua Qin*[1], *Zulun Li*[1], *Guojuan Sun*[2]* *and Shenrui Jin*[3]*

[1]College of Pharmacy, Chengdu University of Traditional Chinese Medicine, Chengdu, China, [2]International Department of Gynecology, Hospital of Chengdu University of Traditional Chinese Medicine, Chengdu, China, [3]College of Basic Medicine, Chengdu University of Traditional Chinese Medicine, Chengdu, China

Sarcandra glabra (Thunb.) Nakai is a folk medicine with a long history in China, which has been applied to treat sore throat, abscess, even tumor and so on. Meanwhile, it is also used as tea in some areas. At present, more than 200 chemical compounds have been isolated and identified from it, such as, sesquiterpenes, flavonoids, phenolic acids, coumarins and so on. Pharmacological studies have already confirmed that the extracts of *S. glabra* have many effects, such as antibacterial, antiviral, anti-inflammatory, anti-tumor, and anti-thrombocytopenia, especially the effects of anti-tumor and anti-thrombocytopenia are confirmed in clinic. Therefore, this paper systematically summarized the traditional uses, botany, phytochemistry, pharmacology, and toxicity of *S. glabra*, in order to provide a beneficial reference of its further research.

Keywords: ***Sarcandra glabra*** **(Thunb.) Nakai, traditional uses, phytochemistry, pharmacology, toxicity**

OPEN ACCESS

Edited by:
Shuai Ji,
Xuzhou Medical University, China

Reviewed by:
Taoufiq Benali,
Cadi Ayyad University, Morocco
Deepak Kumar Semwal,
Uttarakhand Ayurved University, India

***Correspondence:**
Guojuan Sun
sunguojuan@126.com
Shenrui Jin
J15184436539@163.com

Specialty section:
This article was submitted to Ethnopharmacology, a section of the journal Frontiers in Pharmacology

Received: *13 January 2021*
Accepted: *01 April 2021*
Published: *22 April 2021*

Citation:
Zeng Y, Liu J, Zhang Q, Qin X, Li Z, Sun G and Jin S (2021) The Traditional Uses, Phytochemistry and Pharmacology of Sarcandra glabra *(Thunb.) Nakai, a Chinese Herb With Potential for Development: Review. Front. Pharmacol. 12:652926. doi: 10.3389/fphar.2021.652926*

INTRODUCTION

S. glabra is a perennial evergreen plant belonging to the Chloranthaceae family, and its resources are widely distributed throughout China, Japan, Korea, and Southeast Asia (Xu et al., 2011). *S. glabra* is commonly called *Zhong Jie Feng* in Chinese, because its ripe fruits resemble shiny red coral beads, it is also known as *Cao Shan Hu*. Meanwhile, after soaking *S. glabra* in hot water for a period of time, it will emit attractive aroma and taste delicious. Therefore, it is also regarded as tea in some areas (Yang, 1992; Han et al., 2013), also known as *Jiu Jie Cha*.

Abbreviations: Akt, protein kinase B; ALB, albumin; ALT, Alanine aminotransferase; AST, Aspartate aminotransferase; C-IV, procollagen type IV; CAT, catalase; CK, creatine kinase; ERK, extracellular regulated protein kinases; HA, hyaluronia acid; HO-1, heme oxygenase one; IL-6, interleukin-6; IL-18, interleukin-18; iNOS, inducible nitric oxide synthase; MDA, malondialdehyde; NF-κB, nuclear factor kappa B; NO, nitric oxide; Nrf2, nuclear factor erythroid 2-related factor 2; PC-III, procollagen type III; ROS, reactive oxygen species; SOD, superoxide dismutase; SDF-1, stromal cell derived factor-1; TGF-β, transforming growth factor beta; TPO, thermoplastic polyolefin; TNF-α, Tumor necrosis factor alpha; VCAM-1, vascular cell adhesion molecule-1; LN, laminin; TIMP-1, tissue inhibitor of metalloproteinase-1; TG, triglyceride; TC, total cholesterol; LDL-C, low density lipoprotein; T-AOC, total antioxidant capacity; LDH, lactate dehydrogenase.

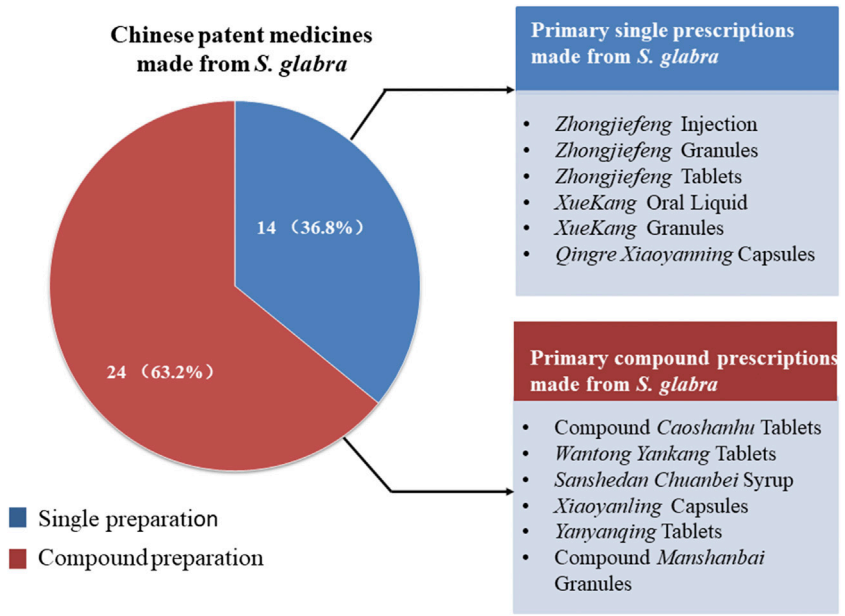

FIGURE 1 | Chinese patent medicines made from *S. glabra*.

S. glabra has high medicinal value. *S. glabra* has been used as a folk medicine since the Qing Dynasty (Chen and Li, 2015), commonly applied by numerous ethnic groups in clinical practice in China, such as Han, Miao, Dong, Yao, Zhuang, *etc*., which has been officially listed in *Chinese Pharmacopoeia* since 1977. Traditionally, *S. glabra* is widely used to treat traumatic fracture, joint swelling and pain, sore throat, abscess, bleeding, and other diseases (Jia and Li, 2005). In modern clinical practice, it also has been applied to treat upper respiratory tract infection (Li, 2003), pneumonia (He et al., 2003), gastritis (Chen et al., 2012), viral myocarditis (Li, 2004), tumor (Cong et al., 2005; Song, 2017), and thrombocytopenia (Jiang and Zhou, 2003; Su and Luo, 2009), with significantly clinical therapeutic effect. Owing to the advantages of definite clinical effect, good safety, and abundant resources, many Chinese patent medicines with *S. glabra* as primary ingredient have been developed in modern times, 38 kinds of which have been approved for marketing by the State Food and Drug Administration of China (**Figure 1**).

In recent decades, considerable work has been done on pharmacology and phytochemistry of *S. glabra*. Many studies have proved that *S. glabra* exhibits a plenty of pharmacological effects, such as anti-inflammatory (Tsai et al., 2017), antibacterial (Jiang et al., 2000), antiviral (Cao et al., 2012), anti-tumor (Zhang et al., 2014), antioxidant (Liu et al., 2016), and anti-thrombocytopenic effects (Lu et al., 2018b). So far, over 200 chemical compounds have been isolated from *S. glabra*, including sesquiterpenes, flavonoids, coumarins, phenolic acids, lignans, anthraquinones and steroids. Among them, flavonoids are considered to be important bioactive components in *S. glabra*, which are also closely related to anti-thrombocytopenic activity of *S. glabra* (Xu et al., 2005). However, findings on pharmacology and phytochemistry are still difficult to comprehensively reflect its pharmacological effects and mechanisms, most pharmacological studies are still focused on exploring the activity of crude extracts, and the correlation between pharmacological effects and chemical components has yet to be fully established. Thus, there are many issues that deserve further investigation.

At present, reviews on *S. glabra* are not comprehensive enough (Han and Wu, 2017; Yang, 2017), and the chemical constituents and mechanism of pharmacological effects are deficiency, which impedes further research of *S. glabra*. In this paper, we used "*Sarcandra glabra*" as the keywords to collect information related to *S. glabra* from Web of Science, Science Direct, Springer, Google Scholar, PubMed, China National Knowledge Infrastructure (CNKI), and other professional websites, as well as classic books of herbal medicine. This paper intended to make a comprehensive and systematic review about *S. glabra*, so as to enhance further understanding of its traditional uses, botany, phytochemistry, pharmacology, and toxicity. This paper would also provide a beneficial reference for its in-depth research, development and utilization.

BOTANY

The genus *Sarcandra* comprises three accepted species worldwide (Chen and Cheng, 1994). *Sarcandra glabra* (Thunberg) Nakai is a species of the genus *Sarcandra*, widely distributed in the south of the Yangtze River in China, as well as other Asian countries, including Korea, Japan, Malaysia, Philippines, Vietnam, India, *etc.* (Zhou, 1993; Chen and Cheng, 1994). It is a semi-shade plant, prefers a warm and humid environment, but avoids direct

FIGURE 2 | *Sarcandra glabra*. **(A–C)** represent the whole plants **(A)**, inflorescence **(B)** and fruits **(C)** of *S. glabra*.

sunlight, thus, it usually grows in ravines, slopes, valleys, and wet places under forests.

S. glabra derives from the dried whole plant of *Sarcandra glabra* (Thunb.) Nakai (synonym: *Chloranthus glaber* (Thunb.) Makino), which belongs to the genus *Sarcandra* of the Chloranthaceae family. It is a perennial evergreen subshrub with a height of approximately 50–120 cm. Its stem is erect, usually branched, and the nodes of the stem and branches are obviously swollen, which also have obvious longitudinal grooves and ridges between the nodes. Its leaves are opposite, leathery or papery, and glabrous on both surfaces. The shape of leaves is ovate or oval, about 6–17 cm long and 2–6 cm in wide. Its leaves are similar to tea leaves, the apex is acuminate, the base is wedge-shaped, the edges are serrated, and the marginal teeth are hard bone. Its petiole is approximately 1 cm in length. The stipule is small, like a sheath. There are small yellow-green flowers on the top of the branches, with a fragrant smell, no perianth, and cluster into spikes. *S. glabra* is monoecious, in which the stamens are clubbed to cylindrical, while the pistil is globose. Its fruit looks like pearl, which turns into shiny red at maturity, about 3–4 mm in diam. The florescence ranges from June to July, and the fruit period is from August to October. The whole plant of *S. glabra* is shown in **Figure 2** [(Cheng, 1982), http://ppbc.iplant.cn/sp/15108].

TRADITIONAL USES

S. glabra was first found in the Tang Dynasty's medical book "*Ben Cao Shi Yi*" (AD 741) under the name of *Jie gu mu*, and then it was recorded in the Ming Dynasty's Plant book "*Ru Nan Pu Shi*" (AD 1620) in the name of *Shan hu* (Chen and Li, 2015). However, its medicinal value was first appeared in "*Sheng Cao Yao Xing Bei Yao*" (AD 1711) in the Qing Dynasty: "Boiling it in water to drink, reducing fever". According to "*Ben Cao Gang Mu Shi Yi*" (AD 1765), *S. glabra* could treat traumatic injury and fracture. In traditional clinical practice, *S. glabra* was effective in the treatment of joint swelling and pain, sore throat, carbuncle, tumor, trauma, bleeding, *etc.* In particular, the production technology of Miao nationality using *S. glabra* to treat traumatic fracture has been included in the list of National Intangible Cultural Heritage Protection at present (http://www.ihchina.cn/). Furthermore, in both ancient and modern times, *S. glabra* has been commonly used by Miao nationality to treat postpartum abdominal pain and dizziness; Dong nationality to treat appendicitis; the nationality of Yao and Zhuang to treat stomachache, dysentery, and influenza; Dai nationality to treat gastric ulcer; the nationality of Jinpo and Lahu to treat many gynecological diseases such as irregular menstruation, dysmenorrhea, and puerperal metrorrhagia (Jia and Li, 2005).

S. glabra has long been regarded as an edible plant in some areas. According to the records of Xingan County Chronicles in Jiangxi Province, people grind *S. glabra* with salt, rice, sesame and houttuynia in pottery bowls, then mix it with well water to drink, which is locally called *Lei Cha*. *Lei Cha* has been popular in the region since the Ming and Qing Dynasties, at present, *Lei Cha* in Gannan of Jiangxi Province has been included in the list of National Intangible Cultural Heritage Protection (http://www.ihchina.cn/). The Dong, Miao, Shui, Buyi and other ethnic groups in Guizhou province use *S. glabra* to make tea instead of ordinary tea in daily life. Especially, the Dong people prefer to make camellia oleifera for consumption through mixing *S. glabra* tea with glutinous rice, peanuts, soybeans and other condiments they like. Hence, the above

TABLE 1 | Compounds presenting in *S. glabra*.

No	Chemical component	Extract	Part	References
	Sesquiterpenes			
1	Chloranthalactone A	Dichloromethane	Aerial parts	Tsui and Brown (1996)
2	Chloranthalactone B	EtOH	Whole plant	Hu et al. (2009)
3	Chloranthalactone E	EtOH	Whole plant	Zhu et al. (2008b)
4	Chloranthalactone E 8-O-β-D-glucopyranoside	EtOH	Whole plant	Li et al. (2006a)
5	Chloranthalactone F	Et_2O	Leaves	Takeda et al. (1993)
6	Chloranthalactone G	Dichloromethane	Aerial parts	Tsui and Brown, (1996)
7	Chloranoside A	EtOH	Whole plant	Hu et al. (2009)
8	Chloranoside B	Et_2O	Leaves	Takeda et al. (1993)
9	Chloranthalactone A photodimer	Acetone	Leaves	Okamura et al. (1995)
10	Sarcandralactone A	EtOH	Whole plant	He et al. (2010)
11	Sarcandralactone B	EtOH	Whole plant	He et al. (2010)
12	Sarcandralactone C	EtOH	Whole plant	Ni et al. (2013)
13	Sarcandralactone D	EtOH	Whole plant	Ni et al. (2013)
14	Sarcandralactone E	EtOH	Whole plant	Ni et al. (2013)
15	8β, 9α-dihydroxylindan-4(5),7(11) -dien-8α,12-olide	EtOH	Whole plant	Zhu et al. (2008b)
16	9-hydroxyheterogorgiolide	EtOH	Whole plant	Hu et al. (2009)
17	Shizukanolide E	EtOH	Whole plant	Hu et al. (2013)
18	Shizukanolide F	EtOH	Whole plant	Hu et al. (2013)
19	Shizukanolide H	EtOAc	Whole plant	Zheng et al. (2014)
20	4α-hydroxy-5α*H*-lindan-8 (9)-en-8,12-olide	EtOH	Whole plant	Li et al. (2011)
21	Chlorajapolide C	EtOAc	Whole plant	Zheng et al. (2014)
22	Sarcaglabrin A	MeOH	Aerial parts	Yang et al. (2020)
23	Glabranol A	EtOH	Aerial parts	Oanh et al. (2010)
24	Glabranol B	EtOH	Aerial parts	Oanh et al. (2010)
25	Sarcaglaboside A	EtOH	Whole plant	Li et al. (2006a)
26	Sarcaglaboside B	EtOH	Whole plant	Li et al. (2006a)
27	Sarcaglaboside C	EtOH	Whole plant	Li et al. (2006a)
28	Sarcaglaboside D	EtOH	Whole plant	Li et al. (2006a)
29	Sarcaglaboside E	EtOH	Whole plant	Li et al. (2006a)
30	Sarcaglaboside F	EtOH	Whole plant	Hu et al. (2009)
31	Sarcaglaboside G	EtOH	Whole plant	Hu et al. (2009)
32	Sarcaglaboside H	EtOH	Whole plant	Hu et al. (2009)
33	Atractylenolide II	Et_2O	Leaves	Takeda et al. (1993)
34	Atractylenolide III	EtOH	Whole plant	Wang et al. (2007)
35	Atractylenolide IV	EtOH	Whole plant	Hu et al. (2013)
36	8β,9α-dihydroxyeudesman-4(15),7(11)-dien-8α,12-olide	EtOH	Whole plant	Zhu et al. (2008b)
37	Neolitacumone B	EtOH	Whole plant	Ni et al. (2013)
38	1α,8α,9α-trihydroxyeudesman-3(4),7(11)-dien-8β,12-olide	EtOH	Whole plant	Wang et al. (2012)
39	3-eudesmene-1β,7, 11-triol	EtOH	Whole plant	He et al. (2010)
40	(-)-istanbulin A	EtOH	Whole plant	Zhu et al. (2008b)
41	Istanbulin A	EtOAc	Whole plant	Zheng et al. (2014)
42	Istanbulin B	EtOAc	Whole plant	Zheng et al. (2014)
43	Furanodienone	EtOH	Whole plant	Luo et al. (2005a)
44	(-)-4β,7α-Dihydromadendrane	Et_2O	Leaves	Takeda et al. (1993)
45	Spathulenol	Dichloromethane	Aerial parts	Tsui and Brown, (1996)
46	PipelolA	EtOH	Whole plant	Wang et al. (2010a)
47	Sarcaboside A	EtOH	Whole plant	Li et al. (2012a)
48	Sarcaboside B	EtOH	Whole plant	Li et al. (2012a)
49	Glabralide A	EtOH	Whole plant	Yang et al. (2018)
50	Glabralide B	EtOH	Whole plant	Yang et al. (2018)
51	Glabralide C	EtOH	Whole plant	Yang et al. (2018)
52	Sarcandrolide A	EtOH	Whole plant	He et al. (2010)
53	Sarcandrolide B	EtOH	Whole plant	He et al. (2010)
54	Sarcandrolide C	EtOH	Whole plant	He et al. (2010)
55	Sarcandrolide D	EtOH	Whole plant	He et al. (2010)
56	Sarcandrolide E	EtOH	Whole plant	He et al. (2010)
57	Sarcandrolide F	EtOH	Whole plant	Ni et al. (2013)
58	Sarcandrolide G	EtOH	Whole plant	Ni et al. (2013)
59	Sarcandrolide H	EtOH	Whole plant	Ni et al. (2013)
60	Sarcandrolide I	EtOH	Whole plant	Ni et al. (2013)
61	Sarcandrolide J	EtOH	Whole plant	Ni et al. (2013)
62	Sarcaglabrin B	MeOH	Aerial parts	Yang et al. (2020)
63	Sarcaglabrin C	MeOH	Aerial parts	Yang et al. (2020)

(Continued on following page)

TABLE 1 | (*Continued*) Compounds presenting in *S. glabra*.

No	Chemical component	Extract	Part	References
64	Shizukaol A	EtOH	Roots	Wei et al. (2019)
65	Shizukaol B	EtOH	Seeds	Wang et al. (2015b)
66	Shizukaol C	EtOH	Seeds	Wang et al. (2015b)
67	Shizukaol D	EtOH	Whole plant	Ni et al. (2013)
68	Shizukaol E	EtOH	Roots	Wei et al. (2019)
69	Shizukaol G	EtOH	Seeds	Wang et al. (2015b)
70	Shizukaol H	EtOH	Whole plant	Ni et al. (2013)
71	Shizukaol I	EtOH	Whole plant	Luo. (2004)
72	Shizukaol N	EtOH	Seeds	Wang et al. (2015b)
73	Sarglabolide A	EtOH	Seeds	Wang et al. (2015b)
74	Sarglabolide B	EtOH	Seeds	Wang et al. (2015b)
75	Sarglabolide C	EtOH	Seeds	Wang et al. (2015b)
76	Sarglabolide D	EtOH	Seeds	Wang et al. (2015b)
77	Sarglabolide E	EtOH	Seeds	Wang et al. (2015b)
78	Sarglabolide F	EtOH	Seeds	Wang et al. (2015b)
79	Sarglabolide G	EtOH	Seeds	Wang et al. (2015b)
80	Sarglabolide H	EtOH	Seeds	Wang et al. (2015b)
81	Sarglabolide I	EtOH	Seeds	Wang et al. (2015b)
82	Sarglabolide J	EtOH	Seeds	Wang et al. (2015b)
83	Sarglabolide K	EtOH	Seeds	Wang et al. (2015b)
84	Chlorajaponilide E	EtOH	Whole plant	Ni et al. (2013)
85	Chloraholide F	EtOH	Whole plant	Ni et al. (2013)
86	Spicachlorantin F	EtOH	Whole plant	Ni et al. (2013)
87	Chloraholide D	EtOH	Roots	Wei et al. (2019)
88	Henriol D	EtOH	Whole plant	Ni et al. (2013)
89	Cycloshizukaol A	EtOH	Roots	Wei et al. (2019)
90	Sarglaperoxide A	EtOH	Seeds	Wang et al. (2016)
91	Sarglaperoxide B	EtOH	Seeds	Wang et al. (2016)
92	Dihydrovomifoliol	Acetone	Whole plant	Wu et al. (2012b)
93	Dihydrovomifoliol-O-β-D-glucopyranoside	Acetone	Whole plant	Wu et al. (2012b)
94	Drovomifoliol-O-β-D-glucopyranoside	Acetone	Whole plant	Wu et al. (2012b)
95	Cis-abscisic acid	Acetone	Whole plant	Wu et al. (2012b)
96	β-D-glucopyranosylabscizate	Acetone	Whole plant	Wu et al. (2012b)
97	Asicariside B1	Acetone	Whole plant	Wu et al. (2012b)
	Diterpenes			
98	15-hydroxy-12-oxolabda-8-(17),13E-dien-19-oicacid	EtOH	Whole plant	Luo. (2004)
99	12R,15-dihydroxylabda-8 (17),13E-dien-19-oicacid	EtOH	Whole plant	Luo. (2004)
100	12S,15-dihydroxylabda-8 (17),13E-dien-19-oicacid	EtOH	Whole plant	Luo. (2004)
101	9R-12S,15-dihydroxylabda-8 (17),13E-dien-19-oic acid	EtOH	Whole plant	Luo. (2004)
	Triterpenes			
102	Sarcandroside A	MeOH	Whole plant	Luo et al. (2005b)
103	Sarcandroside B	MeOH	Whole plant	Luo et al. (2005b)
104	Lupeol	EtOH	Whole plant	Luo et al. (2005a)
105	24-hydroxy lupeol	EtOH	Whole plant	Luo et al. (2005a)
106	Betulinic acid	Dichloromethane	Aerial parts	Tsui and Brown, (1996)
107	Ursolic acid	EtOH	Whole plant	Fu and Liang, (2013)
108	Oleanolic acid	EtOH	Whole plant	Fu and Liang, (2013)
	Flavonoids			
109	Kaempferol	Aqueous	Whole plant	Yuan et al. (2008)
110	Kaempferol-3-O-β-D-glucuronide	Aqueous	Whole plant	Huang et al. (2008)
111	Quercetin	EtOH	Whole plant	Zou et al. (2007)
112	Quercetin-3-O-glucuronide	Aqueous	Stems	Duan et al. (2010)
113	Quercetin-3-O-β-D-glucuronopyranoside methyl ester	Aqueous	Whole plant	Huang et al. (2008)
114	Quercetin-3-O-α-D-glucuronide	Aqueous	Whole plant	Huang et al. (2008)
115	Quercetin-3-O-α-L-rhamnoside	EtOH	Whole plant	Tong et al. (2010)
116	Rutin	EtOH	Whole plant	Fu and Liang, (2013)
117	Hyperoside	EtOH	Whole plant	Fu and Liang, (2013)
118	Epimedin C	Aqueous	Whole plant	Li et al. (2010)
119	Astilbin	EtOH	Whole plant	Wang et al. (2010b)
120	Neoastilbin	EtOH	Whole plant	Wang et al. (2010b)
121	Isoastilbin	EtOH	Whole plant	Wang et al. (2010b)
122	Neoisoastilbin	EtOH	Whole plant	Wang et al. (2010b)
123	Pinostrobin	EtOH	Whole plant	Wang et al. (2007)
124	7-Methylnaringenin	EtOH	Whole plant	Luo et al. (2005a)

(Continued on following page)

TABLE 1 | (*Continued*) Compounds presenting in *S. glabra*.

No	Chemical component	Extract	Part	References
125	5-hydroxy-7-methoxy-dihyflavanones	EtOH	Whole plant	Luo et al. (2005a)
126	5-hydroxy-7, 4′-dimethoxyflavanone	EtOH	Whole plant	Wang et al. (2007)
127	(+)-3,3′,5,5′,7-pentahydroxy-diflavanone	EtOH	Whole plant	Zhu et al. (2008a)
128	5-dihydroxy-7,4′-dimethoxy-dihyflavanones	Dichloromethane	Aerial parts	Tsui and Brown, (1996)
129	5,4′-dihydroxy-7-methoxy-dihyflavanones	EtOH	Whole plant	Luo et al. (2005a)
130	5,7,4′-trihydroxy-8-C-β-D-glucopyranosylflavanone	Aqueous	Whole plant	Huang et al. (2008)
131	5,7,3′,4′-tetrahydroxy-6-C-β-D-glucopyranosylflavanone	Aqueous	Whole plant	Yuan et al. (2008)
132	Isoliquiritigenin	EtOH	Whole plant	Zou et al. (2007)
133	2′,4′-dihydroxy-6′-methoxy-dihydrochalcone	Dichloromethane	Aerial parts	Tsui and Brown, (1996)
134	2′,4′-dihydroxy-4,6′-dimethoxy-dihydrochalcone	Dichloromethane	Aerial parts	Tsui and Brown, (1996)
135	2′,6′-dihydroxy-4′-methoxydihydrochalcone	Dichloromethane	Aerial parts	Tsui and Brown, (1996)
136	2′,6′-dihydroxy-4,4′-dimethoxy-dihydrochalcone; calomelanen	Dichloromethane	Aerial parts	Tsui and Brown, (1996)
137	2′-hydroxy-4′,6′-dimethoxy-dihydrochalcone	Dichloromethane	Aerial parts	Tsui and Brown, (1996)
138	2′-hydroxy-4,4′,6′-timethoxy-dihydrochalcone	Dichloromethane	Aerial parts	Tsui and Brown, (1996)
139	3′-(7″-allylphenyl) -2′,4′,4′-trihydroxy-6′- methoxydihydrochalcone	EtOH	Whole plant	Li et al. (2006b)
140	Cilicicone B	MeOH	Whole plant	Zheng et al. (2016)
141	β,2,3′,4,4′,6-Hexahydroxy-α-(α-L-rhamnopyranosyl) dihydrochalcone	MeOH	Whole plant	Zheng et al. (2016)
142	Catechin 3-O-α-L-rhamnopyranoside	EtOH	Whole plant	Li. (2006)
143	Pelargonidin 3-rhamnosylglucoside	/	Fruits	Ishikura. (1971)
144	Cyaniding 3-rhamnosylglucoside	/	Fruits	Ishikura. (1971)
145	Glabraoside A	EtOH	Whole plant	Li et al. (2006b)
146	Glabraoside B	EtOH	Whole plant	Li. (2006)
147	Glabraoside C	EtOH	Whole plant	Wang et al. (2012)
148	Glabraoside D	EtOH	Whole plant	Wang et al. (2012)
	Organic acids			
149	Rosmarinic acid	Aqueous	Whole plant	Huang et al. (2007)
150	Rosmarinic acid-4-O-β-D-glucoside	Aqueous	Whole plant	Li et al. (2010)
151	Methyl rosmarinate	Aqueous	Whole plant	Huang et al. (2007)
152	Ethyl rosmarinate	EtOH	Whole plant	Zhu et al. (2008a)
153	Caffeic acid	Aqueous	Whole plant	Huang et al. (2007)
154	Caffeic acid ethyl ester	EtOH	Whole plant	Li et al. (2012b)
155	Vinyl caffeate	EtOH	Whole plant	Li et al. (2012b)
156	Caffeic acid 3,4-dihydroxyphenethyl ester	EtOH	Whole plant	Lian. (2006)
157	Chlorogenic acid	EtOH	Whole plant	Li et al. (2012b)
158	Neochlorogenic acid	EtOH	Whole plant	Li et al. (2012b)
159	Cryptochlorogenic acid	EtOH	Whole plant	Li et al. (2012b)
160	Methyl 5-O-caffeoylquinilic acid	Aqueous	Whole plant	Huang et al. (2008)
161	3-O-caffeoylshikimic acid	EtOH	Whole plant	Li et al. (2012b)
162	4-O-caffeoylshikimic acid	EtOH	Whole plant	Li et al. (2012b)
163	5-O-caffeoylshikimic acid	EtOH	Whole plant	Li et al. (2012b)
164	Protocatechuic acid	EtOH	Whole plant	Li et al. (2012b)
165	Isovanillic acid	Aqueous	Stems	Duan et al. (2010)
166	Caryophylic acid	Aqueous	Whole plant	Li et al. (2010)
167	Ferulic acid	EtOH	Whole plant	Li. (2006)
168	N-trans-feruloyltyramine	EtOH	Whole plant	Zhu et al. (2008a)
169	Fumarc acid	Aqueous	Whole plant	Wang and Ma, (1979a)
170	Succinic acid	EtOH	Whole plant	Tong et al. (2010)
171	Phthalic acid	EtOH	Whole plant	Tong et al. (2010)
172	Dibutyl phthalate	Aqueous	Whole plant	Huang et al. (2007)
173	P-hydroxybenzoic acid	Aqueous	Whole plant	Li et al. (2010)
174	3,4-dihydroxy benzoic acid	Aqueous	Whole plant	Huang et al. (2007)
175	3-methoxy-4-hydroxybenzoic acid	Aqueous	Whole plant	Li et al. (2010)
176	Methyl 3,4-dihydroxyphenyll actate	Aqueous	Whole plant	Huang et al. (2007)
177	Benzyl 2-β-glucopyranosyloxybenzoate	Acetone	Whole plant	Wu et al. (2012a)
178	Palmitic acid	EtOH	Whole plant	Wang et al. (2007)
179	Stearic acid	EtOH	Whole plant	Zeng and Luo, (2005)
180	N-pentadecanoic acid	EtOH	Whole plant	Wang et al. (2007)
181	N-docosanoic acid	EtOH	Whole plant	Tong et al. (2010)
182	N-heptadecanoic acid	EtOH	Whole plant	Tong et al. (2010)
	Coumarins			
183	Esculetin	EtOH	Whole plant	Xu et al. (2008)
184	Isoscopoletin	EtOH	Whole plant	Wang et al. (2010b)
185	Scopletin	EtOH	Whole plant	Xu et al. (2008)
186	Fraxetin	EtOH	Whole plant	Xu et al. (2008)

(Continued on following page)

TABLE 1 | (*Continued*) Compounds presenting in *S. glabra*.

No	Chemical component	Extract	Part	References
187	Isofraxidin	EtOH	Whole plant	Wang et al. (2007)
188	Scoparone	EtOH	Whole plant	Wang et al. (2007)
189	Fraxidin	Aqueous	Whole plant	Yuan et al. (2008)
190	Scopolin	Acetone	Whole plant	Wu et al. (2012b)
191	Fraxin	EtOH	Whole plant	Xu et al. (2008)
192	Isofraxidin-7-O-β-D-glucopyranoside	Aqueous	Whole plant	Yuan et al. (2008)
193	Eleutheroside B1	EtOH	Whole plant	Luo et al. (2005a)
194	3,3′-biisofraxidin	EtOH	Whole plant	Wang et al. (2007)
195	4,4′-bisofraxidin	EtOH	Whole plant	Xu et al. (2008)
196	Sarcandracourmarin	Aqueous	Whole plant	Feng et al. (2010)
197	Hemidesmin 1	EtOH	Whole plant	Zhu et al. (2008a)
198	3,5-dihydroxycoumarin-7-O-α-L-rhamnopyranoside	EtOH	Whole plant	Wang et al. (2015a)
	Lignans			
199	(-)-(7S,8R)-dihydrodehydrodiconiferyl alcohol	EtOH	Whole plant	Zhu et al. (2008a)
200	(-)-(7S,8R)-dihydrodehydrodiconiferyl alcohol-9-O-α-D-glucopyranoside	Acetone	Whole plant	Wu et al. (2012a)
201	(-)-(7S,8R)-dihydrodehydrodiconiferyl alcohol-9′-O-α-D-glucopyranoside	Acetone	Whole plant	Wu et al. (2012a)
202	(-)-(7S,8R)-dihydrodehydrodiconiferyl alcohol-4-O-α-D -glucopyranoside	Acetone	Whole plant	Wu et al. (2012a)
203	(-)-(7S,8R)-5-Methoxydihydrodehydrodiconiferyl alcohol-4-O-β-D-glucopyranoside	Acetone	Whole plant	Wu et al. (2012a)
204	Syringaresinol monoside	EtOH	Whole plant	Wang et al. (2010b)
205	Styraxiaponoside B	EtOH	Whole plant	Wang et al. (2010b)
	Anthraquinones			
206	Chrysophanol	EtOH	Whole plant	Fu and Liang, (2013)
207	Emodin	EtOH	Whole plant	Yu et al. (2012)
208	Citreorosein	EtOH	Whole plant	Fu and Liang, (2013)
209	Physcion	EtOH	Whole plant	Yu et al. (2012)
210	Emodin-8-O-β-D-glucopyranoside	EtOH	Whole plant	Fu and Liang, (2013)
	Steroids			
211	β-sitosterol	EtOH	Whole plant	Wang et al. (2007)
212	Daucosterol	EtOH	Whole plant	Wang et al. (2007)

records illustrate the safety of *S. glabra* as a medicine from another point of view.

PHYTOCHEMISTRY

Since the 1970s, the chemical constituents of *S. glabra* have gained the interest of the scholars at home and abroad. Up to now, over 200 compounds have been isolated and identified from *S. glabra*, including sesquiterpenes, flavonoids, phenolic acids, coumarins, lignans, anthraquinones, volatile oil, a small quantity of amino acids, trace elements, polysaccharides and proteoglycans. Among them, flavonoids are considered to be the main active components in *S. glabra*. The chemical constituents reported are listed in **Table 1** and their corresponding structures are shown in **Figures 3–7**.

Terpenoids

There are sesquiterpenes (**1–97**), diterpenes (**98–101**) and triterpenes (**102–108**) in *S. glabra*, among them, sesquiterpenes are the most abundant substances, including the characteristic components such as chloranthalactone, chloranoside, sarcandralactone, shizukaol, and sarglabolide. Sesquiterpenes isolated and identified from *S. glabra* have been reported to possess anti-inflammatory, antibacterial and antitumor effects, *etc.* (He et al., 2010; Wang P. et al., 2015, Wang et al., 2016). For instance, chloranthalactone E (**3**), atractylenolide III (**34**) and sarcandrolides A-C (**52–54**) exhibited reportedly antitumor effects (Wang et al., 2007; He et al., 2010), while shizukaol B (**65**), shizukaol G (**69**) and sarglabolide A (**73**) showed anti-inflammatory activities (Wang P. et al., 2015). Sarglaperoxide A (**90**) possessed anti-inflammatory and antibacterial effects, inhibiting 53.6% nitric oxide (NO) production at 25 μM and 64.5% *Staphylococcus aureus* growth at 25 μg/ml (Wang et al., 2016).

Flavonoids

So far, over 40 flavonoids have been found in *S. glabra* (**109–148**). Flavonoids are the main components within *S. glabra*, and now are considered to be the main bioactive components in the treatment of thrombocytopenia. Flavonoids are also often used as important indicators to control the quality of *S. glabra*. Astilbin (**119**), as one of the active components of *S. glabra*, was reported to play an anti-thrombocytopenic role in rat bone marrow megakaryocytes by up-regulating transforming growth factor beta (TGF-β1) content and down-regulating thermoplastic polyolefin (TPO) content, which may be the effective component against thrombocytopenia (Tang et al., 2014). Besides, there were differences in the content of total flavonoids in different parts of *S. glabra*. The content of total flavonoids in leaves reached 3.17%, which was higher than that in roots (2.38%) and stems (2.11%) (Li et al., 2007). The results suggested that the medicinal part could be selected according to the clinical

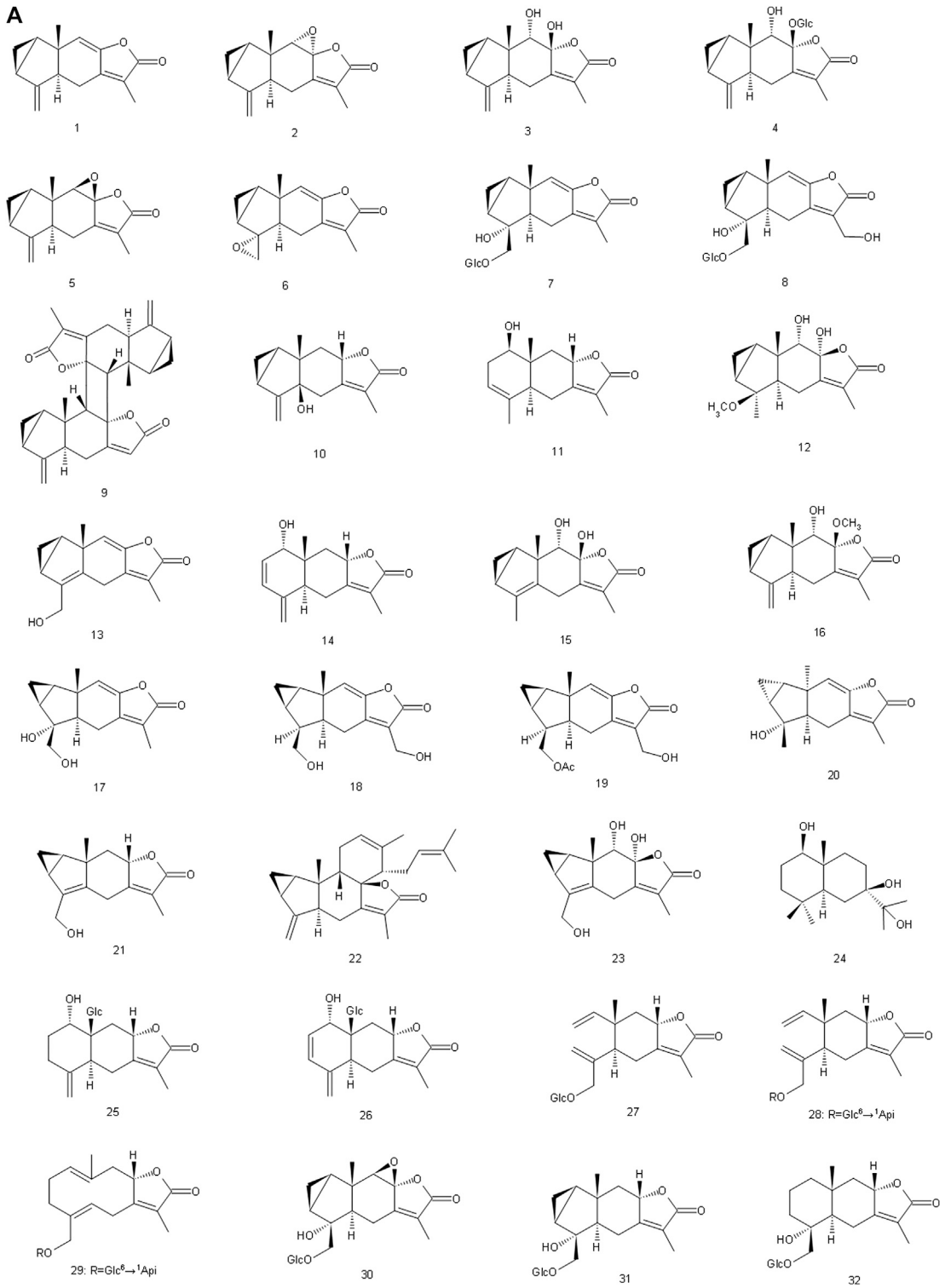

FIGURE 3 | (A) Chemical structures of sesquiterpenes **(A)** identified in *S. glabra* extract. **(B)** Chemical structures of sesquiterpenes **(A)** identified in *S. glabra* extract. **(C)** Chemical structures of sesquiterpenes **(A)** identified in *S. glabra* extract. **(D)** Chemical structures of sesquiterpenes **(A)**, and diterpenes **(B)** identified in *S. glabra* extract. **(E)** Chemical structures of triterpenes **(C)** identified in *S. glabra* extract.

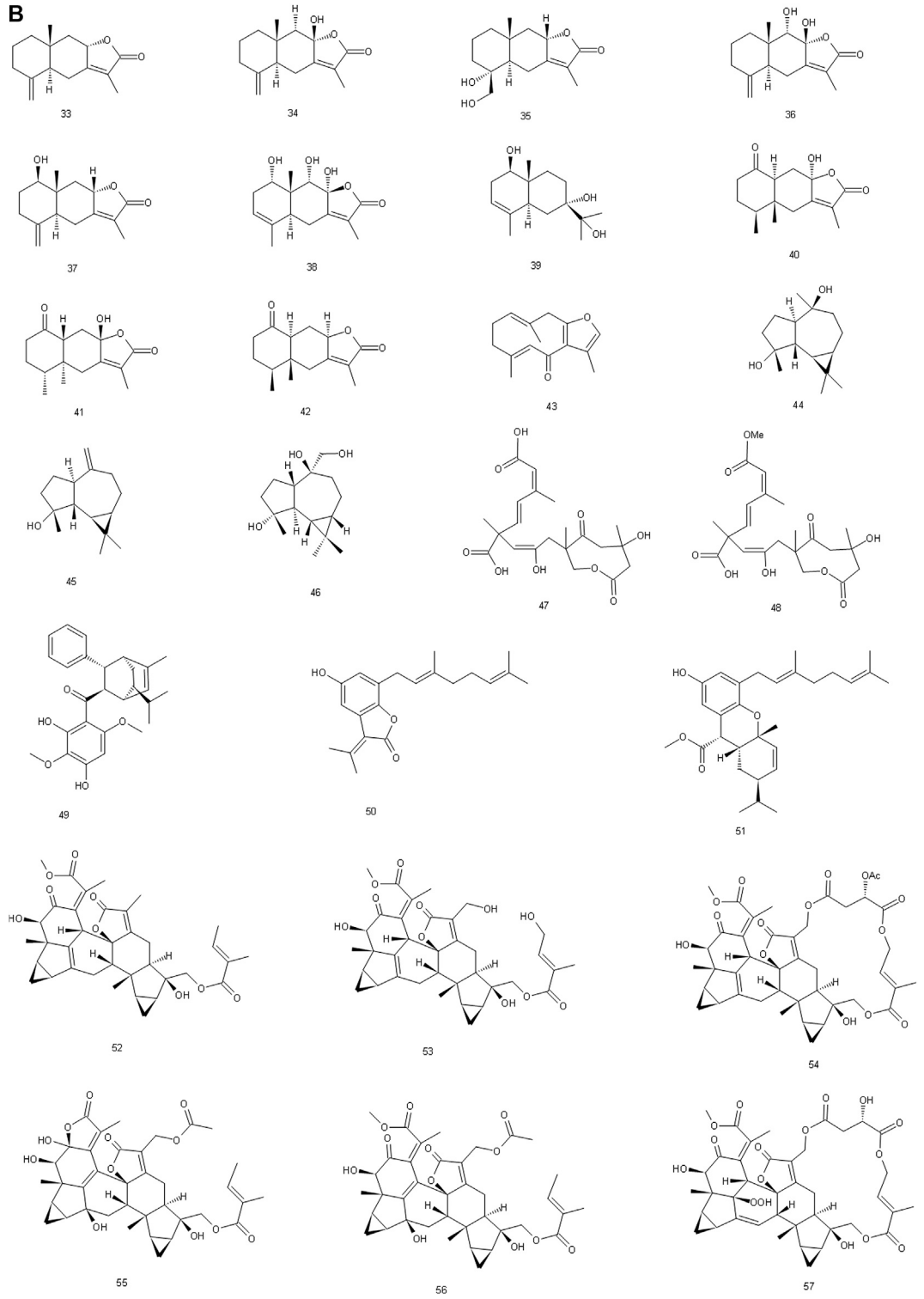

FIGURE 3 | (Continued).

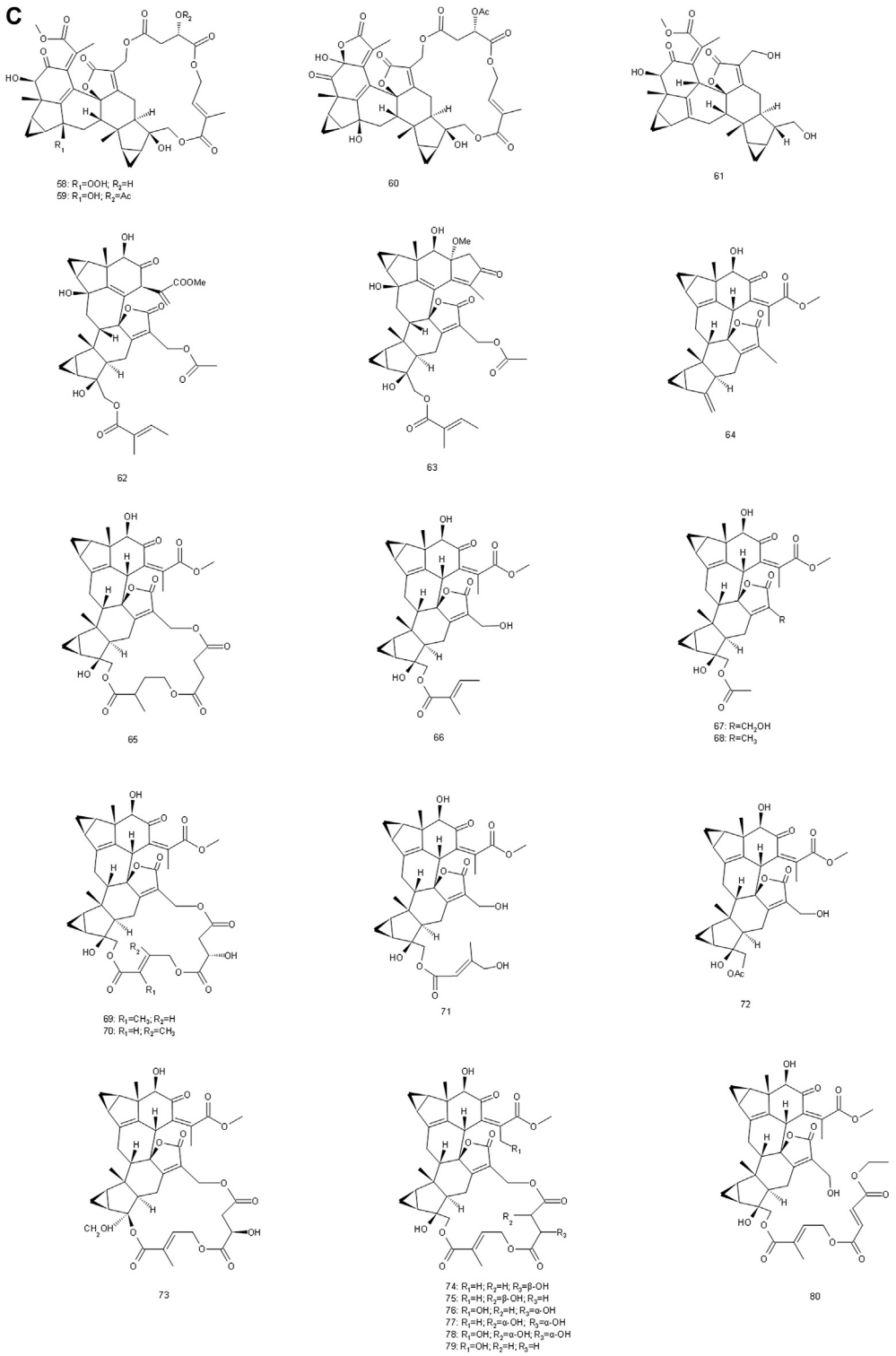

FIGURE 3 | (Continued).

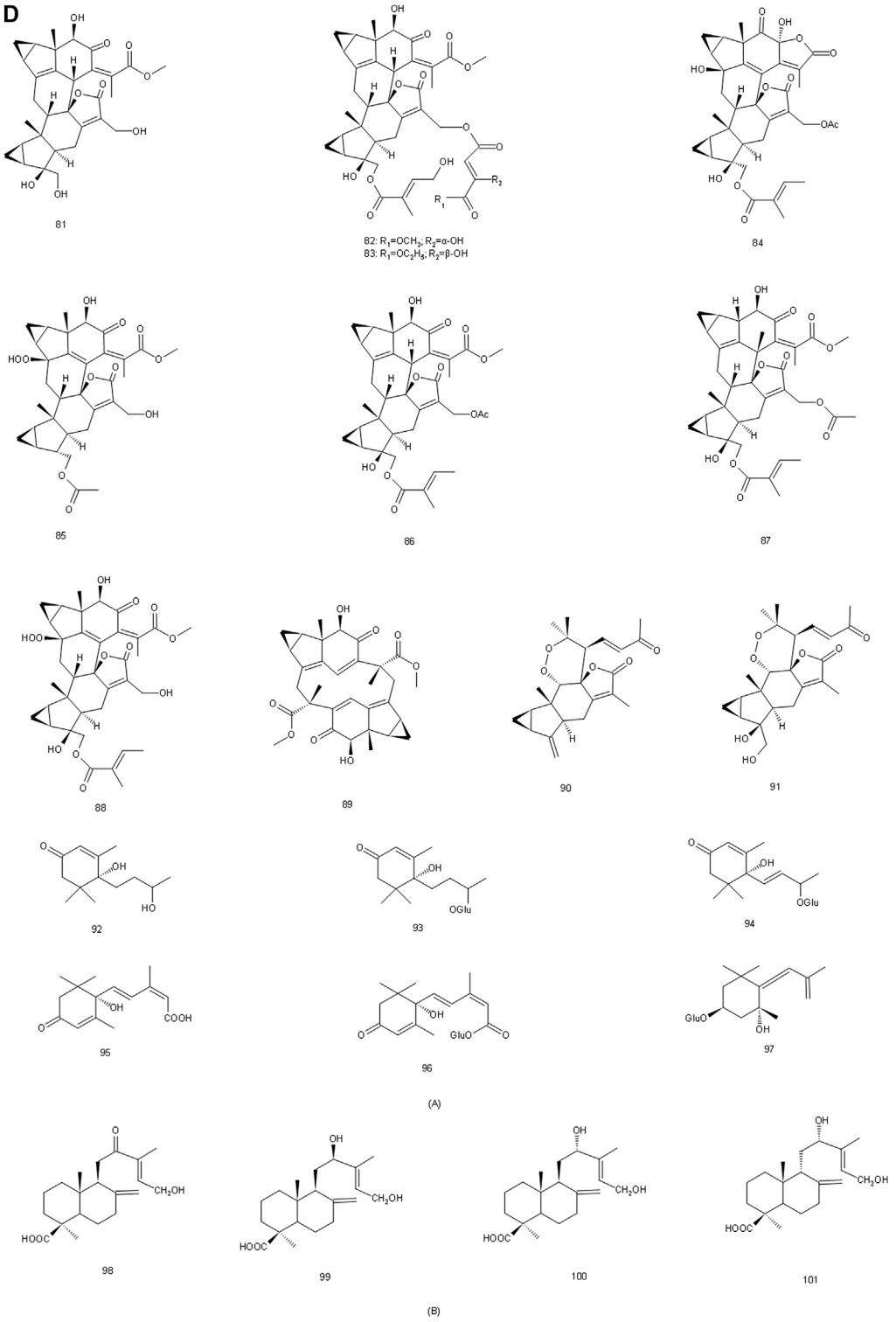

FIGURE 3 | (Continued).

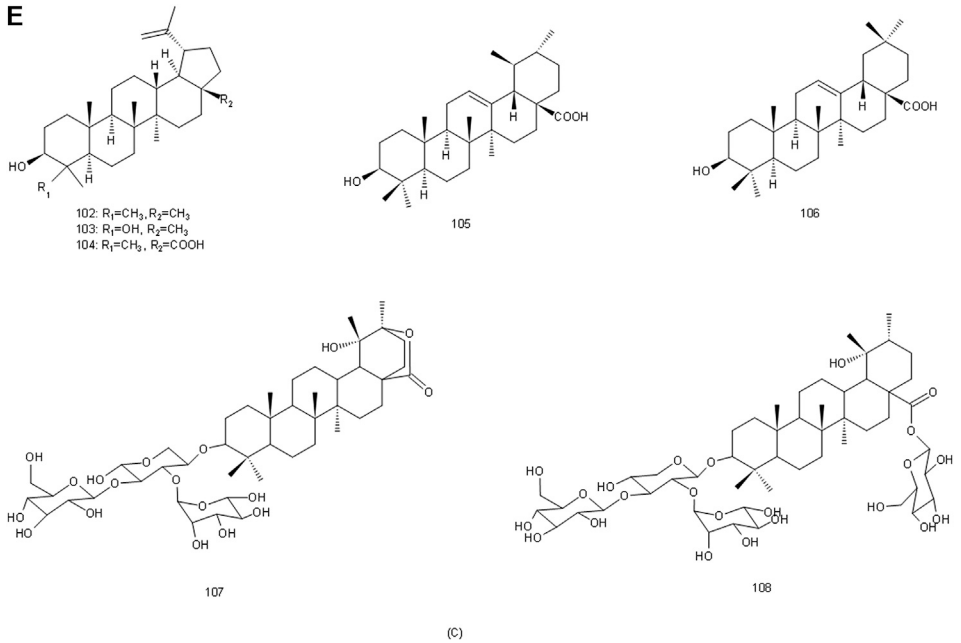

FIGURE 3. | (Continued).

needs, which was beneficial to the sustainable utilization of *S. glabra*.

Organic Acids

At present, more than 20 organic acids have been isolated from *S. glabra* (**149–182**), which can be divided into phenolic acids and fatty acids. Phenolic acids are important components in *S. glabra*, containing rosmarinic acid (**149**), caffeic acid (**153**), chlorogenic acid (**157**), neochlorogenic acid (**158**), cryptochlorogenic acid (**159**), and other components with significant pharmacological activities. They might be the bioactive components of *S. glabra* to exert antibacterial, anti-inflammatory, and antioxidant effects, *etc*. Among them, rosmarinic acid (**149**) possessed various pharmacological effects including anti-inflammatory, antibacterial, antiviral, antioxidant, and anti-tumor effects, its anti-inflammatory and antioxidant effects were particularly significant (Nunes et al., 2017). Rosmarinic acid is also one of the phenolic acids with the highest content within *S. glabra*, serving as a marker in *Chinese pharmacopoeia* for controlling the quality of *S. glabra*.

Coumarins

Currently, more than a dozen coumarins have been isolated from *S. glabra* (**183–198**). As the most representative coumarin with strong pharmacological activity, isofraxidin (**187**) is used as an index for controlling the quality of *S. glabra* and its preparations by *Chinese Pharmacopoeia*. Studies have shown that isofraxidin has a wide range of pharmacological effects (Li et al., 2014; Liu et al., 2015; Jin et al., 2020), including anti-inflammatory, anti-viral, and anti-tumor effects, as well as inhibition of platelet aggregation. Furthermore, 3,3′-biisofraxidin (**194**) had been reported to induce gastric cancer cells apoptosis by activating the mitochondrial-mediated apoptosis pathway (Wu et al., 2015).

Other Compounds

There are lignans (**199–205**), anthraquinones (**206–210**) and steroids (**211–212**) in *S. glabra*. Furthermore, there are abundant volatile components in *S. glabra* (Yang R. et al., 2008), mainly including α-pinene, β-phellandrene, and α-thujene. It also contains 16 kinds of amino acids, such as aspartic acid, glutamic acid, leucine and so on, six kinds of which are essential amino acids for human body, as well as trace elements including iron, zinc, calcium, magnesium and so on (Yang B. et al., 2008). In addition, acidic polysaccharide and proteoglycan are also isolated from *S. glabra* (Liu W. et al., 2017; Sun et al., 2020).

PHARMACOLOGY

Pharmacological studies have indicated that *S. glabra* has a wide range of pharmacological effects, including antibacterial, antiviral, anti-inflammatory, anti-tumor, anti-oxidant, anti-thrombocytopenic effects, *etc*. Pharmacological effects of *S. glabra* and its preparations as well as monomeric compounds were summarized in **Table 2**, which were described in the following sections as well.

Antibacterial

Studies had shown that *S. glabra* possessed a broad spectrum of antibacterial effects, which had inhibitory effects on *Staphylococcus aureus* and its drug resistant bacteria,

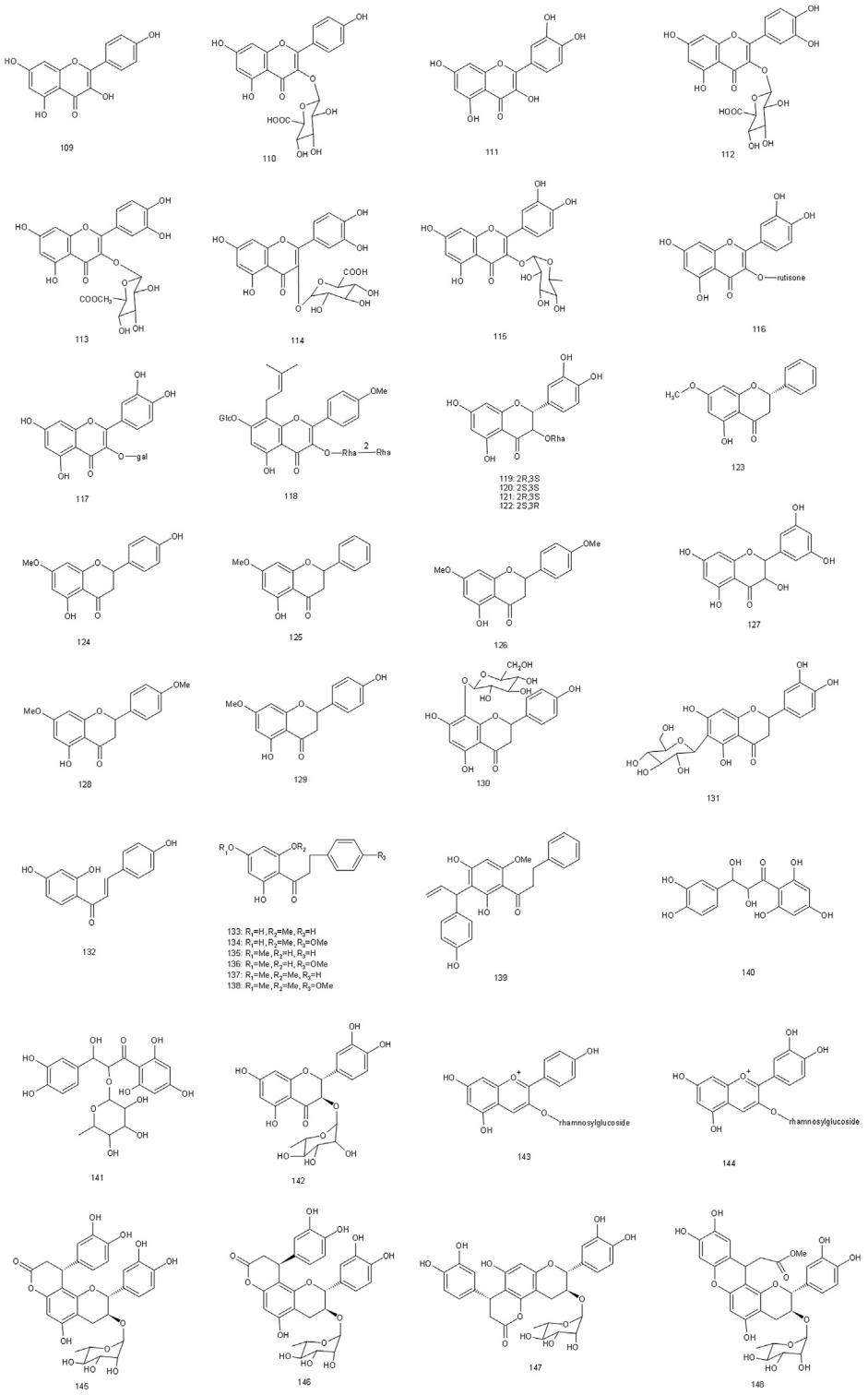

FIGURE 4 | Chemical structures of flavonoids identified in S. glabra extract.

Pseudomonas eruginosa, *Escherichia coli*, *Streptococcus pneumoniae*, *Dysentery bacilli*, *Typhoid* and *Paratyphoid bacilli*, especially on *S. aureus* and *P. aeruginosa*, it showed strong antibacterial activity (Jiang et al., 2000; Wang and Du, 2008). *In vitro* experiment demonstrated that *S. glabra* showed antibacterial effects through inhibiting the growth of

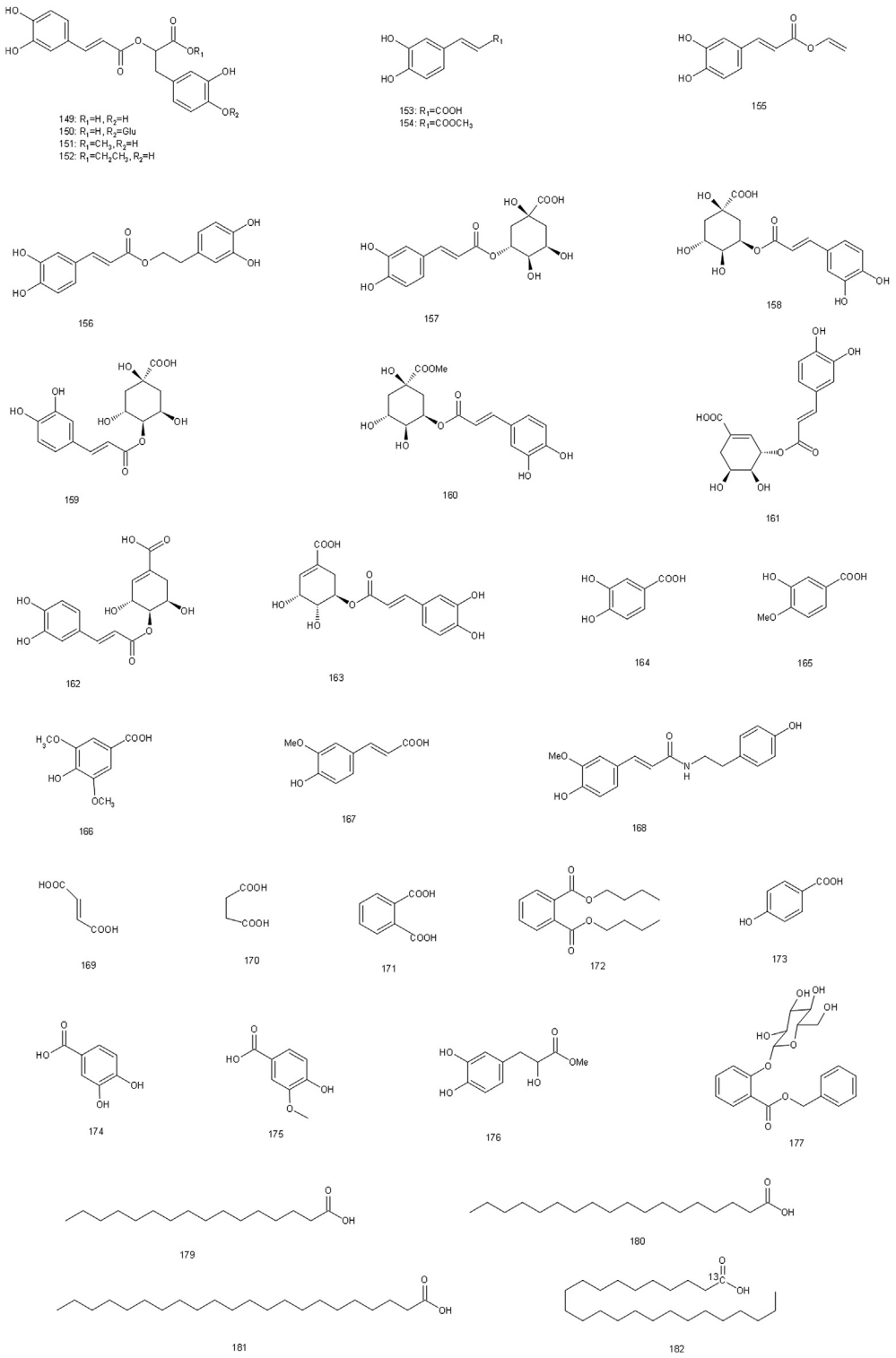

FIGURE 5 | Chemical structures of organic acids identified in S. glabra extract.

Streptococcus mutans along with the activity of its glucosyltransferase (Huang and He, 2001). Besides, the aqueous extract of *S. glabra* could significantly promote the exosmosis of glucose and aspartate amino transferase in *Helicobacter pylori* and its drug-resistant bacteria at the concentration of 95 μg/ml, indicating that its antibacterial

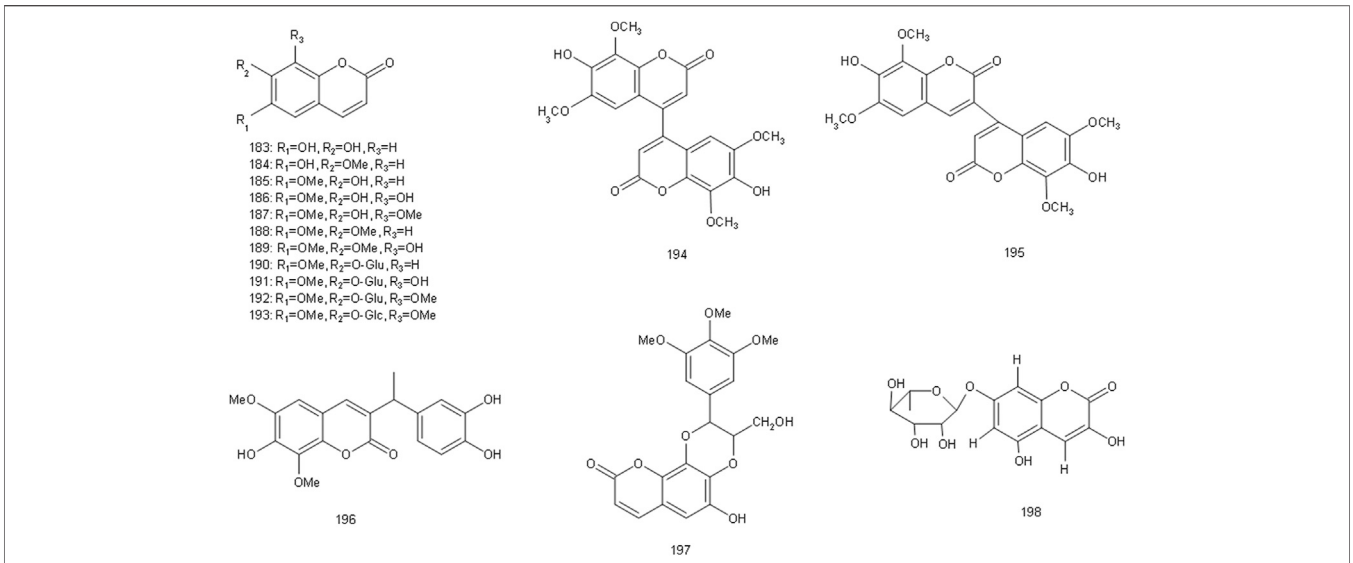

FIGURE 6 | Chemical structures of coumarins identified in S. glabra extract.

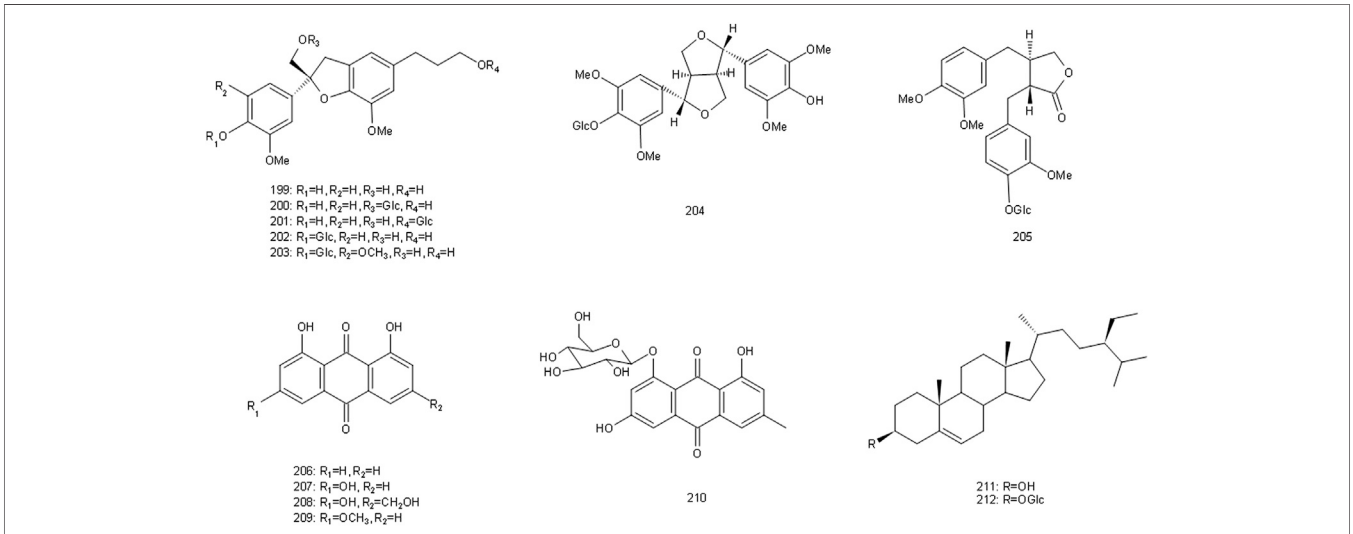

FIGURE 7 | Chemical structures of lignins, anthraquinones and steroids identified in S. glabra extract.

mechanism may be related to the damage of the outer membrane barrier (Guo, 2015). Some phenolic acids, coumarins and flavonoids isolated from the antibacterial fraction of *S. glabra* also showed good antibacterial activity (Wang and Ma, 1979b; Xu et al., 2008; Yuan et al., 2008). Fumaric acid and succinic acid had been proved to have excellent antibacterial effects on *S. aureus* and *P. aeruginosa* (Wang and Ma, 1979b). Isofraxidin (**187**) and 4,4′-bisofraxidin (**195**) showed good antibacterial effects on *Porphyromonas gingivalis* and *Streptococcus transglucosans* respectively, and their corresponding MIC values were 0.078 mg/ml and 0.125 mg/ml (Xu et al., 2008). Also, Kaempferol-3-O-β-D-glucuronide (**110**) exhibited a strong inhibitory effect on *S. aureus*, and its diameter of bacteriostasis circle was 14.67 ± 0.08 mm (Yuan et al., 2008). However, the current pharmacological studies mainly concentrate on *in vitro* models, and lack of discussion on the bioactive components and mechanism of antibacterial effect. Therefore, it is necessary to further evaluate the antibacterial effect and specific mechanism of *S. glabra* on *in vivo* models.

Antiviral

S. glabra extract (250 mg/kg) could reduce the incidence rate and mortality of restraint stress mice caused by H_1N_1 influenza virus *via* reducing the pathological changes and the amount of virus in lung tissue, as well as regulating susceptibility genes and inhibiting the expression of pro-inflammatory factors (Cao

TABLE 2 | Modern Pharmacological studies of *S. glabra*.

Effect	Model	Part of plant/Extracts or compound	Positive control	Formulation/ dosage	Result/mechanism	References
Antibacterial	*Streptococcus mutans*	Ethanol	/	*in vitro*: 3.125, 6.25, 12.5, 25, 50, 100 mg/ml	Inhibiting the bacterial growth and its glucosyltransferase activity	Huang and He. (2001)
	Helicobacter pylori and its drug-resistant bacteria	The whole plant/ Aqueous	/	*in vitro*: 95 μg/ml	Damaging the function of outer membrane barrier	Guo. (2015)
	Streptococcus mutans	Compound **110**	/	*in vitro*: 1.0 mg/ml	Its diameter of bacteriostatic circle was 14.67 ± 0.08 mm	Yuan et al. (2008)
Antiviral	Mice infected with H_1N_1 virus	Ethanol	Ribavirin reduced oxidative stress levels to alleviate lung injury in mice	*in vivo*: 75 mg/kg	Activating Nrf2/HO-1 pathway to regulate SOD, MDA, and NO.	Huo et al. (2020)
	Mice infected with A/FM/1/ 47 H_1N_1 virus	Compound **150**	The high-dose group reduced viral replication in the lungs, and its effect was similar to that of ribavirin (50 mg/kg)	*in vivo*: 20, 50 mg/kg	Reducing pulmonary edema, inflammatory reaction, oxidative damage and viral replication in the lungs	Liu et al. (2017a)
	RNP virus	Compound **193**	/	*in vitro*: 50 μg/ml	Reducing RN mRNA expression	Wang et al. (2017)
Anti-inflammatory	LPS-induced RAW264.7 macrophage	The whole plant/ Ethyl acetate extract and polysaccharide	/	*in vitro*: 100, 200 μg/ml	Inhibiting RAW264.7 cells proliferation and NO expression	Xie et al. (2010)
	LPS-induced RAW264.7 macrophage	Compound **67**	/	*in vitro*: 5, 10, 15, 20 μM	Activating akt mediated Nrf2/ HO-1 pathway and inhibiting NF-κB activation	Wei et al. (2019)
	LPS-induced inflammatory mice	Compound **187**	/	*in vivo*: 1, 5, 15 mg/kg	Down-regulating TNF-α expression by inhibiting NF-κB pathway	Liu et al. (2015)
Anti-tumor	Lung cancer cells A-549, colon cancer cells HCT-29, gastric cancer cells BGC-823	*Zhongjiefeng* injection	/	*in vitro*: 3.125, 6.25, 12.5 25, 50 μg/ml	The IC_{50} values of A-549, HCT-29 and BGC-823 cells were 15.18, 29.21 and 38.58 μg/ml respectively	Zhao et al. (2008)
	Non-small cell lung cancer A549 and H1299	*Zhongjiefeng* tablets	/	*in vitro*: 0.625, 1, 1.25 mg/ml	Up-regulating the TGF-β pathway to induce P21 expression, blocking the cancer cell cycle in the G0/G1 phase	Chen et al. (2018)
	Leukemia cells K562	The whole plant/ Total flavonoids	/	*in vitro*: 25, 50, 100 μg/ml	Down-regulating Bcl-2, Caspase-3 protein expression and up-regulating cleaved Caspase-3 protein expression	Sun et al. (2019)
	Osteosarcoma cells MG-63	The whole plant/ Polysaccharide	/	*in vitro*: 31.25, 62.5, 125 nM	Down-regulating the ERK/ eIF4F/Bcl-XL pathway to promote the release of cytochrome C and activate the caspase protein	Zhang et al. (2014)
	S-180 cell-derived tumor model mice	The whole plant/ Polysaccharide	/	*in vivo*: 25, 50, 100 mg/kg	Inhibition of transplanted tumor growth	Zhang et al. (2014)
Immune regulation	RAW264.7 macrophage cells	The whole plant/ Polysaccharide	/	*in vitro*: 25, 50, 100 mg/l	Increasing CD40, CD14 expression, as well as IL-1β, TNF-α, iNOS and IL-10 mRNA expression, and decreasing CD16/32 expression	Jiang et al. (2014)
	Restrained stress mice	The whole plant/ Aqueous	/	*in vivo*: 125 mg/kg	Improving immune cells proportion and number	He et al. (2009a)
	Restrained stress mice	The whole plant/ Aqueous	/	*in vivo*: 125 mg/kg	Partly through improving the ability of antioxidant to enhance immunity	He et al. (2009b)
Antioxidant	Hydroxy radical	The whole plant/ Aqueous	/	*in vitro*: 0.2, 0.4, 0.6, 1.2 mg/ml	At the concentration of 1.2 mg/ml, its scavenging rate reached 89.89%	Qin et al. (2007)

(Continued on following page)

TABLE 2 | (*Continued*) Modern Pharmacological studies of *S. glabra*.

Effect	Model	Part of plant/Extracts or compound	Positive control	Formulation/ dosage	Result/mechanism	References
	DPPH radical	The whole plant/ Aqueous	Quercetin and lutin half scavenging concentrations were 4.39 mg/L and 7.52 mg/L respectively	*in vitro*: 1, 3, 10, 30, 100 mg/l	Its half scavenging concentration was 13.49 mg/l	Li et al. (2009)
	Hydroxy, superoxide anion, DPPH, and ABTS radicals, and Fe^{2+}	The whole plant/ Polysaccharide	Ascorbic acid (0.5–2.0 mg/ml) showed significant free radical scavenging activity	*in vitro*: 0.5, 1.0, 1.5, 2.0 mg/ml	Scavenging these free radicals effectively and chelating Fe^{2+}	Jin et al. (2012)
	Mesenchymal stem cells	The whole plant/ ethanol, compound **119** and **149**	/	*in vitro*: 10–100 μg/ml, and 20–110 μg/ml	Protecting mesenchymal stem cells from oxidative stress and hydroxy radical mediated DNA damage	Liu et al. (2016)
Anti-thrombocytopenic	Bone marrow stromal cell-Megakaryocyte co-culture system	The whole plant/ Total flavonoids	/	*in vitro*: 1.95, 3.90, 7.80 μg/ml	Increasing the content of TPO, SDF-1 and VCAM-1, and decreasing the content of TGF-β1	Lu et al. (2019)
	Cytarabine-induced thrombocytopenia mice	The whole plant/ Total flavonoids	The activity of prednisolone acetate (10 mg/kg) in promoting TPO and C-mpl expression was weaker than the extract	*in vivo*: 31.5, 63.0, 94.5 mg/kg	Promoting the expression of TPO and its receptor C-mpl	Lu et al. (2018a)
	Cytarabine-induced thrombocytopenia mice	The whole plant/ Total flavonoids	The activity of prednisolone acetate (10 mg/kg) in promoting SDF-1 and CXCR-4 expression was weaker than the extract	*in vivo*: 31.5, 63.0, 94.5 mg/kg	Promoting SDF-1 and its receptor CXCR-4 expression	Lu et al. (2018b)
Hepatoprotec-tive	Dimethylnitrosamine-indued liver injury rat	*Zhongjiefeng* tablets	/	*in vivo*:/	Normalizing the serum protein index, and improving the level of antioxidant index	Jin and Li. (1998)
	p.acnes-LPS-induced immunological hepatitis mice	Extract	The inhibitory effect on ALT activity of cyclosporin a (1 mg/kg) was 85.84%	*in vivo*: 125 mg/kg	Inhibiting ALT activity, and the inhibition rate reached 78.5%	Li et al. (2008)
Hypoglycemic	α-glucosidase	The whole plant/ Polysaccharide	Acarbose (15.63–250 μg/ml) inhibited α-glucosidase activity with a IC_{50} value of 148.3 μg/ml	*in vitro*: 15.63–250 μg/ml	The inhibitory effect of polysaccharide on α-glucosidase (IC_{50} = 49.01 μg/ml) was stronger than that of positive control	Liu et al. (2017b)
	HFD and STZ-induced diabetic mice	The whole plant/ Polysaccharide	Polysaccharide was superior to acarbose (10 mg/kg) and metformin (200 mg/kg) in reducing fasting blood glucose levels and relieve the insulin resistance	*in vivo*: 100, 200 mg/kg	Reducing insulin resistance, improving lipid metabolism, increasing glucose utilization and antioxidant capacity	Liu et al. (2017b)
Hypolipidemic	HFD-induced hyperlipidemic mice	The whole plant/ Total flavonoids	The hypolipidemic effect of the high-dose group was equivalent to that of lovastatin (4.0 mg/d)	*in vivo*: 1.0, 2.0, 4.0 mg/d	Decreasing triglyceride, total cholesterol, and low density lipoprotein	Ji. (2012)

et al., 2012). However, the dose used in this study was too high, and it could be considered to be reduced in future studies. What's more, the ethanol extract of *S. glabra* could reduce pulmonary edema, inhibit viral replication in lung tissue and alleviate oxidative stress level in mice infected with H_1N_1 virus, and its mechanism may be related to activating nuclear factor-erythroid 2-related factor 2 (Nrf-2)/heme oxygenase-1 (HO-1) pathway to regulate superoxide dismutase (SOD), malondialdehyde (MDA) and NO to reduce oxidative stress injury (Huo et al., 2020). In recent years, it has been found that some components from *S. glabra* exhibit antiviral effects (Liu J.-x. et al., 2017; Wang et al., 2017). Rosmarinic acid-4-O-β-D-glucoside (**150**) could reduce the mortality of mice with pneumonia caused by A/FM/1/47 H_1N_1 virus at the concentration of 20 and 50 mg/kg (Liu

J.-x. et al., 2017). Eleutheroside B1 (**193**) could inhibit the influenza virus ribonucleoprotein and the expression of RN mRNA (Wang et al., 2017). These results indicated that *S. glabra* has the potential to be developed as new drugs for the treatment of viral infectious diseases. Thus, in-depth research on active components and mechanism of antiviral activity should be taken into consideration.

Anti-Inflammatory

S. glabra showed significant anti-inflammatory activity, which had a certain degree of inhibitory effect on various inflammation models. *In vitro*, Xie *et al.* confirmed that polysaccharide and ethyl acetate extracts from *S. glabra* could inhibit RAW264.7 cell proliferation and NO expression (Xie et al., 2010). Besides, studies have proved that sesquiterpenes, phenolic compounds and coumarins from *S. glabra* may be the bioactive components of its anti-inflammatory effect (Liu et al., 2015; Tsai et al., 2017; Wei et al., 2019). Wei *et al.* isolated ten sesquiterpenes from the anti-inflammatory fraction of *S. glabra* and found that all of them could inhibit NO production in RAW264.7 cells induced by LPS (Wei et al., 2019). Among them, shizukaol D (**67**: 5, 10, 15, and 20 μM) showed the most significant anti-inflammatory effect with IC_{50} values of 8.13 ± 0.37 μM, and its mechanism may be related to activating protein kinase B (AKT) to regulate Nrf2/HO-1 signaling pathway, thus down-regulating inducible nitric oxide synthase (iNOS) expression, inhibiting phosphorylated nuclear factor kappa B (NF-κB) expression along with nuclear translocation and regulating the activity of oxidation indexes (Wei et al., 2019). Furthermore, isofraxidin (**187**: 1, 5, and 15 mg/kg) had also been proven to improve the survival rate of mice induced by LPS *via* inhibiting the production of pro-inflammatory cytokines such as NF-κB, NO, interleukin-6 (IL-6) along with tumor necrosis factor alpha (TNF-α) and reducing the damage of inflammatory factors to organs. The mechanism may be related to the inhibition of TNF-α expression by regulating NF-κB signaling pathway (Liu et al., 2015). Therefore, *S. glabra* may play its anti-inflammatory effect mainly by regulating the expression of inflammatory factors such as NF-κB, NO, IL-6, TNF-α and the signal pathways related to inflammation, but how to regulate them is not completely clear and needs to be further explored.

Anti-Tumor

S. glabra had been reported to inhibit the growth of gastric cancer, leukemia, liver cancer, lung cancer and other malignant tumors, which played an anti-tumor role by regulating cell cycle and inducing cell apoptosis. *Zhongjiefeng* injection, a Chinese patent medicine made from *S. glabra*, was reported to have a strong cytotoxicity on human lung cancer A-549, colon cancer HCT-29 and gastric cancer BGC-823, with IC_{50} values less than 50 μg/ml (Zhao et al., 2008). *Zhongjiefeng* tablets, made from *S. glabra*, could induce p21 expression by up-regulating TGF-β pathway, and arrested A549 and H1299 cells in G0/G1 phase, thus inducing cell apoptosis and inhibiting cell proliferation (Chen et al., 2018). The total flavonoids extract from *S. glabra* (25, 50 and 100 μg/ml) also showed significant inhibitory effect on leukemic K562 cells, which could promote cell apoptosis by decreasing the expression of Bcl-2 and caspase-3, and increasing expression of Cleaved caspase-3 (Sun et al., 2019). The polysaccharide from *S. glabra* (SGP-2) could inhibit human osteosarcoma cells U2OS proliferation and promote U2OS cells apoptosis at the concentration of 31.25, 62.5, and 125 nM, through down-regulating extracellular regulated protein kinases (ERK)/eIF4F/Bcl-XL signaling pathway to promote the release of cytochromes C and activate caspase protein (Zhang et al., 2014). Moreover, in S-180 cell-derived tumor mice model, it was further confirmed that SGP-2 (25, 50, 100 mg/kg) could inhibit the growth of transplanted tumor and activate endogenous apoptosis pathway through down regulating ERK-eIF4F pathway (Zhang et al., 2014).

Immune Regulation

Jiang *et al.* reported that *S. glabra* could enhance the clearance index of macrophages in mice, but it had no obvious effect on specific humoral immunity, indicating that *S. glabra* mainly acted on the non-specific immunity of the body (Jiang et al., 2001). Meanwhile, *S. glabra* polysaccharide extract played an immune role through promoting the expression of membrane protein-related immune molecules and regulating the expression of pro-inflammatory and anti-inflammatory cytokines in RAW264.7 macrophages (Jiang et al., 2014). Furthermore, *S. glabra* also ameliorated immunodepression caused by stress. In restraint stress model mice, it was found that *S. glabra* extract (125 mg/kg) not only increased the number of lymphocytes, natural killer cells and natural killer T cells, normalized the ratio of T lymphocyte subsets, but also significantly reduced the lipid peroxidation level in spleen cells and increased the activity of oxygen free radicals, which partly through improving the ability of antioxidant to enhance immunity (He R. R. et al., 2009; He R. et al., 2009).

Antioxidant

S. glabra extract exhibited strong free radical scavenging ability. Aqueous extract of *S. glabra* could scavenge hydroxy free radical in a concentration-dependent manner, at the concentration of 1.2 mg/ml, the scavenging rate on hydroxy free radical reached 89.89% (Qin et al., 2007). Aqueous extract of *S. glabra* also had a significant scavenging effect on DPPH radical, with half scavenging concentration of 13.49 mg/l (Li et al., 2009). *S. glabra* polysaccharide had obvious scavenging effect on hydroxy, superoxide anion, DPPH, and ABTS radicals (Jin et al., 2012). The active components of *S. glabra* also had the ability of scavenging free radicals. It was found that phenolic acids isolated from antioxidant active sites, such as rosmarinic acid (**149**), chlorogenic acid (**157**), and cryptochlorogenic acid (**159**), as well as flavonoids, such as quercetin-3-O-α-D-glucuronide (**114**) and neoastibin (**120**), showed antioxidant activity with strong ability of DPPH radical scavenging (Li et al., 2009, Li et al., 2010). In addition, ethanol extract, astilbin (**119**) and rosmarinic acid (**149**) from *S. glabra* had been reported to exhibit significant antioxidant activities, which could directly or indirectly scavenge reactive oxygen species (ROS) to protect mesenchymal stem cells from oxidative stress at the concentration of 10–100 μg/ml and hydroxy free radical mediated DNA damage at the concentration

of 20–110 μg/ml. More importantly, the antioxidant capacity of ethanol extract from *S. glabra* may be related to the presence of total phenolics, especially astilbin and rosmarinic acid (Liu et al., 2016). These studies implied that *S. glabra* had the potential to treat a variety of diseases associated with oxidative stress. But, the current studies on antioxidant activity mainly focus on *in vitro* models, and a variety of *in vivo* models should be established to further evaluate its antioxidant activities, and to explore the relevant targets and pathways.

Anti-Thrombocytopenic

Nowadays, *S. glabra* is commonly used to treat hemorrhagic diseases caused by thrombocytopenia, and its extract has been made into a Chinese patent medicine in China that are used to increase the platelets. Experimental studies had shown that *S. glabra* extract and its single drug preparation--*Xuekang* oral liquid could increase the number of peripheral blood platelets in mice with immune thrombocytopenic purpura, and the experimental results also showed that the total flavonoids from *S. glabra* (TFSG) was better than positive control (prednisone) in increasing the platelets (Xu et al., 2005). Besides, in bone marrow stromal cells-megakaryocyte co-culture system, TFSG (1.95, 3.9, and 7.8 μg/ml) promoted the differentiation and maturation of megakaryocytes in the co-culture system, which may be related to decreasing the rate of stromal cell apoptosis, regulating the content of cytokines that promote megakaryocyte differentiation including TPO, stromal cell derived factor-1 (SDF-1), TGF-β1, and vascular cell adhesion molecule-1 (VCAM-1), thereby affecting the state of stromal cells and secretion function. And the experimental results also suggested that this may be one of the mechanisms of *S. glabra* in the treatment of immune thrombocytopenia (Lu et al., 2019).

At present, most chemotherapeutic drugs can cause bone marrow suppression and lead to thrombocytopenia, *S. glabra* can significantly resist these side effects. Studies had shown that *S. glabra* significantly improved thrombocytopenia induced by 5-FU (Zhong et al., 2005). Based on this, Lu *et al.* established thrombocytopenia mice to explore the mechanism of TFSG on improving thrombocytopenia induced by chemotherapy (Lu et al., 2018a). The results demonstrated that TFSG (31.5, 63, and 94.5 mg/kg) could promote the secretion of TPO from stromal cells in the bone marrow microenvironment and the corresponding receptor C-mpl expression in megakaryocytes, then promote megakaryocyte to release mature platelets by regulating the TPO-C-mpl pathway. In addition, TFSG (31.5, 63, and 94.5 mg/kg) could also promote the proliferation, differentiation and maturation of megakaryocytes by promoting SDF-1 in bone marrow and the corresponding receptor CXCR-4 expression in megakaryocytes, thereby accelerating megakaryocyte to produce platelets (Lu et al., 2018b). These experimental results indicate that TFSG can promote megakaryocyte proliferation through multiple pathways and multiple targets, thereby increasing the number of platelets, but how does the TFSG promote the secretion of TPO or SDF-1 from stromal cells in the bone marrow microenvironment and regulate their corresponding receptors in megakaryocytes are still unclear, and further studies are needed to clarify.

Hepatoprotective

S. glabra had significant protective effects on various liver injury models. In rat with liver injury induced by dimethylnitrosamine, *S. glabra* could significantly improve the pathological changes of liver tissue, and it not only normalized the serum protein index, but also enhanced the level of antioxidant index (Jin and Li, 1998). In mice with liver injury caused by P. acnes-LPS, the plasma alanine aminotransferase (ALT) activity increased, however, *S. glabra* extract could significantly reduce this trend, and the inhibition rate of high dose of the extract was up to 78.5% (Li et al., 2008). Meanwhile, 70% ethanol extract of *S. glabra* and seven sesquiterpenes from the extract showed significant hepatoprotective activity in hepatic epithelial stem cells from WB-F344 rats induced by D-galactosamine, among them, chloranoside A (**7**) and sarcaglaboside A-C (**25–27**) showed stronger liver protection activity than the positive drug dicyclool (Li et al., 2006a). Besides, *S. glabra* also had a good inhibitory effect on liver fibrosis. It was found that *S. glabra* extract reduced the serum liver function indexes (ALT and aspartate aminotransferase (AST)), liver fibrosis indexes (hyaluronic acid (HA), procollagen type III (PC-III), procollagen type IV (C-IV) and laminin (LN)) and tissue inhibitor of metalloproteinase-1 (TIMP-1) in rats with hepatic fibrosis induced by CCl_4, as well as increasing the level of albumin (ALB). In particular, it could reduce the content of TIMP-1 to the normal level, and the related research indicated that the decrease of TIMP-1 expression contributed to the degradation of liver fibrosis, so its mechanism may be related to decreasing the expression of TIMP-1 (Xiong et al., 2015).

Hypolipidemic and Hypoglycemic

In vitro and *in vivo* experiments, the polysaccharide from *S. glabra* showed excellent hypoglycemic effect. *In vitro*, the inhibitory effect of *S. glabra* polysaccharide (SEPR1) on α-glucosidase (IC_{50} = 49.01 μg/ml) was significantly stronger than that of acarbose (IC_{50} = 148.3 μg/ml). While in diabetic mice induced by HFD/STZ, SEPR1 (100 and 200 mg/kg) showed hypoglycemic effect by reducing fasting blood glucose levels and relieving the insulin resistance, which was better than that of positive control Acarbose (10 mg/kg) and Metformin (200 mg/kg). And the experimental results also indicated that SERP1 could increase the activity of antioxidant enzymes and decrease MDA level (Liu W. et al., 2017). In addition, total flavonoids from *S. glabra* reduced the levels of triglyceride (TG), total cholesterol (TC) and low-density lipoprotein (LDL-C) in serum of mice with hyperlipidemia, and the hypolipidemic effect of the high-dose total flavonoids was similar to that of positive control (Ji, 2012).

Others

S. glabra also exhibited other pharmacological effects. Aqueous extract, ethanol extract, and essential oil from *S. glabra* could shorten the healing time of experimental fracture in rabbits, among which aqueous extract had the most significant effect

in promoting fracture healing (Shi et al., 1980). This pharmacological study was consistent with the traditional use of *S. glabra* in the treatment of fractures, but the specific mechanism and effective components were still unclear. In addition, *S. glabra* had a protective effect on sport-injured skeletal muscle cells. In exercise-induced injury rats, it could be observed that the levels of SOD, catalase (CAT) and total antioxidant capacity (T-AOC) in the skeletal muscle and tissues of the rats decreased, the levels of MDA, creatine kinase (CK) and lactate dehydrogenase (LDH) increased, meanwhile, related inflammatory factors such as TNF-α, interleukin-18 (IL-18) and IL-1β levels increased. After the intervention of *S. glabra* polysaccharide, these indexes were significantly improved, suggesting that *S. glabra* polysaccharide could promote the repair and remodeling process of skeletal muscle structure after injury (Liu, 2015; Wang et al., 2020).

TOXICITY

From the long-term medicinal and edible history, it can be found that *S. glabra* is a kind of medicine food homology herb with good safety. Zhang *et al.* indicated that the maximum tolerance dose of aqueous extract of *S. glabra* in mice was more than 20 g kg^{-1}·bw, without obvious genetic toxic effect, and there was no pathological damage in rats fed with the extract for 90 days at a dosage of 1.67, 3.33, and 5 g kg^{-1}·bw (Zhang et al., 2016). These results were consistent with the findings of Xia *et al.* Xia et al. (1996) and Sun *et al.* Sun et al. (1998). In their studies, the results of the acute toxicity test, genetic toxicity test and teratogenicity test of aqueous extract of *S. glabra* were negative, suggesting that *S. glabra* had almost no obvious toxicity. However, these studies have only evaluated the toxicology of aqueous extract of *S. glabra*, and have not yet systematically evaluated the toxicology of its ethanol extract or other extracts. Therefore, future toxicological studies need more abundant experimental models, multiple types of *S. glabra* extracts or its active ingredients for further evaluation.

DISCUSSION AND PROSPECT

As a traditional Chinese medicine, *S. glabra* has a long history of medicinal use and definite clinical curative effect. It is traditionally used to treat many diseases, including joint swelling and pain, sore throat, carbuncle, traumatic fracture, tumor, bleeding, *etc*. Because of its significant pharmacological effects, such as antibacterial, antiviral, anti-inflammatory, anti-tumor and anti-thrombocytopenic effects that are found in modern studies, *S. glabra* has attracted extensive attention. After decades of efforts by scholars, research on *S. glabra* has achieved certain results on chemical constituents and pharmacological effects. However, there is still a lot of work needs to be further explored. The future research of *S. glabra* can be considered from the following aspects:

Firstly, *S. glabra* has used as a folk medicine in China for more than 300 years, and a great quantity of folk empirical prescriptions with remarkable therapeutic effect also have appeared. Among them, the production technology of Miao nationality using *S. glabra* to treat traumatic fracture has been included in the list of National Intangible Cultural Heritage Protection. Nevertheless, research on the relationship between the traditional efficacy and its modern pharmacological activity has not yet been thoroughly investigated. Therefore, we should look for the potential pharmacological effects of *S. glabra* on the basis of its traditional application. For instance, "*Fen Lei Cao Yao Xing*", an herbal medicine book written in the Qing Dynasty (AD 1906), recorded that *S. glabra* was used to treat rheumatic numbness, arthralgia and myalgia. Nevertheless, there is currently a lack of modern pharmacological studies of *S. glabra* on rheumatic arthritis. *S. glabra* has the effect of clearing heat and detoxification, which has a good reputation as "natural antibiotics" in folk, and is often used to treat infective inflammation caused by bacteria and virus in clinic, showing remarkable therapeutic effects. Modern pharmacological research has found that *S. glabra* possesses significant antibacterial, antiviral, and anti-inflammatory effects, which scientifically explains its heat-clearing and detoxifying effects. However, studies on antibacterial, antiviral, and anti-inflammatory effects of *S. glabra* are still in its infancy. Thus, more experiments are urgently needed to clarify its bioactive components and mechanism of action, in order to further establish the correlation between the traditional application and the modern pharmacological activity of *S. glabra*.

Secondly, more than 200 chemical constituents have been isolated from *S. glabra*, such as sesquiterpenes, flavonoids, phenolic acids, coumarins, lignans, anthraquinones, *etc*. However, related research on the pharmacological effects and targets of these components are still insufficient. There are relatively more studies on isofraxidin and rosmarinic acid, which have been used as markers to control the quality of *S. glabra*, but they are not only the characteristic chemical components in *S. glabra* (Alagawany et al., 2017; Majnooni et al., 2020), and whether they are the main active components of *S. glabra* remains to be confirmed. Therefore, the chemical constituents of *S. glabra* need to be further excavated in order to find more potentially active and specific compounds.

Thirdly, *S. glabra* has a good inhibitory effect on leukemia, gastric cancer, liver cancer and other malignant tumors. Ji *et al.* reviewed that *S. glabra* mainly played an anti-tumor role by inhibiting proliferation, inducing apoptosis, inhibiting telomerase activity and improving immune function (Ji et al., 2016). However, the active components, related targets and signaling pathways of its antitumor effects are still unclear. This suggests that the active components of antitumor effect may be polysaccharide, flavonoids, rosmarinic acid, isofraxidin, 3,3′-biisofraxidin, as well as atractylenolide Ⅲ, and the mechanism may be related to regulating ERK-eIF4F signaling pathway, along with apoptosis-related protein including Bcl-2, Bax and caspase-3. Nevertheless, the anti-tumor research on *S. glabra* is not comprehensive enough, its effective anti-tumor components and related mechanism still need to be further studied in the future.

Finally, *S. glabra* possesses an excellent anti-thrombocytopenic effect. In 2013, Dong *et al.* summarized the

research advance of *S. glabra* on thrombocytopenia diseases, and found that the effective part of *S. glabra* against thrombocytopenia was total flavonoids, which could promote megakaryocytes proliferation to increase the platelets (Dong et al., 2013). However, how *S. glabra* regulated megakaryocytes proliferation was not discussed in their review. In this paper, we summarized the mechanism of *S. glabra* against thrombocytopenia, and found that total flavonoids of *S. glabra* could promote megakaryocytes proliferation through regulating the content of cytokines promoted megakaryocyte differentiation including TPO, SDF-1, TGF-β1 along with VCAM-1 and promoting the expression of SDF-1 and TPO in bone marrow microenvironment as well as their corresponding receptors CXCR-4 and C-mpl in megakaryocytes. Furthermore, *Xuekang* oral liquid, a single plant-based drug extracted from *S. glabra*, has a remarkable curative effect on primary and secondary thrombocytopenic purpura, thrombocytopenia caused by chemotherapy and radiotherapy, without side effects, which is a unique Chinese patent medicine for increasing the platelets in China (Xu et al., 1997; Shi, 2009). At present, research on *Xuekang* oral liquid mainly focuses on clinical trials, and there are few studies on its active components and mechanism. In addition, isofraxidin rather than flavonoids is stipulated as a marker by *Chinese Pharmacopoeia* to control the quality of *Xuekang* oral liquid, thus, the components of anti-thrombocytopenic effect still need to be further studied.

In summary, *S. glabra* with a long history and widely distributed resources, has been widely used for anti-bacterial, anti-viral, anti-inflammatory, anti-tumor, and anti-thrombocytopenia in clinic. *S. glabra* as an excellent traditional medicine for the sufficient experience in traditional medicine as well as remarkable curative effect, is also a kind of medicine and food homologous plant with great development potential, which is worthy of in-depth research and exploration in the field of medicine.

AUTHOR CONTRIBUTIONS

SJ and XQ conceived the original idea. YZ wrote the manuscript with help from JL and XQ. QZ gave some suggestions. ZL and GS provided the professional guidance and the financial support. All authors read and approved the final manuscript.

FUNDING

This work was funded by the construction project of Inheritance Studio for National Famous Chinese Medicine Specialists (Grant No. 003111001025) and Sichuan Science and Technology Department Project (Grant No. 2019YFS0412).

REFERENCES

Alagawany, M., Abd El-Hack, M. E., Farag, M. R., Gopi, M., Karthik, K., Malik, Y. S., et al. (2017). Rosmarinic Acid: Modes of Action, Medicinal Values and Health Benefits. *Anim. Health Res. Rev.* 18, 167–176. doi:10.1017/s1466252317000081

Cao, H.-J., Tan, R.-R., He, R.-R., Tang, L.-P., Wang, X.-L., Yao, N., et al. (2012). *Sarcandra glabra* Extract Reduces the Susceptibility and Severity of Influenza in Restraint-Stressed Mice. *Evidence-Based Complement. Altern. Med.* 2012, 1. doi:10.1155/2012/236539

Chen, C., and Li, S. (2015). Herbal Textual Research on *Sarcandra glabra*. *J. Chin. Med. Mater.* 38, 2628–2631. doi:10.13863/j.issn1001-4454.2015.12.043

Chen, H., Chen, P., Bao, Y., and Ao, J. (2012). Treatment of Varioliform Gastritis with Zhongjiefeng Capsule. *Chin. J. Integr. Tradit. West. Med. Dig.* 20, 519–520.

Chen, H., and Cheng, Y. (1994). The Origin, Differentiation and Geography of Chrolanthaceae. *J. Trop. Subtrop. Bot.* 2, 31–44.

Chen, Y., Xie, Q., Li, Z., and Wu, Z. (2018). Study on the Influence of Zhongjiefeng Dispersible Tablet on the Proliferation of Non-small Cell Lung Cancer and its Molecular Mechanism. *J. Qiqihar Med. Univ.* 39, 2626–2630.

Cheng, Y. (1982). *Flora Reipublicae Popularis Sinicae*. Beijing: Science Press.

Cong, S., Bi, W., and Jiang, L. (2005). Zhongjiefeng Injection Combined with Chemotherapy in the Treatment of Advanced Non-small Cell Lung Cancer. *Chin. J. Cancer Prev. Treat.* 12, 156.

Dong, W., Xu, G., Zhang, Q., Shang, G., Li, B., and Tang, X. (2013). Pharmacological Effects of Sarcand Glabra and its Application in Thrombocytopenia. *Pharmacol. Clin. Chin. Mater. Med.* 29, 176–178.

Duan, Y., Dai, Y., Gao, H., Ye, W., and Yao, X. (2010). Chemical Constituents of *Sarcandra glabra*. *Chin. Tradit. Herb. Drugs* 41, 29–32.

Feng, S., Xu, L., Wu, M., Hao, J., Qiu, S. X., and Wei, X. (2010). A New Coumarin from *Sarcandra glabra*. *Fitoterapia* 81, 472–474. doi:10.1016/j.fitote.2009.12.009

Fu, J., and Liang, J. (2013). Studies on the Chemical Constituents of *Sarcandra glabra*. *Strait Pharm. J.* 25, 46–50.

Guo, M. (2015). The Efficacy of Sarcandra glabra Extract Alone or Combined with Antibiotics against *helicobacter Pylori* in vitro. Master's Thesis. (China): Nanchang University.

Han, B., Peng, Y., and Xiao, P. (2013). Systematic Research on Chinese Non-camellia Tea. *Mod. Chin. Med.* 15, 259–269.

Han, Q., and Wu, X. (2017). Advances on Chemical Constituents and Pharmacological Activities of *Sarcandra glabra*. *Agriculture of Jilin*, 63–64.

He, R., Wang, M., Li, Y., Dai, Y., Duan, Y., Yao, X., et al. (2009). [Effects of *Sarcandra glabra* Extract on Immune Activity in Restraint Stress Mice]. *Zhongguo Zhong Yao Za Zhi* 34, 100–103.

He, R. R., Yao, X. S., Li, H. Y., Dai, Y., Duan, Y. H., Li, Y. F., et al. (2009). The Anti-stress Effects of *Sarcandra glabra* Extract on Restraint-Evoked Immunocompromise. *Biol. Pharm. Bull.* 32, 247–252. doi:10.1248/bpb.32.247

He, W., Dong, F., Li, A., and Wang, S. (2003). Comparison of Curative Effect between *Sarcandra glabra* and Ribavirin in Treating Children Viral Pneumonia. *Mod. J. Integr. Tradit. Chin. West. Med.* 12, 605.

He, X.-F., Yin, S., Ji, Y.-C., Su, Z.-S., Geng, M.-Y., and Yue, J.-M. (2010). Sesquiterpenes and Dimeric Sesquiterpenoids from *Sarcandra glabra*. *J. Nat. Prod.* 73, 45–50. doi:10.1021/np9006469

Hu, X.-R., Wu, H.-F., Zhang, X.-P., Yang, J.-S., Dai, Z., Lin, R.-C., et al. (2013). A New Sesquiterpene Lactone from *Sarcandra glabra*. *Nat. Product. Res.* 27, 1197–1201. doi:10.1080/14786419.2012.722084

Hu, X.-r., Yang, J.-s., and Xu, X.-d. (2009). Three Novel Sesquiterpene Glycosides of *Sarcandra glabra*. *Chem. Pharm. Bull.* 57, 418–420. doi:10.1248/cpb.57.418

Huang, F., and He, H. (2001). Effect of Sarcandra on Cariogenicity of *streptococcus Mutans* on Vitro. *Med. J. Chin. Civ. Adm.* 13, 201–203.

Huang, M. J., Zeng, G. Y., Tan, J. B., Li, Y. L., Tan, G. S., and Zhou, Y. J. (2008). [Studies on Flavonoid Glycosides of *Sarcandra glabra*]. *Zhongguo Zhong Yao Za Zhi* 33, 1700–1702.

Huang, M., Li, Y., Zeng, G., Yuan, W., Tan, J., Tan, G., et al. (2007). Chemical Constituents of *Sarcandra glabra*. *Cent. South. Pharm.* 5, 459–461.

Huo, Y., Zhang, Y., An, M., Li, X., Lai, X., Liu, X., et al. (2020). Effects of Different Parts of *Sarcandra glabra* Extract on Oxidative Stress in Mice with Viral Lung Injury. *J. Chin. Med. Mater.* 43, 2555–2559.

Ishikura, N. (1971). Pelargonidin Glycosides in Fruits. *Experientia* 27, 1006. doi:10.1007/bf02138844

Ji, N. (2012). Effects of Total Flavonoids of *Sarcandrae glabra* on Mouse Blood-Fat Content. *J. Mt. Agric. Biol.* 31, 268–270.

Ji, Y., Zhu, X., and Wu, J. (2016). The Progress in the Antitumor Effect and Mechanism of Zhongjiefeng (*Sarcandra glabra*). *Guid. J. Tradit. Chin. Med. Pharmacol.* 22, 44–46.55

Jia, M., and Li, X. (2005). *Zhong Guo Min Zu Yao Zhi Yao*. Beijing: China Medical Science Press.

Jiang, A., and Zhou, H. (2003). Clinical Observation of Xuekang Capsules on Thrombocytopenic Purpura in 52 Cases. *Pract. Clin. J. Integr. Tradit. Chin. West. Med.* 3, 43–44.

Jiang, W., Kong, X., Huang, R., Lin, J., and Dai, M. (2000). Studies on Anti-inflammatory and Antibacterial Effects of Tabellae Sarcandrae. *J. Guangxi Univ. Chin. Med.* 17, 50–52.

Jiang, W., Kong, X., Liang, G., Huang, Z., Chen, J., and Huang, R. (2001). Effects of Tabellae Sarcandrae on Malignant Tumour and Immunity. *J. Guangxi Med. Univ.* 18, 39–41.

Jiang, Z., Chen, Z., Li, X., Zhao, J., Li, S., Hu, J., et al. (2014). Immunomodulatory Effects of *Sarcandra glabra* Polysaccharides on Macrophage RAW264.7. *Chin. J. Exp. Tradit. Med. Formulae* 20, 178–182.

Jin, L., Guan, X., Liu, W., Zhang, X., Yan, W., Yao, W., et al. (2012). Characterization and Antioxidant Activity of a Polysaccharide Extracted from *Sarcandra glabra*. *Carbohydr. Polym.* 90, 524–532. doi:10.1016/j.carbpol.2012.05.074

Jin, L., Ying, Z.-H., Yu, C.-H., Zhang, H.-H., Yu, W.-Y., and Wu, X.-N. (2020). Isofraxidin Ameliorated Influenza Viral Inflammation in Rodents *via* Inhibiting Platelet Aggregation. *Int. Immunopharmacology* 84, 106521. doi:10.1016/j.intimp.2020.106521

Jin, S., and Li, Z. (1998). Experimental Study on Intervention Effect of *Sarcandra glabra* on Rats with Liver Injury Induced by Dimethylnitrosamine. *Shanghai J. Tradit. Chin. Med.*, 43–45.

Li, B., Huang, M., Li, Y., Zeng, G., Tan, J., and Zhou, Y. (2009). Antioxidant Constituents of *Sarcandra glabra* (Thunb.)Nakai. J. Shenyang Pharm. Univ. 26, 900–903.

Li, H., He, R., Liang, T., Ye, W., Yao, X., and Kurihara, H. (2008). Effect of *Sarcandra glabra* (Thunb.) Nakai Extract on Mice Model of Immunological Hepatitis and Acute Inflammation. *Chin. Pharmacol. Bull.* 24, 244–250.

Li, L. (2004). Treatment of 53 Cases of Acute Viral Myocarditis with Zhongjiefeng Injection. *Tradit. Chin. Med. Res.* 17, 48–49.

Li, N., Yang, R., Wang, B., and Zhang, X. (2007). Determination of Total Flavonoids in Different Parts of *Sarcandra glabra*. *Chongqing J. Res. Chin. Drugs Herbs* 16, 16–17.

Li, P., Zhao, Q.-L., Wu, L.-H., Jawaid, P., Jiao, Y.-F., Kadowaki, M., et al. (2014). Isofraxidin, a Potent Reactive Oxygen Species (ROS) Scavenger, Protects Human Leukemia Cells from Radiation-Induced Apoptosis *via* ROS/mitochondria Pathway in P53-independent Manner. *Apoptosis* 19, 1043–1053. doi:10.1007/s10495-014-0984-1

Li, W. (2003). Clinical Observation on 120 Cases of Acute Upper Respiratory Tract Infection in Children Treated with Zhongjiefeng Injection. *Med. J. Liaoning* 17, 186.

Li, X., Zhang, Y. F., Yang, L., Feng, Y., Liu, Y. M., and Zeng, X. (2011). [Sesquiterpenoids from the Whole Plant of *Sarcandra glabra*]. *Yao Xue Xue Bao* 46, 1349–1351. doi:10.16438/j.0513-4870.2011.11.003

Li, X., Huang, M., Li, Y., Zeng, G., Tan, J., Liang, J., et al. (2010). Study on Antioxidant Constituents from *Sarcandra glabra* (Thunb.) Nakai. *Chin. J. Med. Chem.* 20, 57–60.

Li, X., Zhang, Y.-F., Zeng, X., Liu, Y.-M., and Feng, Y. (2012a). Two New-Skeleton Compounds from *Sarcandra glabra*. *Hca* 95, 998–1002. doi:10.1002/hlca.201100352

Li, X., Zhang, Y., Yang, L., Yi, Feng., Liu, Y., and Zeng, X. (2012b). Studies of Phenolic Acid Constituents from the Whole Plant of *Sarcandra glabra*. *Tradit. Chin. Drug Res. Clin. Pharmacol.* 23, 295–298. doi:10.3969/j.issn.1003-9783.2012.03.015

Li, Y. (2006). Studies on the Chemical Constituents and Bioactivities of *Sarcandra glabra, Cercis Chinensis, and Photinia Parvifolia*. Master's Thesis. (China): Chinese Academy of Medical Science, Peking Union Medical College.

Li, Y., Zhang, D.-M., Li, J.-B., Yu, S.-S., Li, Y., and Luo, Y.-M. (2006a). Hepatoprotective Sesquiterpene Glycosides from *Sarcandra glabra*. *J. Nat. Prod.* 69, 616–620. doi:10.1021/np050480d

Li, Y., Zhang, D. M., Yu, S. S., Li, J. B., and Luo, Y. M. (2006b). A Novel Phenylpropanoid-Substituted Catechin Glycoside and a New Dihydrochalcone from *Sarcandra Glabra*. *Chin. Chem. Lett.* 17, 207–210.

Lian, X. (2006). Medical Composition Containing Polyphenols of *Sarcandra glabra* and its Application. *Chin. Patent ZL200610050821* 1.

Liu, J.-x., Zhang, Y., Hu, Q.-P., Liqiang, J.-q. Liu., Liu, Y.-t. Wu, Q. guang., Wu, Q.-g., et al. (2017a). Anti-inflammatory Effects of Rosmarinic Acid-4-O-β-D-Glucoside in Reducing Acute Lung Injury in Mice Infected with Influenza Virus. *Antiviral Res.* 144, 34–43. doi:10.1016/j.antiviral.2017.04.010

Liu, W., Lu, W., Chai, Y., Liu, Y., Yao, W., and Gao, X. (2017b). Preliminary Structural Characterization and Hypoglycemic Effects of an Acidic Polysaccharide SERP1 from the Residue of *Sarcandra glabra*. *Carbohydr. Polym.* 176, 140–151. doi:10.1016/j.carbpol.2017.08.071

Liu, J., Li, X., Lin, J., Li, Y., Wang, T., Jiang, Q., et al. (2016). *Sarcandra glabra* (Caoshanhu) Protects Mesenchymal Stem Cells from Oxidative Stress: A Bioevaluation and Mechanistic Chemistry. *BMC Complement. Altern. Med.* 16, 423. doi:10.1186/s12906-016-1383-7

Liu, L., Mu, Q., Li, W., Xing, W., Zhang, H., Fan, T., et al. (2015). Isofraxidin Protects Mice from LPS Challenge by Inhibiting Pro-inflammatory Cytokines and Alleviating Histopathological Changes. *Immunobiology* 220, 406–413. doi:10.1016/j.imbio.2014.10.007

Liu, Y. (2015). *Sarcandra glabra* Polysaccharides on High-Intensity Exercise in Rat Skeletal Muscle Microinjury under a Protective Mechanism. *J. Sanming Univ.* 32, 97–100.

Lu, X., Sun, H., Zhu, J., Hu, X., Yan, X., and Shang, G. (2019). Effects of Flavonoids from *Sarcandrae glabra* on Differentiation and Maturation of Megakaryocytes in Cell Co-culture System. *Tradit. Chin. Drug Res. Clin. Pharmacol.* 30, 1277–1283. doi:10.1016/j.cclet.2019.09.012

Lu, X., Zhang, J., Peng, W., Wu, Q., Xu, G., Yan, X., et al. (2018a). Effects of Flavonoids Sarcandrae on Bone Marrow Stromal Cells and Mcgakaryocytcs of Mice with Cytarabine-Induced Thrombocytopenia. *Pharmacol. Clin. Chin. Mater. Med.* 34, 32–35.

Lu, X., Zhang, J., Yan, X., Xu, G., and Shang, G. (2018b). Effects of Flavonoids from Sarcandra Herba on Expression of SDF-1 and CXCR-4 in the Bone Marrow of Chemotherapy-Induced Thrombocytopenia Model Mice. *Tradit. Chin. Drug Res. Clin. Pharmacol.* 29, 433–437.

Luo, Y., Liu, A., Yu, B., Kang, L., and Huang, L. (2005a). Studies on Chemical Constituents of *Sarcandra glabra*. *Chin. Pharm. J.* 40, 1296–1298.

Luo, Y.-M., Liu, A.-H., Zhang, D.-M., and Huang, L.-Q. (2005b). Two New Triterpenoid Saponins from *Sarcandra glabra*. *J. Asian Nat. Prod. Res.* 7, 829–834. doi:10.1080/10286020410001721104

Luo, Y. (2004). Study on Jiangxi Characteristic Chinese Medicinal Materials *Sarcandra glabra and Cinnamomum Camphora*. Master's Thesis. (China): Institute of Chinese Materia Medica, China Academy of Chinese Medical Sciences.

Majnooni, M. B., Fakhri, S., Shokoohinia, Y., Mojarrab, M., Kazemi-Afrakoti, S., and Farzaei, M. H. (2020). Isofraxidin: Synthesis, Biosynthesis, Isolation, Pharmacokinetic and Pharmacological Properties. *Molecules* 25, 2040. doi:10.3390/molecules25092040

Ni, G., Zhang, H., Liu, H.-C., Yang, S.-P., Geng, M.-Y., and Yue, J.-M. (2013). Cytotoxic Sesquiterpenoids from *Sarcandra glabra*. *Tetrahedron* 69, 564–569. doi:10.1016/j.tet.2012.11.023

Nunes, S., Madureira, R., Campos, D., Sarmento, B., Gomes, A. M., Pintado, M., et al. (2017). Therapeutic and Nutraceutical Potential of Rosmarinic Acid - Cytoprotective Properties and Pharmacokinetic Profile. *Crit. Rev. Food Sci. Nutr.* 57, 1799–1806. doi:10.1080/10408398.2015.1006768

Oanh, D. T., Ky, P. T., Hang, N. T. B., Yen, P. H., Hanh, T. H., Cuong, N. X., et al. (2010). Two New Sesquiterpenes from *Sarcandra glabra*. *Nat. Prod. Commun.* 5, 1717–1720. doi:10.1177/1934578x1000501102

Okamura, H., Iwagawa, T., and Nakatani, M. (1995). A Revised Structure of Chloranthalactone F and Chloranthalactone A Photodimer. *Bcsj* 68, 3465–3467. doi:10.1246/bcsj.68.3465

Qin, J., Wang, R., Teng, J., Chen, J., and Huang, R. (2007). The Effect of *Sarcandra glabra* Extracts on Oxygen Free Radical. *Lishizhen Med. Mater. Med. Res.* 18, 2945–2946.

Shi, G., Zeng, S., and Chen, J. (1980). Effects of Three Extracts of *Sarcandra glabra* on Experimental Fracture Healing (Animal Experiment Report). *J. Guiyang Coll. Tradit. Chin. Med.*, 59–66.

Shi, J. (2009). Clinical Observation of Xuekang Oral Liquid on Thrombocytopenia. *Chin. J. Mod. Drug Appl.* 3, 110–111.

Song, C. (2017). Clinical Study on Zhongjiefeng Injection Combined with Apatinib in Treatment of Advanced Gastric Cancer. *Drugs Clin.* 32, 1114–1117. doi:10.7501/j.issn.1674-5515.2017.06.036

Su, M., and Luo, C. (2009). Clinical Effect of *Sarcandra glabra* on Abdominal Incision Infection. *China Mod. Med.* 16, 88.

Sun, H., Lu, X., Hu, X., Chen, Z., Zhu, J., Lu, L., et al. (2019). Effect and Mechanism of Total Flavonoids from Sarcandrae Herba on the Apoptosis in Human Leukemia K562 Cells. *Pharmacol. Clin. Chin. Mater. Med.* 35, 54–57. doi:10.13412/j.cnki.zyyl.2019.06.012

Sun, J., Sun, X., Wang, H., Zhan, G., and Zhan, J. (1998). Toxicity Study of *Sarcandra glabra*. *Joural Guiyang Med. Coll.* 23, 43–44.

Sun, X., Zhao, Q., Si, Y., Li, K., Zhu, J., Gao, X., et al. (2020). Bioactive Structural Basis of Proteoglycans from *Sarcandra glabra* Based on Spectrum-Effect Relationship. *J. Ethnopharmacology* 259, 112941. doi:10.1016/j.jep.2020.112941

Takeda, Y., Yamashita, H., Matsumoto, T., and Terao, H. (1993). Chloranthalactone F, A Sesquiterpenoid from the Leaves of *Chloranthus Glaber*. *Phytochemistry* 33, 713–715. doi:10.1016/0031-9422(93)85480-F

Tang, X., Liao, Q., Bao, T., Shang, G., Li, J., Zhu, F., et al. (2014). Effects of Flavonoids Sarcandrae and its Ingredients Rosmarinic Acid and Astilbin on Proliferation of Rat Bone Marrow Megakaryocytes. *Pharmacol. Clin. Chin. Mater. Med.* 30, 47–49. doi:10.13412/j.cnki.zyyl.2014.02.016

Tong, S., Huang, J., Wang, B., and Yan, J. (2010). Study on the Chemical Constituents of *Sarcandra glabra*. *Chin. Tradit. Herb. Drugs* 41, 198–201.

Tsai, Y.-C., Chen, S.-H., Lin, L.-C., and Fu, S.-L. (2017). Anti-inflammatory Principles from *Sarcandra glabra*. *J. Agric. Food Chem.* 65, 6497–6505. doi:10.1021/acs.jafc.6b05125

Tsui, W.-Y., and Brown, G. D. (1996). Cycloeudesmanolides from *Sarcandra glabra*. *Phytochemistry* 43, 819–821. doi:10.1016/j.nuclphysb.2004.12.02510.1016/0031-9422(96)00352-4

Wang, A., and Ma, X. (1979a). Preliminary Study on the Active Constituents of *Sarcandra glabra*. *Chin. Tradit. Herb. Drugs* 8–9.

Wang, A., and Ma, X. (1979b). Study on the Effective Components of *Sarcandra glabra*. *Chin. Tradit. Herb. Drugs* 8–9.

Wang, C., Li, Y., Li, C. J., Yu, S. S., and Zhang, D. M. (2012). Three New Compounds from *Sarcandra glabra*. *Chin. Chem. Lett.* 23, 823–826. doi:10.1016/j.cclet.2012.05.007

Wang, C., Li, Y., Yang, J., Li, C., and Zhang, D. D. (2010a). Study on the Chemical Constituents of *Sarcandra glabra* (Abstract). *10th Natl. Symp. Traditional Chin. Med. Nat. Med.*, 35, 714–717. doi:10.4268/cjcmm20100612

Wang, C., Zhu, L., Yang, J., Li, C., and Zhang, D. (2010b). [Chemical Constituents from *Sarcandra glabra*]. *Zhongguo Zhong Yao Za Zhi* 35, 714–717.

Wang, F., Yuan, S.-T., and Zhu, D.-N. (2007). Active Components of Antitumor Fraction from *Sarcandra glabra*. *Chin. J. Nat. Med.* 5, 174–178.

Wang, J., and Du, M. (2008). Comparison of Antibacterial Effect of Zhongjiefeng Tablets with Chaiyin, Shuanghuanglian and Qutan Oral Liquid In Vitro. *Shanghai Med. Pharm. J.* 29, 80–82. doi:10.1080/01932690701783499

Wang, M., Zhao, J., Zhao, Y., Huang, R.-Y., Li, G., Zeng, X., et al. (2015a). A New Coumarin Isolated from *Sarcandra glabra* as Potential Anti-inflammatory Agent. *Nat. Product. Res.* 30, 1796–1801. doi:10.1080/14786419.2015.1079186

Wang, P., Luo, J., Zhang, Y.-M., and Kong, L.-Y. (2015b). Sesquiterpene Dimers Esterified with Diverse Small Organic Acids from the Seeds of *Sarcandra glabra*. *Tetrahedron* 71, 5362–5370. doi:10.1016/j.tet.2015.05.112

Wang, P., Li, R.-J., Liu, R.-H., Jian, K.-L., Yang, M.-H., Yang, L., et al. (2016). Sarglaperoxides A and B, Sesquiterpene-Normonoterpene Conjugates with a Peroxide Bridge from the Seeds of *Sarcandra glabra*. *Org. Lett.* 18, 832–835. doi:10.1021/acs.orglett.6b00112

Wang, Y., Hou, G., and Liu, Y. (2020). Intervention Effect and Mechanism of Polysaccharides of *Sarcandra glabra* on Exercise-Induced Muscle Damage. *J. Sanming Univ.* 37, 1–9.

Wang, Y., Yan, W., Chen, Q., Huang, W., Yang, Z., Li, X., et al. (2017). Inhibition Viral RNP and Anti-inflammatory Activity of Coumarins against Influenza Virus. *Biomed. Pharmacother.* 87, 583–588. doi:10.1016/j.biopha.2016.12.117

Wei, S., Chi, J., Zhou, M., Li, R., Li, Y., Luo, J., et al. (2019). Anti-inflammatory Lindenane Sesquiterpeniods and Dimers from *Sarcandra glabra* and its Upregulating AKT/Nrf2/HO-1 Signaling Mechanism. *Ind. Crops Prod.* 137, 367–376. doi:10.1016/j.indcrop.2019.05.041

Wu, H., Hu, X., Zhang, X., Chen, S., Yang, J., and Xu, X. (2012a). Benzyl 2-β-Glucopyranosyloxybenzoate, a New Phenolic Acid Glycoside from *Sarcandra glabra*. *Molecules* 17, 5212–5218. doi:10.3390/molecules17055212

Wu, H., Hu, X., Zhang, X., Chen, S., Yang, J., and Xu, X. (2012b). Isolation and Chemotaxonomic Significance of Megastigmane-type Sesquiterpenoids from *Sarcandra glabra*. *J. Med. Plant Res.* 6, 4501–4504. doi:10.5897/JMPR12.523

Wu, J.-T., Lv, S.-M., Lu, C.-H., Gong, J., and An, J.-B. (2015). Effect of 3,3′-Biisofraxidin on Apoptosis of Human Gastric *Cancer* BGC-823 Cells. *Trop. J. Pharm. Res.* 14, 1803–1811. doi:10.4314/tjpr.v14i10.10

Xia, Y., Fu, J., Xu, C., and Wu, H. (1996). Study on Acute Toxicity and Mutagenicity of *Sarcandra glabra*. *J. Zhejiang Coll. TCM* 20, 36–37.

Xie, Y., Zeng, J., Zheng, Y., Lin, P., and Liang, Y. (2010). Study on Anti-inflammatory Active Sites of *Sarcandra glabra* (Thunb.) Nakai Produced in Fujian Province. *J. Fujian Univ. TCM* 20, 35–38.

Xiong, Y., Ying, F., Yu, H., Zi, X., and Yang, H. (2015). Effects of Liquid Extract of *Sarcandra glabra* to Anti-hepatic Fibrosis in Rats. *J. Jiangxi Univ. TCM* 27, 76–78.

Xu, G., Xiao, B., Chen, Q., Xu, Y., and Bi, M. (2005). Effect of Sarcand glabra and its Separated Parts on Amount of Blood Platelet of Immunologic Thrombocytopenic Purpura in Mice. *Chin. J. Exp. Tradit. Med. Formulae* 11, 33–36.

Xu, T., Hu, B., and Zhuang, J. (1997). Clinical Observation of Xuekang in the Treatment of Thrombocytopenia Caused by Chemotherapy. *Acta Univ. Med. Anhui* 663.

Xu, X. D., Hu, X. R., Yuan, J. Q., and Yang, J. S. (2008). [Studies on Chemical Constituents of *Sarcandra glabra*]. *Zhongguo Zhong Yao Za Zhi* 33, 900–902.

Xu, Y., Liu, X., Huang, X., and Ge, F. (2011). Status and Prospect of Studies on *Sarcandra glabra*. *Chin. Tradit. Herb. Drugs* 42, 2552–2559.

Yang, B., Sun, W., Xun, D., and Teng, W. (2008a). Determination of Twelve Elements in Herba Sarcandrae by ICP-MS. *Chin. J. Spectrosc. Lab.* 25, 502–504.

Yang, R., Wang, B., Li, N., and Zhang, X. (2008b). Analysis of Chemical Constituents of Essential Oil from the Leaves of *Sarcandra glabra* by GC-MS. *Chin. Tradit. Pat. Med.* 30, 1703–1704.

Yang, C. (1992). Development and Utilization of Folk Tea Plant Resources of Dong Nationality in Tongdao. *Hunan For. Sci. Technol.* 19, 58–61.

Yang, W.-q., Hai, P., Xiao, H., Gao, Y., Tao, Y.-h., Miao, D.-r., et al. (2018). Glabralides A - C, Three Novel Meroterpenoids from *Sarcandra glabra*. *Tetrahedron* 74, 341–347. doi:10.1016/j.tet.2017.12.001

Yang, X.-R., Tanaka, N., Tsuji, D., Lu, F.-L., Yan, X.-J., Itoh, K., et al. (2020). Sarcaglabrin A, a Conjugate of C15 and C10 Terpenes from the Aerial Parts of *Sarcandra glabra*. *Tetrahedron Lett.* 61, 151916. doi:10.1016/j.tetlet.2020.151916

Yang, X. (2017). Bioactive Material Basis of Medicinal Plants in Genre Sarcandra. *Mod. Chin. Med.* 19, 155–164.

Yu, F., Fu, J., and Liang, J. (2012). Chemical Constituents of *Sarcandra glabra*. *Biotech. World* 5-6, 8.

Yuan, K., Zhu, J. X., Si, J. P., Cai, H. K., Ding, X. D., and Pan, Y. J. (2008). [Studies on Chemical Constituents and Antibacterial Activity from N-Butanol Extract of *Sarcandra glabra*]. *Zhongguo Zhong Yao Za Zhi* 33, 1843–1846.

Zeng, A., and Luo, Y. (2005). Chemical Constituents of *Sarcandra glabra*. *J. Chin. Med. Mater.* 28, 292–293.

Zhang, L., Zou, S., Hu, X., Yu, Z., and Fan, Q. (2016). Toxicology Safety Evaluation of New Food Resources of *Sarcandra glabra*. *J. Nanchang Univ. Sci.* 40, 478–482. doi:10.13764/j.cnki.ncdl.2016.05.014

Zhang, Z., Zheng, Y., Zhu, R., Zhu, Y., Yao, W., Liu, W., et al. (2014). The ERK/eIF4F/Bcl-XL Pathway Mediates SGP-2 Induced Osteosarcoma Cells Apoptosis In Vitro and In Vivo. *Cancer Lett.* 352, 203–213. doi:10.1016/j.canlet.2014.06.015

Zhao, Y., Sun, Y., and Chen, Q. (2008). Studies on the Antitumor Activity of Zhong Jiefeng Injection In Vitro. *Chin. J. ethnomedieine ethnopharmacy* 8-9, 36.

Zheng, X., Liu, H.-Y., and Zhong, H. (2014). Chemical Constituents from *Sarcandra glabra*. *Nat. Prod. Res. Dev.* 26, 1221–1224.

Zheng, Y., Xu, X., Zou, X., Guan, L., Zhang, D., Liu, J., et al. (2016). Chemical Constituents with the Antioxidant Activity in *Sarcandra glabra*. *J. Fujian Norm. Univ. Sci. Ed.* 32, 98–102.

Zhong, L., Liu, T., Chen, Y., Zhong, X., Du, X., Lu, Z., et al. (2005). [The Study on Effect of *Sarcandra glabra* on Prevention and Treatment of Thrombocytopenia by Chemotherapy]. *Zhong Yao Cai* 28, 35–38.

Zhou, Z. (1993). Origin, Systematics and Distribution of Chloranthaceae. *Acta Bot. Yunnanica* 15, 321–331.

Zhu, L., Li, Y., Yang, J., Zuo, L., and Zhang, D. (2008a). Studies on Chemical Constituents of *Sarcandra glabra*. *China J. Chin. Mater. Med.* 33, 155–157.

Zhu, L.-P., Li, Y., Yang, J.-Z., Zuo, L., and Zhang, D.-M. (2008b). Two New Sesquiterpene Lactones from *Sarcandra glabra*. *J. Asian Nat. Prod. Res.* 10, 541–545. doi:10.1080/10286020801966773

Zou, X., Gao, H., Wu, B., Wang, Y., Wang, S., Yang, S., et al. (2007). Study on the Chemical Constituents of *Sarcandra glabra*. *Chin. Tradit. Herb. Drugs* 38, 354–356.

Conflict of Interest: The authors declare that the research was conducted in the absence of any commercial or financial relationships that could be construed as a potential conflict of interest.

frontiers in Pharmacology

ORIGINAL RESEARCH
published: 20 May 2021
doi: 10.3389/fphar.2021.647116

Naofucong Ameliorates High Glucose Induced Hippocampal Neuron Injury Through Suppressing P2X7/NLRP1/Caspase-1 Pathway

Guangchan Jing[1], *Huanyuan Wang*[2], *Fengwei Nan*[3], *Yuqin Liu*[4] *and Mengren Zhang*[1]*

[1]Department of Traditional Chinese Medicine, Peking Union Medical College Hospital, Peking Union Medical College and Chinese Academy of Medical Sciences, Beijing, China, [2]Acupuncture and Tuina Department, Qilu Hospital of Shandong University, Jinan, China, [3]Department of Endocrinology, Kaifeng Hospital of Traditional Chinese Medicine, Kaifeng, China, [4]Department of Cell Resource Center, Institute of Basic Medical Science, Peking Union Medical College and Chinese Academy of Medical Sciences, Beijing, China

P2X7/NLRP1/caspase-1 mediated neuronal injury plays an important role in diabetic cognitive impairment and eventually inflammatory cascade reaction. Chinese herbal compound Naofucong has been mainly used to treat cognitive disorders in Traditional Chinese Medicine The present study aimed to investigate whether its neuroprotective effects might be related to the inhibition of P2X7R/NLRP1/caspase-1 mediated neuronal injury or not. In this study, high glucose-induced HT22 hippocampal neurons were used to determine Naofucong-containing serum neuronal protective effects. Lentiviruses knock out of TXNIP and P2X7R was used to determine that protective effects of Naofucong was related to inflammatory response and P2X7/NLRP1/caspase-1 mediated neuronal injury. NAC was also used to inhibit oxidative stress, so as to determine that oxidative stress is an important starting factor for neuronal injury of HT22 cells cultured with high glucose. Naofucong decreased apoptosis, IL-1β and IL-18 levels in high glucose-induced HT22 hippocampal neuron cells. Naofucong suppressed NLRP1/caspase-1 mediated neuronal injury, and P2X7 was involved in process. HT22 cells cultured in high glucose had an internal environment with elevated oxidative stress, which could promote neuronal injury. The current study demonstrated that Naofucong could significantly improve high glucose-induced HT22 hippocampal neuron injury, which might be related to suppress P2X7R/NLRP1/caspase-1 pathway, which provides novel evidence to support the future clinical use of Naofucong.

Keywords: naofucong, pyroptosis, high glucose, hippocampal neurons, TCM

OPEN ACCESS

Edited by:
Shuai Ji,
Xuzhou Medical University, China

Reviewed by:
Seon-Heui Cha,
Hanseo University, South Korea
Xiao-Ping Pu,
Peking University Health Science Center, China
Peng Luo,
Xijing Hospital, Fourth Military Medical University, China

***Correspondence:**
Mengren Zhang
xh02742@163.com

Specialty section:
This article was submitted to Ethnopharmacology, a section of the journal Frontiers in Pharmacology

Received: *29 December 2020*
Accepted: *28 April 2021*
Published: *20 May 2021*

Citation:
Jing G, Wang H, Nan F, Liu Y and Zhang M (2021) Naofucong Ameliorates High Glucose Induced Hippocampal Neuron Injury Through Suppressing P2X7/NLRP1/Caspase-1 Pathway. Front. Pharmacol. 12:647116. doi: 10.3389/fphar.2021.647116

INTRODUCTION

Diabetes mellitus (DM) is a kind of glucose metabolic disorder involving multiple system damage (Xu et al., 2013). And, DM can cause cognitive decline, manifested as impaired attention, motor speed, executive function and verbal memory, which seriously affects people's health (Palta et al., 2014). Thus, to explore pathogenesis and corresponding therapeutic targets of diabetic cognitive impairment is an important measure to treat diabetic complications. Many studies have shown that diabetes is an autoimmune and low-grade inflammatory disease, and that inflammatory responses

play an important role in diabetic cognitive dysfunction (Romeo et al., 2012). There are many factors and pathways in the damaged neurons of diabetic patients that can cause the inflammatory cascade, and P2X7/NLRP1/caspase-1 is one of the most important pathways.

P2X7/NLRP1/caspase-1 pathway is an important pro-inflammatory pathway, which depends on caspase-1 activation and followed by inflammatory cascade. Under endogenous and exogenous stimulation, apoptosis-related spot-like protein (ASC) activates pro-caspase-1 (Doitsh et al., 2014). It interacts with nucleotide binding oligomerization domain-like receptor protein 1 (NLRP1), which is involved in formation of inflammosomes and activation of caspase-1 (Tan et al., 2015; White et al., 2017; Park et al., 2018). Activated caspase-1 induces the activation of downstream cytokines such as IL-1β and IL-18. Then, cells release intracellular substances such as lactate dehydrogenase (LDH), mediating cell damage. During cell injury, ion channel opening induced by ATP release and binding purine receptor P2X7 is one of the classic pathways of NLRP1 inflammasome activation (Meng et al., 2014). More and more studies have shown the important pathophysiological function of P2X7 receptor (P2X7R) in central nervous system diseases (Divirgilio, 2007). Recent studies have found increased expression of NLRP1, ASC and Caspase-1 in STZ-induced diabetic cortical neurons (Meng et al., 2014). Therefore, P2X7R/NLRP1/caspase-1 mediated neuronal injury plays an important role in diabetic cognitive impairment and eventually inflammatory cascade reaction Bartlett et al. (2014), Sperlágh and Illes (2014), which may provide a new target for the prevention and treatment of diabetic cognitive impairment.

Naofucong is a compound preparation based on traditional Chinese medicine theory and modern pharmacology. NFC consisted of ginseng, salvia, polygonum multiflorum, leeches, poria, berberine, and calamus. Among these herbs, it has been reported that ginseng has beneficial effects in diabetes, and Panax ginseng roots extracts and Polygonum multflorum extracts could improve the learning and memory ability (Jing et al., 2020). Clinical practice has shown that it can significantly improve cognitive dysfunction in diabetics. Animal experiments have also shown that Naofucong can improve the learning and memory function and shorten the incubation period and duration of water maze in diabetic rats through up-regulating the expression of insulin-like growth factor-1 (IGF-1) and glial fibrillary acidic protein (GFAP) and decreasing the expression of nuclear factor-κB (NF-κB) in hippocampus (Zhang et al., 2004; Jing et al., 2020). Our previous studies showed that Naofucong could play a role in improving high glucose-induced neuronal injury (Jing et al., 2016). However, its specific mechanism is unknown. In this study, high glucose-induced HT22 hippocampal neurons were used to determine Naofucong-containing serum neuronal protective effects. Lentiviruses knock out of TXNIP and P2X7R was used to determine that protective effects of Naofucong was related to inflammatory response and P2X7R/NLRP1/caspase-1 mediated neuronal injury. This study can provide novel evidence to support the future clinical use of Naofucong.

MATERIALS AND METHODS

Preparation of Naofucong

Naofucong (NFC) Granules consists of the following dried raw materials: *Panax ginseng* C.A.Mey. [Araliaceae; Ginseng radix et rhizoma], *Salvia miltiorrhiza* Bge. [Lamiaceae; Salviae miltiorrhizae radix et rhizoma], *Polygonum multiflorum* Thunb. [Polygonaceae; Polygoni multiflori radix], *Poria cocos (Schw.)* Wolf [Polyporcee; Poria], *Coptis chinensis* Franch. [Ranunculaceae; Coptidis rhizoma], *Whitemania pigra* Whitman [Hirudinidae; Hirudo] and *Acorus tatarinowii* Schott. [Araceae; Acori tatarinowii rhizoma] (1:3:3:1:1:1:1). These 7 herbs were purchased from Medicinal Materials Company of Beijing Tongrentang (Batch Number: X,157,631), processed by Beijing Kangrentang Pharmaceutical Co., LTD, China, which was prepared into an aqueous solution.

For preparation of the NFC decoction, the mixed crude drugs were soaked with stilled water at room temperature (25°C) for 2 h. For the first decoction, the drugs were refluxed with 10-fold of water (1:10, *w/v*) for 1.5 h before filtered. For the second decoction, the drug residues were refluxed with eightfold of water (1:8, *w/v*) before filtered. The two decoctions were then mixed together and concentrated in vacuum. The concentrated decoction was freeze-dried with an extraction yield of 19%. Then the NFC extract was stored under −80°C and well suspended in water before use.

UPLC/Q-TOF-MS Analysis

The freeze-dried powders of NFC decoction water extract (20 mg) was dissolved in 10 ml of distilled water and then filtered with a 0.22 mm membrane before analysis. UPLC/MS analysis was performed on a UPLC system coupled with XEVO G2 Q-TOF mass spectrometer via an ESI source (Waters Corp. Milford, MA). For UPLC separation, 2 μL of sample solution was injected into an ACQUITY HSS T3 C_{18} column (100 × 2.1 mm, 1.7 μm, Waters). The mobile phase consisted of ACN (A) and water containing 0.1% (v/v) formic acid (B). Linear gradient elution was applied (0–5min, 5–30% A; 5–10min, 30–40% A; 10–20min, 40–65% A; 20–25min, 65–90% A) at a flow rate of 0.4 ml/min. The column temperature was 45°C. For MS detection, accurate mass was maintained by the LockSpray interface of sulfadimethoxine (309.0658 $[MH]^-$). The operating parameters in negative ion mode were as follows: capillary voltage, 3.0 kV; cone voltage, 30 V; desolvation gas flow rate, 750 L/h; source temperature, 120°C; desolvation temperature, 350°C. MS data were acquired in centroid mode and processed by MassLynx software (Waters, version 4.1).

Preparation of Animals and Naofucong-Containing Serum

SPF grade male SD rats (weighing 200–220 g, No. SCXK 2007–004) were provided by Vital River Laboratory Animal Technology Co. Ltd. (Beijing, China), and were kept in the clean animal feeding room of the animal experimental center, with a humidity of 60% and a temperature of 20–22°C. Rats were kept in a cage and fed freely. After

TABLE 1 | Related chromatographic mass spectrometric data of compound in naofucong granule.

No	Rt	*m/z*	Proposed fomula	ppm	MS^n	Identification
1	5.23	197.0455	$C_9H_9O_5$	1.08	MS^2 [197]179; MS^3 [179]135	Tanshinol
2	13.67	342.1705	$C_{20}H_{24}NO_4$	−1.49	[342]297,298,265,311; [297]265,282	Magnoflorine
3	14.76	417.0830	$C_{20}H_{17}O_{10}$	1.36	MS^2 [417]373,175,197; MS^3 [373]175,197	Salvianolic acid G
4	15.15	537.1037	$C_{27}H_{21}O_{12}$	0.95	MS^2 [537]339,295; MS^3 [339]295,321,185	Lithospermic acid
5	15.17	557.1301	$C_{27}H_{25}O_{13}$	1.16	MS^2 [557]313,243,211,405,285	Piceatannol 4′-galloylglucoside
6	15.69	717.1466	$C_{36}H_{29}O_{16}$	1.54	MS^2 [717]519,321; MS^3 [519]321,339	Salvianolic acid L
7	16.02	359.0774	$C_{18}H_{15}O_8$	1.25	MS^2 [359]161,179(24),197,223(13); MS^3 [161]133	Rosmarinate
8	17.24	717.1458	$C_{36}H_{29}O_{16}$	0.8	MS^2 [717]519,321; MS^3 [519]321,339	Salvianolic acid L
9	17.28	322.1079	$C_{19}H_{16}NO_4$	0.52	[322]307,308,294	Thalifendine
10	18.04	493.1138	$C_{26}H_{21}O_{10}$	0.91	MS^2 [493]295; MS^3 [295]159,185,277,157	Salvianolic acid A
11	18.17	493.1138	$C_{26}H_{21}O_{10}$	0.88	MS^2 [493]295; MS^3 [295]159,185,277,157	Salvianolic acid A
12	19.34	338.1372	$C_{20}H_{20}NO_4$	−1.53	[338]323,324,294; [323]294,307,308	Jatrorrhizine
13	19.57	338.1392	$C_{20}H_{20}NO_4$	0.52	[338]323,324,294; [323]294,307	Columbamine
14	20.13	336.1215	$C_{20}H_{18}NO_4$	−1.51	[336]321,320,308; [321]292,293	Berberine
15	20.93	320.0904	$C_{19}H_{14}NO_4$	−1.11	[320]292,290,293; [292]277,264	Coptisine
16	22.59	352.1549	$C_{21}H_{22}NO_4$	−2.00	[352]337,336,338; [337]308,320	Palmatine
17	23.19	336.1214	$C_{20}H_{18}NO_4$	−1.67	[336]321; [321]292,318	Epiberberine
18	31.19	497.3273	C31H45O6	1.12	MS^2 [497]419,435,420,417,269	Poricoic acid A
19	32.75	269.0455	C15H9O5	1.08	MS^2 [269]225,269,226,241,201	Emodin or Aloe-emodin
20	35.34	469.3324	C30H45O4	1.13	MS^2 [469]423,407,337,333,409	3,16-Dihydroxylanosta-7,9 (11),24-trien-21-oic acid
21	35.99	471.3481	C30H47O4	1.19	MS^2 [471]409,337,410,425,407	16 -Hydroxytrametenolic acid
22	36.41	481.3325	C31H45O5	1.28	MS^2 [481]412,421,403,344,382	Poricoic acid C
23	37.13	297.1476	C19H21O3	0.28	MS^2 [297]279,251; MS3 [279]279,264	Cryptotanshinone
24	37.36	529.3534	C32H49O6	1.02	MS^2 [529]453,469,511,451,470	3-O-acetyl-16,26-dihydroxytrametenolic acid
25	37.39	483.3482	C31H47O4	1.35	MS^2 [483]437,337,421; MS^3 [437]421	Dehydrotumulosic acid
26	40.16	481.3325	C31H45O4	1.25	MS^2 [481]311,388,403,335,421	Poricoic acid C
27	41.1	529.3536	C32H49O6	1.27	MS^2 [529]483,460,393,392,461	3-O-acetyl-16, 27-dihydroxytrametenolic acid
28	41.15	483.3482	C31H47O5	1.32	MS^2 [483]437,421,423; MS3 [437]421	Dehydrotumulosic acid
29	46.82	527.3742	C33H51O5	1.11	MS^2 [527]509,481,511,483	Pachymic acid

Naofucong reduced high glucose-induced HT22 hippocampal neuron cell damage.

3 days of adaptive feeding, intragastric administration (Naofucong 4.667 g/kg) was performed, twice per day, for 3 days. After administration, 5 ml/kg 1% pentobarbital sodium was injected intraperitoneally, blood was collected from the abdominal aorta, and Naofucong-containing serum was obtained by centrifugation. Serum was filtered through 0.22 μm filters, inactivated at 56°C for 30 min. This study was performed under the supervision of the Animal Care and Use Committee of Peking Union Medical College Hospital.

Group Processing of Cell Experiments

HT22 (immortalized mouse hippocampal neuronal) cells were kindly provided by Cell bank, Institute of Basic Medicine, Peking Union Medical College. HT22 cells were maintained in DMEM (dulbecco's modified eagle medium)/high-glucose media (Hyclone, Logan, Utah) containing 10% fetal calf serum (Hyclone, Logan, Utah) and were incubated at 5% CO_2/95% O_2 incubation at 37°C. Cells were treated with control (Con, 5.5 mmol/L of glucose) or high-glucose (HG, 75 mmol/L of glucose) medium for 48 h. Besides, 10% Naofucong-containing serum (NFC) and N-acetyl-L-cysteine (NAC, 10 mmol/L) were carried out in high-glucose medium for 48 h.

Preparation of RNAi Lentivirus Clones

The linearized vector was obtained by restriction enzyme digestion; The primers were annealed to prepare the target fragment; The primers were designed to add restriction sites at both ends of the primers, and after annealing, the primer contained the same restriction sites as the two ends of the linearized clone vector. Linearized carrier and annealing product were used to prepare the reaction system, and the products were directly transformed. Monoclones were selected from the plate for PCR identification, and the positive clones were sequenced and the results were analyzed. The high purity plasmid was obtained by expanding culture and extraction of the correct clone bacteria liquid.

Biochemical Assay

After treatment of cells according to experimental grouping requirements, the supernatant of cells was collected for the detection of Cell Counting Kit-8 (CCK-8, C0037, Beyotime, China), Lactate dehydrogenase (LDH, C0017, Beyotime, China), Interleukin-1β (IL-1β, PI301, Beyotime, China) and Interleukin-18 (IL-18, PI553, Beyotime, China). The experimental process was carried out according to instructions.

TUNEL Apoptosis Assay

One Step TUNEL Apoptosis Assay Kit (C1088, Beyotime, China) is a sensitive, rapid and simple method for apoptosis detection. For cells that have been fixed, the apoptotic cells presenting green fluorescence can be detected by fluorescence microscope after

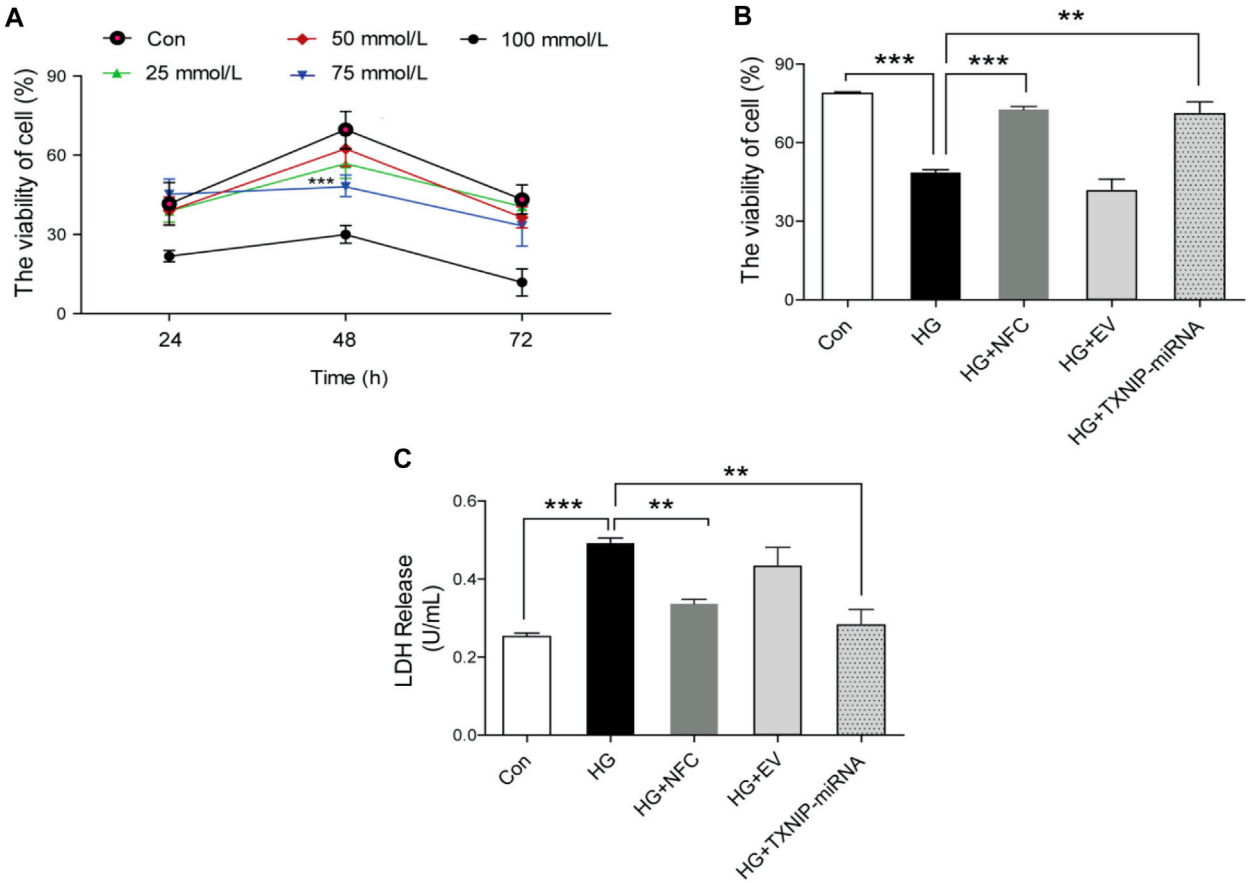

FIGURE 1 | Naofucong reduced high glucose-induced HT22 hippocampal neuron cell damage. **(A)** The activity of HT22 cells cultured with high glucose at different concentrations and at different time points, $^{***}p < 0.001$, 75 mmol/L vs. Con. **(B, C)** HT22 cell activity and LDH release level under high glucose conditions (75 mmol/L and 48 h), NFC or lentivirus knockout of TXNIP treatment. Values are means ± SEM, $n = 5$ per group, $^{*}p < 0.05$, $^{**}p < 0.01$, $^{***}p < 0.001$.

washing after one-step staining. The experimental process was carried out according to instructions.

Real-Time PCR

Total RNA was extracted with Trizol kit in one step (15,596,026, Invitrogen, United States). RNA integrity of each sample was detected by formaldehyde denatured gel electrophoresis. The content of total RNA in each sample was determined by ultraviolet spectrophotometer. According to literature, PCR amplification primers were designed by existing cDNA sequences in gene bank, and PCR amplification conditions of various genes were set according to their characteristics to perform real-time PCR detection. The reaction conditions were as follows: pre-denaturation at 94°C for 5 min, 30 cycles of denaturation at 94°C for 30 s, annealing at 54.5°C for 30 s and extension at 72°C for 30 s, and a final extension at 72°C for 10 min. SDS2.2 fluorescence quantitative operation technology data analysis software was used to process and analyze the data. β-actin was considered as the internal reference of the genes. The expression of target genes was calculated based on the $2^{-\Delta\Delta Ct}$ method, with ΔCt obtained using the following formula: ΔCt = Ct (target gene) −Ct (β-actin), and ΔΔCt = ΔCt (the experiment group) −ΔCt (the control group). The experiment was conducted in triplicates. The primer sequences for RT-PCR assay were summarized in **Supplementary Table S1**.

Western Blot

Cells were added into lysate for homogenization (P0013B, Beyotime biotechnology, Shanghai, China), and centrifuged for supernatant. Then, protein concentration was determined by BCA (23,250, Thermo Fisher Scientific, United States). The supernatant containing 50 μg protein was separated by 8, 10, or 12% SDS-PAGE electrophoresis and transferred to cellulose nitrate film. The non-specific binding was reduced by using TBS-T containing 5% skim milk. Incubate with different primary antibodies (Dilution concentration is 1:1,000), and then incubate with secondary antibodies (Dilution concentration is 1:4,000), and test with ECl kit (32,109, Thermo Fisher Scientific, United States). The strips were scanned and quantified using a computer image analysis system. Detailed information of antibodies was shown in **Supplementary Table S2**.

Statistical Analyses

Data are presented as mean ± SEM, calculated using SPSS 17.0 software (SPSS Inc. Chicago, IL, United States). Differences were

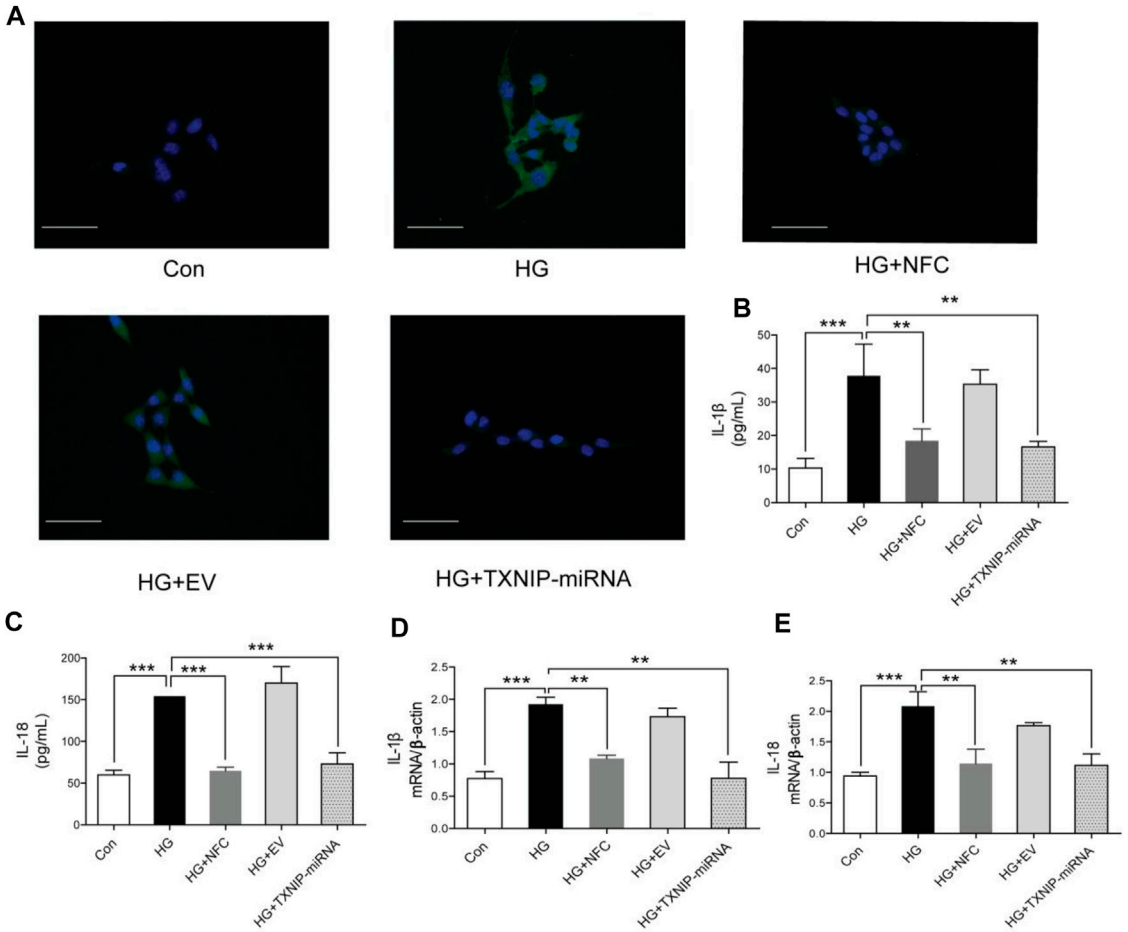

FIGURE 2 | Naofucong decreased apoptosis, IL-1β and IL-18 levels in high glucose-induced HT22 hippocampal neuron cells. **(A)** Morphological photomicrographs of TUNEL staining. TUNEL positive staining cells were labeled as green, scale bar = 30 μm. **(B, C)** Effects of NFC on IL-1β and IL-18 levels of HT22 cells in high glucose. **(D, E)** Effects of NFC on IL-1β and IL-18 mRNA levels of HT22 cells in high glucose. Values are means ± SEM, $n = 5$ per group, $^{*}p < 0.05$, $^{**}p < 0.01$, $^{***}p < 0.001$. Naofucong suppressed NLRP1/caspase-1 mediated neuronal injury in high glucose-induced HT22 hippocampal neuron cells.

analyzed using one-way ANOVA followed by Bonferroni post hoc test or unpaired two-tailed Student's *t*-test with SPSS 17.0 software. $p < 0.05$ was considered statistically significant.

RESULTS

Chemical Profiling of NFC

UPLC/Q-TOF-MS analysis was employed to characterize the chemical composition of NFC. A total of 29 peaks (1–29) were putatively identified by comparing their high-resolution MS data. These compounds have covered most of the main peaks in the chromatogram and different kinds of constituents were involved (**Table 1**, **Supplementary Figure S1**; **Supplementary Table S3**).

In this study, HT22 hippocampal neuron cells were used to determine optimal cell model stimulation conditions after different time and different concentration (**Figure 1A**) of high glucose stimulation. According to results of this study and literature reports Zhang et al. (2018), 75 mmol/L and 48 h were finally determined as optimal stimulus conditions. At the same time, the study found that activity of HT22 cells decreased and LDH level increased under high glucose culture, and NFC could significantly reverse above trend. In addition, lentivirus knockout of TXNIP (a key molecule in inflammatory process), also significantly increased cell activity and decreased LDH release (**Figures 1B,C**). These results suggest that NFC significantly ameliorates high glucose-induced HT22 cell damage and that this effect may be related to its involvement in inflammatory process.

Naofucong decreased apoptosis, IL-1β and IL-18 levels in high glucose-induced HT22 hippocampal neuron cells.

In this study, it was found that apoptosis of HT22 cells was significantly increased in HG group, while NFC and TXNIP-miRNA could significantly reduce number of apoptotic cells (**Figure 2A**). Moreover, high glucose significantly increased expression levels of IL-1β and IL-18 proteins in HT22 cells, and NFC and TXNIP-miRNA significantly reversed above trends (**Figures 2B,C**). And, NFC and TXNIP-miRNA also

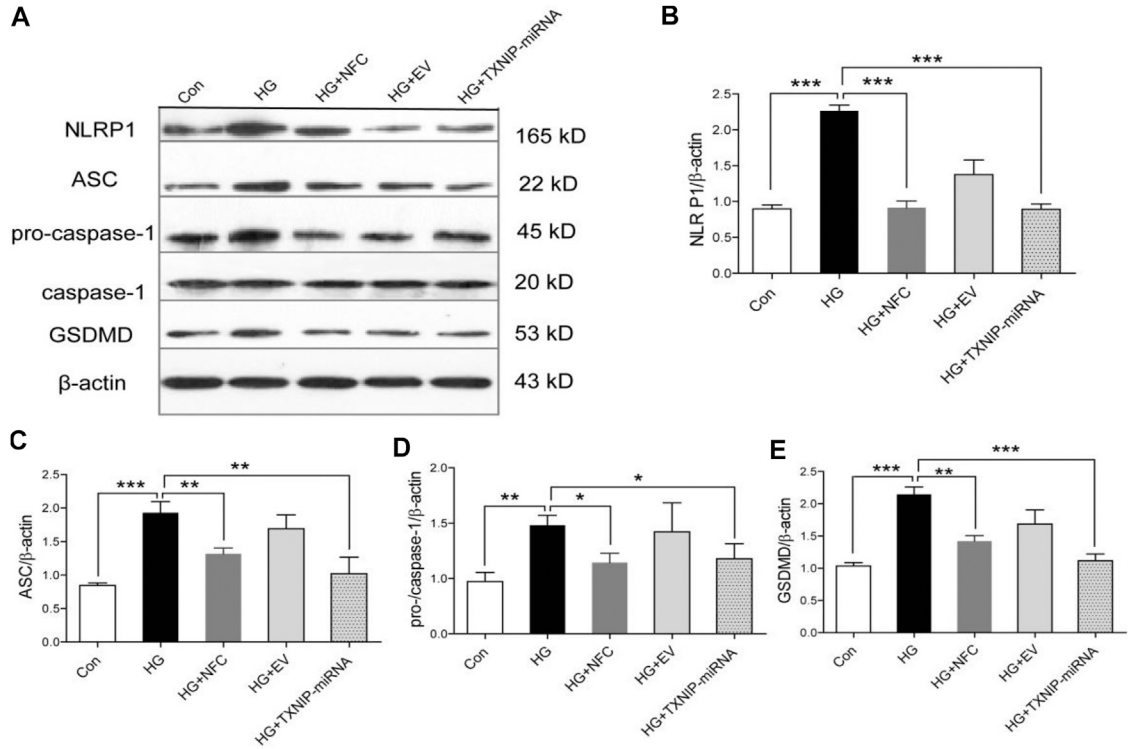

FIGURE 3 | Naofucong suppressed NLRP1/caspase-1 mediated neuronal injury in high glucose-induced HT22 hippocampal neuron cells. **(A)** Effects of NFC on NLRP1, ASC, pro-caspase-1, caspase-1, and GSDMD levels of HT22 cells in high glucose. **(B–E)** Representative protein levels of NLRP1, ASC, pro-caspase-1, caspase-1, and GSDMD levels of HT22 cells in high glucose were assessed by western blotting using specific antibodies. Values are means ± SEM, $n = 4$ per group, $^{*}p < 0.05$, $^{**}p < 0.01$, $^{***}p < 0.001$. Naofucong suppressed P2X7-induced neuronal injury in high glucose-induced HT22 hippocampal neuron cells.

significantly reversed elevated IL-1β and IL-18 mRNA levels in HT22 cells induced by high glucose (**Figures 2B,C**). These data showed that there was inflammatory response activation in HT22 cells induced by high glucose, and NFC could significantly inhibit inflammatory response.

In this study, the expression levels of key proteins in NLRP1/caspase-1 mediated neuronal injury were detected. The results showed that several key proteins in NLRP1/caspase-1 mediated neuronal injury were significantly elevated in high glucose-induced HT22 cells, including NLRP1, ASC, pro-caspase-1, caspase-1 and GSDMD (**Figure 3A**). And, NFC and TXNIP-miRNA significantly reduced expression levels of these proteins (**Figures 3B–E**). These results showed that activation of NLRP1/caspase-1 mediated neuronal injury existed in HT22 cells cultured with high glucose, the activation of NLRP1/caspase-1 mediated neuronal injury was related to TXNIP, and NFC could play a role in inhibiting NLRP1/caspase-1 mediated neuronal injury.

In order to explore roles of P2X7 in NFC improving pyroptosis of high glucose-induced HT22 cells, P2X7R was knocked out in this study. The results showed that in HG group, P2X7R significantly increased and NFC could significantly reduce P2X7R level (**Figures 4A,B**). At the same time, P2X7R-miRNA can significantly reverse rising trend of key proteins in HG group and inhibit NLRP1/caspase-1 mediated neuronal injury (**Figures 4C–F**). And, NFC and P2X7R-miRNA also significantly reversed elevated NLRP1 and ASC mRNA levels in HT22 cells induced by high glucose (**Figures 4G,H**). These results indicated that P2X7 was involved in process of NFC suppressing NLRP1/caspase-1 mediated neuronal injury in high glucose-induced HT22 cells.

Oxidative stress was involved in process of NFC suppressing P2X7/NLRP1/caspase-1 mediated neuronal injury in high glucose-induced HT22 cells.

In order to explore roles of oxidative stress in high glucose-induced neuronal injury of HT22 cells, NAC (an oxidative stress inhibitor) was added in this study as a control drug with NFC. NAC can significantly reverse rising trend of P2X7R and key proteins in HG group and inhibit NLRP1/caspase-1 mediated neuronal injury (**Figures 5A–F**). And, NFC and NAC also significantly reversed elevated P2X7R and GSDMD mRNA levels in HT22 cells induced by high glucose (**Figures 5G,H**). These results indicated that HT22 cells cultured in high glucose had an internal environment with elevated oxidative stress, which could promote P2X7/NLRP1/caspase-1 mediated neuronal injury, while NFC and NAC could reduce oxidative stress and thus alleviate neuronal injury.

DISCUSSION

In this study, HT22 hippocampal neurons were used for high-glucose stimulation to construct a cell damage model, and

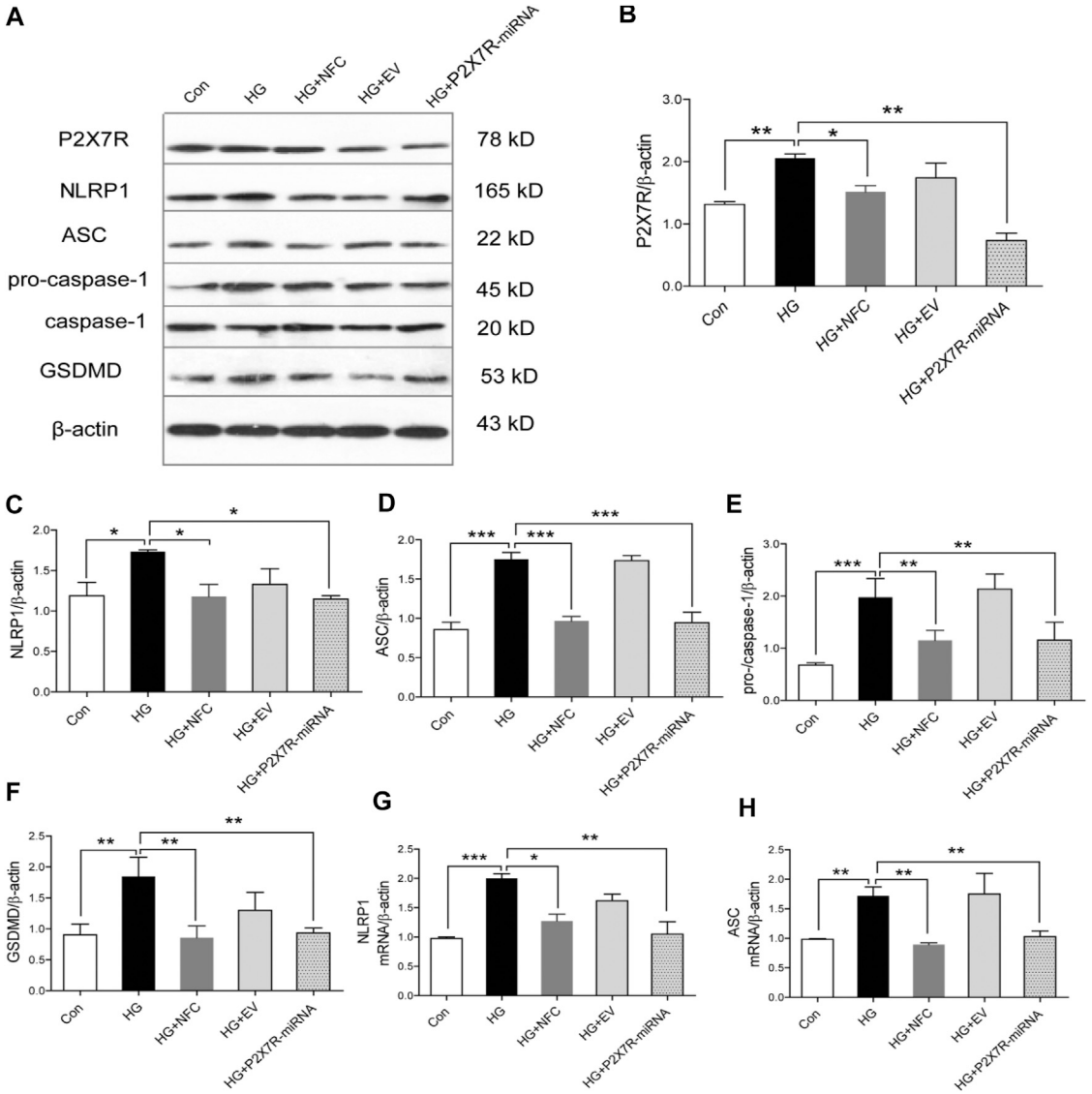

FIGURE 4 | Naofucong suppressed P2X7-induced neuronal injury in high glucose-induced HT22 hippocampal neuron cells. **(A)** Effects of NFC on P2X7R, NLRP1, ASC, pro-caspase-1, caspase-1, and GSDMD levels of HT22 cells in high glucose. **(B–F)** Representative protein levels of P2X7R, NLRP1, ASC, pro-caspase-1, caspase-1, and GSDMD levels of HT22 cells in high glucose were assessed by western blotting using specific antibodies. **(G, H)** Effects of NFC and P2X7R-miRNA on NLRP1 and ASC mRNA levels of HT22 cells in high glucose. Values are means ± SEM, $n = 4$ per group, $^{*}p < 0.05$, $^{**}p < 0.01$, $^{***}p < 0.001$.

Naofucong-containing serum was used to determine neuronal protective effect of Naofucong. Then, lentiviruses were used to knock out TXNIP and P2X7R, respectively, so as to determine that protective effects of Naofucong was related to inflammatory response and P2X7/NLRP1/caspase-1 mediated neuronal injury. Finally, NAC was also used to inhibit oxidative stress, so as to determine that oxidative stress is an important starting factor for P2X7/NLRP1/caspase-1 mediated neuronal injury of HT22 cells cultured with high glucose.

Naofucong is a compound preparation based on traditional Chinese medicine theory and modern pharmacology. It is rich in a variety of intelligence and neuroprotective ingredients. It has effects of tonifying kidney and invigorating spleen, nourishing blood and promoting blood circulation, and improving cognitive function. It has a good effect on patients with mild cognitive dysfunction of spleen and kidney function deficiency, phlegm and blood stasis (Zhang et al., 2004; Jing et al., 2020).

The dosage in this study was determined based on our clinical dosage and previous animal experiments (Jing et al., 2016; Jing et al., 2020). The dose-effect of drug-containing serum is also determined by dose and serum concentration of donor animal. Since serum concentration in this cell culture system has been limited to fixed condition of 10%, blood drug concentration is mainly adjusted according to dose given by donor animal. The dose of Chinese herb *in vitro* test is determined according to dose-effect relationship *in vivo* test under condition that effective

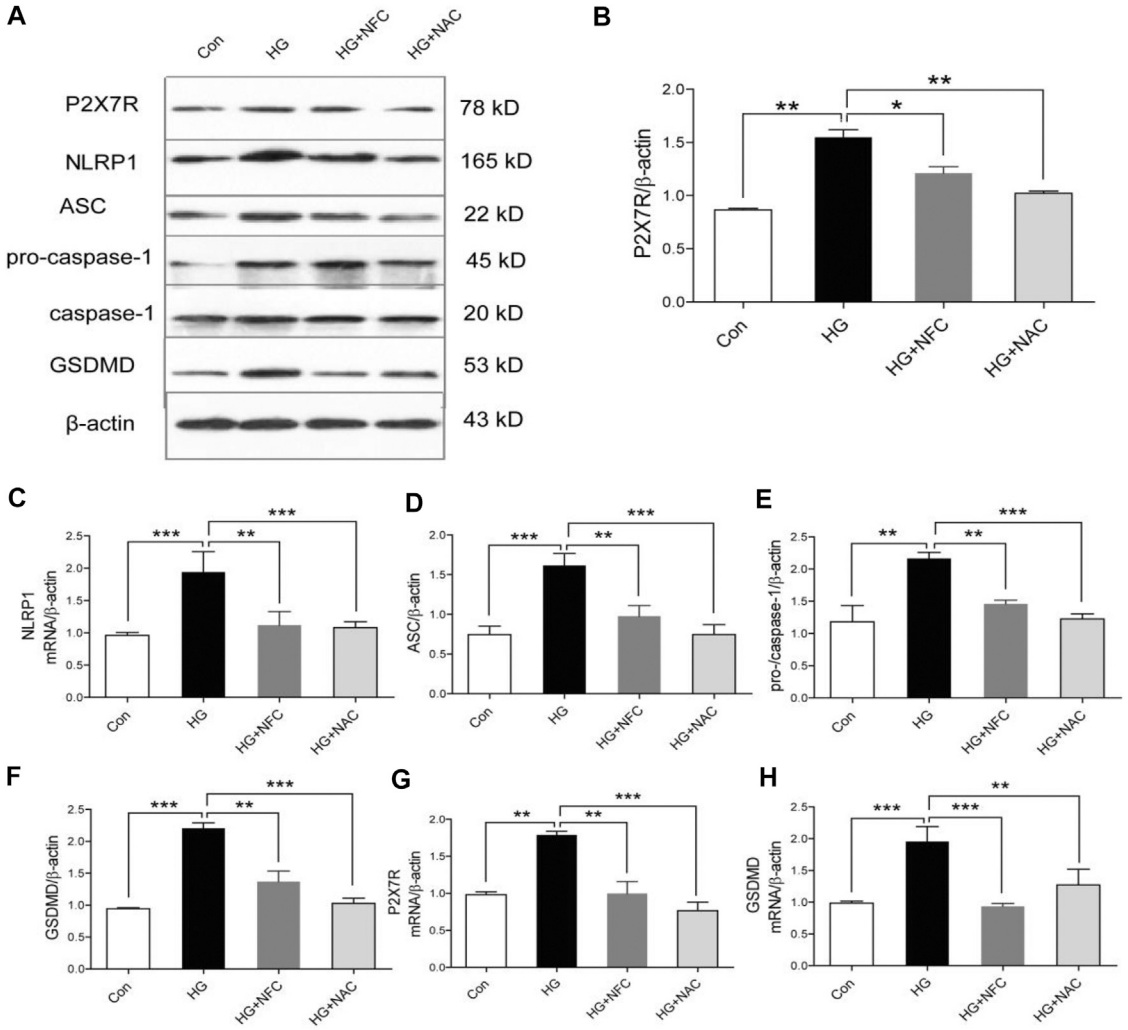

FIGURE 5 | Oxidative stress was involved in process of NFC suppressing P2X7/NLRP1/caspase-1 mediated neuronal injury in high glucose-induced HT22 cells. **(A)** Effects of NAC on P2X7R, NLRP1, ASC, pro-caspase-1, caspase-1, and GSDMD levels of HT22 cells in high glucose. **(B–F)** Representative protein levels of P2X7R, NLRP1, ASC, pro-caspase-1, caspase-1, and GSDMD levels of HT22 cells in high glucose were assessed by western blotting using specific antibodies. **(G, H)** Effects of NFC and NAC on NLRP1, and ASC mRNA levels of HT22 cells in high glucose. Values are means ± SEM, $n = 4$ per group, $^{*}p < 0.05$, $^{**}p < 0.01$, $^{***}p < 0.001$.

components of Chinese herb are not completely clear (Heinrich et al., 2020). The dose used in this study is equivalent to the dose used in human clinical practice.

Hippocampal neurons are main cells in brain for learning and memory, and HT22 cells have been used as well established *in vitro* cellular models for neurodegenerative disorders such as AD. This cell lines has functional cholinergic properties related to the cognitive defects of AD (Liu et al., 2009). In this study, HT22 hippocampal neuron cells were used to determine optimal cell model stimulation conditions after different time and different concentration of high glucose stimulation. According to results of this study and literature reports, 75 mmol/L and 48 h were finally determined as optimal stimulus conditions. Thioredoxin-interacting protein (TXNIP) was a type of thioredoxin binding protein (TRX), which mediated oxidative stress, inhibited cell proliferation, and induced apoptosis by inhibiting function of thioredoxin system. TXNIP is also a central molecule in inflammatory process Singh et al. (2017), and in this study, lentivirus knockout of TXNIP was used to determine relationships between protective effects of Naofucong and inflammatory response. These results suggest that NFC significantly ameliorates high glucose-induced HT22 cell damage. And there was inflammatory response activation in HT22 cells induced by high glucose, and NFC could significantly inhibit inflammatory response.

P2X7/NLRP1/caspase-1 pathway is an important pro-inflammatory pathway, which depends on caspase-1 activation and followed by inflammatory cascade (Tan et al., 2014). In this study, the expression levels of key proteins in NLRP1/caspase-1 mediated neuronal injury were detected. These results showed that activation of NLRP1/caspase-1 mediated neuronal injury existed in HT22 cells cultured with high glucose, the activation of NLRP1/caspase-1 mediated neuronal injury was related to TXNIP, and NFC could play a role in inhibiting NLRP1/caspase-1 mediated neuronal injury. During cell injury, ion channel opening induced by ATP release and binding purine receptor P2X7 is one of

the classic pathways of NLRP1 inflammasome activation. P2X7R, a member of the P2X family of purine receptors, is a type of ion channel that is permeable to potassium, sodium and calcium (Kasuya et al., 2016). It was found that P2X7R binds to NLRP1 inflammasome through Pannexin 1 (Pannexin 1) in the cytoplasm of neurons, inducing caspase-1 activation and IL-1β maturation and release (Meng et al., 2014). In order to explore roles of P2X7 in NFC improving pyroptosis of high glucose-induced HT22 cells, P2X7R was knocked out in this study. These results indicated that P2X7 was involved in process of NFC suppressing NLRP1/caspase-1 mediated neuronal injury in high glucose-induced HT22 cells.

There are many mechanisms of activation of inflammasome complexes in central nervous system. Hyperglycemia causes excessive production of superoxide anions in mitochondria, which will lead to oxidative stress in tissues and cells and eventually lead to various complications of diabetes (Maiese et al., 2007). Many studies have shown that, ROS may be involved in the activation of NLRP1, thereby enhancing the inflammatory response (Xu et al., 2013). Recent studies have shown that hyperglycemia increases the production of ROS in myocardial cells, which in turn upregulates NF-κB and TXNIP. NF-κB in turn upregulates IL-1β precursor, and IL-18 precursor. TXNIP activates Caspase-1 by changing the structure of NLRP1 (Fann et al., 2013), (Masters et al., 2012). The activated Caspase-1, on the one hand, cleases Gasdermin D to form a peptide containing the active domain of nitrogen end of Gasdermin D, which induces the perforation and rupture of myocardial cell membrane, eleases contents, and causes inflammatory reaction. On the other hand, activated caspase-1 excises the precursors of IL-1β and IL-18 to form active IL-1β and IL-18, which are released outside the cell to recruit inflammatory cell aggregation and amplify the inflammatory response (Kıçık et al., 2020). In order to explore roles of oxidative stress in high glucose-induced neuronal injury of HT22 cells, NAC (an oxidative stress inhibitor) was added in this study as a control drug with NFC. These results indicated that HT22 cells cultured in high glucose had an internal environment with elevated oxidative stress, which could promote pyroptosis, while NFC and NAC could reduce oxidative stress and thus alleviate pyroptosis.

The existing problems and future study directions were also summarized as follows. Firstly, because of complicated composition of NFC, only parts of major compounds were identified presently. The key effective constituents remain unknown. Secondly, the complexity of components of Chinese herb determines that effect of Chinese herb on body is a comprehensive embodiment of therapeutic effect of multiple components, multiple targets and multiple channels, while the dose-effect relationship of Chinese herb is still in the stage of accumulation of experience and faces many bottlenecks. At the same time, some influencing factors of Chinese herb itself, such as place of origin, time of collection, processing methods, etc., also need to be considered. Moreover, the drug-containing serum itself does have certain limitations, such as irregular absorption, low bioavailability, and often not obvious dose-effect relationship. The biggest limitation of this experiment is that there is no design of high, medium and low dose drug gradient, and only a single dose was used, and there was a lack of comparison between doses of different concentrations. And, more drug concentration gradients need to be designed in the future to further explore the drug dose-effect relationship. The most appropriated dose of NFC decoction for clinical use still needs more consideration (such as long-term safety) and requires further investigations. Despite this, we should delve deeper to perform further mechanism studies for better understanding the therapeutic effects of NFC decoction and applying it into the management of diabetic cognitive dysfunction.

CONCLUSION

Naofucong significantly improves high glucose-induced HT22 hippocampal neuron injury, which is related to suppress P2X7/NLRP1/caspase-1 pathway. This provides novel evidence to support the future clinical use of Naofucong. However, there is a major defect in current study, which is that the dose is not clearly defined. In this study, there is a lack of effect comparison of multiple doses, which also affects clinical application of NFC. In our follow-up study, we will conduct multiple dose studies to find optimal dose of NFC.

DATA AVAILABILITY STATEMENT

The original contributions presented in the study are included in the article/**Supplementary Material**, further inquiries can be directed to the corresponding author.

ETHICS STATEMENT

The animal study was reviewed and approved by the Animal Care and Use Committee of Peking Union Medical College Hospital.

AUTHOR CONTRIBUTIONS

The study concept and design: GJ, HW, and MZ. Writing of the manuscript: HW, GJ. Data analysis: HW, GJ, YL, and MZ. Obtaining data: GJ, HW, and FN. Interpretation of results: HW, GJ, YL, and MZ. Critical revisions of the manuscript: HW and GJ, and approval of the version for submission: All authors.

FUNDING

This work was supported by the Special Fund for Basic Scientific Research Operating Expenses of Central Universities (No. 3332018044).

SUPPLEMENTARY MATERIAL

The Supplementary Material for this article can be found online at: https://www.frontiersin.org/articles/10.3389/fphar.2021.647116/full#supplementary-material

REFERENCES

Bartlett, R., Stokes, L., and Sluyter, R. (2014). The P2X7 Receptor Channel: Recent Developments and the Use of P2X7 Antagonists in Models of Disease. *Pharmacol. Rev.* 66, 638–675. doi:10.1124/pr.113.008003

Divirgilio, F. (2007). Liaisons Dangereuses: P2X7 and the Inflammasome. *Trends Pharmacological Sciences* 28, 465–472. doi:10.1016/j.tips.2007.07.002

Doitsh, G., Galloway, N. L. K., Geng, X., Yang, Z., Monroe, K. M., Zepeda, O., et al. (2014). Cell Death by Pyroptosis Drives CD4 T-Cell Depletion in HIV-1 Infection. *Nature* 505, 509–514. doi:10.1038/nature12940

Fann, D. Y., Lee, S. Y., Manzanero, S., Tang, S. C., Gelderblom, M., Chunduri, P., et al. (2013). Intravenous Immunoglobulin Suppresses NLRP1 and NLRP3 Inflammasome-Mediated Neuronal Death in Ischemic Stroke. *Cell Death Dis.* 4, e790. doi:10.1038/cddis.2013.326

Heinrich, M., Appendino, G., Efferth, T., Fürst, R., Izzo, A. A., Kayser, O., et al. (2020). Best Practice in Research - Overcoming Common Challenges in Phytopharmacological Research. *J. ethnopharmacology* 246, 112230. doi:10.1016/j.jep.2019.112230

Jing, G.-C., Liu, D., Liu, Y.-Q., and Zhang, M.-R. (2020). Nao-Fu-Cong Ameliorates Diabetic Cognitive Dysfunction by Inhibition of JNK/CHOP/Bcl2-mediated Apoptosis In Vivo and In Vitro. *Chin. J. Nat. medicines* 18, 704–713. doi:10.1016/s1875-5364(20)60009-7

Jing, G.-c., Zhang, M.-r., Ji, C., Zuo, P.-p., Liu, Y.-q., and Gu, B. (2016). Effect of Chinese Herbal Compound Naofucong (脑复聪) on the Inflammatory Process Induced by High Glucose in BV-2 Cells. *Chin. J. Integr. Med.* 22, 832–839. doi:10.1007/s11655-016-2256-0

Kasuya, G., Fujiwara, Y., Takemoto, M., Dohmae, N., Nakada-Nakura, Y., Ishitani, R., et al. (2016). Structural Insights into Divalent Cation Modulations of ATP-Gated P2X Receptor Channels. *Cel Rep.* 14, 932–944. doi:10.1016/j.celrep.2015.12.087

Kıçık, A., Tüzün, E., Erdoğdu, E., Bılgıç, B., Tüfekçıoğlu, Z., Öztürk-Işik, E., et al. (2020). Neuroinflammation Mediators Are Reduced in Sera of Parkinson's Disease Patients with Mild Cognitive Impairment. *Noro psikiyatri arsivi* 57, 15–17.

Liu, J., Li, L., and Suo, W. Z. (2009). HT22 Hippocampal Neuronal Cell Line Possesses Functional Cholinergic Properties. *Life Sci.* 84, 267–271. doi:10.1016/j.lfs.2008.12.008

Maiese, K., Chong, Z. Z., and Shang, Y. C. (2007). Mechanistic Insights into Diabetes Mellitus and Oxidative Stress. *Curr. Med. Chem.* 14, 1729–1738. doi:10.2174/092986707781058968

Masters, S. L., Gerlic, M., Metcalf, D., Preston, S., Pellegrini, M., O'Donnell, J. A., et al. (2012). NLRP1 Inflammasome Activation Induces Pyroptosis of Hematopoietic Progenitor Cells. *Immunity* 37, 1009–1023. doi:10.1016/j.immuni.2012.08.027

Meng, X.-F., Wang, X.-L., Tian, X.-J., Yang, Z.-H., Chu, G.-P., Zhang, J., et al. (2014). Nod-like Receptor Protein 1 Inflammasome Mediates Neuron Injury under High Glucose. *Mol. Neurobiol.* 49, 673–684. doi:10.1007/s12035-013-8551-2

Palta, P., Schneider, A. L. C., Biessels, G. J., Touradji, P., and Hill-Briggs, F. (2014). Magnitude of Cognitive Dysfunction in Adults with Type 2 Diabetes: a Meta-Analysis of Six Cognitive Domains and the Most Frequently Reported Neuropsychological Tests within Domains. *J. Int. Neuropsychol. Soc.* 20, 278–291. doi:10.1017/s1355617713001483

Park, M.-K., Lee, J.-W., Lee, J.-C., Hwang, S.-J., Roh, H. W., Hong, C. H., et al. (2018). NLRP1 and NTN1, Deregulated Blood Differentially Methylated Regions in Mild Cognitive Impairment Patients. *J. Mol. Neurosci.* 66, 561–571. doi:10.1007/s12031-018-1180-5

Romeo, G. R., Lee, J., and Shoelson, S. E. (2012). Metabolic Syndrome, Insulin Resistance, and Roles of Inflammation - Mechanisms and Therapeutic Targets. *Arterioscler Thromb. Vasc. Biol.* 32, 1771–1776. doi:10.1161/atvbaha.111.241869

Singh, L. P., Devi, T. S., and Yumnamcha, T. (2017). The Role of Txnip in Mitophagy Dysregulation and Inflammasome Activation in Diabetic Retinopathy: A New Perspective. *JOJ Ophthalmol.* 4. doi:10.19080/jojo.2017.04.555643

Sperlágh, B., and Illes, P. (2014). P2X7 Receptor: an Emerging Target in Central Nervous System Diseases. *Trends Pharmacological Sciences* 35, 537–547. doi:10.1016/j.tips.2014.08.002

Tan, C.-C., Zhang, J.-G., Tan, M.-S., Chen, H., Meng, D.-W., Jiang, T., et al. (2015). NLRP1 Inflammasome Is Activated in Patients with Medial Temporal Lobe Epilepsy and Contributes to Neuronal Pyroptosis in Amygdala Kindling-Induced Rat Model. *J. neuroinflammation* 12, 18. doi:10.1186/s12974-014-0233-0

Tan, M. S., Tan, L., Jiang, T., Zhu, X. C., Wang, H. F., Jia, C. D., et al. (2014). Amyloid-β Induces NLRP1-dependent Neuronal Pyroptosis in Models of Alzheimer's Disease. *Cel Death Dis.* 5, e1382. doi:10.1038/cddis.2014.348

White, C. S., Lawrence, C. B., Brough, D., and Rivers-Auty, J. (2017). Inflammasomes as Therapeutic Targets for Alzheimer's Disease. *Brain Pathol.* 27, 223–234. doi:10.1111/bpa.12478

Xu, Y., Wang, L., He, J., Bi, Y., Li, M., Wang, T., et al. (2013). Prevalence and Control of Diabetes in Chinese Adults. *Jama* 310, 948–959. doi:10.1001/jama.2013.168118

Zhang, M.-Y., Li, Y., Yin, S.-Y., Kong, L., Liu, X.-L., Yin, X.-X., et al. (2018). Sarsasapogenin Suppresses Aβ Overproduction Induced by High Glucose in HT-22 Cells. *Naunyn-schmiedeberg's Arch. Pharmacol.* 391, 159–168. doi:10.1007/s00210-017-1445-5

Zhang, M. R., Guo, S. S., and Xu, H. Y. (2004). [Study on the Mechanism of Naofucong Granule in Improving Memory of Cerebral Ischemic Mice]. *Zhongguo Zhong Xi Yi Jie He Za Zhi* 24, 147–149.

Conflict of Interest: The authors declare that the research was conducted in the absence of any commercial or financial relationships that could be construed as a potential conflict of interest.

frontiers in Pharmacology

REVIEW
published: 21 June 2021
doi: 10.3389/fphar.2021.696603

The Anti-Obesity Effect of Traditional Chinese Medicine on Lipid Metabolism

Qijing Fan[1], *Furong Xu*[1]*, *Bin Liang*[2]* and *Xiaoju Zou*[1]*

[1]College of Chinese Materia Medica and Yunnan Key Laboratory of Southern Medicinal Utilization, Yunnan University of Chinese Medicine, Kunming, China, [2]Center for Life Sciences, School of Life Sciences, Yunnan University, Kunming, China

With the improvement of living conditions and the popularity of unhealthy eating and living habits, obesity is becoming a global epidemic. Obesity is now recognized as a disease that not only increases the risk of metabolic diseases such as type 2 diabetes (T2D), non-alcoholic fatty liver disease (NAFLD), cardiovascular disease (CVD), and cancer but also negatively affects longevity and the quality of life. The traditional Chinese medicines (TCMs) are highly enriched in bioactive compounds and have been used for the treatment of obesity and obesity-related metabolic diseases over a long period of time. In this review, we selected the most commonly used anti-obesity or anti-hyperlipidemia TCMs and, where known, their major bioactive compounds. We then summarized their multi-target molecular mechanisms, specifically focusing on lipid metabolism, including the modulation of lipid absorption, reduction of lipid synthesis, and increase of lipid decomposition and lipid transportation, as well as the regulation of appetite. This review produces a current and comprehensive understanding of integrative and systematic mechanisms for the use of TCMs for anti-obesity. We also advocate taking advantage of TCMs as another therapy for interventions on obesity-related diseases, as well as stressing the fact that more is needed to be done, scientifically, to determine the active compounds and modes of action of the TCMs.

Keywords: traditional Chinese medicines, obesity-related metabolic diseases, anti-obesity effect, lipid metabolism, mechanisms

OPEN ACCESS

Edited by:
Marcello Locatelli,
University of Studies G. d'Annunzio Chieti and Pescara, Italy

Reviewed by:
Carmine Finelli,
Ospedale Cav. R. Apicella–ASL Napoli 3 Sud, Italy
Giovanni Tarantino,
University of Naples Federico II, Italy

***Correspondence:**
Furong Xu
fxrong99@163.com
Bin Liang
liangb73@yun.edu.cn
Xiaoju Zou
xiaojuzou@163.com

Specialty section:
This article was submitted to Ethnopharmacology, a section of the journal Frontiers in Pharmacology

Received: *17 April 2021*
Accepted: *01 June 2021*
Published: *21 June 2021*

Citation:
Fan Q, Xu F, Liang B and Zou X (2021) The Anti-Obesity Effect of Traditional Chinese Medicine on Lipid Metabolism. Front. Pharmacol. 12:696603. doi: 10.3389/fphar.2021.696603

INTRODUCTION

The state of being overweight and obesity are defined as the abnormal or excessive accumulation of fat, mostly in the form of triacylglycerols (TAGs) and cholesterol esters (CEs) in adipose and non-adipose tissues or organs. The World Health Organization (WHO) classification uses body mass index (BMI) to define overweight as being 25–29.9 kg/m^2 and obesity as being ≥30 kg/m^2 (https://www.who.int/topics/obesity/zh/). Along with an increasing accessibility to food and the popularity of unhealthy lifestyles, obesity is becoming a global epidemic and its metabolic consequences are currently among the most pressing public health challenges (Hossain et al., 2007). The primary consequence of obesity is associated with an increased mortality and a susceptibility to comorbidities, with few viable therapeutic interventions being available. Today, obesity is increasingly gaining attention due to its intimate association with a growing list of diseases beyond T2D, NAFLD, cancers (Stoll, 1998; Arem and Irwin, 2013; Seo et al., 2015; Incio et al., 2018), and CVD (Lazo and Clark, 2008; Zhao et al., 2019), such as atherosclerosis (AS) (Rocha and Libby, 2009; Aboonabi et al., 2019). Meanwhile, obesity also has a substantial impact on the quality of life. Obesity is usually

associated with a lower health-related quality of life than those possessing a normal weight (Pinhas-Hamiel et al., 2006). In children and adolescents, obesity is usually associated with sedentary lifestyles, lower levels of self-esteem, social exclusion, poor educational achievements, and so on (de Beer et al., 2007; Wille et al., 2008). In addition, global health costs associated with obesity and its complications are estimated to be ~US$2 trillion (Dobbs et al., 2014). If the prevalence of obesity continues on its rising trend, almost half of the world's adult population could be overweight or obese by 2030, imposing even greater personal, social, and economic costs (https://www.mckinsey.com/industries/healthcare-systems-and-services).

Effectively combating obesity around the world may require a comprehensive strategy involving multiple interventions (Dobbs et al., 2014). Management of obesity is aimed at weight loss, which improves the quality of life. Studies have shown that weight loss after treatment was associated with varying degrees of improvement in obesity-related psychosocial problems, physical functioning, physical role functioning, bodily pain, general health, mental health, and vitality (Kaukua et al., 2003; Pearl et al., 2018). To lose weight, lifestyle interventions, dietary changes, and physical activity are the first-line approaches, followed by medical treatment and bariatric surgery. Thus far, several drugs have been approved for weight loss, such as orlistat, liraglutide, lorcaserin, and diethylpropion (Solas et al., 2016; Gadde et al., 2018). However, in addition to the considerable financial cost of these drugs, numerous side effects have been increasingly reported, such as headache, dizziness, fatigue, nausea, dry mouth, insomnia, anxiety, and constipation (Smith et al., 2010; Aronne et al., 2013; Pi-Sunyer et al., 2015; Nissen et al., 2016; Solas et al., 2016; Gadde et al., 2018).

The pathogenesis of obesity is complex and determined by the interaction of genetic, environmental, and psychosocial factors acting through several physiological mediators (González-Muniesa et al., 2017). Many studies have reported that lipid metabolic pathways are a potential therapeutic target to prevent or delay the occurrence and progression of obesity and obesity-related metabolic diseases, as the major physiological factor in these diseases is the disturbance of lipid metabolism, such as a dysfunction in lipid absorption, lipid synthesis, lipid decomposition, and/or lipid transportation (Meikle and Summers, 2017). Compared with the modern drugs mentioned above, TCMs have been widely used to treat obesity for a very long time. This fact alone suggests that TCMs may be used as a vast resource for the development of natural anti-obesity drugs possessing fewer side effects (Li et al., 2017; Martel et al., 2017; Zhang Y. et al., 2018; Zhang et al., 2020; Ji-Ping et al., 2021). While some of the anti-obesity effects and mechanisms of TCMs have been studied in the past decade, most of these studies only focused on single/several genes or signaling pathways involved in lipid metabolism. Our goal in this review is to collate these data and give a systematic and comprehensive overview of the anti-obesity effects and mechanisms of TCMs and their major ingredients by targeting lipid metabolism.

THE TRADITIONAL CHINESE MEDICINES WITH ANTI-OBESITY EFFECTS

The diverse evolution of plants represents a near inexhaustible source of biologically active compounds. The importance of these natural products for medicine and health has been immense (Courdavault et al., 2020). For many years, scientists have been researching and applying natural, plant-derived preparations as medicine in clinical treatment. Through these actions, active compounds such as strychnine and brucine (Langley, 1918), quinine (Dickson, 1823), colchicine (1890), caffeine (Bennett, 1873), and artemisinin (Ma et al., 2020) have been discovered. Thus, natural products provide important clues to the identification and development of synergistic drugs.

TCM refers to substances used for the prevention, diagnosis, and treatment of diseases, as well as for rehabilitation and health care under the guidance of TCM theories. It may be the best resource for the use of natural products, and it represents the accumulated experiences of thousands of years of medical practice. The written records of TCM date back at least 2,000 years to *Shen Nong's Classic of Materia Medica*. In the long history of China, TCM has made an indelible contribution to the health of the Chinese people. Moreover, based on 2,000 years of experience in the use of TCMs and modern scientific research, the eleventh edition of the *Pharmacopoeia of the People's Republic of China (ChP)* was promulgated and implemented in 2020. In this volume, the *ChP* stipulated the processing, usage, dosage, and compatibility of TCMs and included many classic prescriptions (Chinese Pharmacopoeia Commission).

Notably, in recent decades, there has been a growing interest in TCM. Since 1973, there have been 2,104 articles related to "traditional Chinese medicine" AND "lipid metabolism" in PubMed, while in 2020 alone, there were 389 articles (PubMed, https://pubmed.ncbi.nlm.nih.gov, last accessed on March 31, 2021). And 35 individual prescriptions from the *ChP (2020 edition)* were identified, each of which is clearly indicated as being anti-obesity and anti-hyperlipidemia (**Table 1**). Based on the formulation of these 35 prescriptions, we searched the Latin name of each single TCM for "anti-obesity" OR "anti-hyperlipidemia" in PubMed and CNKI in recent decades. Five TCMs including *Crataegus pinnatifida* Bunge, *Salvia miltiorrhiza* Bunge, *Polygonum multiflorum* Thunb., *Alisma plantago-aquatica* L., and *Panax notoginseng* (Burkill) F.H. Chen were identified. Each of these plants was implicated not only to function in anti-obesity and anti-hyperlipidemia but also to be mechanistically associated with these processes. Also, based on the widespread use of edible TCMs among people, some medicinal plants appear in diets. We also reviewed commonly used edible TCMs possessing the effects of anti-obesity and anti-hyperlipidemia including *Scutellaria baicalensis* Georgi, *Curcuma longa* L., pu-erh tea, green tea, *Tripterygium wilfordii* Hook. f., chilli peppers, and grape and the main bioactive compounds from them, such as baicalin, curcumin, epigallocatechin gallate, green tea polyphenol, triptolide and celastrol, capsaicin, and resveratrol (Sham et al., 2014; Wang S., et al., 2014; Martel et al., 2017).

TABLE 1 | TCM anti-obesity formulations from the *Pharmacopoeia of the People's Republic of China (ChP) (2020 edition)*.

TCM formulation of anti-obesity and anti-hyperlipidemia		
Dahuang zhechong wan	Liuweidihuang wan	Xuezhikang pian
Danxiang qingzhi keli	Renshen shouwu jiaonang	Xuezhiling pian
Danlou pian	Shanlücha jiangya pian	Xuezhining wan
Dingkun dan	Sangge jiangzhi wan	Xiaokeping pian
Fangfeng tongsheng keli	Songling xuemaikang jiaonang	Yangxinshi pian
Guizhi fuling wan	Shouwu wan	Yindan xinnaotong ruanjiaonang
Hedan pian	Tongxinluo jiaonang	Yixintong pian
Huoxue tongmai pian	Xin'anning pian	Yinxingye jiaonang
Jinshuibao pian	Xinkeshu pian	Zhikang keli
Jiangzhiling pian	Xinxuening pian	Zhimaikang jiaonang
Jiangzhi tongluo ruanjiaonang	Xinyuan jiaonang	Zhengxin jiangzhi pian
Liujunzi wan	Xuefu zhuyu jiaonang	

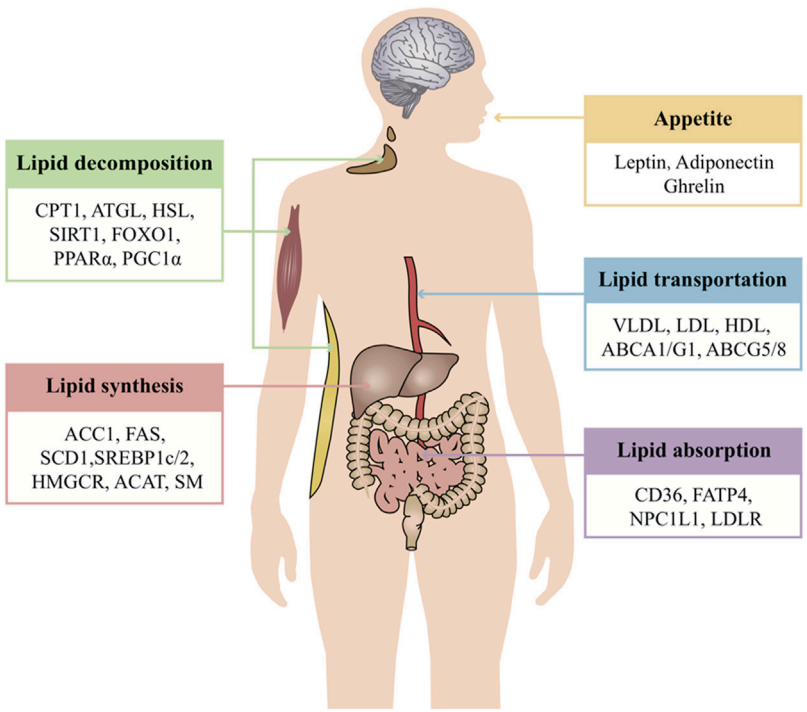

FIGURE 1 | Overview of systematic regulated lipid metabolism of TCMs. TCM treatment of obesity mainly regulates lipid metabolism from five aspects: appetite, lipid absorption, lipid synthesis, lipid decomposition, and lipid transportation. Each link intersects and regulates each other to maintain the stability of the internal environment. One of the advantages of TCM is that it can act on multiple aspects and targets at the same time and systematically regulate life activities. Appetite is regulated by the level of leptin, adiponectin, ghrelin, and so on. These hormones serve as a critical signal to regulate food intake. The small intestine absorbs lipids derived exogenously from the diet. Dietary fat comprises a variety of lipids, while lipids synthesized in the liver are packaged in very low–density lipoproteins and delivered to adipose tissue for storage. CD36, FATP, NPC1L1, and LDLR are the classic regulators of lipid absorption. Apart from lipid absorption, excessive lipid synthesis is another cause of obesity. Some enzymes of lipid synthesis are the key to disease treatment, such as ACC, FAS, SCD, HMGCR, SM, and ACAT. These enzymes may also be regulated by the transcription factors SREBP and LXR. Cytoplasmic lipolysis and lysosomal-mediated autophagy (lipophagy) are two pathways that are known to break down TAGs and CEs in lipid droplets. In this process, ATGL, HSL, and MGL break down TAGs into free fatty acids which then undergo oxidative decomposition in the mitochondria via CPT1 to provide energy. The activity of these enzymes may also be controlled by SIRT1, FOXO1, and PGC1α. Lipoproteins are the major carriers of lipids in circulation. The major forms of lipoproteins are chylomicrons, VLDL, IDL, LDL, and HDL. The lipoproteins are responsible for transportation of FAs and cholesterol. Furthermore, the transportation of cholesterol to the extracellular environment is controlled by ABCA1, ABCG1, and ABCG5/8.

TARGETING LIPID METABOLISM WITH BIOACTIVE COMPOUNDS FROM TCMS WITH ANTI-OBESITY EFFECTS

Over many years of observation and research, it has been found that TCMs can regulate all steps of lipid metabolism, targeting multiple pathways, including the modulation of lipid absorption, reduction of lipid synthesis, and increase of lipid decomposition and lipid transportation, as well as the physiological process of appetite regulation (**Figure 1**). The following is a systematic and comprehensive review of the anti-obesity effect of TCMs by targeting the above-mentioned lipid metabolism.

Regulation of Appetite

Feelings of hunger and satiety are regulated by complex neural and endocrine interactions among the gut, brain, adipose tissues, and other organs. As early as the 1960s, leptin was identified as a hormone linked to obesity. Leptin is secreted by adipose tissue and regulates appetite through inhibiting orexigenic neurons while stimulating anorexigenic pro-opiomelanocortin neurons (Friedman, 1997; Elias et al., 1999). Another hormone, ghrelin, which is released by the gastrointestinal tract when the stomach is empty, induces hunger by acting on hypothalamic brain cells in the central nervous system (CNS) (Ahima and Antwi, 2008). Moreover, the protein hormone adiponectin is secreted by adipocytes and circulates in the plasma. In contrast to leptin, adiponectin is reduced in obesity and increased in response to fasting. Adiponectin deficiency induces insulin resistance (IR) and hyperlipidemia and is associated with increased susceptibility toward vascular injury and atherosclerosis (Kadowaki et al., 2008).

Discovery of leptin brought hopes for treatment of obesity. Data from both humans and animals have established that the leptin level increases and is positively correlated with fat mass, thereby suppressing appetite. Conversely, weight loss leads to a decrease in the leptin level and produces a consequent increase in food intake (Campfield et al., 1995; Halaas et al., 1995; Pelleymounter et al., 1995; Montague et al., 1997; Licinio et al., 2004; Farooqi et al., 2007). Adiponectin levels decrease in obesity. Adiponectin enhances AMPK activity in the arcuate hypothalamus (ARH) *via* its receptor AdipoR1 to stimulate food intake; this stimulation of appetite by adiponectin is attenuated by the dominant-negative AMPK expression in the ARH (Kubota et al., 2007). Ghrelin levels increase during food deprivation in animals and prior to meals in humans and may serve as a critical signal to induce hunger during fasting (Ahima and Antwi, 2008).

As mentioned, TCMs can affect multiple steps in these hormone signaling pathways. *Salvia miltiorrhiza* Bunge can significantly inhibit the appetite and body weight by increasing the sensitivity to leptin and inhibiting ghrelin activity (Xin-Min et al., 2010; Tung et al., 2017). A high-fat diet (HFD) can increase the serum levels of leptin, insulin, and glucose. *Polygonum multiflorum* Thunb. could reverse these changes (Choi et al., 2018). Administration of *Panax notoginseng* (Burkill) F.H. Chen saponins (PNSs) for 30 days resulted in a significant decrease in serum insulin, leptin, body weight, food intake, and serum triglyceride (TG) levels compared with a diabetic control group (Yang et al., 2010). *Curcuma longa* L. may contribute to decreasing body weight and regulating leptin secretion in animals (Song and Choi, 2016) and humans (Navekar et al., 2017). Baicalin, a flavonoid of the herbal medicine *Scutellaria baicalensis* Georgi, also increased the plasma leptin level vs. the diabetic control (Waisundara et al., 2009). Finally, rats fed with fructose/green tea and fructose/pu-erh tea showed the greatest reduction in serum TG, cholesterol, insulin, and leptin levels (Huang and Lin, 2012). Consistent with obesity induction, adiponectin levels were reduced in HFD-fed mice and adiponectin levels were restored after green tea treatment in the wild type (WT) (Bolin et al., 2020). The green tea polyphenols also have the same curative effect (Tian et al., 2013).

Capsaicin is the molecule that is responsible for the pungency of hot peppers. It functions by stimulating the sympathoadrenal system that mediates the thermogenic and anorexigenic effects of capsaicinoids. Capsaicin treatment in mice fed on an HFD for 10 weeks lowered obesity, fasting glucose, insulin, leptin, and hepatic TGs while increasing adiponectin mRNA/protein in the adipose tissue. Furthermore, capsaicin increased GLP1 and decreased ghrelin secretion, indicating a possible interaction between transient receptor potential cation channel subfamily V member 1 (TrpV1) and GLP1 (Smeets and Westerterp-Plantenga, 2009; Kang et al., 2010). Also, leptin levels in the plasma were significantly lower in resveratrol-treated animals (Jimoh et al., 2018; Yu et al., 2019) and humans (Timmers et al., 2011). Celastrol, a compound of *Tripterygium wilfordii* Hook. f., is a leptin sensitizer (Xu et al., 2021). It can suppress appetite, block the reduction of energy expenditures, and lead up to a 45% weight loss in hyperleptinemic diet–induced obese mice by increasing leptin sensitivity (Liu et al., 2015). Celastrol, an NF-κB inhibitor, reduced IR and lipid abnormalities and led to higher plasma adiponectin levels in the *db/db* mice with celastrol treatment for 2 months (Kim et al., 2013).

Regulation of Lipid Uptake From the Intestine

The small intestine absorbs lipids derived exogenously from the diet including non-polar lipids, predominantly TAGs and CEs, and polar PLs. Dietary lipids such as TAGs, CEs, and PLs along with endogenous lipids from the bile are completely digested by pancreatic enzymes in the intestinal lumen, producing fatty acids (FAs), monoacylglycerols (MAGs), cholesterol, and lysophospholipids (Ko et al., 2020). The uptake of FAs and MAGs can be driven by the concentration gradient or facilitated by other proteins such as cluster of differentiation 36 (CD36) and fatty acid transport protein 4 (FATP4). Cholesterol uptake is mediated by Niemann–Pick C1-like 1 (NPC1L1). The TCMs can regulate lipid(s) uptake from the intestine (**Figure 2**).

Regulation of Uptake of FAs

FAs in the liver originate from the diet, *de novo* lipogenesis (DNL), and recycling of FAs released from adipose tissue during fasting (Mashek, 2013). FAs are taken in the intestinal lumen into enterocytes by two distinct mechanisms. In the first process, FAs

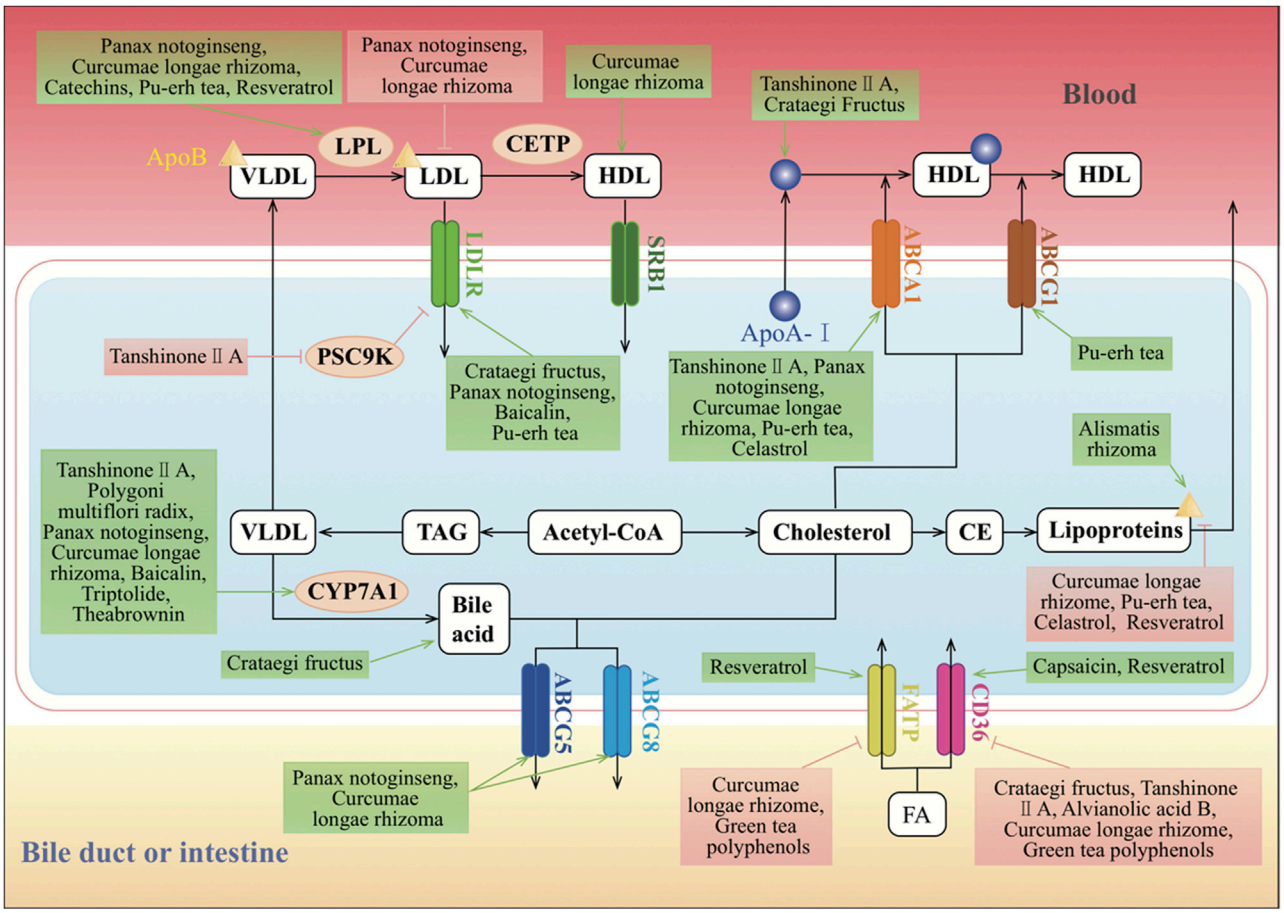

FIGURE 2 | Molecular mechanisms of TCMs in lipid absorption and transportation. CD36, FATP, and LDLR are the classic regulators of lipid absorption. CD36 and FATP mediate the absorption of FA, and LDLR mediates the absorption of LDL. SR-BI can mediate the selective absorption of CE, which plays an important role in HDL metabolism and cholesterol "reversal." Cholesterol is synthesized from acetyl-CoA. Excess cholesterol in hepatic cells is exported to the blood by ABCA1 or the homodimer of ABCG1, or to the intestinal lumen and bile ducts by the ABCG5 and ABCG8 heterodimers. Cholesterol can also be converted to CE by ACAT for storage in lipid droplets or for secretion as lipoproteins. The major forms of lipoproteins are chylomicrons, VLDL, IDL, LDL, and HDL, and they differ in their size, density, composition, and functions. CYP7A1 converts cholesterol into bile acids in the reverse cholesterol transport pathway. In the endogenous pathway, the liver produces VLDL, which interacts with LPL in the circulation to form IDL, with the release of TG and FAs. IDL is rapidly removed by the liver *via* the interaction of its apolipoprotein E component with LDLR. Furthermore, IDL forms LDL upon removal of TG by hepatic lipase. CETP induces LDL to generate HDL, which is an anti-atherogenic lipoprotein or "good cholesterol," as it captures the cholesterol from peripheral tissues or other lipoproteins and transports it back to the liver by the third pathway, which is termed reverse cholesterol transport. ↑/⊥ depicts the positive or negative effect of TCMs in the cellular process, respectively.

diffuse passively through the apical membrane when luminal concentrations are higher than those inside the cell. The other mechanism of FA uptake is saturable and probably protein dependent as this transport occurs when the intracellular FA concentration is higher than that in the lumen.

Tanshinone ⅡA could decrease oxidized low-density lipoprotein (oxLDL)-induced expression of lectin-like oxidized LDL receptor-1 (LOX-1) and CD36 (Wen et al., 2020). And salvianolic acid B inhibited macrophage uptake of modified LDL in a scavenger receptor CD36–dependent manner (Bao et al., 2012). *Curcuma longa* L. suppressed the expression levels of CD36 and FATP, which were increased in HFD groups (Mun et al., 2019). Curcumin, a yellow-colored hydrophobic polyphenol, is the principal curcuminoid of the spice turmeric, the ground rhizome of *Curcuma longa L.*. Curcumin could also downregulate the mRNA level of *Cd36* during adipocyte differentiation of 3T3-L1 cells (Zhao et al., 2011). CD36 mRNA and protein levels were decreased in high-fructose diet–induced rats when treated with green tea polyphenol (Qin et al., 2010). Epigallocatechin gallate (EGCG), a green tea bioactive polyphenol, also dose-dependently reversed HFD-induced effects on intestinal substrate transporters CD36, FATP4, and sodium-dependent glucose transporter 1 (Friedrich et al., 2012). In contrast, capsaicin or capsinoids could upregulate the expression of CD36 (Hong et al., 2015).

Regulation of Cholesterol Uptake

Classical cholesterol metabolism studies have confirmed that there are two main sources of cholesterol in the human body: exogenous cholesterol from the diet absorbed in the intestine and

reabsorbed in the bile and endogenous cholesterol obtained through *de novo* synthesis from acetyl-CoA by the liver and peripheral tissue.

Exogenous cholesterol enters the enterocytes through NPC1L1 and the associated flotillins present on the apical surface of these cells. Curcumin could lower plasma cholesterol and prevent diet-induced hypercholesterolemia through modulating intestinal NPC1L1 expression *via* transcriptional regulation and the involvement of the sterol regulatory element–binding protein 2 (SREBP2) transcription factor (Kumar et al., 2011). In addition to NPC1L1-mediated cholesterol absorption from the intestinal lumen, another pathway is LDL receptor (LDLR)-mediated uptake of cholesterol containing LDL particles (LDL-c) from the blood. LDL in the blood is captured by LDLR on the cell surface and internalized, and as the endosomal pH decreases, LDLR dissociates from LDL and is recycled back to the surface for additional uptake. LDL is further delivered to lysosomes, and the carried cholesteryl esters (CEs) are hydrolyzed to cholesterol.

Tanshinone IIA and *Crataegus pinnatifida* Bunge can regulate the expressions of LDLR in the liver (Hu et al., 2016; Jia et al., 2016b). The *Ldlr* mRNA level was significantly higher in rats by treatment with an *n*-butanol extract (NE3) of *Panax notoginseng* (Burkill) F.H. Chen (Ji and Gong, 2007). The *Scutellaria baicalensis* Georgi extract also activated *Ldlr* genes in the liver. Co-administration of this extract with baicalin and metformin exerted a better effect on obesity-induced IR and lipid metabolism in a rat model system than treatment with metformin alone (Han et al., 2017). Also, proprotein convertase subtilisin/kexin type 9 (PCSK9), a negative regulator of LDLR, is also an SREBP2 target. Tanshinone IIA treatment inhibited the expression of PCSK9 and concomitantly increased LDLR activity (Chen et al., 2016).

Regulation of Gut Microbiota

The community of microorganisms living in the gastrointestinal tract in animals and humans has been shown to participate in various physiological and pathological processes in the gut and many other bodily processes. The link between the microbes in the human gut and the development of obesity and obesity-related diseases is becoming clearer. Studies have shown differences in the gut microbiota between obese individuals and lean individuals. Obesity and the associated metabolic syndromes are associated with microbiota alterations, including an increase in the ratio of Firmicutes to Bacteroidetes and in the relative abundance of Proteobacteria as well as alterations in specific bacteria such as *Lactobacillus* and *Clostridium* (Ley et al., 2005; Turnbaugh et al., 2006; Fei and Zhao, 2013; Cortés-Martín et al., 2020). There are also a reduced bacterial diversity and altered representations of bacterial genes and metabolic pathways (Turnbaugh et al., 2009; Wu et al., 2021).

Studies on both mice and humans show effects of gut microbiota on lipid metabolism by improving energy extraction from food, which is considered an environmental factor contributing to obesity and its comorbidities (Santacruz et al., 2009; Ridaura et al., 2013). Compared to lean mice, the gut microbiota of the obese mice have an increased capacity to harvest energy from the diet (Turnbaugh et al., 2006). Moreover, when compared with conventional mice, germ-free mice were able to resist obesity on a high-fat, high-carbohydrate Western diet, which could be explained by their intake of fewer calories, increased lipid excretion in the feces, and increased lipid oxidation in the intestine and peripheral tissues (Bäckhed et al., 2007; Rabot et al., 2010). In an observational study using fecal microbiota transplantation, the transplantation of feces from twins discordant for obesity into germ-free mice in a diet-dependent manner demonstrated transmissible, rapid, and modifiable effects of diet-by-microbiota interactions (Ridaura et al., 2013).

Many studies have emerged suggesting that the therapeutic potential of TCMs and their bioactive compounds may be due to the interaction with gut microbiota. Theabrownin, one of the most active and abundant pigments in pu-erh tea, altered the gut microbiota in both mice and humans and increased the levels of ileal conjugated bile acids by predominantly suppressing microbes associated with bile-salt hydrolase (BSH) activity. This in turn inhibited the intestinal farnesoid X receptor (FXR)–fibroblast growth factor 15 (FGF15) signaling pathway that increased hepatic production and fecal excretion of bile acids, thereby reducing hepatic cholesterol and decreasing lipogenesis (Huang et al., 2019). Green tea polyphenols decreased the relative abundance of Bacteroidetes and Fusobacteria and increased the relative abundance of Firmicutes as revealed by 16S rRNA gene sequencing analysis in canines with HFD-induced obesity (Li et al., 2020). The gut microbiota played an important role in the anti-obesity effects of celastrol, in which it promoted energy expenditure at a dose of 500 μg/kg body weight and improved the diversity of the gut microbiota with an increased ratio of Bacteroidetes to Firmicutes (Hu et al., 2020). Capsaicin has an anti-obesity effect through alterations in gut microbiota populations and short-chain FA concentrations, which were beneficial in prevention and treatment of obesity (Song et al., 2017; Rosca et al., 2020; Wang Y. et al., 2020). Resveratrol-induced gut microbiota modulated lipid metabolism, stimulated the development of beige adipocytes in white adipose tissue, reduced inflammation, and improved intestinal barrier function in HFD-fed mice. Therefore, the anti-obesity benefits of resveratrol might be through the "gut microbiota–adipose tissue" axis (Wang P, et al., 2020; Zhou et al., 2019).

Regulation of Lipid Transportation

Lipoproteins are the major carriers of lipids in circulation and participate in three major pathways that are responsible for the generation and transport of lipids within the body. The two major forms of circulating lipids in the body, TG and cholesterol, are packaged with apolipoproteins and PLs to form lipoproteins. The major forms of lipoproteins are chylomicrons, very low–density lipoprotein (VLDL), intermediate-density lipoprotein (IDL), low-density lipoprotein (LDL), and high-density lipoprotein (HDL), which differ in their size, density, composition, and functions.

In the exogenous pathway, dietary lipids, which mainly consist of TGs and some PLs, free FAs, and cholesterol, are packaged into chylomicrons by intestinal mucosal cells. These chylomicrons enter the lymphatic system and then the circulation, where TGs are released as free FAs by lipoprotein lipase (LPL) activity on the

capillary endothelium. These free FAs are taken up by the muscle, adipose, and other peripheral tissues, whereas the remnants of chylomicrons are cleared by the liver. In the endogenous pathway, the liver produces VLDL, which interacts with LPL in the circulation to form IDL, with the release of TGs and free FAs. IDL is rapidly removed by the liver *via* the interaction of its apolipoprotein E component with LDLR. Furthermore, IDL forms LDL upon removal of TGs by hepatic lipase (HL). LDL, which is very high in cholesterol content, is in turn removed from the circulation by binding to LDLR in the liver and in extrahepatic tissues. HDL is an anti-atherogenic lipoprotein or "good cholesterol," as it captures the cholesterol from peripheral tissues or other lipoproteins and transports it back to the liver by the third pathway, which is termed reverse cholesterol transport (Luo et al., 2020) (**Figure 2**).

Regulation of Lipoprotein Uptake

The liver has a role in the regulation of systemic lipid metabolism as it assembles and secretes TAG-rich VLDL particles into the systemic circulation for distribution of FAs to the peripheral tissues. Surface LDLR captures the circulating LDL *via* the extracellular ligand–binding domain. Many results suggest that green tea polyphenols inhibit the ubiquitin/proteasome-mediated upregulation of LDLR. This identified molecular mechanism might be related to the previously reported cholesterol-lowering and heart disease–preventative effects of green tea polyphenols (Kuhn et al., 2004). Trans-resveratrol exhibited the anti-atherogenic effect, at least, in part, by increased hepatic LDLR expression *via* proteolytic activation of SREBPs and subsequent LDL uptake (Yashiro et al., 2012).

By contrast, HDLs are generated by the intestine and the liver through the secretion of lipid-free apolipoprotein A-I (ApoA-I). ApoA-I then recruits cholesterol from these organs through the actions of ATP-binding cassette transporter A1 (ABCA1), forming nascent HDLs. In the peripheral tissues, nascent HDLs promote the efflux of cholesterol from tissues, including from macrophages, through the actions of ABCA1. Mature HDLs also promote this efflux, but through the actions of ATP-binding cassette transporter G (ABCA) 1. Tanshinone ⅡA reduced the lipid deposition in the liver. Moreover, it did not affect the serum lipid levels but reduced the levels of HDL middle subfractions and increased the levels of HDL large subfractions (Jia et al., 2016b). Treatment of THP-1 macrophages with baicalin significantly accelerated HDL-mediated but not ApoA-I–mediated cholesterol efflux. However, baicalin treatment increased the expression of scavenger receptor class B type I (SR-BI) in a dose- and time-dependent manner. Furthermore, baicalin increased the expression of peroxisome proliferator–activated receptor (PPAR) γ, a key regulator of reverse cholesterol transport, and liver X receptor (LXR) α (Yu et al., 2016). Administration of *Curcuma longa* L. significantly decreased the serum LDL and ApoB but increased the serum HDL and ApoA of healthy subjects (Ramirez-Bosca et al., 2000). Resveratrol treatment after 6 months decreased LDL-c, ApoB, oxLDL, and oxLDL/ApoB on statin-treated patients in primary cardiovascular disease prevention (Tome-Carneiro et al., 2012). The LPL was increased significantly in muscular tissues and decreased in adipose tissues by treatment with *Crataegus pinnatifida* Bunge flavonoids in mice (Fan et al., 2006). Finally, PNSs could also upregulate the mRNA expression of *Lpl* (Wang et al., 2016).

Regulation of Cholesterol Efflux

Cholesterol export from cells is mediated by ATP-binding cassette transporters. ABCA1 is expressed on the plasma membrane of most cells, including the basolateral surface of enterocytes. ABCG1 is most abundantly expressed on the surface of macrophages, whereas ABCG5 and ABCG8 are expressed at the apical surface of enterocytes and hepatocytes, forming a heterodimer. Excess cholesterol is esterified by acyl coenzyme A–cholesterol acyltransferases (ACATs). ABCA1 mediates cholesterol transport to ApoA-I in the blood, and this generates a nascent HDL that serves as an acceptor for ABCG1-mediated cholesterol efflux, leading to the production of HDL.

Tanshinone IIA treatment suppressed the expression of *miR-33a*, an ABCA1 negative regulator, whereas it upregulated the expression levels of ABCA1, SREBP2, PCSK9, cholesterol 7α-hydroxylase (CYP7A1), CD36, and LDLR in hyperlipidemic rats (Jia et al., 2016a; Jia et al., 2016b). The expression of PPARα and ApoA-Ⅰ was significantly downregulated in the hyperlipidemia group with tanshinone IIA treatment (Yi-Xin et al., 2017). A high dose of *Crataegus pinnatifida* Bunge increased the expressions of ApoA-I gene and HDL-c in HFD-fed mice (Shih et al., 2013). In addition, curcumin increased cholesterol efflux by activating and upregulating the expression of LXR and ABCA1 in subcutaneous adipocytes isolated from rabbits (Dong et al., 2011). The *Curcuma longa* L. oil treatment significantly increased the hepatic expression of PPARα, LXRα, CYP7A1, ABCA1, ABCG5, ABCG8, and LPL accompanied by a reduced SREBP2 and 3-hydroxy-3-methylglutaryl coenzyme A reductase (HMGCR) expression. *Curcuma longa* L. oil treatment also suppressed NPC1L1 expression in the jejunum compared with high-cholesterol diets (Singh et al., 2013). The expression of the reverse cholesterol transporters ABCA1 and ABCG1 was highly expressed in the livers of mice on pu-erh tea intervention (Huang et al., 2019). Furthermore, apolipoprotein B100 (ApoB100) is a constitutive protein of LDL-c, and it was significantly downregulated by pu-erh tea extract (PTE) treatment (Hu et al., 2017).

Cholesterol and sitosterol can be exported by the ABCG5–ABCG8 heterodimers to the intestinal lumen and bile, where cholesterol is extracted by bile salts. Re-synthesis of cholesterol induces pathways for cholesterol export and storage and acts to suppress further cholesterol biosynthesis. When treated with NE3, the concentrations of serum TC, TG, and LDL-c in rats showed a significant dose-dependent decrease. Expression level analysis indicated that both LXR targeting genes including ABCA1, ABCG5, and ABCG8 and FXR targeting genes including ApoC2 and a short heterodimer partner were significantly induced by NE3 (Ji and Gong, 2007). In addition, CE combines with ApoB to form lipoproteins, which are transported outside the cell by

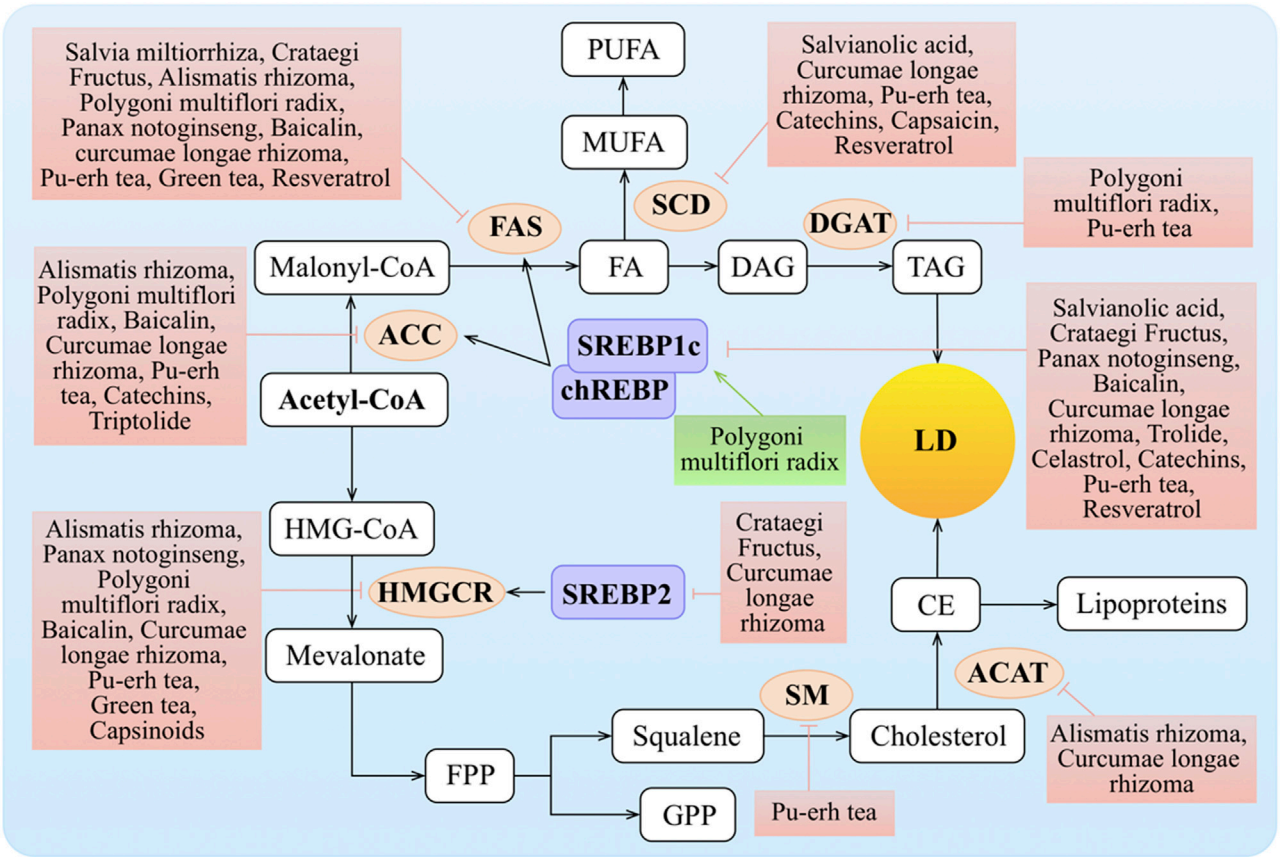

FIGURE 3 | Molecular mechanisms of TCMs in lipid synthesis. FA entering the hepatocyte is rapidly "activated" by acyl-CoA, and this is also termed the *de novo* lipogenesis (DNL) of FA. DNL is mainly regulated *via* the rate-limiting enzymes such as ACC and FAS, while the expression and activation of ACC and FAS are regulated by SREBP1c and chREBP. Transcription of the genes encoding SREBP1c and chREBP is stimulated by insulin *via* LXR and inhibited by FAs. The synthesis of MUFA regulates by SCD. FAs are typically esterified to TG and subsequently packaged into VLDL for export or stored as intracellular LDs. HMGCR and SM as the rate-limiting enzymes are key regulators of the synthesis process of cholesterol. Cholesterol can be converted to CE by ACAT for storage in LDs or for secretion as lipoproteins. Meanwhile, SREBP2 can increase the level of HMGCR. ↑/⊥ depicts the positive or negative effect of TCMs in the cellular process, respectively.

exocytosis. *Curcuma longa* L., resveratrol, and PTE could significantly decrease the level of ApoB (Ramirez-Bosca et al., 2000; Tome-Carneiro et al., 2012; Hu et al., 2017). Celastrol was able to effectively suppress weight and attenuate high-fat–mediated oxidative injury by improving ABCA1 expression, reducing the levels of TC, TG, LDL-c, and ApoB in the plasma, and increasing antioxidant enzyme activities and inhibiting nicotinamide adenine dinucleotide phosphate (NADPH) oxidase activity (Wang C. et al., 2014).

Furthermore, CYP7A1 regulates the balance between cholesterol supply and metabolism by catalyzing the rate-limiting step of bile acid biosynthesis. *Scutellaria baicalensis* Georgi activated the *Cyp7a1* gene in the liver (Han et al., 2017). *Crataegus pinnatifida* Bunge could counteract the downregulation of CYP7A1 and LDLR with the stimulation effect of HFD (Hu et al., 2016). And NE3 significantly decreased the expression level of the *Cyp7a1* gene (Ji and Gong, 2007). In contrast, the expression of *Cyp7a1* was markedly increased in the triptolide-treated group (Yang et al., 2017).

Regulation of Lipid Synthesis

Excessive lipid synthesis is another cause of obesity and hyperlipidemia. Lipids synthesized in the liver are packaged in very low–density lipoproteins (VLDLs) and delivered to adipose tissue for storage. Clearly, TCMs play important roles in lipid synthesis, including FA and TAG synthesis as well as cholesterol biosynthesis (**Figure 3**).

Regulation of Fatty Acid Synthesis

The DNL of FAs from acetyl-CoA to fatty acyl-CoA is mainly regulated by acetyl-CoA carboxylase (ACC) and fatty acid synthase (FAS) as the rate-limiting enzymes. Stearoyl-CoA desaturase (SCD) is a central enzymatic node in the conversion of saturated fatty acids (SFAs) into mono-unsaturated fatty acids (MUFAs) (AM et al., 2017). MUFAs represent the precursors of several lipids essential for plasma membranes, such as TGs, CEs, diacylglycerols, and wax esters. Transcriptional regulation of *Acc* and *Fas* is primarily through SREBP1c and carbohydrate-responsive element–binding protein (chREBP). SCD expression is regulated by diverse hormonal and

nutritional factors and is positively regulated by *Srebp1c*, *chrebp*, and *Lxr* (Wang Y., et al., 2015). Both transcription factors are activated by *Lxr*.

Salvianolic acids, the major water-soluble ingredients of *Salvia miltiorrhiza* Bunge, reduced ovariectomy-induced body weight gain, attenuated the expressions of hepatic lipogenic genes, such as *Srebp1*, *Fas*, and *Scd*, and decreased the TG and TC *via* blocking signal transducer and activator of transcription (STAT)-3/SREBP1 signaling (Chen et al., 2018). The hepatic *Fas* and *Srebp1c* mRNA levels were reduced in mice fed on the *Crataegus pinnatifida* Bunge diet compared to the standard diet (Zhang et al., 2014). The levels of FAS and ACC in the plasma were generally reduced after administration of *Polygonum multiflorum* Thunb. (Xian et al., 2017). *Alisma plantago-aquatica* L. inhibited adipocyte differentiation by downregulating the expression of PPARγ, CCAAT/enhancer-binding protein β (C/EBPβ), and FAS (Park et al., 2014) and blocked hepatic lipid production by regulating hepatic lipogenic genes including *Fas*, *Acc*, and glycerol-3-phosphate acyltransferase (GPAT) (Choi et al., 2019). Alisol B 23-acetate, a natural triterpenoid isolated from *Alisma plantago-aquatica* L., decreased hepatic lipogenesis through decreasing hepatic levels of SREBP1c, FAS, ACC, and SCD (Meng et al., 2017). *Panax notoginseng* (Burkill) F.H. Chen could change the fat and inflammation of liver tissue through decreasing expression levels of SREBP1c, ACC, and FAS (Ji and Gong, 2007; Yan-Xia et al., 2011; Zhang et al., 2020). The expression levels of SREBP1c, ACC, and FAS were downregulated in the *Curcuma longa* L. groups compared to the HFD groups (Ejaz et al., 2009; Ahn et al., 2010; Zhao et al., 2011; Mun et al., 2019). Baicalin treatment significantly attenuated methionine and choline–deficient diet (MCD)–induced hepatic lipid accumulation partly through regulating the expression of SREBP1c, FAS, and ACC (Xi et al., 2015; Zhang J. et al., 2018). Capsaicin inhibited the early adipogenic differentiation, lipogenesis, and maturation of adipocytes with concomitant repression of PPARγ and SCD (Ibrahim et al., 2015). The PTE intake tended to decrease *Srebp1c*, *Acc*, and *Fas* mRNA expressions in the liver of the mice (Shimamura et al., 2013), and PTE also downregulated *Scd* and *Srebp* in *Caenorhabditis elegans* to suppress fat accumulation (Ding et al., 2015; Hu et al., 2017). On treatment with green tea, the expression of lipogenesis-related genes *Acc*, *Fas*, and *Scd* was downregulated in the liver (Kim et al., 2009; Friedrich et al., 2012). The transcriptional activities of Srebp1c and forkhead box protein O1 (FOXO1) were significantly decreased by EGCG (Kim et al., 2010). Resveratrol exerted anti-obesity effects *via* mechanisms involving downregulation of ACC, FAS (Alberdi et al., 2011), and SCD (Zhang et al., 2012) and upregulation of the key adipogenic gene *Srebp1c* (Kim et al., 2011; Khaleel et al., 2018) in an HFD model. Celastrol decreased hepatic SREBP1 expression (Zhang et al., 2017). However, triptolide treatment increased the expression of LXR and its target gene, *Srebp1*, in both male and female rats and increased the expression of ACC only in the female rats (Jiang et al., 2016).

Regulation of TAG Synthesis

TAG production can come from exogenous FAs in the circulation or intracellular FAs generated by glycolysis and lipogenesis from glucose supplied by excess dietary intake. TAG synthesis is catalyzed by diacylglycerol acyltransferase (DGAT) in the last biosynthesis step. *Polygonum multiflorum* Thunb. supplementation significantly downregulated the expression of *Ppar*γ and *Dgat2* genes in obese mice (Choi et al., 2018).

Regulation of Cholesterol Biosynthesis

An increased level of LDL-c and/or TC is a pronounced phenotype of dyslipidemia. Ultimately, it is due to elevated cholesterol. Cholesterol plays an important role in human physiological functions. Almost all cells can synthesize cholesterol, and in this process, three crucial players of the cholesterol biosynthetic pathway are required, SREBP2, which functions as a master transcriptional regulator of cholesterol biosynthesis, and two rate-limiting enzymes of the biosynthetic pathway: HMGCR and squalene monooxygenase (SM).

Regulation of HMGCR and ACAT

As the rate-limiting enzyme for cholesterol biosynthesis, HMGCR is highly regulated at the transcriptional, translational, and post-translational levels (Goldstein and Brown, 1990). The formation of CE is another important means of preventing the accumulation of free cholesterol in cells, as this ACAT-mediated pathway directs the storage or secretion of cholesterol.

Crataegus pinnatifida Bunge could suppress the stimulation effect of HFD on the transcription of *Hmgcr*, and the transcriptional activity of the *Hmgcr* promoter was inhibited by *Crataegus pinnatifida* Bunge in a dose-dependent manner (Hu et al., 2016). HMGCR was generally reduced after administration of *Polygonum multiflorum* Thunb. (Xian et al., 2017). *Alisma plantago-aquatica* L. showed comparatively high inhibition against ACAT and HMGCR activities in rat livers (Choi et al., 2019). *Panax notoginseng* (Burkill) F.H. Chen also reduced the levels of hepatic HMGCR in HFD rats (Xia et al., 2011).

In addition, relative to the HFD control group, hamsters fed a curcumin-supplemented HFD had lower hepatic cholesterol and TG levels and HMGCR and ACAT activities, along with an increased FA β-oxidation activity (Jang et al., 2008). *Scutellaria baicalensis* Georgi, pu-erh tea, or green tea intervention repressed the expression of HMGCR in the liver (Yamashita et al., 2016; Han et al., 2017). However, capsinoids significantly increased HMGCR in the liver (Hong et al., 2015). Treatment with theabrownin, one of the most active and abundant pigments in pu-erh tea, increased two bile acid synthetic genes, *Cyp7a1* and *Cyp7b1*, in HFD-treated mice (Zeng et al., 2015; Huang et al., 2019).

Regulation of Lipid Decomposition

Cytoplasmic lipid droplets (LDs) are multiprotein-coated structures that serve as dynamic TAG storage pools and are involved in several aspects of lipid metabolism. The LDs are

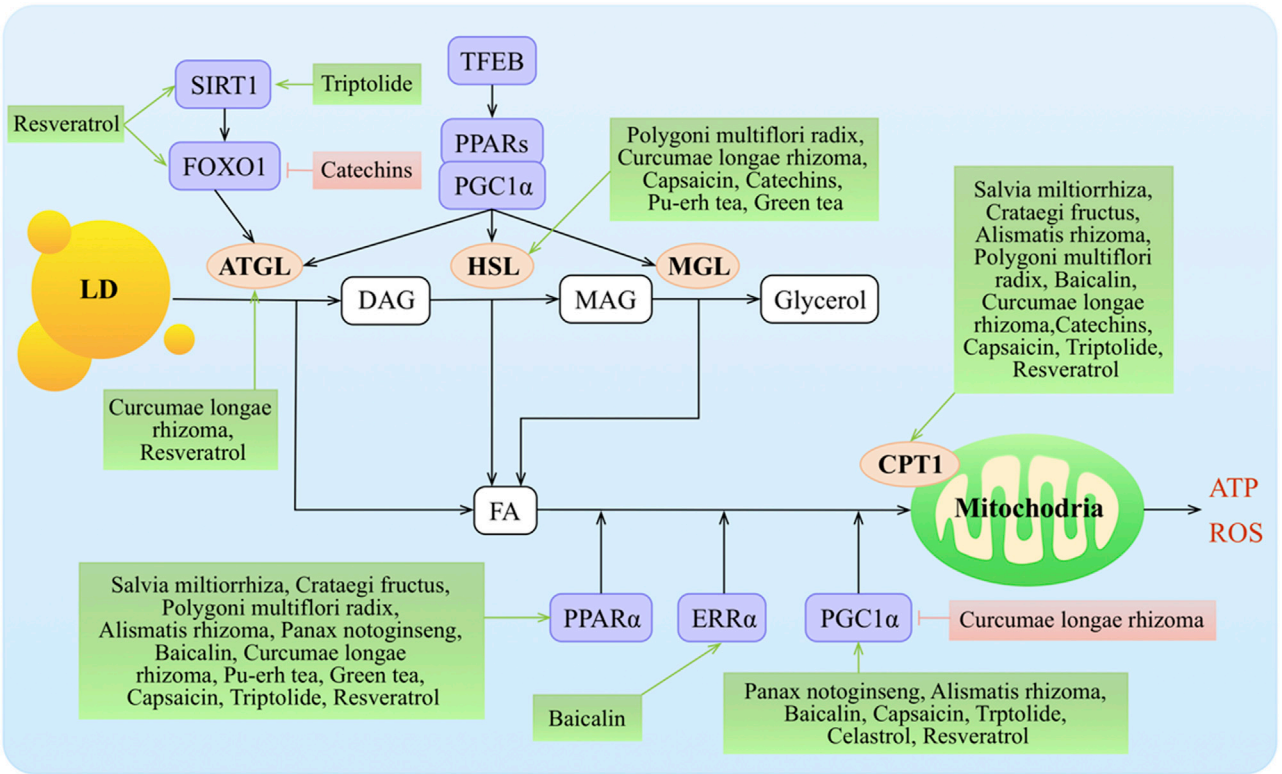

FIGURE 4 | Molecular mechanisms of TCMs in lipid decomposition. TCMs stimulate lipolysis from fat stores in the liver, white adipose tissue, and dietary fat sources (high-fat diets) to generate FAs that enter the hepatic cells *via* protein transporters. TG stored as lipid droplets can be hydrolyzed back to FAs *via* classic lipases (ATGL, HSL, and MGL) and lipophagy (by regulating TFEB, SIRT1, and FOXO1), undergo mitochondrial β-oxidation by the activity of various co-activators or nuclear receptors (such as PPARα, ERRα, and PGC1α), and target the transcription of gene Cpt1. Malonyl-CoA, an intermediate in DNL, inhibits CPT1 action and downregulates FA oxidation. ↑/⊥ depicts the positive or negative effect of TCMs in the cellular process, respectively.

mainly rich in TAGs and CEs. There are two pathways that are known to break down TAGs in LDs: cytoplasmic lipolysis and lysosomal-mediated autophagy (lipophagy). Adipose triglyceride hydrolase (ATGL) plays a key role in the lipolysis pathway, breaking down TAGs into diglycerides (DAGs) and FAs. FAs further undergo oxidative decomposition in the mitochondria *via* carnitine palmitoyl transferase 1 (CPT1) and provide energy (**Figure 4**).

Regulation of LD Decomposition

ATGL initiates TAG hydrolysis to form diacylglycerol and FAs. Hormone-sensitive lipase (HSL) (Lafontan and Langin, 2009; Rodriguez et al., 2010) and monoacylglycerol lipase (MGL) complete the process by consecutively hydrolyzing diacylglycerols into MAGs and FAs and then hydrolyzing MAGs into glycerol and FAs (Zechner et al., 2017). Transcription of *Atgl* is controlled by sirtuin 1 (SIRT1)–mediated deacetylation of FOXO1 and by PPARγ co-activator 1α (PGC1α) (Chakrabarti et al., 2011; Chen et al., 2021). The PPAR–PGC1α axis also regulates the transcriptional expression of *Hsl* (Albert et al., 2014; Farhan et al., 2014) and *Mgl* (Rakhshandehroo et al., 2007).

Curcumin treatment upregulated the expression of ATGL and resulted in acceleration of lipolysis (Valentine et al., 2019). Pu-erh tea administration significantly lowered plasma TC and TG concentrations and the LDL-c level but did not affect HDL-c levels. Moreover, pu-erh tea significantly increased LPL, HL, and HSL activities in epididymal fat tissue in rats with HFD-induced obesity (Cao et al., 2011). Resveratrol acted mainly on ATGL to regulate lipolytic activity in humans and murine adipocytes (Lasa et al., 2012) and increased *Sirt1*, *Foxo1*, and adiponectin mRNA expressions (Costa Cdos et al., 2011; Timmers et al., 2011; Lasa et al., 2012).

Regulation of β-Oxidation of FAs

β-Oxidation in the mitochondria is the predominant oxidative pathway for energy production in the liver. *β*-Oxidation consists of a cycling process involving dehydrogenation, hydration, dehydrogenation, and acylation that produces acetyl-CoA. In this process, the most important enzyme is CPT1 (Houten et al., 2016). The primary regulators of *β*-oxidation are the transcription factors *Pparα* and *Pgc1α*, whose action is upregulated by FAs and glucagon and suppressed *via* insulin (Pawlak et al., 2015).

The expression of PPARα was significantly downregulated in a hyperlipidemia group with tanshinone IIA treatment in rats (Yi-Xin et al., 2017). CPT1, PPARα, and its downstream targets were activated with hawthorn leaf flavonoids in an HFD model (Kuo

TABLE 2 | A summary of studies demonstrating the effects of TCM on lipid metabolism in animal models and humans.

TCM	Appetite	Lipid absorption	Lipid transportation	Lipid synthesis	Lipid decomposition
Crataegus pinnatifida Bunge		CD36↓ LDLR↑	ApoA-I↑	FAS↓ SREBP-1c↓ SREBP2↓	CPT1↑ PPARα↑
Salvia miltiorrhiza Bunge/tanshinone II A/salvianolic acid B	Leptin sensitivity↑ Ghrelin↓	CD36↓ LDLR↓ PCSK9↓	ABCA1↑ CYP7A1↑ ApoA-I↑	FAS↓ SCD↓ SREBP-1c↓	CPT1↑ PPARα↑
Polygonum multiflorum Thunb.	Leptin↓		CYP7A1↑	ACC1↓ FAS↓ DGAT↓ SREBP-1c↑ HMGCR↓;	HSL↑ CPT1↑ PPARα↑
Alisma plantago-aquatica L.	Leptin↓		ApoB↑	ACC1↓ FAS↓ DGAT↓ HMGCR↓ HMGCR↓ ACAT↓	CPT1↑ PPARα↑ PGC1α↑
Panax notoginseng (Burkill) F.H. Chen/ *Panax notoginseng* saponins/*n*-butanol extract of *Panax notoginseng*	Leptin↓	LDLR↑	ABCA1↑ ABCG5/8↑ CYP7A1↑ LPL↑ LDL↓	FAS↓ SREBP-1c↓ HMGCR↓	PPARα↑ PGC1α↑
Curcuma longa L./curcumin	Leptin↓	CD36↓ FATP↓ NPC1L1↓	ABCA1↑ ABCG5/8↑ CYP7A1↑ LPL↑ LDL↓ HDL↑ ApoB↓	ACC1↓ FAS↓; SCD↓ SREBP-1c↓ SREBP2↓ ACAT↓ HMGCR↓	CPT1↑ ATGL↑ HSL↑ PGC1α↓ PPARα↑
Scutellaria baicalensis Georgi/baicalin		LDLR↑;	CYP7A1↑	ACC1↓ FAS↓ SREBP-1c↓ HMGCR↓	CPT1↑ PPARα↑ ERRα↑ PGC1α↑
Pu-erh tea/theabrownin	Leptin↓		ABCA1↑ ABCG11↑ LPL↑ ApoB↓	ACC1↓ FAS↓ SCD↓ DGAT↓ SREBP-1c↓ HMGCR↓ SM↓	HSL↑ PPARα↑
Green tea/green tea polyphenols/EGCG	Leptin↓ Adiponectin↑	CD36↓ FATP↓	LPL↑	FAS↓ ACC1↓ SCD↓ HMGCR↓	HSL↑ FOXO1↓ CPT1↑ PPARα↑
Tripterygium wilfordii Hook. f./celastrol/ triptolide	Leptin sensitivity↑ Adiponectin↑		ABCA1↑ ApoB↓ CYP7A1↑	ACC1↓ SREBP-1c↓	CPT1↑; PPARα↑; PGC1α↑; SIRT1↑;
Capsaicin	Leptin↓ Adiponectin↑ ghrelin↓	CD36↑		SCD↓ HMGCR↓	HSL↑ CPT1↑ PPARα↑ PGC1α↑
Resveratrol	Leptin↓	CD36↑ FATP↑	LPL↑ ApoB↓;	FAS↓ SCD↓ SREBP-1c↓	ATGL↑ SIRT1↑ FOXO1↑ CPT1↑ PPARα↑ PGC1α↑

↑: *increase;* ↓: *decrease.*

et al., 2009; Li et al., 2015; Dong et al., 2017). Alisol B 23-acetate administration increased lipid metabolism *via* inducing PPARα, CPT1α, and LPL (Meng et al., 2017). *Alisma plantago-aquatica* L. suppressed the mRNA levels of hepatic *Pgc1α*, estrogen-related receptor (ERR)*γ*, and PGC1α-dependent enzyme (G6Pase) that are involved in gluconeogenesis in liver tissue (Jeong Hyang Sook %J Korea Journal of Herbology, 2013). *Polygonum multiflorum* Thunb. supplementation significantly upregulated the *Pparα*, *Cpt1*, *Cpt2*, *Ucp1*, and *Hsl* mRNA levels compared with the HFD group (Choi et al., 2018). PNSs regulated lipid metabolism by upregulating the expression of transcriptional factors, such as *Pparα*, *Pparγ*, and *Pgc1α* (Wang et al., 2016). PPARα and CPT1 expressions were upregulated in the *Curcuma longa* L.–treated groups (Mun et al., 2019). Finally, *Curcuma longa* L. treatment in high-fructose diet (HFrD)-fed rats repressed hepatic expression of PGC as compared to the rats fed an HFrD alone, suggesting a protective effect of *Curcuma longa* L. by modulating the expression of lipogenic genes in the liver (Singh et al., 2015). Treatment with baicalin ameliorated diet-induced obesity through directly activating hepatic CPT1 as well as increasing the expression of PPARα (Zhang J. et al., 2018), ERRα, and PGC1α (Takizawa et al., 2015; Dai et al., 2018).

Treatment with capsinoids significantly increased the expression of CPT1, adiponectin, and *Pparα* and *Pgc1α* mRNA in the liver (Kang et al., 2010; Lee et al., 2013; Hong et al., 2015; Panchal et al., 2018). The expression of PPARα was also increased in the HFD/pu-erh tea groups (Sun et al., 2019). Green tea increased the expression of CPT1 and PPARα and decreased the expression of LXR (Chen et al., 2009; Kim et al., 2009; Axling et al., 2012) while increasing HSL in mesenteric adipose tissue concomitantly with the HFD (Cunha et al., 2013). Resveratrol increased CPT1 activities (Gomez-Zorita et al., 2012), had a higher agonistic activity of PPARα (Takizawa et al., 2015), and significantly increased SIRT1 and PGC1α levels and citrate synthase activity and improved muscle mitochondrial respiration (Timmers et al., 2011). Finally, celastrol augmented PGC1α expression in adipocytes and skeletal muscles (Fang et al., 2019).

CONCLUSIONS AND PERSPECTIVES

Human obesity is quickly becoming widespread, and treatment of it and its comorbidities is an important clinical challenge. Targeting lipid metabolism as a potential treatment has attracted a great deal of attention as a primary therapeutic target. TCMs have been widely used as anti-obesity treatments for a very long time. In this review, how TCMs modulate major features of lipid metabolism was systematically summarized. Collation and integration of these data has produced a comprehensive register for the mechanisms of TCMs' action in anti-obesity (**Table 2**).

While TCMs clearly play roles in anti-obesity, the side effects of TCMs should not be overlooked. Hepatotoxicity is the main side effect of TCMs (Tarantino et al., 2009; Frenzel and Teschke, 2016). In many cases, the side effects are caused by incorrect processing, usage, dosage, or compatibility. For example, the use of the processed *Polygonum multiflorum* Thunb. caused less damage to the liver than the unprocessed *Polygonum multiflorum* Thunb. (Tu et al., 2015), while EGCG caused dose-dependent hepatotoxicity in mice under dietary restriction, but not in mice fed a normal diet (Shi et al., 2020). In addition, *Tripterygium wilfordii* Hook. f. is normally hepatotoxic, but the classical compatibility of *Tripterygium wilfordii* Hook. f. and *Lysimachia christinae* Hance can detoxify the poison of *Tripterygium wilfordii* Hook. f. (Wang et al., 2018; Wang J., et al., 2015). Triptolide and celastrol are two major components of *Tripterygium wilfordii* Hook. f.. Interestingly, triptolide is hepatotoxic, while celastrol showed protection from liver injury (Hasnat et al., 2019; Xu et al., 2021). These cases suggest that correct processing, usage, dosage, and compatibility under the application guidance based on long experience can greatly reduce side effects. Therefore, for the use of TCMs in anti-obesity, following the doctor's advice and guidelines of the TCMs is essential to ensure the efficacy of the TCMs and also avoid side effects as much as possible.

Moreover, the capacity of TCMs to inhibit obesity is attracting increasing attention. TCMs are being advocated as another major breakthrough for therapeutic intervention for obesity-related diseases. However, only a fraction of the medically active substances available in TCMs have been identified, and the unidentified natural products have great potential. Modern technologies enable the detailed analysis of TCM extracts to identify active substances. These phytochemicals, in the form of the TCMs themselves, extracts, or purified components, can be combined with existing treatments to reduce the prevalence of obesity and its complications. Taking advantage of TCM effects on therapeutic interventions for the treatment of obesity-related diseases may be another breakthrough for integrated medicine.

AUTHOR CONTRIBUTIONS

QF, FX, and XZ designed the study. QF and XZ wrote the manuscript. BL supervised the work and revised the manuscript. All authors have read and approved the manuscript.

FUNDING

This work was supported by the Ministry of Science and Technology of the People's Republic of China grant (2018YFA0800700), the National Natural Science Foundation of China grants (81700520, U1702288, U1702287, 31671230, 91857113, 31860323, and 32071281), the Yunnan Applied Basic Research Projects 2018FB117 and 2019FY003021, and the Key Project for Yunnan Provincial Traditional Chinese Medicine Joint 2018FF001(-004).

REFERENCES

Aboonabi, A., Meyer, R. R., and Singh, I. (2019). The Association between Metabolic Syndrome Components and the Development of Atherosclerosis. *J. Hum. Hypertens.* 33 (12), 844–855. doi:10.1038/s41371-019-0273-0

Ahima, R. S., and Antwi, D. A. (2008). Brain Regulation of Appetite and Satiety. *Endocrinol. Metab. Clin. North America* 37 (4), 811–823. doi:10.1016/j.ecl.2008.08.005

Ahn, J., Lee, H., Kim, S., and Ha, T. (2010). Curcumin-induced Suppression of Adipogenic Differentiation Is Accompanied by Activation of Wnt/β-Catenin Signaling. *Am. J. Physiology-Cell Physiol.* 298 (6), C1510–C1516. doi:10.1152/ajpcell.00369.2009

Alberdi, G., Rodríguez, V. M., Miranda, J., Macarulla, M. T., Arias, N., Andrés-Lacueva, C., et al. (2011). Changes in white Adipose Tissue Metabolism Induced by Resveratrol in Rats. *Nutr. Metab.* 8 (1), 29. doi:10.1186/1743-7075-8-29

Albert, J. S., Yerges-Armstrong, L. M., Horenstein, R. B., Pollin, T. I., Sreenivasan, U. T., Chai, S., et al. (2014). Null Mutation in Hormone-Sensitive Lipase Gene and Risk of Type 2 Diabetes. *N. Engl. J. Med.* 370 (24), 2307–2315. doi:10.1056/NEJMoa1315496

Am, A., LJohani, D. N., Syed, D. N., and Ntambi, J. M. (2017). Insights into Stearoyl-CoA Desaturase-1 Regulation of Systemic Metabolism. *Trends Endocrinol. Metab.* 28 (12), 831–842. doi:10.1016/j.tem.2017.10.003

Anonymous (1890). Poisoning by Colchicin. *Hospital (Lond 1886)* 9 (214), 75.

Arem, H., and Irwin, M. L. (2013). Obesity and Endometrial Cancer Survival: a Systematic Review. *Int. J. Obes.* 37 (5), 634–639. doi:10.1038/ijo.2012.94

Aronne, L. J., Wadden, T. A., Peterson, C., Winslow, D., Odeh, S., and Gadde, K. M. (2013). Evaluation of Phentermine and Topiramate versus Phentermine/topiramate Extended-Release in Obese Adults. *Obesity* 21 (11), 2163–2171. doi:10.1002/oby.20584

Axling, U., Olsson, C., Xu, J., Fernandez, C., Larsson, S., Ström, K., et al. (2012). Green tea Powder and Lactobacillus Plantarum Affect Gut Microbiota, Lipid Metabolism and Inflammation in High-Fat Fed C57BL/6J Mice. *Nutr. Metab.* 9 (1), 105. doi:10.1186/1743-7075-9-105

Bäckhed, F., Manchester, J. K., Semenkovich, C. F., and Gordon, J. I. (2007). Mechanisms Underlying the Resistance to Diet-Induced Obesity in Germ-free Mice. *Pnas* 104 (3), 979–984. doi:10.1073/pnas.0605374104

Bao, Y., Wang, L., Xu, Y., Yang, Y., Wang, L., Si, S., et al. (2012). Salvianolic Acid B Inhibits Macrophage Uptake of Modified Low Density Lipoprotein (mLDL) in a Scavenger Receptor CD36-dependent Manner. *Atherosclerosis* 223 (1), 152–159. doi:10.1016/j.atherosclerosis.2012.05.006

Bennett, A. (1873). An Experimental Inquiry into the Physiological Actions of Theine, Caffeine, Guaranine, Cocaine, and Theobromine. *Edinb. Med. J.* 19 (4), 323–341.

Bolin, A. P., Sousa-Filho, C. P. B., Marinovic, M. P., Rodrigues, A. C., and Otton, R. (2020). Polyphenol-rich green tea Extract Induces Thermogenesis in Mice by a Mechanism Dependent on Adiponectin Signaling. *J. Nutr. Biochem.* 78, 108322. doi:10.1016/j.jnutbio.2019.108322

Campfield, L., Smith, F., Guisez, Y., Devos, R., and Burn, P. (1995). Recombinant Mouse OB Protein: Evidence for a Peripheral Signal Linking Adiposity and central Neural Networks. *Science* 269 (5223), 546–549. doi:10.1126/science.7624778

Cao, Z.-H., Gu, D.-H., Lin, Q.-Y., Xu, Z.-Q., Huang, Q.-C., Rao, H., et al. (2011). Effect of Pu-Erh tea on Body Fat and Lipid Profiles in Rats with Diet-Induced Obesity. *Phytother. Res.* 25 (2), 234–238. doi:10.1002/ptr.3247

Chakrabarti, P., English, T., Karki, S., Qiang, L., Tao, R., Kim, J., et al. (2011). SIRT1 Controls Lipolysis in Adipocytes via FOXO1-Mediated Expression of ATGL. *J. Lipid Res.* 52 (9), 1693–1701. doi:10.1194/jlr.M014647

Chen, C.-C., Kuo, C.-H., Leu, Y.-L., and Wang, S.-H. (2021). Corylin Reduces Obesity and Insulin Resistance and Promotes Adipose Tissue browning through SIRT-1 and β3-AR Activation. *Pharmacol. Res.* 164, 105291. doi:10.1016/j.phrs.2020.105291

Chen, H.-C., Chen, P.-Y., Wu, M.-J., Tai, M.-H., and Yen, J.-H. (2016). Tanshinone IIA Modulates Low Density Lipoprotein Uptake via Down-Regulation of

PCSK9 Gene Expression in HepG2 Cells. *PLoS One* 11 (9), e0162414. doi:10.1371/journal.pone.0162414

Chen, J., Yue, J., Liu, J., Liu, Y., Jiao, K.-L., Teng, M.-Y., et al. (2018). Salvianolic Acids Improve Liver Lipid Metabolism in Ovariectomized Rats via Blocking STAT-3/SREBP1 Signaling. *Chin. J. Nat. Medicines* 16 (11), 838–845. doi:10.1016/s1875-5364(18)30125-0

Chen, N., Bezzina, R., Hinch, E., Lewandowski, P. A., Cameron-Smith, D., Mathai, M. L., et al. (2009). Green tea, Black tea, and Epigallocatechin Modify Body Composition, Improve Glucose Tolerance, and Differentially Alter Metabolic Gene Expression in Rats Fed a High-Fat Diet. *Nutr. Res.* 29 (11), 784–793. doi:10.1016/j.nutres.2009.10.003

Choi, E., Jang, E., and Lee, J.-H. (2019). Pharmacological Activities of Alisma Orientale against Nonalcoholic Fatty Liver Disease and Metabolic Syndrome: Literature Review. *Evidence-Based Complement. Altern. Med.* 2019, 1–15. doi:10.1155/2019/2943162

Choi, R.-Y., Lee, H.-I., Ham, J. R., Yee, S.-T., Kang, K.-Y., and Lee, M.-K. (2018). Heshouwu (Polygonum Multiflorum Thunb.) Ethanol Extract Suppresses Pre-adipocytes Differentiation in 3T3-L1 Cells and Adiposity in Obese Mice. *Biomed. Pharmacother.* 106, 355–362. doi:10.1016/j.biopha.2018.06.140

Cortés-Martín, A., Iglesias-Aguirre, C. E., Meoro, A., Selma, M. V., and Espín, J. C. (2020). There Is No Distinctive Gut Microbiota Signature in the Metabolic Syndrome: Contribution of Cardiovascular Disease Risk Factors and Associated Medication. *Microorganisms* 8 (3), 416. doi:10.3390/microorganisms8030416

Costa, C. d. S., Rohden, F., Hammes, T. O., Margis, R., Bortolotto, J. W., Padoin, A. V., et al. (2011). Resveratrol Upregulated SIRT1, FOXO1, and Adiponectin and Downregulated PPARγ1-3 mRNA Expression in Human Visceral Adipocytes. *Obes. Surg.* 21 (3), 356–361. doi:10.1007/s11695-010-0251-7

Courdavault, V., O'Connor, S. E., Oudin, A., Besseau, S., and Papon, N. (2020). Towards the Microbial Production of Plant-Derived Anticancer Drugs. *Trends Cancer* 6 (6), 444–448. doi:10.1016/j.trecan.2020.02.004

Cunha, C. A., Lira, F. S., Rosa Neto, J. C., Pimentel, G. D., Souza, G. I. H., da Silva, C. M. G., et al. (2013). Green tea Extract Supplementation Induces the Lipolytic Pathway, Attenuates Obesity, and Reduces Low-Grade Inflammation in Mice Fed a High-Fat Diet. *Mediators Inflamm.* 2013, 1–8. doi:10.1155/2013/635470

Dai, J., Liang, K., Zhao, S., Jia, W., Liu, Y., Wu, H., et al. (2018). Chemoproteomics Reveals Baicalin Activates Hepatic CPT1 to Ameliorate Diet-Induced Obesity and Hepatic Steatosis. *Proc. Natl. Acad. Sci. USA* 115 (26), E5896–E5905. doi:10.1073/pnas.1801745115

de Beer, M., Hofsteenge, G. H., Koot, H., Hirasing, R., Delemarre-van de Waal, H., and Gemke, R. (2007). Health-related-quality-of-life in Obese Adolescents Is Decreased and Inversely Related to BMI. *Acta Paediatr.* 96 (5), 710–714. doi:10.1111/j.1651-2227.2007.00243.x

Dickson, D. J. H. (1823). On the Febrifuge Power of the Sulphate of Quinine. *Edinb. Med. Surg. J.* 19 (77), 571–573.

Ding, Y., Zou, X., Jiang, X., Wu, J., Zhang, Y., Chen, D., et al. (2015). Pu-erh tea Down-Regulates Sterol Regulatory Element-Binding Protein and Stearyol-CoA Desaturase to Reduce Fat Storage in Caenorhaditis Elegans. *PLoS One* 10 (2), e0113815. doi:10.1371/journal.pone.0113815

Dobbs, R., James, M., Woetzel, J., Sawers, C., Thompson, F., Peter, C., et al. 2014. *How the World Could Better Fight Obesity*.

Dong, P., Pan, L., Zhang, X., Zhang, W., Wang, X., Jiang, M., et al. (2017). Hawthorn (Crataegus Pinnatifida Bunge) Leave Flavonoids Attenuate Atherosclerosis Development in apoE Knock-Out Mice. *J. Ethnopharmacology* 198, 479–488. doi:10.1016/j.jep.2017.01.040

Dong, S.-z., Zhao, S.-p., Wu, Z.-h., Yang, J., Xie, X.-z., Yu, B.-l., et al. (2011). Curcumin Promotes Cholesterol Efflux from Adipocytes Related to PPARgamma-LXRalpha-ABCA1 Passway. *Mol. Cel. Biochem.* 358 (1-2), 281–285. doi:10.1007/s11010-011-0978-z

Ejaz, A., Wu, D., Kwan, P., and Meydani, M. (2009). Curcumin Inhibits Adipogenesis in 3T3-L1 Adipocytes and Angiogenesis and Obesity in C57/BL Mice. *J. Nutr.* 139 (5), 919–925. doi:10.3945/jn.108.100966

Elias, C. F., Aschkenasi, C., Lee, C., Kelly, J., Ahima, R. S., Bjorbæk, C., et al. (1999). Leptin Differentially Regulates NPY and POMC Neurons Projecting to the Lateral Hypothalamic Area. *Neuron* 23 (4), 775–786. doi:10.1016/s0896-6273(01)80035-0

Fan, C., Yan, J., Qian, Y., Wo, X., and Gao, L. (2006). Regulation of Lipoprotein Lipase Expression by Effect of Hawthorn Flavonoids on Peroxisome Proliferator Response Element Pathway. *J. Pharmacol. Sci.* 100 (1), 51–58. doi:10.1254/jphs.fp0050748

Fang, P., He, B., Yu, M., Shi, M., Zhu, Y., Zhang, Z., et al. (2019). Treatment with Celastrol Protects against Obesity through Suppression of Galanin-Induced Fat Intake and Activation of PGC-1α/GLUT4 axis-mediated Glucose Consumption. *Biochim. Biophys. Acta (Bba) - Mol. Basis Dis.* 1865 (6), 1341–1350. doi:10.1016/j.bbadis.2019.02.002

Farhan, S. M. K., Robinson, J. F., McIntyre, A. D., Marrosu, M. G., Ticca, A. F., Loddo, S., et al. (2014). A Novel LIPE Nonsense Mutation Found Using Exome Sequencing in Siblings with Late-Onset Familial Partial Lipodystrophy. *Can. J. Cardiol.* 30 (12), 1649–1654. doi:10.1016/j.cjca.2014.09.007

Farooqi, I. S., Bullmore, E., Keogh, J., Gillard, J., O'Rahilly, S., and Fletcher, P. C. (2007). Leptin Regulates Striatal Regions and Human Eating Behavior. *Science* 317 (5843), 1355. doi:10.1126/science.1144599

Fei, N., and Zhao, L. (2013). An Opportunistic Pathogen Isolated from the Gut of an Obese Human Causes Obesity in Germfree Mice. *Isme j* 7 (4), 880–884. doi:10.1038/ismej.2012.153

Frenzel, C., and Teschke, R. (2016). Herbal Hepatotoxicity: Clinical Characteristics and Listing Compilation. *Ijms* 17 (5), 588. doi:10.3390/ijms17050588

Friedman, J. M. (1997). The Alphabet of Weight Control. *Nature* 385 (6612), 119–120. doi:10.1038/385119a0

Friedrich, M., Petzke, K. J., Raederstorff, D., Wolfram, S., and Klaus, S. (2012). Acute Effects of Epigallocatechin Gallate from green tea on Oxidation and Tissue Incorporation of Dietary Lipids in Mice Fed a High-Fat Diet. *Int. J. Obes.* 36 (5), 735–743. doi:10.1038/ijo.2011.136

Gadde, K. M., Apolzan, J. W., and Berthoud, H.-R. (2018). Pharmacotherapy for Patients with Obesity. *Clin. Chem.* 64 (1), 118–129. doi:10.1373/clinchem.2017.272815

Goldstein, J. L., and Brown, M. S. (1990). Regulation of the Mevalonate Pathway. *Nature* 343 (6257), 425–430. doi:10.1038/343425a0

Gómez-Zorita, S., Fernández-Quintela, A., Macarulla, M. T., Aguirre, L., Hijona, E., Bujanda, L., et al. (2012). Resveratrol Attenuates Steatosis in Obese Zucker Rats by Decreasing Fatty Acid Availability and Reducing Oxidative Stress. *Br. J. Nutr.* 107 (2), 202–210. doi:10.1017/s0007114511002753

González-Muniesa, P., Mártinez-González, M.-A., Hu, F. B., Després, J.-P., Matsuzawa, Y., Loos, R. J. F., et al. (2017). Obesity. *Nat. Rev. Dis. Primers* 3, 17034. doi:10.1038/nrdp.2017.34

Halaas, J., Gajiwala, K., Maffei, M., Cohen, S., Chait, B., Rabinowitz, D., et al. (1995). Weight-reducing Effects of the Plasma Protein Encoded by the Obese Gene. *Science* 269 (5223), 543–546. doi:10.1126/science.7624777

Han, K., Bose, S., Wang, J.-H., Lim, S.-k., Chin, Y.-W., Kim, Y.-M., et al. (2017). *In Vivo* therapeutic Effect of Combination Treatment with Metformin and Scutellaria Baicalensis on Maintaining Bile Acid Homeostasis. *PLoS One* 12 (9), e0182467. doi:10.1371/journal.pone.0182467

Hasnat, M., Yuan, Z., Naveed, M., Khan, A., Raza, F., Xu, D., et al. (2019). Drp1-associated Mitochondrial Dysfunction and Mitochondrial Autophagy: a Novel Mechanism in Triptolide-Induced Hepatotoxicity. *Cell. Biol. Toxicol.* 35 (3), 267–280. doi:10.1007/s10565-018-9447-8

Hong, Q., Xia, C., Xiangying, H., and Quan, Y. (2015). Capsinoids Suppress Fat Accumulation via Lipid Metabolism. *Mol. Med. Rep.* 11 (3), 1669–1674. doi:10.3892/mmr.2014.2996

Hossain, P., Kawar, B., and El Nahas, M. (2007). Obesity and Diabetes in the Developing World - A Growing Challenge. *N. Engl. J. Med.* 356 (3), 213–215. doi:10.1056/NEJMp068177

Houten, S. M., Violante, S., Ventura, F. V., and Wanders, R. J. A. (2016). The Biochemistry and Physiology of Mitochondrial Fatty Acid β-Oxidation and its Genetic Disorders. *Annu. Rev. Physiol.* 78, 23–44. doi:10.1146/annurev-physiol-021115-105045

Hu, H.-J., Luo, X.-G., Dong, Q.-Q., Mu, A., Shi, G.-L., Wang, Q.-T., et al. (2016). Ethanol Extract of Zhongtian Hawthorn Lowers Serum Cholesterol in Mice by Inhibiting Transcription of 3-Hydroxy-3-Methylglutaryl-CoA Reductase via Nuclear Factor-Kappa B Signal Pathway. *Exp. Biol. Med. (Maywood)* 241 (6), 667–674. doi:10.1177/1535370215627032

Hu, W.-Y., Ma, X.-H., Zhou, W.-Y., Li, X.-X., Sun, T.-T., and Sun, H. (2017). Preventive Effect of Silibinin in Combination with Pu-Erh tea Extract on Non-alcoholic Fatty Liver Disease in Ob/ob Mice. *Food Funct.* 8 (3), 1105–1115. doi:10.1039/c6fo01591c

Hu, W., Wang, L., Du, G., Guan, Q., Dong, T., Song, L., et al. (2020). Effects of Microbiota on the Treatment of Obesity with the Natural Product Celastrol in Rats. *Diabetes Metab. J.* 44 (5), 747–763. doi:10.4093/dmj.2019.0124

Huang, F., Zheng, X., Ma, X., Jiang, R., Zhou, W., Zhou, S., et al. (2019). Theabrownin from Pu-Erh tea Attenuates Hypercholesterolemia via Modulation of Gut Microbiota and Bile Acid Metabolism. *Nat. Commun.* 10 (1), 4971. doi:10.1038/s41467-019-12896-x

Huang, H.-C., and Lin, J.-K. (2012). Pu-erh tea, green tea, and Black tea Suppresses Hyperlipidemia, Hyperleptinemia and Fatty Acid Synthase through Activating AMPK in Rats Fed a High-Fructose Diet. *Food Funct.* 3 (2), 170–177. doi:10.1039/c1fo10157a

Ibrahim, M., Jang, M., Park, M., Gobianand, K., You, S., Yeon, S.-H., et al. (2015). Capsaicin Inhibits the Adipogenic Differentiation of Bone Marrow Mesenchymal Stem Cells by Regulating Cell Proliferation, Apoptosis, Oxidative and Nitrosative Stress. *Food Funct.* 6 (7), 2165–2178. doi:10.1039/c4fo01069h

Incio, J., Ligibel, J. A., McManus, D. T., Suboj, P., Jung, K., Kawaguchi, K., et al. (2018). Obesity Promotes Resistance to Anti-VEGF Therapy in Breast Cancer by Up-Regulating IL-6 and Potentially FGF-2. *Sci. Transl. Med.* 10 (432), eaag0945. doi:10.1126/scitranslmed.aag0945

Jang, E.-M., Choi, M.-S., Jung, U. J., Kim, M.-J., Kim, H.-J., Jeon, S.-M., et al. (2008). Beneficial Effects of Curcumin on Hyperlipidemia and Insulin Resistance in High-Fat-Fed Hamsters. *Metabolism* 57 (11), 1576–1583. doi:10.1016/j.metabol.2008.06.014

Jeong, Hyang Sook %J Korea Journal of Herbology. 2013. "Efficacy of Alismatis Orientale Rhizoma on Obesity Induced by High Fat Diet." 28 (3):95–106. doi:10.6116/kjh.2013.28.3.95

Ji, W., and Gong, B. Q. (2007). Hypolipidemic Effects and Mechanisms of Panax Notoginseng on Lipid Profile in Hyperlipidemic Rats. *J. Ethnopharmacology* 113 (2), 318–324. doi:10.1016/j.jep.2007.06.022

Ji-Ping, L., Ren-Chao, T., Xiao-Meng, S., Hao-Yue, Z., Shuai, S., Ai-Zhen, X., et al. (2021). Comparison of Main Chemical Composition of Plantago Asiatica L. And *P. depressa* Willd. Seed Extracts and Their Anti-obesity Effects in High-Fat Diet-Induced Obese Mice. *Phytomedicine* 81, 153362. doi:10.1016/j.phymed.2020.153362

Jia, L., Song, N., Yang, G., Ma, Y., Li, X., Lu, R., et al. (2016a). Effects of Tanshinone IIA on the Modulation of miR-33a and the SREBP-2/Pcsk9 Signaling Pathway in Hyperlipidemic Rats. *Mol. Med. Rep.* 13 (6), 4627–4635. doi:10.3892/mmr.2016.5133

Jia, L., Zhang, N., Xu, Y., Chen, W.-n., Zhu, M.-l., Song, N., et al. (2016b). Tanshinone IIA Affects the HDL Subfractions Distribution Not Serum Lipid Levels: Involving in Intake and Efflux of Cholesterol. *Arch. Biochem. Biophys.* 592, 50–59. doi:10.1016/j.abb.2016.01.001

Jiang, Z., Huang, X., Huang, S., Guo, H., Wang, L., Li, X., et al. (2016). Sex-Related Differences of Lipid Metabolism Induced by Triptolide: The Possible Role of the LXRα/SREBP-1 Signaling Pathway. *Front. Pharmacol.* 7, 87. doi:10.3389/fphar.2016.00087

Jimoh, A., Tanko, Y., Ayo, J. O., Ahmed, A., and Mohammed, A. (2018). Resveratrol Increases Serum Adiponectin Level and Decreases Leptin and Insulin Level in an Experimental Model of Hypercholesterolemia. *Pathophysiology* 25 (4), 411–417. doi:10.1016/j.pathophys.2018.08.005

Kadowaki, T., Yamauchi, T., and Kubota, N. (2008). The Physiological and Pathophysiological Role of Adiponectin and Adiponectin Receptors in the Peripheral Tissues and CNS. *FEBS Lett.* 582 (1), 74–80. doi:10.1016/j.febslet.2007.11.070

Kang, J.-H., Tsuyoshi, G., Han, I.-S., Kawada, T., Kim, Y. M., and Yu, R. (2010). Dietary Capsaicin Reduces Obesity-Induced Insulin Resistance and Hepatic Steatosis in Obese Mice Fed a High-Fat Diet. *Obesity (Silver Spring)* 18 (4), 780–787. doi:10.1038/oby.2009.301

Kaukua, J., Pekkarinen, T., Sane, T., and Mustajoki, P. (2003). Health-related Quality of Life in Obese Outpatients Losing Weight with Very-Low-Energy Diet and Behaviour Modification: a 2-y Follow-Up Study. *Int. J. Obes.* 27 (9), 1072–1080. doi:10.1038/sj.ijo.0802366

Khaleel, E. F., Abdel-Aleem, G. A., and Mostafa, D. G. (2018). Resveratrol Improves High-Fat Diet Induced Fatty Liver and Insulin Resistance by Concomitantly Inhibiting Proteolytic Cleavage of Sterol Regulatory Element-Binding Proteins, Free Fatty Acid Oxidation, and Intestinal Triglyceride Absorption. *Can. J. Physiol. Pharmacol.* 96 (2), 145–157. doi:10.1139/cjpp-2017-0001

Kim, H.-J., Jeon, S.-M., Lee, M.-K., Jung, U. J., Shin, S.-K., and Choi, M.-S. (2009). Antilipogenic Effect of green tea Extract in C57BL/6J-Lepob/obmice. *Phytother. Res.* 23 (4), 467–471. doi:10.1002/ptr.2647

Kim, H., Hiraishi, A., Tsuchiya, K., and Sakamoto, K. (2010). (−) Epigallocatechin Gallate Suppresses the Differentiation of 3T3-L1 Preadipocytes through Transcription Factors FoxO1 and SREBP1cEpigallocatechin Gallate Suppresses the Differentiation of 3T3-L1 Preadipocytes through Transcription Factors FoxO1 and SREBP1c. *Cytotechnology* 62 (3), 245–255. doi:10.1007/s10616-010-9285-x

Kim, J. E., Lee, M. H., Nam, D. H., Song, H. K., Kang, Y. S., Lee, J. E., et al. (2013). Celastrol, an NF-Kb Inhibitor, Improves Insulin Resistance and Attenuates Renal Injury in Db/db Mice. *PLoS One* 8 (4), e62068. doi:10.1371/journal.pone.0062068

Kim, S., Jin, Y., Choi, Y., and Park, T. (2011). Resveratrol Exerts Anti-obesity Effects via Mechanisms Involving Down-Regulation of Adipogenic and Inflammatory Processes in Mice. *Biochem. Pharmacol.* 81 (11), 1343–1351. doi:10.1016/j.bcp.2011.03.012

Ko, C.-W., Qu, J., Black, D. D., and Tso, P. (2020). Regulation of Intestinal Lipid Metabolism: Current Concepts and Relevance to Disease. *Nat. Rev. Gastroenterol. Hepatol.* 17 (3), 169–183. doi:10.1038/s41575-019-0250-7

Kubota, N., Yano, W., Kubota, T., Yamauchi, T., Itoh, S., Kumagai, H., et al. (2007). Adiponectin Stimulates AMP-Activated Protein Kinase in the Hypothalamus and Increases Food Intake. *Cel Metab.* 6 (1), 55–68. doi:10.1016/j.cmet.2007.06.003

Kuhn, D. J., Burns, A. C., Kazi, A., and Ping Dou, Q. (2004). Direct Inhibition of the Ubiquitin-Proteasome Pathway by Ester Bond-Containing green tea Polyphenols Is Associated with Increased Expression of Sterol Regulatory Element-Binding Protein 2 and LDL Receptor. *Biochim. Biophys. Acta (Bba) - Mol. Cel Biol. Lipids* 1682 (1-3), 1–10. doi:10.1016/j.bbalip.2003.12.006

Kumar, P., Malhotra, P., Ma, K., Singla, A., Hedroug, O., Saksena, S., et al. (2011). SREBP2 Mediates the Modulation of Intestinal NPC1L1 Expression by Curcumin. *Am. J. Physiology-Gastrointestinal Liver Physiol.* 301 (1), G148–G155. doi:10.1152/ajpgi.00119.2011

Kuo, D.-H., Yeh, C.-H., Shieh, P.-C., Cheng, K.-C., Chen, F.-A., and Cheng, J.-T. (2009). Effect of Shanzha, a Chinese Herbal Product, on Obesity and Dyslipidemia in Hamsters Receiving High-Fat Diet. *J. Ethnopharmacology* 124 (3), 544–550. doi:10.1016/j.jep.2009.05.005

Lafontan, M., and Langin, D. (2009). Lipolysis and Lipid Mobilization in Human Adipose Tissue. *Prog. Lipid Res.* 48 (5), 275–297. doi:10.1016/j.plipres.2009.05.001

Langley, J. N. (1918). On the Stimulation and Paralysis of Nerve Cells and Nerve Endings. *J. Physiol.* 52 (4), 247–266. doi:10.1113/jphysiol.1918.sp001828

Lasa, A., Schweiger, M., Kotzbeck, P., Churruca, I., Simón, E., Zechner, R., et al. (2012). Resveratrol Regulates Lipolysis via Adipose Triglyceride Lipase. *J. Nutr. Biochem.* 23 (4), 379–384. doi:10.1016/j.jnutbio.2010.12.014

Lazo, M., and Clark, J. (2008). The Epidemiology of Nonalcoholic Fatty Liver Disease: a Global Perspective. *Semin. Liver Dis.* 28 (4), 339–350. doi:10.1055/s-0028-1091978

Lee, G.-R., Shin, M. K., Yoon, D.-J., Kim, A.-R., Yu, R., Park, N.-H., et al. (2013). Topical Application of Capsaicin Reduces Visceral Adipose Fat by Affecting Adipokine Levels in High-Fat Diet-Induced Obese Mice. *Obesity* 21 (1), 115–122. doi:10.1002/oby.20246

Ley, R. E., Bäckhed, F., Turnbaugh, P., Lozupone, C. A., Knight, R. D., and Gordon, J. I. (2005). Obesity Alters Gut Microbial Ecology. *Proc. Natl. Acad. Sci.* 102 (31), 11070–11075. doi:10.1073/pnas.0504978102

Li, Y., Wang, X., and Shen, Z. (2017). Traditional Chinese Medicine for Lipid Metabolism Disorders. *Am. J. Transl Res.* 9 (5), 2038–2049.

Li, Y., Rahman, S. U., Huang, Y., Zhang, Y., Ming, P., Zhu, L., et al. (2020). Green tea Polyphenols Decrease Weight Gain, Ameliorate Alteration of Gut Microbiota, and Mitigate Intestinal Inflammation in Canines with High-Fat-Diet-Induced Obesity. *J. Nutr. Biochem.* 78, 108324. doi:10.1016/j.jnutbio.2019.108324

Li, Z., Xu, J., Zheng, P., Xing, L., Shen, H., Yang, L., et al. (2015). Hawthorn Leaf Flavonoids Alleviate Nonalcoholic Fatty Liver Disease by Enhancing the Adiponectin/AMPK Pathway. *Int. J. Clin. Exp. Med.* 8 (10), 17295–17307.

Licinio, J., Caglayan, S., Ozata, M., Yildiz, B. O., de Miranda, P. B., O'Kirwan, F., et al. (2004). Phenotypic Effects of Leptin Replacement on Morbid Obesity, Diabetes Mellitus, Hypogonadism, and Behavior in Leptin-Deficient Adults. *Proc. Natl. Acad. Sci.* 101 (13), 4531–4536. doi:10.1073/pnas.0308767101

Liu, J., Lee, J., Salazar Hernandez, M. A., Mazitschek, R., and Ozcan, U. (2015). Treatment of Obesity with Celastrol. *Cell* 161 (5), 999–1011. doi:10.1016/j.cell.2015.05.011

Luo, J., Yang, H., and Song, B.-L. (2020). Mechanisms and Regulation of Cholesterol Homeostasis. *Nat. Rev. Mol. Cel. Biol.* 21 (4), 225–245. doi:10.1038/s41580-019-0190-7

Ma, N., Zhang, Z., Liao, F., Jiang, T., and Tu, Y. (2020). The Birth of Artemisinin. *Pharmacol. Ther.* 216, 107658. doi:10.1016/j.pharmthera.2020.107658

Martel, J., Ojcius, D. M., Chang, C.-J., Lin, C.-S., Lu, C.-C., Ko, Y.-F., et al. (2017). Anti-obesogenic and Antidiabetic Effects of Plants and Mushrooms. *Nat. Rev. Endocrinol.* 13 (3), 149–160. doi:10.1038/nrendo.2016.142

Mashek, D. G. (2013). Hepatic Fatty Acid Trafficking: Multiple forks in the Road. *Adv. Nutr.* 4 (6), 697–710. doi:10.3945/an.113.004648

Meikle, P. J., and Summers, S. A. (2017). Sphingolipids and Phospholipids in Insulin Resistance and Related Metabolic Disorders. *Nat. Rev. Endocrinol.* 13 (2), 79–91. doi:10.1038/nrendo.2016.169

Meng, Q., Duan, X.-p., Wang, C.-y., Liu, Z.-h., Sun, P.-y., Huo, X.-k., et al. (2017). Alisol B 23-acetate Protects against Non-alcoholic Steatohepatitis in Mice via Farnesoid X Receptor Activation. *Acta Pharmacol. Sin* 38 (1), 69–79. doi:10.1038/aps.2016.119

Montague, C. T., Farooqi, I. S., Whitehead, J. P., Soos, M. A., Rau, H., Wareham, N. J., et al. (1997). Congenital Leptin Deficiency Is Associated with Severe Early-Onset Obesity in Humans. *Nature* 387 (6636), 903–908. doi:10.1038/43185

Mun, J., Kim, S., Yoon, H.-G., You, Y., Kim, O.-K., Choi, K.-C., et al. (2019). Water Extract of Curcuma Longa L. Ameliorates Non-alcoholic Fatty Liver Disease. *Nutrients* 11 (10), 2536. doi:10.3390/nu11102536

Navekar, R., Rafraf, M., Ghaffari, A., Asghari-Jafarabadi, M., and Khoshbaten, M. (2017). Turmeric Supplementation Improves Serum Glucose Indices and Leptin Levels in Patients with Nonalcoholic Fatty Liver Diseases. *J. Am. Coll. Nutr.* 36 (4), 261–267. doi:10.1080/07315724.2016.1267597

Nissen, S. E., Wolski, K. E., Prcela, L., Wadden, T., Buse, J. B., Bakris, G., et al. (2016). Effect of Naltrexone-Bupropion on Major Adverse Cardiovascular Events in Overweight and Obese Patients with Cardiovascular Risk Factors. *Jama* 315 (10), 990–1004. doi:10.1001/jama.2016.1558

Panchal, S., Bliss, E., and Brown, L. (2018). Capsaicin in Metabolic Syndrome. *Nutrients* 10 (5), 630. doi:10.3390/nu10050630

Park, Y.-J., Kim, M.-S., Kim, H.-R., Kim, J.-M., Hwang, J.-K., Yang, S.-H., et al. (2014). Ethanol Extract ofAlismatis rhizomeInhibits Adipocyte Differentiation of OP9 Cells. *Evidence-Based Complement. Altern. Med.* 2014, 1–9. doi:10.1155/2014/4150972014

Pawlak, M., Lefebvre, P., and Staels, B. (2015). Molecular Mechanism of PPARα Action and its Impact on Lipid Metabolism, Inflammation and Fibrosis in Non-alcoholic Fatty Liver Disease. *J. Hepatol.* 62 (3), 720–733. doi:10.1016/j.jhep.2014.10.039

Pearl, R. L., Wadden, T. A., Tronieri, J. S., Berkowitz, R. I., Chao, A. M., Alamuddin, N., et al. (2018). Short- and Long-Term Changes in Health-Related Quality of Life with Weight Loss: Results from a Randomized Controlled Trial. *Obesity* 26 (6), 985–991. doi:10.1002/oby.22187

Pelleymounter, M., Cullen, M., Baker, M., Hecht, R., Winters, D., Boone, T., et al. (1995). Effects of the Obese Gene Product on Body Weight Regulation in Ob/ob Mice. *Science* 269 (5223), 540–543. doi:10.1126/science.7624776

Pi-Sunyer, X., Astrup, A., Fujioka, K., Greenway, F., Halpern, A., Krempf, M., et al. (2015). A Randomized, Controlled Trial of 3.0 Mg of Liraglutide in Weight Management. *N. Engl. J. Med.* 373 (1), 11–22. doi:10.1056/NEJMoa1411892

Pinhas-Hamiel, O., Singer, S., Pilpel, N., Fradkin, A., Modan, D., and Reichman, B. (2006). Health-related Quality of Life Among Children and Adolescents: Associations with Obesity. *Int. J. Obes.* 30 (2), 267–272. doi:10.1038/sj.ijo.0803107

Qin, B., Polansky, M. M., Harry, D., and Anderson, R. A. (2010). Green tea Polyphenols Improve Cardiac Muscle mRNA and Protein Levels of Signal Pathways Related to Insulin and Lipid Metabolism and Inflammation in Insulin-Resistant Rats. *Mol. Nutr. Food Res.* 54 (Suppl. 1), S14–S23. doi:10.1002/mnfr.200900306

Rabot, S., Membrez, M., Bruneau, A., Gérard, P., Harach, T., Moser, M., et al. (2010). Germ-free C57BL/6J Mice Are Resistant to High-Fat-Diet-Induced Insulin Resistance and Have Altered Cholesterol Metabolism. *FASEB J.* 24 (12), 4948–4959. doi:10.1096/fj.10-164921

Rakhshandehroo, M., Sanderson, L. M., Matilainen, M., Stienstra, R., Carlberg, C., de Groot, P. J., et al. (2007). Comprehensive Analysis of PPARα-dependent Regulation of Hepatic Lipid Metabolism by Expression Profiling. *PPAR Res.* 2007, 1–13. doi:10.1155/2007/26839

Ramírez-Boscá, A., Soler, A., Carrión, M. A., Díaz-Alperi, J., Bernd, A., Quintanilla, C., et al. (2000). An Hydroalcoholic Extract of Curcuma Longa Lowers the Apo B/apo A Ratio. Implications for Atherogenesis Prevention. *Mech. Ageing Dev.* 119 (1-2), 41–47. doi:10.1016/s0047-6374(00)00169-x

Ridaura, V. K., Faith, J. J., Rey, F. E., Cheng, J., Duncan, A. E., Kau, A. L., et al. (2013). Gut Microbiota from Twins Discordant for Obesity Modulate Metabolism in Mice. *Science* 341 (6150), 1241214. doi:10.1126/science.1241214

Rocha, V. Z., and Libby, P. (2009). Obesity, Inflammation, and Atherosclerosis. *Nat. Rev. Cardiol.* 6 (6), 399–409. doi:10.1038/nrcardio.2009.55

Rodriguez, J. A., Ben Ali, Y., Abdelkafi, S., Mendoza, L. D., Leclaire, J., Fotiadu, F., et al. (2010). *In Vitro* stereoselective Hydrolysis of Diacylglycerols by Hormone-Sensitive Lipase. *Biochim. Biophys. Acta (Bba) - Mol. Cel Biol. Lipids* 1801 (1), 77–83. doi:10.1016/j.bbalip.2009.09.020

Rosca, A. E., Iesanu, M. I., Zahiu, C. D. M., Voiculescu, S. E., Paslaru, A. C., and Zagrean, A.-M. (2020). Capsaicin and Gut Microbiota in Health and Disease. *Molecules* 25 (23), 5681. doi:10.3390/molecules25235681

Santacruz, A., Marcos, A., Wärnberg, J., Martí, A., Martin-Matillas, M., Campoy, C., et al. (2009). Interplay between Weight Loss and Gut Microbiota Composition in Overweight Adolescents. *Obesity (Silver Spring)* 17 (10), 1906–1915. doi:10.1038/oby.2009.112

Seo, B. R., Bhardwaj, P., Choi, S., Gonzalez, J., Andresen Eguiluz, R. C., Wang, K., et al. (2015). Obesity-dependent Changes in Interstitial ECM Mechanics Promote Breast Tumorigenesis. *Sci. Transl. Med.* 7 (301), 301ra130. doi:10.1126/scitranslmed.3010467

Sham, T.-T., Chan, C.-O., Wang, Y.-H., Yang, J.-M., Mok, D. K.-W., and Chan, S.-W. (2014). A Review on the Traditional Chinese Medicinal Herbs and Formulae with Hypolipidemic Effect. *Biomed. Res. Int.* 2014, 1–21. doi:10.1155/2014/925302

Shi, Z., Zhu, J.-x., Guo, Y.-m., Niu, M., Zhang, L., Tu, C., et al. (2020). Epigallocatechin Gallate during Dietary Restriction - Potential Mechanisms of Enhanced Liver Injury. *Front. Pharmacol.* 11, 609378. doi:10.3389/fphar.2020.609378

Shih, C.-C., Lin, C.-H., Lin, Y.-J., and Wu, J.-B. (2013). Validation of the Antidiabetic and Hypolipidemic Effects of Hawthorn by Assessment of Gluconeogenesis and Lipogenesis Related Genes and AMP-Activated Protein Kinase Phosphorylation. *Evidence-Based Complement. Altern. Med.* 2013, 1–12. doi:10.1155/2013/597067

Shimamura, Y., Yoda, M., Sakakibara, H., Matsunaga, K., and Masuda, S. (2013). Pu-erh tea Suppresses Diet-Induced Body Fat Accumulation in C57BL/6J Mice by Down-Regulating SREBP-1c and Related Molecules. *Biosci. Biotechnol. Biochem.* 77 (7), 1455–1460. doi:10.1271/bbb.130097

Singh, V., Jain, M., Misra, A., Khanna, V., Prakash, P., Malasoni, R., et al. (2015). Curcuma Oil Ameliorates Insulin Resistance & Associated Thrombotic Complications in Hamster & Rat. *Indian J. Med. Res.* 141 (6), 823–832. doi:10.4103/0971-5916.160719

Singh, V., Jain, M., Misra, A., Khanna, V., Rana, M., Prakash, P., et al. (2013). Curcuma Oil Ameliorates Hyperlipidaemia and Associated Deleterious Effects in golden Syrian Hamsters. *Br. J. Nutr.* 110 (3), 437–446. doi:10.1017/S0007114512005363

Smeets, A. J., and Westerterp-Plantenga, M. S. (2009). The Acute Effects of a Lunch Containing Capsaicin on Energy and Substrate Utilisation, Hormones, and Satiety. *Eur. J. Nutr.* 48 (4), 229–234. doi:10.1007/s00394-009-0006-1

Smith, S. R., Weissman, N. J., Anderson, C. M., Sanchez, M., Chuang, E., Stubbe, S., et al. (2010). Multicenter, Placebo-Controlled Trial of Lorcaserin for Weight Management. *N. Engl. J. Med.* 363 (3), 245–256. doi:10.1056/NEJMoa0909809

Solas, M., Milagro, F. I., Martínez-Urbistondo, D., Ramirez, M. J., and Martínez, J. A. (2016). Precision Obesity Treatments Including Pharmacogenetic and Nutrigenetic Approaches. *Trends Pharmacol. Sci.* 37 (7), 575–593. doi:10.1016/j.tips.2016.04.008

Song, J.-X., Ren, H., Gao, Y.-F., Lee, C.-Y., Li, S.-F., Zhang, F., et al. (2017). Dietary Capsaicin Improves Glucose Homeostasis and Alters the Gut Microbiota in

Obese Diabetic Ob/ob Mice. *Front. Physiol.* 8, 602. doi:10.3389/fphys.2017.00602

Song, W.-Y., and Choi, J.-H. (2016). KoreanCurcuma Longa L. Induces Lipolysis and Regulates Leptin in Adipocyte Cells and Rats. *Nutr. Res. Pract.* 10 (5), 487–493. doi:10.4162/nrp.2016.10.5.487

Stoll, B. (1998). Teenage Obesity in Relation to Breast Cancer Risk. *Int. J. Obes.* 22 (11), 1035–1040. doi:10.1038/sj.ijo.0800769

Sun, Y., Wang, Y., Song, P., Wang, H., Xu, N., Wang, Y., et al. (2019). Anti-obesity Effects of Instant Fermented Teas *In Vitro* and in Mice with High-Fat-Diet-Induced Obesity. *Food Funct.* 10 (6), 3502–3513. doi:10.1039/c9fo00162j

Takizawa, Y., Nakata, R., Fukuhara, K., Yamashita, H., Kubodera, H., and Inoue, H. (2015). The 4′-Hydroxyl Group of Resveratrol Is Functionally Important for Direct Activation of PPARα. *PLoS One* 10 (3), e0120865. doi:10.1371/journal.pone.0120865

Tarantino, G., Pezzullo, M. G., Minno, M. N. D. d., Milone, F., Pezzullo, L. S., Milone, M., et al. (2009). Drug-induced Liver Injury Due to "natural Products" Used for Weight Loss: a Case Report. *Wjg* 15 (19), 2414–2417. doi:10.3748/wjg.15.2414

Tian, C., Ye, X., Zhang, R., Long, J., Ren, W., Ding, S., et al. (2013). Green Tea Polyphenols Reduced Fat Deposits in High Fat-Fed Rats via Erk1/2-Pparγ-Adiponectin Pathway. *PLoS One* 8 (1), e53796. doi:10.1371/journal.pone.0053796

Timmers, S., Konings, E., Bilet, L., Houtkooper, R. H., van de Weijer, T., Goossens, G. H., et al. (2011). Calorie Restriction-like Effects of 30 Days of Resveratrol Supplementation on Energy Metabolism and Metabolic Profile in Obese Humans. *Cel Metab.* 14 (5), 612–622. doi:10.1016/j.cmet.2011.10.002

Tomé-Carneiro, J., Gonzálvez, M., Larrosa, M., García-Almagro, F. J., Avilés-Plaza, F., Parra, S., et al. (2012). Consumption of a Grape Extract Supplement Containing Resveratrol Decreases Oxidized LDL and ApoB in Patients Undergoing Primary Prevention of Cardiovascular Disease: a Triple-Blind, 6-month Follow-Up, Placebo-Controlled, Randomized Trial. *Mol. Nutr. Food Res.* 56 (5), 810–821. doi:10.1002/mnfr.201100673

Tu, C., Jiang, B. Q., Zhao, Y. L., Li, C. Y., Li, N., Li, X. F., et al. (2015). [Comparison of Processed and Crude Polygoni Multiflori Radix Induced Rat Liver Injury and Screening for Sensitive Indicators]. *Zhongguo Zhong Yao Za Zhi*. 40 (4), 654–660. doi:10.4268/cjcmm20150416

Tung, N. H., Nakajima, K., Uto, T., Hai, N. T., Long, D. D., Ohta, T., et al. (2017). Bioactive Triterpenes from the Root of Salvia Miltiorrhiza Bunge. *Phytother. Res.* 31 (9), 1457–1460. doi:10.1002/ptr.5877

Turnbaugh, P. J., Hamady, M., Yatsunenko, T., Cantarel, B. L., Duncan, A., Ley, R. E., et al. (2009). A Core Gut Microbiome in Obese and Lean Twins. *Nature* 457 (7228), 480–484. doi:10.1038/nature07540

Turnbaugh, P. J., Ley, R. E., Mahowald, M. A., Magrini, V., Mardis, E. R., and Gordon, J. I. (2006). An Obesity-Associated Gut Microbiome with Increased Capacity for Energy Harvest. *Nature* 444 (7122), 1027–1031. doi:10.1038/nature05414

Valentine, C., Ohnishi, K., Irie, K., and Murakami, A. (2019). Curcumin May Induce Lipolysis via Proteo-Stress in Huh7 Human Hepatoma Cells. *J. Clin. Biochem. Nutr.* 65 (2), 91–98. doi:10.3164/jcbn.19-7

Waisundara, V. Y., Hsu, A., Tan, B. K.-H., and Huang, D. (2009). Baicalin Reduces Mitochondrial Damage in Streptozotocin-Induced Diabetic Wistar Rats. *Diabetes Metab. Res. Rev.* 25 (7), 671–677. doi:10.1002/dmrr.1005

Wang, C., Shi, C., Yang, X., Yang, M., Sun, H., and Wang, C. (2014). Celastrol Suppresses Obesity Process via Increasing Antioxidant Capacity and Improving Lipid Metabolism. *Eur. J. Pharmacol.* 744, 52–58. doi:10.1016/j.ejphar.2014.09.043

Wang, J.-M., Cai, H., Li, J.-H., Chen, R.-X., Zhang, Y.-Y., Li, J.-Y., et al. (2018). Detoxication Mechanisms of Radix Tripterygium Wilfordii via Compatibility with Herba Lysimachia Christinae in S180-Bearing Mice by Involving Nrf2. *Biosci. Rep.* 38 (4). doi:10.1042/bsr20180429

Wang, J., Miao, M., Zhang, Y., Liu, R., Li, X., Cui, Y., et al. (2015). Quercetin Ameliorates Liver Injury Induced with Tripterygium Glycosides by Reducing Oxidative Stress and Inflammation. *Can. J. Physiol. Pharmacol.* 93 (6), 427–433. doi:10.1139/cjpp-2015-0038

Wang, P., Li, D., Ke, W., Liang, D., Hu, X., and Chen, F. (2020). Resveratrol-induced Gut Microbiota Reduces Obesity in High-Fat Diet-Fed Mice. *Int. J. Obes.* 44 (1), 213–225. doi:10.1038/s41366-019-0332-1

Wang, Q., Li, C., Zhang, Q., Wang, Y., Shi, T., Lu, L., et al. (2016). The Effect of Chinese Herbs and its Effective Components on Coronary Heart Disease through PPARs-Pgc1α Pathway. *BMC Complement. Altern. Med.* 16 (1), 514. doi:10.1186/s12906-016-1496-z

Wang, S., Moustaid-Moussa, N., Chen, L., Mo, H., Shastri, A., Su, R., et al. (2014). Novel Insights of Dietary Polyphenols and Obesity. *J. Nutr. Biochem.* 25 (1), 1–18. doi:10.1016/j.jnutbio.2013.09.001

Wang, Y., Tang, C., Tang, Y., Yin, H., and Liu, X. (2020). Capsaicin Has an Anti-obesity Effect through Alterations in Gut Microbiota Populations and Short-Chain Fatty Acid Concentrations. *Food Nutr. Res.* 64. doi:10.29219/fnr.v64.3525

Wang, Y., Viscarra, J., Kim, S.-J., and Sul, H. S. (2015). Transcriptional Regulation of Hepatic Lipogenesis. *Nat. Rev. Mol. Cel. Biol.* 16 (11), 678–689. doi:10.1038/nrm4074

Wen, J., Chang, Y., Huo, S., Li, W., Huang, H., Gao, Y., et al. (2020). Tanshinone IIA Attenuates Atherosclerosis via Inhibiting NLRP3 Inflammasome Activation. *Aging* 13 (1), 910–932. doi:10.18632/aging.202202

Wille, N., Erhart, M., Petersen, C., and Ravens-Sieberer, U. (2008). The Impact of Overweight and Obesity on Health-Related Quality of Life in Childhood - Results from an Intervention Study. *BMC Public Health* 8, 421. doi:10.1186/1471-2458-8-421

Wu, L., Yan, Q., Chen, F., Cao, C., and Wang, S. (2021). Bupleuri Radix Extract Ameliorates Impaired Lipid Metabolism in High-Fat Diet-Induced Obese Mice via Gut Microbia-Mediated Regulation of FGF21 Signaling Pathway. *Biomed. Pharmacother.* 135, 111187. doi:10.1016/j.biopha.2020.111187

Xi, Y., Wu, M., Li, H., Dong, S., Luo, E., Gu, M., et al. (2015). Baicalin Attenuates High Fat Diet-Induced Obesity and Liver Dysfunction: Dose-Response and Potential Role of CaMKKβ/AMPK/ACC Pathway. *Cell. Physiol. Biochem.* 35 (6), 2349–2359. doi:10.1159/000374037

Xia, W., Sun, C., Zhao, Y., and Wu, L. (2011). Hypolipidemic and Antioxidant Activities of Sanchi (Radix Notoginseng) in Rats Fed with a High Fat Diet. *Phytomedicine* 18 (6), 516–520. doi:10.1016/j.phymed.2010.09.007

Xian, Z., Liu, Y., Xu, W., Duan, F., Guo, Z., and Xiao, H. (2017). The Anti-hyperlipidemia Effects of Raw Polygonum Multiflorum Extract *In Vivo*. *Biol. Pharm. Bull.* 40 (11), 1839–1845. doi:10.1248/bpb.b17-00218

Xin-Min, M. O., Liu, R., Jian-Ping, L. I., Fan, J. J., and Gan, G. X. (2010). Effects of Danshen on Non-alcoholic Fatty Liver in Serum Leptin Ghrelin. *Chinese Archives of Traditional Chinese Medicine* 28 (11), 2252–2254. doi:10.13193/j.archtcm.2010.11.14.moxm.064

Xu, S., Feng, Y., He, W., Xu, W., Xu, W., Yang, H., et al. (2021). Celastrol in Metabolic Diseases: Progress and Application Prospects. *Pharmacol. Res.* 167, 105572. doi:10.1016/j.phrs.2021.105572

Yamashita, M., Kumazoe, M., Nakamura, Y., Won, Y. S., Bae, J., Yamashita, S., et al. (2016). The Combination of Green Tea Extract and Eriodictyol Inhibited High-Fat/High-Sucrose Diet-Induced Cholesterol Upregulation Is Accompanied by Suppression of Cholesterol Synthesis Enzymes. *J. Nutr. Sci. Vitaminol* 62 (4), 249–256. doi:10.3177/jnsv.62.249

Yan-Xia, S. U., Xun, Y. H., and Chen, Z. Y. (2011). Effect of Sanchi on Hepatic Expression of SREBP1c in Rats with Alcoholic Liver Disease. *Chinese Journal of Clinical Pharmacology and Therapeutics* 16 (2), 148–154.

Yang, C.-y., Wang, J., Zhao, Y., Shen, L., Jiang, X., Xie, Z.-g., et al. (2010). Anti-diabetic Effects of Panax Notoginseng Saponins and its Major Anti-hyperglycemic Components. *J. Ethnopharmacology* 130 (2), 231–236. doi:10.1016/j.jep.2010.04.039

Yang, J., Sun, L., Wang, L., Hassan, H. M., Wang, X., Hylemon, P. B., et al. (2017). Activation of Sirt1/FXR Signaling Pathway Attenuates Triptolide-Induced Hepatotoxicity in Rats. *Front. Pharmacol.* 8, 260. doi:10.3389/fphar.2017.00260

Yashiro, T., Nanmoku, M., Shimizu, M., Inoue, J., and Sato, R. (2012). Resveratrol Increases the Expression and Activity of the Low Density Lipoprotein Receptor in Hepatocytes by the Proteolytic Activation of the Sterol Regulatory Element-Binding Proteins. *Atherosclerosis* 220 (2), 369–374. doi:10.1016/j.atherosclerosis.2011.11.006

Yi-Xin, M. A., Jia, L. Q., Song, N., Wang, J. Y., Xue, L., Zhang, N., et al. (2017). Effects of Tanshinone ⅡA on Liver Proteome Expression of Hyperlipidemia Rats by iTRAQ Technology. *Chinese Journal of Integrated Traditional and Western Medicine*. doi:10.7661/j.cjim.20170315.041

Yu, H. R., Sheen, J. M., Tiao, M. M., Tain, Y. L., Chen, C. C., Lin, I. C., et al. (2019). Resveratrol Treatment Ameliorates Leptin Resistance and Adiposity Programed by the Combined Effect of Maternal and Post-Weaning High-Fat Diet. *Mol. Nutr. Food Res.* 63 (13), 1802385. doi:10.1002/mnfr.201801385

Yu, R., Lv, Y., Wang, J., Pan, N., Zhang, R., Wang, X., et al. (2016). Baicalin Promotes Cholesterol Efflux by Regulating the Expression of SR-BI in Macrophages. *Exp. Ther. Med.* 12 (6), 4113–4120. doi:10.3892/etm.2016.3884

Zechner, R., Madeo, F., and Kratky, D. (2017). Cytosolic Lipolysis and Lipophagy: Two Sides of the Same coin. *Nat. Rev. Mol. Cel. Biol.* 18 (11), 671–684. doi:10.1038/nrm.2017.76

Zeng, L., Yan, J., Luo, L., and Zhang, D. (2015). Effects of Pu-Erh tea Aqueous Extract (PTAE) on Blood Lipid Metabolism Enzymes. *Food Funct.* 6 (6), 2008–2016. doi:10.1039/c5fo00362h

Zhang, J., Zhang, H., Deng, X., Zhang, N., Liu, B., Xin, S., et al. (2018). Baicalin Attenuates Non-alcoholic Steatohepatitis by Suppressing Key Regulators of Lipid Metabolism, Inflammation and Fibrosis in Mice. *Life Sci.* 192, 46–54. doi:10.1016/j.lfs.2017.11.027

Zhang, X.-H., Huang, B., Choi, S.-K., and Seo, J.-S. (2012). Anti-obesity Effect of Resveratrol-Amplified Grape Skin Extracts on 3T3-L1 Adipocytes Differentiation. *Nutr. Res. Pract.* 6 (4), 286–293. doi:10.4162/nrp.2012.6.4.286

Zhang, X., Zhang, B., Zhang, C., Sun, G., and Sun, X. (2020). Effect of Panax Notoginseng Saponins and Major Anti-obesity Components on Weight Loss. *Front. Pharmacol.* 11, 601751. doi:10.3389/fphar.2020.601751

Zhang, Y., Geng, C., Liu, X., Li, M., Gao, M., Liu, X., et al. (2017). Celastrol Ameliorates Liver Metabolic Damage Caused by a High-Fat Diet through Sirt1. *Mol. Metab.* 6 (1), 138–147. doi:10.1016/j.molmet.2016.11.002

Zhang, Y., Kishi, H., and Kobayashi, S. (2018). Add-on Therapy with Traditional Chinese Medicine: An Efficacious Approach for Lipid Metabolism Disorders. *Pharmacol. Res.* 134, 200–211. doi:10.1016/j.phrs.2018.06.004

Zhang, Y., Zhang, L., Geng, Y., and Geng, Y. (2014). Hawthorn Fruit Attenuates Atherosclerosis by Improving the Hypolipidemic and Antioxidant Activities in Apolipoprotein E-Deficient Mice. *Jat* 21 (2), 119–128. doi:10.5551/jat.19174

Zhao, D., Liu, J., Wang, M., Zhang, X., and Zhou, M. (2019). Epidemiology of Cardiovascular Disease in China: Current Features and Implications. *Nat. Rev. Cardiol.* 16 (4), 203–212. doi:10.1038/s41569-018-0119-4

Zhao, J., Sun, X.-B., Ye, F., and Tian, W.-X. (2011). Suppression of Fatty Acid Synthase, Differentiation and Lipid Accumulation in Adipocytes by Curcumin. *Mol. Cel. Biochem.* 351 (1-2), 19–28. doi:10.1007/s11010-010-0707-z

Zhou, L., Xiao, X., Zhang, Q., Zheng, J., and Deng, M. (2019). Deciphering the Anti-obesity Benefits of Resveratrol: The "Gut Microbiota-Adipose Tissue" Axis. *Front. Endocrinol.* 10, 413. doi:10.3389/fendo.2019.00413

Conflict of Interest: The authors declare that the research was conducted in the absence of any commercial or financial relationships that could be construed as a potential conflict of interest.

GLOSSARY

ABCA ATP-binding cassette transporter A
ABCG ATP-binding cassette transporter G
ACAT acyl coenzyme A–cholesterol acyltransferase
ACC acetyl-CoA carboxylase
ApoA apolipoprotein A
ARH arcuate hypothalamus
AS atherosclerosis
ATGL adipose triglyceride hydrolase
BMI body mass index
BSH bile-salt hydrolase
C/EBPβ CCAAT/enhancer-binding protein β
CD36 cluster of differentiation 36
chREBP carbohydrate-responsive element–binding protein
ChP Pharmacopoeia of the People's Republic of China
CNS central nervous system
CPT1 carnitine palmitoyl transferase 1
CEs cholesterol esters
CVD cardiovascular disease
CYP7A1 cholesterol 7α-hydroxylase
DGAT diacylglycerol acyltransferase
DNL de novo lipogenesis
EGCG epigallocatechin gallate
ERR estrogen-related receptor
FA fatty acid
FAS fatty acid synthase
FATP fatty acid transport protein
FGF15 fibroblast growth factor 15
FOXO1 forkhead box protein O1
FXR farnesoid X receptor
GLP1 glucagon-like peptide 1
GPAT glycerol-3-phosphate acyltransferase
G6Pase PGC1α-dependent enzyme
HDL high-density lipoprotein
HFD high-fat diet
HFrD high-fructose diet
HL hepatic lipase
HMGCR 3-hydroxy-3-methylglutaryl coenzyme A reductase
HNF4α hepatocyte nuclear receptor 4α
HSL hormone-sensitive lipase
IDL intermediate-density lipoprotein
IR insulin resistance
LDL low-density lipoprotein
LDL-c LDL particles
LDLR LDL receptor
LD lipid droplet
LOX-1 lectin-like oxidized LDL receptor-1
LPL lipoprotein lipase
LXR liver X receptor
MAG monoacylglycerol
MCD MCD methionine and choline–deficient diet
MGL monoacylglycerol lipase
MUFA mono-unsaturated fatty acid
NADPH nicotinamide adenine dinucleotide phosphate
NAFLD non-alcoholic fatty liver disease
NE3 n-butanol extract of Panax notoginseng (Burkill) F.H. Chen
NPC1L1 Niemann–Pick C1-like 1
oxLDL oxidized low-density lipoprotein
PCSK9 proprotein convertase subtilisin/kexin type 9
PGC1α PPARγ co-activator 1α
PL phospholipid
PNSs Panax notoginseng (Burkill) F.H. Chen saponins
PPAR peroxisome proliferator–activated receptor
PTE pu-erh tea extract
SCD stearoyl-CoA desaturase
SM squalene monooxygenase
SR-BI scavenger receptor class B type I
SREBP sterol regulatory element–binding protein
T2D type 2 diabetes
TAG triacylglycerol
TC total cholesterol
TCM traditional Chinese medicine
TG triglyceride
TrpV1 transient receptor potential cation channel subfamily V member 1
VLDL very low–density lipoprotein
WHO World Health Organization
WT wild type

frontiers in Pharmacology

ORIGINAL RESEARCH
published: 24 August 2021
doi: 10.3389/fphar.2021.678865

A Polysaccharide From the Whole Plant of *Plantago asiatica* L. Enhances the Antitumor Activity of Dendritic Cell-Based Immunotherapy Against Breast Cancer

Jiafeng Gao[1], Yi-Nan Zhang[2], Jingwen Cui[1], Jiatong Zhang[1], Yuexiang Ming[1], Zhihui Hao[1,3], Huihao Xu[1], Nan Cheng[1], Di Zhang[1], Yipeng Jin[1], Degui Lin[1]* and Jiahao Lin[1,3]**

[1]The Clinical Department, College of Veterinary Medicine, China Agricultural University, Beijing, China, [2]Institute of Biomaterials and Biomedical Engineering, University of Toronto, Toronto, Toronto, Canada, [3]Center of Research and Innovation of Chinese Traditional Veterinary Medicine, China Agricultural University, Beijing, China

OPEN ACCESS

Edited by:
Wei Song,
Peking Union Medical College Hospital (CAMS), China

Reviewed by:
Jen-Tsung Chen,
National University of Kaohsiung, Taiwan
Nai-Yun Sun,
Johns Hopkins University, United States

***Correspondence:**
Yipeng Jin
yipengjin@sina.com
Degui Lin
csama@sina.com
Jiahao Lin
jiahao_lin@cau.edu.cn

Specialty section:
This article was submitted to Ethnopharmacology, a section of the journal Frontiers in Pharmacology

Received: *10 March 2021*
Accepted: *26 July 2021*
Published: *24 August 2021*

Citation:
Gao J, Zhang Y-N, Cui J, Zhang J, Ming Y, Hao Z, Xu H, Cheng N, Zhang D, Jin Y, Lin D and Lin J (2021) A Polysaccharide From the Whole Plant of Plantago asiatica *L. Enhances the Antitumor Activity of Dendritic Cell-Based Immunotherapy Against Breast Cancer. Front. Pharmacol. 12:678865. doi: 10.3389/fphar.2021.678865*

Dendritic cells (DCs) are the most potent professional antigen-presenting cells (APCs) that mediate T-cell immune responses. Breast cancer is one of the most commonly diagnosed diseases and its mortality rate is higher than any other cancer in both humans and canines. Plantain polysaccharide (PLP), extracted from the whole plant of *Plantago asiatica* L., could promote the maturation of DCs. In this research, we found that PLP could upregulate the maturation of DCs both *in vitro* and *in vivo*. PLP-activated DCs could stimulate lymphocytes' proliferation and differentiate naive T cells into cytotoxic T cells. Tumor antigen-specific lymphocyte responses were enhanced by PLP and CIPp canine breast tumor cells lysate-pulsed DCs, and PLP and CIPp-cell-lysate jointly stimulated DCs cocultured with lymphocytes having the great cytotoxicity on CIPp cells. In the 4T1 murine breast tumor model, PLP could control the size of breast tumors and improve immunity by recruiting DCs, macrophages, and $CD4^+$ and $CD8^+$ T cells in the tumor microenvironment. These results indicated that PLP could achieve immunotherapeutic effects and improve immunity in the breast tumor model.

Keywords: ***Plantago asiatica*** **L, dendritic cells, cytotoxic T cells, breast tumor, immunotherapy**

INTRODUCTION

Dendritic cells (DCs) act as initiators of the initial immune response and play an important part in the regulation of the immune system. DCs recognize, capture, process, and present antigen to naive T cells, which stimulate the activation and proliferation of naive T cells for adaptive immune responses (Batra et al., 2012). DCs play a crucial role in triggering anticancer T-cell–mediated immunity against cancer cells. It has been confirmed that the number of DCs is closely related to cancer cell infiltration, lymph node metastasis, and prognosis (Steinman and Banchereau 2007; Palucka and Banchereau 2012).

Breast cancer is one of the most commonly diagnosed diseases and its mortality rate is higher than any other cancer in both humans and canines (KH et al., 2018). As an emerging anticancer therapeutic approach, immunotherapy is designed to harness the patient's own immune system, in which DCs present the cancer antigens to activate antigen-specific T-cell responses for fighting against the cancer cells

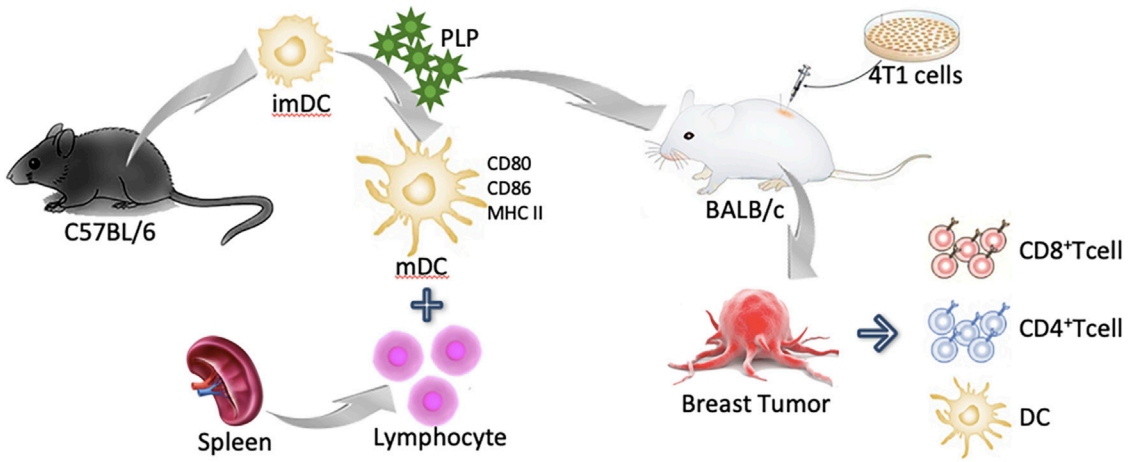

GRAPHICAL ABSTRACT |

(Klingemann, 2018). However, within the tumor microenvironment (TME), the function of DCs was inhibited that limits the effective anticancer T-cell responses, probably because the tumor tissue could secrete certain substances to inhibit the function of DCs (Sabado et al., 2017; Dong et al., 2018).

Chinese herbal extracts, especially their polysaccharide components, exhibit validated therapeutic effects and have shown the ability to promote the maturation of DCs. *Rehmannia glutinosa* polysaccharides (Huang et al., 2016), Cordyceps sinensis extracellular polysaccharides (Song et al., 2011), Kudzu root polysaccharides (Kim et al., 2013), Platycodon grandiflorum polysaccharides (Park et al., 2014), and Ganoderma lucidum polysaccharides (Meng et al., 2011) have all been verified to induce the maturation of DCs. Evidence showed that the clinical effects of these polysaccharides are related to the upregulated expression of costimulatory molecules such as CD80, CD86, and MHC II and the activation of tumor-related T-cell response. These studies provide evidence for the use of Chinese herbal extracts in clinically enhancing host immune function.

Our preliminary experiment had screened extractions of ten different Chinese herbal medicines which have been reported to have the ability of immune upregulation. The results revealed that among the ten candidates, including extraction of *Lycium barbarum* L., dried root of *Rehmannia glutinosa* (Gaertn.) DC., *Schisandra chinensis* (Turcz.) Baill., *Artemisia caruifolia* Buch.-Ham. ex Roxb. (syn. *Artemisia* apiacea), *Ganoderma lucidum* (Curtis) P. Karst., *Panax ginseng* C.A.Mey., *Astragalus mongholicus* Bunge, and *Plantago asiatica* L., etc., the total extraction of *Plantago asiatica* L. (PLPt) showed the most excellent ability to activate DCs.

Plantago asiatica L., belonging to the Plantaginaceae family, is a perennial plant and is widely distributed in eastern Asia. This plant has not only been used as medicine but has also been approved as raw material for healthy foods with a time-honored history (AB 2000; Yin et al., 2018). Polysaccharides from Plantago leaves have also been reported to induce nitric oxide and TNF-α secretion by activating macrophages (Biringanine et al., 2005). Recent studies mainly focused on the seed of *Plantago asiatica* L. and its purified polysaccharide which could upregulate the expression of maturation markers, decrease DCs' endocytosis, and increase intracellular interleukin (IL)-12 levels and heterologous stimulus activity, and promote T-cell proliferation (Huang et al., 2009; Huang et al., 2014; Jiang et al., 2018). Compared with the seed, the whole plants of *Plantago asiatica* L. have the advantages of widespread availability, limited cost, and easy processing. Therefore, the polysaccharide extracted from the whole plant of *Plantago asiatica* L. (PLP) has been screened as the main research object in our experiment. We want to assess if the PLP could induce the maturation of DCs and then stimulate the systemic immune reaction.

In this research, we investigated whether PLP could induce the maturation of mouse myelogenous DCs, and the PLP-activated DCs could stimulate lymphocytes' proliferation and differentiate naive T cells into cytotoxic T cells, which is associated with cellular immune function. Specifically, we evaluated its cytotoxicity on canine breast tumors cell lines and validated its influence on the status of DCs and CTLs against cancer cells. Based on the results, PLP could achieve immunotherapeutic effects and improve immunity in the breast tumor model. In addition, traditional Chinese medicine is expected to play an effective role with DCs in the immunotherapy of breast cancer and to activate the antitumor immune cycle efficiently.

MATERIALS AND METHODS

Animals

6- to 8-week-old female C57BL/6 mice, 4- to 6-week-old female BALB/c mice, and 4- to 6-week-old BALB/c nude mice with cleaning grade were purchased from Beijing Vital River Laboratory Animal Technology Co., Ltd. (Beijing, China, Certificate No. SCXK (Jing) 2016-0008). These animals were taken feeding management with free access to standard chow and water about a week before the experiment to adapt to the environment (24 ± 1°C and 12/12-h light/dark cycle). The mice were fasted overnight except water before the experiment. All animal studies were reviewed and approved by China Agricultural University Laboratory Animal Welfare and Animal Experimental Ethical Committee (Approval ID: CAU 2015121701–1).

Preparation of PLP

The crude *Plantago asiatica* L. herb polysaccharide was extracted using water extraction and alcohol precipitation method. *Plantago asiatica* L. was a kind of biennial herb, and we bought the standard decoction pieces of *Plantago asiatica* L. from Tongrentang Co., Ltd. (Beijing, China). Firstly, the *Plantago asiatica* L. herb was soaked in absolute ethanol with 8 times the amount of the herb overnight. The absolute ethanol part was then discarded, and the drugs were dried for subsequent use. Secondly, the extraction of dried residues was performed using the reflux extraction method 2 times with 2 h for each time. After the extracts were merged and concentrated, 4 times anhydrous ethanol was added and then the mixture was stored at 4°C overnight. Thirdly, the mixture was centrifuged at 3,500 r/min for 15 min to discard the supernatant, while the precipitates were dried and ground into powder. Then the PLP was obtained and stored at 4°C for further use.

The precipitate was redissolved and deproteinized using the Sevag method (Staub et al., 1965). To purify the PLP, 0.2 g PLP powder was dissolved in 40 ml distilled water. Then 10 ml of chloroform and n-butanol (4:1, v/v) were added into the suspension with fully shaking for 20 min. Centrifugal separation was performed five times at 2,500 r/min for 3 min each time to aspirate the supernatant. After the deproteinization procedure, the protein content of the PLP solution was determined using Micro Bicinchoninic Acid (BCA) protein assay method (Thermo Fisher, United States) according to the manufacturer's instructions.

Endotoxin was removed and assayed under endotoxin-free experimental conditions by using EtEraser™ HP Endotoxin Removal Kit and Bioendo™ EC Endotoxin Test Kit (Chinese Horseshoe Crab Reagent Manufactory Co., Fujian Province, China) according to the manufacturer's protocol. In brief, PLP was collected after flowing through the highly efficient endotoxin removal resin prepacked column. After endotoxin removal, 100 μL of PLP, standards, or endotoxin-free water (negative control) was mixed with 100 μL of TAL and the optical density (OD) was measured at 450 nm. The quantity of endotoxin was estimated to be ≤ 0.02 endotoxin unit (EU) per mg of PLP.

Mouse Bone Marrow–Derived DC Culture

Mouse bone marrow–derived DCs (BMDCs) were prepared with some modifications based on the references (Grauer et al., 2002). Briefly, bone marrow cells were harvested from the femurs and tibias of 6- to 8-week-old female C57BL/6 mice and depleted of erythrocytes by Red Blood Cell Lysis Buffer. Cells were washed and cultured at a concentration of 2×10^6 cells/mL in RPMI-1640 supplemented with 10% FBS, 100 U/mL penicillin, 100 U/mL streptomycin (GIBCO BRL, Germany), and 20 ng/ml recombinant mouse (rm) GM-CSF (PeproTech, United States). The medium was changed every 2 days. On Day 7, non-/loosely adherent cells were harvested and cultured in 24-well plates at 1×10^6 cells/mL. The cells were stimulated for 48 h with LPS (2 μg/ml, Sigma-Aldrich, United States), PLP (50 μg/ml), extraction of *Plantago asiatica* L. (PLPt, 50 μg/ml, purchased from Beijing Dongzhimen Hospital), or acteoside (50 μg/ml, purchased from Baoji GuoKang Biotechnology, China) respectively and then analyzed.

Cytotoxicity Assay

Cytotoxicity was evaluated using a commercial Cell Counting Kit-8 (Beyotime, China). Briefly, BMDCs were plated in 96-well plates at 1×10^4 cells per well and treated with RPMI-1640 alone (control group) or with different concentrations of PLP (12.5, 25, 50, 100, and 200 μg/ml). After 24 and 48 h, the CCK-8 solution was added to the cell wells and incubated at 37°C for 1 h to follow the instruction. Cell viability was assessed by measuring the optical density (OD) with a microplate reader (ELx808 TM; BioTek Instruments, United States) at 450 nm.

Maturation Marker Analysis

The effect of PLP on the maturation markers of DCs was examined using flow cytometry. The cultured DCs served as both testing group and control group were harvested on Day 9, and incubated cells were washed by cold PBS containing 2% FBS. Cells were proceeded to be incubated with FITC-conjugated anti-mouse CD11c, PE-conjugated anti-mouse MHC class II (I-A/I-E), PerCP/Cyanine 5.5-conjugated anti-mouse CD80, and APC-conjugated anti-mouse CD86 antibodies (Biolegend, United States) for 30 min at 4°C in the dark. Appropriate isotype-matched monoclonal antibodies served as negative controls. The percentages of CD80, CD86, and MHC class II were detected by a FACS Calibur (BD Pharmingen, United States) and analyzed with FlowJo software (TreeStar, United States).

Cytokine Assays

Interleukin (IL)-12p70, tumor necrosis factor (TNF)-α, IL-1β, IL-4, and IL-6 from the supernatant of cell culture medium were determined by ELISA kits according to the manufacturer's instructions (Proteintech, China). The optical density (OD) at 450 nm was measured with a microplate reader (ELx808TM; BioTek Instruments, United States).

DCs Stimulation with PLP *In Vivo*

- PLP (10 mg/kg) was administered by subcutaneous injection (s.c.), intraperitoneal injection (i.p.), or oral administration (p.o.) to C57BL/6 mice of three groups. Naive mice without PLP injection were used as a negative control, while LPS (2.5 mg/kg) was administered s.c. as a positive control. After 48 h, BMDCs were isolated and cultured until the seventh day to examine the CD80, CD86, and MHC class II expression.

Mixed Lymphocyte Reaction (MLR)

Mouse spleen lymphocytes were isolated by Mouse spleen lymphocytes Separation Solution kits according to the manufacturer's instructions (Solarbio, China). Briefly, 6- to 8-week-old female C57BL/6 mice were killed, and the spleens were transferred aseptically to Petri dishes, then cut into small pieces, minced, and filtered to obtain spleen cells suspension. The spleen cell suspension was slowly added into the lymphocyte separation solution in a ratio of 1:1. After centrifugation, the middle milky white cloud portion was taken to obtain spleen lymphocyte suspension. Finally, the density of cell suspension was set at 5.0×10^6 cells/mL in a complete RPMI-1640 medium. Then, spleen lymphocytes were stained with 1.25 μM carboxyfluorescein

(CFSE, Biolegend, United States) at 37°C for 20 min in dark. Mature DCs (matured in the presence of PLP or LPS) were pretreated with 50 ng/ml mitomycin C (a selective proliferation inhibitor which abrogates DNA synthesis, Sigma-Aldrich, United States) for 30 min at 37°C. After being thoroughly washed, CFSE-stained lymphocytes were cocultured with mature BMDCs in different groups at a BMDC: lymphocyte ratio of 1:4. After 48 h of coculture, cells were collected and incubated with PE-conjugated anti-mouse CD8a and APC-conjugated anti-mouse CD3 antibodies (Biolegend, United States) for flow cytometry analysis, and culture supernatants were collected for cytokine assays by IFN-γ ELISA kits (Proteintech, China).

Tumor Immunotherapy of PLP

Cell Culture

The CIPp cell line, established from a primary lesion of a female dog diagnosed with canine mammary tubular adenocarcinoma at clinical stage IV, was a generous gift from Professor Nobuo Sasaki (University of Tokyo, Japan). And murine breast cancer cell line 4T1 was purchased from ATCC (American Type Culture Collection, Manassas, VA, United States). The CIPp cells were cultured in Dulbecco's modified Eagle's medium (DMEM), supplemented with 10% FBS in a 5% CO_2 air incubator at 37°C. The 4T1 cells were cultured in RPMI-1640, supplemented with 10% FBS in a 5% CO_2 air incubator at 37°C.

Analysis of Tumor-Specific Immunity

Tumor cell lysates were prepared by five freeze–thaw cycles of CIPp cells (1×10^7 cells/mL in PBS). Cellular debris was removed by centrifugation, and the lysate solution was passed through a 0.22 μm membrane filter and stored at −80°C.

BMDCs were cultured in 24-well plates at 1×10^6 cells/mL were stimulated for 48 h with LPS (2 μg/ml), PLP (50 μg/ml), CIPp-cell-lysate, or CIPp-cell-lysate + PLP. DCs were incubated with tumor lysates at a ratio of 3:1 tumor cell equivalent. The stimulated DCs were collected to coculture with lymphocytes for tumor-specific immunity analysis.

Tumor-specific lymphocyte proliferation was determined by a similar method as MLR. Briefly, spleen lymphocytes were stained with 1.25 μM carboxyfluorescein (CFSE, Biolegend, United States) at 37°C for 20 min in dark. After being thoroughly washed, CFSE-stained lymphocytes were cocultured with BMDCs in different groups (LPS, PLP, CIPp-cell-lysate, and CIPp-cell-lysate + PLP) at a BMDC: lymphocyte ratio of 1:4. After 48 h of coculture, cells were collected for flow cytometry analysis. And the supernatants from the aforementioned groups were collected and centrifuged at 1,000 rpm for 10 min. The finally obtained supernatants were collected and stored at −80°C as conditioned medium.

CIPp Inhibitory Effects of PLP and Conditioned Medium

CCK-8 assay was conducted to investigate the effect of PLP and different groups of conditioned medium on the viability of CIPp cells. Cell viability assay was performed by seeding CIPp cells in a 96-well microplate at a density of 1×10^4 cells per well for 24 h before attached. Then cells were divided into different groups including the control group (DMEM) and groups treated with different concentrations of PLP (8, 15, 30, 60, 125, and 250 μg/ml). Cell viability was assessed with a commercial Cell Counting Kit-8 (Beyotime, China) at 24 and 48 h posttreatment according to the manufacturer's instructions. And different groups of conditioned medium (LPS, PLP, CIPp-cell-lysate, and CIPp-cell-lysate + PLP) were added into CIPp cell culture medium for 48 h. The optical density (OD) was measured with a microplate reader (ELx808TM; BioTek Instruments, United States) at 450 nm. All experiments were performed in quadruplicate.

To confirm the impact of PLP-associated T-cell immunity on tumor inhibition, we administered PLP (10 mg/kg) to CIPp tumor-bearing BALB/c nude mice which reveal congenital defects of T cells. BALB/c nude mice were s.c. inoculated with CIPp cells (1×10^5 cells). When tumor size reached approximately 100–200 mm^3 in volume, the mice were administered physiological saline and PLP (10 mg/kg/d, s.c.) every 24 h. The tumor volume was calculated using the following formula: mm^3 = (longest diameter × shortest diameter^2)/2. Mice were sacrificed at Day 28.

Tumor Experiments

4- to 6-week-old female BALB/c mice were used for the breast tumor-bearing model. Subcutaneous tumor models were established by inoculating 5×10^5 4T1 cells into the right flanks of the BALB/c mice. When tumor size reached approximately 100–200 mm^3 in volume, the mice were administered physiological saline, PLP (10 mg/kg/d, s.c.) once every 24 h, and TAXOL® (Harbin Pharmaceutical Group Holding Co., Ltd., Heilongjiang, China, 6 mg/kg, i.p.) and TAXOL®+PLP once every 4 days. Mice were closely monitored every other day for pain/distress, tumor volume, and body weight. The tumor volume was calculated using the following formula: mm^3 = (longest diameter × shortest diameter^2)/2. Mice were sacrificed at Day 22. Tumors were removed and weighed, and tumors, spleens, and inguinal lymph nodes were excised for flow cytometer analysis of immune cell subpopulations. Cells were proceeded to be incubated with FITC anti-mouse CD11c, APC anti-mouse CD3, PE anti-mouse CD8a, PerCP/Cyanine5.5 anti-mouse CD4, FITC anti-mouse IFN-γ, PE/Cyanine7 anti-mouse CD11b, and PE anti-mouse F4/80 antibodies (Biolegend, United States) for 30 min at 4°C in the dark. Cellular supernatant was collected for IFN-γ ELISA analysis.

Statistical Analysis

Statistical analyses were performed using Prism GraphPad 7 software. Each experiment was repeated at least three times. The quantitative data collected were expressed as mean ± S.D. One-way analysis of variance (ANOVA) with Dunnett's posttest was used for analysis of multiple groups, considered statistically significant if $p < 0.05$ ($^*p < 0.05$, $^{**}p < 0.01$, and $^{***}p < 0.001$, unless otherwise indicated).

RESULTS

Morphological Changes in Dendritic Cells after Treatment and Cytotoxicity Evaluation

We studied the DC population, defined as $CD11c^+$ cells using flow cytometry (**Figure 1A**). After being cultured for 7 days, the purity

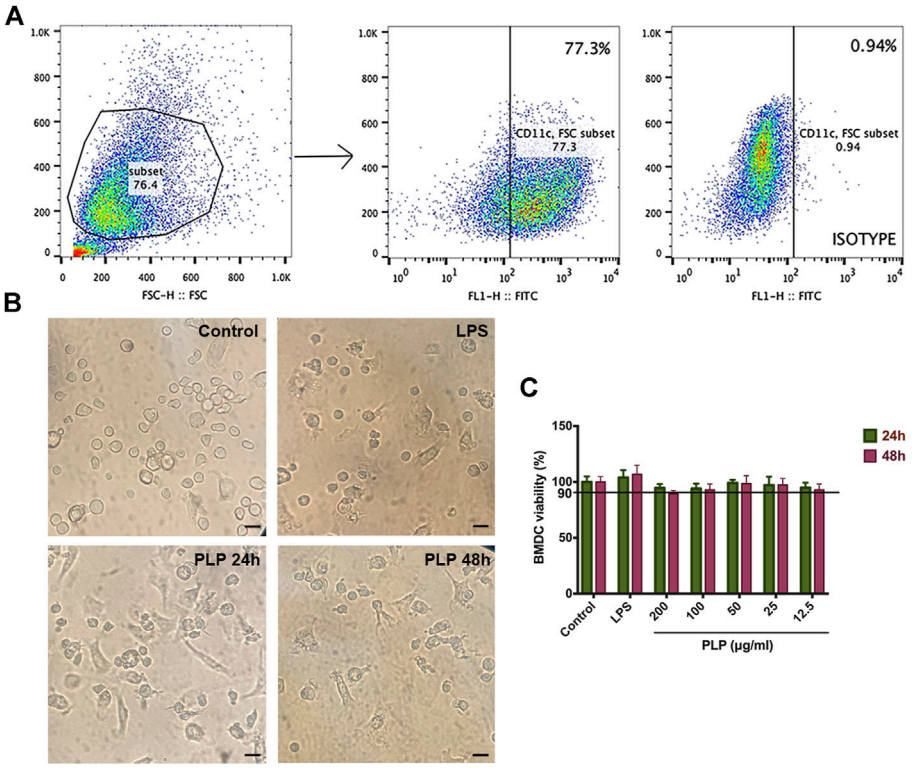

FIGURE 1 | Purity and morphological changes in dendritic cells and cytotoxicity evaluation. **(A)** Subsets of CD11c$^+$ cells were gated. **(B)** Representative microscopic views of BMDCs maturation stimulated with PLP (50 μg/ml) and LPS (positive control) for 48 h (×100). Bar = 150 μm. **(C)** Cytotoxic effects of DCs were analyzed using Cell Counting Kit-8 at 12.5, 25, 50, 100, and 200 μg/ml PLP treatment. Data are shown as mean ± SEM (n = 4) (*p < 0.05, **p < 0.01, and ***p < 0.001).

of CD11c$^+$ cells was detected by flow cytometry with a positive rate of 77.3%, which can be used in the subsequent experiments.

We observed the biological characteristics of BMDCs, and the results are shown in **Figure 1B**. In the control group, the light microscope showed that the semisuspended DCs had a round shape. In the groups treated with PLP and LPS, morphological characteristics of DCs changed to be enlarged, suspended, and displayed more typical dendritic protrusions. These changes in morphological characteristics suggested that DCs treated with PLP were more liable to convert into mature dendritic cells.

We tested the potential cell toxicity of PLP by incubating the DCs with different concentrations of PLP, LPS, and RPMI-1640, respectively. The DCs' viability was assessed by CCK-8 assay. No evidence of DCs toxicity *in vitro* could be observed within the concentration range of PLP from 12.5 to 200 μg/ml (**Figure 1C**).

PLP Induced DC Maturation *In Vitro*

We determined whether PLP could induce DCs' maturation *in vitro*. We studied the expression of DCs surface molecular markers CD86, CD80, and MHC II by flow cytometry. PLP, PLPt, and acteoside groups all revealed significantly upregulated expression of CD86, CD80, and MHC II, compared with the control group after 48 h treatment, and the PLP group was the most prominent among them (**Figure 2A**). Meanwhile, the mean fluorescence intensity (MFI) of three surface markers all increased after acteoside or PLP treatment. The MFI of CD86, CD80, and MHC II increased 1.66-, 1.40-, and 1.37-fold by PLP stimulation compared to the control group. As to acteoside, MFI of CD86 and MHC class II increased 1.26- and 1.13-fold, while no significant difference was observed in MFI of CD80 (**Figure 2B**). PLPt could slightly upregulate the expression percentage of MHC II and costimulatory molecules, but there was no significant difference between PLPt and medium control in MFI. These results indicated that, compared to PLPt and acteoside, PLP demonstrated a better maturation-promoting effect on DCs.

We next determined whether PLP could induce excretion of cytokines from DCs; DCs were stimulated with PLP or LPS for 48 h. The secretion of IL-12p70, TNF-α, IL-1β, and IL-6 was significantly enhanced by the PLP-treated DCs, compared to the control group (**Figure 2C-E,G**). PLP increased IL-12p70 secretion to 9.8-fold at 50 μg/ml. A 4-fold increase was observed for TNF-α in the PLP group. It was noted that PLP with 25 μg/ml and 50 μg/ml concentrations was as potent as LPS with 2 μg/ml concentration in the inductive efficacy of TNF-α's secretion. Conversely, there was no significant difference in the secretion of IL-4 (**Figure 2F**), which indicated Th2 type immune response. It indicated that PLP could increase the secretion of Th1 cytokines such as IL-12p70, TNF-α, IL-1β, and IL-6 of DCs.

PLP Induced DC Maturation *In Vivo*

Since PLP is effective in inducing the maturation of DCs *in vitro*, we further studied the administration routes to validate the safety and efficacy of PLP for DCs maturation *in vivo*. We administered

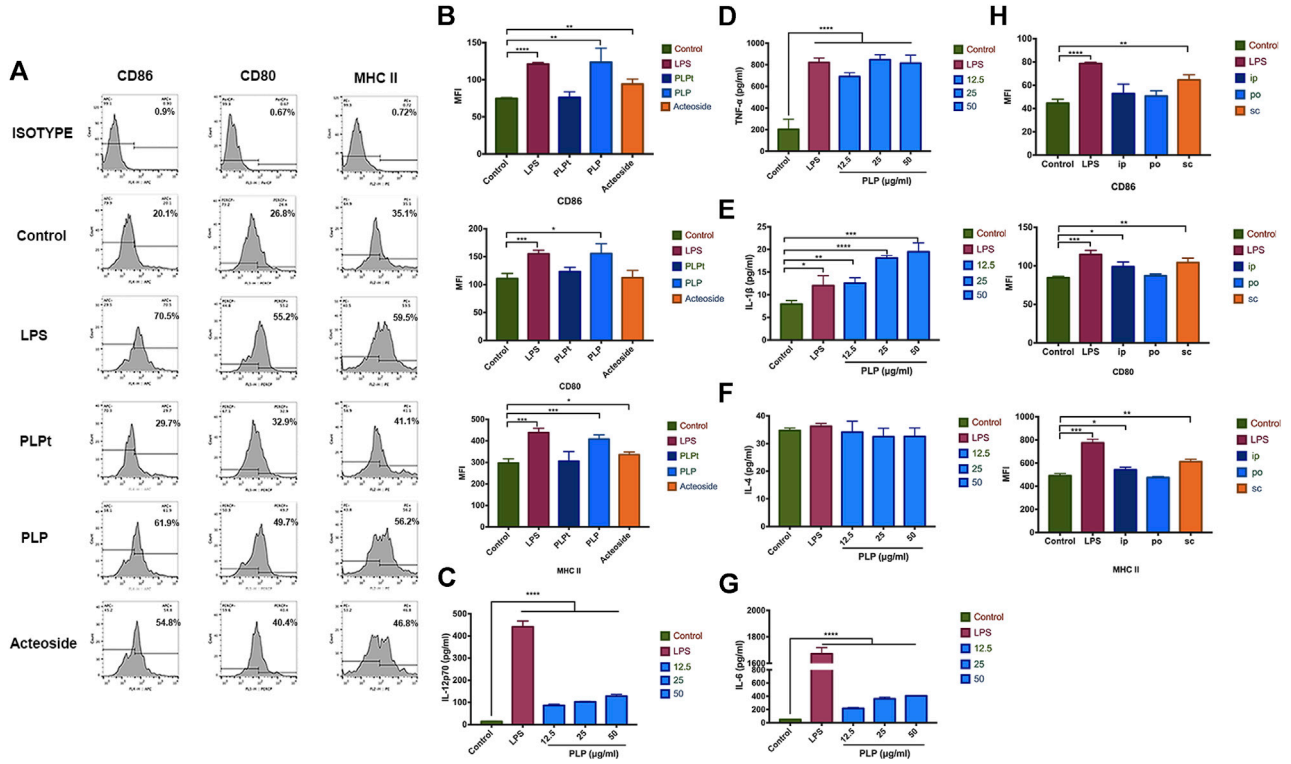

FIGURE 2 | PLP-activated DCs stimulated the expression of costimulator. **(A)** BMDCs were analyzed for expression of $CD86^+$, $CD80^+$, and MHC II^+ by flow cytometry after stimulated with 50 μg/ml PLP, PLPt, and acteoside for 48 h. **(B)** The mean fluorescence intensity (MFI) of three surface markers CD86, CD80, and MHC II expression, respectively, in different groups. Secretion of IL-12p70 **(C)**, TNF-α **(D)**, IL-1β **(E)**, IL-4 **(F)**, and IL-6 **(G)** from DCs treated with different formulations. **(H)** BMDCs were analyzed for the expression of $CD86^+$, $CD80^+$, and MHC II^+ by flow cytometry after stimulated with 10 mg/kg PLP via s.c., i.p., and p.o. for 48 h. All values shown are the average values from three independent experiments ± SEM (*$p < 0.05$, **$p < 0.01$, and ***$p < 0.001$).

PLP with 10 mg/kg dose via s.c., i.p., and p.o., as shown in **Supplementary Figure S2**, LPS (s.c) was used as a positive control. All groups of administration routes exhibited upregulated expression of CD86, CD80, and MHC II at Day 7, compared with the naive control group. S.c. route of PLP was the most effective route to activate DCs. When PLP was administered through i.p. or p.o. route, the efficacy was comparatively weaker than the s.c. administration route (**Figure 2H**). These results indicated that PLP was able to induce DCs maturation *in vivo*.

PLP Strengthened DCs to Stimulate Lymphocyte Proliferation and CTL Differentiation

We studied the ability of PLP pretreated DCs on the stimulation of lymphocytes. We cocultured primed DCs using PLP with lymphocytes to determine if they can induce lymphocyte proliferation. The results showed that DCs activated by PLP and acteoside were relatively more potent in lymphocyte stimulation. It resulted in 47.3 and 37.1% increased rate of proliferation, compared to the control group of 24.4% (**Figures 3A,B**). The results suggested that PLP-treated DCs had the advantage to prime and activate lymphocytes.

We further studied the cytokine production of IFN-γ from coculture supernatants. More IFN-γ was detected in which lymphocytes were cocultured with PLP-stimulated DCs compared to unstimulated DCs after 48 h. IFN-γ produced by the spleen lymphocytes increased 4-fold at a PLP concentration of 50 μg/ml (**Figure 3C**). These results are consistent with that in the CFSE.

Moreover, we investigated whether PLP was attributable to CTL differentiation. Lymphocytes were incubated with anti-CD3 and anti-CD8 antibodies, and the percentage of $CD3^+CD8^+$ T lymphocytes was measured using flow cytometry. As shown in **Figure 3D,E**, an increased percentage of $CD3^+CD8^+$ T lymphocytes was observed in the PLP group (14.1%); though lower than that of the positive control (15.8%), it was still significantly higher than that of the medium group (9.41%). These results implied that PLP significantly elicited $CD3^+CD8^+$ T lymphocyte responses compared to medium controls.

Growth Inhibitory Effects of PLP and Conditioned Medium on CIPp

We quantitatively evaluate the effects of PLP on the growth of CIPp cells using CCK-8 (**Figure 4A**). The results suggested that no obvious cytotoxicity on CIPp cells was observed after the treatment with different doses of PLP for 24 and 48 h. We did not find significant differences among all experimental groups.

To confirm the impact of PLP-associated T-cell immunity on the tumor inhibition and further verify the above results from the animal level, we administered PLP (10 mg/kg) to CIPp tumor-bearing BALB/c nude mice which reveal congenital defect of mature

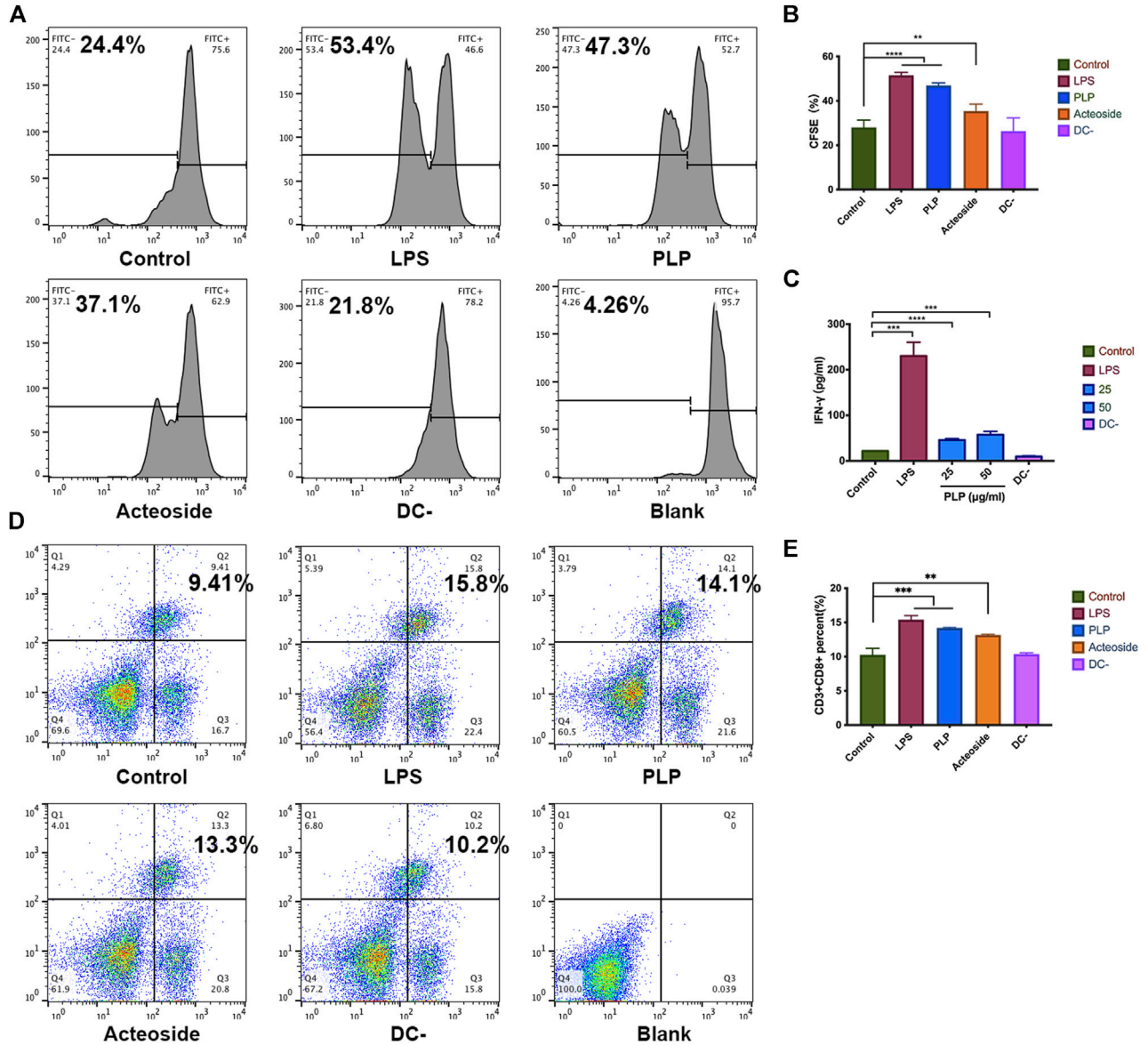

FIGURE 3 | PLP strengthened DCs to stimulate lymphocyte proliferation and CTL differentiation. **(A, B)** CFSE-labeled spleen lymphocytes were stimulated with DCs for 48 h. The fraction of proliferative lymphocytes was measured in a CFSE dilution assay. Representative examples are shown. **(C)** The concentration of IFN-γ secreted by splenic lymphocytes. **(D, E)** Phenotype analysis of $CD3^+CD8^+$ T cells in the spleen. All values shown are the average values from three independent experiments ± SEM (*$p < 0.05$, **$p < 0.01$, and ***$p < 0.001$).

T cells. In this mice model, PLP did not significantly inhibit tumor growth 28 days after the administration (**Figures 4B,C**). These results suggest that T-cell immunity is necessary for the antitumor effect of subcutaneously administered PLP.

Next, we studied the influence of the PLP-induced antitumor activity on the interaction between DCs and lymphocytes using a CFSE dilution assay. The proliferation of spleen lymphocytes with PLP-induced DCs (42.5%) was higher than that of the control group (30.7%). And the proliferation of lymphocytes with CIPp-cell-lysate + PLP-pulsed DCs (64.9%) was higher than that of both the PLP group and CIPp-cell-lysate group (**Figure 4D,E**). It indicated that PLP + CIPp-cell-lysate may stimulate the proliferation of lymphocytes by promoting the maturation of DCs.

We studied the potential antitumor activity of the conditioned medium mediated by PLP on DCs, and CIPp cells were also subjected to different groups of conditioned medium for 48 h. The results of CCK-8 indicated that conditioned medium exerted growth inhibitory effects on CIPp cells, and the toxicity effect of the PLP group (27.1%) was much higher than that of the control group (18.6%). The results showed significant inhibitory effects of the CIPp-cell-lysate + PLP group, which had the most remarkable

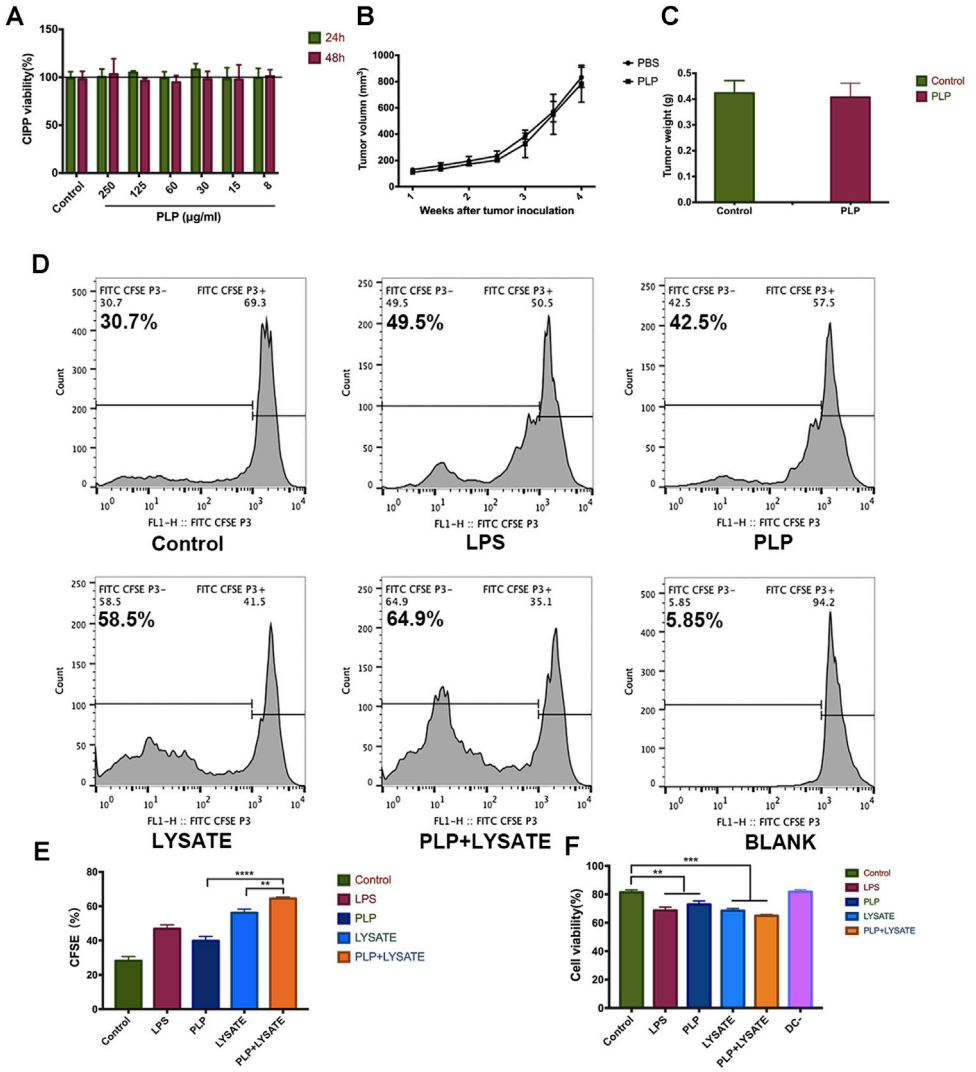

FIGURE 4 | PLP enhanced tumor antigen-specific immune responses against tumor lysate-pulsed DCs. **(A)** Cytotoxic effects of CIPp cells were analyzed using Cell Counting Kit-8 at 8, 15, 30, 60, 125, and 250 μg/ml PLP treatment. **(B)** Mean tumor growth curves given by tumor volume in BALB/c nude mice. Mice were s.c. inoculated with CIPp cells (1×10^5 cells). PLP (10 mg/kg/d, s.c.) was administered to the mice every 48 h, and the tumor growth was measured (n = 6). **(C)** The tumor weight was measured 28 days after tumor challenge in nude mice. **(D, E)** CFSE-labeled spleen lymphocytes were stimulated with DCs for 48 h. The fraction of proliferative lymphocytes was measured in a CFSE dilution assay. Representative examples are shown. **(F)** Cytotoxic effects of CIPp cells were analyzed using Cell Counting Kit-8 by different groups of conditioned medium (LPS, PLP, CIPp-cell-lysate, and CIPp-cell-lysate + PLP). All values shown are the average values from three independent experiments ± SEM (*$p < 0.05$, **$p < 0.01$, and ***$p < 0.001$).

toxicity effect (35.1%), as compared to the PLP group and CIPp-cell-lysate group (**Figure 4F**). It suggested that the conditioned medium mediated by PLP had growth inhibitory effects on CIPp.

PLP Achieved Therapeutic Effects and Improved Immunity in Breast Tumor Model

To investigate the immunotherapy effects of PLP, the BALB/c mice were administered physiological saline, PLP, TAXOL®, and TAXOL®+PLP. There was no significant difference in mice body weight among all groups (**Figure 5A**). As shown in **Figure 5B**, TAXOL®+PLP significantly inhibited 4T1 tumor growth, compared with the control group and TAXOL group. **Figure 5C** showed the photos of tumor completely stripped from mice after sacrificed. Consistently, tumor weight and spleen weight in the TAXOL®+PLP group were significantly decreased at day 21 compared to the control group (**Figures 5D,E**). Expression of cellular supernatant IFN-γ was consistent with the antitumor results (**Figure 5F**).

To demonstrate that PLP induced antitumor immunity, we assessed whether IFN-γ-expressing $CD4^+$ and $CD8^+$ T cells in tumor-bearing mice increased due to administration of PLP on day 21 after tumor inoculation. Intracellular cytokine staining showed that mice administered TAXOL®+PLP had more IFN-

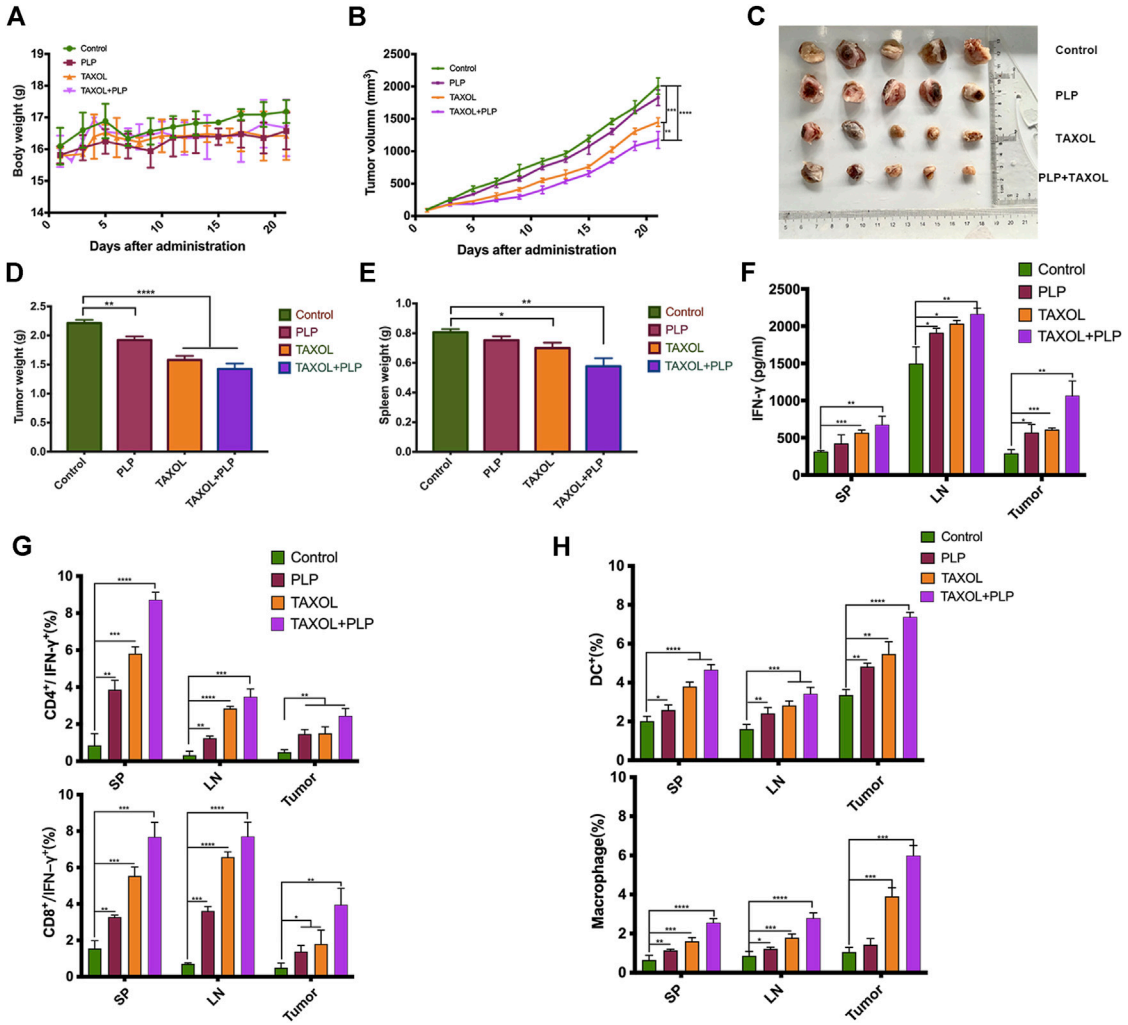

FIGURE 5 | PLP achieved therapeutic effects and improved immunity in the breast tumor model. **(A)** Mice body weight, **(B)** mean tumor growth curves given by tumor volume, **(C)** images of excised tumors from each mouse in each treatment group, **(D)** tumor weight, and **(E)** the spleen weight during the total immunotherapy course. **(F)** IFN-γ released from cellular supernatant of tumor-bearing mice in control, PLP, TAXOL®, and TAXOL®+PLP groups was tested by ELISA. **(G)** Phenotype analysis of $CD4^+$ IFN-γ^+ T cells and $CD8^+$ IFN-γ^+ T cells and **(H)** DCs and macrophages in mice spleen, inguinal lymph node, and tumors 22 days after 4T1 tumor cell inoculation. All values shown are the average values from three independent experiments ± SEM (n = 5) (*p < 0.05, **p < 0.01, and ***p < 0.001).

γ-expressing $CD4^+$ and $CD8^+$ T cells in inguinal lymph node, spleens, and tumors as compared with the control group and TAXOL group. And the PLP group had more IFN-γ-expressing $CD4^+$ T cells in inguinal lymph node and spleens and more IFN-γ-expressing $CD8^+$ T cells in inguinal lymph node, spleen, and tumor as compared with the control group mice (**Figure 5G**; **Supplementary Figures S3, 4**). As shown in **Figure 5H**; **Supplementary Figures S5, 6**, the combination of PLP and TAXOL promoted more $CD11c^+$ DCs and $CD11b^+F4/80^+$ macrophage aggregation in inguinal lymph node, spleen, and tumor as compared with the control group and TAXOL group. And the PLP group had more DCs and macrophages in inguinal lymph node, spleen, and tumor as compared with the control group. Representative gating scheme for flow cytometric analysis of immune cell populations was showed in **Supplementary Figure S1**. These results suggested that PLP achieved therapeutic effects and could improve immunity in the 4T1 breast tumor model.

DISCUSSION

Recent studies approved that polysaccharide components of Chinese herbal extracts exhibit the outstanding ability of immune modulation through activating DCs (Chen et al., 2006). In addition, besides polysaccharides, glycoside was also identified with the same activity. There were also reports which indicated that acteoside, another component isolated from *Plantago asiatica* L., could enhance immunity in mouse splenocytes (Kim et al., 2005). Thus, we first investigated if PLP and acteoside could activate the maturation of DCs. The results showed that PLPt, PLP, and

acteoside all revealed significantly upregulated expression of MHC II and costimulatory molecules. However, at the same concentration, the PLP was the most prominent among them. It manifested that PLP had a stronger maturation-promoting effect on DCs than acteoside, which is consistent with reports by Huang et al. (2009).

In this study, we demonstrated that PLP performed the ability to upregulate DCs' maturation marker and induce its functional maturation *in vivo* and *in vitro*. PLP enhanced the expression of surface molecules, including CD80, CD86, and MHC class II, suggesting that PLP induces the maturation of DCs. This finding was confirmed by the experiments *in vivo*. Groups administered with PLP via s.c., i.p., and p.o. all induced DCs' maturation. Among the three routes of administration, PLP via s.c. route is the most effective, which is consistent with reports by Chen et al. (2009). Perhaps because the subcutaneously administered PLP was taken up by DCs present in hypodermis and lymphatics, which are transported to the sentinel lymph nodes and eventually enter the blood circulation and systemic lymphoid tissues more effectively. DCs primed by PLP cocultured with lymphocytes can further enhance the IL-12 p70 and TNF-α production. This indicates that PLP can induce cytotoxic T-cell activities *in vitro* and *in vivo* (Xiao et al., 2009; Carreno et al., 2013).

Admittedly, PLP is not as strong as LPS in terms of inducing IL-12 production, while it is comparable to LPS with the enhancement of lymphocyte proliferation. LPS is toxic and induces a severe inflammatory response. In contrast, PLP was prepared from the herb, and no substantial toxic effect was detected with relatively high doses in the cytotoxicity evaluation experiments (**Figure 1C**), which indicates a therapeutic safety for the doses pharmacologically. This advantage makes it perform the great potential to be a good supplement for immunosuppressed organisms. Improvement of immunity could be achieved by simply administrating PLP.

As the most important professional antigen-presenting cells, a crucial role of DCs is to present processed antigens to T cells so that T cells can develop a specific immune response to particular antigens (Martinez et al., 2007). We used spleen lymphocytes which were composed of T cells to better simulate the immune environment in the organism. The result demonstrated that DCs could significantly increase the proliferation of spleen lymphocytes when the ratio of DCs: lymphocytes was 1:4. We also used the ratio of 1:10, while the lymphocyte proliferation ability of DCs became weaker (data not shown). And this result is consistent with reports by Huang et al. (2009). The reason might be with the decrease of DCs, and there were not enough IL-2 secreted by DCs, resulting in less lymphocyte proliferation (Guermonprez et al., 2002). Besides, PLP-treated DCs induced higher levels of IFN-γ production from spleen lymphocytes *in vitro*, suggesting they were more potent in priming Th1 response. Immunogenic DCs can induce Th1 cell differentiation and/or CTL priming, depending on the constraints imposed by environmental modifiers, as well as the maturation signal they received (Reis e Sousa 2006).

The CCK-8 results showed that there was no obvious cytotoxicity on CIPp cells after the treatment with PLP (**Figure 4A**), which suggested that PLP could kill tumor cells via enhancing antitumor immunity rather than directly targeting cancer cells. In the BALB/c nude mice model which reveals congenital defect of mature T cells, PLP did not significantly inhibit tumor growth (**Figure 4E**), and it also suggested that T-cell immunity was necessary for the antitumor effect of PLP. We used PLP-activated DCs cocultured with spleen lymphocytes, and the conditioned medium was detected for potential antitumor activity. The results of CCK-8 showed that conditioned medium exerted growth inhibitory effects on CIPp cells. PLP and CIPp-cell-lysate jointly stimulated DCs cocultured with lymphocytes having the strongest killing effects on CIPp cells (**Figure 4B**). On the other hand, in the 4T1 tumor model, PLP and TAXOL® group controlled the size of tumors and exerted better therapeutic effects than that administered TAXOL® or PLP alone (**Figure 5B**), indicating that PLP can exert antitumor effects by upregulating immune responses and improving immunosuppression of the tumor microenvironment.

Antitumor immune responses can be initiated through both the innate and adaptive immune system. Innate immune cells, such as DCs, which process and present antigens to T lymphocytes, activate adaptive immunity. Macrophages can kill tumor cells indirectly by producing effector molecules and exerting phagocytosis (Wang et al., 2020). We chose TAXOL® for combination because there was no general Chinese medicine immunotherapy drug as a positive control, and we also wanted to investigate whether PLP could enhance the effect of conventional chemotherapy medicine. The combination of PLP and TAXOL® recruited more mature DCs and macrophages in inguinal lymph node, spleen, and tumor (**Figure 5H**). Mature DCs secret IL-12, which in turn acts on T cells and promotes Th1 cell differentiation. In addition, subcutaneously administered PLP not only induced IFN-γ expression in the lymph node but also in the spleen and tumor (**Figure 5F**). It suggested that PLP induced the tumor-specific T-cell response to a type 1 cytokine profile and results in successful cancer immunotherapy (Masuda et al., 2013). What is important is that effective anti-tumor immunity is generated during the infiltration of effector cells into tumor microenvironment, and antigen-specific T cells perform effector functions to kill tumor cells (Bos and Sherman 2010). Consistent with the enhancement of expression of IFN-γ, subcutaneously administered PLP significantly increased the infiltration of $CD4^+$ IFN-γ^+ and $CD8^+$ IFN-γ^+ T cells to the tumor sites (**Figure 5G**). These results suggested that PLP might recruit $CD4^+$ and $CD8^+$ T cells to the tumor sites to amplify the Th1 antitumor cellular immunity.

CONCLUSION

Overall, PLP could promote the phenotypic and functional maturation of DCs both *in vivo* and *in vitro*. Mature DCs induced by PLP could enhance the cellular immune function, stimulate lymphocytes' proliferation, and differentiate naive T cells into cytotoxic T cells, which had a cytotoxic effect on breast tumor cells. Tumor antigen-specific T-cell responses were enhanced by PLP and tumor lysate-pulsed DCs. In addition, PLP could achieve therapeutic effects and improve immunity in the breast tumor model. Our study provides scientific support and rationale on

using PLP in various clinical conditions with poor immunity, especially for the tumor immune therapeutic effects in the future.

DATA AVAILABILITY STATEMENT

The original contributions presented in the study are included in the article/**Supplementary Material**; further inquiries can be directed to the corresponding authors.

ETHICS STATEMENT

The animal study was reviewed and approved by the China Agricultural University Laboratory Animal Welfare and Animal Experimental Ethical Committee.

AUTHOR CONTRIBUTIONS

Conceptualization, JG and Y-NZ; methodology, JG and Y-NZ; software, JC and NC; validation, YM, DZ, and YJ; formal analysis, JG; investigation, ZH; resources, HX; data curation, JG and YJ; writing—original draft preparation, JG; writing—review and editing, JL; visualization, ZH; supervision, HX; project administration, JL; funding acquisition, DL. All authors have read and approved this version of the article, and this manuscript, or any part of it, has not been published and will not be submitted elsewhere for publication while being considered by the Frontiers in Pharmacology.

FUNDING

This work was supported by the National Nature Science Foundation of China (Grant no. 31972730), the Talent Cultivation Program of China Agricultural University, and the Special Fund Project of Fundamental Scientific Research Business Expenses of China Agricultural University (Grant no. 2020TC009).

SUPPLEMENTARY MATERIAL

The Supplementary Material for this article can be found online at https://www.frontiersin.org/articles/10.3389/fphar.2021.678865/full#supplementary-material

REFERENCES

Batra, J., Robinson, J. A., Fields, A. P., Radisky, D. C., and Radisky, E. S. (2012). Matrix Metalloproteinase-10 (MMP-10) Interaction with Tissue Inhibitors of Metalloproteinases TIMP-1 and TIMP-2. *J. Biol. Chem.* 287 (19), 15935–15946. doi:10.1074/jbc.m112.341156

Biringanine, G., Vray, B., Vercruysse, V., Vanhaelen-Fastré, R., Vanhaelen, M., and Duez, P. (2005). Polysaccharides Extracted from the Leaves of Plantago Palmata Hook.F. Induce Nitric Oxide and Tumor Necrosis Factor-α Production by Interferon-γ-Activated Macrophages. *Nitric Oxide* 12 (1), 1–8. doi:10.1016/j.niox.2004.10.008

Bos, R., and Sherman, L. A. (2010). CD4+ T-Cell Help in the Tumor Milieu Is Required for Recruitment and Cytolytic Function of CD8+ T Lymphocytes. *Cancer Res.* 70 (21), 8368–8377. doi:10.1158/0008-5472.Can-10-1322

Carreno, B. M., Becker-Hapak, M., Huang, A., Chan, M., Alyasiry, A., Lie, W.-R., et al. (2013). IL-12p70-producing Patient DC Vaccine Elicits Tc1-Polarized Immunity. *J. Clin. Invest.* 123 (8), 3383–3394. doi:10.1172/JCI68395

Chen, X., Yang, L., Howard, O. M., and Oppenheim, J. J. (2006). Dendritic Cells as a Pharmacological Target of Traditional Chinese Medicine. *Cell Mol Immunol* 3 (6), 401–410.

Chen, Z., Lu, J., Srinivasan, N., Tan, B. K. H., and Chan, S. H. (2009). Polysaccharide-Protein Complex fromLycium barbarumL. Is a Novel Stimulus of Dendritic Cell Immunogenicity. *J. Immunol.* 182 (6), 3503–3509. doi:10.4049/jimmunol.0802567

Dong, H., Wen, Z.-f., Chen, L., Zhou, N., Liu, H., Dong, S., et al. (2018). Polyethyleneimine Modification of Aluminum Hydroxide Nanoparticle Enhances Antigen Transportation and Cross-Presentation of Dendritic Cells. *Ijn* Vol. 13, 3353–3365. doi:10.2147/IJN.S164097

Grauer, O., Wohlleben, G., Seubert, S., Weishaupt, A., Kämpgen, E., and Gold, R. (2002). Analysis of Maturation States of Rat Bone Marrow-Derived Dendritic Cells Using an Improved Culture Technique. *Histochem. Cel Biol* 117 (4), 351–362. doi:10.1007/s00418-002-0384-4

Guermonprez, P., Valladeau, J., Zitvogel, L., Théry, C., and Amigorena, S. (2002). Antigenpresentation Andt Cellstimulation Bydendriticcells. *Annu. Rev. Immunol.* 20, 621–667. doi:10.1146/annurev.immunol.20.100301.064828

Huang, D.-F., Tang, Y.-F., Nie, S.-P., Wan, Y., Xie, M.-Y., and Xie, X.-M. (2009). Effect of Phenylethanoid Glycosides and Polysaccharides from the Seed of Plantago Asiatica L. On the Maturation of Murine Bone Marrow-Derived Dendritic Cells. *Eur. J. Pharmacol.* 620 (1-3), 105–111. doi:10.1016/j.ejphar.2009.07.025

Huang, D., Nie, S., Jiang, L., and Xie, M. (2014). A Novel Polysaccharide from the Seeds of Plantago Asiatica L. Induces Dendritic Cells Maturation through Toll-like Receptor 4. *Int. Immunopharmacology* 18 (2), 236–243. doi:10.1016/j.intimp.2013.11.024

Huang, Y., Qin, T., Huang, Y., Liu, Z., Bo, R., Hu, Y., et al. (2016). Rehmannia Glutinosa Polysaccharide Liposome as a Novel Strategy for Stimulating an Efficient Immune Response and Their Effects on Dendritic Cells. *Ijn* Vol. 11, 6795–6808. doi:10.2147/IJN.S119108

Jiang, L., Huang, D., Nie, S., and Xie, M. (2018). Polysaccharide Isolated from Seeds of Plantago Asiatica L. Induces Maturation of Dendritic Cells through MAPK and NF-Kb Pathway. *Saudi J. Biol. Sci.* 25 (6), 1202–1207. doi:10.1016/j.sjbs.2017.09.011

Kim, H. S., Shin, B. R., Lee, H. K., Kim, Y. J., Park, M. J., Kim, S. Y., et al. (2013). A Polysaccharide Isolated from Pueraria Lobata Enhances Maturation of Murine Dendritic Cells. *Int. J. Biol. Macromolecules* 52, 184–191. doi:10.1016/j.ijbiomac.2012.09.011

Kim, S.-S., Son, Y.-O., Chun, J.-C., Kim, S.-E., Chung, G.-H., Hwang, K.-J., et al. (2005). Antioxidant Property of an Active Component Purified from the Leaves of Paraquat-tolerantRehmannia Glutinosa. *Redox Rep.* 10 (6), 311–318. doi:10.1179/135100005x83734

Klingemann, H. (2018). Immunotherapy for Dogs: Running behind Humans. *Front. Immunol.* 9, 133. doi:10.3389/fimmu.2018.00133

Lee, K. H., Park, H. M., Son, K. H., Shin, T. J., and Cho, J. Y. (2018). Transcriptome Signatures of Canine Mammary Gland Tumors and its Comparison to Human Breast Cancers. *Cancers (Basel)* 10 (9). doi:10.3390/cancers10090317

Martínez, D., Vermeulen, M., von Euw, E., Sabatté, J., Maggíni, J., Ceballos, A., et al. (2007). Extracellular Acidosis Triggers the Maturation of Human Dendritic Cells and the Production of IL-12. *J. Immunol.* 179 (3), 1950–1959. doi:10.4049/jimmunol.179.3.1950

Masuda, Y., Inoue, H., Ohta, H., Miyake, A., Konishi, M., and Nanba, H. (2013). Oral Administration of Soluble β-glucans Extracted fromGrifola Frondosainduces Systemic Antitumor Immune Response and Decreases Immunosuppression in Tumor-Bearing Mice. *Int. J. Cancer* 133 (1), 108–119. doi:10.1002/ijc.27999

Meng, J., Hu, X., Shan, F., Hua, H., Lu, C., Wang, E., et al. (2011). Analysis of Maturation of Murine Dendritic Cells (DCs) Induced by Purified Ganoderma

Lucidum Polysaccharides (GLPs). *Int. J. Biol. Macromolecules* 49 (4), 693–699. doi:10.1016/j.ijbiomac.2011.06.029

Palucka, K., and Banchereau, J. (2012). Cancer Immunotherapy via Dendritic Cells. *Nat. Rev. Cancer* 12 (4), 265–277. doi:10.1038/nrc3258

Park, M. J., Ryu, H. S., Kim, J. S., Lee, H. K., Kang, J. S., Yun, J., et al. (2014). Platycodon Grandiflorum Polysaccharide Induces Dendritic Cell Maturation via TLR4 Signaling. *Food Chem. Toxicol.* 72, 212–220. doi:10.1016/j.fct.2014.07.011

Reis e Sousa, C. (2006). Dendritic Cells in a Mature Age. *Nat. Rev. Immunol.* 6 (6), 476–483. doi:10.1038/nri1845

Sabado, R. L., Balan, S., and Bhardwaj, N. (2017). Dendritic Cell-Based Immunotherapy. *Cell Res* 27 (1), 74–95. doi:10.1038/cr.2016.157

Samuelsen, A. B. (2000). The Traditional Uses, Chemical Constituents and Biological Activities of Plantago Major L. A Review. *J. Ethnopharmacol* 71, 1–21. doi:10.1016/s0378-8741(00)00212-9

Song, D., Lin, J., Yuan, F., and Zhang, W. (2011). *Ex Vivo* stimulation of Murine Dendritic Cells by an Exopolysaccharide from One of the Anamorph of Cordyceps Sinensis. *Cell Biochem Funct* 29 (7), 555–561. doi:10.1002/cbf.1787

Staub, A. M. (1965). Removal of Protein—Sevag Method. *Methods Carbohydr. Chem.* 5, 5–6.

Steinman, R. M., and Banchereau, J. (2007). Taking Dendritic Cells into Medicine. *Nature* 449 (7161), 419–426. doi:10.1038/nature06175

Wang, Y., Zhang, Q., Chen, Y., Liang, C.-L., Liu, H., Qiu, F., et al. (2020). Antitumor Effects of Immunity-Enhancing Traditional Chinese Medicine. *Biomed. Pharmacother.* 121, 109570. doi:10.1016/j.biopha.2019.109570

Xiao, Z., Casey, K. A., Jameson, S. C., Curtsinger, J. M., and Mescher, M. F. (2009). Programming for CD8 T Cell Memory Development Requires IL-12 or Type I IFN. *J. Immunol.* 182 (5), 2786–2794. doi:10.4049/jimmunol.0803484

Yin, J.-Y., Huang, X.-Y., Wang, L., Guo, J.-Q., Xie, M.-Y., Wu, J.-Y., et al. (2018). Molecular Properties and Immunomodulatory Activities of a Water-Soluble Heteropolysaccharide Isolated from Plantago Asiatica L. Leaves. *Nat. Product. Res.* 33, 1678–1681. doi:10.1080/14786419.2018.1428584

Conflict of Interest: The authors declare that the research was conducted in the absence of any commercial or financial relationships that could be construed as a potential conflict of interest.

Publisher's Note: All claims expressed in this article are solely those of the authors and do not necessarily represent those of their affiliated organizations, or those of the publisher, the editors, and the reviewers. Any product that may be evaluated in this article, or claim that may be made by its manufacturer, is not guaranteed or endorsed by the publisher.

frontiers in Pharmacology

REVIEW
published: 27 August 2021
doi: 10.3389/fphar.2021.734450

Therapeutic Effects and Molecular Mechanisms of Bioactive Compounds Against Respiratory Diseases: Traditional Chinese Medicine Theory and High-Frequency Use

Jing Wang[1†], Qibiao Wu[2†], Lu Ding[3], Siyu Song[3], Yaxin Li[3], Li Shi[1], Tan Wang[1], Daqing Zhao[4], Zeyu Wang[5] and Xiangyan Li[4]**

[1]Department of Respiratory, Changchun University of Chinese Medicine, Changchun, China, [2]State Key Laboratory of Quality Research in Chinese Medicines, Faculty of Chinese Medicine, Macau University of Science and Technology, Macau, China, [3]College of Integrated Traditional Chinese and Western Medicine, Changchun University of Chinese Medicine, Changchun, China, [4]Jilin Ginseng Academy, Key Laboratory of Active Substances and Biological Mechanisms of Ginseng Efficacy, Ministry of Education, Jilin Provincial Key Laboratory of Bio-Macromolecules of Chinese Medicine, Changchun University of Chinese Medicine, Changchun, China, [5]Department of Scientific Research, Changchun University of Chinese Medicine, Changchun, China

Respiratory diseases, especially the pandemic of respiratory infectious diseases and refractory chronic lung diseases, remain a key clinical issue and research hot spot due to their high prevalence rates and poor prognosis. In this review, we aimed to summarize the recent advances in the therapeutic effects and molecular mechanisms of key common bioactive compounds from Chinese herbal medicine. Based on the theories of traditional Chinese medicine related to lung diseases, we searched several electronic databases to determine the high-frequency Chinese medicines in clinical application. The active compounds and metabolites from the selected medicines were identified using the Traditional Chinese Medicine Systems Pharmacology Database (TCMSP) by analyzing oral bioavailability and drug similarity index. Then, the pharmacological effects and molecular mechanisms of the selected bioactive compounds in the viral and bacterial infections, inflammation, acute lung injury (ALI), chronic obstructive pulmonary disease (COPD), pulmonary fibrosis, asthma, and lung cancer were summarized. We found that 31 bioactive compounds from the selected 10 common Chinese herbs, such as epigallocatechin-3-gallate (EGCG), kaempferol, isorhamnetin, quercetin, and β-sitosterol, can mainly regulate NF-κB, Nrf2/HO-1, NLRP3, TGF-β/Smad, MAPK, and PI3K/Akt/mTOR pathways to inhibit infection, inflammation, extracellular matrix deposition, and tumor growth in a series of lung-related diseases. This review provides novel perspectives on the preclinical study and clinical application of Chinese herbal medicines and their bioactive compounds against respiratory diseases.

Keywords: Chinese herbal medicines, bioactive compounds, respiratory diseases, therapeutic use, molecular mechanisms of pharmacological action

OPEN ACCESS

Edited by:
Wenzhi Yang,
Tianjin University of Traditional Chinese Medicine, China

Reviewed by:
Roodabeh Bahramsoltani,
Tehran University of Medical Sciences, Iran
Rosario Rojas,
Universidad Peruana Cayetano Heredia, Peru

****Correspondence:***
Zeyu Wang
zeyu781022@163.com
Xiangyan Li
xiangyan_li1981@163.com

[†]These authors have contributed equally to this work

Specialty section:
This article was submitted to Ethnopharmacology, a section of the journal Frontiers in Pharmacology

Received: *01 July 2021*
Accepted: *16 August 2021*
Published: *27 August 2021*

Citation:
Wang J, Wu Q, Ding L, Song S, Li Y, Shi L, Wang T, Zhao D, Wang Z and Li X (2021) Therapeutic Effects and Molecular Mechanisms of Bioactive Compounds Against Respiratory Diseases: Traditional Chinese Medicine Theory and High-Frequency Use. Front. Pharmacol. 12:734450. doi: 10.3389/fphar.2021.734450

INTRODUCTION

Respiratory diseases include respiratory infectious diseases, asthma, chronic obstructive pulmonary disease (COPD), interstitial pulmonary disease (ILD), and lung cancer. These diseases are characterized by the injuries of bronchial and alveolar tissue to cause respiratory dysfunction and even respiratory failure. Respiratory infectious diseases mainly caused by viruses or bacteria and often contagious, remain a major global public health problem. For example, since the outbreak of coronavirus disease (COVID-19) at the end of 2019, there have been nearly 180 million confirmed cases, including 3.9 million deaths by June 25, 2021 (Mortality et al., 2019; Berlin et al., 2020). Pneumonia is another common respiratory infection, it can lead to hospitalization and death in all age group, and the annual costs exceed $10 billion in the United States and Europe (Global, 2018; Stets et al., 2019). Chronic respiratory diseases such as COPD, ILD, pulmonary fibrosis (PF), and lung cancer, seriously affect human health, these diseases were associated with more than 4 million deaths (7% of all deaths) worldwide in 2017 (Global, 2018). They are induced by long-term exposure to airborne pollutants, tobacco, or kitchen smoke, and their mortality by 18.0% in the last 30 years (Li et al., 2020a). COPD has become the fourth leading cause of death worldwide (Ferkol and Schraufnagel, 2014). Moreover, the quality of life in patients with ILD and IPF is severely affected due to progressive scarring of the lung parenchyma and impairment of pulmonary function (Wollin et al., 2019; Spagnolo et al., 2021). In addition, lung cancer has poor survival and high mortality, and it is the most common cause of cancer-related death worldwide (Siegel et al., 2021). The concern due to the global burden of respiratory diseases, such as the ongoing global pandemic of COVID-19, COPD, and lung cancer, has stimulated research on the treatment and prevention of respiratory diseases. Therefore, the therapeutic effects and molecular mechanisms of potential intervention strategies have become a hot spot for multidisciplinary research.

Traditional Chinese medicine (TCM) has a history of more than 3,000 years and has been used for the prevention and treatment of many respiratory diseases. The ancient medicine books named "Shennong Ben Cao Jing" and "Shanghan Lun" clearly recorded the theories of traditional Chinese medicine, such as reducing phlegm and relieving cough and asthma, and many prescriptions for the prevention and treatment of lung-related diseases. Based on thousands of years of clinical application and the modernization of TCM research, hundreds of Chinese medicines have been shown to be effective in the current clinical applications for treating respiratory infections, asthma, chronic lung diseases, and lung cancer; these effects are based on the therapeutic and improved effects for acute respiratory symptoms and lung dysfunction (Ren et al., 2020; Zhang et al., 2021). Importantly, bioactive compounds or their metabolites from these medicines with high-frequency use, such as saponins, flavonoids, alkaloids, and phenolic acids, are critical for the prevention and treatment of respiratory diseases (Shahidi and Yeo, 2018; Ory et al., 2019; Russo et al., 2020). Currently, the roles of different medicines are summarized in most review, not for potential active components of these medicines for fighting the diseases of respiratory systems. It is necessary to summarize the recent findings regarding the therapeutic effects and molecular mechanisms of bioactive compounds from commonly used Chinese medicines for preventing and treating a series of lung-related diseases. In this review, we first searched English or Chinese electronic databases for clinical studies of TCM against respiratory diseases to identify the Chinese medicines with high-frequency use in the clinical setting. The active components and their metabolites from the selected medicines were identified using the Traditional Chinese Medicine Systems Pharmacology Database (TCMSP) by analyzing oral bioavailability and drug similarity index. Then, the published studies for advanced research of those bioactive compounds after screening in multiple disorders of respiratory system were collected. Finally, we summarized the pharmacological effects and molecular mechanisms of the selected bioactive compounds in the viral and bacterial infections, inflammation, acute lung injury (ALI), COPD, PF, and lung cancer. This review provides new insights into the clinical use of medicinal herbs for the prevention and treatment of respiratory diseases.

HIGH-FREQUENCY USE OF CHINESE MEDICINE AND LITERATURE COLLECTION

According to the theories of TCM involving lung-related diseases, we searched Chinese or English electronic databases including CNKI database, Wanfang Data Knowledge Service Platform, VIP Chinese Science and Technology Journal database, PubMed database, and Web of Science database with keywords such as "traditional Chinese medicine," "Chinese medicine," or "respiratory diseases." After the literature retrieval, the Chinese medicines widely used in clinical applications for reducing phlegm (*Morus alba* L., *Moraceae* family, Chinese name: Sangbaipi, peel; *Ginkgo biloba* L., *Ginkgoaceae* family, Chinese name: Baiguo, seed; *Aster tataricus* L.f., *Compositae* family, Chinese name: Ziwan, root) and relieving cough and asthma (*Perilla frutescens* (L.) Britton, *Lamiaceae* family, Chinese name: Suzi, seed; *Tussilago farfara* L., *Compositae* family, Chinese name: Kuandonghua, flower; *Datura metel* L., *Solanaceae* family, Chinese name: Yangjinhua, flower; *Ardisia japonica* (Thunb.) Blume, *Primulaceae* family, Chinese name: Aidicha, leaf; *Lepidium apetalum* Willd., *Brassicaceae* family, Chinese name: Tinglizi, seed; *Eriobotrya japonica* (Thunb.) Lindl., *Rosaceae* family, Chinese name: Pipaye leaf; *Prunus mandshurica* (Maxim.) Koehne., *Rosaceae* family, Chinese name: Kuxingren, seed) were selected.

The effective components and their metabolites of the selected 10 medical plants were searched in the Traditional Chinese Medicine Systems Pharmacology Database (TCMSP, https://old.tcmsp-e.com/index.php, version 2.3). The active compounds of each herb were sorted out by the screening criteria with (oral bioavailability ≥30% and drug-likeness ≥0.18) for the ADME (absorption, distribution, metabolism, and excretion) evaluation

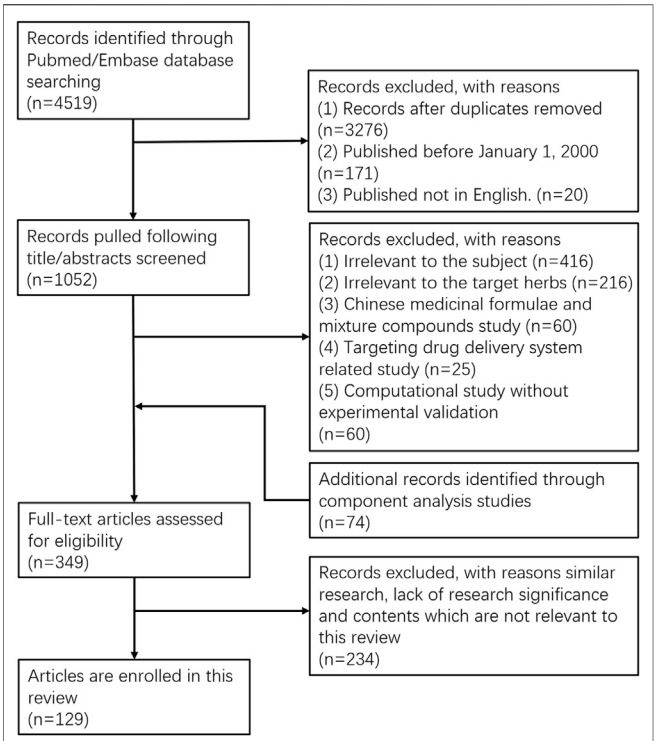

FIGURE 1 | Flow diagram of literature collection methods for bioactive compounds from commonly used of traditional Chinese medicine in clinical applications.

system. After sorting, we identified 165 bioactive compounds from these 10 herbs, such as epigallocatechin-3-gallate (EGCG), kaempferol, apigenin, ellagic acid and resveratrol for further analysis. Then, we searched the databases (PubMed, EMBASE, or Web of Science) using the keywords for one of the ingredients from the TCMSP and a type of disease, such as respiratory infection, COVID-19, inflammation, ALI, PF, COPD, asthma, or lung cancer to obtain articles published from January 2000 to May 2021.

Articles that included both components and disease terms, excluding review articles were identified as reference lists (4,519 articles). Titles and abstracts of all the records were screened to exclude irrelevant studies (duplicates: n = 3,276; publication before 2000: n = 171, non-English: n = 20). We further excluded the irrelevant records for the subject (n = 416), target herbs (n = 216), Chinese medicinal formulae/mixture compounds (n = 60), targeting drug delivery system (n = 25), or computational study without experimental validation (n = 60). Moreover, 74 reports for component analysis were added to obtain 349 full-text articles for eligibility assessment. Finally, 129 articles for the therapeutic effects and molecular mechanisms of 31 bioactive compounds from the selected 10 herbs were enrolled in the final analysis, after excluding similar studies or those not relevant to our topic of this review (n = 234). The detailed flow chart of the published articles collection is shown in **Figure 1**.

THERAPEUTIC EFFECTS AND MOLECULAR MECHANISMS OF BIOACTIVE COMPOUNDS AGAINST RESPIRATORY DISEASES

Viral and Bacterial Infections

Bacterial and viral infections account for up to 70% of all pathogenic diseases in humans (Smith et al., 2014). Influenza is one of the most prevalent respiratory diseases, and accounts for nearly 5–15% of people all respiratory infections. Although most patients recover, about 0.5 million people die of influenza each year (Petrova and Russell, 2018). The outbreak of COVID-19 has become a global health emergency on a pandemic scale, which has given rise to various studies and developments of antiviral drugs and vaccines. Coronaviruses identify the angiotensin-converting enzyme 2 (ACE2) as the main entry point into the respiratory epithelial cells of the host (Zhou et al., 2020a). Potential targets, including retinoic acid-inducible gene I (RIG-I)/melanoma differentiation-associated gene 5/mitochondrial antiviral signaling/TNF receptor-associated factor 3/interferon regulatory factor 3 (IRF3)/IRF7, and Toll-like receptors (TLRs)/TIR-domain-containing adapter-inducing interferon-β/nuclear factor kappa B (NF-κB)/mitogen-activated protein kinase (MAPK)/activating protein-1 (AP-1) pathways as intercellular sensors have been detected to study translation and budding process of SARS-CoV-1 and MERS viruses infection with SARS-CoV-1 using *in vitro* and *in vivo* models (Stertz et al., 2007), which may cause cellular death, hyperinflammation, and cytokine storm during viral infections (Azkur et al., 2020).

TCM could be a great potential resource for the development of innovative pharmacotherapies against infections. It has been reported that Lianhuaqingwen granules (active ingredients including *Forsythia suspensa* (Thunb.) Vahl, *Lonicera japonica* Thunb., and *Prunus mandshurica* (Maxim.) Koehne., *Rosaceae*) (Jia et al., 2015), Shufeng Jiedu capsule (active ingredients including *Forsythia suspensa* (Thunb.) Vahl, *Strobilanthes cusia* (Nees) Kuntze, and *Bupleurum chinense* DC.) (Liu et al., 2019a), Huoxiang Zhengqi dropping pills (active ingredients including *Pogostemon cablin* (Blanco) Benth., *Platycodon grandiflorus* (Jacq.) A.DC., and *Pinellia ternata* (Thunb.) Makino) (Li et al., 2006) and Haishiyi formula (active ingredients including *Ephedra sinica* Stapf, *Prunus mandshurica* (Maxim.) Koehne., and *Atractylodes macrocephala* Koidz.) can improve clinical symptoms, such as fatigue, cough, and fever, reduce the usage rate of antibiotics, and prevent the progression to severe COVID-19 (Xiao et al., 2020a; Tian et al., 2020; Xia et al., 2021). Currently, canti-COVID-19 agents mainly target SARS-CoV-2 spike receptor-binding domain or ACE2 enzyme activity to block the entry of COVID-19 to the cells. EGCG from *Eriobotrya japonica* (Thunb.) Lindl., and *Ginkgo biloba* L., and isorhamnetin found in *Lepidium apetalum* Willd., *Eriobotrya japonica* (Thunb.) Lindl., *Ginkgo biloba* L., and *Aster tataricus* L.f. exhibit the ability to prevent SARS-CoV-2 from entering into $ACE2^{+}$ cells (Henss et al., 2021; Maiti and Banerjee, 2021; Zhan et al., 2021).

TABLE 1 | Summary of effects and mechanisms of bioactive compounds against bacterial and viral infections.

Herbs	Component	Disease/Model	Targets	Mechanism/specific effects	References
Eriobotrya japonica (Thunb.) Lindl., *Ginkgo biloba* L.	EGCG	COVID-19/HEK293T cells transfected with the SARS-CoV-2 delta 19 spike gene	SARS-CoV-2 spike receptor-binding domain	Inhibits coronavirus spike proteins	Henss et al. (2021), Maiti and Banerjee (2021)
Tussilago farfara L.	Neochlorogenic acid	COVID-19/ACE2 enzyme activity measurement	ACE2	Reduces ACE2 enzyme activity	Chen et al. (2021a)
Lepidium apetalum Willd., *Eriobotrya japonica* (Thunb.) Lindl., *Ginkgo biloba* L., *Aster tataricus* L.f.	Isorhamnetin	COVID-19/ACE2 overexpression in HEK293 cells	SARS-CoV-2 spike receptor-binding domain	Inhibits coronavirus spike proteins	Zhan et al. (2021)
Eriobotrya japonica (Thunb.) Lindl.	Hesperidin	Virus infection/A rat model using H1N1 virus infection	MAPK signaling pathways	Inhibits pro-inflammatory cytokine production	Ding et al. (2018)
Eriobotrya japonica (Thunb.) Lindl.	Hyperoside	Virus infection/H1N1-induced acute lung injury in mice	Toll-like receptor signaling pathway	Reduces cytokine secretion and NF-κB p65 phosphorylation for antiviral and anti-inflammatory effects	Ling et al. (2020)
Morus alba L., *Datura metel* L., and other 6 herbs	Kaempferol	Virus infection/H9N2 influenza virus-induced inflammation *in vivo* and *in vitro*	TLR4/MyD88	Reduces ROS and MPO activity, promotes the production of TNF-α, IL-1β and IL-6; and improves SOD activity	Zhang et al. (2017a)
Morus alba L., *Datura metel* L., and other 6 herbs	β-sitosterol	Virus infection/Influenza A virus-induced ALI mice model	Retinoic acid-inducible gene I (RIG-I)	Inhibits RIG-I and STAT1 signaling pathway to improve interferons sensitization	Zhou et al. (2020b)
Prunus mandshurica (Maxim.) Koehne, *Perilla frutescens* (L.) Britton	Benzaldehyde	Bacterial infection/16 bacteria and two yeast species	Not available	Not available	Lee et al. (2014a)

Neochlorogenic acid from *Tussilago farfara* L. and Lianhuaqingwen granules inhibit the ACE2 enzyme activity (Chen et al., 2021a). Hesperidin and hyperoside from *Eriobotrya japonica* (Thunb.) Lindl. show antiviral and anti-inflammatory effects against H1N1 virus (Ding et al., 2018; Ling et al., 2020). In H9N2 virus-induced pneumonia, kaempferol inhibits TLR4/Myeloid differentiation factor 88 (MyD88)/NF-κB signaling pathways to reduce the production of inflammatory factors and enhance antioxidant ability (Zhang et al., 2017a). β-sitosterol from eight herbs, such as *Morus alba* L., and *Datura metel* L., inhibits RIG-I and signal transducer and activator of transcription 1 (STAT1) signaling pathway to improve interferon sensitization (Zhou et al., 2020b). As for bacterial infections, it has been reported that benzaldehyde has a good inhibitory effect on a variety of bacteria (Lee et al., 2014a). SARS-CoV-2 spike receptor-binding domain, ACE2, and inflammatory response are essential targets of these bioactive compounds, which may be related to Toll-like receptor and MAPK signaling pathways. Overall, the antiviral and antibacterial effects of these active compounds mentioned above are shown in **Table 1**.

Inflammation and ALI

ALI is common in pulmonary infection, lung contusion, pulmonary embolism, and near-drowning, it can lead to acute respiratory distress syndrome (ARDS) (Suresh et al., 2000). The mortality of ARDS ranges from 35 to 46%, which is higher than mortality of breast cancer or HIV infection (Fan et al., 2018). Patients recovered from ARDS may experience physical, neuropsychiatric, and neurocognitive morbidity that persistently impair their quality of life (Fan et al., 2014). Inflammation, bacterial and viral infections are the most common causes of ALI (Fan and Fan, 2018). The pathogenesis of ALI is believed to be related to inflammation, oxidative stress, cell apoptosis, and hypoxia, involving major cytokines such as tumor necrosis factor-α (TNF-α), interleukin (IL)-6, and IL-1β, IL-9, and IL-8, as well as the chemokines, such as chemokine-2 (CCL-2), monocyte chemotactic factors (MIP), and macrophage chemoattractant protein (MCP). The critical signaling pathways mainly include NF-κB, MAPK, nucleotide-binding oligomerization domain, NOD-like receptor family pyrin domain containing 3 (NLRP3), TLRs, adrenergic receptors, the Janus kinase (JAK)/STAT, and AMP-activated protein kinase (AMPK)- anti-thymocyte globulin (ATG7) signaling pathways (Chang et al., 2018a; Nadeem et al., 2018). The potential targets include of superoxide dismutase (SOD), glutamate-cysteine ligase catalytic subunit (GCLC), NAD(P)H, quinone-1 (NQO1), catalase (CAT), glutathione peroxidase (GSH-Px), and heme oxygenase-1 (HO-1) (Sun et al., 2018; Zhou et al., 2020a). Collectively, intrapulmonary oxidants derived from either activated lung macrophages or oxidant-generating enzymes delivered into the lung are two main pathways of oxidative stress, which can induce ALI and, more seriously, ARDS (Ward, 2010).

The model of ALI is mainly based on the induction by lipopolysaccharide (LPS) in *in vivo* and *in vitro* experiments. Other inflammatory substances and harmful chemicals such as N-methyl-d-aspartate, methamphetamine, and paraquat (PQ) are also used in ALI studies. TNF-α and other cytokines are commonly used in the *in vitro* model construction of ALI. The changes in pulmonary function, lung wet/dry ratios, the morphology of lung tissue, and inflammatory factors in

alveolar lavage fluid and serum are generally used to evaluate the inflammatory response. Canonical NF-κB pathway directly induces proinflammatory cytokines such as TNF-α, IL-1β, and IL-6. Subsequently, the activation of IL-1R1 and TNFR1 can make a positive feedback to activate the crucial pathway of inflammation via the NF-κB pathway (Yu et al., 2020a). Ellagic acid, apigenin, EGb761, galangin, isorhamnetin, and kaempferol from *Ginkogo biloba*, *Aster tataricus* L.f., *Eriobotrya japonica* (Thunb.) Lindl., and *Lepidium apetalum* Willd. can reduce the production of inflammatory cytokines and oxidative stress to prevent LPS-induced ALI in mice through the NF-κB pathway (Cornélio Favarin et al., 2013; Huang et al., 2013; Lee et al., 2014b; Shu et al., 2014; Wang et al., 2014; Chi et al., 2016; Li et al., 2016; Luan et al., 2016; Liu et al., 2018a; Qian et al., 2019; Júlio de Souza et al., 2020; Ren et al., 2021). TLR4/MYD88, an upstream player of the NF-κB pathway, mediates the inflammation and ALI. Both processes are ameliorated by ferulic acid and hesperidin from *Aster tataricus* L.f. and *Eriobotrya japonica* (Thunb.) Lindl., which have anti-inflammatory activities and protective effects against ALI by downregulating cytokines and chemokines (Ma et al., 2015; Wu et al., 2021). Furthermore, myeloid differentiation 2 (MD2) and high-mobility group box 1 (HMGB1) are the key targets of hesperidin, through which it can effectively inhibit inflammation during ALI (Liu et al., 2015; Ma et al., 2015). Rutin and moracin M from *Eriobotrya japonica* (Thunb.) Lindl. and *Morus alba* L. improve ALI through a crosstalk of the MAPK and the NF-kB signaling pathways (Yeh et al., 2014; Liu et al., 2015; Ma et al., 2015; Huang et al., 2016; Lee et al., 2016; Ye et al., 2019). The NLRP3 inflammasome processes the interleukin precursors into their mature forms, such as IL-1β and IL-18, which results in inflammation (Afonina et al., 2017). The bioactive components from *Prunus mandshurica* (Maxim.) Koehne, *Eriobotrya japonica* (Thunb.) Lindl., and *Morus alba* L. amygdalin and resveratrol suppress NF-κB activity and ROS production *via* inhibiting NLRP3 inflammasome (Jiang et al., 2016a; Zhang et al., 2017b). SIRT1, the NAD^+-dependent protein deacetylase, provides "stop signals" for inflammatory and oxidative stress (Jiang et al., 2016a; de Oliveira et al., 2019; Tsai et al., 2019). Resveratrol and oleanolic acid from *Perilla frutescens* (L.) Britton, *Eriobotrya japonica* (Thunb.) Lindl. and *Morus alba* L. reduce PTEN and NF-κB acetylation through the activation of SIRT1 (Peng et al., 2019; Wang et al., 2020a). Quercetin and formononetin from most of the 10 herbs enhance Nrf2/HO-1-mediated cytoprotective effects and prevent LPS-induced lung inflammation (Ma et al., 2013; Takashima et al., 2014; Wang et al., 2018a; Chen et al., 2021b). Luteolin downregulates cytokine and oxidative stress, ICAM-1 through the NF-κB pathway and induces Treg differentiation against ALI (Rungsung et al., 2018; Xie et al., 2021). According to the role of miRNAs in lung inflammation, it has been shown that resveratrol downregulates miR-193a to target transforming growth factor-β2 (TGF-β2), TGFβ receptor (TGFβR3), and death receptor-6 (Alghetaa et al., 2018). Liquiritin from *Prunus mandshurica* (Maxim.) Koehne inhibits the expression of TRPV1 and TRPA1 thereby providing anti-inflammatory and anticough effects (Liu et al., 2020). Taken together, 16 active compounds in 10 herbs have potential roles in inhibiting lung inflammation and injury through NF-κB, MAPK, NLRP3, PI3K/Akt, SIRT1, and HO-1 pathways. More details for the therapeutic effects and molecular mechanism of these compounds against inflammation and ALI are shown in **Table 2**.

Chronic Obstructive Pulmonary Disease

The pathogenesis of COPD is related to chronic inflammation, oxidative stress, cellular senescence, corticosteroid resistance, cell apoptosis, and changes in pulmonary histology and functions. The proinflammatory cytokines and chemokines (TNF-α, IL-1, IL-6, and IL-8), the signaling pathways (NF-κB and MAPK pathways), and various stress-related molecules (SOD, MDA, GSH) participate in the different pathological stages of COPD (Yang et al., 2020). IL-8 recruits neutrophils and secretes several neutrophil elastases and metalloproteases, e.g., MMP-9, which results in alveolar destruction. GM-CSF and IL-6 contribute to the increase in airway smooth muscle mass and proliferation, leading to bronchial obstruction (Knobloch et al., 2018; Jamal Jameel et al., 2021). Human airway smooth muscle cells (HASMCs) contributing to the secretion of cytokines and chemokines are related to non-type 2 airway inflammation and remodeling processes in COPD (Knobloch et al., 2013; Knobloch et al., 2016; Knobloch et al., 2019). Exposure to gases from cigarette smoking and inhaled particles such as PM2.5 are two archetypical inducing factors of COPD, which means that cigarette smoke and PM2.5 are commonly used for establishing *in vivo* and *in vitro* models of COPD (Rabe and Watz, 2017). Many studies have shown that multiple herbs, such as *Tussilago farfara* L., *Eriobotrya japonica* (Thunb.) Lindl., and *Morus alba* L. can inhibit the progression of COPD. Tussilagone and EGCG from the herbs mentioned above enhance the antiproliferative activity through the inhibition of the NF-κB pathway (Choi et al., 2018; Lakshmi et al., 2020). Amygdalin ameliorates the process of epithelial-mesenchymal transition (EMT) through the TGF-β/Smad pathway in cigarette smoke-exposed BEAS-2B cell line and mice model (Wang et al., 2019). Ursolic acid attenuates emphysema and enhances airway remodeling via unfolded protein response (UPR) signaling pathways (Lin et al., 2019; Li et al., 2020b). Liquiritin can reduce pulmonary inflammation by targeting the TGF-β pathway (Guan et al., 2012). Resveratrol inhibits the autophagic process and decreases IL-1β production by inactivation of NLRP3 inflammasome (Ding et al., 2019) or regulation of p53 destabilization (Navarro et al., 2017). Alveolar macrophages are important immune and inflammatory regulatory cells in the lung tissue (Gerlach et al., 2015). Resveratrol reduces the expression of MMP-9, GM-CSF and inflammatory mediators including IL-6, IL-8, and MCP-1 in alveolar macrophages under the stimulation of different harmful substances (Culpitt et al., 2003; Knobloch et al., 2011). Other reports have shown that resveratrol inhibits cytokines and chemokines (CCL-2, IL-6, IL-8) and ameliorates bronchial obstruction-related secretory proteins (GM-CSF and VEGF) in HASMCs from smokers and COPD patients. Similar to the findings against inflammation and ALI, SIRT1 and p38 MAPK are regarded as therapeutic targets of resveratrol in lipoteichoic acid

TABLE 2 | Summary of effects and mechanisms of bioactive compounds against inflammation.

Herbs	Component	Model	Targets	Mechanism/specific effects	References
Ginkgo biloba L.	EGb761	LPS-induced ALI	NF-κB pathway	Inhibits NF-κB, phosphorylation of JNK and Akt, TNF-α, interleukin IL-6, macrophage inflammatory protein (MIP)-2, MMP-9, inducible nitric oxide synthase (iNOS), and cyclooxygenase-2 (COX-2)	Huang et al. (2013), Lee et al. (2014b)
Aster tataricus L.f.	Apigenin	LPS-induced ALI mice model	NF-κB pathway	Inhibits the expression of NF-κB; reduces IL-6, IL-1β, TNF-α and COX-2	Wang et al. (2014)
Aster tataricus L.f.	Apigenin	PQ-induced ALI mice model	NF-κB pathway	Decreases the lung wet/dry ratios and lipid peroxidation, secretion of IL-6, TNF-α and MDA; increases spleen weight, T cell proliferation, secretion of IL-2, glutathione peroxidase (GSH-Px), CAT, and SOD activity	Luan et al. (2016), Liu et al. (2018a)
Eriobotrya japonica (Thunb.) Lindl.	Ellagic Acid	LPS-induced ALI mice model	NF-κB pathway	Reduces the vascular permeability changes, the activation of NF-κB and AP-1, and the expression of COX-2, CCL-2, IL-1β, IL-6, IL-10	Cornélio Favarin et al. (2013), Júlio de Souza et al. (2020)
Aster tataricus L.f.	Galangin	LPS-induced ALI mice model	NF-κB pathway	Reduces the activation of NF-κB, inflammation and oxidative stress; enhance the expression of HO-1.	Shu et al. (2014)
Lepidium apetalum Willd., *Eriobotrya japonica* (Thunb.) Lindl., *Ginkgo biloba* L., *Aster tataricus* L.f.	Isorhamnetin	LPS-induced ALI mice model and TNF-α induced BEAS-2B	NF-κB pathway	Suppresses the phosphorylation of IκBα, NF-κB(p65), ERK and JNK; reduce the level of IL-1β, IL-6, IL-8, TNF-α, and MPO	Chi et al. (2016), Li et al. (2016), Ren et al. (2021)
Morus alba L., *Datura metel* L., and other 6 herbs	Kaempferol	LPS-induced ALI mice model	NF-κB pathway	Prevents increased NF-κB and K63-linked polyubiquitination; Reducing lung damage	Qian et al. (2019)
Aster tataricus L.f.	Ferulic acid	LPS-induced ALI mice model	TLR4/NF-κB pathway	Reduces the activation of the TLR4 and NF-κB and the secretion of IL-6, IL-1β and TNF-α; ameliorates lung histopathological change	Wu et al. (2021)
Eriobotrya japonica (Thunb.) Lindl.	Hesperidin	LPS-induced ALI mice model	NF-κB pathway; MD2; HMGB1	Upregulates the expression of PPAR-γ and inhibits MD2 and HMGB1 to block the interaction between TLR4 and NF-κB; suppresses cytokines and chemokine (TNF-α, IL-6, IL-1β, and MIP-2), the infiltration of macrophages and production of MCP-1	Liu et al. (2015), Ma et al. (2015), Ye et al. (2019)
Eriobotrya japonica (Thunb.) Lindl.	Rutin	LPS-induced ALI mice model	MAPK-NF-κB pathway	Inhibits oxidative stress, neutrophil infiltration, VCAM-1, iNOS, and NF-κB activation	Yeh et al. (2014), Huang et al. (2016)
Morus alba L.	Moracin M	LPS-induced ALI mice model and alveolar macrophages	MAPK and NF-κB pathways	Downregulates of JNK/c-Jun, NF-κB, IL-6, IL-1β, and iNOS	Lee et al. (2016)
Prunus mandshurica (Maxim.) Koehne	Amygdalin	LPS-induced ALI mice model	NLRP3 and NF-κB signaling pathways	Reduces the activation of NF-κB, NLRP3, inflammatory cytokines production (TNF-α, IL-1β, IL-6, and MPO↓) and protect LPS-induced ALI in mice	Zhang et al. (2017b)
Eriobotrya japonica (Thunb.) Lindl., *Morus alba* L.	Resveratrol	LPS-induced ALI mice model	NLRP3; PI3K/Akt pathways; Src family kinases (SFKs)	Reduces the NLRP3 inflammasome, ERK and PI3K/Akt pathways; suppresses ROS production (MDA↓ and SOD↑); reduces the level of IL-6, KC, MIP-1α, MIP-2, MCP-1; reduces neutrophil activation and ameliorate lung injury	Jiang et al. (2016a), de Oliveira et al. (2019), Tsai et al. (2019)
Perilla frutescens (L.) Britton, *Eriobotrya japonica* (Thunb.) Lindl.	Oleanolic acid	N-methyl-d-aspartate-induced MLE-12 cells apoptosis and lung injury in mice	SIRT1	Activates SIRT1 and reduces the acetylation of NF-κB. Anti-inflammatory (TNF-α, IL-6 and IL-1β) and anti-oxidant (MAD and GSH) functions	Peng et al. (2019)

(Continued on following page)

TABLE 2 | (*Continued*) Summary of effects and mechanisms of bioactive compounds against inflammation.

Herbs	Component	Model	Targets	Mechanism/specific effects	References
Eriobotrya japonica (Thunb.) Lindl., *Morus alba* L.	Resveratrol	Methamphetamine-induced chronic lung injury	SIRT1/PTEN/p-Akt pathway	Activates SIRT1 and reduces PTEN, phosphorylated Akt. Suppresses ROS levels and LDH leakage, inhibits EMT and the apoptosis	Wang et al. (2020a)
Morus alba L., *Datura metel* L., and other 6 herbs	Quercetin	LPS-induced mice model and alveolar macrophage and epithelial cell *in vitro*	heme oxygenase (HO)-1; cAMP	Enhances HO-1-mediated cytoprotective effects for epithelial cell; inhibits the expression of cAMP/Epac, cAMP/PKA, MMP-9, TNF-α, IL-1β, and IL-6; blocks neutrophil recruitment	Takashima et al. (2014), Wang et al. (2018a)
Ginkgo biloba L.	Formononetin	LPS-induced ALI mice model	PPARγ; Nrf2/HO-1	Increases PPAR-γ gene expression, Nrf2 and HO-1; reduces hyperoxia and MPO activity; improves SOD activity	Ma et al. (2013), Chen et al. (2021b)
Eriobotrya japonica (Thunb.) Lindl., *Aster tataricus* L.f.	Luteolin	ALI mouse model with cecal ligation puncture (CLP)	NF-κB; Treg differentiation	Downregulats IL-1β, IL-6, IL-17A, iNOS, MPO, ICAM-1, and NF-κB; induces Treg differentiation, and increases IL-10 to promote the polarization of M2 macrophages	Rungsung et al. (2018), Xie et al. (2021)
Eriobotrya japonica (Thunb.) Lindl., *Morus alba* L.	Resveratrol	Staphylococcal enterotoxin B-exposured mice model	miR-193a	Down-regulates miR-193a targeting TGFβ2, TGFβR3 and death receptor-6; activates apoptotic pathways and promotes anti-inflammatory activities	Alghetaa et al. (2018)
Prunus mandshurica (Maxim.) Koehne	Liquiritin	LPS-induced ALI mice model	TRPV1 and TRPA1	Inhibits the expression of TRPV1 and TRPA1; suppresses NF-κB pathway; anti-inflammatory and anti-coughing	Liu et al. (2020)

(LTA)- or TNF-α-stimulated HASMC models (Knobloch et al., 2010; Knobloch et al., 2014). The abovementioned therapeutic effects and mechanisms of resveratrol have also been demonstrated in animal models (Chen et al., 2016; Wang et al., 2017a). Together, these findings suggest that six main compounds can regulate NF-κB, UPR, TGF-β, MAPK and SIRT1 pathways to inhibit COPD in different cell and animal models (**Table 3**).

Pulmonary Fibrosis

It is now clear that many elements of the innate and adaptive immune response participate in the differentiation and activation of fibroblasts. The pathogenesis of PF is related to adaptive and innate immune activation, inflammation, epithelial/endothelial damage, EMT and cell apoptosis. Specifically, the activation of TGF-β or NF-κB pathway is the primary factor driving the progression of PF (Kitani et al., 2003; Wynn and Ramalingam, 2012). Some natural products, such as β-sitosterol, quercetin, ferulic acid, hesperidin, and EGb761 from various herbs, inhibit PF by downregulating TGF-β. β-sitosterol and ferulic acid suppress EMT and reduce extracellular matrix (ECM) through the TGF-β/Smad-dependent signaling pathways (Park et al., 2019; Ali et al., 2021). Quercetin suppresses Akt/mammalian target of rapamycin (mTOR) pathway in TGF-β-mediated responses and reduces fibrotic factors, such as collagen I, collagen III, and IL-6 (Xiao et al., 2020b). Another study has reported that quercetin enhances the expression of caveolin1 (CAV1), the cell membrane lipid raft and a protective factor for PF, to inhibit ligand-induced apoptosis in fibroblasts (Hohmann et al., 2019). For other bioactive compounds, hesperidin and EGb761 improve the progression of PF by mediating the proinflammatory cytokines and apoptosis-related proteins *via* the crosstalk of NF-κB and TGF-β pathways (Zhou et al., 2019; Pan et al., 2020).

Hyperoside inhibits the EMT *via* the regulation of the Akt/GSK3β pathway (Huang et al., 2020). Ellagic acid suppresses ECM accumulation by regulating the Wnt pathway (Li et al., 2021). EGCG reduces the production of cytokines through the Nrf-2/HO-1 pathway (Sriram et al., 2009; You et al., 2014). Galangin and isorhamnetin attenuate EMT and inflammatory damage in bleomycin or TGF-β-induced PF models (Zheng et al., 2019; Wang et al., 2020b). Kaempferol promotes autophagy in the therapeutic effects on PF (Liu et al., 2019b). Resveratrol regulates miR-21/Smad7 to alleviate serious PF symptoms (Wang et al., 2018b). Rosmarinic acid targets miR-19b-3p/MYPT1 to relieve the pulmonary fibrosis caused by radiotherapy (Zhang et al., 2020). Collectively, these results indicate that these bioactive compounds can reduce EMT and ECM deposition to inhibit progressive lung fibrosis by regulating TGF-β, Akt/GSK3β, Nrf-2/HO-1, or microRNA-mediated pathways (**Table 4**).

Asthma

Asthma is associated with the activation of IgE-mediated mast cells and eosinophilic inflammation. Inhaled corticosteroids which have a therapeutic effect on allergic reactions and sensitivity of type 2 inflammation, are the cornerstone treatment for asthma. Airway inflammation and remodeling, and airway hyperresponsiveness (AHR) promote the pathogenesis of asthma (Mishra et al., 2018). Naïve CD4 T cells are exposed to antigens and differentiate into various T helper (Th) cell types (e.g., Th1, Th2, Th17). Th2 cells play an important role in disease pathogenesis and progression (Chen and Kolls, 2013; Gaurav and Agrawal, 2013). However,

TABLE 3 | Summary of effects and mechanisms of bioactive compounds against COPD.

Herbs	Component	Model	Targets	Mechanism/specific effects	References
Tussilago farfara L.	Tussilagone	EGF or PMA-induced MUC5AC mucin gene expression and production from NCI-H292 cells	NF-κB pathway and MUC5AC mucin gene	Down-regulates MUC5AC protein, phosphorylation of kappa B kinase (IKK), IκBα, and NF-κB p65;	Choi et al. (2018)
Eriobotrya japonica (Thunb.) Lindl., *Ginkgo biloba* L.	EGCG	Cigarette smoke extract-induced normal human bronchial epithelial	NF-κB pathway	Reduces the activation of NF-κB; Anti-oxidative and anti-inflammatory effects	Lakshmi et al. (2020)
Prunus mandshurica (Maxim.) Koehne	Amygdalin	BEAS-2B and mice exposed to cigarette smoke	TGF-β/Smad pathway	Suppresses the expression of TGF-β1 and phosphorylated Smad2/ 3ameliorated EMT process	Wang et al. (2019)
Perilla frutescens (L.) Britton; *Eriobotrya japonica* (Thunb.) Lindl.; *Morus alba* L.	Ursolic Acid	PM2.5-induced COPD in rats; cigarette smoke-induced emphysema in rats	UPR signaling pathways	Reduces the p-Smad2 and p-Smad3 on protein level; attenuates CSE-induced emphysema, airway remodeling, and reduces expression of IL-6, TNF-α	Lin et al. (2019), Li et al. (2020b)
Prunus mandshurica (Maxim.) Koehne	Liquiritin	A549 exposed to cigarette smoke extract *in vivo*; ICR mice exposed to cigarette smoke	TGF-β and TNF-α	Reduces pulmonary inflammation (TGF-β↓, TNF-α↓); increases anti-oxidative levels (GSH↑)	Guan et al. (2012)
Eriobotrya japonica (Thunb.) Lindl.; *Morus alba* L.	Resveratrol	C57BL/6J mice exposed to ambient PM; PM2.5-induced BEAS-2B cells	NLRP3	Reduces the function of NLRP3 inflammasome; inhibits autophagic process and decreased IL-1β production	Ding et al. (2019)
Eriobotrya japonica (Thunb.) Lindl.; *Morus alba* L.	Resveratrol	Prematurely ageing telomerase null ($terc^{-/-}$) mice	p53	Enhances p53 destabilization and the expression of PGC-1α, p-Akt, p-Mdm2, p-PTEN; reduces Bax protein; Slowed aging	Navarro et al. (2017)
Eriobotrya japonica (Thunb.) Lindl.; *Morus alba* L.	Resveratrol	IL-1β or cigarette smoke media CSM stimulated macrophages which were isolated from BALF from cigarette smokers and COPD patients	IL-8 and granulocyte macrophage-colony stimulating factor (GM-CSF)	inhibited basal release of IL-8 and GM-CSF	Culpitt et al. (2003)
Eriobotrya japonica (Thunb.) Lindl.; *Morus alba* L.	Resveratrol	LPS-induced alveolar macrophages from smokers and COPD patients		Reduces secretory protein MMP-9 and inflammatory mediators including IL-6, IL-8, GM-CSF and MCP-1	Knobloch et al. (2011)
Eriobotrya japonica (Thunb.) Lindl.; *Morus alba* L.	Resveratrol	Lipoteichoic acid (LTA) from *Staphylococcus aureus* stimulated HASMCs	SIRT1	Reduces CCL-2, IL-6, IL-8 and GM-CSF through activation of SIRT1 or interaction with class I/II HDACs	Knobloch et al. (2014)
Eriobotrya japonica (Thunb.) Lindl.; *Morus alba* L.	Resveratrol	TNF-α stimulated HASMCs	p38 MAPK	Reduces the transcription level of IL-8, GM-CSF, and VEGF by inhibiting P38 MAPK	Knobloch et al. (2010)
Eriobotrya japonica (Thunb.) Lindl.; *Morus alba* L.	Resveratrol	Cigarette smoke exposure induced rats model	SIRT1 and PGC-1α	Decreases the MDA, IL-6, IL-8 and increases the SOD by increasing SIRT1 and PGC-1α mRNA expression	Wang et al. (2017a)
Eriobotrya japonica (Thunb.) Lindl.; *Morus alba* L.	Resveratrol	LPS and cigarette smoke-induced mouse model	Beclin 1	Attenuats the fibrotic response and mucus hypersecretion; Inhibits IL-17, IL-6, TNF-α, and TGF-β through inhibiting Beclin 1	Chen et al. (2016)

neutrophilic inflammation has also been observed during asthma exacerbations as well asc in severe asthma patients (Ray and Kolls, 2017). Through the literature search, natural products from 10 different medical plants have a good inhibitory effect on the inflammation based on eosinophils and neutrophils in asthma. Unsurprisingly, the dysregulation of the NF-κB and MAPK signaling pathways associated with inflammation and immune response, plays a major role in asthma (Freund-Michel and Frossard, 2008; Zhang et al., 2013). Rosmarinic acid, tussilagone, formononetin, galangin, ellagic acid, and ginkgolide B can downregulate the levels of histamine, ovalbumin (OVA)-specific IgE, Th2 cytokines, and chemokines (IL-4, IL-5, IL-13, CCL5, and CCL11) in serum and bronchial alveolar lavage fluid through the suppression of the NF-κB and MAPK signaling pathways (Chu et al., 2011; Alves et al., 2013; Kim et al., 2013; Zha et al., 2013; Zhou et al., 2014; Liang et al., 2016a; Liang et al., 2016b; Henry et al., 2020; Jin et al., 2020; Yi et al., 2020). EGCG inhibits MMP-9 production, ROS generation, and EMT to reduce airway remodeling by upregulating PTEN (Kim et al., 2006; Yang et al., 2018). Kaempferol ameliorates airway hyperplasia and hypertrophy *via* the Syk-PLCγ and PKCμ-ERK-cPLA2-COX2 and NF-κB signaling pathways (Gong et al., 2012; Shin et al., 2015; Molitorisova et al., 2021). Glabridin, β-sitosterol and quercetin can suppress the level of serum IgE, TNF-α, IL-4, and IL-5, but the mechanism has not been thoroughly explored (Rogerio et al., 2007; Mahajan and Mehta, 2011; Dogan et al., 2020). Luteolin inhibits the

TABLE 4 | Summary of effects and mechanisms of bioactive compounds against PF and IPF.

Herbs	Component	Model	Targets	Mechanism/specific effects	References
Morus alba L., *Datura metel* L., and other 6 herbs	β-sitosterol	TGF-β-induced human lung alveolar epithelial cell (PF)	TGF-β1/Snail pathway	Inhibits the expression of Snail and Smad2; suppresses EMT and ECM effect	Park et al. (2019)
Aster tataricus L.f.	Ferulic acid	silica-induced PF	TGF-β/Smad pathway	Inhibited TGF-β/Smad pathway (CTGF↓, SLUG↓, α-SMA, EMT↓, Vimentin↓, E-cadherin↑); decreases the expression of inflammatory cytokines, and collagen-I; reduces oxidative stress and EMT; attenuates histology	Ali et al. (2021)
Morus alba L., *Datura metel* L., and other 6 herbs	Quercetin	LPS-induced Human embryonic lung fibroblast cells (WI-38) and a trauma-induced rabbit tracheal stenosis model	TGF-β/AKT/mTOR pathway	Downregulates expression of mTOR, AKT, ATG; suppressed fibrotic factors (VEGF, IL-6, TGF-β, COL-1, and COL-3)	Xiao et al. (2020b)
Eriobotrya japonica (Thunb.) Lindl.	Hesperidin	Bleomycin-induced PF in rat	TGF-β/Smad and NF-κB pathways	Up-regulates expression of Nrf2 and HO-1; down-regulates protein level of AMPK, NF-κB, IκBα, and PP2C-α and mRNA level of TNF-α, IL-1β, IL-6, collagen-1, TGF-β; reduce collagen deposition	Zhou et al. (2019)
Ginkgo biloba	EGb761	Bleomycin-Induced PF in Mice	NF-κB/p65 pathway	Reduces protein level of α-SMA and TGF-ß1, phosphorylated NF-κB (p65), caspase-3, and caspase-9; balance of M1/M2 macrophages and NF-κB (p65)-mediated apoptosis	Pan et al. (2020)
Morus alba L., *Datura metel* L., and other 6 herbs.	Quercetin	Bleomycin -induced pulmonary fibrosis in aged mice	Balance of p-AKT and CAV1	Enhances expression of CAV1 and reduces expression of p-AKT; inhibits ligand-induced apoptosis (FasL↓ and TRAIL↓) in fibroblasts	Hohmann et al. (2019)
Eriobotrya japonica (Thunb.) Lindl.	Hyperoside	Bleomycin-induced pulmonary fibrosis in mice	AKT/GSK3β pathway	Reduces the levels of MDA, TNF-α, and IL-6 and increases the activity of SOD; inhibits the EMT (E-cadherin↑, N-cadherin↓, vimentin↓, TWIST1↓, and SNAIL1↓) via the downregulation of AKT/GSK3β pathway	Huang et al. (2020)
Eriobotrya japonica (Thunb.) Lindl.	Ellagic Acid	Bleomycin-induced PF in mice and isolation of primary pulmonary fibroblasts (PPF)	Wnt signaling pathway	Reverses an increase in pro-fibrotic factors hydroxyproline (HYP), ECM accumulation and promotes autophagy of fibroblast through Wnt signaling pathway (Wnt3a↓, β-catenin↓, p-Erk2↓, p-Akt↓, p-mTOR↓, p62↓, Atg16↑, Beclin1↑, LC3-II/I↑)	Li et al. (2021)
Eriobotrya japonica (Thunb.) Lindl., *Ginkgo biloba* L.	EGCG	Bleomycin-induced PF in Wistar rats	Nrf-2/HO-1	Activates the expression of Nrf-2 and its downstream HO-1 and NQO-1; reduces lung index scores and histological changes; suppresses the expression of cytokine (TGF-β1↓, IL-6↓, IL-10↓ and TNF-α↓)	Sriram et al. (2009), You et al. (2014)
Aster tataricus L.f.	Galangin	Bleomycin-induced PF in mouse and TGF-β1-induced A549 and NIH/3T3 cells	$CD4^+$ and $CD8^+$ T cells	Increases in the numbers of $CD4^+$ and $CD8^+$ T cells; attenuates EMT (α-SMA↓, Vimentin↓, E-cadherin↓) and inflammatory damage	Wang et al. (2020b)
Lepidium apetalum Willd., *Eriobotrya japonica* (Thunb.) Lindl., *Ginkgo biloba* L., *Aster tataricus* L.f.	Isorhamnetin	Bleomycin-induced PF in mouse and TGF-β-induced HBECs and A549	PERK signaling	Suppresses the activation of PERK signaling (p-PERK↓, p-eIF2α↓, GRP78↓, CHOP↓); inhibits EMT (α-SMA↓, collagen I↓, Vimentin↓, E-cadherin↑) and fibrotic markers, alleviates lung pathologic abnormalities and collagen deposition	Zheng et al. (2019)
Morus alba L., *Datura metel* L., and other 6 herbs.	Kaempferol	Bleomycin-induced PF in mouse and silicosis models	Autophagy	Induces LC3 lipidation; promotes autophagy (p62↑) in the therapeutic effects on silicosis	Liu et al. (2019b)
Eriobotrya japonica (Thunb.) Lindl.; *Morus alba* L.	Resveratrol	Bleomycin-induced PF in mice and MRC-5 cells	MiR-21	miR-21 targets Smad7 and reduces the phosphorylation levels of ERK, JNK and p38; Decreases the expression of fibronectin, α-SMA, alleviates serious PF symptoms	Wang et al. (2018b)

(Continued on following page)

TABLE 4 | (*Continued*) Summary of effects and mechanisms of bioactive compounds against PF and IPF.

Herbs	Component	Model	Targets	Mechanism/specific effects	References
Perilla frutescens (L.) Britton	Rosmarinic acid	X-ray-induced lung injury	MiR-19b-3p	Attenuates RhoA/Rock signaling through up-regulating miR-19b-3p/MYPT1; relieves the pulmonary fibrosis caused by radiotherapy	Zhang et al. (2020)

inflammatory responses and autophagy via the PI3K/Akt/mTOR pathway (Jang et al., 2017; Wang et al., 2021). Taken together, in asthma, these 10 bioactive compounds can inhibit inflammatory reactions and airway remodeling through the MAPK and NF-κB pathways in OVA-induced animal models (**Table 5**).

Lung Cancer

Lung cancer is the malignant tumor with the highest mortality rate. It causes 1.6 million deaths every year, but treatment can effectively prolong survival and quality of life (Siegel et al., 2021). TCM treatment can effectively improve the quality of life and survival time of patients with advanced lung cancer with or without conventional therapy (Sun et al., 2019; Jiang et al., 2016b; Xu et al., 2011). Active components of TCM participate in the treatment of lung cancer through the regulation of multiple pathways (**Table 6**). Ursolic acid and β-sitosterol show a good lung cancer-inhibiting effect via the TGF-β/Smad pathway (Ruan et al., 2019; Sundarraj et al., 2012; Wang et al., 2017b). Caffeic acid and sanguinarine enhance the antiproliferative effect of paclitaxel in lung cancer A549 and H1299 cells (Lin et al., 2012). Sanguinarine can target NF-κB pathway-mediated autophagy and mitophagy to block lung cancer progression (Yu et al., 2020b). Meanwhile, the p53 protein is a transcription factor that inhibits cell proliferation or survival, acting as a key tumor suppressor protein (Skoulidis and Heymach, 2019). Loss or mutant of p53 induces lung cancer with shortened latency and increases rapid progression and poor prognosis (Donehower et al., 2019). Natural products such as hyperoside, resveratrol, liquiritin, and formononetin have a good effect on improving the antitumor function of p53 and inducing the apoptosis of tumor cells. Hyperoside increases Caspase-9/Caspase-3 activation to induce apoptosis in *in vitro* and *in vivo* models of A549 and H1975 cells (Liu et al., 2016; Lü, 2016). Resveratrol decreases antiapoptotic factors, Bcl-2 and Bcl-xl and the levels of MMP2, and MMP9 by upregulating the p53/HO-1 pathways against lung cancer (Liu et al., 2010; Rasheduzzaman et al., 2018; Li et al., 2019). Liquiritin decreases the expression levels of PCNA, p-PTEN, caspase family, and PARP (Zhou and Ho, 2014). Formononetin promotes Mcl-1 ubiquitination and degradation *via* Fbw7 to enhance the EGFR-TKI sensitivity (Yang et al., 2014; Yu et al., 2020c). The PI3K/Akt signaling pathway is an important dysregulated pathway in tumorigenesis, which controls lung cancer growth, metabolism, motility, and other key cellular processes (Janku et al., 2018). Isorhamnetin and apigenin inhibit EMT and decrease invasion by inhibiting Akt activation (Chang et al., 2018b; Luo et al., 2019). Moracin N induces autophagy mTOR signaling pathway (Gao et al., 2020). Furthermore, isorhamnetin as a potential application in adjuvant radiotherapy inhibits the activation of NF-κB and increases the expression of IL-13 (Du et al., 2020). Resveratrol and ellagic acid promote lung cancer cell apoptosis *via* the PI3K/Akt signaling pathway (Liu et al., 2018b; Li et al., 2019). Amygdalin downregulates the phosphorylation of Akt to inhibit invasion and migration of H1299 and PA cells (Qian et al., 2015). Inactivation of STAT3 is a target for increasing cisplatin sensitivity in lung cancer treatment, galangin, and laricitrin are STAT3 inhibitors in adjuvant chemotherapy (Chang et al., 2016a; Chang et al., 2016b; Yu et al., 2018). Oleanolic acid enhances mitophagy through the PINK1/Parkin axis in A549 cells (Castrejón-Jiménez et al., 2019). Rosmarinic acid could reverse the cisplatin resistance by inhibiting the expression of P-gp, MDR1, and MAPK pathways and plays a key role in the treatment of non-small cell lung cancer (NSCLC) (Liao et al., 2020). EGCG from *Eriobotrya japonica* (Thunb.) Lindl. and *Ginkgo biloba* L. can suppress the levels of Axl and Tyro three to reduce the resistance to platinum (Kim and Lee, 2014). Ginkgolide B and glabridin from *Ginkgo biloba* L. have inhibitory effects on autophagy and angiogenesis, mediated by Beclin-1 or FAK/Src complex, respectively (Tsai et al., 2011; Wang et al., 2020c). In H1975 cell model, ursolic acid inhibits the Wnt/β-catenin pathway to suppress proliferation and induce apoptosis (Yang et al., 2019). As a cisplatin sensitizing agent, ginkgetin enhances the ferroptosis-mediated disruption of the Nrf2/HO-1 axis (Lou et al., 2021). Kaempferol downregulates Nrf2 and upregulates miR-340 to induce apoptosis and autophagy (Han et al., 2018; Fouzder et al., 2021). As for quercetin, it can target aurora B or miR-16-5p/WEE1 pathways to inhibit lung cancer progression and enhance the radiosensitivity of NSCLC cells (Xingyu et al., 2016; Wang et al., 2020d). Hesperidin exhibits antiproliferative and apoptosis induction effects by regulating the miR-132/ZEB2 signaling pathway (Birsu Cincin et al., 2015; Tan et al., 2020). Luteolin inhibits cell proliferation and induces apoptosis via miR-34a-5p targeting MDM4 and RhoA (Jiang et al., 2018; Masraksa et al., 2020). Taken together, these results demonstrate that these bioactive compounds have anticancer effects by targeting multiple pathways, including NF-κB, p53, TGF-β, or miRNAs (**Table 6**).

TABLE 5 | Summary of effects and mechanisms of bioactive compounds against asthma.

Herbs	Component	Model	Targets	Mechanisms/specific effects	References
Perilla frutescens (L.) Britton	Rosmarinic acid	OVA-induced asthmatic mice model	MAPK and NF-κB pathway	Inhibits expression of ERK, JNK and p38 phosphorylation, activation of NF-κB, Th2 cytokines and IgE, reduces in AMCase, CCL11, CCR3, Ym2 and E-selectin mRNA expression	Liang et al. (2016a), Liang et al. (2016b)
Tussilago farfara L.	Tussilagone	OVA-induced asthmatic guinea pigs and IgE-stimulated RBL-2H3 cells	NF-κB and MAPK pathway	suppresses the phosphorylation of Lyn, Syk, Akt, NF-κB p65, ERK and p38 MAPK; down-regulates the levels of histamine, IgE and IL-6 in the serum	Liang et al. (2016a), Liang et al. (2016b), Jin et al. (2020)
Ginkgo biloba L.	Formononetin	OVA-induced asthmatic mice	NF-κB and JNK	Inhibits the activation of NF-κB and JNK; enhances the expression of HO-1; ameliorates collagen deposition and oxidative stress, and increases SOD activity; reduces the expression of IL-4, IL-5, IL-13, Ig E, CCL5, and CCL11	Yi et al. (2020)
Aster tataricus L.f.	Galangin	OVA-induced BALB/c mice and TGF-β1 induced ASMCs	MAPK/Akt axis; NF-κB pathway	Downregulates the expression of VCAM-1 and p-p65; promotes IκB degradation; upregulates the expression of PPARγ; reduces eosinophil infiltration, hyperplasia and the expression of IL-4, IL-5, IL-13, IL-17, TNF-α, NO, ROS, EPO, CXCL10 and OVA-specific IgE	Kim et al. (2013), Zha et al. (2013), Henry et al. (2020)
Ginkgo biloba L.	Ginkgolide B	OVA-induced BALB/c mice	MAPK pathway	Suppresses the expression of MAPK and p-ERK; inhibits the expression of IL-5 and IL-13	Chu et al. (2011)
Eriobotrya japonica (Thunb.) Lindl.	Ellagic acid	OVA-induced mouse asthma model	NF-κB pathway	Inhibited NF-κB activation (p-IκB↓, p- NF-κB p65↓); increases Th2 cytokines and inhibits lung eosinophilic inflammation	Alves et al. (2013), Zhou et al. (2014)
Eriobotrya japonica (Thunb.) Lindl., *Ginkgo biloba* L.	EGCG	OVA-induced asthmatic mice and TGF-β1-induced 16HBE cells	PI3K/Akt pathway	Inhibits p-PI3K, p-Akt expression through up-regulating PTEN; inhibits MMP-9 production, ROS generation and EMT (α-SMA↓, E-cadherin↑); reduces airway remodeling	Kim et al. (2006), Yang et al. (2018)
Morus alba L., *Datura metel* L., and other 6 herbs.	Kaempferol	Bovine serum albumin and OVA-induced BALB/c mice model	Syk-PLCγ, PKCμ-ERK-cPLA2-COX2 and NF-κB pathway	Decreases the levels of IL-5, IL-13, GM-CSF and TGF-β; ameliorates airway hyperplasia and hypertrophy; blunting eosinophil accumulation via suppressing NF-κB pathway	Gong et al. (2012), Shin et al. (2015), Molitorisova et al. (2021)
Ginkgo biloba L.	Glabridin	OVA-induced BALB/c mice model	OVA-specific IgE	Suppresses the level of serum IgE; reduces white blood cells and improves respiratory function	Dogan et al. (2020)
Morus alba L., *Datura metel* L., and other 6 herbs.	β-sitosterol	OVA-induced airway inflammation in guinea pigs	cytokine	Suppresses the levels of TNFα, IL-4 and IL-5; Upregulates the tidal volume and downregulates the respiration rate	Mahajan and Mehta, (2011)
Morus alba L., *Datura metel* L., and other 6 herbs.	Quercetin	OVA-induced BALB/c mice model	IL-5	Reduces neutrophil counts in blood and IL-5 level	Rogerio et al. (2007)
Eriobotrya japonica (Thunb.) Lindl., *Aster tataricus* L.f.	Luteolin	OVA-induced mice model	PI3K/Akt/mTOR pathway	Inhibits the OVA-induced inflammatory responses and autophagy via activating the PI3K/Akt/mTOR pathway and inhibiting the Beclin-1-PI3KC3 protein complex	Jang et al. (2017), Wang et al. (2021)

Collectively, the network of bioactive compounds, targets, signal pathways, and different pulmonary diseases is visualized in **Figure 2**. These bioactive compounds, such as isorhamnetin, formononetin, resveratrol, and galangin are active substances of types of saponins, flavonoids, and alkaloids, which can regulate different key targets (NF-κB, PI3K/Akt, Nrf-2, NLRP3) to regulate cytokine production, oxidative stress or chemotherapy sensitivity against a series of lung-related diseases.

DISCUSSION

According to the theories of TCM and commonly used Chinese medicines in the clinical application against respiratory diseases, this review summarizes the pharmacological effects and molecular mechanisms of 31 active compounds of 10 Chinese herbal medicines in six main lung-related diseases, including pulmonary infection, ALI, PF, COPD, asthma, and lung cancer.

TABLE 6 | Summary of effects and mechanisms of bioactive compounds against lung cancer.

Herbs	Component	Model	Targets	Mechanism/specific effects	References
Perilla frutescens (L.) Britton; *Eriobotrya japonica* (Thunb.) Lindl.; *Morus alba* L.	Ursolic acid	H1975 cells	TGF-β1 signaling pathway	Reduces TGF-β1 pathway to regulate integrin αVβ5 and MMP9 expression; inhibits the cell migration, invasion EMT in H1975 cells	Ruan et al. (2019)
Morus alba L., *Datura metel* L., and other 6 herbs.	β-sitosterol	A549, NCI-H1975 and H1299 cells	TGF-β/Smad2/3 pathway	Inactivates TGF-β, Smad2/3 and c-Myc; inhibits autophagy and induced G_0/G_1 cell cycle arrest and inhibits cell proliferation	Sundarraj et al. (2012), Wang et al. (2017b)
Aster tataricus L.f.	caffeic acid	A549 and H1299 cells	NF-κB pathway	Reduces nuclear translocation of NF-κB p65; sensibilization of paclitaxel; anti-proliferation and apoptosis	Lin et al. (2012)
Morus alba L.	Sanguinarine	A549 and THP-1 *in vivo* model	NF-κB pathway	Inhibits p-p65 expression via exosomes; suppresses the expression of TNF-α, IL-6, and CCL-2; induces autophagy and mitophagy	Yu et al. (2020b)
Eriobotrya japonica (Thunb.) Lindl.	Hyperoside	A549 and H1975 *in vivo* and *in vitro* model	Caspase-3, p53, and NF-κB signaling pathway	Inhibits NF-κB transcriptional activity, enhances Caspase-9/Caspase-3 activation; induces apoptosis and inhibits proliferation	Liu et al. (2016), Lü (2016)
Eriobotrya japonica (Thunb.) Lindl.; *Morus alba* L.	Resveratrol	A549, HCC-15, ASTC-a-1, PC14, H69, and IMR90	p53, PRMT5; HO-1	Decreases the phosphorylated Akt, PRMT5 and NF-κB via upregulation of p53 and HO-1; promotes cancer cell apoptosis (Bcl-2↓, Bcl-xl↓, cyclin D1↓, cyclin E1↓); inhibits invasion (MMP-9↓; MMP-2↓)	Liu et al. (2010), Rasheduzzaman et al. (2018), Li et al. (2019)
Prunus mandshurica (Maxim.) Koehne	Liquiritin	A549 cells	p53 and p21	Upregulates p53 and p21; induces apoptotic pathways (p53↑, p21↑; PCNA↓, MDM2↓, p-GSK3β↓, p-Akt↓, p-c-Raf↓, p-PTEN↑; PARP↓, Bcl-2↓, caspase family↑)	Zhou and Ho, (2014)
Ginkgo biloba L.	Formononetin	A549 and NCI-H23 cells	p53, EGFR-Akt-Mcl-1 axis	Enhances Mcl-1 ubiquitination via degradation of Fbw7; increases the phosphorylation of p53; promotes the EGFR-TKI sensitivity; induces cell cycle arrest and apoptosis	Yang et al. (2014), Yu et al. (2020c)
Lepidium apetalum Willd., *Eriobotrya japonica* (Thunb.) Lindl., *Ginkgo biloba* L., *Aster tataricus* L.f.	Isorhamnetin	A549 cells	Akt/ERK1/2 and NF-κB pathway	Suppresses the expression of Akt, ERK1/2, IL-13, and NF-κB p65; inhibits EMT, MMP-2 and MMP-9 activity	Luo et al. (2019), Du et al. (2020)
Aster tataricus L.f.	Apigenin	A549, CL1–5, HCC827, and H1975 NSCLC *in vitro* and A549 *in vivo* models	CD26/DPPIV	Suppresses the expression of CD26, DPPIV and Akt; modulates EMT (Snail↓, Slug↓) and decreases invasion	Chang et al. (2018b)
Eriobotrya japonica (Thunb.) Lindl.	Ellagic acid	A549 cells	PI3K/Akt signaling pathway	Reduces the phosphorylation of PI3K and Akt; suppresses cell proliferation, induces apoptosis (Bax↑, Bcl-2↓, Caspase-3↑, p21↑)	Liu et al. (2018b)
Morus alba L.	Moracin N	A549 and PC9 cells	mTOR signaling pathway	Inhibits the expression of p-S6 EGFR; reduces ROS generation, promotes cancer cell autophagy (p-AKT↓, p-mTOR↓) and apoptosis (Bax↑, Bcl-2↓, Caspase-9↑)	Gao et al. (2020)
Prunus mandshurica (Maxim.) Koehne	Amygdalin	H1299 and PA cell	Akt and RICTOR	Down-regulates the expression of cell integrin β1/4 and FAK; inhibits the *in vitro* invasion and migration (E-cadherin↑)	Qian et al. (2015)
Ardisia japonica (Thunb.) Blume	Laricitrin	A549, CL1-5, and H1395 *in vivo*; LLC cells implanted into C57BL/6	BRAF; STAT3	Inhibits the phosphorylation of STAT3 and expression of IL-10; changes the $CD4^+$ T cell phenotype from Th2 to Th1; ameliorates BRAF mutation-induced lung cancer; enhances the DDP sensitivity	Chang et al. (2016a), Chang et al. (2016b)

(Continued on following page)

TABLE 6 | (*Continued*) Summary of effects and mechanisms of bioactive compounds against lung cancer.

Herbs	Component	Model	Targets	Mechanism/specific effects	References
Aster tataricus L.f.	Galangin	A549 and A549/DDP	STAT3	Suppresses the NF-κB, Bcl-2/Bax ratio via inactivating p-STAT3/p65; enhances the DDP sensitivity	Yu et al. (2018)
Perilla frutescens (L.) Britton; *Eriobotrya japonica* (Thunb.) Lindl.	Oleanolic acid	A549 cells	PINK1/Parkin axis	Decrease p62 and Nrf2 proteins, induces an ROS production; promotes ROS production and mitophagy (p-AKT↓; p-mTOR↓)	Castrejón-Jiménez et al. (2019)
Perilla frutescens (L.) Britton	Rosmarinic acid	A549 cisplatin-resistant cells	MAPK signaling pathway	Inhibits the expression of P-gp and MDR1, enhances p-JNK, p-c-JUN, p21 and p53 expression; DDP resistance reversal agent in NSCLC	Liao et al. (2020)
Eriobotrya japonica (Thunb.) Lindl.; *Ginkgo biloba* L.	EGCG	A549 and H460 platinum-resistant cells	Axl, Tyro3	Suppresses the expression of both Axl and Tyro 3 receptor tyrosine kinases; reduces platinum-resistance	Kim and Lee, (2014)
Ginkgo biloba L.	Ginkgolide B	A549 and H1975 cells	Beclin-1	Reduces Beclin-1, induces inhibition of NLRP3 and autophagy (Bcl-2↓, PCNA↓, p62↑)	Wang et al. (2020c)
Ginkgo biloba L.	Glabridin	A549 cells	FAK/Src complex	Inhibits the FAK/Src complex; suppresses the activation of Akt and RhoA; promotes inhibition of migration, invasion, and angiogenesis	Tsai et al. (2011)
Morus alba L.; *Perilla frutescens* (L.) Britton; *Eriobotrya japonica* (Thunb.) Lindl	Ursolic acid	H1975 cells *in vitro* and *in vivo* models	Wnt/β-catenin signaling pathway	Suppresses CT45A2 gene transcription by inhibiting TCF4 and β-catenin; inhibits proliferation and enhances apoptosis of H1975	Yang et al. (2019)
Ginkgo biloba	Ginkgetin	A549, NCI-H460, and SPC-A-1 cells and A549 xenograft nude mouse model	Nrf2/HO-1 axis	Regulates ferroptosis-mediated disruption of the Nrf2/HO-1 axis (Nrf2↓, HO-1↓, SLC7A11↓, GPX4↓); decreased GSH/GSSG ratio, enhances ROS formation and apoptosis as a cisplatin sensitizing agent	Lou et al. (2021)
Morus alba L., *Datura metel* L., and other 6 herbs	Kaempferol	A549, H460 cells	Nrf2 and miR-340	Suppresses the expression of GST, NQO1 and HO1 through downregulating Nrf2; upregulates miR-340 and PTEN; induces apoptosis and autophagy (cyclinD1↓, Bcl-2↓, Bax↑, Caspase-3↑, Caspase-9↑)	Han et al. (2018), Fouzder et al. (2021)
Morus alba L., *Datura metel* L., and other 6 herbs	Quercetin	Radiation-resistant NSCLC cell lines	MiR-16-5p/WEE1 axis	Increases the expression of miR-16-5p to target WEE1; enhances the radiosensitivity of NSCLC cells	Wang et al. (2020d)
Morus alba L., *Datura metel* L., and other 6 herbs	Quercetin	A549, H441 and H1975 *in vitro* and A549 *in vivo* models	Aurora B	Suppresses CT45A2 gene transcription by inhibiting TCF4 and β-catenin; reduces the growth of lung cancer cells	Xingyu et al. (2016)
Eriobotrya japonica (Thunb.) Lindl.	Hesperidin	A549, NCI-H358, H460 cells	FGF/NF-κB and miR-132/ZEB2 signaling pathway	Suppresses the expression of FGF and NF-κB and enhances apoptosis-related nucleosomal enrichment factor; upregulates miR-132 which inhibits the expression of ZEB2; anti-proliferation, apoptosis; induces cell death (Annexin V, Caspase-3, JC-1)	Birsu Cincin et al. (2015), Tan et al. (2020)
Eriobotrya japonica (Thunb.) Lindl., *Aster tataricus* L.f.	Luteolin	A549, H1975, and H460 cells	miR-34a-5p, Src/FAK	Inhibits cell proliferation and induces apoptosis via miR-34a-5p targeting MDM4; diminishes the p-FAK, p-Src, Rac1, Cdc42, and RhoA	Jiang et al. (2018), Masraksa et al. (2020)

Many studies have demonstrated that bioactive compounds can ameliorate bacterial, virus, and LPS-induced pulmonary infection by targeting the NF-κB, MAPK, Nrf2/HO-1, and NLRP3 pathways, reducing the release of cytokines and chemokines, and suppressing inflammation by pathological reaction, oxidative stress, and ROS production. *Eriobotrya japonica*

FIGURE 2 | Network of bioactive compounds, targets, pathways, and six main respiratory diseases.

(Thunb.) Lindl. and its compounds (EGCG, isorhamnetin, hesperidin, hyperoside, kaempferol, β-sitosterol) may be considered an effective Chinese herbal medicine for the treatment of viral infections. Flavonoids, including apigenin, galangin, isorhamnetin, rutin, moracin M, amygdalin, hesperidin, quercetin, formononetin, luteolin, and liquiritin, exhibit good bioactivity against ALI. As for inflammation, bioactive compounds from *Aster tataricus* L.f. and *Eriobotrya japonica (Thunb.) Lindl.* have potential anti-inflammatory activity, suggesting that apigenin, quercetin, luteolin, and isorhamnetin are effective anti-inflammatory compounds. In the studies of COPD, bioactive compounds have mainly attenuated cigarette smoke-induced emphysema, airway remodeling, and inflammation through the NF-κB, MAPK, and TGF-β/Smad pathways, and resveratrol is one of the important and effective bioactive substances against COPD. Multiple components, including β-sitosterol, ferulic acid, quercetin, hesperidin, EGb761, and resveratrol, are directly or indirectly related to TGF-β/Smad, which is a crucial target for PF. These components can effectively suppress biological process of EMT and ECM. In asthma, rosmarinic acid, tussilagone, formononetin, and galangin targeting the MAPK and NF-κB pathways to reduce OVA-specific IgE, and ameliorate airway hyperplasia and hypertrophy. Importantly, these active components such as organic acids and flavonoids can inhibit the proliferation and migration of lung cancer and increase its sensitivity to radiotherapy and chemotherapy. Hyperoside, resveratrol, glabridin, luteolin, and kaempferol are considered potential candidates for the treatment of lung cancer based on a large number of studies. Collectively, ECCG, kaempferol, isorhamnetin, quercetin, and β-sitosterol are important bioactive compounds for prevention and treatment of ALI, PF, and lung cancer. Taken together, multiple bioactive compounds from the 10 different herbs have potential therapeutic effects against respiratory diseases by regulating various molecular pathways (**Figures 2**, **3**).

However, in the studies of different bioactive compounds on respiratory diseases, three important aspects should be considered. Firstly, only key and common active ingredients in each herb are summarized, which might not be fully representative of the herb. More active components should be further identified to explore their pharmacological effects against respiratory diseases. Secondly, multiple compounds In a herb can target similar or different signaling pathways to play the potential roles in those diseases. The network of various targets of different components might be used to explain the combined effect of the formula. Thirdly, different signaling pathways or pathological procedures in infection, inflammation, COPD, or lung cancer are potential targets for these active ingredients. However, the potential targets and the binding role of these active compounds still remain unclear. It should be a future direction for most researchers to confirm specific targets of those potential drug candidates using multiple modern techniques. Finally, the quantitative analysis for the biological activity, toxicity and selectivity of 31 bioactive compounds should be performed in a kind of respiratory diseases to predict the

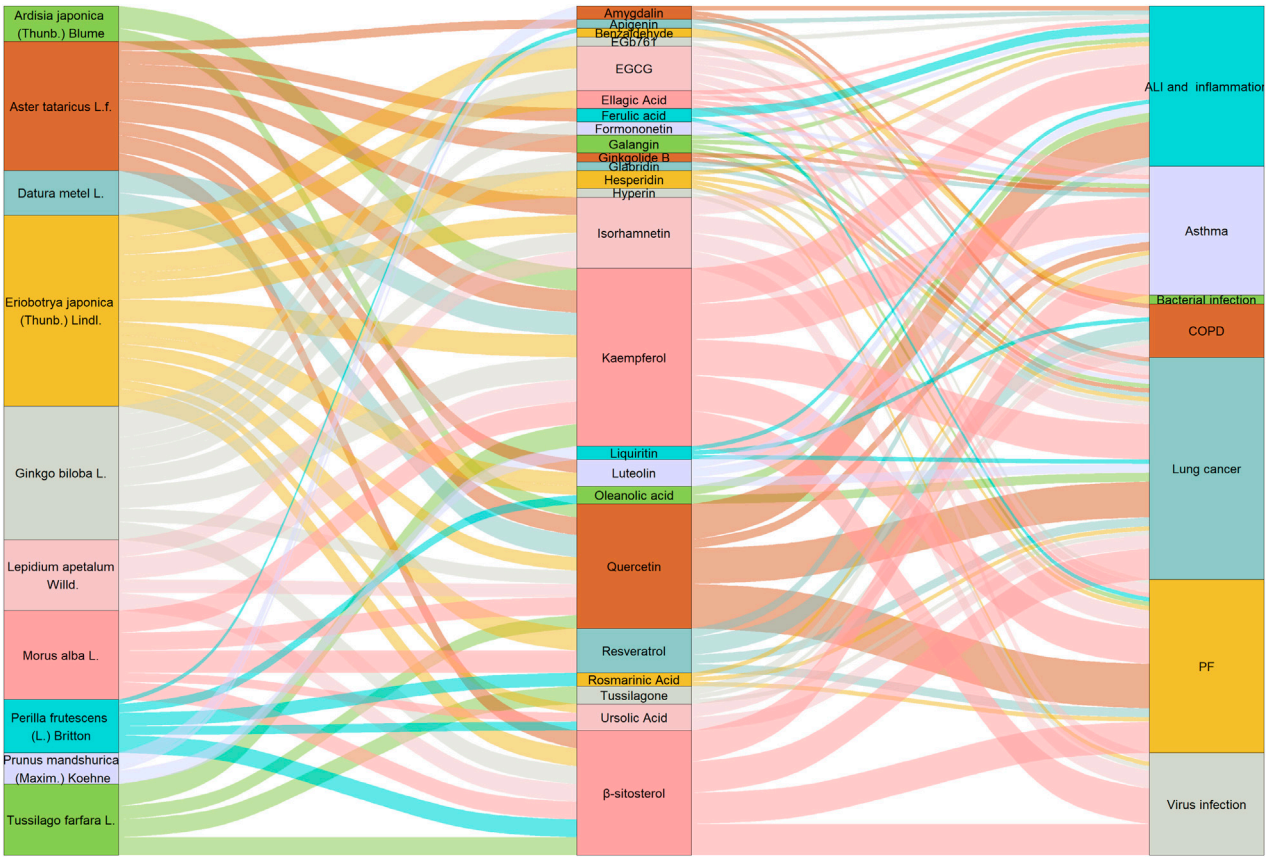

FIGURE 3 | Network of different herbs, main bioactive compounds, and a series of lung-related diseases.

promising candidates for drug development using systematic review and meta-analysis. Overall, this review provides novel perspectives on the preclinical study and clinical application of herbal medicines and their bioactive compounds against respiratory diseases.

CONCLUSION

In summary, 10 Chinese herbal medicines were selected based on the theories of TCM and high-frequency use of Chinese medicines in clinical application. The pharmacological effects and molecular mechanisms of 31 bioactive compounds from these 10 Chinese herbs in infection, ALI, PF, COPD, asthma, and lung cancer were summarized. The bioactive compounds, such as epigallocatechin-3-gallate, kaempferol, isorhamnetin, quercetin, and β-sitosterol, can mainly regulate the NF-κB, Nrf2/HO-1, NLRP3, TGF-β/Smad, MAPK, and PI3K/Akt/mTOR pathways to inhibit infection, inflammation, extracellular matrix deposition, and tumor growth in a series of lung-related diseases. This review provides novel perspectives on the preclinical study and clinical application of Chinese herbal medicines and their bioactive compounds against respiratory diseases.

AUTHOR CONTRIBUTIONS

JW and QW collected, analyzed, and reviewed the literatures and wrote the draft manuscript; JW, QW, LD, SS, and YL added/checked references and assembled figures/tables; LS, TW, and DZ supervised the manuscript; ZW and XL designed and revised the whole manuscript. All authors have read and agreed to the published version of the manuscript.

FUNDING

This study was supported by the Science and Technology Development Plan Project of Jilin Province (20201222235JC, 20200404057YY, 20200901003SF), National Natural Science Foundation of China (81804013), and Science and Technology Project of Education Department of Jilin Province (JJKH20210964KJ).

ACKNOWLEDGMENTS

We thank LetPub (www.letpub.com) for its linguistic assistance during the preparation of this manuscript.

REFERENCES

Afonina, I. S., Zhong, Z., Karin, M., and Beyaert, R. (2017). Limiting Inflammation-The Negative Regulation of NF-Kb and the NLRP3 Inflammasome. *Nat. Immunol.* 18 (8), 861–869. doi:10.1038/ni.3772

Alghetaa, H., Mohammed, A., Sultan, M., Busbee, P., Murphy, A., Chatterjee, S., et al. (2018). Resveratrol Protects Mice against SEB-Induced Acute Lung Injury and Mortality by miR-193a Modulation that Targets TGF-β Signalling. *J. Cel Mol. Med.* 22 (5), 2644–2655. doi:10.1111/jcmm.13542

Ali, S. A., Saifi, M. A., Pulivendala, G., Godugu, C., and Talla, V. (2021). Ferulic Acid Ameliorates the Progression of Pulmonary Fibrosis via Inhibition of TGF-B/smad Signalling. *Food Chem. Toxicol.* 149, 111980. doi:10.1016/j.fct.2021.111980

Alves, Cde. F., Angeli, G. N., Favarin, D. C., de Andrade, E. L., Chica, J. E., Faccioli, L. H., et al. (2013). The Effects of Proresolution of Ellagic Acid in an Experimental Model of Allergic Airway Inflammation. *Mediators Inflamm.* 2013, 863198. doi:10.1155/2013/863198

Azkur, A. K., Akdis, M., Azkur, D., Sokolowska, M., van de Veen, W., Brüggen, M. C., et al. (2020). Immune Response to SARS-CoV-2 and Mechanisms of Immunopathological Changes in COVID-19. *Allergy* 75 (7), 1564–1581. doi:10.1111/all.14364

Berlin, D. A., Gulick, R. M., and Martinez, F. J. (2020). Severe Covid-19. *N. Engl. J. Med.* 383 (25), 2451–2460. doi:10.1056/NEJMcp2009575

Birsu Cincin, Z., Unlu, M., Kiran, B., Sinem Bireller, E., Baran, Y., and Cakmakoglu, B. (2015). Anti-proliferative, Apoptotic and Signal Transduction Effects of Hesperidin in Non-small Cell Lung Cancer Cells. *Cel Oncol (Dordr)* 38 (3), 195–204. doi:10.1007/s13402-015-0222-z

Castrejón-Jiménez, N. S., Leyva-Paredes, K., Baltierra-Uribe, S. L., Castillo-Cruz, J., Campillo-Navarro, M., Hernández-Pérez, A. D., et al. (2019). Ursolic and Oleanolic Acids Induce Mitophagy in A549 Human Lung Cancer Cells. *Molecules* 24 (19). doi:10.3390/molecules24193444

Chang, H. Y., Chen, Y. C., Lin, J. G., Lin, I. H., Huang, H. F., Yeh, C. C., et al. (2018). Asatone Prevents Acute Lung Injury by Reducing Expressions of NF-[Formula: See text]B, MAPK and Inflammatory Cytokines. *Am. J. Chin. Med.* 46 (3), 651–671. doi:10.1142/s0192415x18500349

Chang, J. H., Cheng, C. W., Yang, Y. C., Chen, W. S., Hung, W. Y., Chow, J. M., et al. (2018). Downregulating CD26/DPPIV by Apigenin Modulates the Interplay between Akt and Snail/Slug Signaling to Restrain Metastasis of Lung Cancer with Multiple EGFR Statuses. *J. Exp. Clin. Cancer Res.* 37 (1), 199. doi:10.1186/s13046-018-0869-1

Chang, W. A., Hung, J. Y., Jian, S. F., Lin, Y. S., Wu, C. Y., Hsu, Y. L., et al. (2016). Laricitrin Ameliorates Lung Cancer-Mediated Dendritic Cell Suppression by Inhibiting Signal Transducer and Activator of Transcription 3. *Oncotarget* 7 (51), 85220–85234. doi:10.18632/oncotarget.13240

Chang, W. A., Hung, J. Y., Tsai, Y. M., Hsu, Y. L., Chiang, H. H., Chou, S. H., et al. (2016). Laricitrin Suppresses Increased Benzo(a)pyrene-Induced Lung Tumor-Associated Monocyte-Derived Dendritic Cell Cancer Progression. *Oncol. Lett.* 11 (3), 1783–1790. doi:10.3892/ol.2016.4153

Chen, J., Yang, X., Zhang, W., Peng, D., Xia, Y., Lu, Y., et al. (2016). Therapeutic Effects of Resveratrol in a Mouse Model of LPS and Cigarette Smoke-Induced COPD. *Inflammation* 39 (6), 1949–1959. doi:10.1007/s10753-016-0430-3

Chen, K., and Kolls, J. K. (2013). T Cell-Mediated Host Immune Defenses in the Lung. *Annu. Rev. Immunol.* 31, 605–633. doi:10.1146/annurev-immunol-032712-100019

Chen, X., Wu, Y., Chen, C., Gu, Y., Zhu, C., Wang, S., et al. (2021). Identifying Potential Anti-COVID-19 Pharmacological Components of Traditional Chinese Medicine Lianhuaqingwen Capsule Based on Human Exposure and ACE2 Biochromatography Screening. *Acta Pharm. Sin B* 11 (1), 222–236. doi:10.1016/j.apsb.2020.10.002

Chen, Y., Wei, D., Zhao, J., Xu, X., and Chen, J. (2021). Reduction of Hyperoxic Acute Lung Injury in Mice by Formononetin. *PloS one* 16 (1), e0245050. doi:10.1371/journal.pone.0245050

Chi, G., Zhong, W., Liu, Y., Lu, G., Lü, H., Wang, D., et al. (2016). Isorhamnetin Protects Mice from Lipopolysaccharide-Induced Acute Lung Injury via the Inhibition of Inflammatory Responses. *Inflamm. Res.* 65 (1), 33–41. doi:10.1007/s00011-015-0887-9

Choi, B. S., Kim, Y. J., Yoon, Y. P., Lee, H. J., and Lee, C. J. (2018). Tussilagone Suppressed the Production and Gene Expression of MUC5AC Mucin via Regulating Nuclear Factor-Kappa B Signaling Pathway in Airway Epithelial Cells. *Korean J. Physiol. Pharmacol.* 22 (6), 671–677. doi:10.4196/kjpp.2018.22.6.671

Chu, X., Ci, X., He, J., Wei, M., Yang, X., Cao, Q., et al. (2011). A Novel Anti-inflammatory Role for Ginkgolide B in Asthma via Inhibition of the ERK/MAPK Signaling Pathway. *Molecules* 16 (9), 7634–7648. doi:10.3390/molecules16097634

Cornélio Favarin, D., Martins Teixeira, M., Lemos de Andrade, E., de Freitas Alves, C., Lazo Chica, J. E., Artério Sorgi, C., et al. (2013). Anti-inflammatory Effects of Ellagic Acid on Acute Lung Injury Induced by Acid in Mice. *Mediators Inflamm.* 2013, 164202. doi:10.1155/2013/164202

Culpitt, S. V., Rogers, D. F., Fenwick, P. S., Shah, P., De Matos, C., Russell, R. E., et al. (2003). Inhibition by Red Wine Extract, Resveratrol, of Cytokine Release by Alveolar Macrophages in COPD. *Thorax* 58 (11), 942–946. doi:10.1136/thorax.58.11.942

de Oliveira, M. T. P., de Sá Coutinho, D., Tenório de Souza, É., Stanisçuaski Guterres, S., Pohlmann, A. R., Silva, P. M. R., et al. (2019). Orally Delivered Resveratrol-Loaded Lipid-Core Nanocapsules Ameliorate LPS-Induced Acute Lung Injury via the ERK and PI3K/Akt Pathways. *Int. J. Nanomedicine* 14, 5215–5228. doi:10.2147/ijn.S200666

Ding, S., Wang, H., Wang, M., Bai, L., Yu, P., and Wu, W. (2019). Resveratrol Alleviates Chronic "Real-World" Ambient Particulate Matter-Induced Lung Inflammation and Fibrosis by Inhibiting NLRP3 Inflammasome Activation in Mice. *Ecotoxicol Environ. Saf.* 182, 109425. doi:10.1016/j.ecoenv.2019.109425

Ding, Z., Sun, G., and Zhu, Z. (2018). Hesperidin Attenuates Influenza A Virus (H1N1) Induced Lung Injury in Rats through its Anti-inflammatory Effect. *Antivir. Ther.* 23 (7), 611–615. doi:10.3851/imp3235

Dogan, M. F., Parlar, A., Cam, S. A., Tosun, E. M., Uysal, F., and Arslan, S. O. (2020). Glabridin Attenuates Airway Inflammation and Hyperresponsiveness in a Mice Model of Ovalbumin-Induced Asthma. *Pulm. Pharmacol. Ther.* 63, 101936. doi:10.1016/j.pupt.2020.101936

Donehower, L. A., Soussi, T., Korkut, A., Liu, Y., Schultz, A., Cardenas, M., et al. (2019). Integrated Analysis of TP53 Gene and Pathway Alterations in the Cancer Genome Atlas. *Cell Rep.* 28 (11), 1370–e5. doi:10.1016/j.celrep.2019.08.06110.1016/j.celrep.2019.07.001

Du, Y., Jia, C., Liu, Y., Li, Y., Wang, J., and Sun, K. (2020). Isorhamnetin Enhances the Radiosensitivity of A549 Cells through Interleukin-13 and the NF-Kb Signaling Pathway. *Front. Pharmacol.* 11, 610772. doi:10.3389/fphar.2020.610772

Fan, E., Brodie, D., and Slutsky, A. S. (2018). Acute Respiratory Distress Syndrome: Advances in Diagnosis and Treatment. *Jama* 319 (7), 698–710. doi:10.1001/jama.2017.21907

Fan, E., Dowdy, D. W., Colantuoni, E., Mendez-Tellez, P. A., Sevransky, J. E., Shanholtz, C., et al. (2014). Physical Complications in Acute Lung Injury Survivors: a Two-Year Longitudinal Prospective Study. *Crit. Care Med.* 42 (4), 849–859. doi:10.1097/ccm.0000000000000040

Fan, E. K. Y., and Fan, J. (2018). Regulation of Alveolar Macrophage Death in Acute Lung Inflammation. *Respir. Res.* 19 (1), 50. doi:10.1186/s12931-018-0756-5

Ferkol, T., and Schraufnagel, D. (2014). The Global burden of Respiratory Disease. *Ann. Am. Thorac. Soc.* 11 (3), 404–406. doi:10.1513/AnnalsATS.201311-405PS

Fouzder, C., Mukhuty, A., and Kundu, R. (2021). Kaempferol Inhibits Nrf2 Signalling Pathway via Downregulation of Nrf2 mRNA and Induces Apoptosis in NSCLC Cells. *Arch. Biochem. Biophys.* 697, 108700. doi:10.1016/j.abb.2020.108700

Freund-Michel, V., and Frossard, N. (2008). The Nerve Growth Factor and its Receptors in Airway Inflammatory Diseases. *Pharmacol. Ther.* 117 (1), 52–76. doi:10.1016/j.pharmthera.2007.07.003

Gao, C., Sun, X., Wu, Z., Yuan, H., Han, H., Huang, H., et al. (2020). A Novel Benzofuran Derivative Moracin N Induces Autophagy and Apoptosis through ROS Generation in Lung Cancer. *Front. Pharmacol.* 11, 391. doi:10.3389/fphar.2020.00391

Gaurav, R., and Agrawal, D. K. (2013). Clinical View on the Importance of Dendritic Cells in Asthma. *Expert Rev. Clin. Immunol.* 9 (10), 899–919. doi:10.1586/1744666x.2013.837260

Gerlach, K., Köhler-Bachmann, S., Jungck, D., Körber, S., Yanik, S., Knoop, H., et al. (2015). Endothelin Receptor-Antagonists Suppress Lipopolysaccharide-Induced Cytokine Release from Alveolar Macrophages of Non-smokers, Smokers and COPD Subjects. *Eur. J. Pharmacol.* 768, 123–130. doi:10.1016/j.ejphar.2015.10.040

Global, regional. (2018). Global, Regional, and National Incidence, Prevalence, and Years Lived with Disability for 354 Diseases and Injuries for 195 Countries and Territories, 1990-2017: a Systematic Analysis for the Global Burden of Disease Study 2017. *Lancet* 392 (10159), 1789–1858. doi:10.1016/s0140-6736(18)32279-7

Gong, J. H., Shin, D., Han, S. Y., Kim, J. L., and Kang, Y. H. (2012). Kaempferol Suppresses Eosionphil Infiltration and Airway Inflammation in Airway Epithelial Cells and in Mice with Allergic Asthma. *J. Nutr.* 142 (1), 47–56. doi:10.3945/jn.111.150748

Guan, Y., Li, F. F., Hong, L., Yan, X. F., Tan, G. L., He, J. S., et al. (2012). Protective Effects of Liquiritin Apioside on Cigarette Smoke-Induced Lung Epithelial Cell Injury. *Fundam. Clin. Pharmacol.* 26 (4), 473–483. doi:10.1111/j.1472-8206.2011.00956.x

Han, X., Liu, C. F., Gao, N., Zhao, J., and Xu, J. (2018). Kaempferol Suppresses Proliferation but Increases Apoptosis and Autophagy by Up-Regulating microRNA-340 in Human Lung Cancer Cells. *Biomed. Pharmacother.* 108, 809–816. doi:10.1016/j.biopha.2018.09.087

Henry, L. J. K., Ramar, M. K., Palanisamy, S., Natesan, S., and Kandasamy, R. (2020). Mechanistic Investigation of PPARγ-Facilitated Anti-asthmatic Effects of Galangin (Norizalpinin): Insights from In Silico and In vivo Analyses. *Biochem. Biophys. Res. Commun.* 526 (3), 833–840. doi:10.1016/j.bbrc.2020.03.158

Henss, L., Auste, A., Schürmann, C., Schmidt, C., von Rhein, C., Mühlebach, M. D., et al. (2021). The green tea Catechin Epigallocatechin Gallate Inhibits SARS-CoV-2 Infection. *J. Gen. Virol.* 102 (4). doi:10.1099/jgv.0.001574

Hohmann, M. S., Habiel, D. M., Coelho, A. L., Verri, W. A., Jr., and Hogaboam, C. M. (2019). Quercetin Enhances Ligand-Induced Apoptosis in Senescent Idiopathic Pulmonary Fibrosis Fibroblasts and Reduces Lung Fibrosis *In Vivo*. *Am. J. Respir. Cel Mol. Biol.* 60 (1), 28–40. doi:10.1165/rcmb.2017-0289OC

Huang, C. H., Yang, M. L., Tsai, C. H., Li, Y. C., Lin, Y. J., and Kuan, Y. H. (2013). Ginkgo Biloba Leaves Extract (EGb 761) Attenuates Lipopolysaccharide-Induced Acute Lung Injury via Inhibition of Oxidative Stress and NF-κb-dependent Matrix Metalloproteinase-9 Pathway. *Phytomedicine* 20 (3-4), 303–309. doi:10.1016/j.phymed.2012.11.004

Huang, J., Tong, X., Zhang, L., Zhang, Y., Wang, L., Wang, D., et al. (2020). Hyperoside Attenuates Bleomycin-Induced Pulmonary Fibrosis Development in Mice. *Front. Pharmacol.* 11, 550955. doi:10.3389/fphar.2020.550955

Huang, Y. C., Horng, C. T., Chen, S. T., Lee, S. S., Yang, M. L., Lee, C. Y., et al. (2016). Rutin Improves Endotoxin-Induced Acute Lung Injury via Inhibition of iNOS and VCAM-1 Expression. *Environ. Toxicol.* 31 (2), 185–191. doi:10.1002/tox.22033

Jamal Jameel, K., Gallert, W. J., Yanik, S. D., Panek, S., Kronsbein, J., Jungck, D., et al. (2021). Biomarkers for Comorbidities Modulate the Activity of T-Cells in COPD. *Int. J. Mol. Sci.* 22 (13). doi:10.3390/ijms22137187

Jang, T. Y., Jung, A. Y., Kyung, T. S., Kim, D. Y., Hwang, J. H., and Kim, Y. H. (2017). Anti-allergic Effect of Luteolin in Mice with Allergic Asthma and Rhinitis. *Cent. Eur. J. Immunol.* 42 (1), 24–29. doi:10.5114/ceji.2017.67315

Janku, F., Yap, T. A., and Meric-Bernstam, F. (2018). Targeting the PI3K Pathway in Cancer: Are We Making Headway? *Nat. Rev. Clin. Oncol.* 15 (5), 273–291. doi:10.1038/nrclinonc.2018.28

Jia, W., Wang, C., Wang, Y., Pan, G., Jiang, M., Li, Z., et al. (2015). Qualitative and Quantitative Analysis of the Major Constituents in Chinese Medical Preparation Lianhua-Qingwen Capsule by UPLC-DAD-QTOF-MS. *ScientificWorldJournal* 2015, 731765. doi:10.1155/2015/731765

Jiang, L., Zhang, L., Kang, K., Fei, D., Gong, R., Cao, Y., et al. (2016). Resveratrol Ameliorates LPS-Induced Acute Lung Injury via NLRP3 Inflammasome Modulation. *Biomed. Pharmacother.* 84, 130–138. doi:10.1016/j.biopha.2016.09.020

Jiang, Y., Liu, L. S., Shen, L. P., Han, Z. F., Jian, H., Liu, J. X., et al. (2016). Traditional Chinese Medicine Treatment as Maintenance Therapy in Advanced Non-small-cell Lung Cancer: A Randomized Controlled Trial. *Complement. Ther. Med.* 24, 55–62. doi:10.1016/j.ctim.2015.12.006

Jiang, Z. Q., Li, M. H., Qin, Y. M., Jiang, H. Y., Zhang, X., and Wu, M. H. (2018). Luteolin Inhibits Tumorigenesis and Induces Apoptosis of Non-small Cell Lung Cancer Cells via Regulation of MicroRNA-34a-5p. *Int. J. Mol. Sci.* 19 (2). doi:10.3390/ijms19020447

Jin, C., Ye, K., Luan, H., Liu, L., Zhang, R., Yang, S., et al. (2020). Tussilagone Inhibits Allergic Responses in OVA-Induced Allergic Rhinitis guinea Pigs and IgE-Stimulated RBL-2H3 Cells. *Fitoterapia* 144, 104496. doi:10.1016/j.fitote.2020.104496

Júlio de Souza, A. L., Beatriz Mahler Pereira, A., Robison de Oliveira, J., Santos Ramalho, L., Ismarsi de Souza, H., Lacerda Nascimento, A., et al. (2020). Dermatophagoides Pteronyssinus-Induced Pro-inflammatory Responses Mediated via STAT3 and NF-kappaB Signaling Pathways in Human Bronchial Epithelial Cells - Inhibitory Effects of Lafoensia Pacari and Ellagic Acid. *J. Pharmacol. Sci.* 142 (4), 157–164. doi:10.1016/j.jphs.2020.01.004

Kim, H. H., Bae, Y., and Kim, S. H. (2013). Galangin Attenuates Mast Cell-Mediated Allergic Inflammation. *Food Chem. Toxicol.* 57, 209–216. doi:10.1016/j.fct.2013.03.015

Kim, K. C., and Lee, C. (2014). Reversal of Cisplatin Resistance by Epigallocatechin Gallate Is Mediated by Downregulation of Axl and Tyro 3 Expression in Human Lung Cancer Cells. *Korean J. Physiol. Pharmacol.* 18 (1), 61–66. doi:10.4196/kjpp.2014.18.1.61

Kim, S. H., Park, H. J., Lee, C. M., Choi, I. W., Moon, D. O., Roh, H. J., et al. (2006). Epigallocatechin-3-gallate Protects Toluene Diisocyanate-Induced Airway Inflammation in a Murine Model of Asthma. *FEBS Lett.* 580 (7), 1883–1890. doi:10.1016/j.febslet.2006.02.052

Kitani, A., Fuss, I., Nakamura, K., Kumaki, F., Usui, T., and Strober, W. (2003). Transforming Growth Factor (TGF)-beta1-producing Regulatory T Cells Induce Smad-Mediated Interleukin 10 Secretion that Facilitates Coordinated Immunoregulatory Activity and Amelioration of TGF-Beta1-Mediated Fibrosis. *J. Exp. Med.* 198 (8), 1179–1188. doi:10.1084/jem.20030917

Knobloch, J., Hag, H., Jungck, D., Urban, K., and Koch, A. (2011). Resveratrol Impairs the Release of Steroid-Resistant Cytokines from Bacterial Endotoxin-Exposed Alveolar Macrophages in Chronic Obstructive Pulmonary Disease. *Basic Clin. Pharmacol. Toxicol.* 109 (2), 138–143. doi:10.1111/j.1742-7843.2011.00707.x

Knobloch, J., Jungck, D., Charron, C., Stoelben, E., Ito, K., and Koch, A. (2018). Superior Anti-inflammatory Effects of Narrow-Spectrum Kinase Inhibitors in Airway Smooth Muscle Cells from Subjects with Chronic Obstructive Pulmonary Disease. *J. Allergy Clin. Immunol.* 141 (3), 1122–1124. doi:10.1016/j.jaci.2017.09.026

Knobloch, J., Jungck, D., Kronsbein, J., Stoelben, E., Ito, K., and Koch, A. (2019). LABAs and p38MAPK Inhibitors Reverse the Corticosteroid-Insensitivity of IL-8 in Airway Smooth Muscle Cells of COPD. *J. Clin. Med.* 8 (12). doi:10.3390/jcm8122058

Knobloch, J., Lin, Y., Konradi, J., Jungck, D., Behr, J., Strauch, J., et al. (2013). Inflammatory Responses of Airway Smooth Muscle Cells and Effects of Endothelin Receptor Antagonism. *Am. J. Respir. Cel Mol. Biol.* 49 (1), 114–127. doi:10.1165/rcmb.2012-0287OC

Knobloch, J., Sibbing, B., Jungck, D., Lin, Y., Urban, K., Stoelben, E., et al. (2010). Resveratrol Impairs the Release of Steroid-Resistant Inflammatory Cytokines from Human Airway Smooth Muscle Cells in Chronic Obstructive Pulmonary Disease. *J. Pharmacol. Exp. Ther.* 335 (3), 788–798. doi:10.1124/jpet.110.166843

Knobloch, J., Wahl, C., Feldmann, M., Jungck, D., Strauch, J., Stoelben, E., et al. (2014). Resveratrol Attenuates the Release of Inflammatory Cytokines from Human Bronchial Smooth Muscle Cells Exposed to Lipoteichoic Acid in Chronic Obstructive Pulmonary Disease. *Basic Clin. Pharmacol. Toxicol.* 114 (2), 202–209. doi:10.1111/bcpt.12129

Knobloch, J., Yanik, S. D., Körber, S., Stoelben, E., Jungck, D., and Koch, A. (2016). Tnfα-induced Airway Smooth Muscle Cell Proliferation Depends on Endothelin Receptor Signaling, GM-CSF and IL-6. *Biochem. Pharmacol.* 116, 188–199. doi:10.1016/j.bcp.2016.07.008

Lakshmi, S. P., Reddy, A. T., Kodidhela, L. D., and Varadacharyulu, N. C. (2020). Epigallocatechin Gallate Diminishes Cigarette Smoke-Induced Oxidative Stress, Lipid Peroxidation, and Inflammation in Human Bronchial Epithelial Cells. *Life Sci.* 259, 118260. doi:10.1016/j.lfs.2020.118260

Lee, C. Y., Yang, J. J., Lee, S. S., Chen, C. J., Huang, Y. C., Huang, K. H., et al. (2014). Protective Effect of Ginkgo Biloba Leaves Extract, EGb761, on Endotoxin-Induced Acute Lung Injury via a JNK- and Akt-dependent NFκB Pathway. *J. Agric. Food Chem.* 62 (27), 6337–6344. doi:10.1021/jf501913b

Lee, H. H., Ahn, J. H., Kwon, A. R., Lee, E. S., Kwak, J. H., and Min, Y. H. (2014). Chemical Composition and Antimicrobial Activity of the Essential Oil of Apricot Seed. *Phytother Res.* 28 (12), 1867–1872. doi:10.1002/ptr.5219

Lee, J. H., Ko, H. J., Woo, E. R., Lee, S. K., Moon, B. S., Lee, C. W., et al. (2016). Moracin M Inhibits Airway Inflammation by Interrupting the JNK/c-Jun and

NF-Kb Pathways *In Vitro* and *In Vivo*. *Eur. J. Pharmacol.* 783, 64–72. doi:10.1016/j.ejphar.2016.04.055

Li, C., Chen, J., Yuan, W., Zhang, W., Chen, H., and Tan, H. (2020). Preventive Effect of Ursolic Acid Derivative on Particulate Matter 2.5-induced Chronic Obstructive Pulmonary Disease Involves Suppression of Lung Inflammation. *IUBMB life* 72 (4), 632–640. doi:10.1002/iub.2201

Li, K., Yuan, J., and Su, W. (2006). Determination of Liquiritin, Naringin, Hesperidin, Thymol, Imperatorin, Honokiol, Isoimperatorin, and Magnolol in the Traditional Chinese Medicinal Preparation Huoxiang-Zhengqi Liquid Using High-Performance Liquid Chromatography. *Yakugaku Zasshi* 126 (11), 1185–1190. doi:10.1248/yakushi.126.1185

Li, X., Huang, K., Liu, X., Ruan, H., Ma, L., Liang, J., et al. (2021). Ellagic Acid Attenuates BLM-Induced Pulmonary Fibrosis via Inhibiting Wnt Signaling Pathway. *Front. Pharmacol.* 12, 639574. doi:10.3389/fphar.2021.639574

Li, X., Cao, X., Guo, M., Xie, M., and Liu, X. (2020). Trends and Risk Factors of Mortality and Disability Adjusted Life Years for Chronic Respiratory Diseases from 1990 to 2017: Systematic Analysis for the Global Burden of Disease Study 2017. *BMJ* 368, m234. doi:10.1136/bmj.m234

Li, Y., Chi, G., Shen, B., Tian, Y., and Feng, H. (2016). Isorhamnetin Ameliorates LPS-Induced Inflammatory Response through Downregulation of NF-Kb Signaling. *Inflammation* 39 (4), 1291–1301. doi:10.1007/s10753-016-0361-z

Li, Y., Yang, Y., Liu, X., Long, Y., and Zheng, Y. (2019). PRMT5 Promotes Human Lung Cancer Cell Apoptosis via Akt/Gsk3β Signaling Induced by Resveratrol. *Cel Transpl.* 28 (12), 1664–1673. doi:10.1177/0963689719885083

Liang, Z., Nie, H., Xu, Y., Peng, J., Zeng, Y., Wei, Y., et al. (2016). Therapeutic Effects of Rosmarinic Acid on Airway Responses in a Murine Model of Asthma. *Int. Immunopharmacol* 41, 90–97. doi:10.1016/j.intimp.2016.10.010

Liang, Z., Xu, Y., Wen, X., Nie, H., Hu, T., Yang, X., et al. (2016). Rosmarinic Acid Attenuates Airway Inflammation and Hyperresponsiveness in a Murine Model of Asthma. *Molecules* 21 (6). doi:10.3390/molecules21060769

Liao, X. Z., Gao, Y., Sun, L. L., Liu, J. H., Chen, H. R., Yu, L., et al. (2020). Rosmarinic Acid Reverses Non-small Cell Lung Cancer Cisplatin Resistance by Activating the MAPK Signaling Pathway. *Phytother Res.* 34 (5), 1142–1153. doi:10.1002/ptr.6584

Lin, C. L., Chen, R. F., Chen, J. Y., Chu, Y. C., Wang, H. M., Chou, H. L., et al. (2012). Protective Effect of Caffeic Acid on Paclitaxel Induced Anti-proliferation and Apoptosis of Lung Cancer Cells Involves NF-Kb Pathway. *Int. J. Mol. Sci.* 13 (5), 6236–6245. doi:10.3390/ijms13056236

Lin, L., Hou, G., Han, D., Kang, J., and Wang, Q. (2019). Ursolic Acid Protected Lung of Rats from Damage Induced by Cigarette Smoke Extract. *Front. Pharmacol.* 10, 700. doi:10.3389/fphar.2019.00700

Ling, L. J., Lu, Y., Zhang, Y. Y., Zhu, H. Y., Tu, P., Li, H., et al. (2020). Flavonoids from Houttuynia Cordata Attenuate H1N1-Induced Acute Lung Injury in Mice via Inhibition of Influenza Virus and Toll-like Receptor Signalling. *Phytomedicine* 67, 153150. doi:10.1016/j.phymed.2019.153150

Liu, H., Yu, H., Cao, Z., Gu, J., Pei, L., Jia, M., et al. (2019). Kaempferol Modulates Autophagy and Alleviates Silica-Induced Pulmonary Fibrosis. *DNA Cel Biol.* 38 (12), 1418–1426. doi:10.1089/dna.2019.4941

Liu, P. L., Tsai, J. R., Charles, A. L., Hwang, J. J., Chou, S. H., Ping, Y. H., et al. (2010). Resveratrol Inhibits Human Lung Adenocarcinoma Cell Metastasis by Suppressing Heme Oxygenase 1-mediated Nuclear Factor-kappaB Pathway and Subsequently Downregulating Expression of Matrix Metalloproteinases. *Mol. Nutr. Food Res.* 54 (Suppl. 2), S196–S204. doi:10.1002/mnfr.200900550

Liu, Q., Liang, X., Niu, C., and Wang, X. (2018). Ellagic Acid Promotes A549 Cell Apoptosis via Regulating the Phosphoinositide 3-kinase/protein Kinase B Pathway. *Exp. Ther. Med.* 16 (1), 347–352. doi:10.3892/etm.2018.6193

Liu, X., Zhang, H., Xu, J., Gong, S., Han, Y., Zhang, T., et al. (2019). Identification of Absorbed Components and Their Metabolites in Rat Plasma after Oral Administration of Shufeng Jiedu Capsule Using Ultra-performance Liquid Chromatography/quadrupole Time-Of-Flight Mass Spectrometry. *Rapid Commun. Mass. Spectrom.* 33 (19), 1494–1501. doi:10.1002/rcm.8498

Liu, X. X., Yu, D. D., Chen, M. J., Sun, T., Li, G., Huang, W. J., et al. (2015). Hesperidin Ameliorates Lipopolysaccharide-Induced Acute Lung Injury in Mice by Inhibiting HMGB1 Release. *Int. Immunopharmacol* 25 (2), 370–376. doi:10.1016/j.intimp.2015.02.022

Liu, Y., Li, Z., Xue, X., Wang, Y., Zhang, Y., and Wang, J. (2018). Apigenin Reverses Lung Injury and Immunotoxicity in Paraquat-Treated Mice. *Int. Immunopharmacol* 65, 531–538. doi:10.1016/j.intimp.2018.10.046

Liu, Y. H., Liu, G. H., Mei, J. J., and Wang, J. (2016). The Preventive Effects of Hyperoside on Lung Cancer *In Vitro* by Inducing Apoptosis and Inhibiting Proliferation through Caspase-3 and P53 Signaling Pathway. *Biomed. Pharmacother.* 83, 381–391. doi:10.1016/j.biopha.2016.06.035

Liu, Z., Wang, P., Lu, S., Guo, R., Gao, W., Tong, H., et al. (2020). Liquiritin, a Novel Inhibitor of TRPV1 and TRPA1, Protects against LPS-Induced Acute Lung Injury. *Cell calcium* 88, 102198. doi:10.1016/j.ceca.2020.102198

Lou, J. S., Zhao, L. P., Huang, Z. H., Chen, X. Y., Xu, J. T., Tai, W. C., et al. (2021). Ginkgetin Derived from Ginkgo Biloba Leaves Enhances the Therapeutic Effect of Cisplatin via Ferroptosis-Mediated Disruption of the Nrf2/HO-1 axis in EGFR Wild-type Non-small-cell Lung Cancer. *Phytomedicine* 80, 153370. doi:10.1016/j.phymed.2020.153370

Lü, P. (2016). Inhibitory Effects of Hyperoside on Lung Cancer by Inducing Apoptosis and Suppressing Inflammatory Response via Caspase-3 and NF-Kb Signaling Pathway. *Biomed. Pharmacother.* 82, 216–225. doi:10.1016/j.biopha.2016.05.006

Luan, R. L., Meng, X. X., and Jiang, W. (2016). Protective Effects of Apigenin against Paraquat-Induced Acute Lung Injury in Mice. *Inflammation* 39 (2), 752–758. doi:10.1007/s10753-015-0302-2

Luo, W., Liu, Q., Jiang, N., Li, M., and Shi, L. (2019). Isorhamnetin Inhibited Migration and Invasion via Suppression of Akt/ERK-Mediated Epithelial-To-Mesenchymal Transition (EMT) in A549 Human Non-small-cell Lung Cancer Cells. *Biosci. Rep.* 39 (9). doi:10.1042/bsr20190159

Ma, H., Feng, X., and Ding, S. (2015). Hesperetin Attenuates Ventilator-Induced Acute Lung Injury through Inhibition of NF-Kb-Mediated Inflammation. *Eur. J. Pharmacol.* 769, 333–341. doi:10.1016/j.ejphar.2015.11.038

Ma, Z., Ji, W., Fu, Q., and Ma, S. (2013). Formononetin Inhibited the Inflammation of LPS-Induced Acute Lung Injury in Mice Associated with Induction of PPAR Gamma Expression. *Inflammation* 36 (6), 1560–1566. doi:10.1007/s10753-013-9700-5

Mahajan, S. G., and Mehta, A. A. (2011). Suppression of Ovalbumin-Induced Th2-Driven Airway Inflammation by β-sitosterol in a guinea Pig Model of Asthma. *Eur. J. Pharmacol.* 650 (1), 458–464. doi:10.1016/j.ejphar.2010.09.075

Maiti, S., and Banerjee, A. (2021). Epigallocatechin Gallate and Theaflavin Gallate Interaction in SARS-CoV-2 Spike-Protein central Channel with Reference to the Hydroxychloroquine Interaction: Bioinformatics and Molecular Docking Study. *Drug Dev. Res.* 82 (1), 86–96. doi:10.1002/ddr.21730

Masraksa, W., Tanasawet, S., Hutamekalin, P., Wongtawatchai, T., and Sukketsiri, W. (2020). Luteolin Attenuates Migration and Invasion of Lung Cancer Cells via Suppressing Focal Adhesion Kinase and Non-receptor Tyrosine Kinase Signaling Pathway. *Nutr. Res. Pract.* 14 (2), 127–133. doi:10.4162/nrp.2020.14.2.127

Mishra, V., Banga, J., and Silveyra, P. (2018). Oxidative Stress and Cellular Pathways of Asthma and Inflammation: Therapeutic Strategies and Pharmacological Targets. *Pharmacol. Ther.* 181, 169–182. doi:10.1016/j.pharmthera.2017.08.011

Molitorisova, M., Sutovska, M., Kazimierova, I., Barborikova, J., Joskova, M., Novakova, E., et al. (2021). The Anti-asthmatic Potential of Flavonol Kaempferol in an Experimental Model of Allergic Airway Inflammation. *Eur. J. Pharmacol.* 891, 173698. doi:10.1016/j.ejphar.2020.173698

Mortality, Morbidity, and Hospitalisations Due to Influenza Lower Respiratory Tract Infections, 2017: an Analysis for the Global Burden of Disease Study 2017. *Lancet Respir. Med.* (2019) 7(1):69–89. doi:10.1016/s2213-2600(18)30496-x

Nadeem, A., Al-Harbi, N. O., Ahmad, S. F., Ibrahim, K. E., Siddiqui, N., and Al-Harbi, M. M. (2018). Glucose-6-phosphate Dehydrogenase Inhibition Attenuates Acute Lung Injury through Reduction in NADPH Oxidase-Derived Reactive Oxygen Species. *Clin. Exp. Immunol.* 191 (3), 279–287. doi:10.1111/cei.13097

Navarro, S., Reddy, R., Lee, J., Warburton, D., and Driscoll, B. (2017). Inhaled Resveratrol Treatments Slow Ageing-Related Degenerative Changes in Mouse Lung. *Thorax* 72 (5), 451–459. doi:10.1136/thoraxjnl-2016-208964

Ory, L., Nazih, E. H., Daoud, S., Mocquard, J., Bourjot, M., Margueritte, L., et al. (2019). Targeting Bioactive Compounds in Natural Extracts - Development of a Comprehensive Workflow Combining Chemical and Biological Data. *Anal. Chim. Acta* 1070, 29–42. doi:10.1016/j.aca.2019.04.038

Pan, L., Lu, Y., Li, Z., Tan, Y., Yang, H., Ruan, P., et al. (2020). Ginkgo Biloba Extract EGb761 Attenuates Bleomycin-Induced Experimental Pulmonary Fibrosis in Mice by Regulating the Balance of M1/M2 Macrophages and

Nuclear Factor Kappa B (NF-Kb)-Mediated Cellular Apoptosis. *Med. Sci. Monit.* 26, e922634. doi:10.12659/msm.922634

Park, Y. J., Bang, I. J., Jeong, M. H., Kim, H. R., Lee, D. E., Kwak, J. H., et al. (2019). Effects of β-Sitosterol from Corn Silk on TGF-B1-Induced Epithelial-Mesenchymal Transition in Lung Alveolar Epithelial Cells. *J. Agric. Food Chem.* 67 (35), 9789–9795. doi:10.1021/acs.jafc.9b02730

Peng, X. P., Li, X. H., Li, Y., Huang, X. T., and Luo, Z. Q. (2019). The Protective Effect of Oleanolic Acid on NMDA-Induced MLE-12 Cells Apoptosis and Lung Injury in Mice by Activating SIRT1 and Reducing NF-Kb Acetylation. *Int. Immunopharmacol* 70, 520–529. doi:10.1016/j.intimp.2019.03.018

Petrova, V. N., and Russell, C. A. (2018). The Evolution of Seasonal Influenza Viruses. *Nat. Rev. Microbiol.* 16 (1), 47–60. doi:10.1038/nrmicro.2017.118

Qian, J., Chen, X., Chen, X., Sun, C., Jiang, Y., Qian, Y., et al. (2019). Kaempferol Reduces K63-Linked Polyubiquitination to Inhibit Nuclear Factor-Kb and Inflammatory Responses in Acute Lung Injury in Mice. *Toxicol. Lett.* 306, 53–60. doi:10.1016/j.toxlet.2019.02.005

Qian, L., Xie, B., Wang, Y., and Qian, J. (2015). Amygdalin-mediated Inhibition of Non-small Cell Lung Cancer Cell Invasion *In Vitro*. *Int. J. Clin. Exp. Pathol.* 8 (5), 5363–5370.

Rabe, K. F., and Watz, H. (2017). Chronic Obstructive Pulmonary Disease. *Lancet* 389 (10082), 1931–1940. doi:10.1016/s0140-6736(17)31222-9

Rasheduzzaman, M., Jeong, J. K., and Park, S. Y. (2018). Resveratrol Sensitizes Lung Cancer Cell to TRAIL by P53 Independent and Suppression of Akt/NF-Kb Signaling. *Life Sci.* 208, 208–220. doi:10.1016/j.lfs.2018.07.035

Ray, A., and Kolls, J. K. (2017). Neutrophilic Inflammation in Asthma and Association with Disease Severity. *Trends Immunol.* 38 (12), 942–954. doi:10.1016/j.it.2017.07.003

Ren, J. L., Zhang, A. H., and Wang, X. J. (2020). Traditional Chinese Medicine for COVID-19 Treatment. *Pharmacol. Res.* 155, 104743. doi:10.1016/j.phrs.2020.104743

Ren, X., Han, L., Li, Y., Zhao, H., Zhang, Z., Zhuang, Y., et al. (2021). Isorhamnetin Attenuates TNF -α-induced Inflammation, Proliferation, and Migration in Human Bronchial Epithelial Cells via MAPK and NF-κB Pathways. *Anat. Rec.* 304 (4), 901–913. doi:10.1002/ar.24506

Rogerio, A. P., Kanashiro, A., Fontanari, C., da Silva, E. V., Lucisano-Valim, Y. M., Soares, E. G., et al. (2007). Anti-inflammatory Activity of Quercetin and Isoquercitrin in Experimental Murine Allergic Asthma. *Inflamm. Res.* 56 (10), 402–408. doi:10.1007/s00011-007-7005-6

Ruan, J. S., Zhou, H., Yang, L., Wang, L., Jiang, Z. S., Sun, H., et al. (2019). Ursolic Acid Attenuates TGF-B1-Induced Epithelial-Mesenchymal Transition in NSCLC by Targeting Integrin αVβ5/MMPs Signaling. *Oncol. Res.* 27 (5), 593–600. doi:10.3727/096504017x15051723858706

Rungsung, S., Singh, T. U., Rabha, D. J., Kumar, T., Cholenahalli Lingaraju, M., Parida, S., et al. (2018). Luteolin Attenuates Acute Lung Injury in Experimental Mouse Model of Sepsis. *Cytokine* 110, 333–343. doi:10.1016/j.cyto.2018.03.042

Russo, M., Moccia, S., Spagnuolo, C., Tedesco, I., and Russo, G. L. (2020). Roles of Flavonoids against Coronavirus Infection. *Chem. Biol. Interact* 328, 109211. doi:10.1016/j.cbi.2020.109211

Shahidi, F., and Yeo, J. (2018). Bioactivities of Phenolics by Focusing on Suppression of Chronic Diseases: A Review. *Int. J. Mol. Sci.* 19 (6). doi:10.3390/ijms19061573

Shin, D., Park, S. H., Choi, Y. J., Kim, Y. H., Antika, L. D., Habibah, N. U., et al. (2015). Dietary Compound Kaempferol Inhibits Airway Thickening Induced by Allergic Reaction in a Bovine Serum Albumin-Induced Model of Asthma. *Int. J. Mol. Sci.* 16 (12), 29980–29995. doi:10.3390/ijms161226218

Shu, Y. S., Tao, W., Miao, Q. B., Lu, S. C., and Zhu, Y. B. (2014). Galangin Dampens Mice Lipopolysaccharide-Induced Acute Lung Injury. *Inflammation* 37 (5), 1661–1668. doi:10.1007/s10753-014-9894-1

Siegel, R. L., Miller, K. D., Jemal, A., and Jemal, A. (2021). Cancer Statistics, 2017. *CA Cancer J. Clin.* 67 (1), 7–30. doi:10.3322/caac.2165410.3322/caac.21387

Skoulidis, F., and Heymach, J. V. (2019). Co-occurring Genomic Alterations in Non-small-cell Lung Cancer Biology and Therapy. *Nat. Rev. Cancer* 19 (9), 495–509. doi:10.1038/s41568-019-0179-8

Smith, K. F., Goldberg, M., Rosenthal, S., Carlson, L., Chen, J., Chen, C., et al. (2014). Global Rise in Human Infectious Disease Outbreaks. *J. R. Soc. Interf.* 11 (101), 20140950. doi:10.1098/rsif.2014.0950

Spagnolo, P., Kropski, J. A., Jones, M. G., Lee, J. S., Rossi, G., Karampitsakos, T., et al. (2021). Idiopathic Pulmonary Fibrosis: Disease Mechanisms and Drug Development. *Pharmacol. Ther.* 222, 107798. doi:10.1016/j.pharmthera.202010.1016/j.pharmthera.2020.107798107798

Sriram, N., Kalayarasan, S., and Sudhandiran, G. (2009). Epigallocatechin-3-gallate Exhibits Anti-fibrotic Effect by Attenuating Bleomycin-Induced Glycoconjugates, Lysosomal Hydrolases and Ultrastructural Changes in Rat Model Pulmonary Fibrosis. *Chem. Biol. Interact* 180 (2), 271–280. doi:10.1016/j.cbi.2009.02.017

Stertz, S., Reichelt, M., Spiegel, M., Kuri, T., Martínez-Sobrido, L., García-Sastre, A., et al. (2007). The Intracellular Sites of Early Replication and Budding of SARS-Coronavirus. *Virology* 361 (2), 304–315. doi:10.1016/j.virol.2006.11.027

Stets, R., Popescu, M., Gonong, J. R., Mitha, I., Nseir, W., Madej, A., et al. (2019). Omadacycline for Community-Acquired Bacterial Pneumonia. *N. Engl. J. Med.* 380 (6), 517–527. doi:10.1056/NEJMoa1800201

Sun, K., Huang, R., Yan, L., Li, D. T., Liu, Y. Y., Wei, X. H., et al. (2018). Schisandrin Attenuates Lipopolysaccharide-Induced Lung Injury by Regulating TLR-4 and Akt/FoxO1 Signaling Pathways. *Front. Physiol.* 9, 1104. doi:10.3389/fphys.2018.01104

Sun, L., Yim, W. S., Fahey, P., Wang, S., Zhu, X., Qiao, J., et al. (2019). Investigation on Advanced Non-small-cell Lung Cancer Among Elderly Patients Treated with Chinese Herbal Medicine versus Chemotherapy: A Pooled Analysis of Individual Data. *Evid. Based Complement. Alternat Med.* 2019, 1898345. doi:10.1155/2019/1898345

Sundarraj, S., Thangam, R., Sreevani, V., Kaveri, K., Gunasekaran, P., Achiraman, S., et al. (2012). γ-Sitosterol from Acacia Nilotica L. Induces G2/M Cell Cycle Arrest and Apoptosis through C-Myc Suppression in MCF-7 and A549 Cells. *J. Ethnopharmacol* 141 (3), 803–809. doi:10.1016/j.jep.2012.03.014

Suresh, R., Kupfer, Y., and Tessler, S. (2000). Acute Respiratory Distress Syndrome. *N. Engl. J. Med.* 343 (9), 660–661. doi:10.1056/nejm200008313430914

Takashima, K., Matsushima, M., Hashimoto, K., Nose, H., Sato, M., Hashimoto, N., et al. (2014). Protective Effects of Intratracheally Administered Quercetin on Lipopolysaccharide-Induced Acute Lung Injury. *Respir. Res.* 15 (1), 150. doi:10.1186/s12931-014-0150-x

Tan, S., Dai, L., Tan, P., Liu, W., Mu, Y., Wang, J., et al. (2020). Hesperidin Administration Suppresses the Proliferation of Lung Cancer Cells by Promoting Apoptosis Via targeting the miR-132/ZEB2 S-ignalling P-athway. *Int. J. Mol. Med.* 46 (6), 2069–2077. doi:10.3892/ijmm.2020.4756

Tian, J., Yan, S., Wang, H., Zhang, Y., Zheng, Y., Wu, H., et al. (2020). Hanshiyi Formula, a Medicine for Sars-CoV2 Infection in China, Reduced the Proportion of Mild and Moderate COVID-19 Patients Turning to Severe Status: A Cohort Study. *Pharmacol. Res.* 161, 105127. doi:10.1016/j.phrs.2020.105127

Tsai, Y. F., Chen, C. Y., Chang, W. Y., Syu, Y. T., and Hwang, T. L. (2019). Resveratrol Suppresses Neutrophil Activation via Inhibition of Src Family Kinases to Attenuate Lung Injury. *Free Radic. Biol. Med.* 145, 67–77. doi:10.1016/j.freeradbiomed.2019.09.021

Tsai, Y. M., Yang, C. J., Hsu, Y. L., Wu, L. Y., Tsai, Y. C., Hung, J. Y., et al. (2011). Glabridin Inhibits Migration, Invasion, and Angiogenesis of Human Non-small Cell Lung Cancer A549 Cells by Inhibiting the FAK/rho Signaling Pathway. *Integr. Cancer Ther.* 10 (4), 341–349. doi:10.1177/1534735410384860

Wang, J., He, F., Chen, L., Li, Q., Jin, S., Zheng, H., et al. (2018). Resveratrol Inhibits Pulmonary Fibrosis by Regulating miR-21 through MAPK/AP-1 Pathways. *Biomed. Pharmacother.* 105, 37–44. doi:10.1016/j.biopha.2018.05.104

Wang, J., Liu, Y. T., Xiao, L., Zhu, L., Wang, Q., and Yan, T. (2014). Anti-inflammatory Effects of Apigenin in Lipopolysaccharide-Induced Inflammatory in Acute Lung Injury by Suppressing COX-2 and NF-kB Pathway. *Inflammation* 37 (6), 2085–2090. doi:10.1007/s10753-014-9942-x

Wang, L., Liu, H., He, Q., Gan, C., Li, Y., Zhang, Q., et al. (2020). Galangin Ameliorated Pulmonary Fibrosis *In Vivo* and *In Vitro* by Regulating Epithelial-Mesenchymal Transition. *Bioorg. Med. Chem.* 28 (19), 115663. doi:10.1016/j.bmc.2020.115663

Wang, Q., Chen, Y., Lu, H., Wang, H., Feng, H., Xu, J., et al. (2020). Quercetin Radiosensitizes Non-small Cell Lung Cancer Cells through the Regulation of miR-16-5p/WEE1 axis. *IUBMB life* 72 (5), 1012–1022. doi:10.1002/iub.2242

Wang, S., Wuniqiemu, T., Tang, W., Teng, F., Bian, Q., Yi, L., et al. (2021). Luteolin Inhibits Autophagy in Allergic Asthma by Activating PI3K/Akt/mTOR Signaling and Inhibiting Beclin-1-Pi3kc3 Complex. *Int. Immunopharmacol* 94, 107460. doi:10.1016/j.intimp.2021.107460

Wang, X., Li, M., Hu, M., Wei, P., and Zhu, W. (2017). BAMBI Overexpression Together with β-sitosterol Ameliorates NSCLC via Inhibiting Autophagy and

Inactivating TGF-β/Smad2/3 Pathway. *Oncol. Rep.* 37 (5), 3046–3054. doi:10.3892/or.2017.5508

Wang, X., Liu, M., Zhu, M. J., Shi, L., Liu, L., Zhao, Y. L., et al. (2020). Resveratrol Protects the Integrity of Alveolar Epithelial Barrier via SIRT1/PTEN/p-Akt Pathway in Methamphetamine-Induced Chronic Lung Injury. *Cell Prolif* 53 (3), e12773. doi:10.1111/cpr.12773

Wang, X., Shao, Q. H., Zhou, H., Wu, J. L., Quan, W. Q., Ji, P., et al. (2020). Ginkgolide B Inhibits Lung Cancer Cells Promotion via Beclin-1-dependent Autophagy. *BMC Complement. Med. Ther.* 20 (1), 194. doi:10.1186/s12906-020-02980-x

Wang, X. F., Song, S. D., Li, Y. J., Hu, Z. Q., Zhang, Z. W., Yan, C. G., et al. (2018). Protective Effect of Quercetin in LPS-Induced Murine Acute Lung Injury Mediated by cAMP-Epac Pathway. *Inflammation* 41 (3), 1093–1103. doi:10.1007/s10753-018-0761-3

Wang, X. L., Li, T., Li, J. H., Miao, S. Y., and Xiao, X. Z. (2017). The Effects of Resveratrol on Inflammation and Oxidative Stress in a Rat Model of Chronic Obstructive Pulmonary Disease. *Molecules* 22 (9). doi:10.3390/molecules22091529

Wang, Z., Fang, K., Wang, G., Guan, X., Pang, Z., Guo, Y., et al. (2019). Protective Effect of Amygdalin on Epithelial-Mesenchymal Transformation in Experimental Chronic Obstructive Pulmonary Disease Mice. *Phytother Res.* 33 (3), 808–817. doi:10.1002/ptr.6274

Ward, P. A. (2010). Oxidative Stress: Acute and Progressive Lung Injury. *Ann. N. Y Acad. Sci.* 1203, 53–59. doi:10.1111/j.1749-6632.2010.05552.x

Wollin, L., Distler, J. H. W., Redente, E. F., Riches, D. W. H., Stowasser, S., Schlenker-Herceg, R., et al. (2019). Potential of Nintedanib in Treatment of Progressive Fibrosing Interstitial Lung Diseases. *Eur. Respir. J.* 54 (3). doi:10.1183/13993003.00161-2019

Wu, X., Lin, L., and Wu, H. (2021). Ferulic Acid Alleviates Lipopolysaccharide-induced Acute Lung Injury through Inhibiting TLR4/NF-κB Signaling Pathway. *J. Biochem. Mol. Toxicol.* 35 (3), e22664. doi:10.1002/jbt.22664

Wynn, T. A., and Ramalingam, T. R. (2012). Mechanisms of Fibrosis: Therapeutic Translation for Fibrotic Disease. *Nat. Med.* 18 (7), 1028–1040. doi:10.1038/nm.2807

Xia, L., Shi, Y., Su, J., Friedemann, T., Tao, Z., Lu, Y., et al. (2021). Shufeng Jiedu, a Promising Herbal Therapy for Moderate COVID-19:Antiviral and Anti-inflammatory Properties, Pathways of Bioactive Compounds, and a Clinical Real-World Pragmatic Study. *Phytomedicine* 85, 153390. doi:10.1016/j.phymed.2020.153390

Xiao, M., Tian, J., Zhou, Y., Xu, X., Min, X., Lv, Y., et al. (2020). Efficacy of Huoxiang Zhengqi Dropping Pills and Lianhua Qingwen Granules in Treatment of COVID-19: A Randomized Controlled Trial. *Pharmacol. Res.* 161, 105126. doi:10.1016/j.phrs.2020.105126

Xiao, Y., Zhou, L., Zhang, T., Qin, C., Wei, P., Luo, L., et al. (2020). Anti-fibrosis Activity of Quercetin Attenuates Rabbit Tracheal Stenosis via the TGF-β/AKT/mTOR Signaling Pathway. *Life Sci.* 250, 117552. doi:10.1016/j.lfs.2020.117552

Xie, K., Chai, Y.-s., Lin, S.-h., Xu, F., and Wang, C.-j. (2021). Luteolin Regulates the Differentiation of Regulatory T Cells and Activates IL-10-Dependent Macrophage Polarization against Acute Lung Injury. *J. Immunol. Res.* 2021, 1–12. doi:10.1155/2021/8883962

Xingyu, Z., Peijie, M., Dan, P., Youg, W., Daojun, W., Xinzheng, C., et al. (2016). Quercetin Suppresses Lung Cancer Growth by Targeting Aurora B Kinase. *Cancer Med.* 5 (11), 3156–3165. doi:10.1002/cam4.891

Xu, Z. Y., Jin, C. J., Zhou, C. C., Wang, Z. Q., Zhou, W. D., Deng, H. B., et al. (2011). Treatment of Advanced Non-small-cell Lung Cancer with Chinese Herbal Medicine by Stages Combined with Chemotherapy. *J. Cancer Res. Clin. Oncol.* 137 (7), 1117–1122. doi:10.1007/s00432-011-0975-3

Yang, K., Chen, Y., Zhou, J., Ma, L., Shan, Y., Cheng, X., et al. (2019). Ursolic Acid Promotes Apoptosis and Mediates Transcriptional Suppression of CT45A2 Gene Expression in Non-small-cell Lung Carcinoma Harbouring EGFR T790M Mutations. *Br. J. Pharmacol.* 176 (24), 4609–4624. doi:10.1111/bph.14793

Yang, N., Zhang, H., Cai, X., and Shang, Y. (2018). Epigallocatechin-3-gallate Inhibits Inflammation and Epithelial-mesenchymal T-ransition through the PI3K/AKT P-athway via U-pregulation of PTEN in A-sthma. *Int. J. Mol. Med.* 41 (2), 818–828. doi:10.3892/ijmm.2017.3292

Yang, Y., Zhao, Y., Ai, X., Cheng, B., and Lu, S. (2014). Formononetin Suppresses the Proliferation of Human Non-small Cell Lung Cancer through Induction of Cell Cycle Arrest and Apoptosis. *Int. J. Clin. Exp. Pathol.* 7 (12), 8453–8461.

Yang, Y., Jin, X., Jiao, X., Li, J., Liang, L., Ma, Y., et al. (2020). Advances in Pharmacological Actions and Mechanisms of Flavonoids from Traditional Chinese Medicine in Treating Chronic Obstructive Pulmonary Disease. *Evidence-Based Complement. Altern. Med.* 2020, 1–10. doi:10.1155/2020/8871105

Ye, J., Guan, M., Lu, Y., Zhang, D., Li, C., Li, Y., et al. (2019). Protective Effects of Hesperetin on Lipopolysaccharide-Induced Acute Lung Injury by Targeting MD2. *Eur. J. Pharmacol.* 852, 151–158. doi:10.1016/j.ejphar.2019.02.042

Yeh, C. H., Yang, J. J., Yang, M. L., Li, Y. C., and Kuan, Y. H. (2014). Rutin Decreases Lipopolysaccharide-Induced Acute Lung Injury via Inhibition of Oxidative Stress and the MAPK-NF-Kb Pathway. *Free Radic. Biol. Med.* 69, 249–257. doi:10.1016/j.freeradbiomed.2014.01.028

Yi, L., Cui, J., Wang, W., Tang, W., Teng, F., Zhu, X., et al. (2020). Formononetin Attenuates Airway Inflammation and Oxidative Stress in Murine Allergic Asthmaflammation and Oxidative Stress in Murine Allergic Asthma. *Front. Pharmacol.* 11, 533841. doi:10.3389/fphar.2020.533841

You, H., Wei, L., Sun, W. L., Wang, L., Yang, Z. L., Liu, Y., et al. (2014). The green tea Extract Epigallocatechin-3-Gallate Inhibits Irradiation-Induced Pulmonary Fibrosis in Adult Rats. *Int. J. Mol. Med.* 34 (1), 92–102. doi:10.3892/ijmm.2014.1745

Yu, H., Lin, L., Zhang, Z., Zhang, H., and Hu, H. (2020). Targeting NF-Kb Pathway for the Therapy of Diseases: Mechanism and Clinical Study. *Signal. Transduct Target. Ther.* 5 (1), 209. doi:10.1038/s41392-020-00312-6

Yu, S., Gong, L. S., Li, N. F., Pan, Y. F., and Zhang, L. (2018). Galangin (GG) Combined with Cisplatin (DDP) to Suppress Human Lung Cancer by Inhibition of STAT3-Regulated NF-Kb and Bcl-2/Bax Signaling Pathways. *Biomed. Pharmacother.* 97, 213–224. doi:10.1016/j.biopha.2017.10.059

Yu, X., Gao, F., Li, W., Zhou, L., Liu, W., and Li, M. (2020). Formononetin Inhibits Tumor Growth by Suppression of EGFR-Akt-Mcl-1 axis in Non-small Cell Lung Cancer. *J. Exp. Clin. Cancer Res.* 39 (1), 62. doi:10.1186/s13046-020-01566-2

Yu, Y., Luo, Y., Fang, Z., Teng, W., Yu, Y., Tian, J., et al. (2020). Mechanism of Sanguinarine in Inhibiting Macrophages to Promote Metastasis and Proliferation of Lung Cancer via Modulating the Exosomes in A549 Cells. *Onco Targets Ther.* 13, 8989–9003. doi:10.2147/ott.S261054

Zha, W.-J., Qian, Y., Shen, Y., Du, Q., Chen, F.-F., Wu, Z.-Z., et al. (2013). Galangin Abrogates Ovalbumin-Induced Airway Inflammation via Negative Regulation of NF-Kb. *Evidence-Based Complement. Altern. Med.* 2013, 1–14. doi:10.1155/2013/767689

Zhan, Y., Ta, W., Tang, W., Hua, R., Wang, J., Wang, C., et al. (2021). Potential Antiviral Activity of Isorhamnetin against SARS-CoV -2 Spike Pseudotyped Virus *In Vitro*. *Drug Dev. Res.* doi:10.1002/ddr.21815

Zhang, A., Pan, W., Lv, J., and Wu, H. (2017). Protective Effect of Amygdalin on LPS-Induced Acute Lung Injury by Inhibiting NF-Kb and NLRP3 Signaling Pathways. *Inflammation* 40 (3), 745–751. doi:10.1007/s10753-017-0518-4

Zhang, R., Ai, X., Duan, Y., Xue, M., He, W., Wang, C., et al. (2017). Kaempferol Ameliorates H9N2 Swine Influenza Virus-Induced Acute Lung Injury by Inactivation of TLR4/MyD88-Mediated NF-Kb and MAPK Signaling Pathways. *Biomed. Pharmacother.* 89, 660–672. doi:10.1016/j.biopha.2017.02.081

Zhang, T., Ma, S., Liu, C., Hu, K., Xu, M., and Wang, R. (2020). Rosmarinic Acid Prevents Radiation-Induced Pulmonary Fibrosis through Attenuation of ROS/MYPT1/TGFβ1 Signaling via miR-19b-3p. *Dose Response* 18 (4), 1559325820968413. doi:10.1177/1559325820968413

Zhang, Y., Cardell, L. O., Edvinsson, L., and Xu, C. B. (2013). MAPK/NF-κB-dependent Upregulation of Kinin Receptors Mediates Airway Hyperreactivity: a New Perspective for the Treatment. *Pharmacol. Res.* 71, 9–18. doi:10.1016/j.phrs.2013.02.004

Zhang, Y., Lu, P., Qin, H., Zhang, Y., Sun, X., Song, X., et al. (2021). Traditional Chinese Medicine Combined with Pulmonary Drug Delivery System and Idiopathic Pulmonary Fibrosis: Rationale and Therapeutic Potential. *Biomed. Pharmacother.* 133, 111072. doi:10.1016/j.biopha.2020.111072

Zheng, Q., Tong, M., Ou, B., Liu, C., Hu, C., and Yang, Y. (2019). Isorhamnetin Protects against Bleomycin-Induced Pulmonary Fibrosis by Inhibiting Endoplasmic Reticulum Stress and Epithelial-Mesenchymal Transition. *Int. J. Mol. Med.* 43 (1), 117–126. doi:10.3892/ijmm.2018.3965

Zhou, B. X., Li, J., Liang, X. L., Pan, X. P., Hao, Y. B., Xie, P. F., et al. (2020). β-Sitosterol Ameliorates Influenza A Virus-Induced Proinflammatory

Response and Acute Lung Injury in Mice by Disrupting the Cross-Talk between RIG-I and IFN/STAT Signaling. *Acta Pharmacol. Sin* 41 (9), 1178–1196. doi:10.1038/s41401-020-0403-9

Zhou, E., Fu, Y., Wei, Z., and Yang, Z. (2014). Inhibition of Allergic Airway Inflammation through the Blockage of NF-Kb Activation by Ellagic Acid in an Ovalbumin-Induced Mouse Asthma Model. *Food Funct.* 5 (9), 2106–2112. doi:10.1039/c4fo00384e

Zhou, P., Yang, X. L., Wang, X. G., Hu, B., Zhang, L., Zhang, W., et al. (2020). A Pneumonia Outbreak Associated with a New Coronavirus of Probable Bat Origin. *Nature* 579 (7798), 270–273. doi:10.1038/s41586-020-2012-7

Zhou, Y., and Ho, W. S. (2014). Combination of Liquiritin, Isoliquiritin and Isoliquirigenin Induce Apoptotic Cell Death through Upregulating P53 and P21 in the A549 Non-small Cell Lung Cancer Cells. *Oncol. Rep.* 31 (1), 298–304. doi:10.3892/or.2013.2849

Zhou, Z., Kandhare, A. D., Kandhare, A. A., and Bodhankar, S. L. (2019). Hesperidin Ameliorates Bleomycin-Induced Experimental Pulmonary Fibrosis via Inhibition of TGF-beta1/Smad3/AMPK and IkappaBalpha/NF-kappaB Pathways. *EXCLI J.* 18, 723–745. doi:10.17179/excli2019-1094

Conflict of Interest: The authors declare that the research was conducted in the absence of any commercial or financial relationships that could be construed as a potential conflict of interest.

Publisher's Note: All claims expressed in this article are solely those of the authors and do not necessarily represent those of their affiliated organizations, or those of the publisher, the editors and the reviewers. Any product that may be evaluated in this article, or claim that may be made by its manufacturer, is not guaranteed or endorsed by the publisher.

frontiers in Pharmacology

ORIGINAL RESEARCH
published: 10 September 2021
doi: 10.3389/fphar.2021.720886

Metabolomics Analysis Reveals Interaction of Base-Line Chemotherapy and Shiyiwei Shenqi Tablets in Breast Cancer Treatment

Hong Wan[1†], Xiaojun Xu[2,3†], Xiaowei Yang[2,3†], Angqing Li[3], Xiaopeng Ma[4], Aman Xu[1], Xiao Yuan[1], Wenbin Wang[1], Tao Guo[1], Guangtao Luo[2,3], Xiaobo He[3], Wang Li[5], Zhaorui Wang[2,3], Qiang Sun[6], Jing Pei[2,3], Yongzhen Guo[7]* and Yong Zhu[1]**

[1]Department of General Surgery, The Fourth Affiliated Hospital of Anhui Medical University, Hefei, China, [2]Department of Breast Surgery, The First Affiliated Hospital of Anhui Medical University, Hefei, China, [3]Department of General Surgery, The First Affiliated Hospital of Anhui Medical University, Hefei, China, [4]Department of Thyroid and Breast Surgery, The First Affiliated Hospital of University of Science and Technology of China, Hefei, China, [5]Department of Head and Neck Surgery, The First Affiliated Hospital of University of Science and Technology of China, Hefei, China, [6]Cancer Institute, Xuzhou Medical University, Xuzhou, China, [7]Department of Pathology, The Third Affliated Hospital of Zhengzhou University, Zhengzhou, China

OPEN ACCESS

Edited by:
Wei Song,
Peking Union Medical College Hospital (CAMS), China

Reviewed by:
Xinzhao Wang,
Shandong University, China
Guangguo Tan,
Fourth Military Medical University, China

***Correspondence:**
Yong Zhu
zhuyong0831@163.com
Yongzhen Guo
gyz1988@foxmail.com
Jing Pei
peijing@ahmu.edu.cn

[†]These authors have contributed equally to this work

Specialty section:
This article was submitted to Ethnopharmacology, a section of the journal Frontiers in Pharmacology

Received: *05 June 2021*
Accepted: *24 August 2021*
Published: *10 September 2021*

Citation:
Wan H, Xu X, Yang X, Li A, Ma X, Xu A, Yuan X, Wang W, Guo T, Luo G, He X, Li W, Wang Z, Sun Q, Pei J, Guo Y and Zhu Y (2021) Metabolomics Analysis Reveals Interaction of Base-Line Chemotherapy and Shiyiwei Shenqi Tablets in Breast Cancer Treatment. Front. Pharmacol. 12:720886. doi: 10.3389/fphar.2021.720886

Shiyiwei Shenqi Tablet (SSTs) has been widely used for treatment of different types of cancer including breast cancer. SST has drawn more and more interest due to the low rate of side effects. The aim of this study was to investigate the metabolites in serums of breast cancer patients who received base-line chemotherapy only or combination treatment with SST. An untargeted metabolomics method was developed to investigate the alteration of metabolism in patients' serums using ultra-high-performance liquid chromatography/Q-exactive Orbitrap mass spectrometry. The patients were separated based on the metabolomics data, and further analyses showed that SST treatment can affect the metabolism of glucose, fatty acid, bile acid and amino acid. In particular, SST treatment significantly reduced some short peptides which are potential tumor neoantigens. This study may provide novel insights into the mechanism underlying interaction between SST and base-line chemotherapy in terms of affecting metabolic pathways and thereby changing metabolic products, which might shed new light for clinical medication.

Keywords: shiyiwei shenqi tablets, breast cancer, untargeted metabolomics, amino acid metabolism, side effects

INTRODUCTION

Breast cancer is the leading female cancer (2,261,419 cases worldwide in 2020) and the leading cause of cancer-related deaths around the world (684,996 deaths worldwide in 2020) (DeSantis et al., 2019; Sung et al., 2021). Despite dramatic improvements achieved in breast cancer diagnosis and treatments, the prognosis of breast cancer patients, especially those with metastasis, remains unsatisfactory (Miller et al., 2019). In China, the breast cancer incidence and mortality are rising (Chen et al., 2016). According to the report of Centers for disease Control of China, breast cancer has become the most common cancer type in Chinese women. There were 416,371 new breast cancer cases in 2020 in China, and 117,174 breast cancer-induced death in 2020, which impose a heavy burden on the public health system (Cao et al., 2021). The influence of some recognized risk factors such as alcohol use, tobacco use, hormone levels, and body weight on breast cancer generation, and the roles of metabolism in breast cancer etiology and treatment remain unclear and need further study (Li et al., 2016).

Metabolomics is characterized as a technique that can comprehensively and simultaneously identify small molecule metabolites and quantify their changes under different conditions (Johnson et al., 2016; Cui et al., 2018; Jang et al., 2018; Guo et al., 2019). Metabolomics aims to identify indicators to reflect interactions between biological systems. So, it is an ideal holistic method for investigation of drug-drug interactions to obtain further insights into pharmacodynamic mechanisms (Kalwat and Cobb, 2017). Non-targeted metabolomics provides high-throughput analysis of metabolites in samples, which is very helpful for investigating new drug-drug interactions (Li et al., 2017; Zhang et al., 2020). Several analytical platforms including nuclear magnetic resonance (NMR), high performance liquid chromatography mass spectrometry (HPLC-MS), and gas chromatography mass spectrometry (GC-MS) are used for non-targeted metabolomics analysis (Alonso et al., 2015). MS based metabolomics approaches have been widely applied due to their high throughput and sensitivity, and highly quantitative and reproducible data (Cui et al., 2018). Furthermore, the negative and positive ionization also enhances the examination sensitivity.

Although surgery chemotherapy, radiotherapy, and targeted therapy have been combined and widely utilized for breast cancer treatment, recurrence and metastasis remain leading to a high mortality of advanced breast cancer patients (Harbeck et al., 2019). Furthermore, chemotherapy can lead to substantial side effects as well as drug resistance, resulting in therapeutic failure eventually (Ponde et al., 2019). Therefore, it is urgent to seek novel treatment methods for breast cancer. Traditional Chinese medicine (TCM) has been widely used to treat various types of cancers (Yan et al., 2017; Xiang et al., 2019), particularly, TCM has been applied in almost half patients who have breast cancer in China (Poo et al., 2020; Yang et al., 2021). Notably, the utilization of TCM in Western countries is also rising. Previous studies showed that the extract of *Astragalus* membranaceus can induce apoptosis of several breast cancer cells *via* suppressing PI3K/AKT/mTOR pathway (Zhou et al., 2018; Liu et al., 2019). Scutellaria barbata plus Hedyotis diffusa has shown high efficacy in breast cancer therapy (Fang et al., 2020). These studies indicate the promising prospects of TCM in breast cancer therapy.

TCM has drawn more and more interest due to its high safety and efficacy, low toxicity and side effects, as well as potential synergistic effects when combined with chemotherapy (Xiang et al., 2019). Shiyiwei Shenqi Tablet (SST) is a traditional Chinese decoction that has been utilized for treatment of leucopenia and relief of chemotherapy related symptoms: lassitude, vomiting, weakness, nausea, emaciation, and dizziness. SST consists of 11 Chinese herbs including Panax ginseng C. A. Mey, *Astragalus* abbreviatus Kar. and Kir, Angelica acutiloba (Siebold & Zucc.) Kitag, Gastrodia elata Blume, Rehmannia glutinosa (Gaertn.) DC, Catsia tora Linn, Rhizoma Alismatis, Cuscuta abyssinica A. Rich, Asarum acuminatum (Ashe), E. P. Bicknell, Cornu Cervi, and Lycium chinense Mill) (Dong et al., 2010; Chen et al., 2011; Yang et al., 2017). The mechanisms of pharmacodynamics and drug-drug interaction for SST still remain unclear. Moreover, the influence of compounds on metabolism of each other is very complicated. Therefore, new strategy is needed to investigate the drug-drug interactions in combination treatment with base-line chemotherapy and SST. In this study, we performed non-targeted metabolomics analysis using HPLC-MS to explore the interactions between base-line chemotherapy and SST in breast cancer treatment. Patients with sole base-line chemotherapy treatment or combination treatments were prospectively enrolled, and the changes of metabolites in serum were examined to elucidate the mechanism of interaction between base-line chemotherapy and SST.

MATERIALS AND METHODS

Study Subjects

30 Chinese female patients aged from 30 to 70 years with a definite diagnosis of breast cancer were prospectively enrolled. The clinicopathological characteristics of the patients involved were assessed independently by two senior pathologists. In addition, patients with any prior treatment for breast cancer, preinvasive carcinoma, distant metastasis, other malignancies, active rheumatism, or heart failure were excluded. All the involved patients were informed about the participation benefits and risks, and were provided written informed consent. Studies were approved by the Institutional Review Board of the Fourth Affiliated Hospital of Anhui Medical University, and conducted in compliance with the Declaration of Helsinki principles (PJ-YX2020-011).

Study Design

The 30 patients were randomly divided into two groups: 1) base-line chemotherapy treatment group (n = 15); 2) adjuvant SST treatment group (n = 15). Patients from the adjuvant SST treatment group were given epirubicin combined with cyclophosphamide as the neoadjuvant chemotherapy and SST. Patients from the base-line chemotherapy treatment group received epirubicin combined with cyclophosphamide as neoadjuvant therapy. The dosages of epirubicin and cyclophosphamide were 90 mg/m^2 and 600 mg/m^2 per course, respectively. The dosage of SST was 2 g three times a day. Before treatment and 14 days after treatment, the whole blood samples were clot and centrifuged for 10 min at 1,000×g, and serum was isolated and stored at −80 °C until further use.

Formula of SST

First, Panax ginseng C.A.Mey [Araliaceae; Panax quinquefolius var. ginseng], 67 g *Astragalus* mongholicus Bunge [Fabaceae; Astragalus membranaceus Fisch. ex Bunge], 89 g Angelica sinensis (Oliv.) Diels [Apiaceae; Angelica polymorpha var. sinensis Oliv], 44.5 g Gastrodia elata Blume [Orchidaceae; Gastrodia elata var. gracilis Pamp], 89 g Rehmannia glutinosa (Gaertn.) DC. [Orobanchaceae; Rehmannia Libosch. ex Fisch. and C.A.Mey.], 66.5 g Alisma plantago-aquatica subsp. orientale (Sam.) Sam. [Alismataceae; Alisma plantago-aquatica var. orientale Sam.], 89 g *Senna* tora (L.) Roxb. [Fabaceae; *Cassia* contorta Vogel], 22 g Cornu Cervi Pantotrichum [Cervidae;

antler of *Cervus* nippon Temminck], 66.5 g Cuscuta chinensis Lam. [Convolvulaceae; Pentake chinense (Lam.) Raf.], 2.5 g Asarum sieboldii Miq. [Aristolochiaceae; Asarum sieboldii var. cornutum Y.N.Lee], 66.5 g Lycium barbarum L. [Solanaceae; Lycium barbatum Thunb.]. All of these herbs were grounded into powder. The powder were then boiled at high pressure for 20 h. Further, the residues were filtrated, and the paste was concentrated to a relative density of 1.20–1.25 (55–60°C) at reduced pressure, then spray-dried and crushed into fine powder. Finally, the sucrose were added to the powder to make 1000 g SST.

Untargeted Metabolomics Analysis

Sample preparation: The metabolites in serum were identified using HPLC-MS. For HPLC-MS analysis, 200 μL serum sample was added into a tube with 1,200 μL ice methanol and acetonitrile (50/50, v/v). After a 10-min standing at -20°C, the solution was centrifuged for 10 min at 10000 rpm. Then the supernatant was dried by rotary evaporation, and 50 μL acetonitrile was added for re-dissolving and further analysis by LC-MS.

LC-MS conditions: LC experiment was conducted on a waters e2695 UPLC (waters, the USA). A Fortis C18 column (2.1 × 100 mm, 1.7 μm) was used at 40°C. Water containing acetic acid (99.9/0.1, v/v, solvent A) and acetonitrile (solvent B) were used as mobile phase. A gradient of 0 min, 5% (B); 1 min, 25% (B); 3 min, 45% (B); 6 min, 95% (B); and 12 min, 95% (B) was used in both positive and negative mode. The posting time was set as 2 min. The injection volume and flow rate of the mobile phase were 5 μL and 0.3 ml/min, respectively. Electrospray ionization (ESI) with both negative and positive full scan was used for detection. Solutions were infused at 0.3 ml/min with the following parameters: temperature: 350°C, capillary: 4000 V, and speed of drying gas using nitrogen: 12 L/min. The samples for quality control (QC) were prepared by mixing all the serum samples from patients and injected six times before test for system stability checking and also injected every 10 samples during test.

Data and Statistical Analysis

The untargeted metabolomics was carried out as described previously (Sha et al., 2020). Briefly, deconvolution of LC-MS spectrum, including peak alignment, noise processing and baseline correction was performed using Thermo Data Analysis software. Compound Discoverer TM2.0 was then used for normalization to obtain the matrix. The raw intensities were transformed and normalized. For multiple peaks mapped to the same metabolites, the average intensity values were used. The matrix was then subjected to orthogonal partial least squares discrimination analysis (OPLS-DA) and principal component analysis (PCA) using the R ropls package (version 1.21.0) to obtain the differential metabolites between groups (Thevenot et al., 2015). Metabolites with variable importance in projection (VIP) > 1 were further analyzed by one-way analysis of variance (One-way ANOVA), followed by Benjamini-Hochberg correction and fold change analysis. Metabolites with fold change >2 or <0.5 and FDR <0.05 were considered to have statistically significant difference. Finally, the metabolites were traced to metabolite pathways through the Kyoto encyclopedia of genes and genomes (KEGG) by MetaboAnalyst (https://www.metaboanalyst.ca/MetaboAnalyst/home.xhtml) (Chong et al., 2018). All the statistics were performed using the R software (version 3.4.4).

TABLE 1 | Demographic and baseline disease characteristics of the patients.

Characteristic	SST group (N = 12)	Base line group (N = 14)	*p* Value
Age			ns
<45 yr	5	6	-
≥45 yr	7	8	
ER status			ns
Positive	6	7	-
Negative	6	7	
PR status			ns
Positive	7	8	-
Negative	5	6	
Her-2 status			ns
Positive	4	5	-
Negative	8	9	
Tumor size			ns
≤2 cm	2	3	-
>2 cm	10	11	
Nodal status			ns
Positive	12	13	-
Negative	0	1	
TNM stage			ns
Stage II	8	9	-
Stage III	4	5	

Yr = years; p *value was calculated using Chi-square* test.

RESULTS

Identification of Key Compounds in SST

Serum samples from 30 breast cancer patients were used for untargeted metabolomics analysis. Among them, sample 1 and 3 from base-line chemotherapy and adjuvant SST treatment groups failed in untargeted metabolomics analysis due to their relatively low data quality. Baseline characteristics are presented in **Table 1**. The clinical characteristics including age, tumor TNM stage, tumor size, and PR, ER, HER2 and lymph node metastasis status showed no significant differences between the two groups to ensure the accuracy of this study. We used magnetic resonance imaging (MRI) to evaluate the efficacy of the two groups, and the results showed the SST group exhibited a better efficacy on breast cancer after a 14-day treatment (**Supplementary Figure S1**).

SST is mainly composed of eleven traditional Chinese medicine ingredients. Through our detection, we have found six key components including ginsenoside, artemisia iactone, astragaloside, gastrodin, emodin, and quercetin in SQEI by LC-HRMS (**Figure 1**). Therefore, we considered these six compounds as the main pharmaceutical components.

Untargeted Metabolomics Analysis of Serum Samples After Base Line Treatment

To confirm the stability of our HPLC-MS system, we performed PCA on the untargeted metabolomics data based on both

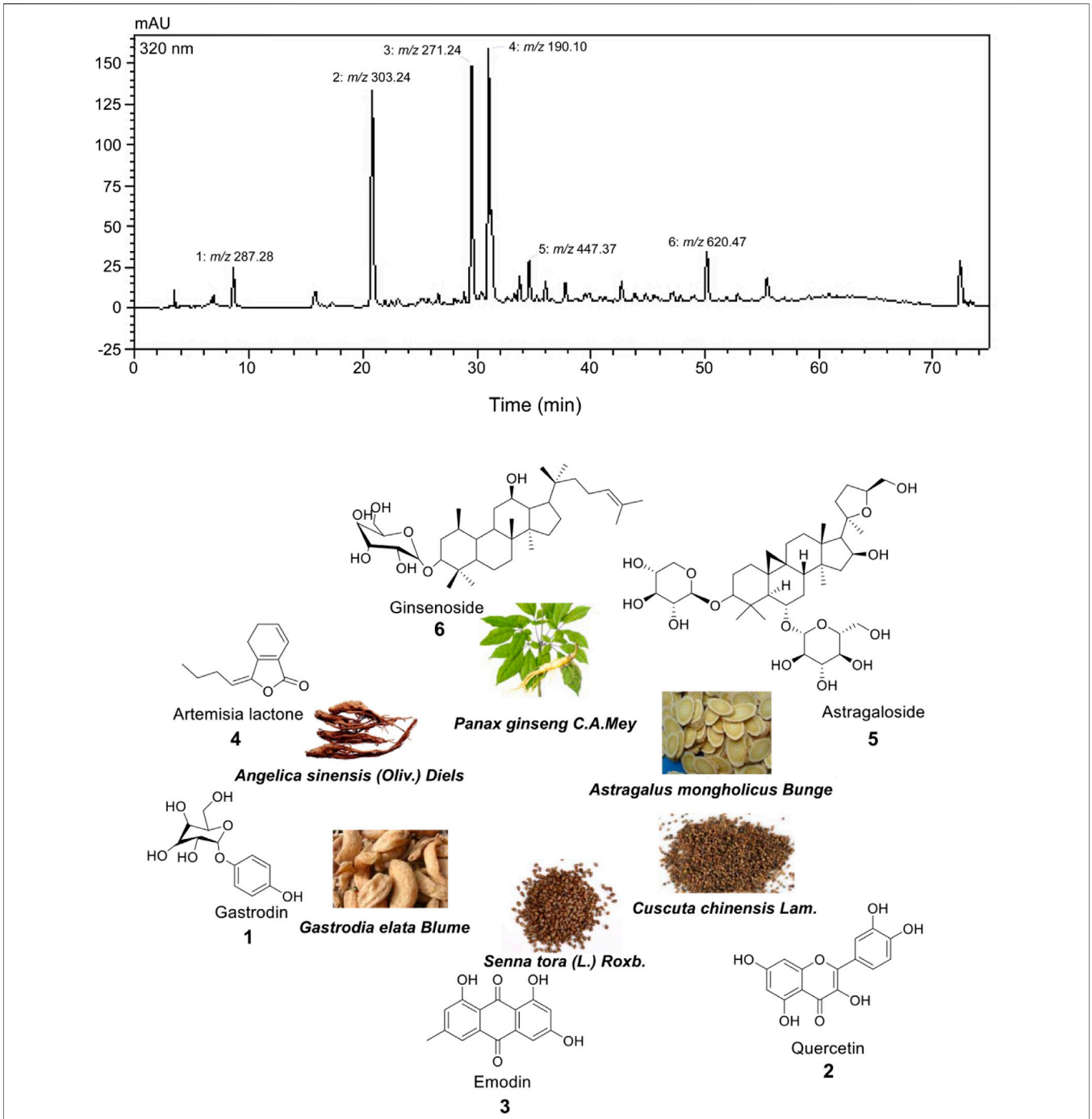

FIGURE 1 | Structures of compounds identified from Shiyiwei Shenqi Tablets.

positive and negative ion models. The results showed that the QC samples could be discriminated from the real samples in both positive and negative ion models. Furthermore, the QC samples tended to be clustered, which demonstrated the stability of our HPLC-MS system (**Supplementary Figure S2A**). We also calculated the relative standard deviation (RSD) of each metabolite identified. The results showed that the RSD values of different peaks of QC samples were small, further confirming the stability of our HPLC-MS system (**Supplementary Figure S2B**).

We also performed untargeted metabolomics analysis using an HPLC-QE-Orbitrap-MS platform for 14 serum samples from breast cancer patients who received base line chemotherapy before surgery. Serum samples from patients before and after base line chemotherapy treatment were subjected to metabolomics analysis using an optimized HPLC-QE-

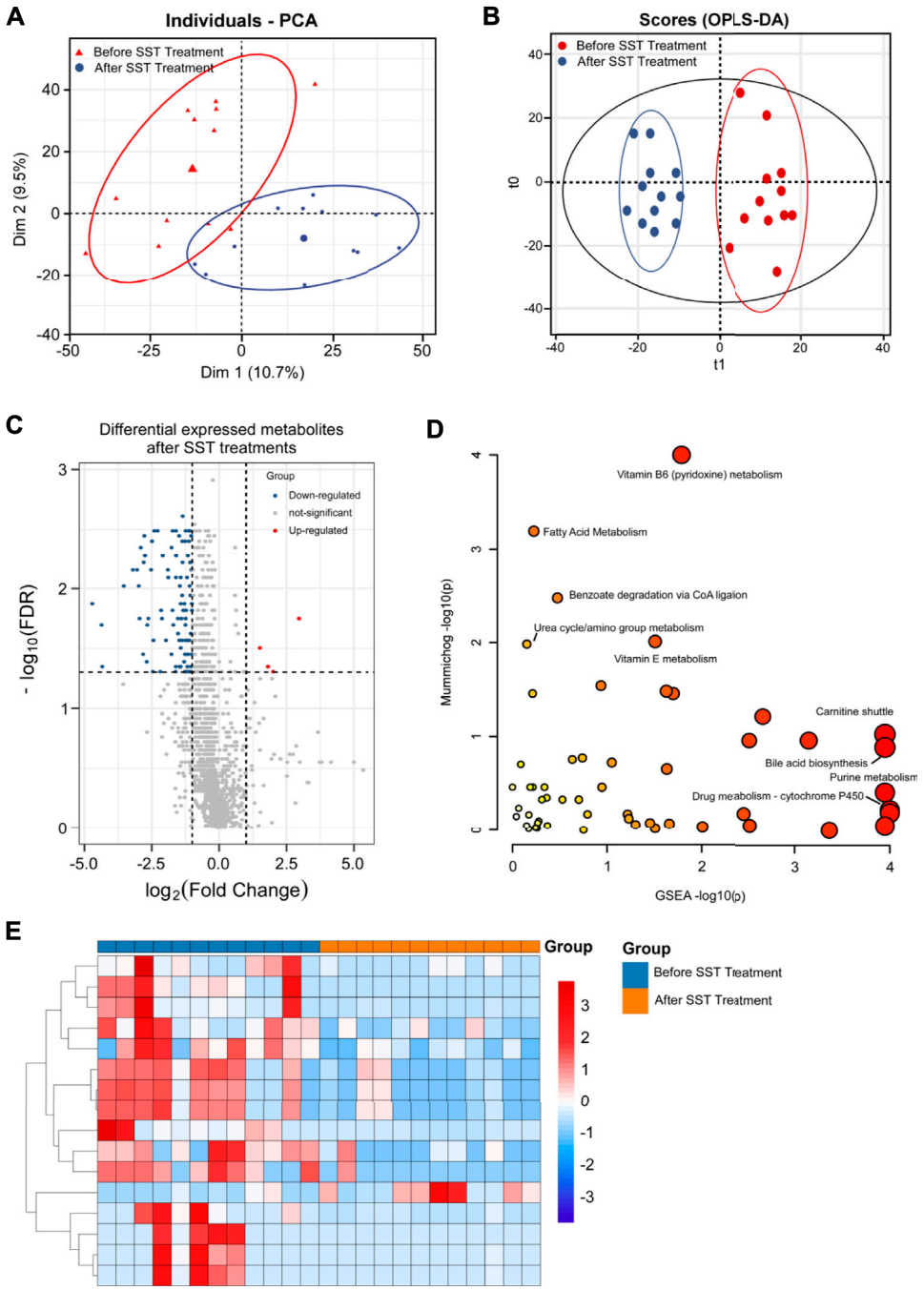

FIGURE 2 | Metabolomics analysis of breast cancer patients' serums after base-line chemotherapy. **(A, B)** PCA **(A)** and OPLS-DA **(B)** plots of the metabolites detected in serums of breast cancer patients before and after base-line chemotherapy (n = 14). **(C)** Volcano plot showing the DEMs identified in serums of breast cancer patients after base-line chemotherapy. **(D)** The bubble plot showing the enriched pathways of DEMs identified in serums of breast cancer patients after base-line chemotherapy. **(E)** The heatmap illustrating the levels of DEMs identified in serums of breast cancer patients after base-line chemotherapy; each row represents one metabolite, and each column represents one sample.

Orbitrap-MS method. The raw MS data of both negative and positive modes were imported into Thermo Data Analysis software for peak detection, correspondence, normalization and alignment. A data matrix was then subjected OPLS-DA and PCA using R ropls package. The PCA score plot (**Figure 2A**) showed that serum samples after base line chemotherapy could be discriminated from those before base line chemotherapy (R2X = 0.526). Further OPLS-DA confirmed that serum samples after base line chemotherapy were clearly distinguished from those before base line chemotherapy

TABLE 2 | The representative differential metabolites identified in serum samples after base-line treatment.

Compound	m/z	R_t	Molecular formula	VIP	FC	FDR	Change	Metabolic pathway
1-(4Z,7Z,10Z,13Z,16Z,19Z-docosahexaenoyl)-sn-glycero-3-phosphocholine	567.3312	5.744	$C_{30}H_{50}NO_7P$	2.023	0.252	0.0014	Down	Phospholipid metabolism
1-[(11Z,14Z)]-icosadienoyl-sn-glycero-3-phosphocholine	547.3628	6.401	$C_{28}H_{54}NO_7P$	2.006	0.426	0.0022	Down	Phospholipid metabolism
1-[(8Z,11Z,14Z)-icosatrienoyl]-sn-glycero-3-phosphocholine	545.3476	6.131	$C_{28}H_{52}NO_7P$	1.110	0.470	0.0468	Down	Phospholipid metabolism
1-[(9Z)-hexadecenoyl]-sn-glycero-3-phosphocholine	493.3160	5.68	$C_{24}H_{48}NO_7P$	1.596	0.430	0.0261	Down	Phospholipid metabolism
Ala-Pro	186.1001	0.688	$C_8H_{14}N_2O_3$	1.232	4.006	0.0152	Up	Amino acid metabolism
Gly-Pro	172.0848	0.79	$C_7H_{12}N_2O_3$	1.375	2.656	0.0152	Up	Amino acid metabolism
H-Gly-Pro-Pro-OH	269.1370	0.877	$C_{12}H_{19}N_3O_4$	1.208	3.268	0.0261	Up	Amino acid metabolism
leu-leu-leu-leu	470.3460	2.624	$C_{24}H_{46}N_4O_5$	1.792	0.276	0.0019	Down	Amino acid metabolism
Linoleamide	279.2556	6.829	$C_{18}H_{33}NO$	1.339	0.382	0.0082	Down	Fatty acid metabolism
Methyl L-leucyl-L-leucinate	258.1939	2.429	$C_{13}H_{26}N_2O_3$	1.785	0.217	0.0026	Down	Amino acid metabolism
N5-Ethyl-L-glutamine	174.1004	1.706	$C_7H_{14}N_2O_3$	1.547	2.301	0.0082	Up	Amino acid metabolism
N-Acetyl-D-alloisoleucine	173.1044	2.816	$C_8H_{15}NO_3$	1.759	2.403	0.0026	Up	Amino acid metabolism
N-Acetyl-DL-norvaline	159.0886	2.227	$C_7H_{13}NO_3$	1.834	2.234	0.0011	Up	Amino acid metabolism
PC	757.5612	13.71	$C_{42}H_{80}NO_8P$	1.987	0.406	0.0064	Down	Phospholipid metabolism
Val-Arg	273.1799	2.594	$C_{11}H_{23}N5O_3$	1.041	2.604	0.0173	Up	Amino acid metabolism
[FAtrihydroxy(18:0)]9_10_13-trihydroxy-11-octadecenoicacid	330.2402	4.596	$C_{18}H_{34}O_5$	1.639	0.356	0.0046	Down	Fatty acid metabolism
[FA(18:4)]6Z_9Z_12Z_15Z-octadecatetraenoicacid	276.2083	5.782	$C1_8H_{28}O_2$	1.813	0.433	0.0040	Down	Fatty acid metabolism
[FAhydroxy(20:4)]5S-hydroxy-12-keto-6Z_8E_10E_14Z-eicosatetraenoicacid	334.2132	7.307	$C_{20}H_{30}O_4$	1.942	0.172	0.0011	Down	Fatty acid metabolism
(Dichloromethyl)phosphonate	161.9056	0.656	$CHCl_2O_3P$	1.642	0.203	0.0298	Down	Phospholipid metabolism
Val-Leu-Gly-Lys	415.2773	2.575	$C_{19}H_{37}N5O_5$	1.171	2.502	0.0229	Up	Amino acid metabolism

(**Figure 2B**), and the Q2Y and R2Y values were 0.883 and 0.984, respectively.

VIP, which is frequently used in metabolomic analysis, was employed to identify the differentially expressed metabolites (DEMs) after treatments. High-resolution MS peaks were annotated to known metabolites by Thermo Data Analysis software according to the database including HMDB, KEGG, and in-house reference metabolites. The VIP score and fold change for each metabolite before and after treatments were then calculated. In total, 186 metabolites including 41 up-regulated and 145 down-regulated metabolites showed significant changes after treatments (**Figure 2C and 2E**, FDR <0.05 and fold change >2 or <0.5 and VIP >1) (the complete DEMs list is shown in **Supplementary Table S1**). The DEMs included amino acid, fatty acids and phospholipids, such as 1-[(9Z)-hexadecenoyl]-sn-glycero-3 -phosphocholine, [FA (18:4)] 6Z_9Z_12Z_15Z-octadecatetraenoic acid, Ala-Pro, and Gly-Pro (**Table 2**).

The changes of metabolic pathways were analyzed using MetaboAnalyst webtool, and the results showed that the potential metabolic pathways related to base line chemotherapy were those involved in metabolism of amino acids, fatty acids, and vitamins. In particular, pathways involved in metabolism of glycosphingolipid, linoleate, and leukotriene, and carnitine shuttle were considered the most probably involved metabolic pathways after base line chemotherapy (**Figure 2D** and **Supplementary Table S2**).

Untargeted Metabolomics Analysis of Patient Serums After SST Treatment

Untargeted metabolomics analysis of patient serum samples was conducted using HPLC-QE-Orbitrap-MS platform. After peak detection, alignment, correspondence, and normalization, the PCA score plot showed that the serum samples after SST treatment could be distinguished from those before SST treatment (**Figure 3A**, R^2X = 0.540). Further OPLS-DA confirmed that serum samples after SST treatment were clearly discriminated from those before SST treatment, and the R^2Y and Q^2Y values were 0.921 and 0.583, respectively (**Figure 3B**).

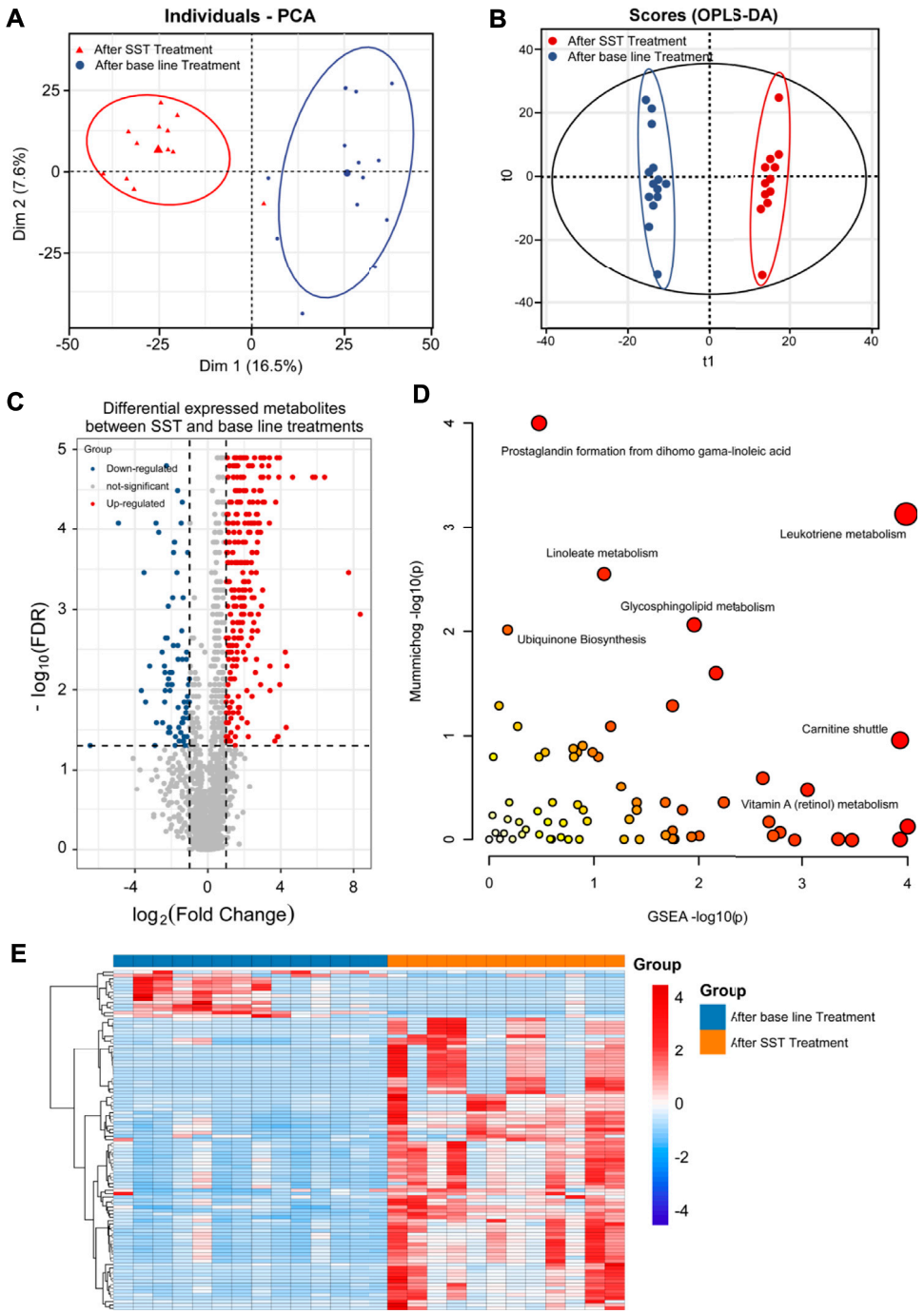

FIGURE 3 | Metabolomics analysis of breast cancer patients' serums after SST treatment. **(A, B)** PCA **(A)** and OPLS-DA **(B)** plots of the metabolites detected in serums of breast cancer patients before and after SST treatment (n = 12). **(C)** Volcano plot showing the DEMs identified in serums of breast cancer patients after SST treatment. **(D)** The bubble plot showing the enriched pathways of DEMs identified in serums of breast cancer patients after SST treatment. **(E)** The heatmap illustrating the levels of DEMs identified in serums of breast cancer patients after SST treatment; each row represents one metabolite, and each column represents one sample.

To identify the DEMs after SST treatment, the high-resolution MS peaks of the LC-MS chromatograms were annotated to known candidates by Thermo Data Analysis software according to the database including HMDB, KEGG, and in-house reference metabolites. The VIP score for each metabolite was then calculated by combing the peaks mapped to one metabolite. Totally 76 down-regulated and 3 up-regulated metabolites exhibited significant changes after SST treatment (**Figure 3C and 3E**, FDR <0.05 and fold change >2 or <0.5 and VIP >1) (the complete DEMs list is shown in **Supplementary**

TABLE 3 | The representative differential metabolites identified in serum samples after SST treatment.

Compound	m/z	R_t	Molecular formula	VIP	FC	FDR	Change	Metabolic pathway
His-Trp	341.1479	1.815	$C_{17}H_{19}N_5O_3$	1.594	7.792	0.018	Up	Amino acid metabolism
Cystathionine	222.0672	2.883	$C_7H_{14}N_2O_4S$	2.110	0.109	0.007	Down	Amino acid metabolism
Adenosine	267.0962	0.872	$C_{10}H_{13}N_5O_4$	1.695	0.141	0.035	Down	Nucleotide metabolism
Histidinate	154.0620	2.086	$C_6H_8N_3O_2$	1.411	0.205	0.003	Down	Amino acid metabolism
Arg-Phr	321.1790	1.025	$C_{15}H_{23}N_5O_3$	1.560	0.427	0.015	Down	Amino acid metabolism
Deoxycholic Acid	392.2926	6.832	$C_{24}H_{40}O_4$	1.818	0.496	0.015	Down	Bile acid metabolism
L-Phe-L-Phe	312.1470	3.003	$C_{18}H_{20}N_2O_3$	1.581	4.004	0.049	Up	Amino acid metabolism
D-Ala-D-Ala	160.0847	1.956	$C_6H_{12}N_2O_3$	1.502	0.495	0.013	Down	Amino acid metabolism
Adenine	135.0546	2.029	$C_5H_5N_5$	2.142	0.488	0.004	Down	Nucleotide metabolism
DL-α-Aminocaprylic acid	159.1259	2.720	$C_8H_{17}NO_2$	1.365	0.396	0.015	Down	Amino acid metabolism

Table S3). Interestingly, two dipeptides His-Trp and L-Phe-L-Phe were significantly up-regulated in serum after SST treatment (**Table 2**). In contrast, several metabolites involved in metabolism of nucleotides such as adenine and adenosine were dramatically down-regulated after SST treatment (**Table 3**).

We further analyzed the alterations of metabolic pathways after SST treatment using the MetaboAnalyst web tool. As shown in **Figure 3D** and **Supplementary Table S4**, the changes of metabolic pathways were mainly involved in metabolism of Vitamin B6 (pyridoxine), Vitamin E, and purine, carnitine shuttle, biosynthesis of bile acid, and regulation of drug metabolism-cytochrome P450. The scatter plot displayed the most possible metabolic pathways *via* circle size. Therefore, the metabolism of Vitamin B6 and purine, and carnitine shuttle were considered to have most altered metabolic pathways after SST treatment.

Untargeted Metabolomics Analysis of Patient Serum Between SST Treatment and Base Line Chemotherapy

Since dramatic metabolic changes happened after SST treatment and base line chemotherapy, we next analyzed and compared these metabolic alterations between patients who received SST treatment or only base line chemotherapy. The PCA score plot clearly separated patients receiving SST treatment from those receiving base line chemotherapy based on the serum metabolomics data (**Figure 4A**, $R^2X = 0.522$). The OPLS-DA results further demonstrated that serum samples after SST treatment were clearly discriminated from those after base line chemotherapy, the R^2Y and Q^2Y values were 0.898 and 0.655, respectively (**Figure 4B**).

DEMs were also identified by the VIP score of each metabolite. A total of 287 metabolites including 50 down-regulated and 237 up-regulated metabolites exhibited significant changes in serum between SST and base line chemotherapy treatments (**Figure 4C and 4E**, FDR <0.05 and fold change >2 or <0.5 and VIP >1) (the complete DEMs list is shown in **Supplementary Table S5**). In particular, metabolites such as phospholipids, amino acids, and fatty acids showed significant changes between SST and base line chemotherapy treatments (**Table 4**). The metabolic pathway changes between SST and base line chemotherapy treatments were further analyzed using the MetaboAnalyst web tool. As shown in **Figure 4D** and **Supplementary Table S6**, metabolic pathways involved in carnitine shuttle, saturated fatty acids beta-oxidation, parathio degradation, bile acid biosynthesis, and leukotriene metabolism were considered the most altered metabolic pathways between SST and base line chemotherapy treatments.

Amino Acid Metabolism Was Identified as an Important Pathway After SST Treatment by Untargeted Metabolomics Analysis

Amino acid metabolism enhances tumor cell proliferation survival by supporting building block synthesis, producing immunosuppressive metabolites for immune escape, and reducing the production of agents mitigating oxidative stress (Pavlova and Thompson, 2016; Tabe et al., 2019). At the same time, numerous short peptides are generated during cancer initiation and progression. Untargeted metabolomics analysis results revealed that many short peptides such as val-pro-gly-val-gly, tyr-lys-pro-asn, and D-Ala-D-Ala were dramatically reduced after SST treatment, while these metabolites remained unchanged after base line chemotherapy (**Figure 5A**). In addition, some amino acids including N-Acetyl-L-Carnosine and arginine were also significantly reduced after SST treatment (**Figure 5A**). Intriguingly, the dipeptide his-trp was significantly increased after SST treatment, indicating SST treatment might induce the expression of some protective peptides (**Figure 5A**). Furthermore, some nucleotides such as adenine and adenosine were dramatically decreased after SST treatment compared with those after base line chemotherapy. These results showed that SST may exert its effect in breast cancer treatment through modulating amino acid metabolism.

Glycometabolism Pathways Were Demonstrated as Co-regulatory Pathways in Both SST and Base Line Chemotherapy Treatments by Untargeted Metabolomics Analysis

Glycometabolism pathways including the tricarboxylic acid (TCA) cycle and glycolysis are reported to play important

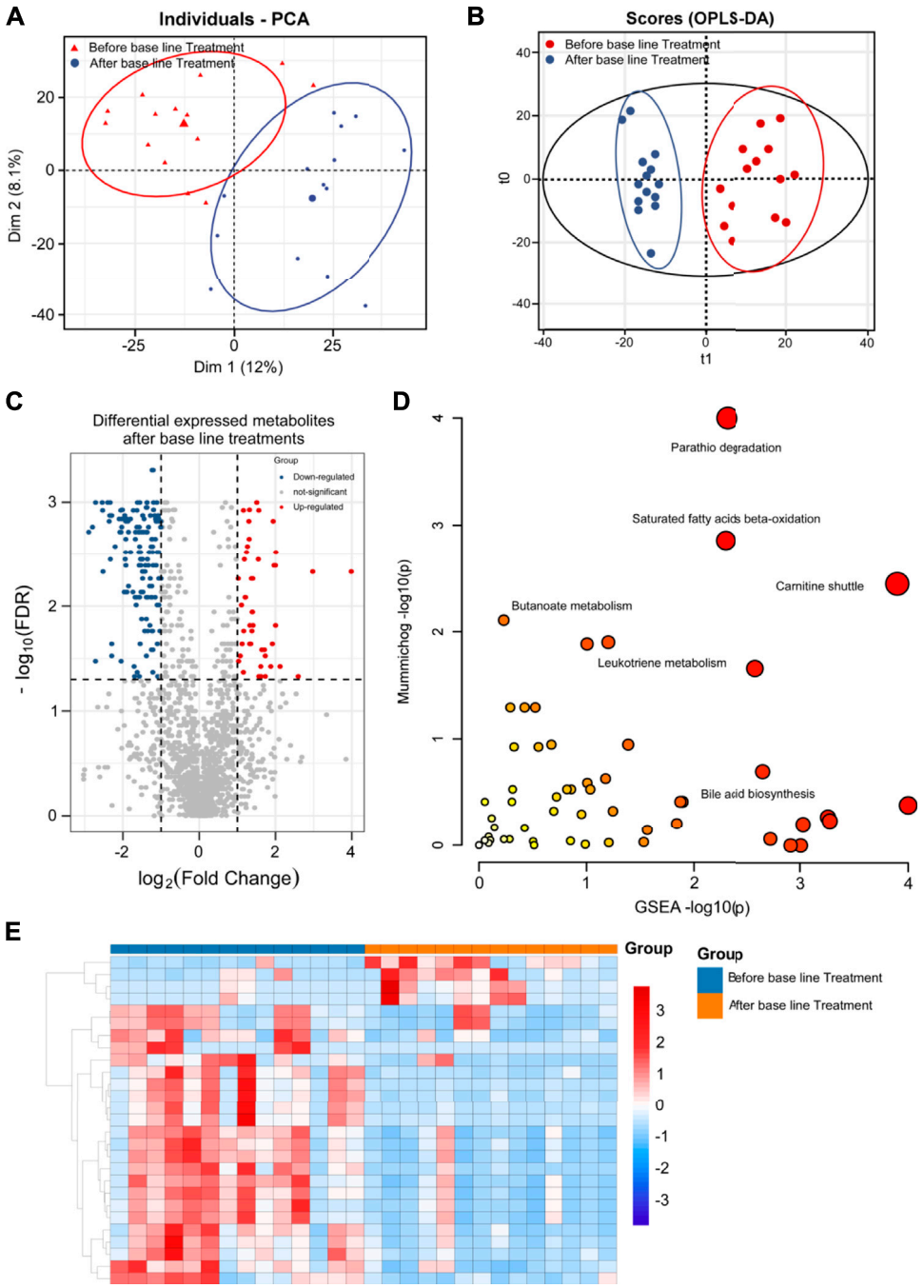

FIGURE 4 | Metabolomics analysis of breast cancer patients' serums between base-line chemotherapy and SST treatments. **(A, B)** PCA **(A)** and OPLS-DA **(B)** plots of the metabolites detected in serums of breast cancer patients between base-line chemotherapy and SST treatments (n = 12 for SST group, n = 14 for base-line chemotherapy group). **(C)** Volcano plot showing the DEMs identified in serums of breast cancer patients between base-line chemotherapy and SST treatments. **(D)** The bubble plot showing the enriched pathways of DEMs identified in serums of breast cancer patients between base-line chemotherapy and SST treatments. **(E)** The heatmap illustrating the levels of DEMs identified in serums of breast cancer patients between base-line chemotherapy and SST treatments; each row represents one metabolite, and each column represents one sample.

roles including promoting proliferation, growth, and long-term maintenance in carcinogenesis. (Pavlova and Thompson, 2016; Martinez-Outschoorn et al., 2017). The common characteristics of cancer cells known as Warburg Effect include enhancing uptake of glucose and glucose fermentation to lactate. Normal cells mainly produce energy through glycolysis, followed by TCA cycle and oxidative phosphorylation (Vander Heiden et al., 2009). However, cancer cells principally produce their energy through

TABLE 4 | The representative differential metabolites identified in serum samples between SST treatment and base-line treatment.

Compound	m/z	R_t	Molecular formula	VIP	FC	FDR	Change	Metabolic pathway
leu-leu-leu-leu	470.346	2.624	$C_{24}H_{46}N_5$	1.912	7.464	0.0001	Up	Amino acid metabolism
LysoPC(20:5(5Z,8Z,11Z,14Z,17Z))	541.3163	5.445	$C_{28}H_{48}N_7P$	1.559	5.797	0.0007	Up	Phospholipid metabolism
LysoPC(22:4(7Z,10Z,13Z,16Z))	571.3629	6.335	$C_{30}H_{54}N_7P$	1.670	2.926	0.0009	Up	Phospholipid metabolism
LysoPC(22:5(7Z,10Z,13Z,16Z,19Z))	569.347	6.013	$C_{30}H_{52}N_7P$	1.651	3.764	0.0009	Up	Phospholipid metabolism
N5-Ethyl-L-glutamine	174.1004	1.706	$C_7H_{14}N_{23}$	1.440	0.496	0.0073	Down	Amino acid metabolism
N-Acetyl-L-methionine	191.0612	2.264	$C_7H_{13}NOS$	1.285	0.447	0.0034	Down	Amino acid metabolism
N-Acetyl-L-tyrosine	223.0841	2.173	$C_{11}H_{13}N_4$	1.496	0.464	0.0001	Down	Amino acid metabolism
Omega	321.2144	5.143	$C_{15}H_{31}N_6$	1.180	3.107	8.23E-	Up	Fatty acid metabolism
PC	757.5612	13.71	$C_{42}H_{80}N_8P$	1.671	2.589	0.0014	Up	Phospholipid metabolism
Pyrimidine	80.03746	11.15	$C_4H_4N_2$	1.665	1.420	0.0018	Up	Nucleotide metabolism
Stearic acid	284.2714	8.208	$C_{18}H_{36}O_2$	1.569	1.800	0.0050	Up	Fatty acid metabolism
Ubiquinone-1(CoQ1)	250.1202	5.035	$C_{14}H_{18}O_4$	1.589	1.450	0.0014	Up	Energy metabolism
val-leu-gly-lys	415.2774	2.575	$C_{19}H_{37}N_5$	1.045	0.271	0.0001	Down	Amino acid metabolism
[FA(16:2)]N-hexadecyl-ethanolamine	299.2819	5.945	C_{18} $H_{37}NO_2$	1.393	2.191	0.0004	Up	Fatty acid metabolism
[FA(18:2)]9Z_11E-octadecadienoicacid	280.2399	6.174	$C_{18}H_{32}O_2$	1.713	1.846	0.0005	Up	Fatty acid metabolism
[FA(18:4)]6Z_9Z_12Z_15Z-octadecatetraenoicacid	276.2084	5.782	$C_{18}H_{28}O_2$	1.669	3.871	0.0001	Up	Fatty acid metabolism
Ala-Pro	186.1001	0.688	C_8 $H_{14}N_2O_3$	1.292	0.154	0.0001	Down	Amino acid metabolism
Arachidonic acid	304.2401	7.147	$C_{20}H_{32}O_2$	1.294	1.293	0.0086	Up	Fatty acid metabolism
asp-gly-lys	318.153	0.587	$C_{12}H_{22}N_6$	1.500	6.844	0.0011	Up	Amino acid metabolism
Creatine	131.0697	0.706	$C_4H_9N_3O_2$	1.234	1.458	0.0034	Up	Amino acid metabolism
Creatinine	113.0591	2.904	$C_4H_7N_3O$	1.581	1.860	0.0073	Up	Amino acid metabolism
Gly-Pro	172.0849	0.79	$C_7H_{12}N_{23}$	1.173	0.415	0.0495	Down	Amino acid metabolism
Lauryl glucoside	348.2507	4.264	$C_{18}H_{36}O_6$	1.237	1.522	0.0258	Up	Glycometabolism

enhanced glycolysis, followed by lactic acid fermentation in the presence of abundant oxygen in microenvironment. Interestingly, citric acid and L-(+)-lactic acid were dramatically upregulated after both SST and base line chemotherapy treatments (**Figure 6**). Together, these upregulations may have resulted from cancer cells that are killed by chemotherapy or SST.

DISCUSSION

Nowadays, surgery combined with radiotherapy, chemotherapy, targeted therapy, hormonal therapy, and immunotherapy has been extensively used for treating patients with breast cancer (Harbeck et al., 2019). Chemotherapy is commonly used for treatment of different stages of breast cancer. Moreover, neoadjuvant chemotherapy has been used to shrink tumors before surgery (Early Breast Cancer Trialists' Collaborative Group (EBCTCG), 2018; Untch et al., 2014). Normally, the chemotherapeutic strategy is established by combining two or more agents to achieve a better effect for breast cancer. Although chemotherapy shows significant efficacy in killing cancer cells, it also results in non-negligible side effects such as alopecia, vomiting, constipation, diarrhea, immune dysfunction, and myelosuppression (Tao et al., 2015). The severity of these adverse effects is highly related to the regimen type, drug dosage, treatment length, and general health of patients. Furthermore, some breast cancer patients also show significant chemotherapy resistance. Thus, an adjuvant treatment aimed at managing side effects and increasing chemotherapy sensitivity is expected.

TCM has been increasingly combined with regular chemotherapy in breast cancer treatment because it can enhance chemotherapy sensitivity and alleviate the side effects induced by chemotherapy (Li et al., 2020). Some meta-analyses and systematic reviews have shown that the adjuvant use of TCM with chemotherapy can attenuate a series of side effects induced by chemotherapy including alopecia, vomiting, diarrhea, constipation, myelosuppression, and immune dysfunction (Li et al., 2020). For example, previous studies have shown that a TCM named Yiqi Jianpi Hewei could alleviate the occurrence rate of chemotherapy induced constipation in breast cancer patients (Wu et al., 2019; Li et al., 2020). The SST has been used to restore the immune function of chemotherapeutic or post-operational period gastric cancer patients (Lu et al., 2020). However, the mechanisms of pharmacodynamics and drug-drug interaction remain unclear. Moreover, the impacts of compounds on drug metabolism is not just simply the sum of effects from individual compounds.

In this study, we applied an untargeted metabolomics analysis method using HPLC-MS to examine the metabolite changes in serum of breast cancer patients following base line chemotherapy and SST adjuvant therapy. In addition, the mass spectrometry analysis data were further subjected to OPLS-DA and PCA analyses to obtain good division. Numerous differentially expressed metabolites especially those involved in fatty acid or amino acid metabolism have been identified after base line chemotherapy and SST adjuvant therapy, and treatments had shown significant impacts on the metabolites. We also analyzed the metabolic pathways involved based on the differentially expressed metabolites. The carnitine shuttle, bile acid biosynthesis, drug metabolism-cytochrome P450, and vitamin B6 (pyridoxine), Vitamin E, and purine metabolism pathways were considered as the potential pathways affected by SST treatment.

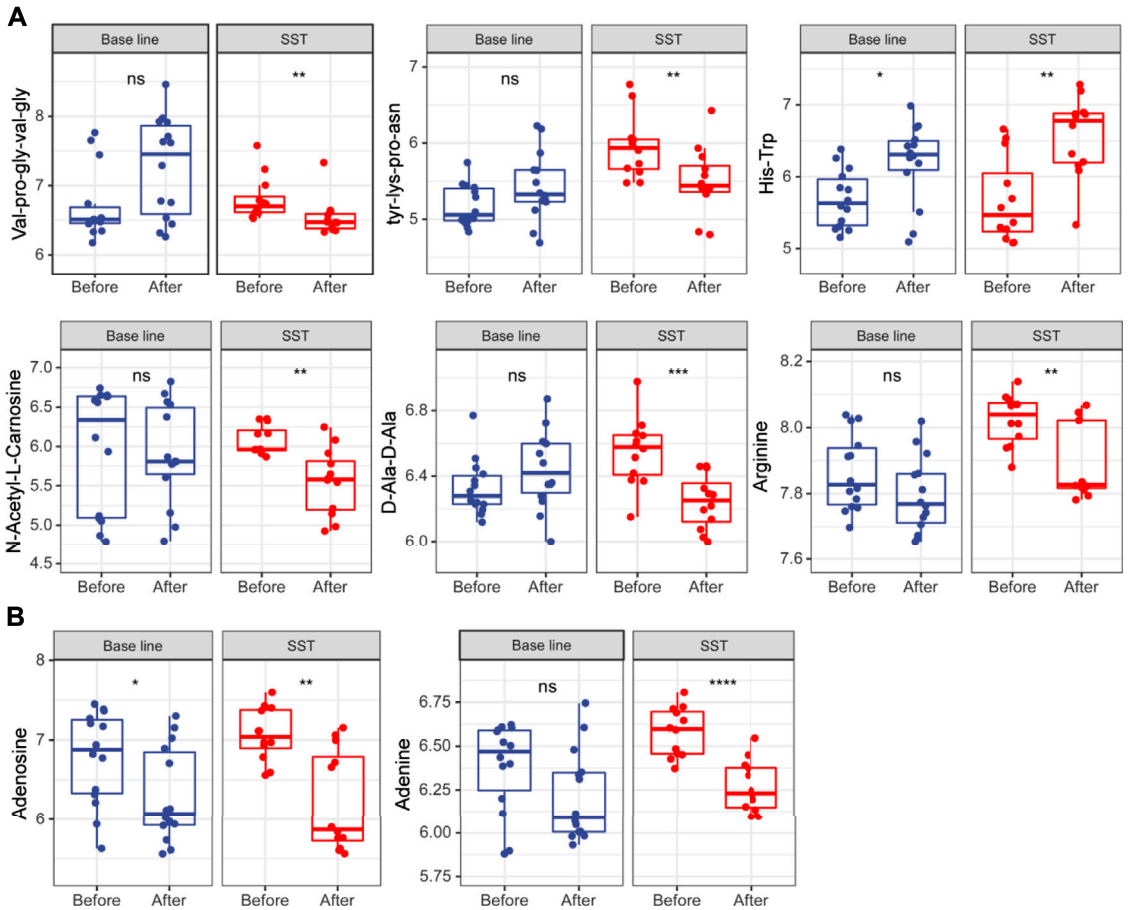

FIGURE 5 | Levels of amino acid **(A)** and nucleotide **(B)** metabolism related metabolites in serums of breast cancer patients receiving base-line chemotherapy or adjuvant SST treatment; ns, not significant; *$p < 0.05$, **$p < 0.01$, ***$p < 0.001$, and ****$p < 0.0001$ by student's *t* test.

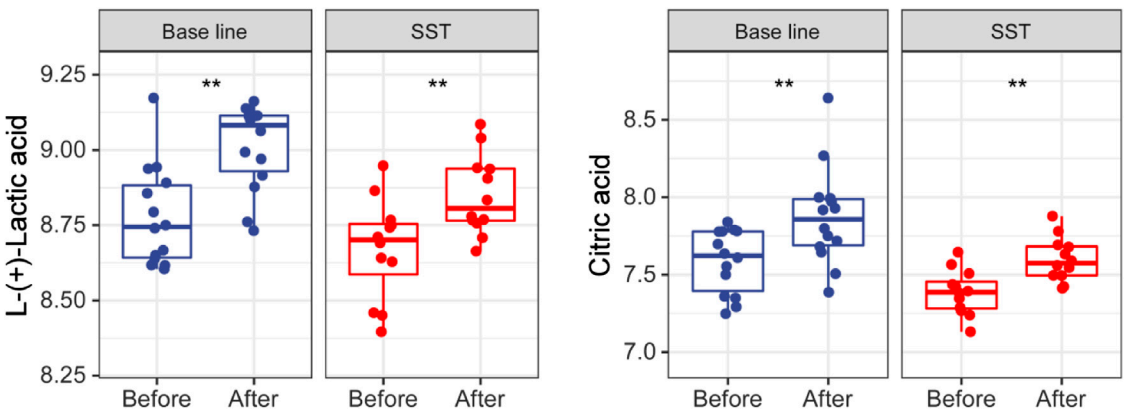

FIGURE 6 | Levels of glucose metabolism related metabolites in serums of breast cancer patients receiving base-line chemotherapy or adjuvant SST treatment. **$p < 0.01$ by student's *t* test.

Amino acid metabolic disorder plays acritical role in breast cancer (Pavlova and Thompson, 2016; Tabe et al., 2019). The differentially expressed metabolites we found, such as val-pro-gly-val-gly, tyr-lys-pro-asn, and D-Ala-D-Ala were significantly reduced after adjuvant SST treatment. In breast cancer initiation and progression, many peptides called neoantigens are generated

by disrupted alternative splicing processes and gene mutations (Benvenuto et al., 2019). In addition, amino acid metabolism disruption also leads to aberrant expression of short peptides in cancer. In this study, a lot of short peptides were detected with a remarkable decrease in breast cancer patients after adjuvant SST treatment. This result means that adjuvant SST treatment can inhibit the production of potential neoantigens, thereby alleviating tumor burden by affecting the amino acid metabolism disorder. Warburg effect has been known as an important phenomenon in cancer development: different from normal cells which primarily use oxidative phosphorylation in mitochondria to generate energy, most cancer cells primarily use aerobic glycolysis to obtain energy for development. We found the differential metabolites were all involved in aerobic glycolysis, such as L-(+)-lactic acid and citric acid, suggesting that the adjuvant SST treatment can improve the prognosis of breast cancer, thereby affect the glucose metabolism disorder.

We systematically performed untargeted metabolic analysis to investigate the potential mechanism of SST in breast cancer treatment. The results revealed that SST may enhance chemotherapy sensitivity and alleviate side-effects mainly by affecting the amino acid and glucose metabolism pathways. However, the detailed mechanisms of how SST impacts the cancer cell malignant biological properties remain further study. Furthermore, SST led to significant alleviation of side effects induced by chemotherapy, which may be related to drug and vitamin metabolism pathways. Hypothetically, SST may protect patients from vomiting and aspirating gastric contents through affecting the patients' gut microbiota, thereby influencing the secondary metabolites.

At present, although TCM has been widely applied in breast cancer therapy for many years in China and also some other Asian counties (Xiang et al., 2019), it remains a challenge to introduce TCM to western countries. Currently, most reported clinical trials about the use of TCM in treating breast cancer were performed in Chinese patients. Therefore, more clinical trials are needed to be performed in western countries to facilitate the use of TCM worldwide. Another concern is whether TCM influences the pharmacokinetics of chemotherapeutic agents in combination treatments. Some *in vivo* studies showed that there were no interactions between chemotherapeutic agents and TCM such as berberine. However, pharmacokinetic studies of chemotherapeutic agents in combination with TCM are quite few. Moreover, the mechanisms about how TCM alleviates the side-effects induced by chemotherapy also need further research.

CONCLUSION

We used an HPLC-MS-based untargeted metabolomics analysis method to investigate drug interactions between base line chemotherapy and SST treatment. Based on the HPLC-MS results, we have identified several differential metabolites after base line chemotherapy and SST treatment, respectively. The metabolites exhibited different changes before and after treatment of only base line chemotherapy or combination treatment with SST, indicating that the SST treatment can affect the glycometabolism, fatty acid, bile acid and amino acid metabolism. Especially, some short peptides which are potential tumor neoantigens were significantly reduced after adjuvant SST treatment. This work has elucidated the interaction mechanism between base line chemotherapy and SST treatment based on analysis of metabolite changes, and identified potential metabolic pathways involved, which might shed new light on clinical medication.

DATA AVAILABILITY STATEMENT

The original contributions presented in the study are included in the article/**Supplementary Material**, further inquiries can be directed to the corresponding authors.

ETHICS STATEMENT

The studies involving human participants were reviewed and approved by The Fourth Affiliated Hospital of Anhui Medical University. The patients/participants provided their written informed consent to participate in this study.

AUTHOR CONTRIBUTIONS

HW, YZ, JP, QS, and YG performed the experiments and participated in article writing. HW, YG, QS, and YZ designed and performed the bioinformatic data analyses. HW, XX, XYa, and AL collected the clinical samples. XM, AX, WW, and TG interpreted the results. XYu, WW, YG, and GL provided help for statistical analyses. YG, XH, WL, and ZW revised the article. All authors contributed to the article and approved the submitted version.

FUNDING

This work was supported by the National and provincial key specialty construction plan (Z155080000004), the Basic and Clinical Cooperative Research Promotion Program of Anhui Medical University (2019xkjT029), and the Clinical Medicine Discipline Construction Project of Anhui Medical University (2020lcxk032).

SUPPLEMENTARY MATERIAL

The Supplementary Material for this article can be found online at: https://www.frontiersin.org/articles/10.3389/fphar.2021.720886/full#supplementary-material

REFERENCES

Alonso, A., Marsal, S., and Julià, A. (2015). Analytical Methods in Untargeted Metabolomics: State of the Art in 2015. *Front. Bioeng. Biotechnol.* 3, 23. doi:10.3389/fbioe.2015.00023

Benvenuto, M., Focaccetti, C., Izzi, V., Masuelli, L., Modesti, A., and Bei, R. (2021). Tumor Antigens Heterogeneity and Immune Response-Targeting Neoantigens in Breast Cancer. *Semin. Cancer Biol.* 72, 65–75. doi:10.1016/j.semcancer.2019.10.023

Cao, W., Chen, H. D., Yu, Y. W., Li, N., and Chen, W. Q. (2021). Changing Profiles of Cancer burden Worldwide and in China: a Secondary Analysis of the Global Cancer Statistics 2020. *Chin. Med. J. (Engl)* 134, 783–791. doi:10.1097/CM9.0000000000001474

Chen, W., Zheng, R., Baade, P. D., Zhang, S., Zeng, H., Bray, F., et al. (2016). Cancer Statistics in China, 2015. *CA Cancer J. Clin.* 66, 115–132. doi:10.3322/caac.21338

Chen, Y. Z., Lin, F., Zhuang, G. B., Ren, Y., and Li, P. P. (2011). Protective Effect of Renshen Yangrong Decoction (人参养荣汤) on Bone Marrow against Radiation Injury in Mouse. *Chin. J. Integr. Med.* 17, 453–458. doi:10.1007/s11655-011-0634-1

Chong, J., Soufan, O., Li, C., Caraus, I., Li, S., Bourque, G., et al. (2018). MetaboAnalyst 4.0: towards More Transparent and Integrative Metabolomics Analysis. *Nucleic Acids Res.* 46, W486–W494. doi:10.1093/nar/gky310

Cui, L., Lu, H., and Lee, Y. H. (2018). Challenges and Emergent Solutions for LC-MS/MS Based Untargeted Metabolomics in Diseases. *Mass. Spectrom. Rev.* 37, 772–792. doi:10.1002/mas.21562

DeSantis, C. E., Ma, J., Gaudet, M. M., Newman, L. A., Miller, K. D., Goding Sauer, A., et al. (2019). Breast Cancer Statistics, 2019. *CA Cancer J. Clin.* 69, 438–451. doi:10.3322/caac.21583

Dong, J., Su, S. Y., Wang, M. Y., and Zhan, Z. (2010). Shenqi Fuzheng, an Injection Concocted from Chinese Medicinal Herbs, Combined with Platinum-Based Chemotherapy for Advanced Non-small Cell Lung Cancer: a Systematic Review. *J. Exp. Clin. Cancer Res.* 29, 137. doi:10.1186/1756-9966-29-137

Early Breast Cancer Trialists' Collaborative Group (EBCTCG) (2018). Long-term Outcomes for Neoadjuvant versus Adjuvant Chemotherapy in Early Breast Cancer: Meta-Analysis of Individual Patient Data from Ten Randomised Trials. *Lancet Oncol.* 19, 27–39. doi:10.1016/S1470-2045(17)30777-5

Fang, T., Yan, Y. X., Yang, Y., Lv, Y. X., Chang, Q. Q., and Zhang, D. D. (2020). Ethyl Acetate Fraction from Hedyotis Diffusa Plus Scutellaria Barbata Suppresses Migration of Bone-Metastatic Breast Cancer Cells via OPN-FAK/ERK/NF-κB Axis. *Evid. Based Complement. Alternat Med.* 2020, 3573240. doi:10.1155/2020/3573240

Guo, M. Z., Wang, T. Y., Yang, J., Chang, H., Ji, S., and Tang, D. Q. (2019). Interaction of Clopidogrel and Fufang Danshen Dripping Pills Assay in Coronary Heart Disease Based on Non-target Metabolomics. *J. Ethnopharmacol* 234, 189–196. doi:10.1016/j.jep.2019.01.030

Harbeck, N., Penault-Llorca, F., Cortes, J., Gnant, M., Houssami, N., Poortmans, P., et al. (2019). Breast Cancer. *Nat. Rev. Dis. Primers* 5, 66. doi:10.1038/s41572-019-0111-2

Jang, C., Chen, L., and Rabinowitz, J. D. (2018). Metabolomics and Isotope Tracing. *Cell* 173, 822–837. doi:10.1016/j.cell.2018.03.055

Johnson, C. H., Ivanisevic, J., and Siuzdak, G. (2016). Metabolomics: beyond Biomarkers and towards Mechanisms. *Nat. Rev. Mol. Cel Biol* 17, 451–459. doi:10.1038/nrm.2016.25

Kalwat, M. A., and Cobb, M. H. (2017). Mechanisms of the Amplifying Pathway of Insulin Secretion in the β Cell. *Pharmacol. Ther.* 179, 17–30. doi:10.1016/j.pharmthera.2017.05.003

Li, B., He, X., Jia, W., and Li, H. (2017). Novel Applications of Metabolomics in Personalized Medicine: A Mini-Review. *Molecules* 22, 1173. doi:10.3390/molecules22071173

Li, S., So, T. H., Tang, G., Tan, H. Y., Wang, N., Ng, B. F. L., et al. (2020). Chinese Herbal Medicine for Reducing Chemotherapy-Associated Side-Effects in Breast Cancer Patients: A Systematic Review and Meta-Analysis. *Front. Oncol.* 10, 599073. doi:10.3389/fonc.2020.599073

Li, T., Mello-Thoms, C., and Brennan, P. C. (2016). Descriptive Epidemiology of Breast Cancer in China: Incidence, Mortality, Survival and Prevalence. *Breast Cancer Res. Treat.* 159, 395–406. doi:10.1007/s10549-016-3947-0

Liu, C., Wang, K., Zhuang, J., Gao, C., Li, H., Liu, L., et al. (2019). The Modulatory Properties of Astragalus Membranaceus Treatment on Triple-Negative Breast Cancer: An Integrated Pharmacological Method. *Front. Pharmacol.* 10, 1171. doi:10.3389/fphar.2019.01171

Lu, X., Zheng, Y., Wen, F., Huang, W., and Shu, P. (2020). Effectiveness and Safety of Oral Chinese Patent Medicines Combined with Chemotherapy for Gastric Cancer: A Bayesian Network Meta-Analysis. *Evid. Based Complement. Alternat Med.* 2020, 8016531. doi:10.1155/2020/8016531

Martinez-Outschoorn, U. E., Peiris-Pagés, M., Pestell, R. G., Sotgia, F., and Lisanti, M. P. (2017). Cancer Metabolism: a Therapeutic Perspective. *Nat. Rev. Clin. Oncol.* 14, 11–31. doi:10.1038/nrclinonc.2016.60

Miller, K. D., Nogueira, L., Mariotto, A. B., Rowland, J. H., Yabroff, K. R., Alfano, C. M., et al. (2019). Cancer Treatment and Survivorship Statistics, 2019. *CA Cancer J. Clin.* 69, 363–385. doi:10.3322/caac.21565

Pavlova, N. N., and Thompson, C. B. (2016). The Emerging Hallmarks of Cancer Metabolism. *Cell Metab* 23, 27–47. doi:10.1016/j.cmet.2015.12.006

Pondé, N. F., Zardavas, D., and Piccart, M. (2019). Progress in Adjuvant Systemic Therapy for Breast Cancer. *Nat. Rev. Clin. Oncol.* 16, 27–44. doi:10.1038/s41571-018-0089-9

Poo, C. L., Dewadas, H. D., Ng, F. L., Foo, C. N., and Lim, Y. M. (2021). Effect of Traditional Chinese Medicine on Musculoskeletal Symptoms in Breast Cancer: A Systematic Review and Meta-Analysis. *J. Pain Symptom Manage.* 62, 159–173. doi:10.1016/j.jpainsymman.2020.11.024

Sha, Q., Lyu, J., Zhao, M., Li, H., Guo, M., and Sun, Q. (2020). Multi-Omics Analysis of Diabetic Nephropathy Reveals Potential New Mechanisms and Drug Targets. *Front. Genet.* 11, 616435. doi:10.3389/fgene.2020.616435

Sung, H., Ferlay, J., Siegel, R. L., Laversanne, M., Soerjomataram, I., Jemal, A., et al. (2021). Global Cancer Statistics 2020: GLOBOCAN Estimates of Incidence and Mortality Worldwide for 36 Cancers in 185 Countries. *CA Cancer J. Clin.* 71, 209–249. doi:10.3322/caac.21660

Tabe, Y., Lorenzi, P. L., and Konopleva, M. (2019). Amino Acid Metabolism in Hematologic Malignancies and the Era of Targeted Therapy. *Blood* 134, 1014–1023. doi:10.1182/blood.2019001034

Tao, J. J., Visvanathan, K., and Wolff, A. C. (2015). Long Term Side Effects of Adjuvant Chemotherapy in Patients with Early Breast Cancer. *Breast* 24 Suppl 2 (Suppl. 2), S149–S153. doi:10.1016/j.breast.2015.07.035

Thévenot, E. A., Roux, A., Xu, Y., Ezan, E., and Junot, C. (2015). Analysis of the Human Adult Urinary Metabolome Variations with Age, Body Mass Index, and Gender by Implementing a Comprehensive Workflow for Univariate and OPLS Statistical Analyses. *J. Proteome Res.* 14, 3322–3335. doi:10.1021/acs.jproteome.5b00354

Untch, M., Konecny, G. E., Paepke, S., and von Minckwitz, G. (2014). Current and Future Role of Neoadjuvant Therapy for Breast Cancer. *Breast* 23, 526–537. doi:10.1016/j.breast.2014.06.004

Vander Heiden, M. G., Cantley, L. C., and Thompson, C. B. (2009). Understanding the Warburg Effect: the Metabolic Requirements of Cell Proliferation. *Science* 324, 1029–1033. doi:10.1126/science.1160809

Wu, J., Liu, Y., Fang, C., Zhao, L., Lin, L., and Lu, L. (2019). Traditional Chinese Medicine Preparation Combined Therapy May Improve Chemotherapy Efficacy: A Systematic Review and Meta-Analysis. *Evid. Based Complement. Alternat Med.* 2019, 5015824. doi:10.1155/2019/5015824

Xiang, Y., Guo, Z., Zhu, P., Chen, J., and Huang, Y. (2019). Traditional Chinese Medicine as a Cancer Treatment: Modern Perspectives of Ancient but Advanced Science. *Cancer Med.* 8, 1958–1975. doi:10.1002/cam4.2108

Yan, Z., Lai, Z., and Lin, J. (2017). Anticancer Properties of Traditional Chinese Medicine. *Comb. Chem. High Throughput Screen.* 20, 423–429. doi:10.2174/1386207320666170116141818

Yang, Y., Ting, W., Xiao, L., Shufei, F., Wangxiao, T., Xiaoying, W., et al. (2017). Immunoregulation of Shenqi Fuzheng Injection Combined with Chemotherapy in Cancer Patients: A Systematic Review and Meta-Analysis. *Evid. Based Complement. Alternat Med.* 2017, 5121538. doi:10.1155/2017/5121538

Yang, Z., Zhang, Q., Yu, L., Zhu, J., Cao, Y., and Gao, X. (2021). The Signaling Pathways and Targets of Traditional Chinese Medicine and Natural Medicine in Triple-Negative Breast Cancer. *J. Ethnopharmacol* 264, 113249. doi:10.1016/j.jep.2020.113249

Zhang, Z., Yi, P., Yang, J., Huang, J., Xu, P., Hu, M., et al. (2020). Integrated Network Pharmacology Analysis and Serum Metabolomics to Reveal the Cognitive Improvement Effect of Bushen Tiansui Formula on Alzheimer's Disease. *J. Ethnopharmacol* 249, 112371. doi:10.1016/j.jep.2019.112371

Zhou, R., Chen, H., Chen, J., Chen, X., Wen, Y., and Xu, L. (2018). Extract from Astragalus Membranaceus Inhibit Breast Cancer Cells Proliferation via PI3K/AKT/mTOR Signaling Pathway. *BMC Complement. Altern. Med.* 18, 83. doi:10.1186/s12906-018-2148-2

Conflict of Interest: The authors declare that the research was conducted in the absence of any commercial or financial relationships that could be construed as a potential conflict of interest.

Publisher's Note: All claims expressed in this article are solely those of the authors and do not necessarily represent those of their affiliated organizations, or those of the publisher, the editors and the reviewers. Any product that may be evaluated in this article, or claim that may be made by its manufacturer, is not guaranteed or endorsed by the publisher.

frontiers in Pharmacology

ORIGINAL RESEARCH
published: 21 September 2021
doi: 10.3389/fphar.2021.719532

Proteomic Analysis Reveals the Protective Effects of Yiqi Fumai Lyophilized Injection on Chronic Heart Failure by Improving Myocardial Energy Metabolism

*Xiaoying Han[1†], Yi Zhang[1†], Ou Qiao[1], Haixia Ji[1], Xinyu Zhang[1], Wenzhe Wang[1], Xia Li[1], Juan Wang[1], Dekun Li[2], Aichun Ju[2], Changxiao Liu[3] and Wenyuan Gao[1]**

[1]School of Pharmaceutical Science and Technology, Tianjin University, Tianjin, China, [2]Tasly Pride Pharmaceutical Company Limited, Tianjin, China, [3]Tianjin Pharmaceutical Research Institute, Tianjin, China

OPEN ACCESS

Edited by:
Wenzhi Yang,
Tianjin University of Traditional Chinese Medicine, China

Reviewed by:
Lifeng Han,
Tianjin University of Traditional Chinese Medicine, China
Qilong Wang,
Tianjin University of Traditional Chinese Medicine, China

***Correspondence:**
Wenyuan Gao
pharmgao@tju.edu.cn

[†]These authors have contributed equally to this work

Specialty section:
This article was submitted to Ethnopharmacology, a section of the journal Frontiers in Pharmacology

Received: 02 June 2021
Accepted: 03 September 2021
Published: 21 September 2021

Citation:
Han X, Zhang Y, Qiao O, Ji H, Zhang X, Wang W, Li X, Wang J, Li D, Ju A, Liu C and Gao W (2021) Proteomic Analysis Reveals the Protective Effects of Yiqi Fumai Lyophilized Injection on Chronic Heart Failure by Improving Myocardial Energy Metabolism. Front. Pharmacol. 12:719532. doi: 10.3389/fphar.2021.719532

Yiqi Fumai lyophilized injection (YQFM) is the recombination of Sheng mai san (SMS).YQFM has been applied clinically to efficaciously and safely treat chronic heart failure (CHF). However, the mechanism of YQFM is still not fully elucidated. The purpose of our study was to investigate the protective mechanism of YQFM against abdominal aortic coarctation (AAC) in rats by proteomic methods. After YQFM treatment, the cardiac function were obviously meliorated. One hundred and fifty-seven important differentially expressed proteins (DEPs) were identified, including 109 in model rat compared with that in control rat (M:C) and 48 in YQFM-treated rat compared with that in model rat (T:M) by iTRAQ technology to analyze the proteomic characteristics of heart tissue. Bioinformatics analysis showed that DEPs was mainly involved in the body's energy metabolism and was closely related to oxidative phosphorylation. YQFM had also displayed efficient mitochondrial dysfunction alleviation properties in hydrogen peroxide (H_2O_2)-induced cardiomyocyte damage by Transmission Electron Microscope (TEM), Metabolic assay, and Mitotracker staining. What's more, the levels of total cardiomyocyte apoptosis were markedly reduced following YQFM treatment. Furthermore, Western blot analysis showed that the expressions of peroxisome proliferator activated receptor co-activator-1α(PGC-1α) ($p < 0.01$ or $p < 0.001$), perixisome proliferation-activated receptor alpha (PPAR-α) ($p < 0.001$)and retinoid X receptor alpha (RXR-α) were upregulated ($p < 0.001$), PGC-1α as well as its downstream effectors were also found to be upregulated in cardiomyocytes after YQFM treatment($p < 0.001$).These results provided evidence that YQFM could enhance mitochondrial function of cardiomyocytes to play a role in the treatment of CHF by regulating mitochondrial biogenesis-related proteins.

Keywords: chronic heart failure, Yiqi Fumai lyophilized injection, oxidative phosphorylation, mitochondrial biogenesis, perixisome proliferation-activated receptor alpha

Abbreviations: AAC, Abdominal aortic coarctation; Bax, Bcl-2-associated X protein; Bcl-2, B-cell lymphoma-2; CHF, Chronic heart failure; DEPs, Differentially expressed proteins; GO, Gene Ontology; HE, hematoxylin and eosin; H_2O_2, hydrogen peroxide; KEGG, Kyoto Encyclopedia of Genes and Genome; LVEF, left ventricular rejection fraction; LVFS, left ventricular fractional Shortening; NRF-1, nuclear respiratory factor 1; PAS, Periodic Acid Schiff; PGC-1α, Peroxisome proliferator-activated receptor-γ coactivator-1α; PPAR-α, perixisome proliferation-activated receptor alpha; RXR-α, retinoid X receptor alpha; SMS, Sheng mai san; TCM, Traditional Chinese medicine; TEM, Transmission Electron Microscope; Tfam, mitochondrial transcription factor A; TMT, tandem mass tags; YQFM, Yiqi Fumai lyophilized injection.

BACKGROUND

Chronic heart failure is myocardial damage caused by various reasons, resulting in injures the function and structure of the myocardium, and finally resulting in low ventricular pumping or filling function (Mosterd and Hoes, 2007). The mortality rate of patients with CHF(4-year) is up to 50%, and the mortality rate of patients (1-year) with severe heart failure is as high as 50% (Heo et al., 2008; Yancy et al., 2013; Wang et al., 2017). Therefore, CHF is an important challenge facing the cardiovascular field in the 21st century. With the deepening of the understanding of the pathogenesis of heart failure, Western medicine's treatment of CHF has gradually shifted from a cardiotonic, diuretic, and vasodilator-based cardiac circulation model to prevent ventricular remodeling, improve prognosis, and recover. Targeting the synchrony of ventricular function, these drugs can alleviate patient mortality and relieve symptoms with advantage. However, there are some adverse events that may limit the use of TCM (Fu et al., 2010; Faris et al., 2012; Wang et al., 2015a), so conventional treatment of western medicine is often combined with TCM syndrome differentiation and treatment, and the advantages of Chinese and Western medicine are complemented.

YQFM derives from the classic name "Sheng Mai SAN," made by Radix of Panax ginseng C.A. Mey. (Araliaceae), Fructus of Schisandra chinensis (Turcz.) Baill (Schisandraceae), and Radix of *Ophiopogon japonicus* (L.f) Ker-Gawl. YQFM is a TCM powder injection produced by Tasly Pharmaceutical Co., Ltd., It is mainly used for coronary heart disease fatigue angina pectoris syndrome of Qi and Yin deficiency, and chronic left ventricular insufficiency caused by coronary heart disease II and III Qi and Yin deficiency. Since its official launch in 2007, the quality is stable and the curative effect is accurate, and it has been wide-ranging recognized by doctors and patients. Past studies have shown that its active ingredients could melioration HF by inhibiting the activity of NF-κB (Xing et al., 2013), and reduce hypoxia-induced myocardial injury (Feng et al., 2016; Li et al., 2016). In addition, YQFM can regulate MAPKs and alleviate myocardial remodeling and heart failure caused by coronary artery ligation (CAL) (Pang et al., 2017). Many components of YQFM show mitochondrial regulation (Zheng et al., 2018), including ginsenosides Rb1, Rb3, Rg1, Rg3, Schisandra B, and

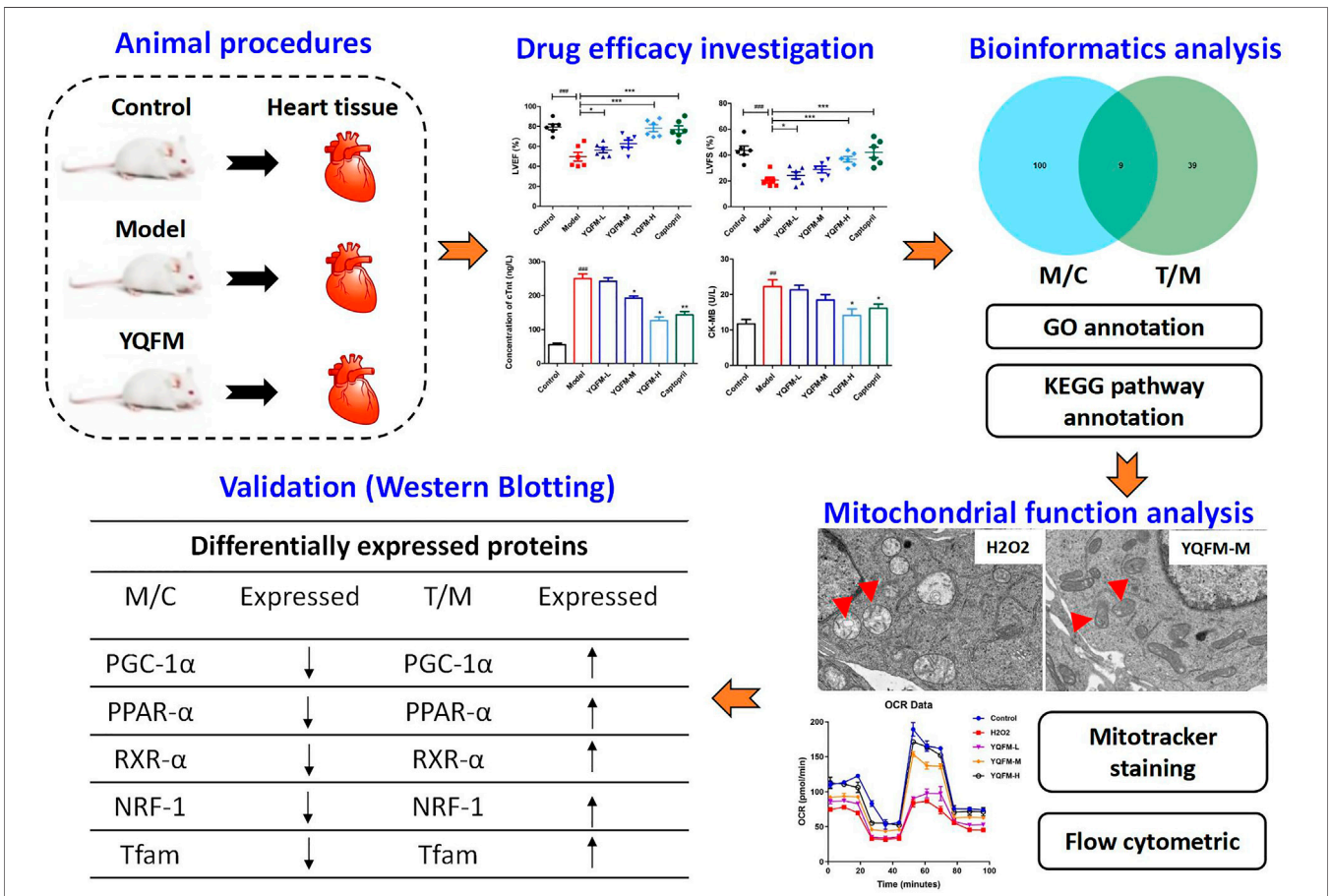

Graphical Abstract | Potential mechanism of YQFM in the treatment of chronic heart failure is to improve myocardial energy metabolism via enhancing the mitochondrial function of myocardial.

ophiopogon D (Chiu et al., 2007; Chen and Ko, 2010; Sun et al., 2013; Mu et al., 2015; Dong et al., 2016; Chen et al., 2019; Park et al., 2019; Li et al., 2021). Nevertheless, the mechanism of YQFM in treating chronic heart failure remains to be further elucidated. Differential proteomics is a method to clarify the pathological changes of diseases or the mechanism of therapeutic intervention through differential expression analysis of proteins (Wilhelm et al., 2014), to obtain "panoramic information" about life activities within a short period. Differential proteomics analyzes the dynamic evolution process of protein expression in the body under different conditions from a holistic perspective. Its research method is very consistent with the method of TCM syndrome differentiation and treatment, and the comprehensive regulation of TCM prescriptions. With the help of the development and breakthrough of proteomics technology, it is now possible to study the changes in the overall protein expression of various organs in the organism under different internal and external interventions and influences, such as in the onset of cardiovascular disease, and to detect the changes in the cell The composition, expression and regularity of this protein (Suo et al., 2016; Wei et al., 2019). The application of proteomics to the research of TCM can effectively help researchers to find the targets of TCM compounds, analyze the biological processes involved in the pharmacological effects of TCM, and further explain the mechanism of TCM from the perspective of molecular biology.

This study was aimed to explore the therapeutic effect and mechanism by which YQFM attenuates AAC-induced CHF in rats and H_2O_2-induced cardiomyocyte damage in H_9C_2 cells. However, due to the complexity of TCM prescriptions and various causes of CHF, the mechanism of the optimized prescription is not very clear. Therefore, this experiment used differential proteomics to investigate the targets protein regulated by YQFM in treating CHF rats, and combined with biological function analysis to explore the possible biological basis of the therapeutic effect of the formula. Western blot verification were used to confirm that the mechanism of YQFM in the treatment of CHF.

MATERIALS AND METHODS

Chemicals and Materials

YQFM was donated by Tasly Pride Pharmaceutical Company Limited. Lactate dehydrogenase (LDH) assay kit, rat cardiac troponin-T (cTnT) and creatine kinase isoenzyme-MB (CK-MB) ELISA kits were obtained from Nanjing Jiancheng Bioengineer Institute. Antibodies against cleaved cTnT, Bax, Bcl-2, PGC-1α, PPAR-α, RXR-α, Tfam and NRF-1 and secondary anti-rabbit antibodies were purchased from Abcam, (Cambridge, United Kingdom). Hydrogen peroxide (H_2O_2, Aladdin®, 700 μmol/L).

HPLC-QQQ-MS/MS Analysis Condition

Sample solutions for qualitative analysis. 2.60 g of YQFM was accurately weighed and dissolved in 30% methanol (10 ml). Sample solution was added into C8 solid-phase extraction (SPE). The samples were eluted in turn with the following solutions: 30% methanol solution containing 2 ml sodium hydroxide (0.5 mol/L), 30% methanol (5 ml) and 100% methanol (5 ml). The 100% methanol eluent was collected and diluted to 5 ml. The obtained test solution should be filtered through a 0.22 mm syringe filter. Accurately weigh the ginsenosides Rb1, Rf, Re, Rc, Rb2, Rb3, Rg1, Rh1, Rc, Rd, Rf2, Rg2, Schisandrin A, Schisandrin B, Schisandrin A, and Schisandrin B reference substance, add 50% Methanol is dissolved, and the mass concentration of ginsenoside Rb1, Rf, Re, Rc, Rb2, Rb3, Rg1, Rh1, Rc, Rd, Rf2, Rg2, schisandrin A, and schisandrin B are each 20 μg/ml. A mixed reference solution of ethyl alcohol and schisandrin A 10 μg/ml.

Sample solutions for qualitative analysis. Chemical analysis was performed on high performance liquid chromatography (HPLC) system. Two mobile phases were used for chromatographic separation on kromasil 100-5-C18 column (5 μm, 4.6 mm × 250 mm): Phase A is ultrapure water with 0.1% formic acid and Phase B is acetonitrile. Gradient elution program: 0–8 min, 20–30% B; 8–10 min, 30–32% B; 10–15 min, 32–35% B; 15–26 min, 35–35% B; 26–35 min, 35–40% B; 35–40 min, 40–45% B; 40–50 min, 45–55% B; 50–60 min, 55–70% B; 60–65 min, 70–95% B; 65–72 min, 95–98% B; 72–81 min, 98–20% B. When the injection volume was 10 μl, the flow rate: 1 ml/min, and the column temperature was 28°C.

Model Establishment

Sprague-Dawley (SD) male rats weighing (220–240) g were obtained from the Beijing HFK Biotechnology Co., Ltd (SCXK-2018-0004). All the rats were then subjected to 1 week of domestication before experiment. The rats were kept in a 22 ± 2°C cage with light/dark circulation for 12 h and humidity of 40 ± 5%. In addition, the rats were fed rat chow and given free water.

Abdominal aortic coarctation (AAC) establishes a pressure overload CHF model. Its mechanism is that by narrowing the abdominal aorta, aortic pressure increases, cardiac afterload increases, myocardial compensatory hypertrophy, ventricular volume increases, heart expands, cardiac decompensation in the later stage, resulting in myocardial function and structural damage, and finally heart failure. AAC model in rats was established by referring to the reference method (Cops et al., 2019). The steps were as follows. After intraperitoneal injection of 2% sodium pentobarbital at 0.2 ml/100 g (Sigma-Aldrich, St. Louis, MO, United States) and preparation of the skin (shaved), the rat was fixed on the operating table supine. The abdominal aorta above the renal artery branch was blunt dissociated. The needle of No. 7 syringe was parallel to the abdominal aorta, and No. 4 non absorbable surgical silk thread was used to connect the abdominal aorta and syringe. The needle was ligated together, and then the syringe was slowly withdrawn, the abdomen was closed, and layered sutures were used to narrow the diameter of the rat's abdominal aorta to 0.7 mm, and then 0.1 ml of penicillin was injected into the abdominal cavity to prevent infection.

Animal Grouping and Administration

Except for 10 rats in the blank control group, 55 of the 70 rats were made into AAC models. They were then grouped randomly into control, AAC, AAC+YQFM low-dose (YQFM-L, 20 mg/kg/d) arms, AAC+YQFM medium-dose (YQFM-M, 40 mg/kg/d) arms, AAC+YQFM high-dose (YQFM-H, 80 mg/kg/d) arms and

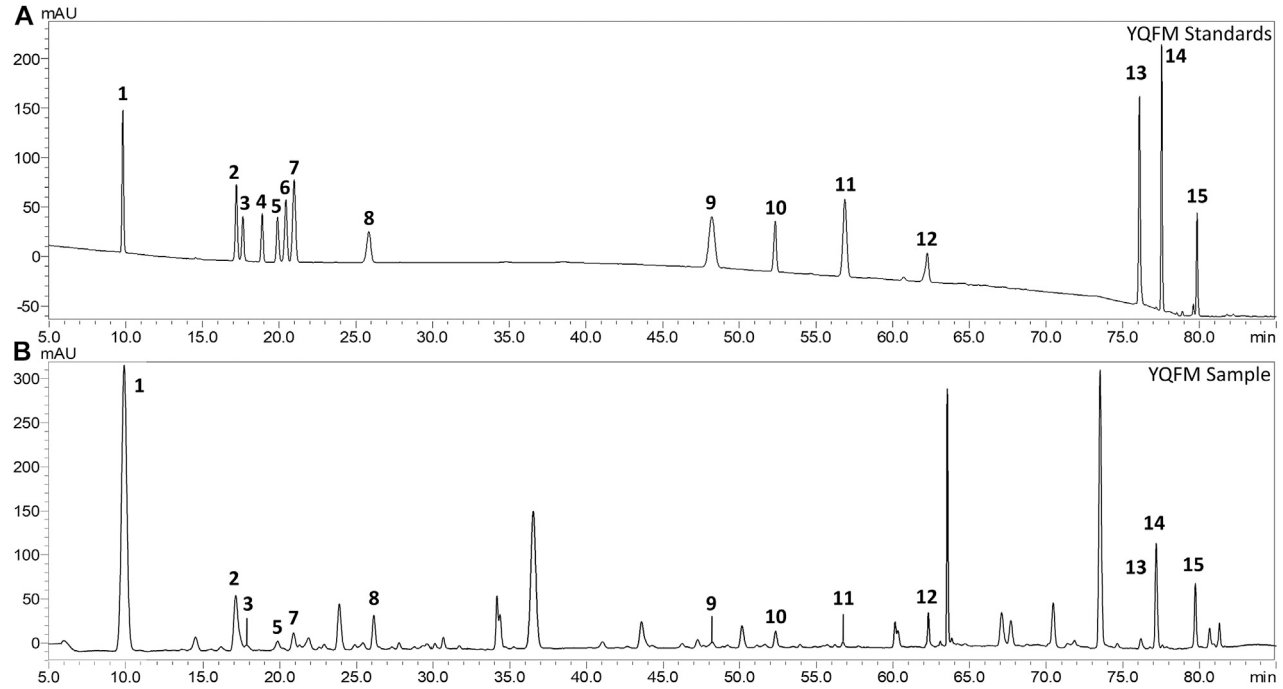

FIGURE 1 | Comparison of the liquid chromatogram of the mixed reference substance and YQFM sample. **(A)** Standard solution and **(B)** Sample solution: 1: ginsenoside Rg1, 2: ginsenoside Rf, 3: ginsenoside Rb1, 4: ginsenoside Rc, 5: ginsenoside Rb2, 6: ginsenoside Rb3, 7: ginsenoside Re, 8: ginsenoside Rd, 9: schizandrol A, 10:20(S)-ginsenoside F2, 11: schizandrol B, 12: ginsenoside Rg2, 13: schisandrin A, 14: schisandrin B, 15: ginsenoside Rh1.

captopril (Capt., 40 mg/kg/d) group. The dose of rats in the middle group received an adult equivalent dose of 70 kg, the dose of rats in the high group received twice the adult equivalent dose, and the dose of rats in the low group received half of the adult equivalent dose.

After 4 weeks of intervention, the rats were anesthetized. 2% sodium pentobarbital (Shanghai, China) (0.2 ml/100 g) was injected intraperitoneally. The blood was gathered from the femoral artery, centrifuged and stored at −80°C for analysis. After perfusing the heart with cold PBS to remove blood, filter paper was used to remove free PBS. The heart tissue was immersed with 4% paraformaldehyde (Google Biotechnology, Wuhan, China), and a biopsy was performed to monitor the morphology of the myocardial tissue. The remaining heart tissue was saved in liquid nitrogen for 1 h and stored at −80°C before proteomics and Western blot analysis.

Echocardiography

Four weeks after administration, the rats were anesthetized with 2% sodium pentobarbital and underwent echocardiography on an ultrasound machine. Left ventricular posterior wall thickness (LVPWd, LVPWs) during diastolic and systolic periods was recorded in M mode to examine left ventricular thickening (Luo et al., 2015).

Biochemical Parameters

cTnT, LDH and CK-MB in serum are unique biomarkers of myocardial injury after heart failure (Bertinchant et al., 2000; Giannitsis and Katus, 2013). After 28 days, the serum CK-MB and LDH were detected by blood biochemical examination to evaluate the cardiomyocyte repair. Quantitative examination of cTn T and CK-MB and LDH analysis on serum samples from different research groups using assay kits.

Cardiac Histopathological Examination

The left ventricular region of each group was fixed in 4% paraformaldehyde for 24 h. After fixation, it was embedded with paraffin and stained with hematoxylin and eosin (HE), Masson and Periodic Acid Schiff (PAS) respectively.The pathological changes of myocardial fibers in each group of rat were observed by an optical microscope (JEOL, Tokyo, Japan).

Immunohistochemical Measurement of cTnt

Immunohistochemical analysis of cTnt expression in the heart. Paraffin-embedded tissue was sectioned continuously at 4 μm, dewaxed with xylene and hydrated with gradient alcohol. The sections were incubated with goat serum (10%) for 1 h, then combined with primary antibody and incubated overnight at 4°C. Follow the instructions in the manufacturer's agreement for subsequent procedures. The Image Pro Plus software was used to evaluate images.

Protein Extraction and Tandem Mass Tags Protein Labelling

Randomly collect rat myocardial tissue, three samples in control arm, three samples in model arm, and three samples in the

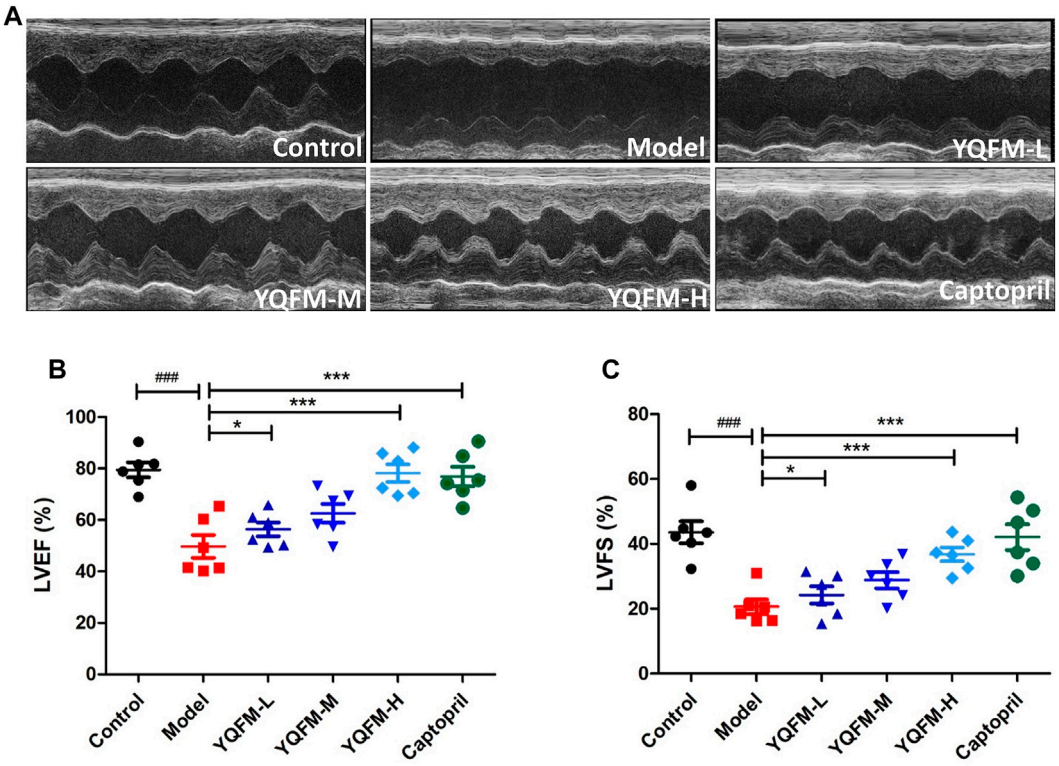

FIGURE 2 | The effect of YQFM on cardiac function in CHF rat after being treated for 28 days. **(A)** Representative echocardiograph from the various groups. **(B)** Left ventricle ejection fraction (LVEF) (n = 6 animals/group). **(C)** Left ventricle fractional shortening (LVFS) (n = 6 animals/group). Data are means ± SD. $^{\#}p < 0.05$, $^{\#\#}p < 0.01$, $^{\#\#\#}p < 0.001$ vs the Control group, $^{*}p < 0.05$, $^{**}p < 0.01$, $^{***}p < 0.001$ vs the Model group.

YQFM-H treatment group. All frozen samples were took out and ground them with liquid nitrogen. Then the same amount of samples was transferred to MP shaker tubes, and moderate dose of protein lysis solution (1% SDS + 8 M urea, containing protease inhibitors) was added. FastPrep®-24 instrument (MP Biomedicals, OH, United States) was used to homogenize heart tissue samples in pyrolysis buffer (TEAB, 25 mM Triethylammonium bicarbonate, 2% sodium dodecyl sulfate (SDS)). The protein was quantified according to the BCA kit instructions. Samples from each animal in the group were then divided into equal groups. Tissue samples, 50 μg of reference cell containing the same amount of all samples and 50 μg of total protein in each combination group, were reduced by DL-Dithiothreitol and then trypsin was digested using the membrane assisted sample preparation method modified by Wiśniewski et al. (2009).The sample diluted with 8 M urea was used to filter (Nanosep 30 k Omega, Pall Life Sciences, Washington, New York, United States), and the SDS was washed repeatedly with 8 M urea.

Methyl methane thiosulfonate diluted in digestion buffer (20 mM TEAB, 1% sodium deoxycholate (SDC)) was used for alkylation, and the membrane was washed repeatedly with digestion buffer. Trypsin was added to 25 mM TEAB at a ratio of 1:100 relative to protein mass, and the samples were incubated overnight at 37°C. The next morning, another portion of trypsin was added and the samples were incubated at 37°C for 4 h (Boersema et al., 2009; Xu et al., 2014; Liu et al., 2017). According to the manufacturer's instructions, the peptide was labeled with isobaric mass labeling reagent TMT®. In one group, each reference and sample were labelled with a unique label from the TMT 6 plex or 10 plex isobaric mass labelling kit. After TMT labeling, a set of samples were combined, concentrated and acidified to about pH 2 to precipitate SDC.

High Performance Liquid Chromatography Fractionation

Trypsin samples were separated into fractions by high-pH reverse HPLC with ACQUITY UPLC BEH C18 (1.7 μm particles, 2.1 mm ID, and 250 mm length) (Wang et al., 2010; Song et al., 2011). The procedure was as follows: Within 48 min, a gradient of 0–100% acetonitrile (pH = 10.0) was used to separate peptides. According to the time and peak type, 20 fractions were collected for each group, and they were combined into 10 fractions. After vacuum centrifugation, they were dissolved in mass spectrometry loaded buffer for two-dimensional analysis.

LC-MS/MS Analysis

Tryptic peptide was dissolved in 0.1% (V/V) formic acid, and then 9RKFSG2_NCS-3500RS (Thermo, United States) Ultra High Performance Liquid System was used for separation (Motoyama and Yates, 2008). 0.1% formic acid and 2% acetonitrile were contained in Solvent A, while 0.1% formic acid and 80%

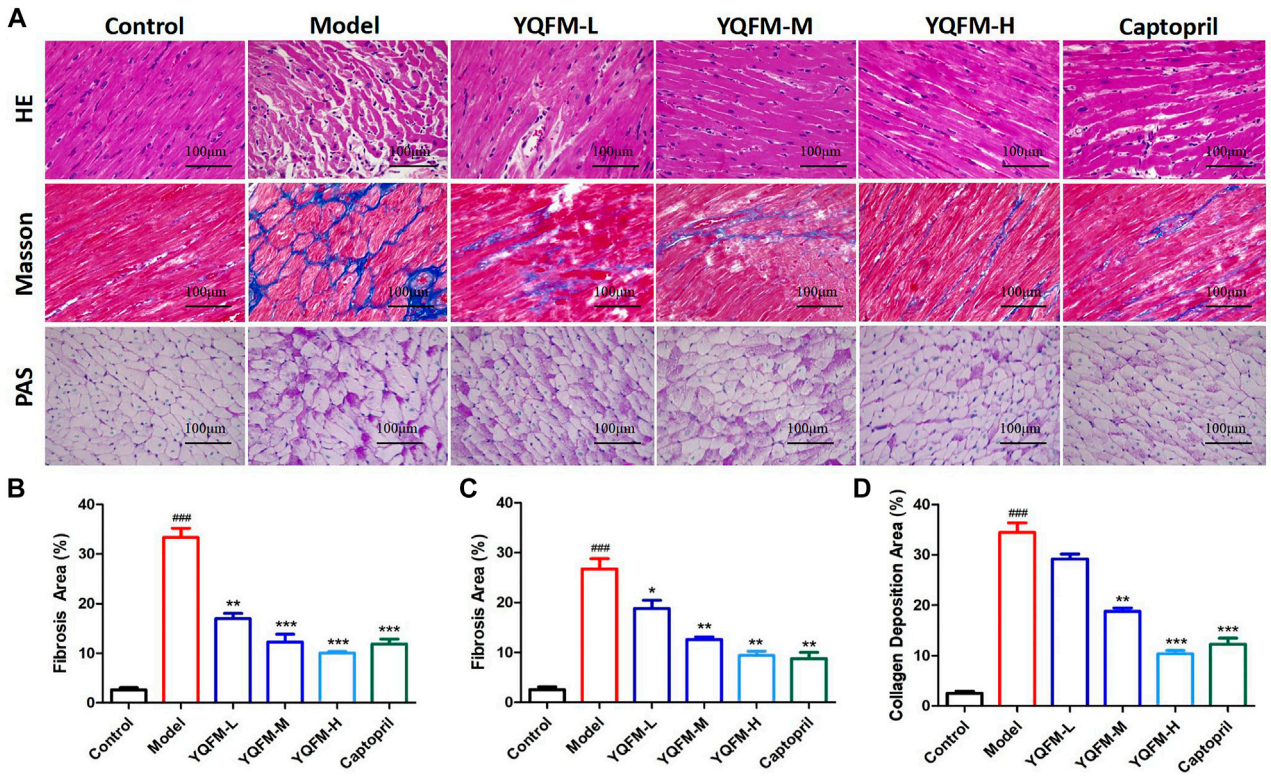

FIGURE 3 | The effect of YQFM on Cardiac Morphology in CHF rat after being treated for 28 d. **(A)** HE, Masson and PAS pathology section **(B–D)** staining of the myocardial. (n = 6 animals/group). Data are means ± SD. $^{\#}p < 0.05$, $^{\#\#}p < 0.01$, $^{\#\#\#}p < 0.001$ vs the Control group, $^{*}p < 0.05$, $^{**}p < 0.01$, $^{***}p < 0.001$ vs the Model group.

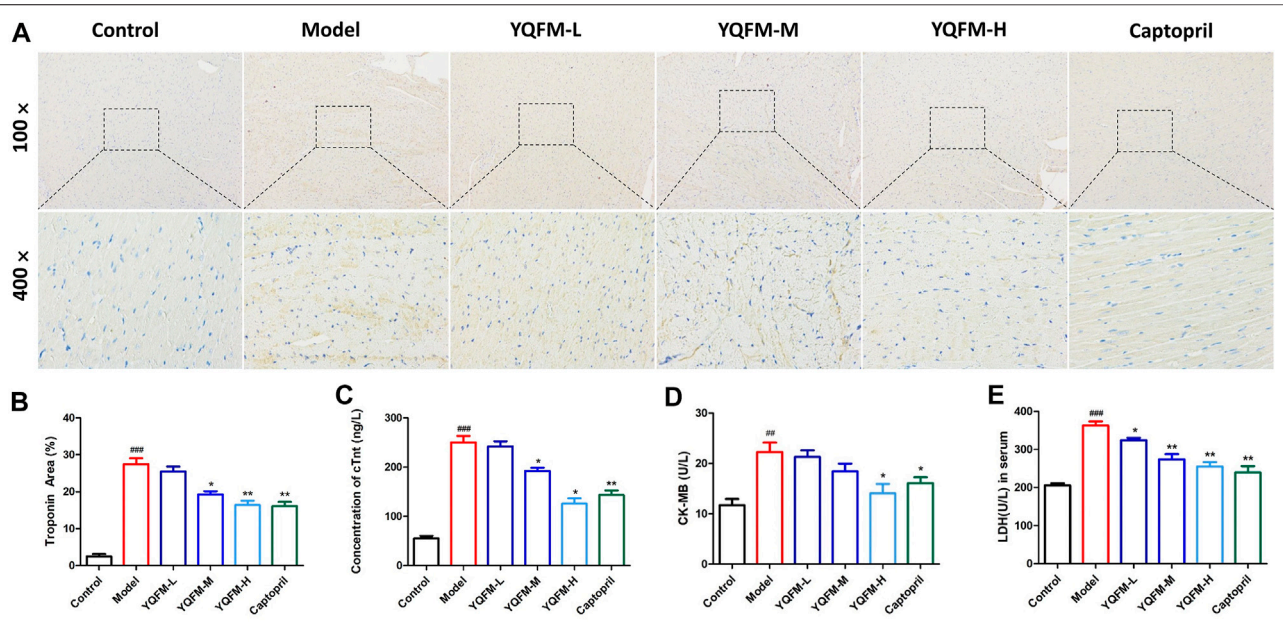

FIGURE 4 | The effect of YQFM on Cardiac Morphology in CHF rat after being treated for 28 days. **(A,B)** Immunohistochemistry analysis of cTnt expression in heart sections of different groups. The diseased areas in the heart are magnified in the panel below (n = 3 per group). Concentration of cTn t **(C)**, CK-MB **(D)** and LDH **(E)** in CHF rat after being treated for 28 days (n = 6 animals/group). Data are means ± SD. $^{*}p < 0.05$, $^{**}p < 0.01$, $^{***}p < 0.001$ vs the Model group, $^{\#}p < 0.05$, $^{\#\#}p < 0.01$, $^{\#\#\#}p < 0.001$ vs the Control group.

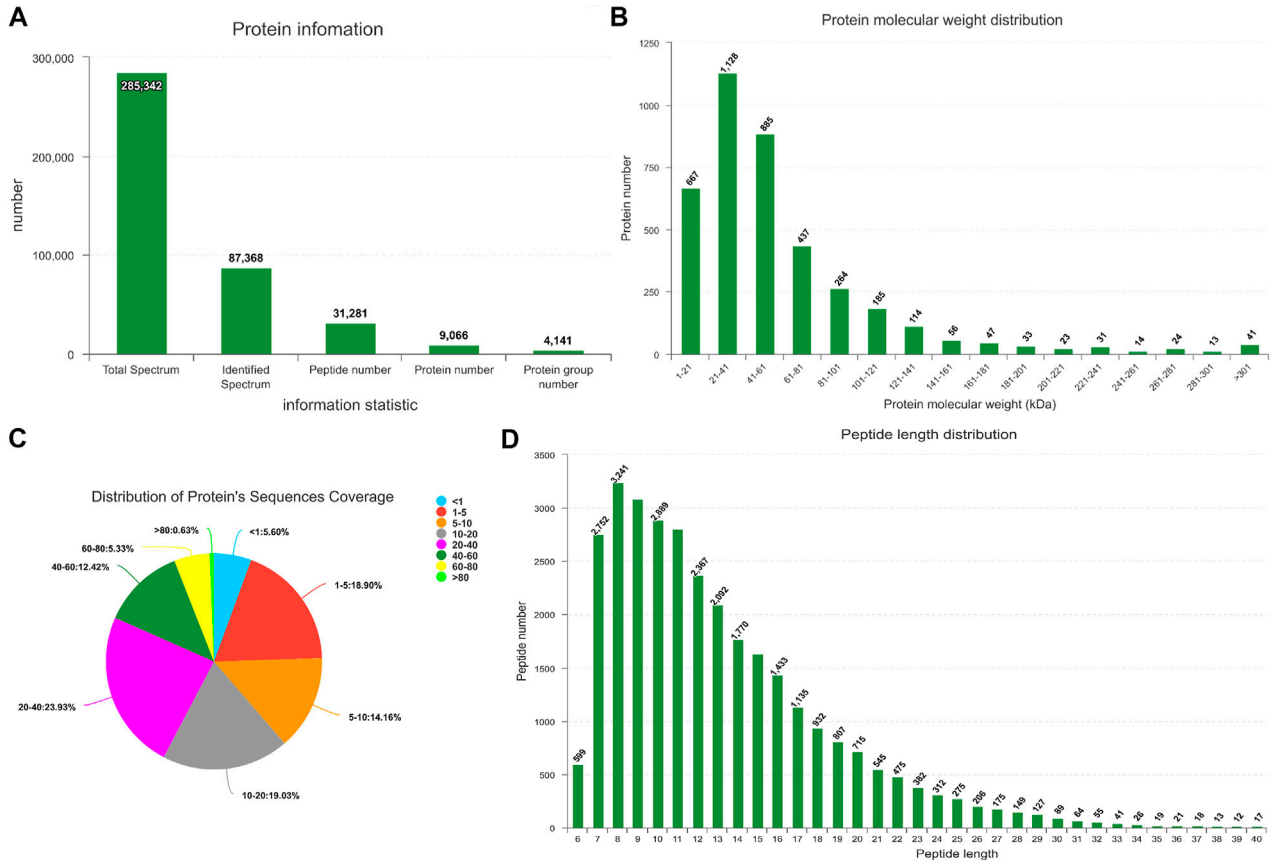

FIGURE 5 | Quality control of protein data validation. **(A)** Protein information. The x-axis in the figure represents the identified protein information, from left to right: the total number of secondary spectra, the number of matched spectra, the number of identified peptides, the number of identified proteins, and the number of identified protein groups. **(B)** Protein mass distribution of all identified proteins. **(C)** Distribution of protein's sequences coverage. **(D)** Protein length distribution of all identified peptides.

acetonitrile were contained in solvent B. Gradient elution: 0–6 min, 0–7% solvent B; 7–68 min, 7–24% solvent B; 69–80 min, 24–29% solvent B; 80–90 min, 29–39% solvent B; 90–94 min, 39–52% solvent B; 94–97 min, 52–100% solvent B; 97–105 min, 100–100% solvent B; and 105–106 min, 0% solvent B. The flow rate was kept at 300 nl/min.

The peptides has passed a nano-electrospray ionization source and then analyzed by Q-Exactive Plus(Thermo, United States)mass spectrometry.The resolution of the primary mass spectrometer is 70,000, AGC target 3e6, the fragmentation method was HCD, and maximum injection time is 20 ms; the secondary resolution was 35,000, AGC target 1e5, the maximum injection time was 50 ms. In the MS investigation scan, the first 20 precursor ions above the threshold ion count 5E4 were scanned once, and then the alternate data dependence program between 20 ms/MS scans was performed, and 18.0 s was excluded dynamically. Automatic gain control was used to prevent the ion trap from being over full. m/z scan range: 350–1300.

Database Search

The software version used by the database was Proteome Discoverer ^{TM} Software 2.2. When searching the database, the original file has been submitted to the Proteome Discoverer server, and then the database was searched in the established database.

Bioinformatics Analysis

Gene Ontology (GO) annotated proteome comes from Genebank database. Then, through GO annotation, proteins were classified according to biological process, cell composition and molecular function. The KEGG database was accustomed to explain the pathways of identified proteins.

Cell Culture and Treatment

H9C2 cells were obtained from the Chinese Academy of Sciences (Shanghai, China). Dulbecco's modified eagle's medium (DMEM) containing 10% (v/v) FBS, 1% (V/V) penicillin-streptomycin solution was used for cell culture, and placed in the incubator at 37°C with a humidified 5% CO_2. To stimulate cardiomyocyte injury, H_2O_2 was used to stimulate H_9C_2 cells. H_9C_2 cells were treated with 45 μg/ml (YQFM-L), 90 μg/ml (YQFM-M) or 180 μg/ml (YQFM-H) YQFM for 24 h.

Transmission Electron Microscopy

H9C2 cells were inoculated on 6-well plates and H_2O_2 was used to cause myocardial cell damage. After 24 h, the cells were treated with YQFM (90 μg/ml) for 24 h. The cultured cells were fixed on 2.5% glutaraldehyde for 1 h respectively with glutaraldehyde,

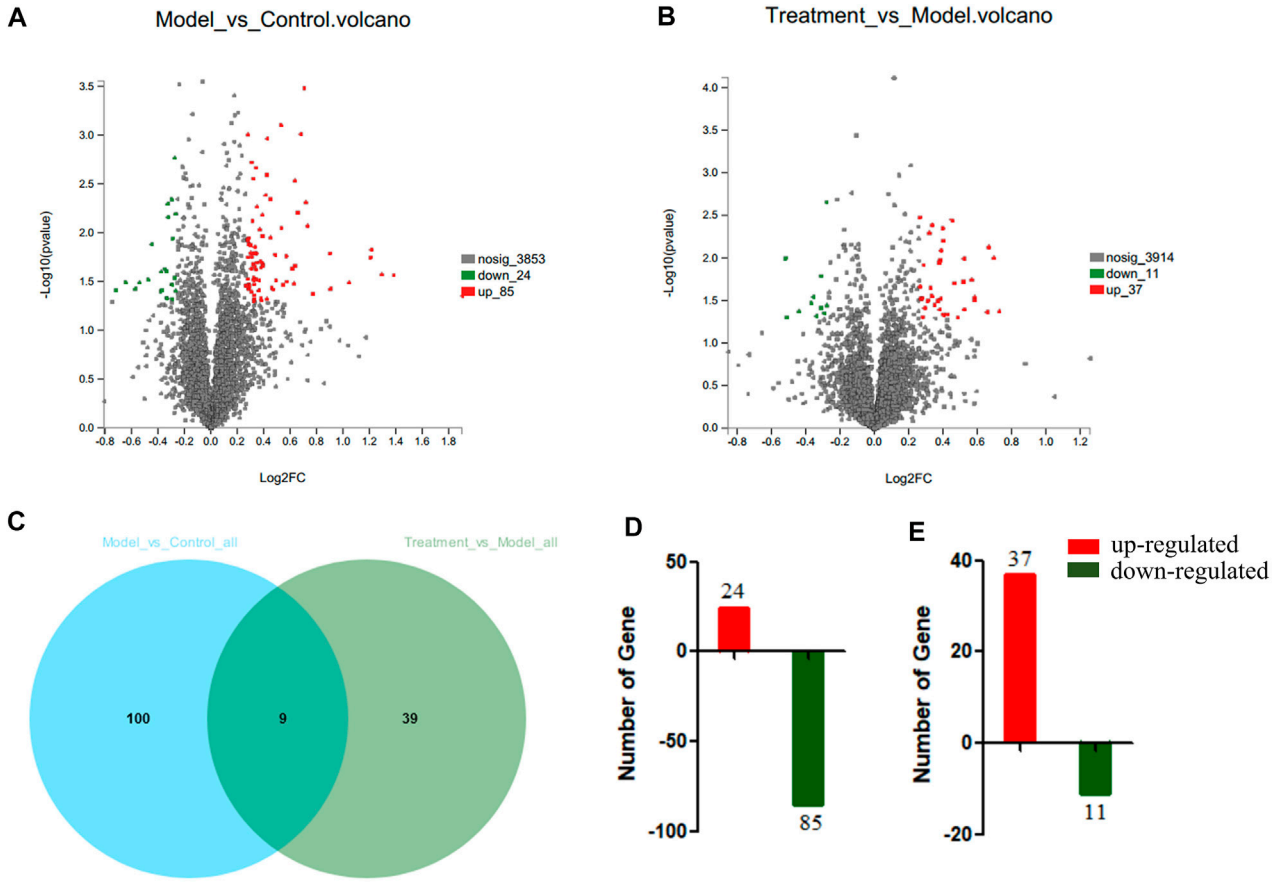

FIGURE 6 | The differentially abundant proteins (DEPs) in serum between Model:Control and Treatment: Model. **(A)** Volcano Plots of DEPs of Model:Control. **(B)** Volcano Plots of DEPs of Treatment:Model. **(C)** Venn-diagram showing the overlap of all DEPs. **(D)** DEPs involved in Model:Control. **(E)** DEPs involved in Treatment: Model. Red or Green represents the numbers of upregulated and downregulated proteins, respectively.

dehydrated, critical-point dried, metal sputtering, and analyzed by TEM at 6,000 × magnification.

Metabolic Assay

H9C2 cells were inoculated in 96-well plates. Except for control group, H_2O_2 was used to simulate myocardial cell injury in other groups. After 24 h, cells were treated with different dose of YQFM (45, 90, and 180 μg/ml) for 24 h. DMEM medium was replaced with 100 μl XF containing 4,500 mg/L glucose. The cells were then incubated in the absence of CO_2 at 37°C for 1 h. According to the manufacturer's agreement, oxygen consumption rate (OCR) was measured by SeaHorse XF96 Extracellular Analyzer as a measure of oxidative metabolism.

Immunofluorescence Staining

After the indicated treatments, H_9C_2 cells were seeded in chamber slides at a density of 1×10^6 cells/well. Take a slice of cardiomyocytes that have been cultured for 24 h. After treated with or without YQFM for 24 h, immunostaining of the cells was carried out with Mitotracker (Thermo Fisher Scientific, Waltham, MA, United States). Incubate with DAPI staining solution for 10 min, and wash with PBS three times; immediately after mounting with anti-fluorescence quenching solution, observe under a confocal microscope.

Apoptosis Assay

FITC-labeled annexin V and propidium iodide staining were used to evaluate the apoptosis of the treated cells, and FACS calibur flow cytometry (Becton Dickinson, United States) was used to examine the level of apoptosis. The cell cycle was subsequently checked using FlowJo software.

Western Blot Analysis

The left ventricular protein was extracted with RIPA lysate containing protease inhibitors, and the protein concentration was determined by BCA method. The SDS-PAGE was performed, electrophoresed to nitrocellulost membrane, and blocked with 5% bovine serum albumin for 1 h. Next, antibodies and dilutions as follows: Bax (Abcam, ab32503, rabbit), Bcl-2 (Abcam, ab182858, rabbit), PGC-1α (Abcam, ab176328, rabbit), PPAR-α (Abcam, ab245119, rabbit), RXR-α (Abcam, ab125001, rabbit), NRF-1 (Abcam, ab55744, rabbit) and Tfam (Abcam, ab176558, rabbit).The fluorescently labeled secondary antibodies are then conjugated by incubation. The blotted proteins were examined

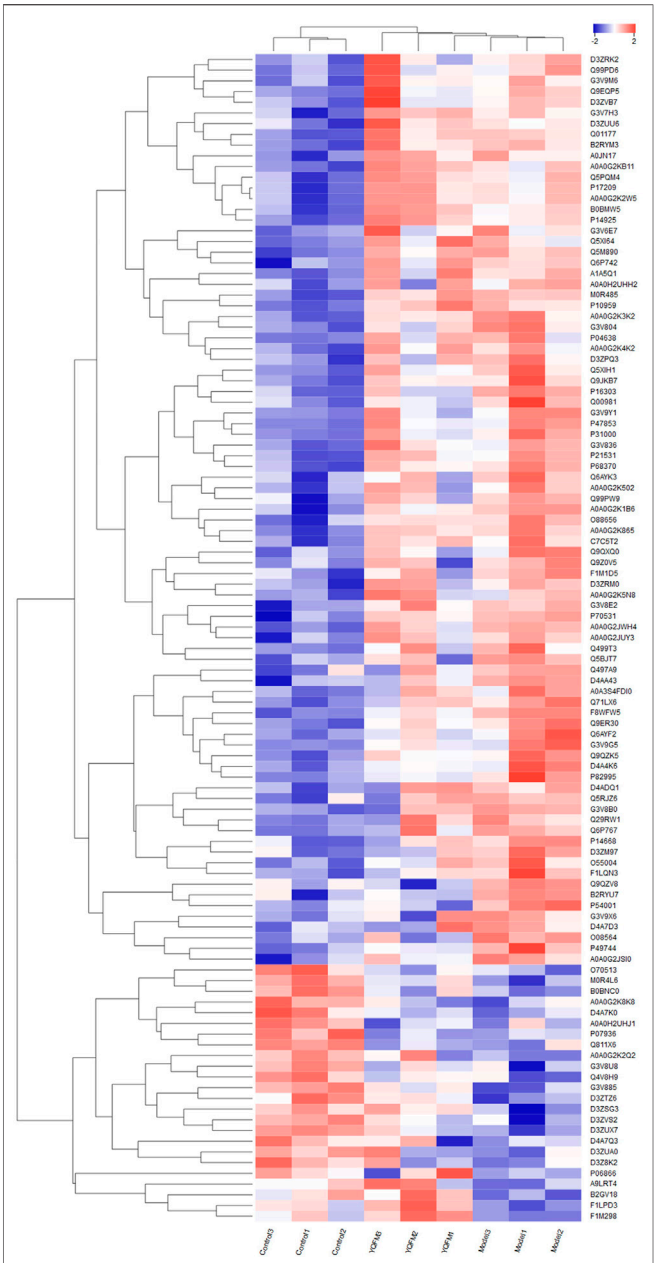

FIGURE 7 | Cluster analysis of differentially expressed proteins among the three groups. Color changes with protein expression, blue indicates negative correlation, red indicates positive correlation, the stronger the color, the strongest correlation.

and quantified on the Odyssey Infrared Imaging system. The ratio of the target protein to the internal reference protein β-actin reflects the relative expression of the protein.

Statistical Analyses

All data are expressed as the means ± SD. GraphPad Prism statistical software was used for analysis, and one-way analysis of variance was used for comparison between groups; $p < 0.05$ was considered statistically significant.

RESULTS

Analysis of Chemical Components of Yiqi Fumai Lyophilized Injection

In order to detect the chemical constituents of YQFM, an HPLC method was established. After analyzing the HPLC of YQFM standard solution and sample solution (**Figures 1A,B**). A total of 14 compounds were identified from YQFM.

Effects of Yiqi Fumai Lyophilized Injection on Cardiac Dysfunction in Chronic Heart Failure Rat

As indicated on the **Figure 2A**, echocardiography was used as a method to assess cardiac function. Compared with the control group, the titers of left ventricular rejection fraction (LVEF) and left ventricular shortening fraction (LVFS) in the model group were significantly decreased by 30 and 23%, respectively, indicating that the AAC model was successfully constructed. Notably, in CHF rat administered YQFM LVEF% and LVFS% were effectively restored to normal levels, respectively (**Figures 2B,C**).

Effects of Yiqi Fumai Lyophilized Injection on Cardiac Morphology in Chronic Heart Failure Rat

In order to examine the therapeutic efficiency of YQFM against CHF *in vivo*, we applied YQFM to rats with cardiac dysfunction. At 28 days after treatment, the effect of YQFM was examined by histological evaluation of cardiac tissue. After YQFM treatment, myocardial cell interstitial edema, intracellular space enlargement and vacuolization, and inflammatory cell infiltration were alleviated (**Figures 3A,B**). Compared with the model group and captopril group, less sedimentary fiber was observed in LV as a result of YQFM treatment. It demonstrates a significantly reduced level of scar tissue (**Figures 3A,C**). PAS staining was consistent with Masson's results (**Figures 3A, D**). Less sedimentary collagen was observed in LV after YQFM treatment.

Effects of Yiqi Fumai Lyophilized Injection on the Biochemical Parameters of Chronic Heart Failure Rat

To elucidate cardiac function, the cTnt titer was determined by immunohistochemical evaluation. The results are indicated in **Figures 4A,B**, indicating that the model groups treated by YQFM show a significant reduction. Considering the absolutely heart tissue specificity, cTnt, CK-MB, and LDH were used as the primary biometric characteristics for the diagnosis of cardiac damage. Changes in the concentrations of cTnt, CK-MB and LDH can describe the severity of myocardial injury. Our data show that cTnt, CK-MB and LDH concentrations were lower in the YQFM processing arm than in the model (AAC) group (**Figures 4C–E**). It implied that YQFM treatment could reduce the degree of damage and the necrosis of myocardial tissue in rats with heart failure.

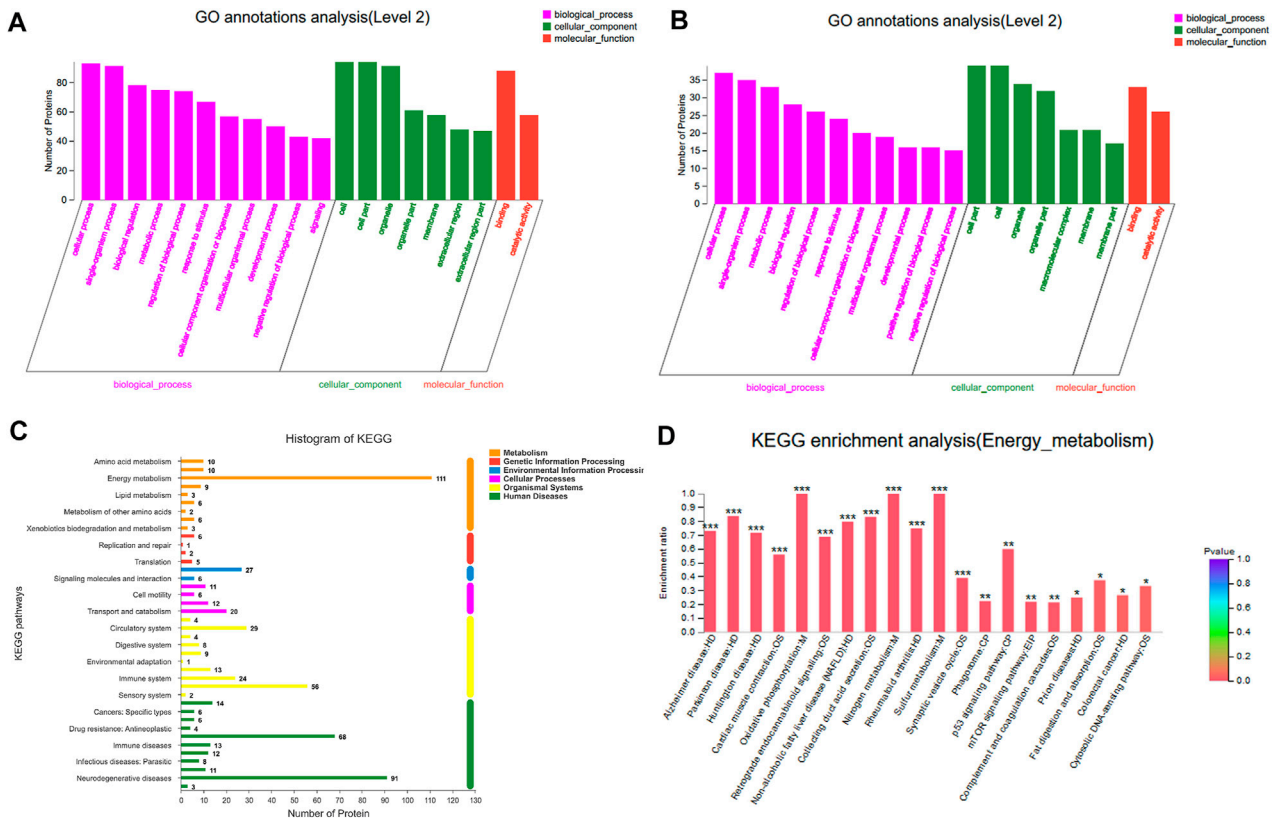

FIGURE 8 | Functional annotation and categories of DEPs. **(A)** GO annotations analisis of Model:Control. **(B)** GO annotations analisis of Treatment:Model. **(C)** KEGG analyses of protein functions. **(D)** Enrichment analysis of KEGG energy metabolism pathway.

LC-MS/MS

In this study, iTRAQ technology was used to analyze the proteomic characteristics of heart tissue. 9,066 proteins in total were identified (**Figure 5A**). The quality control of protein data revealed that the molecular weight of the protein was in the range of 1–100 kDa (**Figures 5B,C**), and many peptides were between 7 and 14 amino acids in length (**Figure 5D**).

Identification of Differentially Expressed Proteins in Heart Tissue of Yiqi Fumai Lyophilized Injection-Treated Rat

To probe the mechanisms of YQFM, the MaxQuant was used to obtain the general summary of proteomics change in Model: Control and Treatment: Model. The ratio of Model: Control and Treatment: Model was compared to probe changes in key protein expression among the three groups (**Figures 6A,B**) ($p < 0.05$). 148 DEPs are displayed in a Venn diagram (**Figure 6C**). At the same time, 109 differentially accumulated proteins were explicated in Model: Control, 84 of which were down regulated and 24 were up regulated. 48 proteins were explicated in Treatment: Model, of which 11 were down regulated and 37 were up-regulated (**Figures 6D,E**).

Clustering Analysis

The results of hierarchical clustering were shown in a heat map, where blue means down regulation and red means up regulation. The difference in protein expression observed between the groups were displayed in **Figure 7**. It was clear that the overall protein expression pattern in the model and treatment groups was different from that in the control group. In the model group, many proteins showed a down regulated expression pattern (blue band), while in the control and treatment groups, many proteins were up regulated.

Function Notes and Categories of Differentially Expressed Proteins

To better explore the biological correlation of protein expression changes and retrieve information about biological processes or pathways, the identified DEPs have been analyzed by bioinformatics methods. From the GO analysis results (**Figures 8A,B**), it can be seen that in the biological process analysis, 157 differentially expressed proteins were mainly distributed in the metabolic process, cellular process and single-organism process. In the cell location analysis among them, most proteins were mainly concentrated in the three types of cells, cell parts and organelles. As far as molecular functions were concerned, proteins related to catalytic activity and binding dominate most.

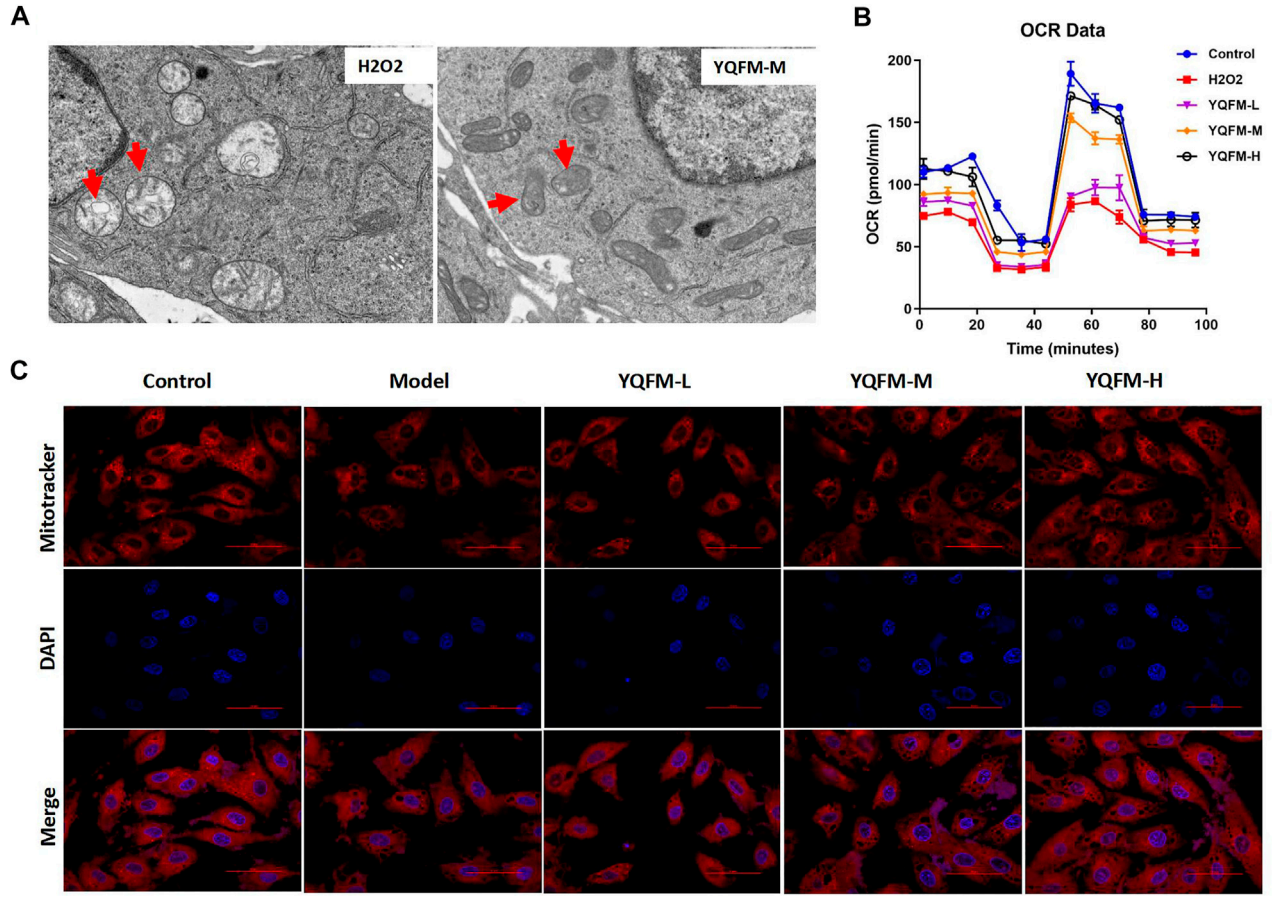

FIGURE 9 | YQFM ameliorated the mitochondrial dysfunction induced by H_2O_2 *in vitro*. **(A)** TEM images of the ultrastructural morphology of H_9C_2 cells mitochondria. **(B)** Oxygen consumption rates (OCR) in H_9C_2 cells treated with YQFM-L, YQFM-M& YQFM-H. **(C)** H_9C_2 cells were subjected to Mitotracker red staining. The model group refers to H_9C_2 cells induced by H_2O_2.

In order to further explore the biological pathway in response to YQFM protection, KEGG pathway annotation was used to explore all DEPs (**Figures 8C,D**). The results showed that most proteins were enriched in energy metabolism pathway. Metabolic pathway analysis was performed on the proteins in the obtained energy metabolism pathway. As shown in the figure, the oxidative phosphorylation pathway apparently plays a very important role in treatment.

Effects of Yiqi Fumai Lyophilized Injection on H_2O_2 Induced Mitochondrial Dysfunction *In Vitro*

Next, we investigated effects of YQFM on the mitochondrial dysfunction by using TEM, Metabolic assay, and Mitotracker staining. The ultrastructural morphology of mitochondria in H9C2 cells was observed by conventional TEM (**Figures 9A,B**). After hypoxia, the mitochondria of cardiomyocytes swelled, the number of mitochondria decreased, and the mitochondrial matrix appeared cristae and vacuole-like phenomena. After YQFM treatment, the damage of cardiomyocyte mitochondria was significantly reduced. We detected the effect of YQFM on OCR in H_9C_2 cells with H_2O_2 stimulation. OCR was significantly reduced in H_9C_2 cells stimulated by H_2O_2, all of which were ameliorated by YQFM. We also found that mitochondrial content of H_9C_2 cells was increased significantly after 24 h of YQFM treatment with 180 μg/ml, determined by the red fluorescence intensity and mitochondrial size of the mitotracker (**Figure 9C**). All of these results implied that YQFM ameliorated mitochondrial function in H_9C_2 cells stimulated by H_2O_2.

Effect of Yiqi Fumai Lyophilized Injection on Apoptosis of Cardiomyocytes Induced by H_2O_2 *In Vitro*

In the process of oxidative phosphorylation, the imbalance of intracellular ROS levels will lead to oxidative stress and ultimately lead to cell apoptosis. Therefore, we hypothesized

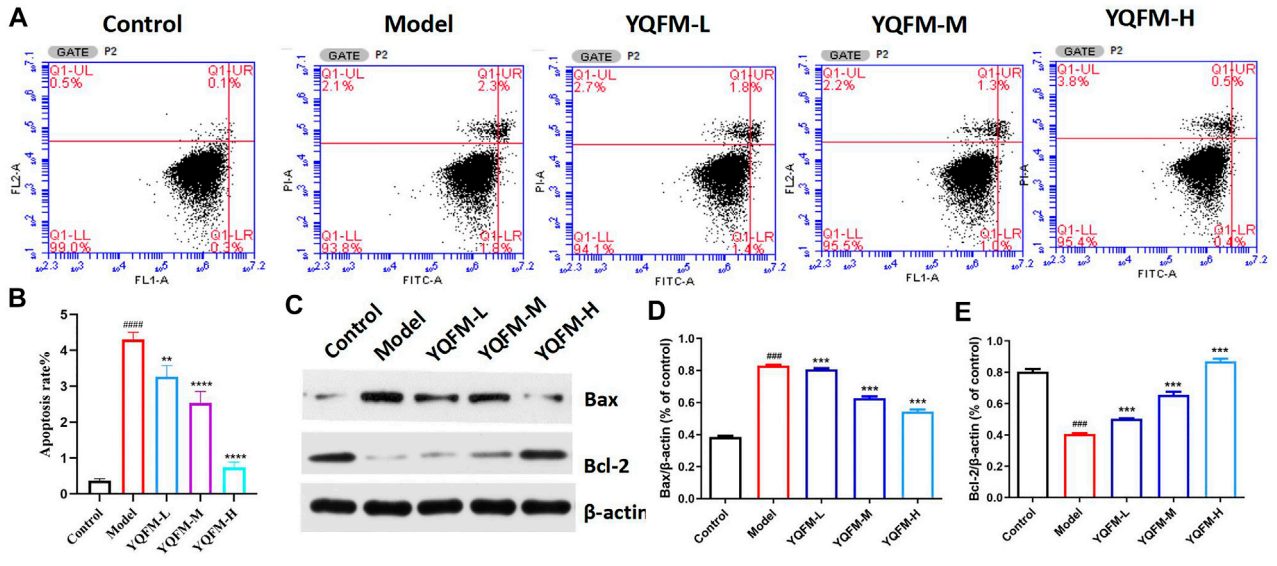

FIGURE 10 | YQFM suppressed cardiomyocyte apoptosis caused by H_2O_2. **(A,B)** Flow cytometric measurement of H9C2 cells apoptosis caused by H2O2. **(C)** The amount of Bax and Bcl-2 from H9C2 cells lysate was examined by Western blot analysis. **(D,E)** Relative protein levels were measured by densitometry for Bax and Bcl-2 (n = 3 per group). Data are means ± SD. $^{*}p < 0.05$, $^{**}p < 0.01$, $^{***}p < 0.001$ vs the Model group, $^{\#}p < 0.05$, $^{\#\#}p < 0.01$, $^{\#\#\#}p < 0.001$ vs the Control group.

that YQFM may improve mitochondrial function by inhibiting apoptosis. In this study, the flow cytometry and Western blot were used to evaluate the effect of YQFM on cell apoptosis. Research results indicated that YQFM significantly inhibited H2O2 induced apoptosis (**Figure 10A**), accompanied by decreased Bax cleavage and increased bcl-2 expression (**Figures 10B–D**).

Effects of Yiqi Fumai Lyophilized Injection on Mitochondrial Biogenesis-Related Proteins *In Vitro*

To determine the molecular mechanisms of mitochondrial dysfunction enhancement through YQFM treatment, we detected the expression of mitochondrial biogenic related proteins by Western blot (**Figure 11A**). Since previous studies have described the key role of PGC-1 α in regulating mitochondrial biogenesis, the 24-hour treatment with YQFM of 180 μg/ml can lead to a significant increase the expression of PGC-1 α. Western blot analysis further corroborated the regulatory effect of YQFM on PGC-1 α (**Figure 11B**). PGC-1α and PPAR-α/RXR-α jointly regulate the increase of mitochondrial activity to coordinate mitochondrial biogenesis, so YQFM-treated cardiomyocytes displayed significant increase in all of these proteins (**Figures 11C,D**).

In H_9C_2 cells treated with 180 μg/ml YQFM, NRF-1, the downstream target of PGC-1 α, was also increased at 24 h, while Tfam, the downstream target of NRF-1 and mitochondrial DNA expression regulator, had similar changes with NRF-1 (**Figure 11H**). These results revealed that YQFM treatment increased mitochondrial content by activating PGC-1 α and activating mitochondrial biogenesis related proteins.

DISCUSSION

The incidence of CHF greatly increased with the aging of the world population. (Yancy et al., 2013) Hence, seeking safe and effective therapy has become a common concern in the global medical community and has been widely concerned. Current clinical studies have indicated that YQFM could availably alleviate the clinical symptoms of CHF patients (Nie et al., 2020). At the same time, studies have shown that YQFM can improve heart failure through a variety of ways (Li et al., 2019; Zhang et al., 2019). Notwithstanding, the exact mechanism of action remains to be explored in depth. In this research, we used a proteomic based method to investigate the mechanism of YQFM in ACC model rats and on H_9C_2 cells, and developed a better understanding of YQFM.

CHF is a syndrome caused by the inability of the heart pump to meet the body's energy needs (Bertero and Maack, 2018). Despite a lot of work, the pathogenesis of cardiomyocyte abnormalities caused by CHF is still not fully understood. Factors that cause abnormal contraction and relaxation of heart failure include abnormal metabolic pathways that lead to energy production, energy transfer, and reduced energy utilization (Zhou and Tian, 2018). CHF also affects the surroundings. Early muscle fatigue and motor intolerance are always present in CHF patients, in which the reduction of mitochondrial ATP production and energy transfer through phosphotransferase kinase play an important role.

Yiqi Fumai for injection is mainly extracted from the traditional Chinese medicine red ginseng, Ophiopogon japonicus and Schisandra. Its active ingredients are diverse, and it has the advantages of multiple pathways, multiple targets, and safety and effectiveness. Therefore, YQFM may

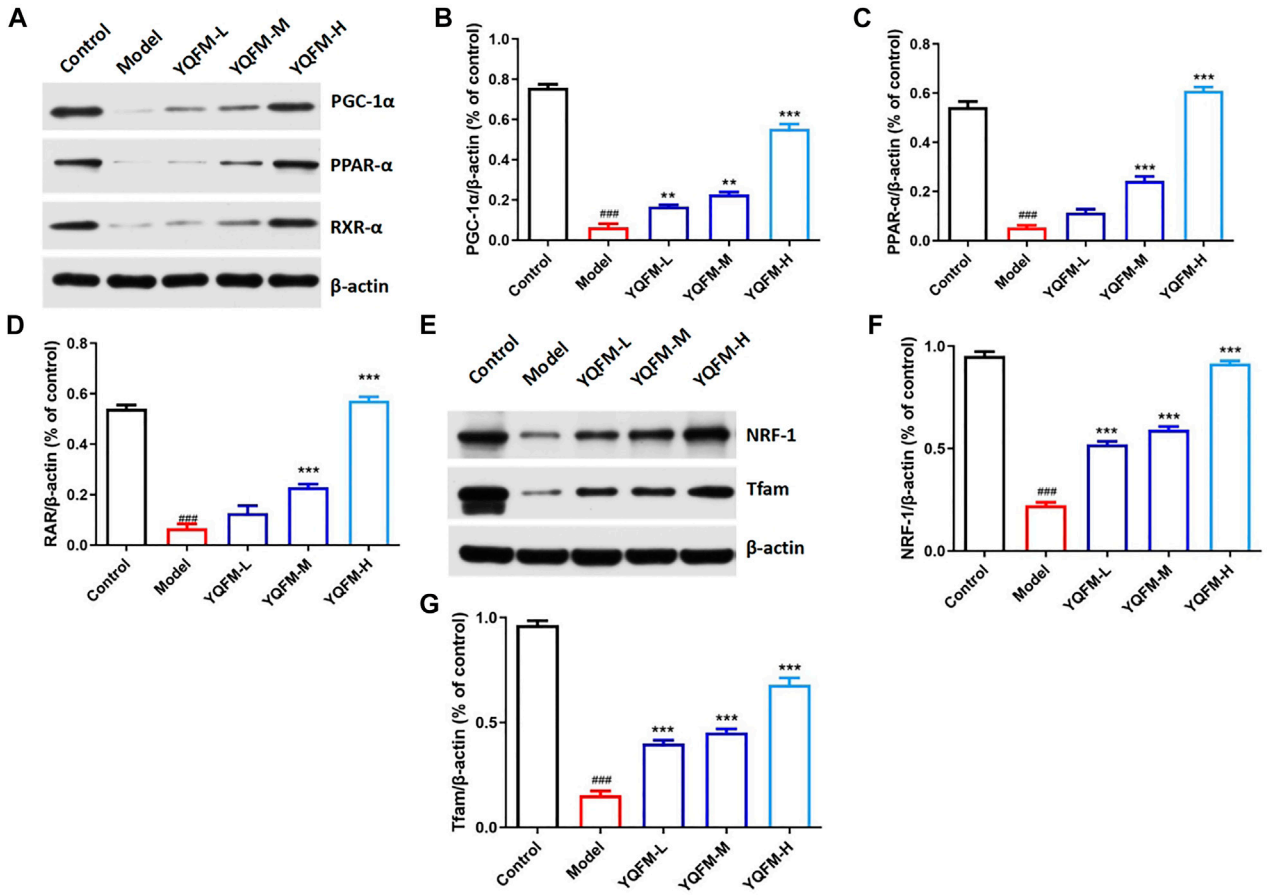

FIGURE 11 | YQFM upregulated mitochondrial biogenesis-related genes with PGC-1α activation. **(A)** The amount of PGC-1α,PPAR-α and RXR-α from H9C2 cells lysate was examined by Western blot analysis. **(B–D)** Relative protein levels were measured by densitometry for PGC-1α,PPAR-α and RXR-α. **(E)** The amount of NRF-1 and Tfam from H9C2 cells lysate was examined by Western blot analysis. **(F,G)** Relative protein levels were measured by densitometry for NRF-1 and Tfam (n = 3 per group). Data are means ± SD. $^{*}p < 0.05$, $^{**}p < 0.01$, $^{***}p < 0.001$ vs the Model group, $^{\#}p < 0.05$, $^{\#\#}p < 0.01$, $^{\#\#\#}p < 0.001$ vs the Control group.

also have a certain regulatory effect on myocardial energy. Studies have shown that YQFM ginsenoside Rb1, ginsenoside Rb3, ginsenoside Rg1, ginsenoside Rg3, Schizandrin B, Ophiopogonin D and other natural products can regulate energy metabolism by increasing the activity of mitochondria. In 3T3-L1 mature adipocytes, ginsenoside Rb1 can activates the mRNA expression of PGC-1α, UPC-1 and PRDM16, which in turn increased basal glucose uptake and promoted browning (Mu et al., 2015; Park et al., 2019). Ginsenoside Rb3 can regulates energy metabolism and apoptosis of cardiac myocytes by activating PPAR α pathway (Chen et al., 2019).

Ginsenoside Rg1 can protect cardiomyocytes from Hypoxia/reperfusion (H/R) by regulating GDH and MFN2 to maintain mitochondrial dynamics (Dong et al., 2016). Ginsenoside Rg3 activates PGC-1α and Nrf2 in rat myocardium, and the mRNA levels of Tfam and NRF-1 downstream of PGC-1α are enhanced (Sun et al., 2013). Schizandrin B improves mitochondrial function in damaged myocardium (Chiu et al., 2007; Chen and Ko, 2010). Ophiopogonin D intervention can reduce lipid accumulation and mitochondrial damage of heart and cardiomyocytes stimulated by palmitic acid in diabetic mice (Li et al., 2021). The enhanced mitochondrial function of these natural products is helpful to support the protective effect of YQFM on CHF.

It is well known that cTnT is the main feature of myocardial injury in CHF (Barberi and van den Hondel, 2018). The results of heart histopathology and cTn t showed that YQFM could reverse myocardial injury and alleviate CHF. In proteomics analysis, 157 DEPs was identified. GO clearly confirmed that the DEPs of Model: Control and Treatment: Model participated in various biological processes. KEGG pathway results showed that most proteins were significantly enriched in the energy metabolism pathway, especially in oxidative phosphorylation pathway.

In the process of oxidative phosphorylation, the electrons escaping from the mitochondrial electron transport chain react with oxygen to form O_2 (Saybaşili et al., 2001).Convert it into hydrogen peroxide and other reactive oxygen species (ROS).The imbalance of intracellular ROS levels can cause oxidative stress,

leading to DNA damage and eventually apoptosis. And our results demonstrate that YQFM inhibited cardiomyocyte apoptosis, improved the vacuolation state of mitochondria in cardiomyocytes, examined oxidative metabolism, and H_9C_2 cells mitochondrial content was significantly increased. This result further shows that YQFM can improve mitochondrial function through oxidative phosphorylation.

Mitochondria are cardinal for the survival of cardiomyocytes and the maintenance of normal heart function (Hammerling and Gustafsson, 2014). More and more evidences show that mitochondrial dysfunction can cause CHF, which indicates that there is a close relationship between mitochondrial biology and heart function (Aubert et al., 2013; Wang et al., 2015b; Tao et al., 2015). Studies have shown that PGC-1α is a key molecule of mitochondria, and PGC-1α is involved in mitochondrial energy metabolism and plays a key role in oxidative stress and inflammation (Jeganathan et al., 2017). PGC-1α is an important synergistic factor of PPAR/RXR (Warren et al., 2018), which regulates the metabolism of lipids and sugars by acting with PPAR/RXR. In addition to its action with PPARs, PGC-1α mainly binds to two other transcription factors to regulate the function of cardiac mitochondria. That is, activation of PGC-1α protein can activate downstream transcription factors like NRFs and Tfam, thereby promoting mitochondrial biosynthesis. At the same time, it promotes physiological processes such as glucose utilization and fatty acid oxidation (Huang et al., 2017). In our study, the expressions of PGC-1α, PPAR-α and RXR-α were up regulated in cells treated with YQFM for 180 μg/ml for 24 h, and PGC-1 α and its downstream effectors, including NRF-1 and TFAM, were also found to be up regulated in cardiac myocytes.

These results provide evidence that YQFM could enhance mitochondrial function and improve mitochondrial energy metabolism of cardiomyocytes by regulating PGC-1α and its related proteins.

CONCLUSION

In summary, we performed proteomic characteristics of heart tissue analysis of protein expression in heart tissue of AAC rats treated with YQFM using an iTRAQ technology. A total of 157 important DEPs were identified, including 109 in M: C and 48 in T: M. Intensive bioinformatics analysis identified metabolic process, cellular process and single-organism process as significant biological processes. The oxidative phosphorylation process were mainly involved, especially the mitochondrial PGC-1α signaling pathway. In general, the results of this study were helpful to understand of the mechanisms of YQFM. In addition, this work demonstrated the potential application of the iTRAQ technique in Anti-CHF studies.

DATA AVAILABILITY STATEMENT

The datasets presented in this study can be found in online repositories. The names of the repository/repositories and accession number(s) can be found below: ProteomeXchange (https://www.ebi.ac.uk/pride/archive/login) via the PRIDE repository with the dataset identifier PXD027442.

ETHICS STATEMENT

All procedures were conducted in accordance with the "Guiding Principles in the Care and Use of Animals" and were approved by The Institutional Animal Care and Use Committee of Tianjin Medical University (SYXK-2014-0002).

AUTHOR CONTRIBUTIONS

YZ and XH conceived and designed the experiments. CL and WG provided technical support. YZ, XH, OQ, and HJ performed all the experiments. XZ, WW, JW, and XL analyzed the data. DL and AJ provided material support. All authors read and approved the final manuscript.

FUNDING

This work was supported by National Natural Science Foundation of China (No. 81673535); the Science and Technology project of Tianjin (NO. 18ZXXYSY00080).

SUPPLEMENTARY MATERIAL

The Supplementary Material for this article can be found online at: https://www.frontiersin.org/articles/10.3389/fphar.2021.719532/full#supplementary-material

REFERENCES

Aubert, G., Vega, R. B., and Kelly, D. P. (2013). Perturbations in the Gene Regulatory Pathways Controlling Mitochondrial Energy Production in the Failing Heart. *Biochim. Biophys. Acta* 1833, 840–847. doi:10.1016/j.bbamcr.2012.08.015

Barberi, C., and van den Hondel, K. E. (2018). The Use of Cardiac Troponin T (cTnT) in the Postmortem Diagnosis of Acute Myocardial Infarction and Sudden Cardiac Death: A Systematic Review. *Forensic Sci. Int.* 292, 27–38. doi:10.1016/j.forsciint.2018.09.002

Bertero, E., and Maack, C. (2018). Metabolic Remodelling in Heart Failure. *Nat. Rev. Cardiol.* 15, 457–470. doi:10.1038/s41569-018-0044-6

Bertinchant, J. P., Robert, E., Polge, A., Marty-Double, C., Fabbro-Peray, P., Poirey, S., et al. (2000). Comparison of the Diagnostic Value of Cardiac Troponin I and T Determinations for Detecting Early Myocardial Damage and the Relationship with Histological Findings after Isoprenaline-Induced Cardiac Injury in Rats. *Clin. Chim. Acta* 298, 13–28. doi:10.1016/s0009-8981(00)00223-0

Boersema, P. J., Raijmakers, R., Lemeer, S., Mohammed, S., and Heck, A. J. (2009). Multiplex Peptide Stable Isotope Dimethyl Labeling for Quantitative Proteomics. *Nat. Protoc.* 4, 484–494. doi:10.1038/nprot.2009.21

Chen, N., and Ko, M. (2010). Schisandrin B-Induced Glutathione Antioxidant Response and Cardioprotection Are Mediated by Reactive Oxidant Species Production in Rat Hearts. *Biol. Pharm. Bull.* 33, 825–829. doi:10.1248/bpb.33.825

Chen, X., Wang, Q., Shao, M., Ma, L., Guo, D., Wu, Y., et al. (2019). Ginsenoside Rb3 Regulates Energy Metabolism and Apoptosis in Cardiomyocytes via Activating PPARα Pathway. *Biomed. Pharmacother.* 120, 109487. doi:10.1016/j.biopha.2019.109487

Chiu, P. Y., Leung, H. Y., Siu, A. H., Poon, M. K., and Ko, K. M. (2007). Schisandrin B Decreases the Sensitivity of Mitochondria to Calcium Ion-Induced Permeability Transition and Protects against Ischemia-Reperfusion Injury in Rat Hearts. *Acta Pharmacol. Sin* 28, 1559–1565. doi:10.1111/j.1745-7254.2007.00614.x

Cops, J., Haesen, S., De Moor, B., Mullens, W., and Hansen, D. (2019). Current Animal Models for the Study of Congestion in Heart Failure: an Overview. *Heart Fail. Rev.* 24, 387–397. doi:10.1007/s10741-018-9762-4

Dong, G., Chen, T., Ren, X., Zhang, Z., Huang, W., Liu, L., et al. (2016). Rg1 Prevents Myocardial Hypoxia/reoxygenation Injury by Regulating Mitochondrial Dynamics Imbalance via Modulation of Glutamate Dehydrogenase and Mitofusin 2. *Mitochondrion* 26, 7–18. doi:10.1016/j.mito.2015.11.003

Faris, R., Flather, M. D., Purcell, H., Poole-Wilson, P. A., and Coats, A. J. (2012). Diuretics for Heart Failure. *Cochrane Database Syst. Rev.* (2), CD003838. doi:10.1002/14651858.CD003838

Feng, Y. Q., Ju, A. C., Liu, C. H., Wang, T., Yu, B. Y., and Qi, J. (2016). Protective Effect of the Extract of Yi-Qi-Fu-Mai Preparation on Hypoxia-Induced Heart Injury in Mice. *Chin. J. Nat. Med.* 14, 401–406. doi:10.1016/S1875-5364(16)30035-8

Fu, S., Zhang, J., Gao, X., Xia, Y., Ferrelli, R., Fauci, A., et al. (2010). Clinical Practice of Traditional Chinese Medicines for Chronic Heart Failure. *Heart Asia* 2, 24–27. doi:10.1136/ha.2009.001123

Giannitsis, E., and Katus, H. A. (2013). Cardiac Troponin Level Elevations Not Related to Acute Coronary Syndromes. *Nat. Rev. Cardiolcardiology* 10, 623–634. doi:10.1038/nrcardio.2013.129

Hammerling, B. C., and Gustafsson, Å. B. (2014). Mitochondrial Quality Control in the Myocardium: Cooperation between Protein Degradation and Mitophagy. *J. Mol. Cel Cardiol* 75, 122–130. doi:10.1016/j.yjmcc.2014.07.013

Heo, S., Doering, L. V., Widener, J., and Moser, D. K. (2008). Predictors and Effect of Physical Symptom Status on Health-Related Quality of Life in Patients with Heart Failure. *Am. J. Crit. Care* 17, 124–132. doi:10.4037/ajcc2008.17.2.124

Huang, T. Y., Zheng, D., Houmard, J. A., Brault, J. J., Hickner, R. C., and Cortright, R. N. (2017). Overexpression of PGC-1α Increases Peroxisomal Activity and Mitochondrial Fatty Acid Oxidation in Human Primary Myotubes. *Am. J. Physiol. Endocrinol. Metab.* 312, E253–E263. doi:10.1152/ajpendo.00331.2016

Jeganathan, J., Saraf, R., Mahmood, F., Pal, A., Bhasin, M. K., Huang, T., et al. (2017). Mitochondrial Dysfunction in Atrial Tissue of Patients Developing Postoperative Atrial Fibrillation. *Ann. Thorac. Surg.* 104, 1547–1555. doi:10.1016/j.athoracsur.2017.04.060

Li, F., Pang, L. Z., Zhang, L., Zhang, Y., Zhang, Y. Y., Yu, B. Y., et al. (2019). YiQiFuMai Powder Injection Ameliorates Chronic Heart Failure through Cross-Talk between Adipose Tissue and Cardiomyocytes via Up-Regulation of Circulating Adipokine Omentin. *Biomed. Pharmacother.* 119, 109418. doi:10.1016/j.biopha.2019.109418

Li, F., Zheng, X., Fan, X., Zhai, K., Tan, Y., Kou, J., et al. (2016). YiQiFuMai Powder Injection Attenuates Ischemia/Reperfusion-Induced Myocardial Apoptosis through AMPK Activation. *Rejuvenation Res.* 19, 495–508. doi:10.1089/rej.2015.1801

Li, W., Ji, L., Tian, J., Tang, W., Shan, X., Zhao, P., et al. (2021). Ophiopogonin D Alleviates Diabetic Myocardial Injuries by Regulating Mitochondrial Dynamics. *J. Ethnopharmacol.* 271, 113853. doi:10.1016/j.jep.2021.113853

Liu, J., Xu, B., Liu, Z., Dong, M., Mao, J., Zhou, Y., et al. (2017). Specific Mixing Facilitates the Comparative Quantification of Phosphorylation Sites with Significant Dysregulations. *Anal. Chim. Acta* 950, 129–137. doi:10.1016/j.aca.2016.10.044

Luo, T., Chen, B., and Wang, X. (2015). 4-PBA Prevents Pressure Overload-Induced Myocardial Hypertrophy and Interstitial Fibrosis by Attenuating Endoplasmic Reticulum Stress. *Chem. Biol. Interact* 242, 99–106. doi:10.1016/j.cbi.2015.09.025

Mosterd, A., and Hoes, A. W. (2007). Clinical Epidemiology of Heart Failure. *Heart* 93, 1137–1146. doi:10.1136/hrt.2003.025270

Motoyama, A., and Yates, J. R., 3rd (2008). Multidimensional LC Separations in Shotgun Proteomics. *Anal. Chem.* 80, 7187–7193. doi:10.1021/ac8013669

Mu, Q., Fang, X., Li, X., Zhao, D., Mo, F., Jiang, G., et al. (2015). Ginsenoside Rb1 Promotes browning through Regulation of PPARγ in 3T3-L1 Adipocytes. *Biochem. Biophys. Res. Commun.* 466, 530–535. doi:10.101610.1016/j.bbrc.2015.09.064

Nie, H., Li, S., Liu, M., Zhu, W., Zhou, X., and Yan, D. (2020). Yiqi Fumai Injection as an Adjuvant Therapy in Treating Chronic Heart Failure: A Meta-Analysis of 33 Randomized Controlled Trials. *Evid. Based Complement. Alternat Medecam* 2020, 1876080. doi:10.1155/2020/1876080

Pang, L. Z., Ju, A. C., Zheng, X. J., Li, F., Song, Y. F., Zhao, Y., et al. (2017). YiQiFuMai Powder Injection Attenuates Coronary Artery Ligation-Induced Myocardial Remodeling and Heart Failure through Modulating MAPKs Signaling Pathway. *J. Ethnopharmacol.* 202, 67–77. doi:10.1016/j.jep.2017.02.032

Park, S. J., Park, M., Sharma, A., Kim, K., and Lee, H. J. (2019). Black Ginseng and Ginsenoside Rb1 Promote Browning by Inducing UCP1 Expression in 3T3-L1 and Primary White Adipocytes. *Nutrients* 11, 2747. doi:10.3390/nu11112747

Saybaşili, H., Yüksel, M., Haklar, G., and Yalçin, A. S. (2001). Effect of Mitochondrial Electron Transport Chain Inhibitors on Superoxide Radical Generation in Rat Hippocampal and Striatal Slices. *Antioxid. Redox Signaling* 3, 1099–1104. doi:10.1089/152308601317203602

Song, C., Wang, F., Ye, M., Cheng, K., Chen, R., Zhu, J., et al. (2011). Improvement of the Quantification Accuracy and Throughput for Phosphoproteome Analysis by a Pseudo Triplex Stable Isotope Dimethyl Labeling Approach. *Anal. Chem.* 83, 7755–7762. doi:10.1021/ac201299j

Sun, M., Huang, C., Wang, C., Zheng, J., Zhang, P., Xu, Y., et al. (2013). Ginsenoside Rg3 Improves Cardiac Mitochondrial Population Quality: Mimetic Exercise Training. *Biochem. Biophys. Res. Commun.* 441, 169–174. doi:10.1016/j.bbrc.2013.10.039

Suo, T., Wang, H., and Li, Z. (2016). Application of Proteomics in Research on Traditional Chinese Medicine. *Expert Rev. Proteom.* 13, 873–881. doi:10.1080/14789450.2016.1220837

Tao, L., Bei, Y., Lin, S., Zhang, H., Zhou, Y., Jiang, J., et al. (2015). Exercise Training Protects against Acute Myocardial Infarction via Improving Myocardial Energy Metabolism and Mitochondrial Biogenesis. *Cell Physiol. Biochem.* 37, 162–175. doi:10.1159/000430342

Wang, F., Chen, R., Zhu, J., Sun, D., Song, C., Wu, Y., et al. (2010). A Fully Automated System with Online Sample Loading, Isotope Dimethyl Labeling and Multidimensional Separation for High-Throughput Quantitative Proteome Analysis. *Anal. Chem.* 82, 3007–3015. doi:10.1021/ac100075y

Wang, H., Bei, Y., Lu, Y., Sun, W., Liu, Q., Wang, Y., et al. (2015). Exercise Prevents Cardiac Injury and Improves Mitochondrial Biogenesis in Advanced Diabetic Cardiomyopathy with PGC-1α and Akt Activation. *Cel Physiol Biochem* 35, 2159–2168. doi:10.1159/000374021

Wang, H. Z., Tian, J. B., and Yang, K. H. (2015). Efficacy and Safety of LCI699 for Hypertension: a Meta-Analysis of Randomized Controlled Trials and Systematic Review. *Eur. Rev. Med. Pharmacol. Sci.* 19, 296–304.

Wang, Q., Dong, L., Jian, Z., and Tang, X. (2017). Effectiveness of a PRECEDE-Based Education Intervention on Quality of Life in Elderly Patients with Chronic Heart Failure. *BMC Cardiovasc. Disord.* 17, 262. doi:10.1186/s12872-017-0698-8

Warren, J. S., Tracy, C. M., Miller, M. R., Makaju, A., Szulik, M. W., Oka, S. I., et al. (2018). Histone Methyltransferase Smyd1 Regulates Mitochondrial Energetics in the Heart. *Proc. Natl. Acad. Sci. U S A.* 115, E7871–E7880. doi:10.1073/pnas.1800680115

Wei, J., Guo, F., Zhang, M., Xian, M., Wang, T., Gao, J., et al. (2019). Signature-oriented Investigation of the Efficacy of Multicomponent Drugs against Heart Failure. *FASEB J.* 33, 2187–2198. doi:10.1096/fj.201800673RR

Wilhelm, M., Schlegl, J., Hahne, H., Gholami, A. M., Lieberenz, M., Savitski, M. M., et al. (2014). Mass-spectrometry-based Draft of the Human Proteome. *Nature* 509, 582–587. doi:10.1038/nature13319

Wiśniewski, J. R., Zougman, A., Nagaraj, N., and Mann, M. (2009). Universal Sample Preparation Method for Proteome Analysis. *Nat. Methods* 6, 359–362. doi:10.1038/nmeth.1322

Xing, L., Jiang, M., Dong, L., Gao, J., Hou, Y., Bai, G., et al. (2013). Cardioprotective Effects of the YiQiFuMai Injection and Isolated Compounds on Attenuating

Chronic Heart Failure via NF-Kb Inactivation and Cytokine Suppression. *J. Ethnopharmacol* 148, 239–245. doi:10.1016/j.jep.2013.04.019

Xu, B., Wang, F., Song, C., Sun, Z., Cheng, K., Tan, Y., et al. (2014). Large-scale Proteome Quantification of Hepatocellular Carcinoma Tissues by a Three-Dimensional Liquid Chromatography Strategy Integrated with Sample Preparation. *J. Proteome Res.* 13, 3645–3654. doi:10.1021/pr500200s

Yancy, C. W., Jessup, M., Bozkurt, B., Butler, J., Casey, D. E., Drazner, M. H., et al. (2013). 2013 ACCF/AHA Guideline for the Management of Heart Failure: Executive Summary: a Report of the American College of Cardiology Foundation/American Heart Association Task Force on Practice Guidelines. *Circulation* 128, 1810–1852. doi:10.1016/j.jacc.2013.05.019

Zhang, Y., Zhang, L., Zhang, Y., Fan, X., Yang, W., Yu, B., et al. (2019). YiQiFuMai Powder Injection Attenuates Coronary Artery Ligation-Induced Heart Failure through Improving Mitochondrial Function via Regulating ROS Generation and CaMKII Signaling Pathways. *Front. Pharmacol.* 10, 381. doi:10.3389/fphar.2019.00381

Zheng, H. R., Chu, Y., Zhou, D. Z., Ju, A. C., Li, W., Li, X., et al. (2018). Integrated Pharmacokinetics of Ginsenosides after Intravenous Administration of YiQiFuMai Powder Injection in Rats with Chronic Heart Failure by UFLC-MS/MS. *J. Chromatogr. B Analyt Technol. Biomed. Life Sci.* 1072, 282–289. doi:10.1016/j.jchromb.2017.10.056

Zhou, B., and Tian, R. (2018). Mitochondrial Dysfunction in Pathophysiology of Heart Failure. *J. Clin. Invest.* 128, 3716–3726. doi:10.1172/JCI120849

Conflict of Interest: Authors DL and AJ were employed by the company Tasly Pride Pharmaceutical Company Limited.

The remaining authors declare that the research was conducted in the absence of any commercial or financial relationships that could be construed as a potential conflict of interest.

Publisher's Note: All claims expressed in this article are solely those of the authors and do not necessarily represent those of their affiliated organizations, or those of the publisher, the editors and the reviewers. Any product that may be evaluated in this article, or claim that may be made by its manufacturer, is not guaranteed or endorsed by the publisher.

frontiers in Pharmacology

ORIGINAL RESEARCH
published: 23 September 2021
doi: 10.3389/fphar.2021.645140

Inhibitory Effects of Rhaponticin on Osteoclast Formation and Resorption by Targeting RANKL-Induced NFATc1 and ROS Activity

Jianbo He[1,2†], Kai Chen[2†], Tiancheng Deng[1], Jiewei Xie[1], Kunjing Zhong[1], Jinbo Yuan[2], Ziyi Wang[2], Zhifeng Xiao[1], Ronghe Gu[2,3], Delong Chen[4], Xiaojuan Li[5], Dingkun Lin[1]* and Jiake Xu[2]**

[1]The Second Affiliated Hospital of Guangzhou University of Chinese Medicine, Guangdong Provincial Hospital of Chinese Medicine, Guangzhou, China, [2]School of Biomedical Sciences, University of Western Australia, Perth, WA, Australia, [3]Department of Orthopedics, First People's Hospital of Nanning, Fifth Affiliated Hospital of Guangxi Medical University, Nanning, China, [4]The First Affiliated Hospital of Guangzhou University of Chinese Medicine, Guangzhou, China, [5]Formula-Pattern Research Center, School of Traditional Chinese Medicine, Jinan University, Guangzhou, China

The extravagant osteoclast formation and resorption is the main cause of osteoporosis. Inhibiting the hyperactive osteoclastic resorption is considered as an efficient treatment for osteoporosis. Rhaponticin (RH) is a small molecule that has been reported to possess anti-inflammatory, anti-allergic, anti-fibrotic, and anti-diabetic activities. However, the influence of RH on osteoclasts differentiation and function is still unclear. To this end, an array of assays including receptor activator of nuclear factor kappa-B (NF-κB) ligand (RANKL) induced osteoclastogenesis, tartrate-resistant acidic phosphatase (TRAcP) staining, immunofluorescence, and hydroxyapatite resorption were performed in this study. It was found that RH had significant anti-catabolic effects by inhibiting osteoclastogenesis and bone resorption without cytotoxicity. Mechanistically, the expression of NADPH oxidase 1 (Nox1) was found to be suppressed and antioxidant enzymes including catalase, superoxide dismutase 2 (SOD-2), and heme oxygenase-1(HO-1) were enhanced following RH treatment, suggesting RH exhibited antioxidant activity by reducing the generation of reactive oxygen species (ROS) as well as enhancing the depletion of ROS. In addition, MAPKs, NF-κB, and intracellular Ca^{2+} oscillation pathways were significantly inhibited by RH. These changes led to the deactivation of osteoclast master transcriptional factor-nuclear factor of activated T cells 1 (NFATc1), as examined by qPCR and Western blot assay, which led to the decreased expression of downstream integrin β3, c-Fos, cathepsin K, and Atp6v0d2. These results suggested that RH could effectively suppress RANKL-regulated osteoclast formation and bone resorption. Therefore, we propose that RH can represent a novel natural small molecule for the treatment of osteoporosis by inhibiting excessive osteoclast activity.

Keywords: osteoclast, NFATc1, ROS, rhaponticin, bone

OPEN ACCESS

Edited by:
Wenzhi Yang,
Tianjin University of Traditional Chinese Medicine, China

Reviewed by:
Young-Ji Shiao,
National Research Institute of Chinese Medicine, Taiwan
Pin Ju Chueh,
Institute of Biomedical Sciences, National Chung Hsing University, Taiwan

****Correspondence:***
Xiaojuan Li
lixiaojuan@jnu.edu.cn
Dingkun Lin
lindingkuntcm@126.com
Jiake Xu
jiake.xu@uwa.edu.au

[†]These authors have contributed equally to this work

Specialty section:
This article was submitted to Ethnopharmacology, a section of the journal Frontiers in Pharmacology

Received: *22 December 2020*
Accepted: *06 April 2021*
Published: *23 September 2021*

Citation:
He J, Chen K, Deng T, Xie J, Zhong K, Yuan J, Wang Z, Xiao Z, Gu R, Chen D, Li X, Lin D and Xu J (2021) Inhibitory Effects of Rhaponticin on Osteoclast Formation and Resorption by Targeting RANKL-Induced NFATc1 and ROS Activity. Front. Pharmacol. 12:645140. doi: 10.3389/fphar.2021.645140

INTRODUCTION

The well-orchestrated bone formation and bone resorption is vital for bone modelling and remodelling (Baron & Kneissel, 2013). Excessive bone resorption is considered to be the main cause of osteoporosis which is characterized by reduced bone mass, with the high risk of bone fractures (Rachner, Khosla, & Hofbauer, 2011). Estrogen deficiency and glucocorticoid administration are the top two primary causes of osteoporosis (Adami & Saag, 2019; Manolagas, O'Brien, & Almeida, 2013) and subsequent vertebral or hip fractures pose heavy economic burdens to patients and society (Melton, 2003). Clinically available osteoporosis treatments such as hormone replacement therapy, bisphosphates, and RANKL antibody have acceptable therapeutic outcome by exhibiting an appreciated suppression on bone resorption. However, a series of potential adverse impacts including breast cancer, endometrial carcinoma, heart attack, and jaw osteonecrosis will have some limitation on their application (Ross, Paganini-Hill, Wan, & Pike, 2000; Lopez-Jornet, Camacho-Alonso, Molina-Minano, & Gomez-Garcia, 2010; Wang et al., 2017). Therefore, it is urgent to provide more effective alternative options to alleviate these osteoclast-related bone disorders.

Osteoclasts (OCs) are bone-resorbing and multinucleated cells, differentiating from the bone marrow monocytes (BMMs) (Ibbotson, Roodman, McManus, & Mundy, 1984). Mature osteoclasts are the unique cell lineage which can resorb bone tissue and thus highly involved in the bone metabolism. During the process of differentiation, there are two indispensable factors: macrophage colony-stimulating factor (M-CSF) and RANKL (Teitelbaum, 2000). M-CSF maintains the proliferation and survival of osteoclast precursor BMMs (Teitelbaum, 2000). RANKL mediates the differentiation of osteoclast precursor cells and regulates the function of mature osteoclasts by binding to its receptor–RANK (Wada, Nakashima, Hiroshi, & Penninger, 2006). RANKL-induced intracellular signalling pathways include reactive oxygen species (ROS), NF-κB, mitogen-activated protein kinase (MAPK) and calcium oscillation, which collaboratively induce the differentiation and function of osteoclasts (Wada, et al., 2006). Eventually, two main transcription factors–activator protein 1 (AP-1) and nuclear factor of activated T cells 1 (NFATc1) are activated to enhance osteoclast-specific markers such as tartrate-resistant acid phosphatase (TRAcP) and cathepsin K (CTSK) (Indo et al., 2013; Wada, et al., 2006). Hence, strategies on suppressing the RANKL-induced pathways in osteoclasts are deemed practical for the treatment of osteoporosis.

Rhaponticin (RH) is a natural compound originally isolated from the famous Chinese medicinal herb *Rheum undulatum L.*. It is well-known for anti-inflammatory, anti-allergic, anti-fibrotic, and anti-cancer effects (Kim & Ma, 2018; Tao et al., 2017; Wei et al., 2017). RH suppresses the spread and expansion of cancer cells by decreasing its transmutation and angiogenic functions (Kim & Ma, 2018). RH also effectively prevents pulmonary fibrosis via the modification of AMP activated protein kinase (AMPK) activation and transforming growth factor beta (TGF-β)/Smad pathway *in vitro* and *in vivo* (Tao, et al., 2017). Given the wide range of bioactivities that RH exhibited, we hypothesized RH may affect osteoclast formation and function. In this study, we identified that RH could significantly inhibit RANKL-induced osteoclast formation and resorption by targeting RANKL-induced ROS and NFATc1. The underlying mechanisms include the suppression on MAPK, NF-κB and Ca^{2+} oscillations. Therefore, these results suggested the potential and beneficial anti-catabolic effects of RH on osteoclast-related bone disorders.

MATERIALS AND METHODS

Materials and Reagents

Rhaponticin (purity >98%) was purchased from Ruifensi company (Chengdu, China) and dissolved with dimethyl sulfoxide (DMSO), stocking at the concentration of 100 mM in −20°C freezer. Further dilution was achieved through adding phosphate-buffered saline (PBS) to the original stock. The complete cell medium consisted of Alpha modified minimal essential medium, penicillin/streptomycin (1%), and fetal bovine serum (10%), obtained from Thermo Fisher Scientific (Scoresby, Vic, Australia). Recombinant M-CSF and glutathione S-transferase-recombinant RNAKL (GST-rRANKL) were used as previously described (Xu et al., 2000). The regents for MTS and luciferase assay were purchased from Promega (Madison, WI, United States). The primary antibodies special for NFATc1, c-Fos, CTSK, V-ATPase-d2, integrin β3, extracellular signal regulated kinase (ERK), phosphorylated ERK (*p*-ERK), P38, phosphorylated P38 (p-P38), and β-actin were obtained from Cell Signaling Technology, Santa Cruz Biotechnology and Abcam companies.

Cell Culture

The BMMs were extracted from the femur and tibia of 10 weeks C57BL/6J mice, and the procedures were in conformity with the principles of the Animal Ethics Committee of the University of Western Australia (RA/3/100/1601). The bone marrow was flushed from the long bones, with the filtering and centrifuge, the bone marrow extracts were cultured in osteoclast cells special medium with the existence of M-CSF at the concentration of 50 ng/ml, and changed the medium every 2 days.

Cytotoxicity Assay

The BMMs were seeded into the 96-well plate (5×10^3 cells per well) with the M-CSF kit, without the stimulation of RANKL. On the following day, different concentrations of RH were added to the medium for culturing 48 hours. Then the cell viability was determined at the 490 nm absorbance after 2 hours incubation with MTS kit (10 μl/well).

In vitro Osteoclastogenesis Assay

BMMs at the stage of passage 2 were seeded into the 96-well plate (5×10^3 cells per well) and cultured with complete medium containing M-CSF with the overnight to adhere. On the following day, the BMMs were changed to the medium with RANKL (50 ng/ml), in the presence or absence of RH at the varying

concentrations (6.25,12.5, 25 and 50 μM). The culturing cell medium needed to be changed about three times every 2 days until the osteoclasts formed after RANKL stimulus. Then the mature cells were fixed with 2.5% glutaraldehyde for 10 mins, with the washing by PBS three times, they were well prepared for TRAcP staining. The cells with more than three nuclei were recognized as the TRAcP-positive osteoclasts, counting under the light microscope.

Furthermore, the time course was undertaken to investigate the effects of RH on definite stages of osteoclastogenesis. The RH was added to the medium with RANKL at an early stage (1–2 days), middle-stage (3–4 days), late-stage (5–6 days) and the whole stage (1–6 days). Finally, the osteoclasts were fixed for TRAcP staining as described above.

Immunofluorescent Staining

The BMMs were seeded in the 96-well plates with the culturing of M-CSF at the above concentration overnight. Cells were then stimulated by the consistent concentration of RANKL, with the RH treatment (25 and 50 μM, respectively) or not. When the mature osteoclasts formed, 4% paraformaldehyde was added in the wells to fix about 15 minutes at room temperature. After the wash with PBS and permeabilization with 0.25% Triton X-100, the prepared cells were then blocked at the room tempreture for 1 hour with 3% bovine serum albumin. Next, they were probed with the effects of Rhodamine-Phalloidin for the staining of F-actin in the dark. And the nuclei of mature osteoclasts were counterstained with DAPI. Then, they were visualized on the confocal fluorescence microscope (Nikon, A1S confocal microscopy).

Hydroxyapatite Resorption Assay

The bone resorption could be detected with the hydroxyapatite resorption assay induced by the osteoclasts as described previously (Chen et al., 2019). The primary BMMs were planted into the 6-well collagen-coated plate with the stimulation of M-CSF and RANKL with the above concentration. The mature osteoclast cells were transferred into the 96-well plate with the coat of hydroxyapatite after gently detaching them from the previous plate with special cell dissociation solution (Sigma-Aldrich). With the stimulation of RANKL, the osteoclasts in 96-well hydroxyapatite plate were incubated with the RH at indicated 25 and 50 μM concentrations for 48 hours to fully display the bone resorption function. Then one half of wells were fixed for TRAcP staining for counting the number of multinucleated TRAcP-positive cells in the well, as described above, and the other half wells were flushed with the bleach to remove the adhering cells and measure the resorbed areas on hydroxyapatite surface by osteoclasts.

RNA Isolation and RT-PCR Analysis

After the maturation of osteoclasts from the primary BMMs by the stimulation of M-CSF and RANKL, with the treatment of RH or not, as mentioned above, the total RNA of different groups was isolated with 1 ml Trizol reagent per well, the procedures were practised according to the manufacturer's protocol. cDNA was then generated from the RNA samples, with the reagents of M-MLV reverse transcriptase and oligo dT primers. The specific amplification sequences of polymerase chain reaction (PCR) was underdone with the detection of SYBR Green MasterMix, following the special conditions. The related primers were used for detecting gene expression as shown: *Nfatc1* (Forward: 5′-CA ACGCCCTGACCACCGATAG-3′; Reverse: 5′-GGCTGC CTTCCGTCTCATAGT- 3′), *Atp6v0d2* (Forward: 5′-GTGAGA CCTTGGAAGACCTGAA-3′; Reverse: 5′-GAGAAATGTGCT CAGGGGCT-3′), *Ctsk* (Forward: 5′-GGGAGAAAAACCTGA AGC-3'; Reverse: 5′-ATTCTGGGGACTCAGAGC-3′), *c-Fos* (Forward: 5′-GCGAGCAACTGAGAAGAC-3′; Reverse: 5′-TTGAAACCCGAGAACATC- 3′), and *Hprt* (Forward: 5′-CAGTCCCAGCGTCGTGATTA-3′'; Reverse: 5′-TGGCCT CCCATCTCCTTCAT-3′) was used as a housekeeping gene. The perforation of the reaction was running on the ViiA™ 7 Real-time PCR machine (Applied Biosystems, Paisley, United Kingdom).

Luciferase Reporter Assays

The luciferase reporter construct was performed to investigate the activation of NFATc1 and NF-κB transcription with the transfected RAW264.7 cells (Wang et al., 2003; Cheng et al., 2018). Briefly, the prepared transfected cells were seeded in the 48-well plate with 1.0×10^5 cells per well overnight. After the pretreatment with 50 μM RH for 1 hour, the cells were cultured with the presence of RANKL (100 ng/ml) about 24 hours for NFATc1 luciferase reporter and 6 hours for NF-κB luciferase reporter. The cells were subjected to luciferase reporter assay system according to the manufacturer's protocol (Promega).

Western Blot Analysis

The BMMs were cultured in 6-well plates and with the adding of RANKL (50 ng/ml) at the concentration of 1.5×10^5 per well, with the presence or absence of RH in the medium. At the stated culturing times, the cells were lysed in special RIPA lysis buffer. After the cells protein samples were resolved and collected, the SDS gel electrophoresis was used for protein separation. The protein was then transferred to Nitrocellulose blotting membranes (Amersham, Germany). The membranes were gently blocked with 5% skim milk for 2 hours, and incubated in the targeted specific primary antibodies by gently shaking overnight at 4°C. The following day, with the wash by PBS for 3 times per 10 minutes, the membranes were incubated in the secondary Rat/Mouse antibodies for 1 hour at the room temperature. Finally, the antibody reactivity was detected with Extreme Sensitivity Chemiluminescence Substrate (PerkinElmer, Waltham, MA, Unites States). The protein images were visualized on the machine of Image Quant LAS 4000 (GE Healthcare) and then analyzed with the tool of ImageJ software.

Intracellular Ca^{2+} Measurement

Intracellular Ca^{2+} oscillation assay was used to measure the effects of RH on the calcium signalling, involving in the progress of the osteoclast differentiation as previously described (Wang et al., 2019). Briefly, after the culturing of BMMs for overnight in 48-well plates, the cells were pretreated 1 hour with or without RH (50 μM) and then added RANKL to the complete medium for

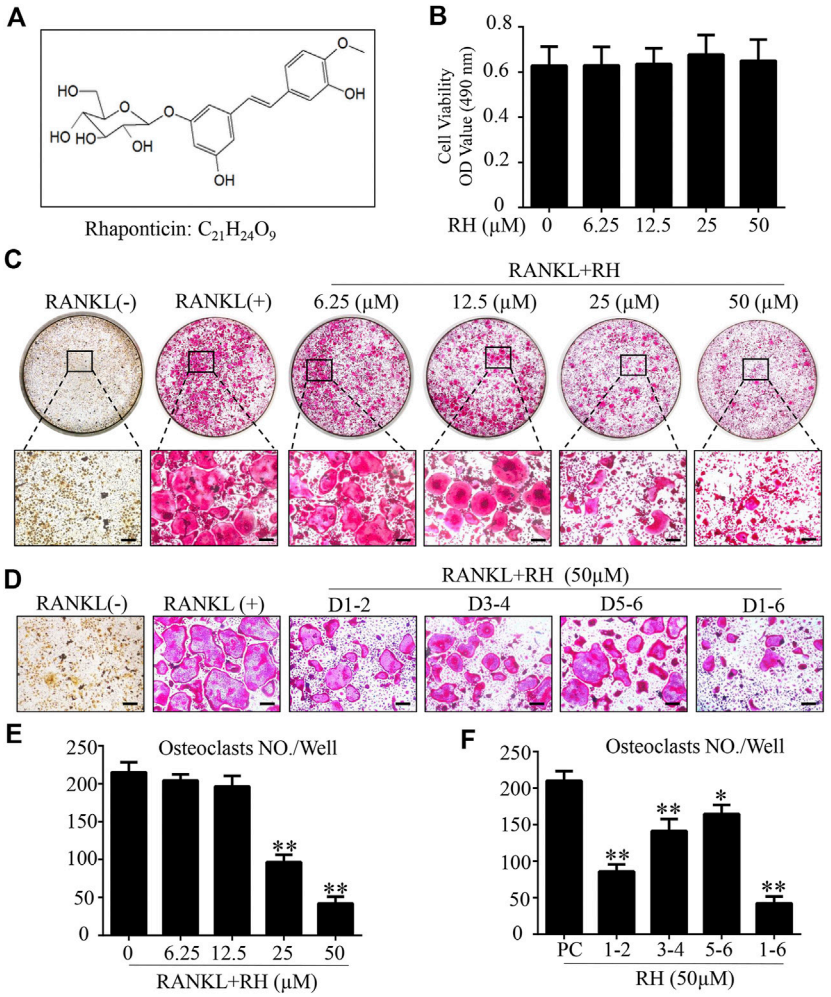

FIGURE 1 | Rhaponticin (RH) suppressed RANKL-induced osteoclastogenesis *in vitro*. **(A)** Chemical structure and formula of RH. **(B)** MTS assay of the BMMs cultured with various concentrations of RH. **(C, D)** Representative images of optical microscope and TRAcP staining of BMMs treated with RH in different concentrations for 6 days **(C)** and in 50 μM, at different time phase of 1–2 days (D1-2), 3–4 days (D3-4), 5–6 days (D5-6), 1–6 days (D1-6), during differentiation **(D)** were shown. **(E, F)** Quantification of TRAcP positive multinucleated osteoclasts (nuclei > 3) with the treatment of RH (n = 3). *p < 0.05, **p < 0.01 relative to RANKL-induced control group. Scale bar = 200 μm.

another coculturing of 24 hours. The treated cells were washed with assay buffer, consisting of Hanks' buffer and the supplement of 1 mmol/L probenecid and 1% Fetal Bovine Serum. Then the intracellular free calcium was labeled by Fluo4 staining solution for 45 minutes (Chen et al., 2019a). Then the free calcium was detected at the fluorescent light (488 nm excitation wavelength) and the images were scanned and obtained at 2s intervals for 3 minutes with the fluorescence microscope. Oscillating cells with two intensity peaks at the observed time were positively identified and their oscillation intensity changes were counted by the minus of the maximum and the minimum peak (Wang, et al., 2019).

Statistical Analysis

All data were presented as mean ± standard deviation, representing at least three experiments and performance in triplicate. One-way analysis of variance and Student's t-test was used to determine the significance of differences between results, with $p < 0.05$ considered to be significant.

RESULTS

RH Inhibits RANKL-Induced Osteoclastogenesis

The MTS assay was performed to assess the cytotoxicity of RH on BMM cells. BMMs were cultured with M-CSF and RH for 48 hours at the varying dosages. RH had no effect on the proliferation and viability of BMM cells when compared with the control group at the concentration of 50 μM or lower (**Figure 1A and 1B**). To determine the influence of RH on the formation progress of osteoclasts from BMMs induced by RANKL, we performed an osteoclastogenesis assay as

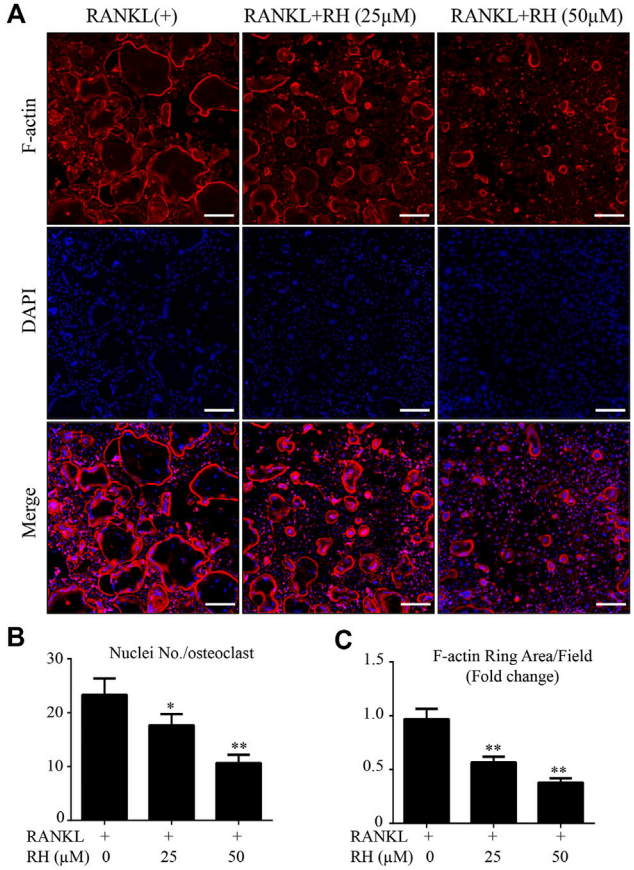

FIGURE 2 | RH inhibited the formation of F-actin belt during the osteoclast formation induced by RANKL. **(A)** The confocal images of F-actin ring formation were detected with Rhodamine Phalloidin, combined DAPI staining for nuclei respectively. Scale bar, 200 μm. **(B)** Quantification of the nucleus number per osteoclast under the different concentrations of RH. **(C)** Quantification of the average of actin ring area per field ($n = 3$). *$p < 0.05$, **$p < 0.01$ relative to RANKL-induced control group. Scale bar = 200 μm.

mentioned above (Chen et al., 2019). The primary BMMs were cultured with the presence of M-CSF and the stimulation of RANKL around 6 days by the treatment of RH in various concentrations. The TRAcP staining result indicated that RH could significantly reduce the osteoclastogenesis in a dose-dependent manner. The TRAcP-positive multinucleated cell numbers at 25 and 50 μM concentrations were significantly less than the positive control group (**Figures 1C,E**). In the time-course experiment, BMM cells were treated with RH at different time phases (1–2, 3–4, 5–6, 1–6 days), which could investigate the stage that the inhibitory effects of RH treatment mainly exhibits. The results suggested that RH displayed the various levels of effect at the different stages during osteoclast differentiation (**Figures 1D,F**). To observe the effects of RH on the morphological changes of F-actin ring, a vital structure during the formation of mature OC, BMMs were stimulated with RANKL and the treatmnent of doses of RH until they became mature osteoclasts, then the Rhodamine Phalloidin was used to stain actin ring and DAPI for the nuclei. The nuclei number of the osteoclasts was counted under the microscope (**Figure 2A**). It showed that both nuclei number per osteoclast and average area of F-actin belt per field were decreased in the presence of RH as compared with that in the RANKL-positive group (**Figures 2B,C**). Therefore, RH may possess potential inhibitory effects on the osteoclastogenesis induced by RANKL.

RH Decreases the Hydroxyapatite Resorption by Osteoclastic Cells

As RH could inhibit the osteoclastogenesis and formation of F-actin ring, hydroxyapatite resorption assay was carried out to examine the outcome of RH on osteoclast-induced bone resorptive function. Following the incubation of mature osteoclasts with RANKL for 48 hours, the number of osteoclasts was reduced by RH at 50 μM (**Figures 3A,B**), and the average resorbed area in hydroxyapatite-coated well by per cell was significantly decreased by the treatment of RH (25 and 50 μM) in comparison with the control group (**Figure 3C**). The hydroxyapatite resorption result was consistent with osteoclastogenesis assay, demonstrating that RH possesses potential anticatabolic influence on osteoclast formation and bone resorptive function.

RH Inhibits Osteoclast Marker Gene Expression

To further explore the mechanisms of inhibitory effects on osteoclastogenesis and osteoclastic bone resorption by RH, BMMs were cultured with RANKL and M-CSF and treated with RH (25 and 50 μM) for about 6 days till the mature osteoclasts formed. PCR assay was then performed to distinguish the expression levels of osteoclast cells-related marker genes including *Nfatc1, c-Fos, Ctsk*, and *Atp6v0d2*. As demonstrated in **Figure 3**, the expression of *Nfatc1*, was effectively inhibited by RH in a dose-dependent manner when compared with the control group (**Figure 3D**). Additionally, the expression levels of other genes, such as *c-Fos*, *Ctsk*, and *Atp6v0d2* were also down-regulated by RH treatment (**Figures 3E–G**).

RH Suppresses the Expression Activity of NFATc1 and the Related Proteins

To determine the effects of RH on NFATc1 transcriptional activity induced by RANKL, the NFATc1 luciferase assay was performed. RH pretreatment showed a significant inhibition on RANKL-induced NFATc1 activity (**Figure 4A**). Additionally, the Western blot results showed that RH could significantly suppress the NFATc1 expression at protein level in osteoclast cells following the induction of RANKL at day 3 and 5 (**Figures 4B,C**). And the other expressions of osteoclast-related proteins were also down-regulated with RH, including integrin β3, c-Fos, CTSK, and V-ATPase-d2 when compared with the untreated group (**Figure 4B-G**). Thus, the NFATc1 activity was significantly inhibited via influencing downstream signaling and transcription by RH.

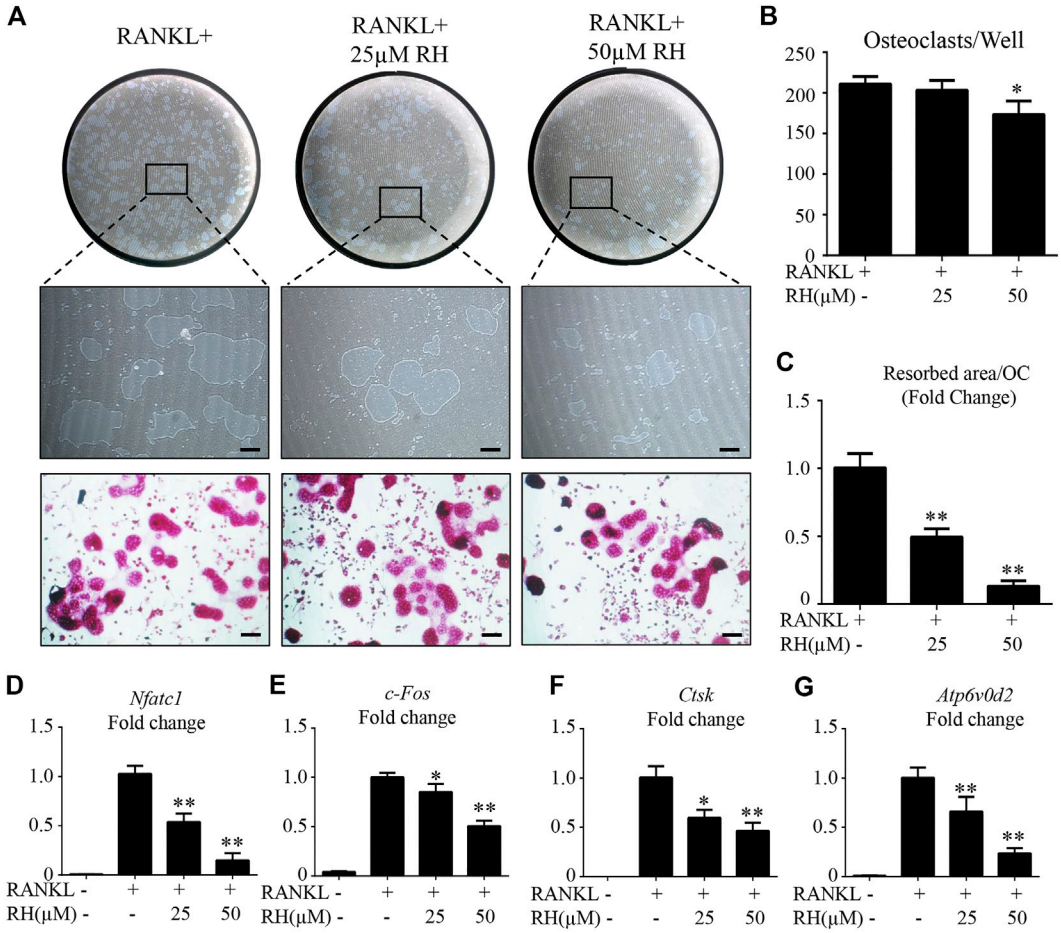

FIGURE 3 | RH attenuated osteoclast hydroxyapatite resorption and osteoclast-specific genes expression. **(A)** Representative images of the resorption on hydroxyapatite-coated plates and TRAcP staining after treatment of RH for 48 hr. **(B)** Quantification of TRAcP-positive osteoclasts numbers per well (n = 3). **(C)** Quantification of resorption area on hydroxyapatite surface per osteoclast (n = 3). **(D–G)** PCR results of osteoclast-specific genes *Nfatc1*, *c-Fos*, *Ctsk*, and *Atp6v0d2*. Gene expression levels were standardized to Hprt expression. $^{*}p < 0.05$, $^{**}p < 0.01$ relative to RANKL-induced control group. Scale bar = 200 μm.

RH Suppresses ROS Activity and Ca^{2+} Oscillation in the Osteoclastogenesis Induced by RANKL

To inspect the effect of RH on the intracellular ROS level at the stage of osteoclast differentiation induced by RANKL, oxidation-sensitive protein makers were tested with Western blot assay. Nox1 was known as the protein marker contributing to ROS generation (Sasaki et al., 2009). The Nox1 protein expression level was significantly improved by the stimulation of RANKL, but significantly suppressed with the treatment of RH (**Figures 5A,B**). The antioxidant enzymes including HO-1, catalase and SOD-2 were enhanced dose-dependently by RH treatment as examined by Western blot (**Figures 5A,C–E**). The results indicated that RH is able to reduce the intracellular ROS generation and enhance the scavenging ability of ROS level. As reported by other studies, calcium oscillation initiation plays a grave role in the activation of NFATc1 (Takayanagi et al., 2002). Furthermore, to explore the molecular mechanism of the inhibition of osteoclast formation and function by RH, the intracellular calcium oscillation activity was also performed. In the results, Ca^{2+} oscillation was increased with the stimulation of RANKL. While this trend was dramatically attenuated after the treatment of RH (**Figures 5F–I**).

RH Represses NF-κB Activation and the Phosphorylation of ERK and P38 in MAPK Pathways

We also investigated the effects of RH on NF-κB activity induced by RANKL. With the luciferase reporter assay, RANKL stimulation could increase the activity of NF-κB luciferase, while the treatment of RH significantly inhibited the obvious trend (**Figure 6A**). NF-κB complex is bound with IκB-α and is prevented from translocating to nucleus for futher activation. Western blot results further indicated that the degradation of IκB-α was induced by RANKL but was suppressed by RH treatment

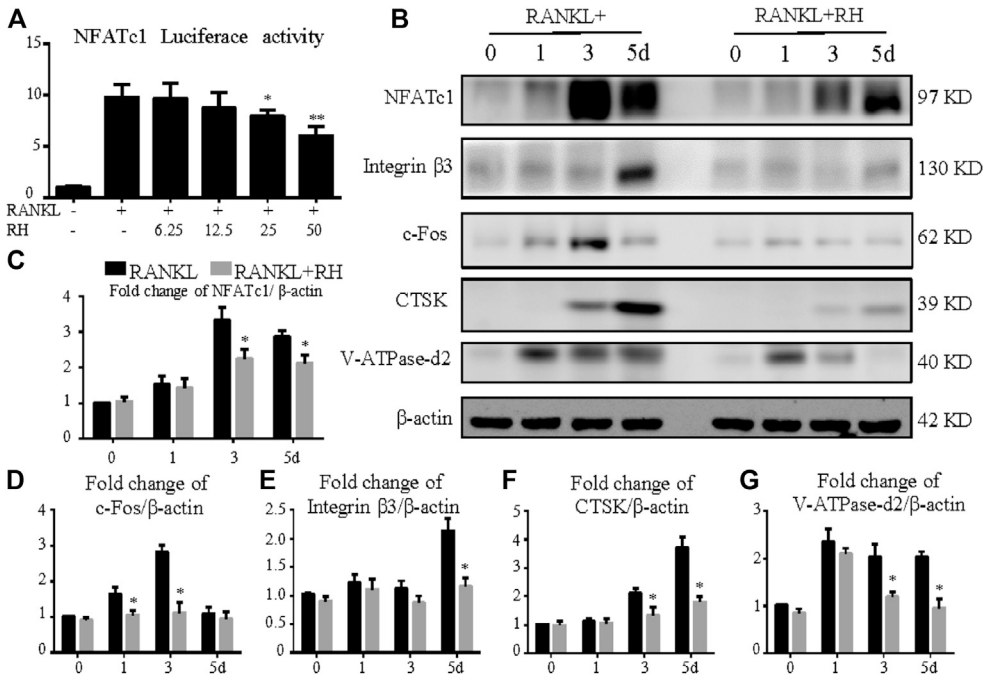

FIGURE 4 | RH suppressed NFATc1 activation and its downstream protein expression. **(A)** RH inhibited the NFATc1 activity of RAW 264.7 cells transfected with luciferase report construct. The cells were pretreated with RH for 1 hour, followed by RANKL stimulation at 50 ng/ml concentration for 24 hours (n = 4). **(B)** Representative Western blot images of the effects of RH on the protein expression of NFATc1, integrin β3, CTSK, c-Fos, and V-ATPase-d2 at day 0, 1, 3, and 5 with the stimulation of RANKL (50 ng/mL). **(C–G)** Quantification of the ratios of band intensity of NFATc1, integrin β3, CTSK, c-Fos, and V-ATPase-d2 relative to β-actin (n = 3). *p < 0.05, **p < 0.01 relative to RANKL-induced control group.

(**Figures 6B,C**). Therefore, it was revealed that RH treatment had an attenuating effect on NF-κB activity during the progress of osteoclastogenesis.

The MAPK signalling pathway members of P38 and ERK are vital in the activation of c-Fos and NFATc1 (Chen et al., 2019a; Huang, Chang, et al., 2006). Therefore, the effects of RH treatment on MAPK pathway activation during RANKL-induced osteoclastogenesis was investigated. BMMs were preincubated in serum-free medium for 4 hours, then stimulated by RANKL with the presence of RH or not, at 0, 10, 20, 30, and 60 minutes. RH pretreatment had attenuated the phosphorylation of ERK at 10, 20, and 30 minutes (**Figures 6B,D,E**). Additionally, the phosphorylation of P38 was significantly inhibited by RH treatment at 10 and 20 minutes compared to the control group (**Figures 6B,F**). These results suggested that RH could down-regulate osteoclast formation and function against the RANKL stimulation by suppressing the MAPK signalling pathways.

DISCUSSION

Osteoporosis is a highly prevalent disease which can cause a substantial economic burden to individuals and society due to the increased risk of bone fractures (Harvey, Dennison, & Cooper, 2010). And the excessive osteoclastic activity and bone resorption are considered as the main reasons for bone loss (Baron & Kneissel, 2013). The serious side effects induced by the long-term and large-usage of the traditional clinical anti-osteoporotic agents have limited their wide application in treating osteoporosis (Lopez-Jornet, et al., 2010; Ross, et al., 2000; Wang, et al., 2017). Therefore, alternative therapeutic agents to prevent osteolytic diseases are urgent to be exploited. Many herbs have been proved possessing the effects to treat osteoporosis (Chen et al., 2019; Jin et al., 2019). RH, an important stilbene-type component extracted from the root of *Rheum undulatum L.*, possesses various biological activities, such as anti-allergic, anti-cancer, anti-diabetic and anti-inflammatory activities in the previous reports (A. Kim & Ma, 2018; Li, Tian, Wang, & Ma, 2014; Tao, et al., 2017). However, there is no research regarding its potential effects on bone cells. In this study, firstly, RH was proved to be able to suppress the osteoclastogenesis and osteoclastic resorption.

Osteoclasts are the monocyte-macrophage lineage-derived large multinucleated cells, acting with the vital role in bone remodelling by resorbing bone matrix. M-CSF and RANKL play a leading role in osteoclast biology and are used to induce osteoclastogenesis in our study. M-CSF provides signals required for the survival and proliferation of early osteoclast precursors. It is also imperative for macrophage maturation in the presence of RANKL. Upon these stimulations, the precursors differentiate into the mature osteoclasts characterized by the F-actin ring foramtion with resorptive function (Teitelbaum, 2000). TRAcP is an acid phosphatase and abundant in osteoclasts,

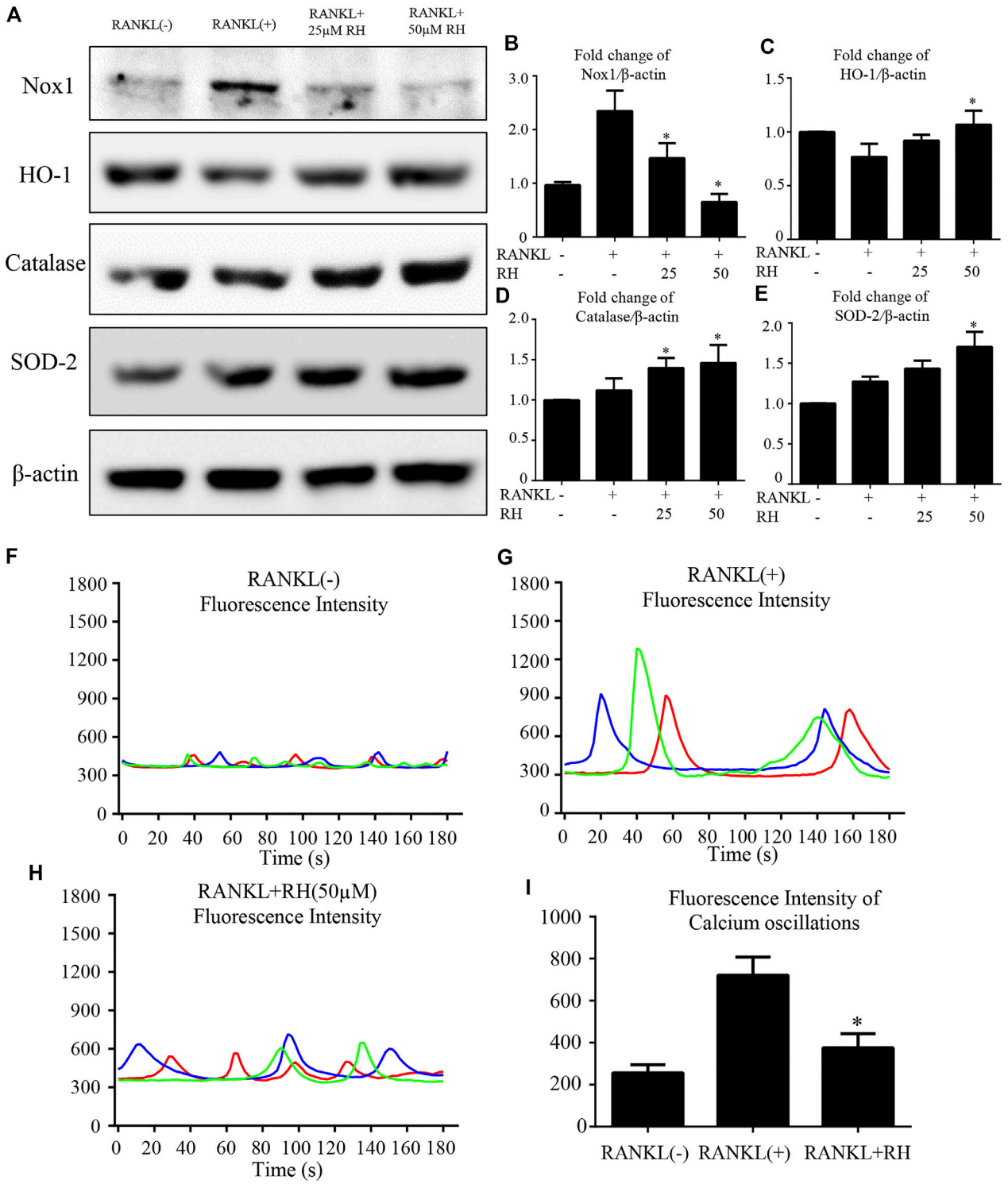

FIGURE 5 | RH suppressed RANKL-induced ROS activity and Ca^{2+} oscillation. **(A)** Representative Western blot images of the Nox1, catalase, HO-1, and SOD-2 expression with the treatment of RH, the Nox1 expression was significantly suppressed by RH, and the antioxidant enzymes of HO-1, catalase and SOD-2 were enhanced. BMMs were stimulated with RANKL (50 ng/mL) with RH at the concentration of 25 and 50 μM or PBS for 2 days before collecting protein. **(B–E)** Quantification of the ratios of band intensity of Nox1, HO-1, catalase, and SOD-2 relative to *β*-actin ($n = 3$ per group). $^{*}p < 0.05$, $^{**}p < 0.01$ comparison with the RANKL-induced positive control group. **(F–H)** Representative images of fluorescence intensity waves of Ca^{2+} oscillation in negative group, RANKL stimulated positive group and RH (50 μM) treated group. There were three colours indicating different cells in each group. **(I)** Quantification of fluorescence intensity change of Ca^{2+} oscillation in each group. $^{*}p < 0.05$, $^{**}p < 0.01$ relative to RANKL-induced positive control group.

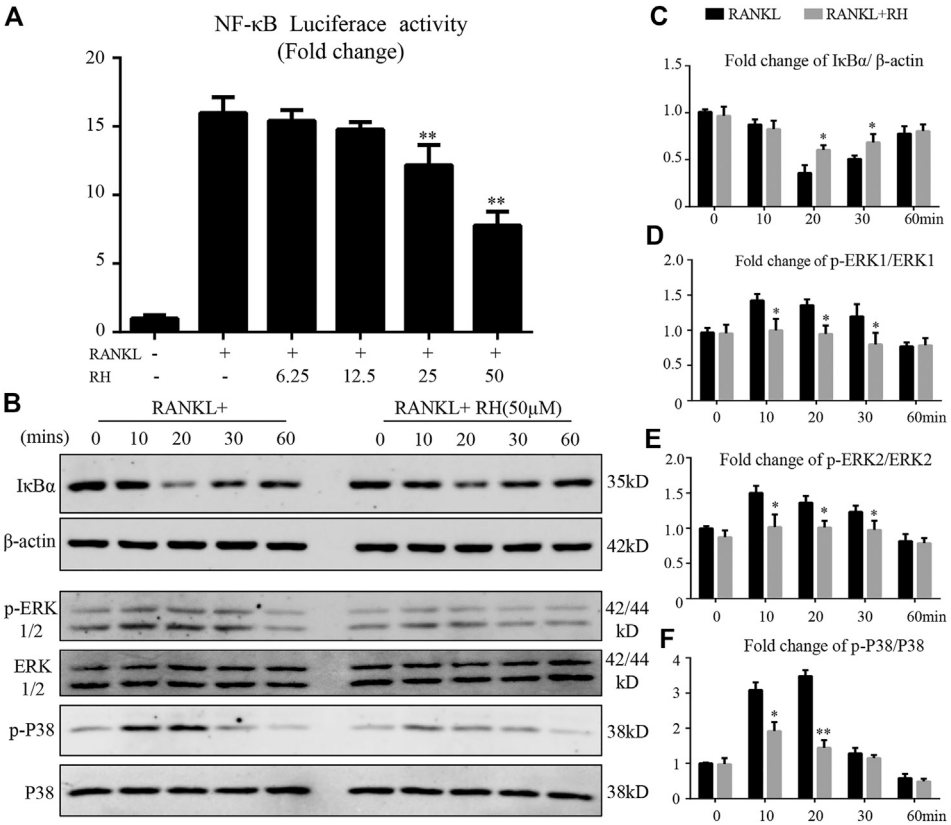

FIGURE 6 | RH suppressed the activation of NF-κB and the phosphorylation of ERK and P38 induced by RANKL. **(A)** RH inhibited the NF-κB activity of RAW 264.7 cells with luciferase report construct at the different concentrations of RH as indicated. The cells were pretreated with varying densities of RH and stimulated with RANKL at 50 ng/mL for 6 hours. **(B–C)** Representative images of the expression level of IκB-α and *β*-actin in Western blot assay and the quantification of the ratios of band intensity of IκB-α to *β*-actin. **(B–F)** Representative images of the expression phosphorylation level of ERK and P38 with or without the treatment of 50 μM RH, and the quantification of the fold change ratios of band intensity of p-ERK to ERK and p-P38 to P38 ($n = 3$). $^{*}p < 0.05$, $^{**}p < 0.01$ relative to RANKL-induced positive group.

a specific marker for osteoclast cells activity (Janckila, Takahashi, Sun, & Yam, 2001). In our study, the MTS results found that the viability of BMM cells was not influenced by RH, even at the high concentration of 50 μM, while the quantity of RANKL-induced TRAcP-positive cells was meaningfully lower by RH treatment compared with the positive group, indicating the osteoclast formation was efficiently inhibited by RH. Furthermore, in the time-course assay, the number of TRAcP-positive mature osteoclasts was effectively reduced at different times as indicated, especially with fewer osteoclasts at the early and middle stages. It may be related with the early inhibition of RH on the upstream of ROS, NF-κB, and MAPK pathways and then the NFATc1 protein expression according to the results below. Additionally, the mature osteoclasts are featured by resorbing the bone tissues through multiple processes (Croucher, McDonald, & Martin, 2016). In the bone resorption pit assay, we found that RH-treated group displayed a significantly reduced resorption area as compared with the positive control group, indicating the inhibition of RH on bone resorption.

Next, we explored the mechanisms for the anti-catabolic effects of RH. During osteoclast differentiation and maturation stimulated by RANKL, the BMM will highly express NFATc1 protein at about 2 or 3 days after the stiulation of RANKL, acting as a master transcriptional factor to promote the expression of the numerous genes which are prerequisites for bone resorption (Negishi-Koga & Takayanagi, 2009; Zhao, Wang, Liu, He, & Jia, 2010). The physiological implication of NFATc1 for osteoclasts has been well elucidated. Firstly, osteoclast precursor cells with the deficiency of NFATc1 fail to differentiate into the mature osteoclasts (Zhao, Shao, Chen, & Li, 2007). Secondly, NFATc1 regulates the expression of target genes and proteins that empower osteoclastic resorption as evidenced by the osteopetrosis in the conditional NFATc1-deficient mice (Aliprantis et al., 2008). In our study, we found that RH significantly suppressed the expressions of NFATc1 at both gene and protein levels, which further caused the downregulation of related proteins and genes including integrin β3, c-Fos, V-ATPase-d2, and CTSK. This was also supported by the suppressed NFATc1 transcriptional activity as examined by luciferase assay. These findings suggested the involvement of NFATc1-mediated mechanisms by which RH inhibited osteoclastogenesis and osteoclastic resorption.

The physiological intracellular ROS activity rests on the equilibrium between the rates of generation and scavenging (Chen et al., 2019). RANKL-induced ROS production is

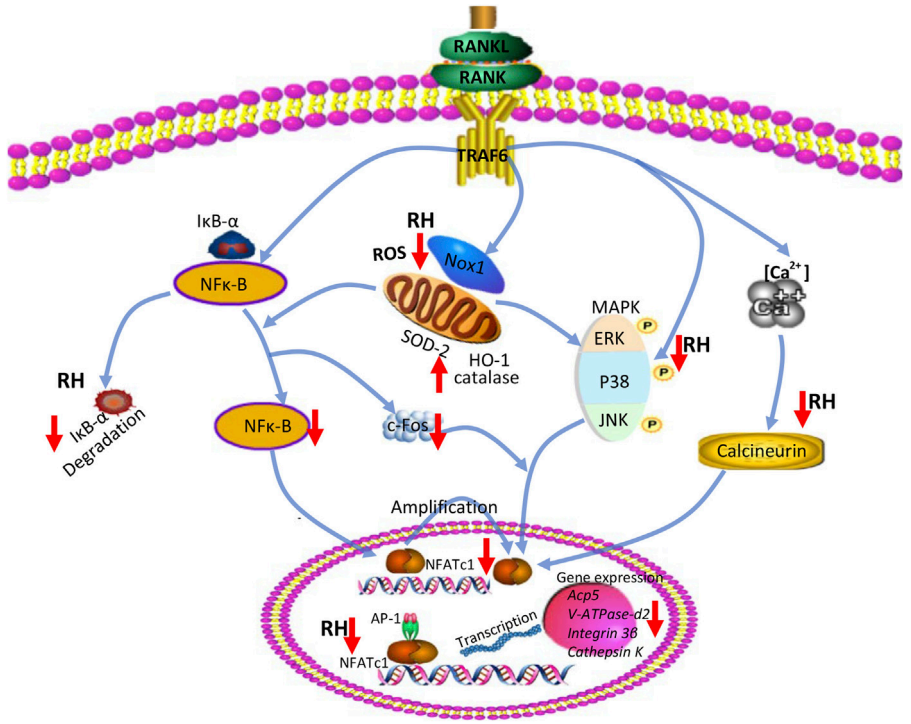

FIGURE 7 | A proposed diagram depicts the RH treatment on the inhibition of osteoclast formation and function. RH suppresses NF-κB activity, ERK, and P38 phosphorylation and Ca^{2+} oscillation, eventually leading to the deactivation of NFATc1 and its downstream osteoclast-specific genes. In addition, RH treatment also reduced ROS level by inhibiting ROS production and boosting ROS scavenging activity.

mainly mediated by Nox1 (Lee et al., 2005) and ROS were essential in mediating osteoclastogenesis by facilitating MAPKs and NF-κB (Koh et al., 2006; Kim, Lee, Kim, Lee, & Kim, 2017). Our results showed that the expression of Nox1 was effectively inhibited by RH. We then examined the RH's effect on antioxidant enzymes (HO-1, catalase, and SOD-2) which contribute to ROS scavenging. Previous studies showed that HO-1 was an antioxidant protein which can protect organs from the onset of tumorigenesis, and regulate osteoclastogenesis and bone resorption (Zwerina et al., 2005; Chen et al., 2016). Catalase could protect tumour cells against specific apoptosis induction by inhibiting the intercellular ROS generation (Bechtel & Bauer, 2009). SOD-2 was a vital factor for bone metabolism. The knockdown of SOD-2 would be inductive for ROS generation, leading to increasing osteoclasts formation. Whilst SOD-2 overexpression significantly suppressed the differentiation of mature osteoclast by attenuating ROS level (Kim, et al., 2017). These ROS scavenging proteins were significantly upregulated following RH treatment. Taken together, RH suppressed the ROS level during the osteoclastogenesis by significantly inhibiting ROS production and boosting ROS scavenging activity.

Upon RANKL binding to RANK, a series of downstream signalling cascades are initiated to regulate osteoclast formation. The expression of NFATc1 would be activated by the upstream cascades of TNF receptor-associated factor 6 (TRAF6), NF-κB, MAPK, and calcium-signalling pathways (Huang, Ryu, et al., 2006). IκB-α binds to NF-κB complex and prevents its translocation into the nucleus (Ghosh & Hayden, 2008). Following the stimulation of RANKL, IκB-α is degraded in the cytoplasm and releases NF-κB which subsequently induces osteoclastogenesis. Our results demonstrated that the treatment of RH inhibits the degradation of IκB-α in the presence of RANKL, indicating the suppression on NF-κB activity.

Furthermore, ERK and P38 are the essential members of the MAPK family. RANKL could enhance the phosphorylation levels of ERK and P38 to regulate the differentiation and function of osteoclasts (Liu et al., 2019). It was reported that the inhibitors of P38 (SB202190) and ERK (PD98059) could block the activation of the MAPK pathway and thus exerted a strong suppression on RANKL-induced osteoclast formation (Lee et al., 2002). The Western blot results demonstrated that RH could inhibit the expression levels of p-ERK1/2 and p-P38 induced by RANKL. This may also partly due to the decreased ROS level following RH treatment. The longlasting Ca^{2+} oscillation is essential to guarantee the vigorous induction of NFATc1 in an auto-amplification manner, which is initially triggered by the stimulation of RANKL (Asagiri et al., 2005). Calcineurin inhibitors potently suppressed RANKL-induced osteoclast formation via decreasing the translocation of nuclear NFATc1, suggesting the crucial role of the Ca^{2+}-NFATc1 pathway in osteoclastogenesis (Takayanagi, et al., 2002). Interestingly, we found that RH treatment downregulated the activity of RANKL-induced Ca^{2+} oscillation, which may largely contribute to the suppression of NFATc1 in our study.

In summary, our studies indicated that RH has inhibitory effects on RANKL-induced osteoclastogenesis and osteoclastic

resorption via effecting vital signaling including ROS, NF-κB, MAPK, Ca^{2+} oscillation, and eventually NFATc1 activation (**Figure 7**). The results propose that RH, a natural compound from *Rheum undulatum L.*, may be a potential and therapeutic candidate for the prevention and treatment of osteoclast-related bone disorders. However, in our study, the effected concentration for RH to exhibit the antiosteoporotic function is about 50μM, without cellular toxicity for BMMs, so the higher concentration should be considered in the future studies. Meanwhile the therapeutic effects on osteoporosis *in vivo* and the precise molecular target of RH in osteoclasts may require further investigations.

DATA AVAILABILITY STATEMENT

The original contributions presented in the study are included in the article/Supplementary material, further inquiries can be directed to the corresponding authors.

ETHICS

The study received animal ethics approval for the basic principle for the mice according to the animal ethics Committee of UWA (RA/3/100/1601).

AUTHOR CONTRIBUTIONS

JH and KC contributed equally to this work. JH and KC conceived the idea and wrote the manuscript. TC, JW, and KJ helped modify the language and the revision. JB, ZY, and ZF collected the literature. JK, DK, and XJ helped supervise the research and contribute to the final draft of the paper. We thanked RH and DL for the help of this review. All authors reviewed and approved the final manuscript.

FUNDING

This study was supported in part by the Australian National Health and Medical Research Council (NHMRC, Nos. 1107828, 1127156, 1163933), National Natural Science Foundation of China Youth Fund (No. 81904091) and Fundamental Research Funds for the Central Universities (No. 21619307).

ACKNOWLEDGMENTS

We acknowledge the facilities and technical assistance of the Center for Microscopy, Characterization and Analysis, The University of Western Australia.

REFERENCES

Adami, G., and Saag, K. G. (2019). Glucocorticoid-induced Osteoporosis: 2019 Concise Clinical Review. *Osteoporos. Int.* 30, 1145. doi:10.1007/s00198-019-04906-x

Aliprantis, A. O., Ueki, Y., Sulyanto, R., Park, A., Sigrist, K. S., Sharma, S. M., et al. (2008). NFATc1 in Mice Represses Osteoprotegerin during Osteoclastogenesis and Dissociates Systemic Osteopenia from Inflammation in Cherubism. *J. Clin. Invest.* 118, 3775–3789. doi:10.1172/jci35711

Asagiri, M., Sato, K., Usami, T., Ochi, S., Nishina, H., Yoshida, H., et al. (2005). Autoamplification of NFATc1 Expression Determines its Essential Role in Bone Homeostasis. *J. Exp. Med.* 202, 1261–1269. doi:10.1084/jem.20051150

Baron, R., and Kneissel, M. (2013). WNT Signaling in Bone Homeostasis and Disease: from Human Mutations to Treatments. *Nat. Med.* 19, 179–192. doi:10.1038/nm.3074

Bechtel, W., and Bauer, G. (2009). Catalase Protects Tumor Cells from Apoptosis Induction by Intercellular ROS Signaling. *Anticancer Res.* 29, 4541–4557.

Chen, K., Qiu, P., Yuan, Y., Zheng, L., He, J., Wang, C., et al. (2019). Pseurotin A Inhibits Osteoclastogenesis and Prevents Ovariectomized-Induced Bone Loss by Suppressing Reactive Oxygen Species. *Theranostics* 9, 1634–1650. doi:10.7150/thno.30206

Chen, K., Yuan, Y., Wang, Z., Song, D., Zhao, J., Cao, Z., et al. (2019a). Helvolic Acid Attenuates Osteoclast Formation and Function via Suppressing RANKL-Induced NFATc1 Activation. *J. Cel Physiol* 234, 6477–6488. doi:10.1002/jcp.27385

Chen, X., Wang, C., Qiu, H., Yuan, Y., Chen, K., Cao, Z., et al. (2019b). Asperpyrone A Attenuates RANKL-induced Osteoclast Formation through Inhibiting NFATc1, Ca 2+ Signalling and Oxidative Stress. *J. Cel Mol Med* 23, 8269–8279. doi:10.1111/jcmm.14700

Chen, X., Wei, S. Y., Li, J. S., Zhang, Q. F., Wang, Y. X., Zhao, S. L., et al. (2016). Overexpression of Heme Oxygenase-1 Prevents Renal Interstitial Inflammation and Fibrosis Induced by Unilateral Ureter Obstruction. *PLoS One* 11–e0147084. doi:10.1371/journal.pone.0147084

Cheng, J., Zhou, L., Liu, Q., Tickner, J., Tan, Z., Li, X., et al. (2018). Cyanidin Chloride Inhibits Ovariectomy-Induced Osteoporosis by Suppressing RANKL-Mediated Osteoclastogenesis and Associated Signaling Pathways. *J. Cel Physiol* 233, 2502–2512. doi:10.1002/jcp.26126

Croucher, P. I., McDonald, M. M., and Martin, T. J. (2016). Bone Metastasis: the Importance of the Neighbourhood. *Nat. Rev. Cancer* 16, 373–386. doi:10.1038/nrc.2016.44

Ghosh, S., and Hayden, M. S. (2008). New Regulators of NF-Kb in Inflammation. *Nat. Rev. Immunol.* 8, 837–848. doi:10.1038/nri2423

Harvey, N., Dennison, E., and Cooper, C. (2010). Osteoporosis: Impact on Health and Economics. *Nat. Rev. Rheumatol.* 6, 99–105. doi:10.1038/nrrheum.2009.260

Huang, H., Chang, E.-J., Ryu, J., Lee, Z. H., Lee, Y., and Kim, H.-H. (2006). Induction of C-Fos and NFATc1 during RANKL-Stimulated Osteoclast Differentiation Is Mediated by the P38 Signaling Pathway. *Biochem. Biophysical Res. Commun.* 351, 99–105. doi:10.1016/j.bbrc.2006.10.011

Huang, H., Ryu, J., Ha, J., Chang, E.-J., Kim, H. J., Kim, H.-M., et al. (2006a). Osteoclast Differentiation Requires TAK1 and MKK6 for NFATc1 Induction and NF-Kb Transactivation by RANKL. *Cell Death Differ* 13, 1879–1891. doi:10.1038/sj.cdd.4401882

Ibbotson, K. J., Roodman, G. D., McManus, L. M., and Mundy, G. R. (1984). Identification and Characterization of Osteoclast-like Cells and Their Progenitors in Cultures of Feline Marrow Mononuclear Cells. *J. Cel Biol* 99, 471–480. doi:10.1083/jcb.99.2.471

Indo, Y., Takeshita, S., Ishii, K.-A., Hoshii, T., Aburatani, H., Hirao, A., et al. (2013). Metabolic Regulation of Osteoclast Differentiation and Function. *J. Bone Miner Res.* 28, 2392–2399. doi:10.1002/jbmr.1976

Janckila, A. J., Takahashi, K., Sun, S. Z., and Yam, L. T. (2001). Tartrate-resistant Acid Phosphatase Isoform 5b as Serum Marker for Osteoclastic Activity. *Clin. Chem.* 47, 74–80. doi:10.1093/clinchem/47.1.74

Jin, H., Yao, L., Chen, K., Liu, Y., Wang, Q., Wang, Z., et al. (2019). Evodiamine Inhibits RANKL-Induced Osteoclastogenesis and Prevents Ovariectomy-Induced Bone Loss in Mice. *J. Cel Mol Med* 23, 522–534. doi:10.1111/jcmm.13955

Kim, A., and Ma, J. Y. (2018). Rhaponticin Decreases the Metastatic and Angiogenic Abilities of Cancer Cells via Suppression of the HIF-1α P-athway. *Int. J. Oncol.* 53, 1160–1170. doi:10.3892/ijo.2018.4479

Kim, H., Lee, Y. D., Kim, H. J., Lee, Z. H., and Kim, H.-H. (2017). SOD2 and Sirt3 Control Osteoclastogenesis by Regulating Mitochondrial ROS. *J. Bone Miner Res.* 32, 397–406. doi:10.1002/jbmr.2974

Koh, J.-M., Lee, Y.-S., Kim, Y. S., Kim, D. J., Kim, H.-H., Park, J.-Y., et al. (2006). Homocysteine Enhances Bone Resorption by Stimulation of Osteoclast

Formation and Activity through Increased Intracellular ROS Generation. *J. Bone Miner Res.* 21, 1003–1011. doi:10.1359/jbmr.060406

Lee, N. K., Choi, Y. G., Baik, J. Y., Han, S. Y., Jeong, D.-w., Bae, Y. S., et al. (2005). A Crucial Role for Reactive Oxygen Species in RANKL-Induced Osteoclast Differentiation. *Blood* 106, 852–859. doi:10.1182/blood-2004-09-3662

Lee, S. E., Woo, K. M., Kim, S. Y., Kim, H.-M., Kwack, K., Lee, Z. H., et al. (2002). The Phosphatidylinositol 3-kinase, P38, and Extracellular Signal-Regulated Kinase Pathways Are Involved in Osteoclast Differentiation. *Bone* 30, 71–77. doi:10.1016/s8756-3282(01)00657-3

Li, P., Tian, W., Wang, X., and Ma, X. (2014). Inhibitory Effect of Desoxyrhaponticin and Rhaponticin, Two Natural Stilbene Glycosides from the Tibetan Nutritional Food Rheum Tanguticum Maxim. Ex Balf., on Fatty Acid Synthase and Human Breast Cancer Cells. *Food Funct.* 5, 251–256. doi:10.1039/c3fo60484e

Liu, Y., Wang, C., Wang, G., Sun, Y., Deng, Z., Chen, L., et al. (2019). Loureirin B Suppresses RANKL-Induced Osteoclastogenesis and Ovariectomized Osteoporosis via Attenuating NFATc1 and ROS Activities. *Theranostics* 9, 4648–4662. doi:10.7150/thno.35414

López-Jornet, P., Camacho-Alonso, F., Molina-Miñano, F., and Gomez-Garcia, F. (2010). Bisphosphonate-associated Osteonecrosis of the Jaw. Knowledge and Attitudes of Dentists and Dental Students: a Preliminary Study. *J. Eval. Clin. Pract.* 16, 878–882. doi:10.1111/j.1365-2753.2009.01203.x

Manolagas, S. C., O'Brien, C. A., and Almeida, M. (2013). The Role of Estrogen and Androgen Receptors in Bone Health and Disease. *Nat. Rev. Endocrinol.* 9, 699–712. doi:10.1038/nrendo.2013.179

Melton, L. J., 3rd. (2003). Adverse Outcomes of Osteoporotic Fractures in the General Population. *J. Bone Miner Res.* 18, 1139–1141. doi:10.1359/jbmr.2003.18.6.1139

Negishi-Koga, T., and Takayanagi, H. (2009). Ca2+-NFATc1 Signaling Is an Essential axis of Osteoclast Differentiation. *Immunol. Rev.* 231, 241–256. doi:10.1111/j.1600-065x.2009.00821.x

Rachner, T. D., Khosla, S., and Hofbauer, L. C. (2011). Osteoporosis: Now and the Future. *The Lancet* 377, 1276–1287. doi:10.1016/s0140-6736(10)62349-5

Ross, R. K., Paganini-Hill, A., Wan, P. C., and Pike, M. C. (2000). Effect of Hormone Replacement Therapy on Breast Cancer Risk: Estrogen versus Estrogen Plus Progestin. *J. Natl. Cancer Inst.* 92, 328–332. doi:10.1093/jnci/92.4.328

Sasaki, H., Yamamoto, H., Tominaga, K., Masuda, K., Kawai, T., Teshima-Kondo, S., et al. (2009). NADPH Oxidase-Derived Reactive Oxygen Species Are Essential for Differentiation of a Mouse Macrophage Cell Line (RAW264.7) into Osteoclasts. *J. Med. Invest.* 56, 33–41. doi:10.2152/jmi.56.33

Takayanagi, H., Kim, S., Koga, T., Nishina, H., Isshiki, M., Yoshida, H., et al. (2002). Induction and Activation of the Transcription Factor NFATc1 (NFAT2) Integrate RANKL Signaling in Terminal Differentiation of Osteoclasts. *Develop. Cel* 3, 889–901. doi:10.1016/s1534-5807(02)00369-6

Tao, L., Cao, J., Wei, W., Xie, H., Zhang, M., and Zhang, C. (2017). Protective Role of Rhapontin in Experimental Pulmonary Fibrosis In Vitro and In Vivo. *Int. Immunopharmacology* 47, 38–46. doi:10.1016/j.intimp.2017.03.020

Teitelbaum, S. L. (2000). Bone Resorption by Osteoclasts. *Science* 289, 1504–1508. doi:10.1126/science.289.5484.1504

Wada, T., Nakashima, T., Hiroshi, N., and Penninger, J. M. (2006). RANKL-RANK Signaling in Osteoclastogenesis and Bone Disease. *Trends Mol. Med.* 12, 17–25. doi:10.1016/j.molmed.2005.11.007

Wang, C., Steer, J. H., Joyce, D. A., Yip, K. H., Zheng, M. H., and Xu, J. (2003). 12-O-tetradecanoylphorbol-13-acetate (TPA) Inhibits Osteoclastogenesis by Suppressing RANKL-Induced NF-Kb Activation. *J. Bone Miner Res.* 18, 2159–2168. doi:10.1359/jbmr.2003.18.12.2159

Wang, K., Li, F., Chen, L., Lai, Y.-M., Zhang, X., and Li, H.-Y. (2017). Change in Risk of Breast Cancer after Receiving Hormone Replacement Therapy by Considering Effect-Modifiers: a Systematic Review and Dose-Response Meta-Analysis of Prospective Studies. *Oncotarget* 8, 81109–81124. doi:10.18632/oncotarget.20154

Wang, Q., Yao, L., Xu, K., Jin, H., Chen, K., Wang, Z., et al. (2019). Madecassoside Inhibits Estrogen Deficiency-Induced Osteoporosis by Suppressing RANKL-Induced Osteoclastogenesis. *J. Cel Mol Med* 23, 380–394. doi:10.1111/jcmm.13942

Wei, W., Wang, L., Zhou, K., Xie, H., Zhang, M., and Zhang, C. (2017). Rhapontin Ameliorates Colonic Epithelial Dysfunction in Experimental Colitis through SIRT1 Signaling. *Int. Immunopharmacology* 42, 185–194. doi:10.1016/j.intimp.2016.11.024

Xu, J., Tan, J. W., Huang, L., Gao, X.-H., Laird, R., Liu, D., et al. (2000). Cloning, Sequencing, and Functional Characterization of the Rat Homologue of Receptor Activator of NF-Kb Ligand. *J. Bone Miner Res.* 15, 2178–2186. doi:10.1359/jbmr.2000.15.11.2178

Zhao, Q., Shao, J., Chen, W., and Li, Y. P. (2007). Osteoclast Differentiation and Gene Regulation. *Front. Biosci.* 12, 2519–2529. doi:10.2741/2252

Zhao, Q., Wang, X., Liu, Y., He, A., and Jia, R. (2010). NFATc1: Functions in Osteoclasts. *Int. J. Biochem. Cel Biol.* 42, 576–579. doi:10.1016/j.biocel.2009.12.018

Zwerina, J., Tzima, S., Hayer, S., Redlich, K., Hoffmann, O., Hanslik-Schnabel, B., et al. (2005). Heme Oxygenase 1 (HO-1) Regulates Osteoclastogenesis and Bone Resorption. *FASEB j.* 19, 2011–2013. doi:10.1096/fj.05-4278fje

Conflict of Interest: The authors declare that the research was conducted in the absence of any commercial or financial relationships that could be construed as a potential conflict of interest.

Publisher's Note: All claims expressed in this article are solely those of the authors and do not necessarily represent those of their affiliated organizations, or those of the publisher, the editors, and the reviewers. Any product that may be evaluated in this article, or claim that may be made by its manufacturer, is not guaranteed or endorsed by the publisher.

frontiers in Pharmacology

ORIGINAL RESEARCH
published: 24 September 2021
doi: 10.3389/fphar.2021.748684

A New Strategy to Investigate the Efficacy Markers Underlying the Medicinal Potentials of *Orthosiphon stamineus* Benth.

Zheng Li[1,2†], Biao Qu[3†], Lei Zhou[1], Hongwei Chen[4], Jue Wang[3], Wei Zhang[3] and Caifa Chen[1*]*

[1]Jiangsu Engineering Research Center of Cardiovascular Drugs Targeting Endothelial Cells, College of Health Sciences, School of Life Sciences, Jiangsu Normal University, Xuzhou, China, [2]State Key Laboratory of Natural and Biomimetic Drugs, Peking University, Beijing, China, [3]State Key Laboratory of Quality Research in Chinese Medicines, Macau University of Science and Technology, Macau, China, [4]School of Public Health (Shenzhen), Sun Yat-sen University, Shenzhen, China

OPEN ACCESS

Edited by:
Wei Song,
Peking Union Medical College Hospital (CAMS), China

Reviewed by:
Yu Pan,
Yunnan University, China
Yan Lin,
Guizhou Medical University, China

***Correspondence:**
Zheng Li
lizhengcpu@163.com
Caifa Chen
chencaifa@jsnu.edu.cn

[†]These authors have contributed equally to this work

Specialty section:
This article was submitted to Ethnopharmacology, a section of the journal Frontiers in Pharmacology

Received: 28 July 2021
Accepted: 08 September 2021
Published: 24 September 2021

Citation:
Li Z, Qu B, Zhou L, Chen H, Wang J, Zhang W and Chen C (2021) A New Strategy to Investigate the Efficacy Markers Underlying the Medicinal Potentials of Orthosiphon stamineus Benth.. Front. Pharmacol. 12:748684. doi: 10.3389/fphar.2021.748684

Orthosiphon stamineus Benth. (OSB) is a well-known herbal medicine exerting various pharmacological effects and medicinal potentials. Owing to its complex of phytochemical constituents, as well as the ambiguous relationship between phytochemical constituents and varied bioactivities, it is a great challenge to explore which constituents make a core contribution to the efficacy of OSB, making it difficult to determine the efficacy makers underlying the varied efficacies of OSB. In our work, a new strategy was exploited and applied for investigating efficacy markers of OSB consisting of phytochemical analysis, *in vivo* absorption analysis, bioactive compound screening, and bioactive compound quantification. Using liquid chromatography coupled with mass spectrometry, a total of 34 phytochemical components were detected in the OSB extract. Subsequently, based on *in vivo* absorption analysis, 14 phytochemical constituents in the form of prototypes were retained as potential bioactive compounds. Ten diseases were selected as the potential indications of OSB based on previous reports, and then the overall interaction between compounds, action targets, action pathways, and diseases was revealed based on bioinformatic analysis. After refining key pathways and targets, the interaction reversing from pathways, targets to constituents was deduced, and the core constituents, including tanshinone IIA, sinensetin, salvianolic acid B, rosmarinic acid, and salvigenin, were screened out as the efficacy markers of OSB. Finally, the contents of these five constituents were quantified in three different batches of OSB extracts. Among them, the content of salvianolic acid B was the highest while the content of tanshinone IIA was the lowest. Our work could provide a promising direction for future research on the quality control and pharmacological mechanism of OSB.

Keywords: herbal medicine, efficacy markers, *Orthosiphon stamineus* benth., quality control, phytochemical analysis

INTRODUCTION

The usage of herbal products as drugs for disease treatment, cosmetics, and health supplements is truly universal as can be seen in different regions of the world. Moreover, herbs, commonly containing various primary and secondary metabolites, have been exploited as a valuable source of leading compounds, and many of the approved drugs have been directly or indirectly derived from them (Bauer et al., 2014). *Orthosiphon stamineus* Benth. (syn: *Orthosiphon aristatus* (Blume) Miq.) (OSB) is a medicinal plant from the Lamiaceae family which is widely distributed in southern China and Southeast Asia. In China, the dried whole plant of OSB is also named "Shen Cha," which is a popular folk medicine of Dai nationality (Chen et al., 2009). As a traditional medicinal herb, OSB has been widely used for the treatment of kidney stones and other urinary tract diseases on empiricism (Arafat et al., 2008). In past decades, many studies have explored the pharmacological effects and medicinal potentials of OSB. The reported therapeutic effects of OSB included a diuretic effect for treating urinary diseases (Adam et al., 2009), glucose-lowering ability for treating type 2 diabetes mellitus (T2DM) (Lokman et al., 2019), anti-inflammatory activities for managing arthritis (Tabana et al., 2016), hepatoprotective effect for alleviating liver injury (Yam et al., 2007), and neuroprotective ability for improving Alzheimer's disease (AD) (Retinasamy et al., 2020), etc.

Many constituents have been identified in this herb and the major compounds included phenolic acids, polymethoxylated flavonoids, terpenoids, hexoses, and saponins (Malterud et al., 1989; Tezuka et al., 2000; Nguyen et al., 2004; Hossain et al., 2013; Guo et al., 2019b). In previous studies, the water-soluble constituents, such as protocatechuic acid, caffeic acid, and danshensu, were regarded as the key bioactive constituents, since they were found to possess anti-oxidant and anti-inflammatory properties (Nuengchamnong et al., 2011; Alshawsh et al., 2012). Meanwhile, the alcohol-soluble constituents including sinensetin, eupatorin, and 3′-hydroxy-5,6,7,4′-tetramethoxyflavone (TMF), were also reported to exert various pharmacological activities, thus the efficacy of OSB has also been attributed to them in several studies (Yam et al., 2008; Yam et al., 2009; Chan et al., 2017). However, there are dozens of constituents in OSB, so many of them have been reported to exhibit bioactivities. Furthermore, the multiple constituents could synergistically act on targets to yield a holistic therapeutic effect. Consequently, it is a great challenge to explore which constituents make a core contribution to the efficacy of OSB. Likewise, these issues also make it difficult to elucidate the relationship between the phytochemicals and the holistic efficacy.

In the most recent decade, bioinformatics, represented by network pharmacology, have become efficient tools for revealing the scientific basis and systematic features of herbal medicines. These approaches provide a holistic insight into the relationship between compounds, targets, and signaling pathways behind drug efficacy (Hopkins, 2008; Chen et al., 2016). Interestingly, recent studies have utilized network analysis to screen bioactive constituents as efficacy markers for quality control of herbal medicines (Liao et al., 2018; Xiang et al., 2018; Luo L. et al., 2020). However, challenges are still hanging over many of those related studies. For instance, the predicted phytochemicals from databases could show significant deviation from the realistic constituents of herbs. Moreover, the latest analytical techniques might provide more and newer phytochemicals which go beyond the content of databases. The predicted oral bioavailability (OB) is often used in preliminary screening of phytochemicals, whereas, the screened constituents might differ from the constituents actually absorbed in blood. In addition, one herb could have medicinal potentials for the treatment of different diseases. Nevertheless, often, many studies only focus on one indication, thus resulting in biased conclusions of bioactive constituents to one specific disease. Consequently, these constituents fail to account for the overall efficacy of the herb, which results in the fragile reliability of determining them as efficacy markers.

In this work, a new strategy, consisting of phytochemical analysis, *in vivo* absorption analysis, bioactive compound screening, and bioactive compound quantification, was exploited for investigating efficacy markers underlying the medicinal potentials of OSB. Using liquid chromatography coupled with quadrupole time-of-flight mass spectrometry (LC-Q/TOF-MS), the constituents in OSB extract were comprehensively characterized. Then, the blood-absorbed constituents were identified in plasma samples from rats after oral administration of OSB extract, which were retained as potential bioactive compounds. After selecting the potential indications of OSB, bioinformatic analysis was used to reveal the interaction between compounds, action targets, action pathways, and different diseases, and the core bioactive constituents were screened out as the efficacy markers of OSB. Finally, the quantitative analysis of efficacy markers was carried out by an established LC-MS/MS method.

MATERIALS AND METHODS

Reagents and Materials

Raw materials of OSB were purchased from Yunnan Jianping Biotechnology Co., Ltd. (Origin: Xishuangbanna, Yunnan, China). Analytical grade ethanol and chloroform were obtained from Anaqua Global International Inc. Limited (Cleveland, OH, United States). LC-MS-grade acetonitrile was supplied from J. T. Baker (Phillipsburg, NJ, United States of America). LC-MS-grade formic acid was obtained from Fisher Scientific (Fair Lawn, NJ, United States). Ultra-pure water produced from a Milli-Q Gradient Water System (Millipore Corp Bedford, United States) was used throughout the study. Chromatographic column Sepax GP-C18 (2.1 × 150 mm, 1.8 μm) was purchased from Sepax Technologies (Newark, DE, United States). Reference substances of protocatechuic acid and cichoric acid were obtained from National Institutes for Food and Drug Control (Beijing, China); danshensu, rosmarinic acid, salvianolic acid A, salvianolic acid B, and sinensetin were

purchased from Macklin Biochemical Co., Ltd. (Shanghai, China); eupatorin, salvigenin, and TMF were provided by Shanghai yuanye Bio-Technology Co., Ltd. (Shanghai, China). All reference substances possessed high purities up to 97%.

Preparation of OSB Extract Samples

The dried herb of OSB was smashed to powder. A total of 10 g powder was extracted twice with 100 ml of ethanol-water (80:20, v/v) in an ultrasonic bath for 30 min. The mixture was filtered and the filtrate was combined. The obtained solution was evaporated to a concrete under reduced pressure at 55°C. Then it was dissolved in methanol to remove starch and polysaccharides. After standing at room temperature for 24 h, the solution was centrifuged to remove the precipitate (12,000×*g*, 15 min). The obtained filtrate was evaporated under reduced pressure at 40°C until dry to yield the OSB extract. For qualitative analysis, OSB extract (3.0 mg) was dissolved in 10.0 mL of methanol, followed by filtration through a 0.22 μm nylon membrane filter before LC-MS analysis. Respective standard stock solutions of eight reference substances were prepared in methanol, and stored at −20°C before use.

Preparation of OSB Plasma Samples

Male Sprague-Dawley rats (200 ± 20 g, $n = 3$) were provided by Guangdong Medical Laboratory Animal Center (Guangzhou, China), and fed at the Experimental Animal Center of Macau University of Science and Technology (Macau, China). Rats were kept at an ambient temperature of 22–25°C and a relative humidity of 55 ± 5% with 12 h light/dark cycles. They were fed with free access to water and food, and fasted with free access to water for 12 h before drug administration. The experimental protocol was approved by the Ethics Review Committee for Animal Experimentation of Macau University of Science and Technology. All procedures were in accordance with the Guide for the Care and Use of Laboratory Animals (National Institutes of Health). OSB extract was dissolved in 0.5% carboxymethyl cellulose sodium aqueous solution to give an apparent concentration of 0.2 g/mL for oral administration. Then the OSB extract was administered to rats orally with a single dose of 1.0 g/kg. Blood samples were then collected from the tail vein at 1 h after administration and centrifuged to separate plasma. A total of 100 μL of plasma was mixed with methanol/acetonitrile (1:2; v:v) solution (300 μL), followed by vortex for 1 min. After centrifugation, the collected supernatant was evaporated until dry under nitrogen gas. The residue was re-dissolved in 200 μL of methanol and then centrifuged to separate the supernatant for LC-MS analysis.

Qualitative Analysis of Phytochemical Constituents in OSB Samples

Qualitative analysis was carried out on an Agilent 6550 ultra-performance liquid chromatography coupled with a quadrupole time-of-flight mass spectrometry (UPLC-Q/TOF-MS) system. Chromatographic separation was achieved on a Sepax GP-C18 column with an ambient temperature of 35°C. The mobile phase was composed of 0.1% formic acid aqueous solution (A) and acetonitrile (B), and delivered at a flow rate of 0.25 mL/min using the following gradient program: 0–5 min, 25–35% B; 5–10 min, 35–50% B; 10–15 min, 50–53% B; 15–20 min, 53–56% B; 20–25 min, 56–80% B; 25–30 min, 80–85% B; 30–35 min, 85–90% B; 35–40 min, 90–95% B; 40–45 min, 95–25% B. The autosampler was set at 4°C and the injection volume was 5 μL. The MS equipped with an electrospray ionization (ESI) source was carried out in both positive and negative modes using the following optimized parameters: ion spray voltage, 3500 V for positive mode and 3000 V for negative mode; vaporizer temperature, 280°C; sheath gas pressure, 50 psi; capillary temperature, 320°C; and auxiliary gas pressure, 15 psi. The full scan data were acquired from 100 to 1,000 Da, and MS/MS fragmentation was carried out with different collision energy. Identification of the phytochemical compounds was achieved by matching their retention times (RT), molecular ions, and product ions obtained from LC-MS and LC-MS/MS analysis with corresponding reference substances and literature data.

Constituent Screening and Target Collection

For constituents detected in OSB extract, the OB parameters were extracted from the TCMSP database (http://tcmspw.com/index.php), and OB ≥ 30% was selected as a threshold for screening potential bioactive constituents. For constituents detected in plasma samples, all of them were considered as potential bioactive constituents. Based on comparison, the potential active constituents were determined. Then, the TCMSP (http://tcmspw.com/index.php) and STITCH (http://stitch.embl.de/) databases were used to predict potential action targets of OSB. Moreover, a text mining of PubMed (2016–2021) with each constituent as a search term was carried out to manually extract potential targets for updates and supplementation.

Based on the reported efficacies of OSB, ten diseases were chose as its potential clinical indications, including AD, arthritis, chronic glomerulonephritis, chronic renal failure, gout, hepatic cirrhosis, hepatic fibrosis, hyperlipidemia, nephrolithiasis, and T2DM. The targets of these diseases were extracted from the human gene database GeneCards (http://www.genecards.org/). The items "Symbol" and "Score" of genes were reserved, in which the "Score" represents the relevance degree between disease and target. The intersection targets between OSB and each disease were generated through target mapping. The contribution of each constituent to the intersection targets was analyzed.

Bioinformatic Analysis of Compounds, Targets, Enriched Pathways, and Their Interaction

Since different constituents in OSB had the same targets, the repetitive targets were merged and the repetition quantity of each target was counted as n, followed by normalization with the maximum normalized to 1. For each disease, the "Score" values of their targets were also normalized by being divided by the maximum. Subsequently, the quantitative datasets of OSB targets and disease targets were combined to build a data

matrix of OSB-disease targets. Then it was imported into software SIMCA-P (Ver.12.0) and Heml (Ver.1.0.3) for multivariate data analysis to investigate the relevance degree between OSB target profile and disease target profile.

The target data of each OSB-disease pair were combined to generate a whole dataset. After it was imported into Cytoscape (Ver.3.7), the network visualizing the relationship of OSB-compound-target-disease was constructed. For each OSB-disease pair, the top 7 constituents and top 20 targets were extracted according to their degree values. For each OSB-disease pair, the intersection targets were imported into STRING (http://www.string-db.org/) to predict the protein-protein interaction (PPI). Subsequently, the top 20 targets from each PPI network were extracted and combined. These targets were used to generate a new PPI network, and the key regulatory targets were predicted. KEGG pathway enrichment was performed, and a *p* value was given along with each enriched pathway. Based on *p* values, the top 20 pathways were extracted for each OSB-disease pair, respectively. Then these top pathways were combined, and among them the shared pathways by all OSB-disease pairs were retained. Meanwhile, the embedded targets and signaling pathways were also labeled.

Screening the Efficacy Markers of OSB Through Reversing Bioinformatics Analysis

Based on the enriched pathways, the raw data of key KEGG pathways consisting of embedded signaling pathways and targets were retrieved. After PPI analysis, the raw data of the key target-target interaction were retrieved. From the compound-target network, the raw data of the compound-target interaction were retrieved. Subsequently, the retrieved datasets were combined to generate a new whole dataset. After it was imported into Cytoscape (Ver.3.7), a comprehensive network, that strung together pathway-target pairs, target-target pairs, and target-compound pairs, was finally constructed. Based on topological analysis, the core signaling pathways were firstly deduced then the core targets, and finally the core constituents were screened out as the efficacy markers of OSB.

Quantitative Analysis of the Efficacy Markers in OSB

Liquid chromatography coupled with triple-quadrupole mass spectrometry (LC-QQQ-MS/MS) was used for simultaneous quantitation of efficacy markers in OSB. A Waters ACQUITY BEH C18 column (3.0 × 100 mm, 2.5 μm) was used for chromatographic separation. The column temperature was maintained at 35°C. Mobile phase consisted of 0.1% formic acid solution (A) and acetonitrile (B). To obtain a short run time and good chromatographic behaviors, the LC conditions were optimized. The flow rate was set at 0.3 mL/min using the following gradient program: 0–5 min, 5–35% B; 5–7 min, 35–60% B; 7–8 min, 65–70% B; 8–9 min, 70–90% B; 9–10 min, 90–5% B. ESI-MS/MS was carried out in both positive and negative modes. The ESI parameters were as follows: ESI temperature was 500°C; ion spray voltage was 5500 V and 4500 V in the negative and positive modes, respectively; curtain gas was 20 psi. Meanwhile, the MS/MS parameters for analyte determination in multiple reaction monitoring (MRM) mode were optimized. The calibration curves were created by running mixed standards of efficacy markers at a series of concentrations. The contents of each efficacy marker in three batches of OSB extracts were determined based on the calibration curve created on the same day.

RESULTS

Constituent Identification and Screening in OSB

The identification of phytochemical constituents in OSB extract was performed by LC-Q/TOF-MS analysis. As shown in chromatograms, a larger peak number was generated in the negative mode (**Figure 1A**) while a stronger MS response was obtained in the positive mode (**Figure 1B**). The detailed fragment information of parent ions was obtained from MS/MS fragmentation. For these detected peaks, they were deduced and identified based on the retention time, exact mass, and fragment information through matching with reference substances or related data reported in the literature (Malterud et al., 1989; Awale et al., 2001; Akowuah et al., 2004; Guo et al., 2019a; Guo et al., 2019b). As represented in **Table 1** and **Figure 1**, a total of 34 peaks with significant responses were detected. For peaks 1, 3, 8, 10, 12, 14, 18, 22, 24, and 28, these compounds were unambiguously identified by comparison with their reference substances. The identified constituents were categorized as 12 phenylpropenoic acids, 2 benzoic acids, 1 flavonoid glycoside, 12 polymethoxylated flavones, 6 diterpenes, and 1 triterpenoid. Among them, phenylpropenoic acids and polymethoxylated flavones were the top two categories in the OSB extract. Most phenylpropenoic acids displayed the same fragment ion at m/z 179 which was the precursor ion of caffeic acid, and these compounds were regarded as its derivatives. For polymethoxylated flavones, most of them presented same fragment ions at m/z 313 and 298 that were produced by continuous loss of OCH_3. For diterpenoids, some compounds presenting the same fragment ion at m/z 121 due to the presence of the benzoyl group belonged to the orthosiphol class, and some compounds giving the same fragment ion at m/z 249 belonged to the tanshinone class. In a word, a total of 34 main phytochemical constituents were identified in the OSB extract.

The developed method was then applied to investigate the blood-absorbed phytochemicals in rats after oral administration of OSB extract. **Figures 2A,B** showed the representative chromatograms of plasma samples generated in negative and positive modes, respectively. A total of 17 phytochemical constituents of OSB were identified in rat plasma samples. These constituents including danshensu, caffeic acid, protocatechuic acid, orthosiphoic acid A, cichoric acid, rosmarinic acid, salvianolic acid A, salvianolic acid B, rhamnazin, TMF, sinensetin, eupatorin,

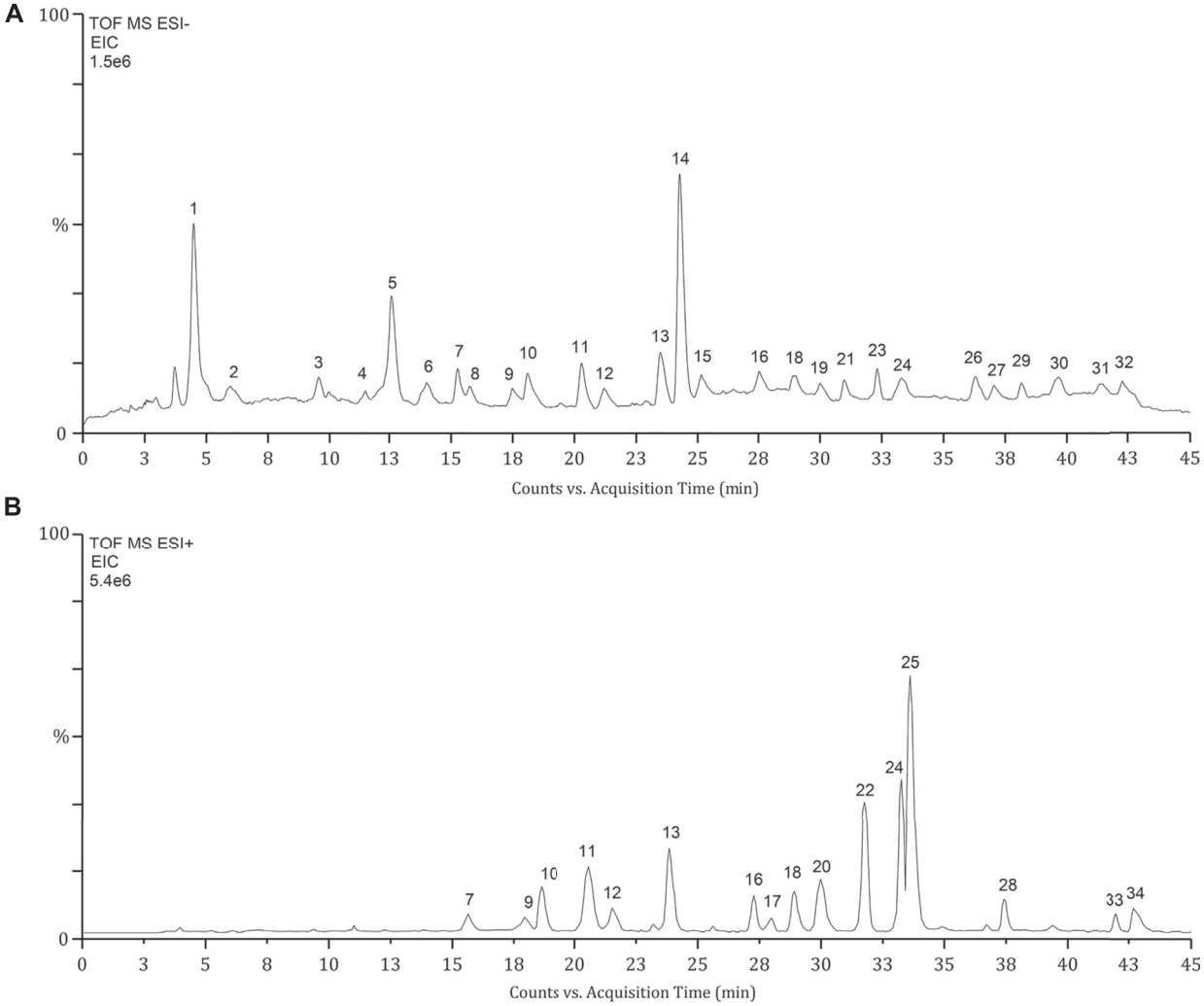

FIGURE 1 | Extracted ion chromatograms (EIC) of OSB samples obtained from LC-Q/TOF-MS analysis. EIC of OSB extract samples in negative mode **(A)** and positive mode **(B)**. LC-Q/TOF-MS, liquid chromatography coupled with quadrupole time-of-flight mass spectrometry; OSB, *Orthosiphon stamineus* Benth.

tetramethylscutellarein, pillion, salvigenin, orthosiphol A, and tanshinone IIA. Consistent with the above phytcochemical characterization, phenylpropenoic acids and polymethoxylated flavones were also the top two categories that could be absorbed in the circulatory system.

Based on the OB parameter, a total of 20 constituents were screened out from 34 constituents. Several constituents with large OB, such as trimethylapigenin (OB 39.83%), however, were not detected in rat plasma. By contrast, several constituents with small OB, such as rosmarinic acid (OB 1.38%), however, were detected in rat plasma. Nevertheless, these screened constituents still showed a lot of overlapping with the phytochemicals detected in plasma samples. For the constituents detected in plasma samples, preliminary collection of their targets was carried out. Finally, the constituents with reported targets were screened out as potential bioactive constituents, including protocatechuic acid, danshensu, caffeic acid, orthosiphoic acid A, cichoric acid, rosmarinic acid, salvianolic acid A, salvianolic acid B, TMF, sinensetin, eupatorin, salvigenin, orthosiphol A, and tanshinone IIA. The chemical structures of these phytochemicals were provided in **Figures 2A,B**.

Bioinformatic Analysis of the Interaction From Compounds to Targets and Pathways

OSB constituents generated a total of 488 potential targets. After overlapping, OSB shared 410, 383, 208, 421, 164, 339, 392, 210, 137, and 439 targets with AD, arthritis, chronic glomerulonephritis, chronic renal failure, gout, hepatic cirrhosis, hepatic fibrosis, hyperlipidemia, nephrolithiasis, and T2DM, respectively (**Figure 3A**). As detailed in each phytochemical constituent, the contribution to targets varied from constituent to constituent. Salvianolic acid A, protocatechuic acid, and tanshinone IIA were the top three in terms of counting their contribution to the total targets of OSB

TABLE 1 | Constituents identified in the extract of *Orthosiphon stamineus* Benth.

Peak No	Precursor ion	Measured mass (m/z)	Calculated mass (m/z)	Error (ppm)	Formula	Fragments (m/z)	Identification	Categories
1	$[M–H]^-$	197.0432	197.0449	8.5	$C_9H_{10}O_5$	197, 179, 135, 109	Danshensu	Phenylpropenoic acids
2	$[M–H]^-$	179.0335	179.0343	4.6	$C_9H_8O_4$	179, 135	Caffeic acid	Phenylpropenoic acids
3	$[M–H]^-$	153.0173	153.0187	8.9	$C_7H_6O_4$	153, 109	Protocatechuic acid	Benzoic acids
4	$[M–H]^-$	167.0349	167.0343	–3.5	$C_8H_8O_4$	167, 138, 109	Protocatechuic acid methyl ester	Benzoic acids
5	$[M–H]^-$	179.0329	179.0343	7.9	$C_9H_8O_4$	179, 170, 154, 134	Caffeic acid isomer	Phenylpropenoic acids
6	$[M–H]^-$	207.0641	207.0656	7.3	$C_{11}H_{12}O_4$	207, 179, 135	Caffeic acid ethyl ester	Phenylpropenoic acids
7	$[M–H]^-$	521.1098	521.1083	–2.9	$C_{27}H_{22}O_{11}$	521, 323, 197, 161	Orthosiphoic acid A	Phenylpropenoic acids
8	$[M–H]^-$	473.0738	473.0725	–2.7	$C_{22}H_{18}O_{12}$	473, 179, 149	Cichoric acid	Phenylpropenoic acids
9	$[M–H]^-$	717.1436	717.1454	2.6	$C_{36}H_{30}O_{16}$	717, 519, 537	Salvianolic acid E	Phenylpropenoic acids
10	$[M–H]^-$	359.0751	359.0766	4.1	$C_{18}H_{16}O_8$	359, 197, 179	Rosmarinic acid	Phenylpropenoic acids
11	$[M–H]^-$	537.1049	537.1032	–3.2	$C_{27}H_{22}O_{12}$	537, 493, 356	Lithospermic acid	Phenylpropenoic acids
12	$[M–H]^-$	493.1152	493.1134	–3.7	$C_{26}H_{22}O_{10}$	493, 295, 267	Salvianolic acid A	Phenylpropenoic acids
13	$[M–H]^-$	491.0961	491.0977	3.3	$C_{26}H_{20}O_{10}$	491, 293	Salvianolic acid C	Phenylpropenoic acids
14	$[M–H]^-$	717.1473	717.1454	–2.6	$C_{36}H_{30}O_{16}$	717, 519, 321, 295	Salvianolic acid B	Phenylpropenoic acids
15	$[M–H]^-$	463.0857	463.0875	4.0	$C_{21}H_{20}O_{12}$	463, 300271	Isoquercitrin	Flavonoid glycosides
16	$[M–H]^-$	329.0675	329.0660	–4.5	$C_{17}H_{14}O_7$	329, 245, 151	Rhamnazin	Polymethoxylated flavones
17	$[M + H]^+$	313.1090	313.1077	–4.1	$C_{18}H_{16}O_5$	313, 298, 283	Trimethylapigenin	Polymethoxylated flavones
18	$[M–H]^-$	357.0956	357.0973	4.8	$C_{19}H_{18}O_7$	357, 345, 296, 269	3′-Hydroxy-5,6,7,4′-tetramethoxyflavone	Polymethoxylated flavones
19	$[M–H]^-$	313.0724	313.0711	–4.2	$C_{17}H_{14}O_6$	313, 299, 285	Ermanin	Polymethoxylated flavones
20	$[M + H]^+$	343.1171	343.1183	3.5	$C_{19}H_{18}O_6$	343, 329, 315	Tetramethoxyluteolin	Polymethoxylated flavones
21	$[M–H]^-$	313.0720	313.0711	–2.9	$C_{17}H_{14}O_6$	313, 298, 283	Cirsimaritin	Polymethoxylated flavones
22	$[M + H]^+$	373.1270	373.1288	4.9	$C_{20}H_{20}O_7$	373, 358, 343, 315	Sinensetin	Polymethoxylated flavones
23	$[M–H]^-$	569.2360	569.2386	4.5	$C_{31}H_{38}O_{10}$	569, 121	Orthosiphol I	Diterpenoids
24	$[M–H]^-$	343.0833	343.0817	–4.8	$C_{18}H_{16}O_7$	343, 328, 313, 285	Eupatorin	Polymethoxylated flavones
25	$[M + H]^+$	343.1173	343.1183	2.9	$C_{19}H_{18}O_6$	343, 328, 313, 285	Tetramethylscutellarein	Polymethoxylated flavones
26	$[M–H]^-$	313.0723	313.0711	–3.8	$C_{17}H_{14}O_6$	313, 298, 83, 255	Pilloin	Polymethoxylated flavones
27	$[M–H]^-$	327.0881	327.0867	–4.1	$C_{18}H_{16}O_6$	327, 313, 298	5-Hydroxy-3′,4′,7-trimethoxyflavone	Polymethoxylated flavones
28	$[M + H]^+$	329.1038	329.1026	–3.6	$C_{18}H_{16}O_6$	329, 314, 296	Salvigenin	Polymethoxylated flavones
29	$[M–H]^-$	631.2527	631.2542	2.4	$C_{36}H_{40}O_{10}$	631, 121	Orthosiphol N	Diterpenoids
30	$[M–H]^-$	675.2828	675.2804	–3.5	$C_{38}H_{44}O_{11}$	675, 637, 589, 505	Orthosiphol A	Diterpenoids
31	$[M–H]^-$	677.2573	677.2597	3.5	$C_{37}H_{42}O_{12}$	677, 631, 121	Norstaminol A	Diterpenoids
32	$[M–H]^-$	455.3540	455.3524	–3.5	$C_{30}H_{48}O_3$	455	Oleanolic acid	Triterpenoids
33	$[M + H]^+$	277.0877	277.0866	–4.0	$C_{18}H_{12}O_3$	277, 249, 231	Tanshinone A	Diterpenoids
34	$[M + H]^+$	295.1346	295.1335	–3.6	$C_{19}H_{18}O_3$	295, 277, 249	Tanshinone IIA	Diterpenoids

(**Figure 3B**). By comparison, there was a remarkable variation in the overall profile of target contribution after intersection with disease targets (**Figure 3B**). Rosmarinic acid, sinensetin, salvigenin danshensu, cichoric acid, and orthosiphoic acid A were the representatives, in which the first four constituents showed increased contribution after intersection while the last two showed decreased contribution after intersection. Tanshinone IIA, rosmarinic acid, and sinensetin were the top three constituents in contribution percentage after intersection, in contrast, rosmarinic acid and sinensetin showed a very low contribution percentage before intersection. These results suggested that, for constituents, the effective targets they possessed for diseases were more meaningful than the amount of total targets.

Based on multivariate data analysis employing principal component analysis (PCA) and hierarchical cluster analysis (HCA) models, the relevance degree between OSB target profile and disease target profile was investigated. A 3D score plot was generated in SIMCA using the PCA model, and it visualized the relevance of overall targets between groups (**Figure 3C**). The OSB group showed clear separation from the disease groups, and most disease groups were located in the same dimension. Interestingly, only the AD group was located in the same dimension as the OSB group, and was the nearest to the

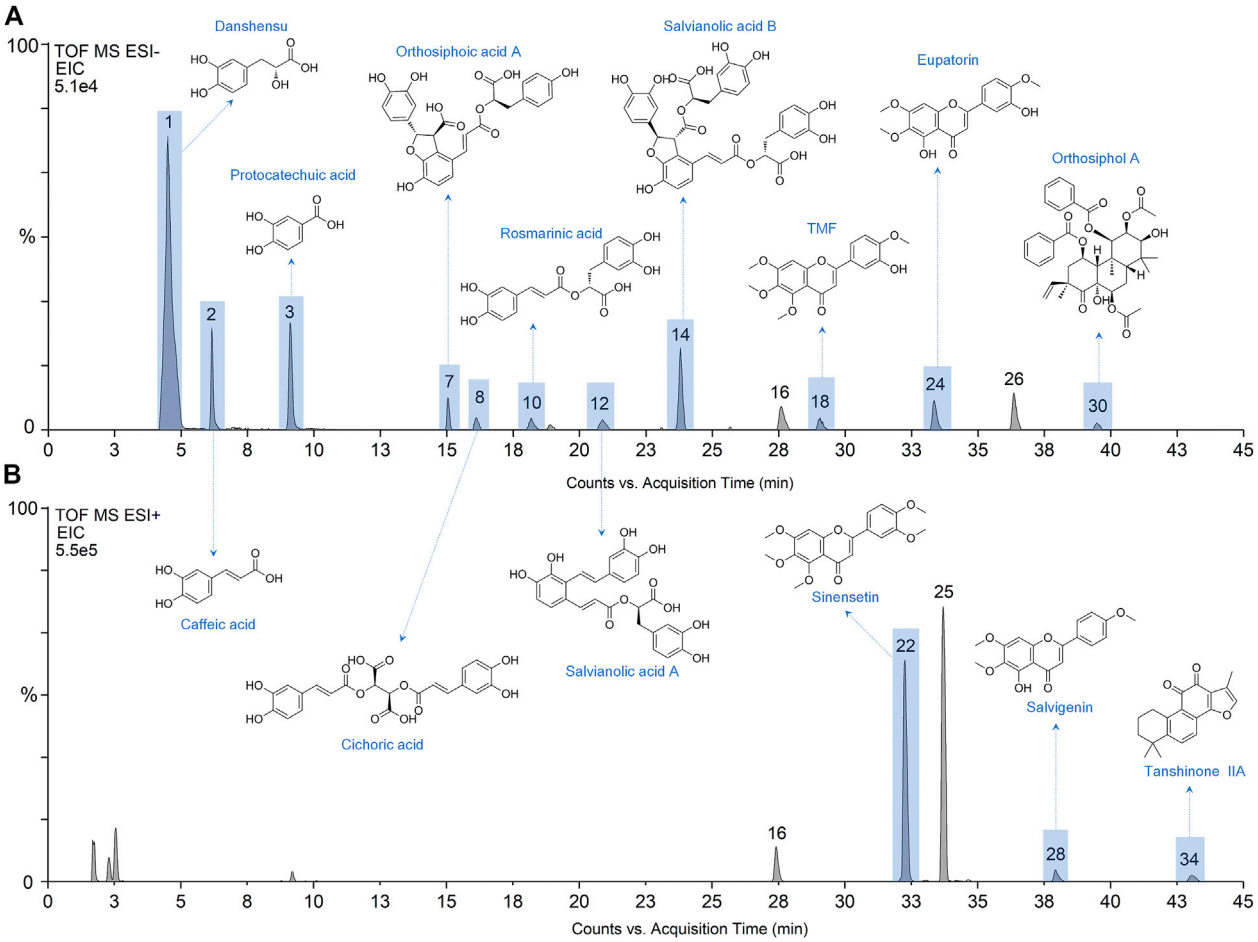

FIGURE 2 | Extracted ion chromatograms (EIC) of plasma samples from rats after administration of OSB extract in negative mode **(A)** and positive mode **(B)**. OSB *Orthosiphon stamineus* Benth.

OSB group, followed by the arthritis and chronic glomerulonephritis groups (**Figure 3C**). Consistently, the heatmap generated in Heml using the HCA model showed similar results, which visualized the relevance of both individual and overall targets between groups (**Figure 3D**). Based on integrative comparison, AD, arthritis, and chronic glomerulonephritis had a strong affinity with OSB in terms of target profile.

The interaction of OSB-compound-target-disease was visualized in a network which integrated all OSB-disease pairs (**Figure 4**). In this network, the top 7 constituents and top 20 targets were magnified into a sub-network for each OSB-disease pair. Among these top constituents, up to six constituents were shared by all OSB-disease pairs as follows: protocatechuic acid, rosmarinic acid, salvianolic acid B, salvigenin, sinensetin, and tanshinone IIA. Among these top targets, up to six targets were shared by all OSB-disease pairs as follows: IL1B, IL6, MMP2, MMP9, NOS2, and TNF. For each OSB-disease pair, the top 20 targets were respectively extracted from the PPI network. Then a refined PPI network was then constructed through integrating these top targets (**Supplementary Figure S1**). Based on the topological properties, the key regulatory targets were screened out as follows: AKT1, JAK2, JUN, MAPK1, MAPK8, PIK3CA, PIK3R1, RELA, STAT3, TNF, and TP53. After pathway enrichment, the top 20 pathways for each OSB-disease pair were combined. After merging duplicates, only 37 non-repetitive pathways were retained, suggesting extensive overlapping among the top pathways from each OSB-disease pair (**Figure 5**). After analysis, a total of eight KEGG pathways shared by all OSB-disease pairs were screened out. The detailed information of these pathways is provided in **Supplementary Table S1**. One representative pathway is shown in **Figure 5** in which OSB-disease intersection targets were labeled with color.

Screening of the Efficacy Markers of OSB Through Reversing Bioinformatics Analysis

Based on extraction, 8 key KEGG pathways generated 17 different signaling pathways. As shown in **Figure 6**, a KEGG pathway contained several signaling pathways, while a signaling pathway was also embedded in several KEGG pathways. These signaling pathways contained 209 OSB-disease intersection targets after

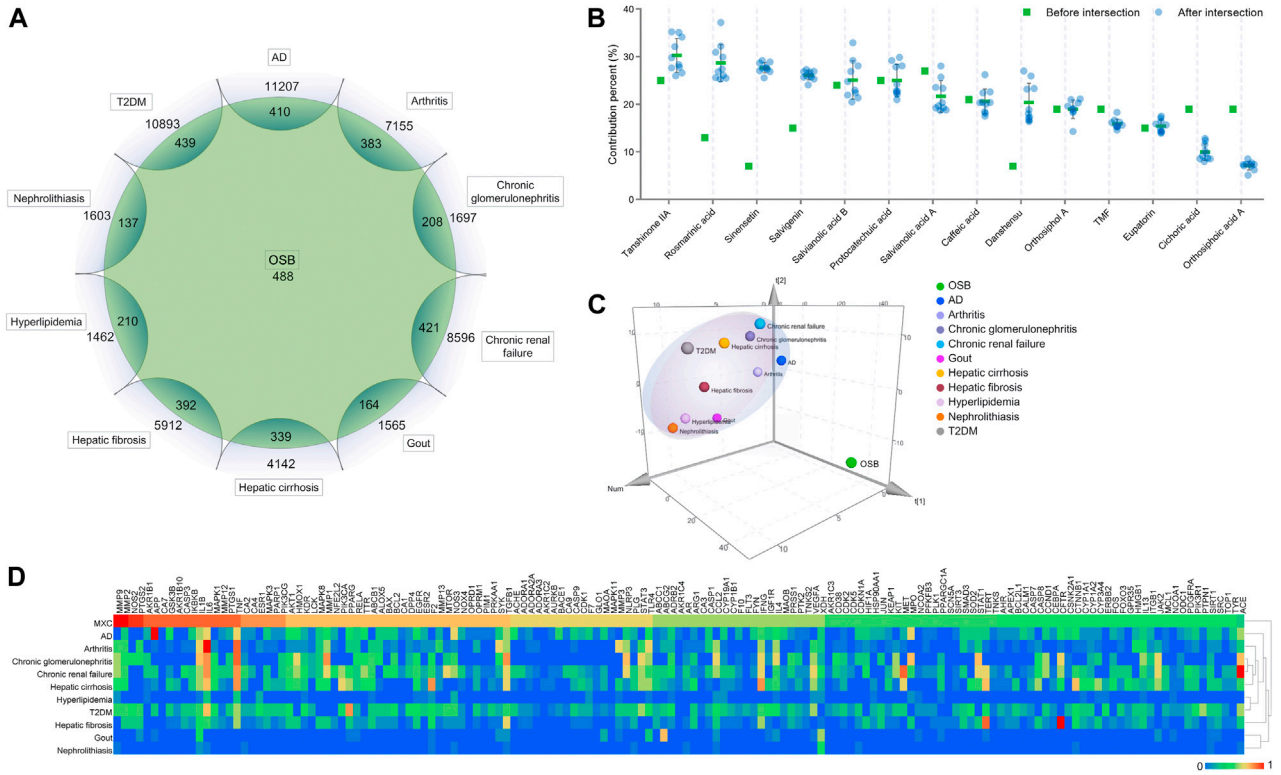

FIGURE 3 | Analysis of the intersection targets between OSB and different diseases. **(A)** Sketch profile of intersection targets between OSB and different diseases; **(B)** Contribution of each constituent to the intersection targets of all OSB-disease pairs; **(C)** 3D score plot generated in SIMCA software using the PCA model for visualizing the overall relevance of targets between groups; **(D)** Heatmap integrating the HCA model for visualizing the relevance of both individual and overall targets between groups. AD, Alzheimer's disease; HCA, hierarchical cluster analysis; OSB, *Orthosiphon stamineus* Benth.; PCA, principal component analysis; T2DM, type 2 diabetes mellitus.

merging duplicates. As expected, there was a great overlap of these targets among different signaling pathways. Pathway-target connection was firstly established, and then target-target connection. Based on topological properties, two signaling pathways: PI3K-AKT signaling pathway and MAPK signaling pathway, were screened out as the core action pathways. After integrating target-compound interaction, a full-scale network was constructed which reversely deduced the interaction from KEGG pathways to signaling pathways, then targets, and finally compounds. The topological profile of targets was significantly different from that in the original network as shown in **Figure 4**. Meanwhile, the core targets were screened out as follows: PIK3CA, PIK3R1, MAPK1, MAPK3, AKT1, PIK3CB, HSP90AA1, IKBKB, MAPK8, and RELA, which also showed a significant difference from the results in **Figure 3**. Based on topological analysis, the core compounds were finally screened out as follows: tanshinone IIA, sinensetin, salvianolic acid B, rosmarinic acid, and salvigenin. These constituents showed the interaction with all of core targets, and were finally selected as the efficacy markers underlying the various medicinal potentials of OSB.

Quantitative Analysis of the Efficacy Markers in OSB

The optimized MS/MS parameters in MRM mode for the determination of five efficacy markers were provided in **Table 2**, including ion transitions, declustering potential (DP), and collision energy (CE). Calibration curve for each analyte was created with a series of concentrations of standard solution. Acceptable linear correlation was confirmed by the correlation coefficient (r, 0.9990–0.9999). The detailed information regarding calibration curves and linear ranges are shown in **Table 3**. The proposed method was applied in the quantification of five efficacy markers in three different batches of OSB extracts. All compounds were quantified with the content of more than 2.50 mg/g (**Table 3**). Among them, the content of salvianolic acid B was the highest with the average content of 220.86 mg/g while the content of tanshinone IIA was the lowest with 2.78 mg/g.

DISCUSSION

As a traditional herbal medicine, OSB has been empirically used for the treatment of urinary tract diseases. Recent studies demonstrated its various medicinal potentials owing to different pharmacological effects, such as anti-oxidation (Nuengchamnong et al., 2011), anti-inflammation (Yam et al., 2010), diuretic (Adam et al., 2009), anti-diabetic (Mohamed et al., 2013), and hepatoprotection (Yam et al., 2007). The phytochemicals in OSB represent the material basis of its

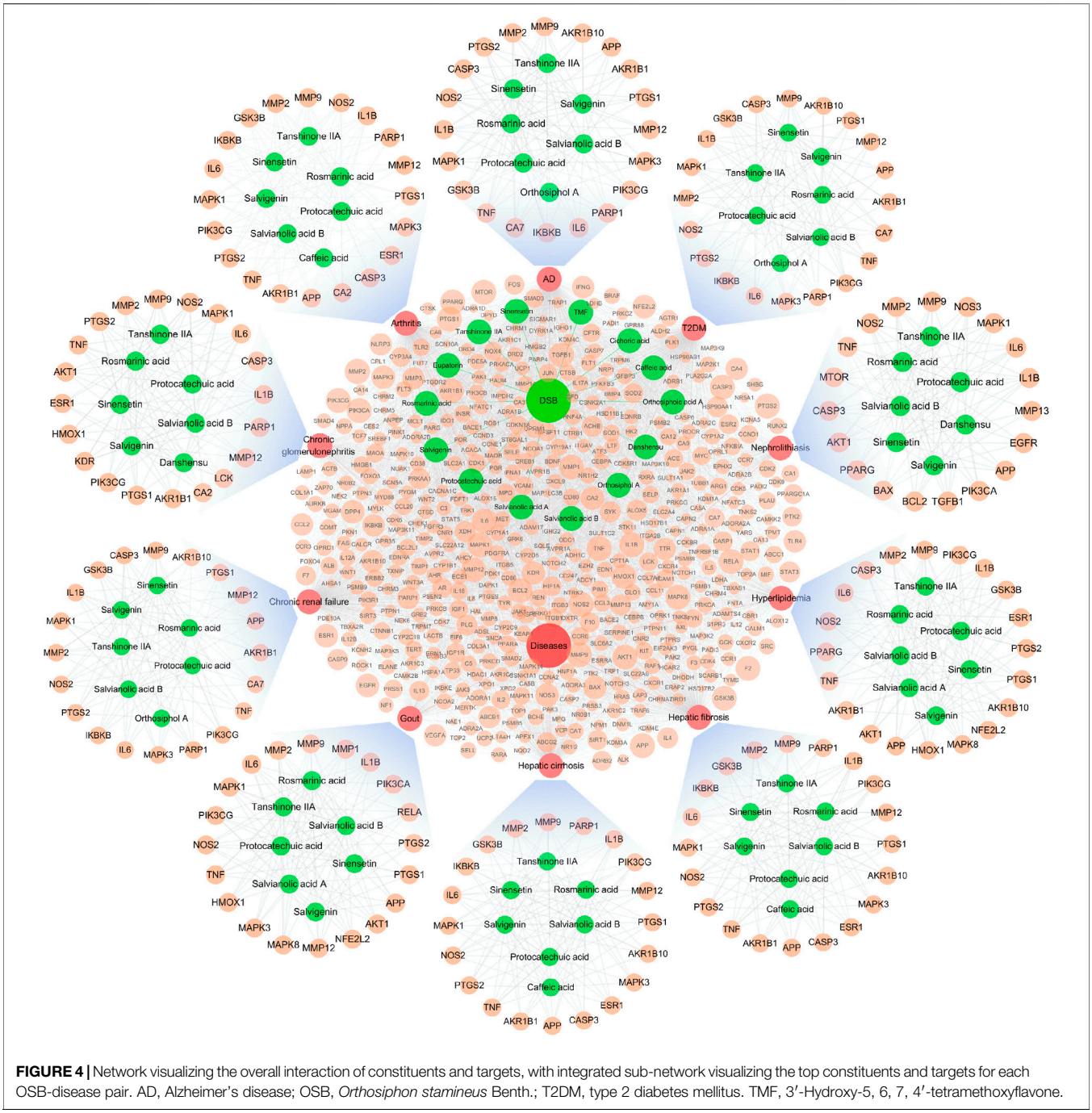

FIGURE 4 | Network visualizing the overall interaction of constituents and targets, with integrated sub-network visualizing the top constituents and targets for each OSB-disease pair. AD, Alzheimer's disease; OSB, *Orthosiphon stamineus* Benth.; T2DM, type 2 diabetes mellitus. TMF, 3′-Hydroxy-5, 6, 7, 4′-tetramethoxyflavone.

pharmacological effects. Taking advantage of modern analytical techniques, it was reported that OSB contained dozens of phytochemical constituents (Malterud et al., 1989; Tezuka et al., 2000; Nguyen et al., 2004; Hossain et al., 2013; Guo et al., 2019b). The constituents in OSB extract could vary with the polarities of extract solvents, which thus has a considerable effect on the bioactivities. Several studies suggested that the aqueous extract fraction of OSB could show weaker bioactivities than the extract fraction with strong polarity (Abdelwahab et al., 2011; Choo et al., 2018). Therefore, large percentage ethanol solution was used as the extract solvent in this study. As a result, a total of 34 constituents were detected in OSB extract. Among them, phenylpropenoic acids, polymethoxylated flavones, and terpenoids represented the predominant structural classes.

The identification of blood-absorbed phytochemicals could be regarded as a preliminary screening of bioactive constituents from oral herbs. Several studies have reported the quantitative analysis of several specified constituents of OSB in rat plasma (Loon et al., 2005; Guo et al., 2019a). However, there is a lack of

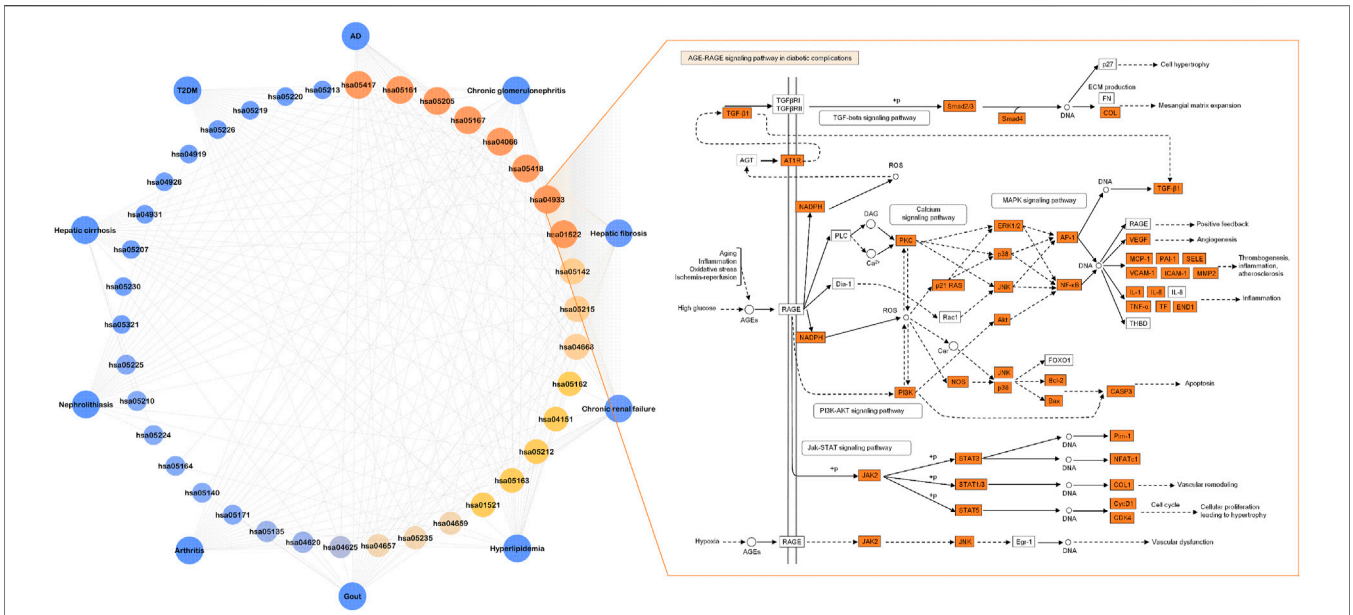

FIGURE 5 | The terms of 37 non-repetitive KEGG pathways retained from the pool of top KEGG pathways for each OSB-disease pair. Among them, eight KEGG pathways were shared by all OSB-disease pairs and a representative KEGG pathway was shown in which OSB-disease intersection targets were labeled with color. hsa05417: lipid and atherosclerosis; hsa05161: hepatitis B; hsa05205: proteoglycans in cancer; hsa05167: kaposi sarcoma-associated herpesvirus infection; hsa04066: HIF-1 signaling pathway, hsa05418: fluid shear stress and atherosclerosis; hsa04933: AGE-RAGE signaling pathway in diabetic complications, hsa01522: endocrine resistance. OSB *Orthosiphon stamineus* Benth.

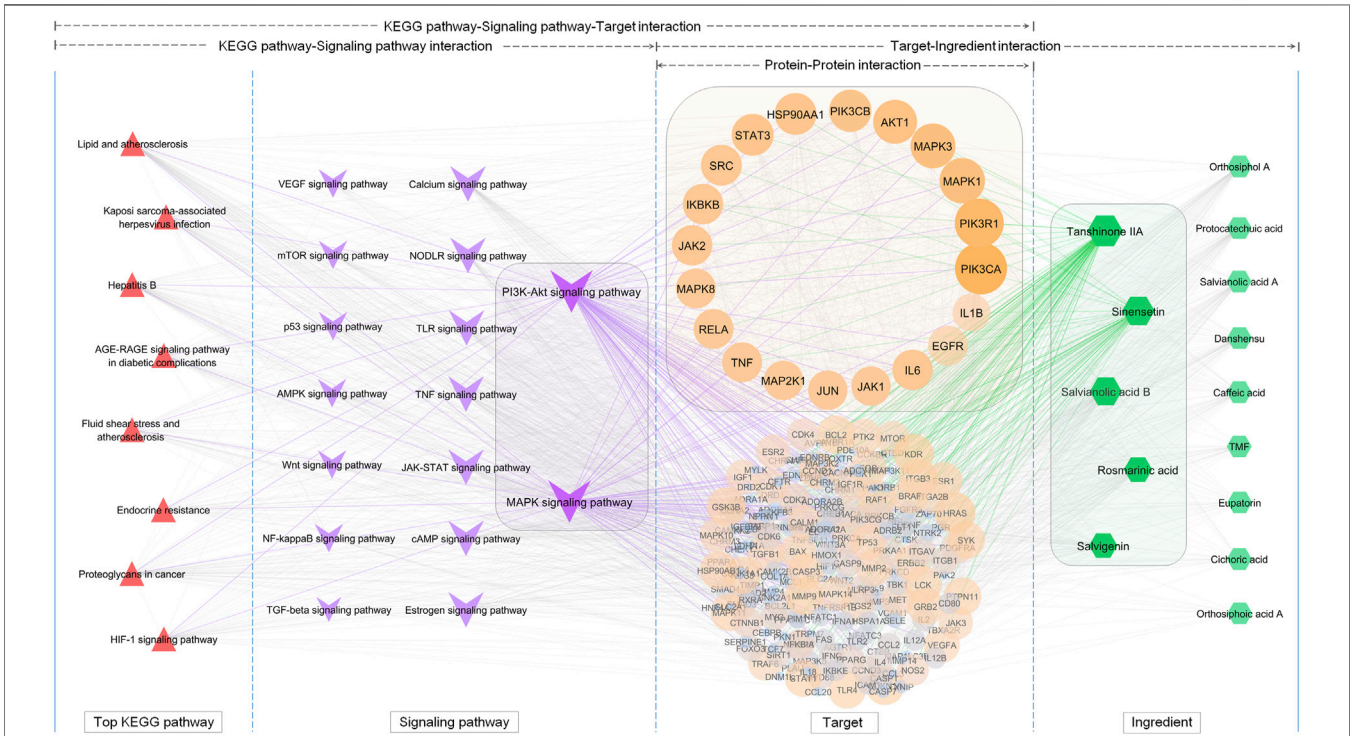

FIGURE 6 | Screening of the efficacy markers underlying the varied medicinal potentials of OSB through reversing bioinformatics analysis which deduced the interaction from key KEGG pathways to signaling pathways, followed by targets, and finally compounds. OSB *Orthosiphon stamineus* Benth.; TMF, 3′-Hydroxy-5, 6, 7, 4′-tetramethoxyflavone.

TABLE 2 | MS/MS parameters for analyte determination in MRM mode.

Analytes	Precursor-product ion pairs (m/z)	DP (V)	CE (V)	ESI mode
Tanshinone IIA	295.3 → 277.3	70	28	Positive
Sinensetin	373.1 → 343.0	130	38	Positive
Salvigenin	329.1 → 296.1	110	36	Positive
Rosmarinic acid	359.1 → 161.1	69	20	Negative
Salvianolic acid B	717.1 → 519.1	116	24	Negative

TABLE 3 | Calibration curves, linear ranges and determined contents of five efficacy markers in OSB extracts.

Compounds	Calibration curves	Linear range (ng/mL)	Contents (mg/g)
Tanshinone IIA	y = 0.001x + 0.0861 (r = 0.9995)	20–1,000	2.78 ± 0.25
Sinensetin	y = 0.0137x − 0.048 (r = 0.9999)	20–1,000	7.18 ± 0.63
Salvianolic acid B	y = 0.0000498x + 0.0109 (r = 0.9996)	200–10,000	220.86 ± 20.92
Rosmarinic acid	y = 0.000551x + 0.0871(r = 0.9990)	100–10,000	129.98 ± 16.49
Salvigenin	y = 0.00373x − 0.0014 (r = 0.9997)	20–1,000	3.01 ± 0.34

characterization of the phytochemicals absorbed in the circulatory system. In the present work, a total of 17 phytochemicals were identified in plasma samples from rats after oral administration of OSB extract. On the other hand, the predicted OB parameter, representing the fraction of the orally-administered drug that reaches systemic circulation unchanged, is widely used for preliminary screening of active constituents (Xu et al., 2012). Based on OB, a total of 20 constituents were screened out from 34 constituents that were detected in OSB extract. Interestingly, despite extensive overlapping, a remarkable difference was still found between the two pools of constituents respectively generated by plasma detection and OB screening. Some constituents detected in plasma had small OB, while some constituents with large OB were not actually detected in plasma. These findings suggested that virtual screening using OB resulted in constituent distortion compared with practical detection. In worse cases, this distortion might lead to a cascade of deviation in deduced bioactive constituents and mechanism. Therefore, practical detection of realistic samples could be a more reliable approach.

In following bioinformatic analysis, the key constituents were screened out for each OSB-disease pair based on the degree from topological analysis. This is a well-accepted paradigm for identifying key bioactive constituents in many related studies (Liao et al., 2018; Wang et al., 2019a; Wang et al., 2019b). However, the intersection targets between OSB and diseases varied with paired diseases, thus the screened key constituents could also vary. Furthermore, different targets had varied relevance to diseases as indicated by different "Score" values. However, the targets with weak relevance were treated equally with the targets with strong relevance due to the unbiased strategy. Consequently, a mass of targets with weak relevance, however, might play a prominent part in the screening of key constituents. In our work, the active compounds were screened through reversing bioinformatics analysis. It began with disassembling the enriched key pathways to extract the embedded key targets, thus excluding many targets with weak relevance. After re-constructing the interaction between pathways, targets, and compounds, a new network was generated which was significantly different from the original target-compound network. The core targets in the new network were mainly involved in the PI3K-AKT signaling pathway and MAPK signaling pathway. There was considerable overlapping between the two signaling pathways regarding the contained targets, and the NF-κB signaling pathway was one of the important intersections between them. Now there is no clear clue to the relationship between deduced action mechanisms (PI3K-AKT signaling pathway/MAPK signaling pathways) and traditional therapeutic effects of OSB owing to the limited modern pharmacological studies regarding OSB. However, the NF-κB signaling pathway was reported as the action pathway of OSB accounting for its traditional pharmacological activities in several studies (Li et al., 2016; Retinasamy et al., 2020). Undoubtedly, more effort should be put into the investigation of the precise therapeutic mechanism of OSB. Moreover, the core targets showed minor overlapping with that in the original network. These results suggested that the unbiased strategy for all targets might lead to significant distortion of screened core targets. The core constituents in the new network showed large overlapping with that in the original network, although a slight deviation was still found especially in terms of compound sorting. These results demonstrated the robustness of the core bioactive constituents of OSB for the treatment of different diseases, which were extremely appropriate as the efficacy markers of OSB.

Bioactive constituents including tanshinone IIA, sinensetin, salvianolic acid B, rosmarinic acid, and salvigenin, were selected as the efficacy markers accounting for the varied efficacies of OSB. Surprisingly, in previous OSB-related

studies, there were few points of focus on tanshinone IIA. The major interest was fastened on rosmarinic acid and flavonoids (Yuliana et al., 2009; Shafaei et al., 2016; Cai et al., 2018). Only recently, one study that aimed at qualitative and quantitative analysis of phytochemicals in OSB characterized tanshinone IIA in OSB extract (Guo et al., 2019b). In contrast to its nonentity in previous OSB-related studies, tanshinone IIA has been reported to exert various therapeutic activities, such as improving renal function (Zhang et al., 2020), relieving myocardial ischemia reperfusion injury (Li Q. et al., 2016), alleviating neuroinflammation (Maione et al., 2018), and exerting an antifibrotic effect (Shi et al., 2020). The action mechanism was suggested to be mainly involved in activating the PI3K-AKT signaling pathway and/or suppressing the MAPK and NF-κB signaling pathways. This evidence underlined the reliability for selecting tanshinone IIA as an efficacy marker of OSB. In previous studies, the constituents selected as efficacy contributors of OSB, varied with studied diseases. Even caffeic acid and protocatechuic acid, which widely exist in a variety of herbs and lack specificity, were also regarded as the core bioactive constituents and included in the quality control of OSB (Guo et al., 2019a; Guo et al., 2019b). Nevertheless, in most studies, rosmarinic acid, salvianolic acid B, and methoxy flavonoids were widely accepted as the bioactive constituents of OSB (Loon et al., 2005; Nuengchamnong et al., 2011; Cai et al., 2018; Yam et al., 2018), which was consistent with our results. Indeed, these phytochemical monomers have been reported with definite pharmacological effects for the treatment of various diseases (Mohamed et al., 2012; Tongqiang et al., 2016; Serino et al., 2021; Yamamoto et al., 2021). Rosmarinic acid is contained mainly in the family Lamiaceae, and numerous studies have demonstrated its health benefits, especially in management of inflammatory diseases via inhibition of oxidative stress, apoptosis, and inflammation (Joardar et al., 2019; Luo et al., 2020). Salvianolic acid B was remarkably abundant in OSB, and several studies indicated that it had strong anti-inflammatory and anti-fibrotic effects through targeting the MAPK and NF-κB pathways (Li et al., 2019; Wu et al., 2019). Polymethoxylated flavonoids, such as sinensetin, have been widely reported with anti-inflammatory, anti-oxidant, anti-dementia, and vasorelaxant activities and the action mechanisms could be involved in the regulation of different targets and signaling pathways including AKT and NF-κB signaling pathways (Lee et al., 2020). In sum, these reported evidence strengthened the reliability of selecting these phytochemicals as efficacy makers of OSB.

CONCLUSION

In this work, a new strategy was exploited to investigate the efficacy markers underlying the varied pharmacological effects of OSB. By LC-MS analysis, a total of 34 phytochemical constituents were characterized in OSB, and 14 blood-absorbed phytochemicals were retained as potential active compounds. The results from bioinformatic analysis revealed the overall interaction between compounds, action targets, action pathways, and diseases. Through refining key pathways and targets, the interaction reversing from signaling pathways, targets to constituents was deduced, and then the core signaling pathways, targets, and compounds were screened out. Five constituents, including tanshinone IIA, sinensetin, salvianolic acid B, rosmarinic acid, and salvigenin, were finally selected as the efficacy markers accounting for the efficacies of OSB against different diseases. The corresponding action mechanism was suggested to closely relate with the PI3K-AKT signaling pathway and/or MAPK signaling pathway, but further experimental studies are necessary to validate the deduced mechanism. Finally, the contents of the five efficacy markers in OSB extracts were quantified, and the content of salvianolic acid B was the highest while the content of tanshinone IIA was the lowest. It is believed that our findings could provide promising directions for future research on the quality control and pharmacological mechanism of OSB.

DATA AVAILABILITY STATEMENT

The original contributions presented in the study are included in the article/**Supplementary Material**, further inquiries can be directed to the corresponding authors.

ETHICS STATEMENT

The animal study was reviewed and approved by Ethics Review Committee for Animal Experimentation of Macau University of Science and Technology.

AUTHOR CONTRIBUTIONS

ZL and CC conceived and supervised the research; ZL, BQ, and LZ performed the experiment and analyzed the data; HC and JW validated the data analysis; ZL and BQ wrote the articles; ZL and WZ revised the articles.

FUNDING

This research was supported by the National Natural Science Foundation of China (Grant No.82104525), Natural Science Foundation of Jiangsu Normal University (Grant No.20XSRX002) and State Key Laboratory of Natural and Biomimetic Drugs (Grant No.K202114).

SUPPLEMENTARY MATERIAL

The Supplementary Material for this article can be found online at: https://www.frontiersin.org/articles/10.3389/fphar.2021.748684/full#supplementary-material

REFERENCES

Abdelwahab, S. I., Mohan, S., Mohamed Elhassan, M., Al-Mekhlafi, N., Mariod, A. A., Abdul, A. B., et al. (2011). Antiapoptotic and Antioxidant Properties of Orthosiphon Stamineus Benth (Cat's Whiskers): Intervention in the Bcl-2-Mediated Apoptotic Pathway. *Evid. Based. Complement. Alternat. Med.* 2011, 156765. doi:10.1155/2011/156765

Adam, Y., Somchit, M. N., Sulaiman, M. R., Nasaruddin, A. A., Zuraini, A., Bustamam, A. A., et al. (2009). Diuretic Properties of Orthosiphon Stamineus Benth. *J. Ethnopharmacol* 124 (1), 154–158. doi:10.1016/j.jep.2009.04.014

Akowuah, G., Zhari, I., Norhayati, I., Sadikun, A., and Khamsah, S. (2004). Sinensetin, Eupatorin, 3′-hydroxy-5, 6, 7, 4′-tetramethoxyflavone and Rosmarinic Acid Contents and Antioxidative Effect of Orthosiphon Stamineus from Malaysia. *Food Chem.* 87 (4), 559–566. doi:10.1016/j.foodchem.2004.01.008

Alshawsh, M. A., Abdulla, M. A., Ismail, S., Amin, Z. A., Qader, S. W., Hadi, H. A., et al. (2012). Free Radical Scavenging, Antimicrobial and Immunomodulatory Activities of Orthosiphon Stamineus. *Molecules* 17 (5), 5385–5395. doi:10.3390/molecules17055385

Arafat, O. M., Tham, S. Y., Sadikun, A., Zhari, I., Haughton, P. J., and Asmawi, M. Z. (2008). Studies on Diuretic and Hypouricemic Effects of Orthosiphon Stamineus Methanol Extracts in Rats. *J. Ethnopharmacol* 118 (3), 354–360. doi:10.1016/j.jep.2008.04.015

Awale, S., Tezuka, Y., Banskota, A. H., Kouda, K., Tun, K. M., and Kadota, S. (2001). Five Novel Highly Oxygenated Diterpenes of Orthosiphon Stamineus from Myanmar. *J. Nat. Prod.* 64 (5), 592–596. doi:10.1021/np000607t

Bauer, A., and Brönstrup, M. (2014). Industrial Natural Product Chemistry for Drug Discovery and Development. *Nat. Prod. Rep.* 31 (1), 35–60. doi:10.1039/c3np70058e

Cai, X., Xiao, C., Xue, H., Xiong, H., Hang, Y., Xu, J., et al. (2018). A Comparative Study of the Antioxidant and Intestinal Protective Effects of Extracts from Different Parts of Java tea (Orthosiphon Stamineus). *Food Sci. Nutr.* 6 (3), 579–584. doi:10.1002/fsn3.584

Chan, C. H., See, T. Y., Yusoff, R., Ngoh, G. C., and Kow, K. W. (2017). Extraction of Bioactives from Orthosiphon Stamineus Using Microwave and Ultrasound-Assisted Techniques: Process Optimization and Scale up. *Food Chem.* 221, 1382–1387. doi:10.1016/j.foodchem.2016.11.016

Chen, Y., Kern, T. S., Kiser, P. D., and Palczewski, K. (2016). Eyes on Systems Pharmacology. *Pharmacol. Res.* 114, 39–41. doi:10.1016/j.phrs.2016.09.026

Chen, Y. L., Tan, C. H., Tan, J. J., Zhao, X. M., Jiang, S. H., and Zhu, D. Y. (2009). Progress of Chemical and Pharmacological Studies on Clerodendranthus Spicatus. *Nat. Prod. Res. Dev.* 21 (05), 885–891. doi:10.16333/j.1001-6880.2009.05.041

Choo, B. K. M., Kundap, U. P., Kumari, Y., Hue, S. M., Othman, I., and Shaikh, M. F. (2018). Orthosiphon Stamineus Leaf Extract Affects TNF-α and Seizures in a Zebrafish Model. *Front. Pharmacol.* 9, 139. doi:10.3389/fphar.2018.00139

Guo, Z., Li, B., Gu, J., Zhu, P., Su, F., Bai, R., et al. (2019a). Simultaneous Quantification and Pharmacokinetic Study of Nine Bioactive Components of *Orthosiphon Stamineus* Benth. Extract in Rat Plasma by UHPLC-MS/MS. *Molecules* 24 (17), 3057. doi:10.3390/molecules24173057

Guo, Z., Liang, X., and Xie, Y. (2019b). Qualitative and Quantitative Analysis on the Chemical Constituents in Orthosiphon Stamineus Benth. Using Ultra High-Performance Liquid Chromatography Coupled with Electrospray Ionization Tandem Mass Spectrometry. *J. Pharm. Biomed. Anal.* 164, 135–147. doi:10.1016/j.jpba.2018.10.023

Han Jie, L., Jantan, I., Yusoff, S. D., Jalil, J., and Husain, K. (2020). Sinensetin: An Insight on its Pharmacological Activities, Mechanisms of Action and Toxicity. *Front. Pharmacol.* 11, 553404. doi:10.3389/fphar.2020.553404

Hopkins, A. L. (2008). Network Pharmacology: the Next Paradigm in Drug Discovery. *Nat. Chem. Biol.* 4 (11), 682–690. doi:10.1038/nchembio.118

Hossain, M. A., and Ismail, Z. (2013). Isolation and Characterization of Triterpenes from the Leaves of Orthosiphon Stamineus. *Arabian J. Chem.* 6 (3), 295–298. doi:10.1016/j.arabjc.2010.10.009

Joardar, S., Dewanjee, S., Bhowmick, S., Dua, T. K., Das, S., Saha, A., et al. (2019). Rosmarinic Acid Attenuates Cadmium-Induced Nephrotoxicity via Inhibition of Oxidative Stress, Apoptosis, Inflammation and Fibrosis. *Int. J. Mol. Sci.* 20 (8), 2027. doi:10.3390/ijms20082027

Li, C., Mo, Z., Xie, J., Xu, L., Tan, L., Luo, D., et al. (2016a). Chongcao-Shencha Attenuates Liver and Kidney Injury through Attenuating Oxidative Stress and Inflammatory Response in D-Galactose-Treated Mice. *Evid. Based. Complement. Alternat. Med.* 2016, 3878740. doi:10.1155/2016/3878740

Li, Q., Shen, L., Wang, Z., Jiang, H. P., and Liu, L. X. (2016b). Tanshinone IIA Protects against Myocardial Ischemia Reperfusion Injury by Activating the PI3K/Akt/mTOR Signaling Pathway. *Biomed. Pharmacother.* 84, 106–114. doi:10.1016/j.biopha.2016.09.014

Li, S., Wang, R., Wu, B., Wang, Y., Song, F., Gu, Y., et al. (2019). Salvianolic Acid B Protects against ANIT-Induced Cholestatic Liver Injury through Regulating Bile Acid Transporters and Enzymes, and NF-Kb/ικb and MAPK Pathways. *Naunyn Schmiedebergs Arch. Pharmacol.* 392 (9), 1169–1180. doi:10.1007/s00210-019-01657-8

Liao, M., Shang, H., Li, Y., Li, T., Wang, M., Zheng, Y., et al. (2018). An Integrated Approach to Uncover Quality Marker Underlying the Effects of Alisma Orientale on Lipid Metabolism, Using Chemical Analysis and Network Pharmacology. *Phytomedicine* 45, 93–104. doi:10.1016/j.phymed.2018.04.006

Lokman, E. F., Saparuddin, F., Muhammad, H., Omar, M. H., and Zulkapli, A. (2019). Orthosiphon Stamineus as a Potential Antidiabetic Drug in Maternal Hyperglycemia in Streptozotocin-Induced Diabetic Rats. *Integr. Med. Res.* 8 (3), 173–179. doi:10.1016/j.imr.2019.05.006

Loon, Y. H., Wong, J. W., Yap, S. P., and Yuen, K. H. (2005). Determination of Flavonoids from Orthosiphon Stamineus in Plasma Using a Simple HPLC Method with Ultraviolet Detection. *J. Chromatogr. B Analyt Technol. Biomed. Life Sci.* 816 (1-2), 161–166. doi:10.1016/j.jchromb.2004.11.021

Luo, C., Zou, L., Sun, H., Peng, J., Gao, C., Bao, L., et al. (2020a). A Review of the Anti-inflammatory Effects of Rosmarinic Acid on Inflammatory Diseases. *Front. Pharmacol.* 11, 153. doi:10.3389/fphar.2020.00153

Luo, L., Gao, W., Zhang, Y., Liu, C., Wang, G., Wu, H., et al. (2020b). Integrated Phytochemical Analysis Based on UPLC-MS and Network Pharmacology Approaches to Explore the Quality Control Markers for the Quality Assessment of *Trifolium Pratense* L. *Molecules* 25(17). 3787doi:doi:10.3390/molecules25173787

Maione, F., Piccolo, M., De Vita, S., Chini, M. G., Cristiano, C., De Caro, C., et al. (2018). Down Regulation of Pro-inflammatory Pathways by Tanshinone IIA and Cryptotanshinone in a Non-genetic Mouse Model of Alzheimer's Disease. *Pharmacol. Res.* 129, 482–490. doi:10.1016/j.phrs.2017.11.018

Malterud, K. E., Hanche-Olsen, I. M., and Smith-Kielland, I. (1989). Flavonoids from Orthosiphon Spicatus. *Planta Med.* 55 (6), 569–570. doi:10.1055/s-2006-962099

Mohamed, E. A., Siddiqui, M. J., Ang, L. F., Sadikun, A., Chan, S. H., Tan, S. C., et al. (2012). Potent α-glucosidase and α-amylase Inhibitory Activities of Standardized 50% Ethanolic Extracts and Sinensetin from Orthosiphon Stamineus Benth as Anti-diabetic Mechanism. *BMC Complement. Altern. Med.* 12, 176. doi:10.1186/1472-6882-12-176

Mohamed, E. A., Yam, M. F., Ang, L. F., Mohamed, A. J., and Asmawi, M. Z. (2013). Antidiabetic Properties and Mechanism of Action of Orthosiphon Stamineus Benth Bioactive Sub-fraction in Streptozotocin-Induced Diabetic Rats. *J. Acupunct Meridian Stud.* 6 (1), 31–40. doi:10.1016/j.jams.2013.01.005

Nguyen, M. T., Awale, S., Tezuka, Y., Chien-Hsiung, C., and Kadota, S. (2004). Staminane- and Isopimarane-type Diterpenes from Orthosiphon Stamineus of Taiwan and Their Nitric Oxide Inhibitory Activity. *J. Nat. Prod.* 67 (4), 654–658. doi:10.1021/np030471+

Nuengchamnong, N., Krittasilp, K., and Ingkaninan, K. (2011). Characterisation of Phenolic Antioxidants in Aqueous Extract of Orthosiphon Grandiflorus tea by LC-ESI-MS/MS Coupled to DPPH Assay. *Food Chem.* 127 (3), 1287–1293. doi:10.1016/j.foodchem.2011.01.085

Retinasamy, T., Shaikh, M. F., Kumari, Y., Abidin, S. A. Z., and Othman, I. (2020). Orthosiphon Stamineus Standardized Extract Reverses Streptozotocin-Induced Alzheimer's Disease-like Condition in a Rat Model. *Biomedicines* 8 (5), 104. doi:10.3390/biomedicines8050104

Serino, E., Chahardoli, A., Badolati, N., Sirignano, C., Jalilian, F., Mojarrab, M., et al. (2021). Salvigenin, a Trimethoxylated Flavone from Achillea Wilhelmsii C. Koch, Exerts Combined Lipid-Lowering and Mitochondrial Stimulatory Effects. *Antioxidants (Basel)* 10 (7), 1042. doi:10.3390/antiox10071042

Shafaei, A., Sultan Khan, M. S., F A Aisha, A., Abdul Majid, A. M., Hamdan, M. R., Mordi, M. N., et al. (2016). Flavonoids-rich Orthosiphon Stamineus Extract as New Candidate for Angiotensin I-Converting Enzyme

Inhibition: A Molecular Docking Study. *Molecules* 21(11). 1500doi: doi:10.3390/molecules21111500

Shi, M. J., Yan, X. L., Dong, B. S., Yang, W. N., Su, S. B., and Zhang, H. (2020). A Network Pharmacology Approach to Investigating the Mechanism of Tanshinone IIA for the Treatment of Liver Fibrosis. *J. Ethnopharmacol* 253, 112689. doi:10.1016/j.jep.2020.112689

Tabana, Y. M., Al-Suede, F. S., Ahamed, M. B., Dahham, S. S., Hassan, L. E., Khalilpour, S., et al. (2016). Cat's Whiskers (Orthosiphon Stamineus) tea Modulates Arthritis Pathogenesis via the Angiogenesis and Inflammatory cascade. *BMC Complement. Altern. Med.* 16 (1), 480. doi:10.1186/s12906-016-1467-4

Tezuka, Y., Stampoulis, P., Banskota, A. H., Awale, S., Tran, K. Q., Saiki, I., et al. (2000). Constituents of the Vietnamese Medicinal Plant Orthosiphon Stamineus. *Chem. Pharm. Bull. (Tokyo)* 48 (11), 1711–1719. doi:10.1248/cpb.48.1711

Tongqiang, L., Shaopeng, L., Xiaofang, Y., Nana, S., Xialian, X., Jiachang, H., et al. (2016). Salvianolic Acid B Prevents Iodinated Contrast media-induced Acute Renal Injury in Rats via the PI3K/Akt/Nrf2 Pathway. *Oxid. Med. Cel. Longev.* 2016, 7079487. doi:10.1155/2016/7079487

Wang, N., Zhu, F., Shen, M., Qiu, L., Tang, M., Xia, H., et al. (2019a). Network Pharmacology-Based Analysis on Bioactive Anti-diabetic Compounds in Potentilla Discolor Bunge. *J. Ethnopharmacol* 241, 111905. doi:10.1016/j.jep.2019.111905

Wang, Y., Sun, Y. W., Wang, Y. M., Ju, Y., and Meng, D. L. (2019b). Virtual Screening of Active Compounds from Artemisia Argyi and Potential Targets against Gastric Ulcer Based on Network Pharmacology. *Bioorg. Chem.* 88, 102924. doi:10.1016/j.bioorg.2019.102924

Wu, C., Chen, W., Ding, H., Li, D., Wen, G., Zhang, C., et al. (2019). Salvianolic Acid B Exerts Anti-liver Fibrosis Effects via Inhibition of MAPK-Mediated Phospho-Smad2/3 at Linker Regions *In Vivo* and *In Vitro*. *Life Sci.* 239, 116881. doi:10.1016/j.lfs.2019.116881

Xiang, W., Suo, T. C., Yu, H., Li, A. P., Zhang, S. Q., Wang, C. H., et al. (2018). A New Strategy for Choosing "Q-Markers" via Network Pharmacology, Application to the Quality Control of a Chinese Medical Preparation. *J. Food Drug Anal.* 26 (2), 858–868. doi:10.1016/j.jfda.2017.10.003

Xu, X., Zhang, W., Huang, C., Li, Y., Yu, H., Wang, Y., et al. (2012). A Novel Chemometric Method for the Prediction of Human Oral Bioavailability. *Int. J. Mol. Sci.* 13 (6), 6964–6982. doi:10.3390/ijms13066964

Yam, M. F., Ang, L. F., Basir, R., Salman, I. M., Ameer, O. Z., and Asmawi, M. Z. (2009). Evaluation of the Anti-pyretic Potential of Orthosiphon Stamineus Benth Standardized Extract. *Inflammopharmacology* 17 (1), 50–54. doi:10.1007/s10787-008-8038-3

Yam, M. F., Asmawi, M. Z., and Basir, R. (2008). An Investigation of the Anti-inflammatory and Analgesic Effects of Orthosiphon Stamineus Leaf Extract. *J. Med. Food* 11 (2), 362–368. doi:10.1089/jmf.2006.065

Yam, M. F., Basir, R., Asmawi, M. Z., and Ismail, Z. (2007). Antioxidant and Hepatoprotective Effects of Orthosiphon Stamineus Benth. Standardized Extract. *Am. J. Chin. Med.* 35 (1), 115–126. doi:10.1142/S0192415X07004679

Yam, M. F., Lim, V., Salman, I. M., Ameer, O. Z., Ang, L. F., Rosidah, N., et al. (2010). HPLC and Anti-inflammatory Studies of the Flavonoid Rich Chloroform Extract Fraction of Orthosiphon Stamineus Leaves. *Molecules* 15 (6), 4452–4466. doi:10.3390/molecules15064452

Yam, M. F., Tan, C. S., and Shibao, R. (2018). Vasorelaxant Effect of Sinensetin via the NO/sGC/cGMP Pathway and Potassium and Calcium Channels. *Hypertens. Res.* 41 (10), 787–797. doi:10.1038/s41440-018-0083-8

Yamamoto, S., Kayama, T., Noguchi-Shinohara, M., Hamaguchi, T., Yamada, M., Abe, K., et al. (2021). Rosmarinic Acid Suppresses Tau Phosphorylation and Cognitive Decline by Downregulating the JNK Signaling Pathway. *NPJ Sci. Food* 5 (1), 1. doi:10.1038/s41538-021-00084-5

Yuliana, N. D., Khatib, A., Link-Struensee, A. M., Ijzerman, A. P., Rungkat-Zakaria, F., Choi, Y. H., et al. (2009). Adenosine A1 Receptor Binding Activity of Methoxy Flavonoids from Orthosiphon Stamineus. *Planta Med.* 75 (2), 132–136. doi:10.1055/s-0028-1088379

Zhang, X. W., Zhou, M., An, L., Zhang, P., Li, P., and Chen, J. (2020). Lipophilic Extract and Tanshinone IIA Derived from Salvia Miltiorrhiza Attenuate Uric Acid Nephropathy through Suppressing Oxidative Stress-Activated MAPK Pathways. *Am. J. Chin. Med.* 48 (6), 1455–1473. doi:10.1142/S0192415X20500718

Conflict of Interest: The authors declare that the research was conducted in the absence of any commercial or financial relationships that could be construed as a potential conflict of interest.

Publisher's Note: All claims expressed in this article are solely those of the authors and do not necessarily represent those of their affiliated organizations, or those of the publisher, the editors and the reviewers. Any product that may be evaluated in this article, or claim that may be made by its manufacturer, is not guaranteed or endorsed by the publisher.

frontiers in Pharmacology

ORIGINAL RESEARCH
published: 28 September 2021
doi: 10.3389/fphar.2021.732716

LC–MS Based Metabolomics Study of the Effects of EGCG on A549 Cells

Tingyu Pan[1], *Di Han*[1], *Yong Xu*[1], *Wenpan Peng*[1], *Le Bai*[1], *Xianmei Zhou*[1,2]* and *Hailang He*[1,2,3]*

[1]*Affiliated Hospital of Nanjing University of Chinese Medicine, Nanjing, China,* [2]*Department of Respiratory Medicine, Jiangsu Province Hospital of Chinese Medicine, Nanjing, China,* [3]*Arizona Metabolomics Laboratory, College of Health Solutions, Arizona State University, Scottsdale, AZ, United States*

(–)-Epigallocatechin-3-gallate (EGCG) is the main bioactive catechin in green tea. The antitumor activity of EGCG has been confirmed in various types of cancer, including lung cancer. However, the precise underlying mechanisms are still largely unclear. In the present study, we investigated the metabolite changes in A549 cells induced by EGCG *in vitro* utilizing liquid chromatography-mass spectrometry (LC-MS)-based metabolomics. The result revealed 33 differentially expressed metabolites between untreated and 80 μM EGCG-treated A549 cells. The altered metabolites were involved in the metabolism of glucose, amino acid, nucleotide, glutathione, and vitamin. Two markedly altered pathways, including glycine, serine and threonine metabolism and alanine, aspartate and glutamate metabolism, were identified by MetaboAnalyst 5.0 metabolic pathway analysis. These results may provide potential clues for the intramolecular mechanisms of EGCG's effect on A549 cells. Our study may contribute to future molecular mechanistic studies of EGCG and the therapeutic application of EGCG in cancer management.

Keywords: EGCG, A549 cells, metabolomics, arginine and proline metabolism, glutamate metabolism, histidine metabolism

OPEN ACCESS

Edited by:
Shuai Ji,
Xuzhou Medical University, China

Reviewed by:
Sanmoy Karmakar,
Jadavpur University, India
Anika Wagner,
University of Giessen, Germany

***Correspondence:**
Xianmei Zhou
zhouxianmeijs@aliyun.com
Hailang He
lyghehailang@163.com

Specialty section:
This article was submitted to Ethnopharmacology, a section of the journal Frontiers in Pharmacology

Received: *29 June 2021*
Accepted: *15 September 2021*
Published: *28 September 2021*

Citation:
Pan T, Han D, Xu Y, Peng W, Bai L, Zhou X and He H (2021) LC–MS Based Metabolomics Study of the Effects of EGCG on A549 Cells. Front. Pharmacol. 12:732716. doi: 10.3389/fphar.2021.732716

INTRODUCTION

As one of the most common cancers globally, lung cancer causes a severe social burden (Ferlay et al., 2015; Siegel et al., 2016). Worldwide, an estimated 2.2 million new lung cancer cases occurred in 2020 (Sung et al., 2021). As the second most commonly diagnosed cancer, lung cancer remained the leading cause of cancer death, with an estimated 1.8 million deaths in 2020 (Sung et al., 2021). Despite significant advances that have been made in the interventions, including surgery, radiation therapy, chemotherapy, targeted therapy, and immunotherapy on lung cancer, the 5 years survival of lung cancer only remains 21% (Miller et al., 2019; Siegel et al., 2021). It is critical to consider other preventive and therapeutic measures for lung cancer not only to decrease its incidence and mortality but also to overcome the toxicity, side effects, and cost of existing treatments (Hirsch et al., 2017).

Epigallocatechin-3-gallate (EGCG) is the most abundant and effective catechin in numerous types of white tea and green tea (Sano et al., 2001; Tang et al., 2019). It has been shown that EGCG can inhibit tumor growth and stimulate cancer cell apoptosis in various human cancers *in vivo* and *vitro* studies (Huh et al., 2004; Chen et al., 2016; Yang et al., 2016; Huang et al., 2017; Liu et al., 2017; Borutinskaite et al., 2018; Gan et al., 2018; Zhou et al., 2018; Wei et al., 2019; Wu et al., 2019; Yoshimura et al., 2019; Almatroodi et al., 2020; Panji et al., 2021; Romano and Martel, 2021). Many studies have demonstrated that EGCG may take a role in the initiation, promotion, and progression

of cancer through the modulation of various mechanisms, including cellular proliferation, differentiation, apoptosis, angiogenesis, and metastasis, which leads to its anticarcinogenic activities (Chen and Dou, 2008; Ma et al., 2013; Luo et al., 2014; Luo et al., 2017; Moradzadeh et al., 2018; Pal et al., 2018; Li et al., 2019; Almatroodi et al., 2020; Yin et al., 2021). Increasing evidence has shown that EGCG possesses anti-tumorigenic property against non-small cell lung cancer (Sonoda et al., 2014; Shi et al., 2015; Gu et al., 2018; Hu et al., 2019). Even though the antitumor activity of EGCG in lung cancer has been extensively investigated, the underlying mechanism remains unclear.

Metabolomics is an exciting tool to detect small metabolic compounds and monitor small global molecule endogenous metabolite changes induced by biochemical reactions in biological systems (Dunn et al., 2011; Griffin et al., 2011; Reaves and Rabinowitz, 2011; Gu et al., 2012; Carroll et al., 2015; Zampieri et al., 2017; McCartney et al., 2018; Yan and Xu, 2018; Yeung, 2018; Shi et al., 2019; Eghlimi et al., 2020; He et al., 2020; Lim et al., 2020; Wei et al., 2021). Metabolomics is a promising approach to searching potential biomarkers and novel therapeutic strategies for lung cancer (Luengo et al., 2017; Seijo et al., 2019; Noreldeen et al., 2020; Schmidt et al., 2021). To date, the precise molecular mechanisms of antitumor activity in lung cancer induced by EGCG still keep unclear and need more investigation, especially from a metabolism point of view. Therefore, in this study, we applied liquid chromatography-mass spectrometry (LC-MS) based metabolomics and employed A549 cells as an *in vitro* model to further explore the effect of EGCG on lung cancer cell metabolism.

MATERIALS AND METHODS

Reagents and Materials

EGCG was purchased from Sigma-Aldrich (St. Louis, MO, United States). A549 cell line (ATCC NO. CCL-185) was purchased from American Type Culture Collection (ATCC, Manassas, VA, United States). The Cell Counting Kit-8 (CK04-05) was obtained from Dojindo Molecular Technologies (Gaithersburg, MD, United States). 4′,6-diamindino-2-phenylinodole (DAPI) staining kit was purchased from FcmacsBiotechCo., Ltd. (Jiangsu, China). BCA™ Protein Assay Kit was obtained from Thermo Scientific (Waltham, MA, 84 United States). LC-MS-grade isopropanol (IPA), acetonitrile (ACN), MeOH, and CH_2Cl_2 were purchased from Fisher Scientific (Pittsburgh, PA). HPLC grade acetic acid, U-^{13}C glucose, N-tert-butyldimethylsilyl-N-methyltrifluoroacetamide (MTBSTFA), methoxyamine hydrochloride, ammonia acetate, anhydrous pyridine, and dimethyl sulfoxide (DMSO) and all of the standard compounds used for metabolic identification were acquired from Sigma-Aldrich (St. Louis, MO, United States).

Cell Culture

The A549 cells were cultured in Dulbecco's modified eagle medium (DMEM) (Corning, 10-013-CV) supplemented with 10% fetal bovine serum (FBS) (Corning, 35-010-CV). Cells were grown at 37°C and 5% CO_2 in a humidified atmosphere.

Cell Viability Assay

Cells were seeded in 96-well plates (8.0×10^3 per well) and treated with different concentrations of EGCG (20, 40, 60, 80, 100, 120, 160, 200 μM) for 24 h. After treatment, the viability of A549 cells was measured via the Cell Counting Kit-8 assay. Briefly, 10 μl of CCK-8 reagents were inserted into each well before incubation in an incubator with 5% CO_2 at 37°C for 3 h. Subsequently, absorbance at 450 nm was measured using a microplate reader (Molecular Devices, CA, United States). Viability is expressed as a cell activity percentage between the EGCG group and the control group.

LC-MS Metabolomics Analysis

In this study, we utilized a pathway-specific LC-MS method that can cover more than 300 metabolites from >35 metabolic pathways (Carroll et al., 2015; Gu et al., 2015; Sperber et al., 2015; Li et al., 2018; Jasbi et al., 2019; Liu et al., 2019; Shi et al., 2019). Briefly, A549 cells were seeded in 6-well plates (4.5×10^5 cells/well) with 10% FBS supplemented with DMEM. Then, cells were incubated overnight in an incubator with 5% CO_2 at 37°C. The cells were then treated with EGCG for 24 h. For sample preparation, the cells were first rinsed with PBS. Then 1.2 ml of 80% MeOH was added into each well for extraction of intracellular metabolites. Samples were completely lysed using an ultrasonic homogenizer in an ice bath for 20 min and centrifuged at 14,000 rpm under 4°C for 10 min. Following that, 500 μl of each supernatant was retained and dried under vacuum for 4 h. The dried samples were reconstituted using 150 μl of solvent (PBS: ACN = 4:6) and then centrifuged at 14,000 rpm under 4°C for 10 min. Sets of samples of identical volume were combined for quality-control specimens solvent (B) to assess instrument performance.

The supernatants were analyzed by liquid chromatography-mass spectrometry (LC-MS) simultaneously after centrifugation. 100 μl of the supernatant was transferred to a new vial and analyzed by an Agilent 1290 LC-6490 Triple Quadrupole mass spectrometer system equipped with an electrospray ionization (ESI) source. LC was performed on a Waters XBridge BEH Amide column (150 × 2.1 mm, 2.5 μm particle size, Waters Corporation, Milford, MA). The mobile phase for chromatographic separation was composed of solvent (A): 10 mM ammonium hydroxide, 10 mM ammonium acetate in 95% H_2O/5% ACN, and solvent (B): 10 mM ammonium hydroxide, 10 mM ammonium acetate in 95% ACN/5% H_2O. Following a 1 min isocratic elution of 90% solvent (B), solvent (B) was gradually reduced to 40% in 10 min (t = 11 min) and then kept at 40% for 4 min (t = 15 min). Subsequently, solvent (B) was returned to 90% to run the next sample. Each sample was injected twice, 4 μl for positive ion electrospray ionization analysis and 10 μl for negative ion analysis. Multiple reaction monitoring (MRM) mode was employed for targeted data acquisition.

The QQQ-MS system was operated with a capillary voltage of 3.5 kV. The nebulizer gas (N2) pressure was set at 30 psi with a drying gas (N2) flow rate of 15 L/min, and the temperature was 175°C. The flow rate of sheath gas (N2) was set to 11 L/min with a

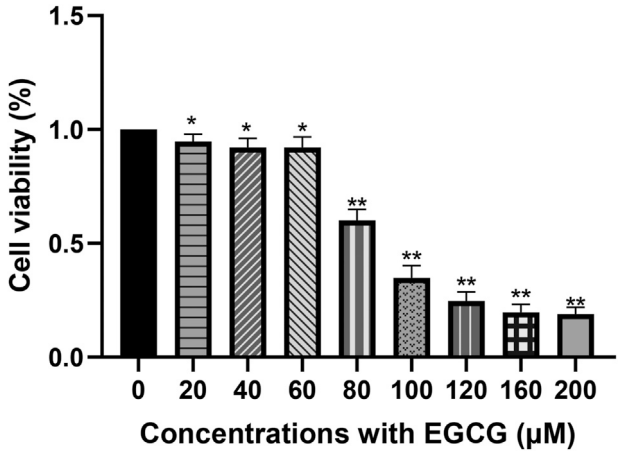

FIGURE 1 | Cell viability of A549 cells after EGCG exposure. A549 cells were exposed to 20–200 μM EGCG for 24 h, and cell viability was determined utilizing a CCK-8 assay. The experimental data are expressed as the mean value with SD of three independent replicates. (*$p < 0.05$, **$p < 0.005$).

temperature of 225°C. A CE range of 5–50 V in increments of 5 V, and 4 CAV values (2 V, 4 V, 6 V, 8 V) were evaluated for MRM optimization; optimized CE and CAV values were determined from the highest MRM response.

The software programs used to control the LC-MS system and integrate extracted MRM peaks were Agilent MassHunter Workstation and Agilent MassHunter Quantitative Data Analysis, respectively. Protein concentrations in each sample were utilized to normalize metabolite levels.

The post-preparative stability of the sample was tested by running five prepared quality control (QC) samples kept in an autosampler (maintained at 4°C). In addition, one QC sample was inserted every 3–4 test samples during the whole process to validate system suitability and stability.

Statistical Analysis

Measurement data are the mean ± standard deviation (SD) and analyzed via the Student's two-tailed *t*-test or one-way analysis of variance (ANOVA) with Tukey's post hoc analysis, and $p < 0.05$ was considered as a significant difference.

Principal component analysis (PCA), partial least squares discriminant analysis (PLS-DA), pathway analysis overview, and heatmap clustering of altered metabolic profiling analysis were performed using MetaboAnalyst 5.0 (https://www.metaboanalyst.ca/). In pathway analysis, "*Homo sapiens* (KEGG)" library was selected, as well as Hypergeometric test for pathway enrichment analysis and relative betweenness centrality for pathway topology analysis.

RESULTS

EGCG Suppressors Cell Viability of A549 Cells

After exposure to EGCG for 24 h, the A549 cell viability was downregulated in a dose-dependent manner within the concentration range of 60–100 μM (**Figure 1**). Cell viability was 92.10 ± 3.23% at 40 μM ($p < 0.05$) and reduced to 60.01 ± 4.02% at 80 μM ($p < 0.005$). As shown in **Supplementary Figure S1**, abnormal nucleus margin and shortening of nucleus diameter occurred at EGCG exposure groups, especially at the concentrations of 100 μM. Considering the balance between cell viability and data interpretability, a concentration of 40 μM was chosen for further experiments. The concentration of 80 μM was also selected in the subsequent metabolomics experiments to help capture more responses on cell metabolism related to the effect of EGCG.

LC-MS Metabolite Profiling of A549 Cells After EGCG Treated

LC-MS of Metabolic Profiles

In total, we found that 173 metabolites were reliably detected with relative abundances >1,000 in more than 80% of all samples. After normalization by averaged values from the QC injection data, 142 metabolites had a coefficient of variation (CV) value of <30%. We analyzed the metabolic profiles of these 142 metabolites of 40 μM, 80 μM EGCG-treated and untreated A549 cells. Based on the LC-MS data, the PCA score plot of metabolites showed an obvious separation among the control group, 40 μM EGCG-treated group, and 80 μM EGCG-treated group (**Figure 2A**). No outlier detection was performed from the data overview. PLS-DA was further undertaken to reveal the metabolic deviations between the EGCG-treated groups and the control group. As shown in **Figure 2B**, the metabolite profiles of the three groups were distributed in significantly separated clusters. Although it is a supervised classification method, component 1 and component 2 in the PLS-DA model (**Figure 2B**) accounted for 23 and 22.9% of the total variance in the data respectively, which indicated that significant metabolic disturbances were induced in A549 cells treated by EGCG.

As the volcano plot shows (**Figure 3**, **Supplementary Figure S2**), the up-regulated metabolites between the control and the EGCG exposure groups were presented on the right-hand side of the valley, while the left-hand side of the valley represents those that were down-regulated. The number of significantly altered metabolic abundances in the 80 μM group was greater than that in the 40 μM group, which indicated that EGCG disturbed the A549cells in a dose-dependent manner. The ANOVA test analysis was utilized to identify potential biomarkers contributing most to the difference between control and the EGCG-treated groups. The results with metabolites ($p < 0.05$) are shown in **Table 1** and separately in **Figure 4**. The top 25 significantly changed metabolites were visualized using a heat map in a red-blue scale (from higher to lower metabolite levels) (**Figure 5**). In pairwise comparison, metabolites with a *p*-value below 0.05 and fold change above 1.5 or below 0.75 were selected as potential biomarkers. As shown in **Supplementary Table S1**, the identified metabolites were summarized, and a total of 11 features were selected as potentially altered metabolite markers in A549 cells exposed to 80 μM EGCG compared with the control group. In addition, all of the disturbed metabolites with $p < 0.05$

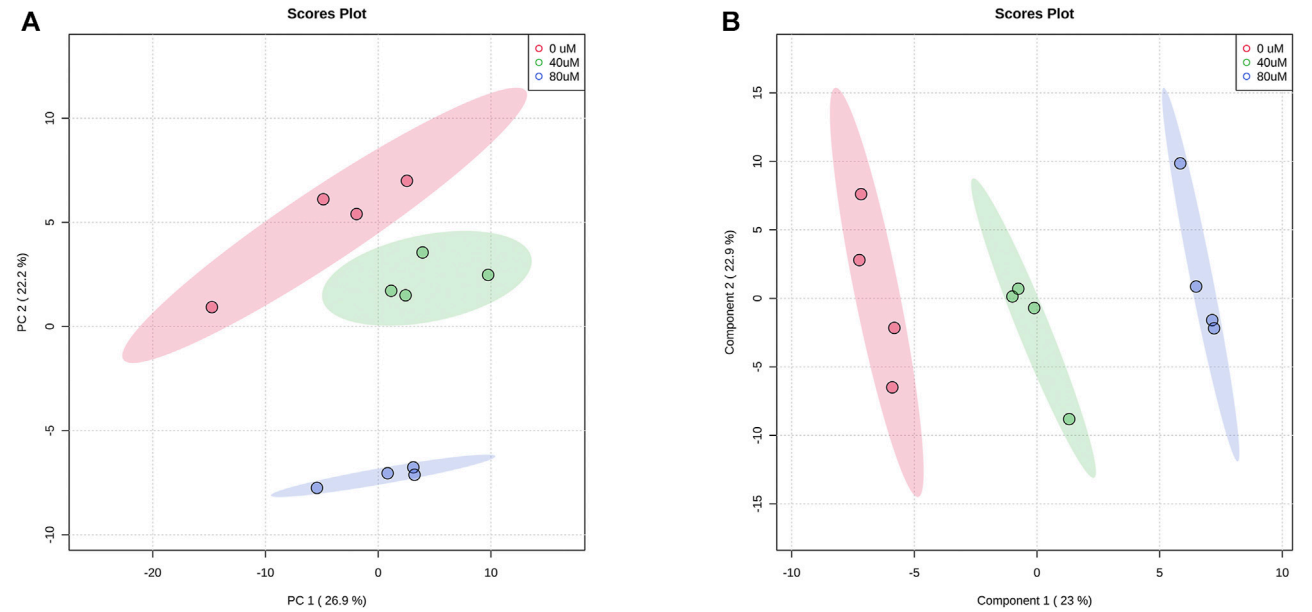

FIGURE 2 | Score plots of PCA **(A)** and PLS-DA **(B)** models for the metabolome data obtained by LC-MS, showing the metabolic profile differences between control and EGCG-treated groups. Red cycle: control group; green cycle: 40 μM EGCG-treated group; blue cycle: 80 μM EGCG-treated group.

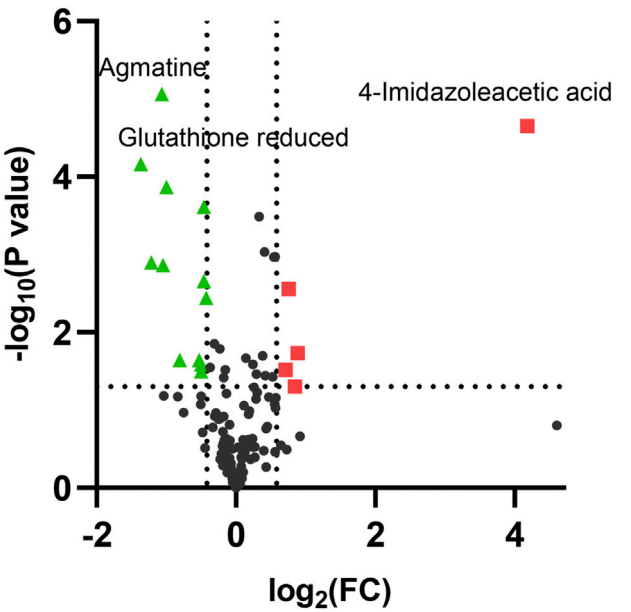

FIGURE 3 | Volcano plot analysis of differential metabolites in A549 cells after exposure to 80 μM EGCG. The *x*-axis represents $\log_2$ (fold change), while the *y*-axis represents *p*-value in $-\log_{10}$ scale. The significantly up-regulated metabolites were indicated in red squares and down-regulated in green triangles. ($p < 0.05$ and fold change >1.5 or <0.75).

in 80 μM EGCG-treated A549 cells compared to controls were summarized in **Table 2**. The corresponding results between the 40 μM EGCG-treated group and the control group are shown in **Supplementary Tables S2, S3** respectively.

Analysis of Metabolic Pathways

We used MetaboAnalyst 5.0 and metabolites with $p < 0.05$ to analyze metabolic pathways. Compared to the control group, 27 metabolic pathways were affected (**Supplementary Table S4**) in the 80 μM EGCG-treated group. Of these, two markedly altered pathways were filtered according to specific criteria (raw $p < 0.05$ and impact value >0.2): Glycine, serine and threonine metabolism (impact value = 0.628), Alanine, aspartate and glutamate metabolism (impact value = 0.272). Each metabolic pathway was represented by a colored circle within the diagram. As shown in **Figure 6** and **Supplementary Table S4**, EGCG induced significant perturbations in Glycine, serine and threonine metabolism, Alanine, aspartate and glutamate metabolism, Aminoacyl-tRNA biosynthesis, Glyoxylate and dicarboxylate metabolism, Arginine and proline metabolism in the 80 μM EGCG group (**Figure 6**), as well as Histidine metabolism, arginine and proline metabolism in the 40 μM EGCG group (**Supplementary Figure S3**).

DISCUSSION

The anticancer ability of EGCG has been shown to be related to its antiproliferative and proapoptotic effects (Ahmad et al., 1997; Khan et al., 2006; Ma et al., 2013; Pal et al., 2018; Almatroodi et al., 2020). Similar to previous reports (Jiang et al., 2016; Li et al., 2016), our data suggest that EGCG concentrations at 40 μM or greater showed evident cell growth inhibition on A549 cells compared to the control group. Considering the balance between cell viability and data interpretability and exploring cell metabolism changes caused by different concentrations of EGCG, 40 and 80 μM were chosen for further experiments in this

TABLE 1 | Significantly altered metabolites among the control and the EGCG-treated groups by ANOVA test analysis with Tukey's post hoc analysis.

	p. value	Tukey's HSD
4-Imidazoleacetic acid	4.970E-07	40 μM-0 μM; 80 μM-0 μM
Glutathione reduced	3.730E-06	40 μM-0 μM; 80 μM-0 μM
Agmatine	1.160E-05	40 μM-0 μM; 80 μM-0 μM
Cytosine	2.710E-05	40 μM-0 μM; 80 μM-0 μM
Aspartate	1.126E-04	40 μM-0 μM; 80 μM-0 μM
2-Deoxycytidine	1.900E-04	40 μM-0 μM; 80 μM-0 μM
2/3-Aminoisobutyric acid/Dimethylglycine	3.167E-04	40 μM-0 μM; 80 μM-0 μM
Proline	3.484E-04	40 μM-0 μM; 80 μM-0 μM
6-Methyl-DL-Tryptophan	4.916E-04	80-0 μM
Serine	0.001	80-0 μM
R5P	0.001	80-0 μM
2-Methylglutaric acid	0.001	40 μM-0 μM; 80 μM-0 μM
Asparagine	0.001	80-0 μM
Acetohydroxamic acid	0.002	80-0 μM

R5P, Ribose-5-phosphate.

study, corresponding to 92 and 60% survival rate respectively (Chu et al., 2018; Daskalaki et al., 2018; Zhang et al., 2020). It has been proved that treatment with green tea-based food supplements has acceptable safety, but high doses of EGCG can induce certain toxic side effects (Peter et al., 2017). Intake up to 300 mg EGCG/person/day is a tolerable upper intake level proposed for food supplements (Dekant et al., 2017). In a previous study, the maximum plasma concentration of EGCG was 695.8 ng/ml after receiving oral EGCG in 10 day's repeated doses of 400 mg (Ullmann et al., 2004).

Studies have demonstrated various biological and pharmacological activities of EGCG, such as antioxidant, anti-inflammatory, antiangiogenic, antiproliferative, proapoptotic, and antimetastatic properties (Gu et al., 2013; Lee et al., 2013; Zhang et al., 2013; Chen et al., 2016; Liu et al., 2016; Fujiki et al., 2017; Almatroodi et al., 2020). *In vitro*, EGCG has been shown to inhibit growth by increasing the percentage of cells at the G0/G1 phase of the cell cycle (Fujiki et al., 2017) and inhibit epithelial-mesenchymal transition and migration via downregulation of HIF-1α, VEGF, pAkt/ERK, COX-2 and vimentin in A549 lung cancer cell (Shi et al., 2015). Also, research has shown that EGCG stimulates apoptosis in the H1299 lung cancer cell line by inhibiting the activation of PI3K/Akt serine/threonine kinase 1 signaling pathway (Gu et al., 2018). One study demonstrated that the inhibition of A549 cell proliferation by EGCG might be achieved via suppressing the expression of the cell death-inhibiting gene, Bcl-xL (Sonoda et al., 2014). Another study showed EGCG also upregulated the expression of the apoptosis-promoting factor Bax by regulating Ku70 acetylation that blocks the interaction between Ku70 and Bax (Li et al., 2016). The amino acids alanine and glutamate were found to be significantly up-regulated in apoptotic HepG2 and HEK293 cells irrespective of the apoptosis inducer (Halama et al., 2013). Disturbed alanine, aspartate and glutamate metabolism in A549 cells under 80 μM EGCG exposure in this study may be related to the proapoptotic effect of EGCG. Long non-coding RNAs (lncRNAs) have emerged as new players in the cancer paradigm. Real-time quantitative reverse transcription-polymerase chain reaction proved a downregulation of *HMMR-AS1, AL392089.1, PSMC3IP,* and *LINC02643* lncRNAs and upregulation of *RP1-74M1.3, AC087273.2, SNAI3-AS1, LINC02532,* and *AC007319.1* lncRNAs in A549 cell lines treated with EGCG (Hu et al., 2019). Various lncRNAs, mRNAs, or proteins regulated by EGCG identified in these studies could affect the metabolic results of A549 cells. Synergistic inhibition of lung cancer cells by EGCG with other drugs has also been reported, such as leptomycin B (Cromie and Gao, 2015), NF-κB inhibitor BAY11-7082 (Zhang et al., 2019), gefitinib (Meng et al., 2019), and cisplatin (Jiang et al., 2016). However, the precise underlying mechanisms of the antitumor activity of EGCG in lung cancer are still largely unclear.

In this study, we used a metabolic approach to further uncover the likely mechanisms underlying the anticancer activity of EGCG in A549 cells. This approach led us to identify 32 differential metabolites (15 upregulated/17 downregulated) in the 80 μM EGCG treated group compared to the control (**Table 2**). Among the identified metabolites, 11 compounds were significantly changed (fold change >1.5 or <0.75) (**Supplementary Table S2**). Glycine, serine and threonine metabolism and alanine, aspartate and glutamate metabolism were the two most significantly disturbed pathways under 80 μM EGCG exposure. Histidine metabolism and arginine and proline metabolism were the two most significantly disturbed by exposure to 40 μM EGCG. A schematic diagram of the modulated metabolites and potential disturbed metabolic pathways is shown in **Figure 7**. A more specific analysis of metabolites is as follows.

Energy Metabolism

In this study, the metabolomics data suggested that EGCG altered the cellular energy metabolism of A459 cells through glycolysis and the tricarboxylic acid (TCA) cycle. Consumption of glucose by tumors increased markedly compared to the nonproliferating normal tissues to meet the biosynthetic demands associated with proliferation (Warburg et al., 1927). Usually, cancer cells predominantly use glycolysis rather than the TCA cycle for energy production, a phenomenon known as the Warburg effect (Panieri and Santoro, 2016). In previous studies, EGCG

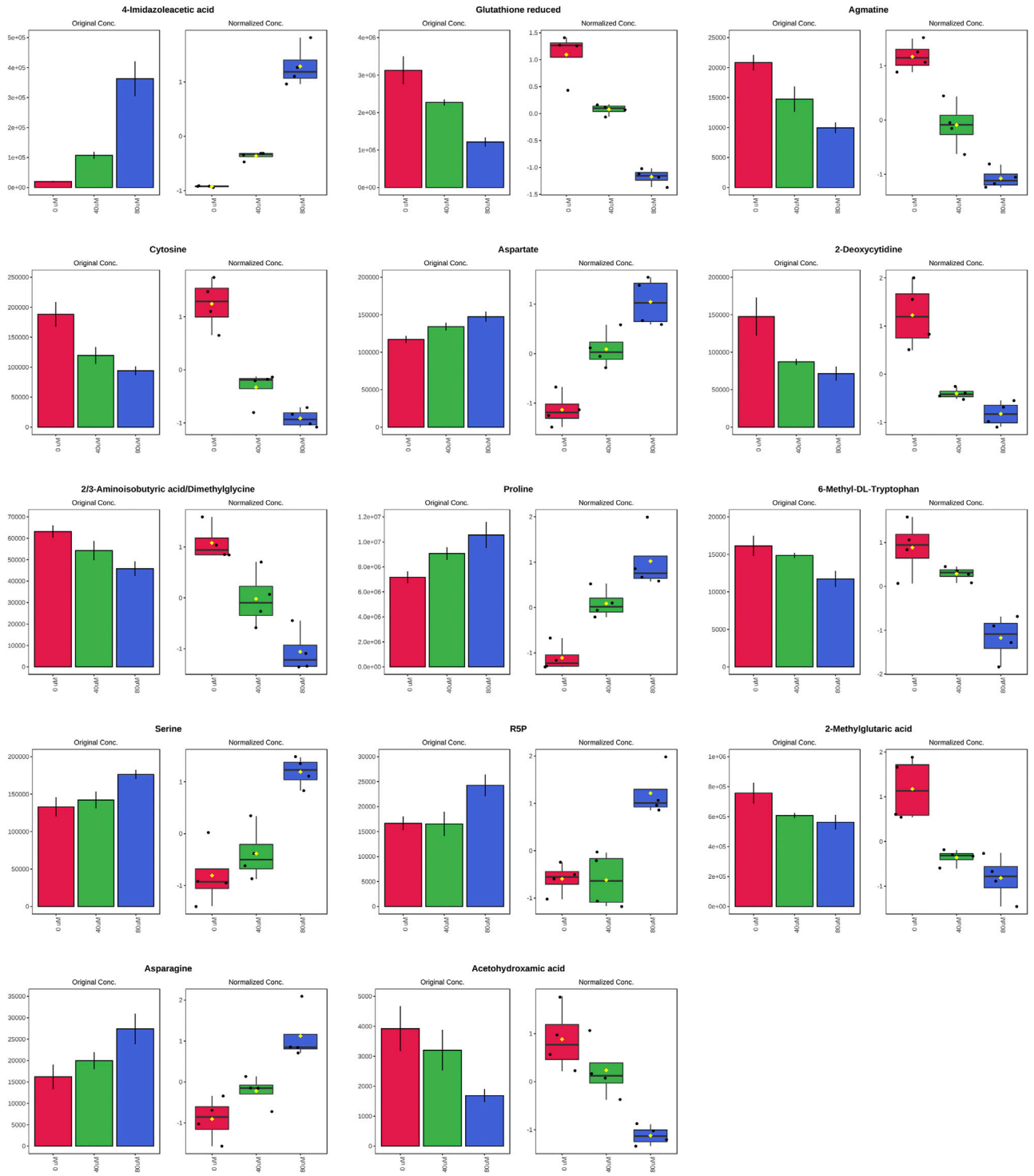

FIGURE 4 | Significantly altered metabolites among the control and the EGCG-treated groups. The bar plots on the left show the original peak intensity values (mean ± SD). The box and whisker plots on the right summarize the normalized values.

significantly reduced lactate production, anaerobic glycolysis, glucose consumption and glycolytic rate in pancreatic adenocarcinoma MIA PaCa-2 cells (Lu et al., 2015). A decrease in glycolysis intermediate glyceraldehyde 3-phosphate was observed in 80 μM EGCG induced cells compared with control cells in this study. However, there were no significant differences in glycolysis intermediates such as glucose-6-phosphate/fructose-6-phosphate (G6P/F6P) and lactate

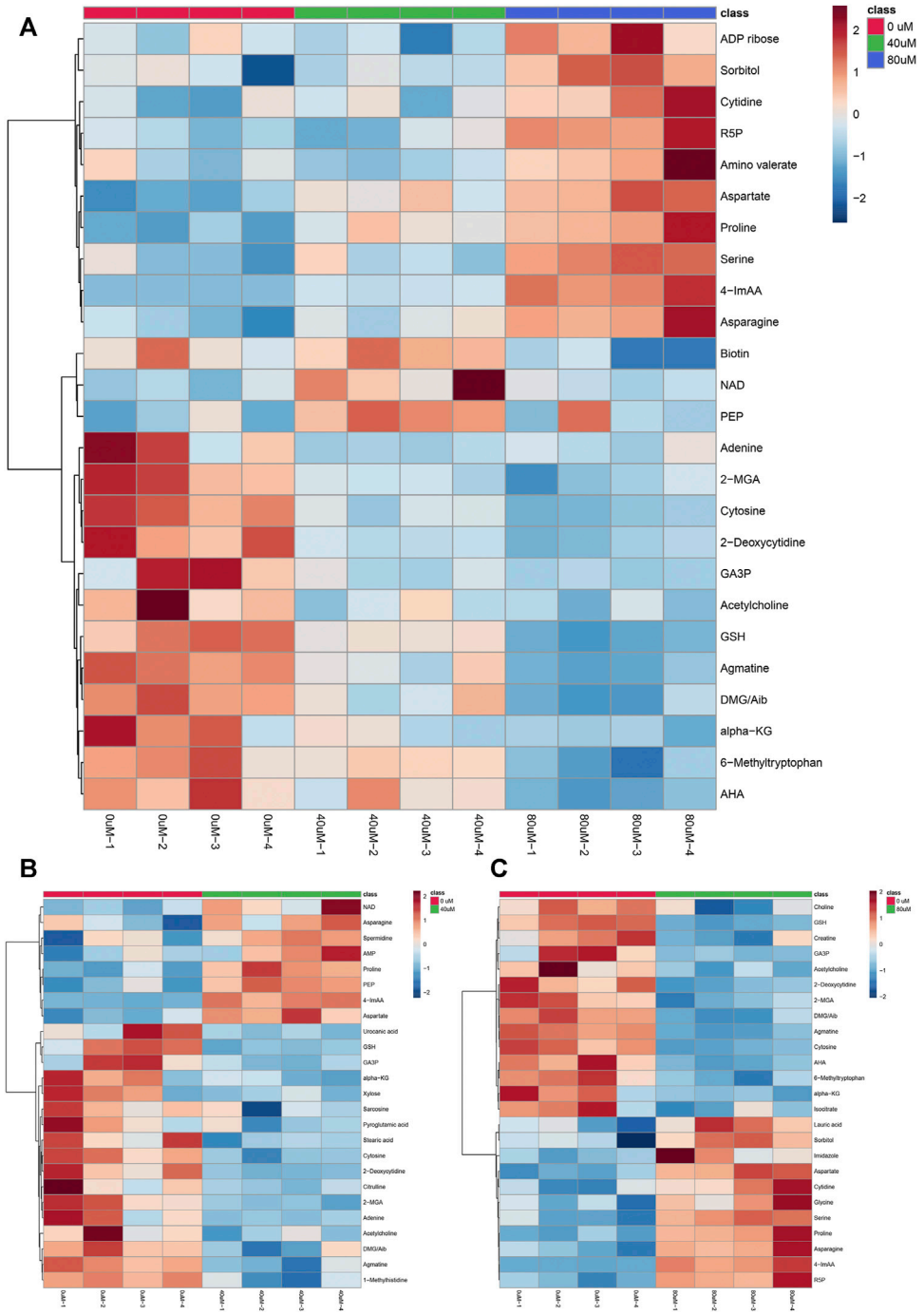

FIGURE 5 | Hierarchical clustering heat map of the top 25 differential metabolites selected based on t-tests/ANOVA, with the degree of change marked with red (up-regulation) and blue (down-regulation). The distance measure was set to "Euclidean" and the clustering algorithm was set to "Ward". **(A)**: control group, 40 μM EGCG-treated group and 80 μM EGCG-treated group; **(B)**: control group and 40 μM EGCG-treated group; **(C)**: control group and 80 μM EGCG-treated group. **Abbreviations:** R5P, Ribose-5-phosphate; 4-ImAA, 4-Imidazoleacetic acid; NAD, nicotinamide adenine dinucleotide; PEP, phosphoenolpyruvate; 2-MGA, 2-Methylglutaric Acid; GA3P, glyceraldehyde 3-phosphate; GSH, glutathione; DMG, Dimethylglycine; Aib, 2/3-Aminoisobutyric acid; alpha-KG, alpha-Ketoglutaric acid; AHA, Acetohydroxamic acid.

between the control group and EGCG induced group, neither 40 μM nor 80 μM. Interestingly, phosphoenolpyruvate (PEP) was found to increase in the 40 μM group compared to the control. An increase in Glucose-6-phosphate isomerase (GPI), ATP-dependent 6-phosphofructokinase platelet type (PFK-P) and fructose-bisphosphate aldolase A (ALDA) were detected by

TABLE 2 | The disturbed metabolites with $p < 0.05$ in 80 μM EGCG-treated A549 cells compared to controls.

Metabolite	*p*. value	Fold change
Agmatine	8.640E-06	0.48
4-Imidazoleacetic acid	2.220E-05	18.13
Glutathione reduced	6.860E-05	0.39
Cytosine	1.360E-04	0.50
2/3-Aminoisobutyric acid/Dimethylglycine	2.450E-04	0.73
Aspartate	3.240E-04	1.26
Serine	0.001	1.33
Proline	0.001	1.47
R5P	0.001	1.46
Acetohydroxamic acid	0.001	0.43
2-Deoxycytidine	0.001	0.48
6-Methyl-DL-Tryptophan	0.002	0.73
Asparagine	0.003	1.69
2-Methylglutaric acid	0.004	0.74
alpha-KG	0.014	0.81
Creatine	0.016	0.85
Cytidine	0.019	1.84
Lauric acid	0.020	1.30
Glycine	0.022	1.10
GA3P	0.023	0.69
Acetylcholine	0.023	0.57
Choline	0.026	0.71
Sorbitol	0.026	1.18
IsoCitrate	0.028	0.77
Imidazole	0.030	1.64
Sarcosine	0.030	0.90
Biotin	0.032	0.71
UDP-GlcNAc	0.035	1.22
ADP ribose	0.036	1.34
Adipic acid	0.037	1.44
Pantothenic acid	0.038	0.88
Amino valerate	0.050	1.80

R5P, Ribose-5-phosphate; alpha-KG, alpha-Ketoglutaric acid; GA3P, glyceraldehyde 3-phosphate; UDP-GlcNAc, Uridine diphosphate-N-acetylglucosamine.

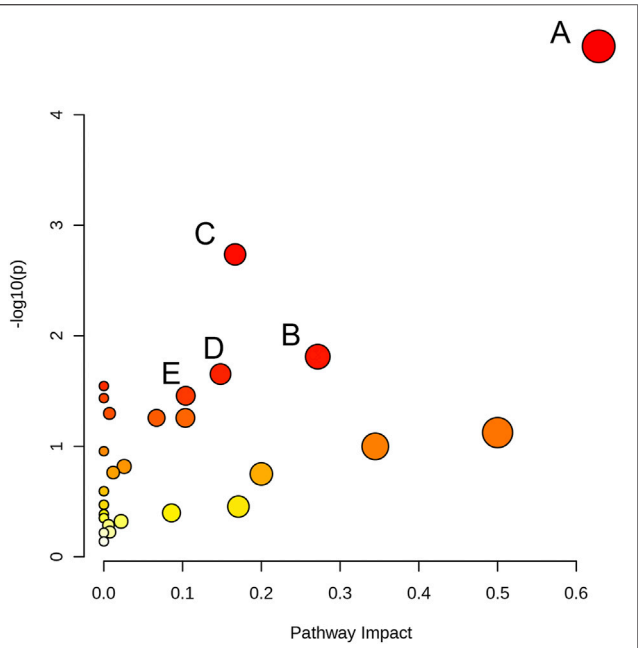

FIGURE 6 | Pathway analysis overview depicting altered metabolic pathways in A549 cells from control and 80 μM EGCG-treated groups. The metabolic pathways are displayed as distinctly colored circles depending on their enrichment analysis scores (vertical axis, shade of red) and topology (pathway impact, horizontal axis, circle diameter) via MetaboAnalyst 5.0. **(A)**: Glycine, serine and threonine metabolism, **(B)**: Alanine, aspartate and glutamate metabolism, **(C)**: Aminoacyl-tRNA biosynthesis, **(D)**: Glyoxylate and dicarboxylate metabolism E: Arginine and proline metabolism.

Wu et al. (2017) in Dox-induced senescent cells compared with control cells, suggesting an up-regulation of the glycolytic pathway during senescence. So, we couldn't refuse the assumption that the inhibitory effect on glycolysis may be counteracted by induced cell senescence in our research.

Ribose-5-phosphate, which can be generated by the pentose phosphate pathway (PPP), a constituent of nucleotides, was found to increase in the 80 μM group compared to the control. Wu et al. (2017) also found the activation of PPP in senescent cells. We could infer that A549 cells would produce more nucleotide precursors to fulfill the increased need for nucleosides for DNA damage repair by activating PPP when challenged with EGCG treatment.

Our data revealed an elevated level of Uridine diphosphate-N-acetylglucosamine (UDP-Glc-NAc) in the 80 μM EGCG induced group compared to the control one. UDP-Glc-NAc is the end product of a well-established pathway for nutrient sensing-the hexosamine biosynthetic pathway (HBP) and also the donor substrate for modification of nucleocytoplasmic proteins at serine and threonine residues with N-acetylglucosamine (O-GlcNAc) (Wells et al., 2003). Elevated HBP has been reported in cancers and much evidence suggests the HBP helps fuel cancer cell metabolism, growth, survival, and spread (Ferrer et al., 2016; Akella et al., 2019). Interestingly, not only in the cancer cells but also in senescent cells, up-regulation of HBP has been suggested (Wu et al., 2017). The reason for the up-regulation of the UDP-Glc-NAc induced by EGCG in A549 cells needs to be further explored.

The tricarboxylic acid (TCA) cycle is the main pathway of glucose degradation and the primary energy supplier for universal organisms. The 80 μM EGCG induced group showed a down-regulated TCA cycle activity in the A549 cell line, manifested as a decrease in two main TCA cycle intermediates: α-ketoglutarate and isocitrate. However, we didn't find similar down-regulated TCA cycle intermediates in 40 μM EGCG induced group. This suggested that downregulated TCA cycle in A549 cells induced by EGCG may be dose-dependent and relates to the downregulation of cell viability.

Amino Acid Metabolism

TCA cycle provides metabolic precursors for the biosynthesis of non-essential amino acids, including aspartate and asparagine. In our study, the level of aspartate and asparagine was increased in 80 μM EGCG induced group, which indicated that there were other ways to supplement the synthesis of aspartic acid.

The significantly increased expression of 4-Imidazoleacetic acid (histidine's metabolite) was observed in EGCG-treated A549 cells, which implied the disturbance of histidine metabolism. The presented evidence indicates that histamine is an important

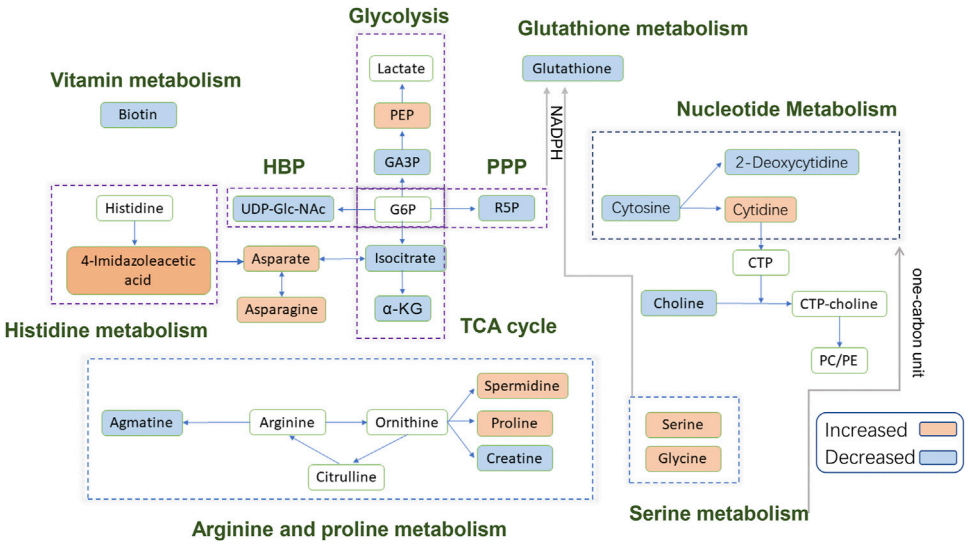

FIGURE 7 | Schematic diagram of the modulated metabolites and potential disturbed metabolic pathways. Up-regulated metabolites detected are shown in the orange background; down-regulated metabolites detected are shown in the blue background; blank background means no statistically significant change or undetected. **Abbreviations:** PEP, phosphoenolpyruvate; GA3P, glyceraldehyde 3-phosphate; G6P, glucose-6-phosphate; α-KG, alpha-Ketoglutaric acid; R5P, Ribose-5-phosphate; CTP, cytidine triphosphate; PC, phosphatidylcholine; PE, phosphatidylethanolamine; HBP, hexosamine biosynthetic pathway; PPP, pentose phosphate pathway; TCA, tricarboxylic acid.

mediator in cancer development and progression (Rivera et al., 2000), and the effects of histamine's receptor antagonists on cancer cell proliferation have been explored (Blaya et al., 2010). 4-Imidazoleacetic acid is the most apparent upregulated metabolite among the statistically different metabolites in our study, by 18.13-fold and 5.36-fold in 80 and 40 μM EGCG induced group respectively compared to the control group. 4-Imidazoleacetic acid can be generated from oxidative deamination of histamine and then transform to aspartate. So, the increased level of aspartate and asparagine is not strange in the 80 μM EGCG induced group. Asparagine has also been reported to potentiate $CD8^+$ T-cell activation and antitumor responses (Wu et al., 2021). As tumors frequently outgrow their supply, cancer cells reside in oxygen-poor environments. Low oxygen activates a transcriptional program that induces glucose uptake and glycolysis while suppressing the electron transport chain (ETC) activity (Ackerman and Simon, 2014). Studies show that aspartate synthesis plays an essential role in the electron transport chain in cell proliferation (Birsoy et al., 2015; Sullivan et al., 2015). Therefore, aspartate may be a limiting metabolite for tumor growth, and aspartate availability may be targeted for cancer therapy (Garcia-Bermudez et al., 2018).

The metabolites of arginine are involved in multiple pathways. Creatine participates in ATP production, whereas ornithine can be converted to putrescine and spermidine for cell proliferation (Wei et al., 2001; Abraham et al., 2013). Ornithine can also be converted to proline and hydroxyproline for collagen formation and new extracellular matrix deposition (Tan et al., 1983). A meta-analysis of metabolic enzyme expression across diverse tumor types identified pyrroline-5-carboxylate reductase (PYCR1), the principal enzyme in proline biosynthesis, as one of the most commonly overexpressed genes in tumors (Nilsson et al., 2014). Compared with the normal, increased levels of spermidine (in 40 μM EGCG induced group) and proline (both in 40 and 80 μM EGCG induced group) were found in our research. However, the level of CTP itself was not changed. In addition, we found decreased levels of creatine in the 80 μM EGCG induced group, another metabolite of arginine which participates in ATP production (Abraham et al., 2013). Agmatine, which can be converted from arginine by the action of arginine decarboxylase on the cell mitochondrial membrane, was also found to decrease in the EGCG group. Agmatine can induce a decrease in cell proliferation due to decreased intracellular levels of polyamines putrescine, spermidine, and spermine (Higashi et al., 2004). Studies have indicated that agmatine administration to tumor cells *in vitro* results in a suppression of cell proliferation (Molderings et al., 2004; Mayeur et al., 2005). In our research, the antitumor effect of EGCG may counteract the endogenous production of agmatine.

Serine is crucial for multiple metabolic pathways required for cell growth and proliferation, including phospholipid, purine and glutathione biosynthesis, as well as being a methyl source for single carbon metabolism. Serine has been reported to be the third most consumed metabolite by cancer cells after glucose and glutamine (Jain et al., 2012; Dolfi et al., 2013). When a significant amount of serine is converted into glycine, serine releases a one-carbon unit to the one-carbon pool. Glycine could also contribute to the one-carbon pool through the glycine cleavage system. One-carbon pathway metabolites contribute to a number of cellular biosynthetic and regulatory processes. Serine was found to be elevated in our research and glycine slightly, which may indicate the decrease consumption of them for one-carbon unit generation.

Nucleotide Metabolism

The change of carbon flow in the metabolic stream will cause the abnormality of nucleotide metabolism. The increase of serine level can promote serine-mediated pyruvate kinase 2 (PKM2) activity by inducing allosteric changes of the enzyme (Mazurek, 2011; Chaneton et al., 2012). PKM2 reduces the carbon flux into the serine biosynthesis pathway and the nucleotide biosynthesis pathway, ultimately affecting nucleotide metabolism (Mazurek, 2011; Chaneton et al., 2012). In our study, the decrease of cytosine and 2-deoxycytidine in the 80 μM EGCG-treated group may be related to the up-regulation of serine. This trend is not applicable to cytidine, but it's not strange when the trend of choline is down-regulated. It has been reported that the reduction of choline and glutathione metabolites is associated with apoptosis (Rainaldi et al., 2008; Halama et al., 2013). Cytidine is a precursor of cytidine triphosphate (CTP) needed in the phosphatidylcholine (PC) and phosphatidylethanolamine (PE) biosynthetic pathways. The down-regulation of choline may lead to a reduction in cytidine consumption.

From **Supplementary Table S3**, we can find that adenine was downregulated by 0.38-fold which was the most obvious reduction among all the statistically different metabolites in the 40 μM group compare to the control. Clear signaling roles for extracellular adenosine have been established in immunomodulation, vascular remodeling, and promotion of cell growth and proliferation (Chen et al., 2018; Di Virgilio et al., 2018; Morandi et al., 2018; Antonioli et al., 2019). In recent years, it has also been found that adenosine can be used as a signal molecule to affect the biological behavior of tumor cells through different signaling pathways, such as triggering cell cycle arrest, inducing tumor cell apoptosis and affecting cell proliferation (Yang et al., 2007).

Glutathione Metabolism

In our study, glutathione expression was downregulated in 80 μM EGCG-treated group by 0.39-fold compared with that in the control group. In a metabolomics study of EGCG acting on colorectal cancer cells (HT-29), glutathione expression was also downregulated in EGCG-treated cells (Zhang et al., 2020). Generation of reactive oxygen species (ROS) at high levels can damage nucleotides, proteins and lipids, so impair cell viability. In cancer cells, glutathione oxidation-reduction coupled to NADPH reduction-oxidation is a major pathway for ROS detoxification (Lv et al., 2019). NADPH for ROS turnover through this pathway can be generated from glucose via the pentose phosphate pathway or serine via one-carbon metabolism. As analyzed above, the former one was up-regulated. Taken together, disturbance of glutathione metabolism is a potential pathway involved in the antitumor mechanism of EGCG.

Vitamin Metabolism

Biotin (vitamin H) is an essential micronutrient vital for normal cellular function (Livaniou et al., 2000). To thrive and multiply rapidly, cancer cells need extra biotin compared with normal cells. Biotin overexpression is observed in wide types of cancer cells, including renal (RENCA, RD0995), leukemia (L1210FR), lung (A549, M109), ovarian (OV 2008; ID8), mastocytoma (P815), and breast (4T1, JC, MMT06056) cancer (Russell-Jones et al., 2004; Chen et al., 2010; Shi et al., 2014). The decreased biotin implied a slowdown in the proliferation of 80 μM EGCG-treated A549 cells compared to the control group.

Finally, there are several limitations in the present study. Firstly, although some previous *in vitro* studies employed the A549 cell line to explore the mechanism of the antitumor effects of EGCG, the A549 cell line cannot represent the true lung cancer cell environment *in vivo*. The concentrations of EGCG from 10 to 100 μM used in most of the studies in cell culture systems, as well as in this paper, are much higher than the concentrations monitored in human plasma (usually lower than 1 μM) after tea ingestion. Thus, it is necessary to verify the high concentration findings in cell lines utilizing lower concentrations in the human body. Secondly, in metabolomics studies, the differences in viability between the control and treated cells would affect the accuracy of the results. The dose of IC50 has been used in the metabolomics research of toxicology in recent years (Yu et al., 2019; He et al., 2020; Hou et al., 2020). To capture more responses on cell metabolism related to the anticancer effect of EGCG and explore the changes in metabolic processes with increasing EGCG concentration, the dosages of 40 and 80 μM were both used in our metabolomics experiment. Thirdly, even though we used a pathway-specific LC-MS/MS method that can cover more than 300 metabolites from over 35 metabolic pathways, there were still many important metabolites left out. This has an impact on the analysis of metabolic pathways. In addition, quantitative proteomics is needed to detect whether there was an increase or decrease in enzymes involved better to explain the upregulation or downregulation of the metabolic pathway. Further experiments are needed to investigate the specific relationship between genetic changes and metabolite changes.

CONCLUSION

In this study, the metabolite changes in A549 cells induced by EGCG were investigated utilizing LC-MS-based metabolomics. Our data demonstrated that altered metabolites were involved in the metabolism of glucose, amino acid, nucleotide, glutathione, vitamin and especially associated with serine and threonine metabolism, alanine, aspartate and glutamate metabolism, and histidine metabolism. These findings contribute to understanding the intramolecular metabolic processes of A549 cells caused by EGCG and may provide potential clues for the underlying mechanisms of the anti-cancer property of EGCG. Further researches are required for the therapeutic application of EGCG in cancer management.

DATA AVAILABILITY STATEMENT

The original contributions presented in the study are included in the article/**Supplementary Material**, further inquiries can be directed to the corresponding authors.

AUTHOR CONTRIBUTIONS

XZ and HH conceived and designed the study. HH, DH, YX, and TP carried out the experiments. TP, HH, WP, and LB drafted this

manuscript and analyzed the data. HH and XZ provided final approval of the version to be published. All of the authors discussed the complete dataset to establish an integral and coherent analysis. All authors have read and approved the final manuscript.

SUPPLEMENTARY MATERIAL

The Supplementary Material for this article can be found online at: https://www.frontiersin.org/articles/10.3389/fphar.2021.732716/full#supplementary-material

REFERENCES

Abraham, M. R., Bottomley, P. A., Dimaano, V. L., Pinheiro, A., Steinberg, A., Traill, T. A., et al. (2013). Creatine Kinase Adenosine Triphosphate and Phosphocreatine Energy Supply in a Single kindred of Patients with Hypertrophic Cardiomyopathy. *Am. J. Cardiol.* 112 (6), 861–866. doi:10.1016/j.amjcard.2013.05.017

Ackerman, D., and Simon, M. C. (2014). Hypoxia, Lipids, and Cancer: Surviving the Harsh Tumor Microenvironment. *Trends Cell Biol.* 24 (8), 472–478. doi:10.1016/j.tcb.2014.06.001

Ahmad, N., Feyes, D. K., Nieminen, A. L., Agarwal, R., and Mukhtar, H. (1997). Green tea Constituent Epigallocatechin-3-Gallate and Induction of Apoptosis and Cell Cycle Arrest in Human Carcinoma Cells. *J. Natl. Cancer Inst.* 89 (24), 1881–1886. doi:10.1093/jnci/89.24.1881

Akella, N. M., Ciraku, L., and Reginato, M. J. (2019). Fueling the Fire: Emerging Role of the Hexosamine Biosynthetic Pathway in Cancer. *BMC Biol.* 17 (1), 52. doi:10.1186/s12915-019-0671-3

Almatroodi, S. A., Almatroudi, A., Khan, A. A., Alhumaydhi, F. A., Alsahli, M. A., and Rahmani, A. H. (2020). Potential Therapeutic Targets of Epigallocatechin Gallate (EGCG), the Most Abundant Catechin in Green Tea, and its Role in the Therapy of Various Types of Cancer. *Molecules* 25 (14), 3146. doi:10.3390/molecules25143146

Antonioli, L., Fornai, M., Blandizzi, C., Pacher, P., and Haskó, G. (2019). Adenosine Signaling and the Immune System: When a Lot Could Be Too Much. *Immunol. Lett.* 205, 9–15. doi:10.1016/j.imlet.2018.04.006

Birsoy, K., Wang, T., Chen, W. W., Freinkman, E., Abu-Remaileh, M., and Sabatini, D. M. (2015). An Essential Role of the Mitochondrial Electron Transport Chain in Cell Proliferation Is to Enable Aspartate Synthesis. *Cell* 162 (3), 540–551. doi:10.1016/j.cell.2015.07.016

Blaya, B., Nicolau-Galmés, F., Jangi, S. M., Ortega-Martínez, I., Alonso-Tejerina, E., Burgos-Bretones, J., et al. (2010). Histamine and Histamine Receptor Antagonists in Cancer Biology. *Inflamm. Allergy Drug Targets* 9 (3), 146–157. doi:10.2174/187152810792231869

Borutinskaitė, V., Virkšaitė, A., Gudelytė, G., and Navakauskienė, R. (2018). Green tea Polyphenol EGCG Causes Anti-cancerous Epigenetic Modulations in Acute Promyelocytic Leukemia Cells. *Leuk. Lymphoma* 59 (2), 469–478. doi:10.1080/10428194.2017.1339881

Carroll, P. A., Diolaiti, D., McFerrin, L., Gu, H., Djukovic, D., Du, J., et al. (2015). Deregulated Myc Requires MondoA/Mlx for Metabolic Reprogramming and Tumorigenesis. *Cancer Cell* 27 (2), 271–285. doi:10.1016/j.ccell.2014.11.024

Chaneton, B., Hillmann, P., Zheng, L., Martin, A. C. L., Maddocks, O. D. K., Chokkathukalam, A., et al. (2012). Serine Is a Natural Ligand and Allosteric Activator of Pyruvate Kinase M2. *Nature* 491 (7424), 458–462. doi:10.1038/nature11540

Chen, D., and Dou, Q. P. (2008). Tea Polyphenols and Their Roles in Cancer Prevention and Chemotherapy. *Int. J. Mol. Sci.* 9 (7), 1196–1206. doi:10.3390/ijms9071196

Chen, M., Wei, L., Law, C. T., Tsang, F. H., Shen, J., Cheng, C. L., et al. (2018). RNA N6-Methyladenosine Methyltransferase-like 3 Promotes Liver Cancer Progression through YTHDF2-dependent Posttranscriptional Silencing of SOCS2. *Hepatology* 67 (6), 2254–2270. doi:10.1002/hep.29683

Chen, S., Zhao, X., Chen, J., Chen, J., Kuznetsova, L., Wong, S. S., et al. (2010). Mechanism-based Tumor-Targeting Drug Delivery System. Validation of Efficient Vitamin Receptor-Mediated Endocytosis and Drug Release. *Bioconjug. Chem.* 21 (5), 979–987. doi:10.1021/bc9005656

Chen, S. J., Yao, X. D., Peng, B. O., Xu, Y. F., Wang, G. C., Huang, J., et al. (2016). Epigallocatechin-3-gallate Inhibits Migration and Invasion of Human Renal Carcinoma Cells by Downregulating Matrix Metalloproteinase-2 and Matrix Metalloproteinase-9. *Exp. Ther. Med.* 11 (4), 1243–1248. doi:10.3892/etm.2016.3050

Chu, K. O., Chan, K. P., Chan, S. O., Ng, T. K., Jhanji, V., Wang, C. C., et al. (2018). Metabolomics of Green-Tea Catechins on Vascular-Endothelial-Growth-Factor-Stimulated Human-Endothelial-Cell Survival. *J. Agric. Food Chem.* 66 (48), 12866–12875. doi:10.1021/acs.jafc.8b05998

Cromie, M. M., and Gao, W. (2015). Epigallocatechin-3-gallate Enhances the Therapeutic Effects of Leptomycin B on Human Lung Cancer A549 Cells. *Oxid Med. Cell Longev* 2015, 217304. doi:10.1155/2015/217304

Daskalaki, E., Pillon, N. J., Krook, A., Wheelock, C. E., and Checa, A. (2018). The Influence of Culture media upon Observed Cell Secretome Metabolite Profiles: The Balance between Cell Viability and Data Interpretability. *Anal. Chim. Acta* 1037, 338–350. doi:10.1016/j.aca.2018.04.034

Dekant, W., Fujii, K., Shibata, E., Morita, O., and Shimotoyodome, A. (2017). Safety Assessment of green tea Based Beverages and Dried green tea Extracts as Nutritional Supplements. *Toxicol. Lett.* 277, 104–108. doi:10.1016/j.toxlet.2017.06.008

Di Virgilio, F., Sarti, A. C., Falzoni, S., De Marchi, E., and Adinolfi, E. (2018). Extracellular ATP and P2 Purinergic Signalling in the Tumour Microenvironment. *Nat. Rev. Cancer* 18 (10), 601–618. doi:10.1038/s41568-018-0037-0

Dolfi, S. C., Chan, L. L., Qiu, J., Tedeschi, P. M., Bertino, J. R., Hirshfield, K. M., et al. (2013). The Metabolic Demands of Cancer Cells Are Coupled to Their Size and Protein Synthesis Rates. *Cancer Metab.* 1 (1), 20. doi:10.1186/2049-3002-1-20

Dunn, W. B., Broadhurst, D. I., Atherton, H. J., Goodacre, R., and Griffin, J. L. (2011). Systems Level Studies of Mammalian Metabolomes: the Roles of Mass Spectrometry and Nuclear Magnetic Resonance Spectroscopy. *Chem. Soc. Rev.* 40 (1), 387–426. doi:10.1039/b906712b

Eghlimi, R., Shi, X., Hrovat, J., Xi, B., and Gu, H. (2020). Triple Negative Breast Cancer Detection Using LC-MS/MS Lipidomic Profiling. *J. Proteome Res.* 19 (6), 2367–2378. doi:10.1021/acs.jproteome.0c00038

Ferlay, J., Soerjomataram, I., Dikshit, R., Eser, S., Mathers, C., Rebelo, M., et al. (2015). Cancer Incidence and Mortality Worldwide: Sources, Methods and Major Patterns in GLOBOCAN 2012. *Int. J. Cancer* 136 (5), E359–E386. doi:10.1002/ijc.29210

Ferrer, C. M., Sodi, V. L., and Reginato, M. J. (2016). O-GlcNAcylation in Cancer Biology: Linking Metabolism and Signaling. *J. Mol. Biol.* 428 (16), 3282–3294. doi:10.1016/j.jmb.2016.05.028

Fujiki, H., Sueoka, E., Rawangkan, A., and Suganuma, M. (2017). Human Cancer Stem Cells Are a Target for Cancer Prevention Using (-)-epigallocatechin Gallate. *J. Cancer Res. Clin. Oncol.* 143 (12), 2401–2412. doi:10.1007/s00432-017-2515-2

Gan, R. Y., Li, H. B., Sui, Z. Q., and Corke, H. (2018). Absorption, Metabolism, Anti-cancer Effect and Molecular Targets of Epigallocatechin Gallate (EGCG): An Updated Review. *Crit. Rev. Food Sci. Nutr.* 58 (6), 924–941. doi:10.1080/10408398.2016.1231168

Garcia-Bermudez, J., Baudrier, L., La, K., Zhu, X. G., Fidelin, J., Sviderskiy, V. O., et al. (2018). Aspartate Is a Limiting Metabolite for Cancer Cell Proliferation under Hypoxia and in Tumours. *Nat. Cell Biol* 20 (7), 775–781. doi:10.1038/s41556-018-0118-z

Griffin, J. L., Atherton, H., Shockcor, J., and Atzori, L. (2011). Metabolomics as a Tool for Cardiac Research. *Nat. Rev. Cardiol.* 8 (11), 630–643. doi:10.1038/nrcardio.2011.138

Gu, H., Gowda, G. A., and Raftery, D. (2012). Metabolic profiling: are we en route to better diagnostic tests for cancer. *Future Oncol.* 8 (10), 1207–1210. doi:10.2217/fon.12.113

Gu, H., Zhang, P., Zhu, J., and Raftery, D. (2015). Globally Optimized Targeted Mass Spectrometry: Reliable Metabolomics Analysis with Broad Coverage. *Anal. Chem.* 87 (24), 12355–12362. doi:10.1021/acs.analchem.5b03812

Gu, J. J., Qiao, K. S., Sun, P., Chen, P., and Li, Q. (2018). Study of EGCG Induced Apoptosis in Lung Cancer Cells by Inhibiting PI3K/Akt Signaling Pathway. *Eur. Rev. Med. Pharmacol. Sci.* 22 (14), 4557–4563. doi:10.26355/eurrev_201807_15511

Gu, J. W., Makey, K. L., Tucker, K. B., Chinchar, E., Mao, X., Pei, I., et al. (2013). EGCG, a Major green tea Catechin Suppresses Breast Tumor Angiogenesis and Growth via Inhibiting the Activation of HIF-1α and NFκB, and VEGF Expression. *Vasc. Cell* 5 (1), 9. doi:10.1186/2045-824X-5-9

Halama, A., Riesen, N., Möller, G., Hrabě de Angelis, M., and Adamski, J. (2013). Identification of Biomarkers for Apoptosis in Cancer Cell Lines Using Metabolomics: Tools for Individualized Medicine. *J. Intern. Med.* 274 (5), 425–439. doi:10.1111/joim.12117

He, H., Shi, X., Lawrence, A., Hrovat, J., Turner, C., Cui, J. Y., et al. (2020). 2,2',4,4'-tetrabromodiphenyl Ether (BDE-47) Induces Wide Metabolic Changes Including Attenuated Mitochondrial Function and Enhanced Glycolysis in PC12 Cells. *Ecotoxicol Environ. Saf.* 201, 110849. doi:10.1016/j.ecoenv.2020.110849

Higashi, K., Yoshida, K., Nishimura, K., Momiyama, E., Kashiwagi, K., Matsufuji, S., et al. (2004). Structural and Functional Relationship Among Diamines in Terms of Inhibition of Cell Growth. *J. Biochem.* 136 (4), 533–539. doi:10.1093/jb/mvh150

Hirsch, F. R., Scagliotti, G. V., Mulshine, J. L., Kwon, R., Curran, W. J., Jr., Wu, Y. L., et al. (2017). Lung Cancer: Current Therapies and New Targeted Treatments. *Lancet* 389 (10066), 299–311. doi:10.1016/S0140-6736(16)30958-8

Hou, L., Guan, S., Jin, Y., Sun, W., Wang, Q., Du, Y., et al. (2020). Cell Metabolomics to Study the Cytotoxicity of Carbon Black Nanoparticles on A549 Cells Using UHPLC-Q/TOF-MS and Multivariate Data Analysis. *Sci. Total Environ.* 698, 134122. doi:10.1016/j.scitotenv.2019.134122

Hu, D. L., Wang, G., Yu, J., Zhang, L. H., Huang, Y. F., Wang, D., et al. (2019). Epigallocatechin-3-gallate M-odulates L-ong N-on-coding RNA and mRNA E-xpression P-rofiles in L-ung C-ancer C-ells. *Mol. Med. Rep.* 19 (3), 1509–1520. doi:10.3892/mmr.2019.9816

Huang, C. Y., Han, Z., Li, X., Xie, H. H., and Zhu, S. S. (2017). Mechanism of EGCG Promoting Apoptosis of MCF-7 Cell Line in Human Breast Cancer. *Oncol. Lett.* 14 (3), 3623–3627. doi:10.3892/ol.2017.6641

Huh, S. W., Bae, S. M., Kim, Y. W., Lee, J. M., Namkoong, S. E., Lee, I. P., et al. (2004). Anticancer Effects of (-)-Epigallocatechin-3-Gallate on Ovarian Carcinoma Cell Lines. *Gynecol. Oncol.* 94 (3), 760–768. doi:10.1016/j.ygyno.2004.05.031

Jain, M., Nilsson, R., Sharma, S., Madhusudhan, N., Kitami, T., Souza, A. L., et al. (2012). Metabolite Profiling Identifies a Key Role for glycine in Rapid Cancer Cell Proliferation. *Science* 336 (6084), 1040–1044. doi:10.1126/science.1218595

Jasbi, P., Wang, D., Cheng, S. L., Fei, Q., Cui, J. Y., Liu, L., et al. (2019). Breast Cancer Detection Using Targeted Plasma Metabolomics. *J. Chromatogr. B Analyt Technol. Biomed. Life Sci.* 1105, 26–37. doi:10.1016/j.jchromb.2018.11.029

Jiang, P., Wu, X., Wang, X., Huang, W., and Feng, Q. (2016). NEAT1 Upregulates EGCG-Induced CTR1 to Enhance Cisplatin Sensitivity in Lung Cancer Cells. *Oncotarget* 7 (28), 43337–43351. doi:10.18632/oncotarget.9712

Khan, N., Afaq, F., Saleem, M., Ahmad, N., and Mukhtar, H. (2006). Targeting Multiple Signaling Pathways by green tea Polyphenol (-)-Epigallocatechin-3-Gallate. *Cancer Res.* 66 (5), 2500–2505. doi:10.1158/0008-5472.CAN-05-3636

Lee, I. T., Lin, C. C., Lee, C. Y., Hsieh, P. W., and Yang, C. M. (2013). Protective Effects of (-)-Epigallocatechin-3-Gallate against TNF-α-Induced Lung Inflammation via ROS-dependent ICAM-1 Inhibition. *J. Nutr. Biochem.* 24 (1), 124–136. doi:10.1016/j.jnutbio.2012.03.009

Li, C. Y., Dempsey, J. L., Wang, D., Lee, S., Weigel, K. M., Fei, Q., et al. (2018). PBDEs Altered Gut Microbiome and Bile Acid Homeostasis in Male C57BL/6 Mice. *Drug Metab. Dispos* 46 (8), 1226–1240. doi:10.1124/dmd.118.081547

Li, M., Li, J. J., Gu, Q. H., An, J., Cao, L. M., Yang, H. P., et al. (2016). EGCG Induces Lung Cancer A549 Cell Apoptosis by Regulating Ku70 Acetylation. *Oncol. Rep.* 35 (4), 2339–2347. doi:10.3892/or.2016.4587

Li, T., Zhao, N., Lu, J., Zhu, Q., Liu, X., Hao, F., et al. (2019). Epigallocatechin Gallate (EGCG) Suppresses Epithelial-Mesenchymal Transition (EMT) and Invasion in Anaplastic Thyroid Carcinoma Cells through Blocking of TGF-β1/Smad Signaling Pathways. *Bioengineered* 10 (1), 282–291. doi:10.1080/21655979.2019.1632669

Lim, J. J., Li, X., Lehmler, H. J., Wang, D., Gu, H., and Cui, J. Y. (2020). Gut Microbiome Critically Impacts PCB-Induced Changes in Metabolic Fingerprints and the Hepatic Transcriptome in Mice. *Toxicol. Sci.* 177 (1), 168–187. doi:10.1093/toxsci/kfaa090

Liu, J., Hanavan, P. D., Kras, K., Ruiz, Y. W., Castle, E. P., Lake, D. F., et al. (2019). Loss of SETD2 Induces a Metabolic Switch in Renal Cell Carcinoma Cell Lines toward Enhanced Oxidative Phosphorylation. *J. Proteome Res.* 18 (1), 331–340. doi:10.1021/acs.jproteome.8b00628

Liu, L., Ju, Y., Wang, J., and Zhou, R. (2017). Epigallocatechin-3-gallate Promotes Apoptosis and Reversal of Multidrug Resistance in Esophageal Cancer Cells. *Pathol. Res. Pract.* 213 (10), 1242–1250. doi:10.1016/j.prp.2017.09.006

Liu, S., Xu, Z. L., Sun, L., Liu, Y., Li, C. C., Li, H. M., et al. (2016). (-)-Epigallocatechin-3-gallate I-nduces A-poptosis in H-uman P-ancreatic C-ancer C-ells via PTEN. *Mol. Med. Rep.* 14 (1), 599–605. doi:10.3892/mmr.2016.5277

Livaniou, E., Costopoulou, D., Vassiliadou, I., Leondiadis, L., Nyalala, J. O., Ithakissios, D. S., et al. (2000). Analytical Techniques for Determining Biotin. *J. Chromatogr. A.* 881 (1-2), 331–343. doi:10.1016/s0021-9673(00)00118-7

Lu, Q. Y., Zhang, L., Yee, J. K., Go, V. W., and Lee, W. N. (2015). Metabolic Consequences of LDHA Inhibition by Epigallocatechin Gallate and Oxamate in MIA PaCa-2 Pancreatic Cancer Cells. *Metabolomics* 11 (1), 71–80. doi:10.1007/s11306-014-0672-8

Luengo, A., Gui, D. Y., and Vander Heiden, M. G. (2017). Targeting Metabolism for Cancer Therapy. *Cell Chem Biol* 24 (9), 1161–1180. doi:10.1016/j.chembiol.2017.08.028

Luo, H. Q., Xu, M., Zhong, W. T., Cui, Z. Y., Liu, F. M., Zhou, K. Y., et al. (2014). EGCG Decreases the Expression of HIF-1α and VEGF and Cell Growth in MCF-7 Breast Cancer Cells. *J. BUON* 19 (2), 435–439.

Luo, K. W., Wei Chen, C., Lung, W. Y., Wei, X. Y., Cheng, B. H., Cai, Z. M., et al. (2017). EGCG Inhibited Bladder Cancer SW780 Cell Proliferation and Migration Both *In Vitro* and *In Vivo* via Down-Regulation of NF-Kb and MMP-9. *J. Nutr. Biochem.* 41, 56–64. doi:10.1016/j.jnutbio.2016.12.004

Lv, H., Zhen, C., Liu, J., Yang, P., Hu, L., and Shang, P. (2019). Unraveling the Potential Role of Glutathione in Multiple Forms of Cell Death in Cancer Therapy. *Oxid Med. Cell Longev* 2019, 3150145. doi:10.1155/2019/3150145

Ma, J., Shi, M., Li, G., Wang, N., Wei, J., Wang, T., et al. (2013). Regulation of Id1 Expression by Epigallocatechin-3-gallate and its E-ffect on the P-roliferation and A-poptosis of P-oorly D-ifferentiated AGS G-astric C-ancer C-ells. *Int. J. Oncol.* 43 (4), 1052–1058. doi:10.3892/ijo.2013.2043

Mayeur, C., Veuillet, G., Michaud, M., Raul, F., Blottière, H. M., and Blachier, F. (2005). Effects of Agmatine Accumulation in Human colon Carcinoma Cells on Polyamine Metabolism, DNA Synthesis and the Cell Cycle. *Biochim. Biophys. Acta* 1745 (1), 111–123. doi:10.1016/j.bbamcr.2004.12.004

Mazurek, S. (2011). Pyruvate Kinase Type M2: a Key Regulator of the Metabolic Budget System in Tumor Cells. *Int. J. Biochem. Cell Biol* 43 (7), 969–980. doi:10.1016/j.biocel.2010.02.005

McCartney, A., Vignoli, A., Biganzoli, L., Love, R., Tenori, L., Luchinat, C., et al. (2018). Metabolomics in Breast Cancer: A Decade in Review. *Cancer Treat. Rev.* 67, 88–96. doi:10.1016/j.ctrv.2018.04.012

Meng, J., Chang, C., Chen, Y., Bi, F., Ji, C., and Liu, W. (2019). EGCG Overcomes Gefitinib Resistance by Inhibiting Autophagy and Augmenting Cell Death through Targeting ERK Phosphorylation in NSCLC. *Onco Targets Ther.* 12, 6033–6043. doi:10.2147/OTT.S209441

Miller, K. D., Nogueira, L., Mariotto, A. B., Rowland, J. H., Yabroff, K. R., Alfano, C. M., et al. (2019). Cancer Treatment and Survivorship Statistics, 2019. *CA Cancer J. Clin.* 69 (5), 363–385. doi:10.3322/caac.21565

Miller, K. D., Siegel, R. L., Lin, C. C., Mariotto, A. B., Kramer, J. L., Rowland, J. H., et al. (2016). Cancer Treatment and Survivorship Statistics, 2016. *CA Cancer J. Clin.* 66 (1), 271–289. doi:10.3322/caac.2133210.3322/caac.21349

Molderings, G. J., Kribben, B., Heinen, A., Schröder, D., Brüss, M., and Göthert, M. (2004). Intestinal Tumor and Agmatine (Decarboxylated Arginine): Low Content in colon Carcinoma Tissue Specimens and Inhibitory Effect on Tumor Cell Proliferation *In Vitro*. *Cancer* 101 (4), 858–868. doi:10.1002/cncr.20407

Moradzadeh, M., Roustazadeh, A., Tabarraei, A., Erfanian, S., and Sahebkar, A. (2018). Epigallocatechin-3-gallate Enhances Differentiation of Acute

Promyelocytic Leukemia Cells via Inhibition of PML-Rarα and HDAC1. *Phytother Res.* 32 (3), 471–479. doi:10.1002/ptr.5990

Morandi, F., Horenstein, A. L., Rizzo, R., and Malavasi, F. (2018). The Role of Extracellular Adenosine Generation in the Development of Autoimmune Diseases. *Mediators Inflamm.* 2018, 7019398. doi:10.1155/2018/7019398

Nilsson, R., Jain, M., Madhusudhan, N., Sheppard, N. G., Strittmatter, L., Kampf, C., et al. (2014). Metabolic Enzyme Expression Highlights a Key Role for MTHFD2 and the Mitochondrial Folate Pathway in Cancer. *Nat. Commun.* 5, 3128. doi:10.1038/ncomms4128

Noreldeen, H. A. A., Liu, X., and Xu, G. (2020). Metabolomics of Lung Cancer: Analytical Platforms and Their Applications. *J. Sep. Sci.* 43 (1), 120–133. doi:10.1002/jssc.201900736

Pal, D., Sur, S., Roy, R., Mandal, S., and Kumar Panda, C. (2018). Epigallocatechin Gallate in Combination with Eugenol or Amarogentin Shows Synergistic Chemotherapeutic Potential in Cervical Cancer Cell Line. *J. Cell Physiol* 234 (1), 825–836. doi:10.1002/jcp.26900

Panieri, E., and Santoro, M. M. (2016). ROS Homeostasis and Metabolism: a Dangerous Liason in Cancer Cells. *Cell Death Dis* 7 (6), e2253. doi:10.1038/cddis.2016.105

Panji, M., Behmard, V., Zare, Z., Malekpour, M., Nejadbiglari, H., Yavari, S., et al. (2021). Suppressing Effects of green tea Extract and Epigallocatechin-3-Gallate (EGCG) on TGF-β- Induced Epithelial-To-Mesenchymal Transition via ROS/Smad Signaling in Human Cervical Cancer Cells. *Gene* 794, 145774. doi:10.1016/j.gene.2021.145774

Peter, B., Bosze, S., and Horvath, R. (2017). Biophysical Characteristics of Proteins and Living Cells Exposed to the green tea Polyphenol Epigallocatechin-3-Gallate (EGCg): Review of Recent Advances from Molecular Mechanisms to Nanomedicine and Clinical Trials. *Eur. Biophys. J.* 46 (1), 1–24. doi:10.1007/s00249-016-1141-2

Rainaldi, G., Romano, R., Indovina, P., Ferrante, A., Motta, A., Indovina, P. L., et al. (2008). Metabolomics Using 1H-NMR of Apoptosis and Necrosis in HL60 Leukemia Cells: Differences between the Two Types of Cell Death and independence from the Stimulus of Apoptosis Used. *Radiat. Res.* 169 (2), 170–180. doi:10.1667/RR0958.1

Reaves, M. L., and Rabinowitz, J. D. (2011). Metabolomics in Systems Microbiology. *Curr. Opin. Biotechnol.* 22 (1), 17–25. doi:10.1016/j.copbio.2010.10.001

Rivera, E. S., Cricco, G. P., Engel, N. I., Fitzsimons, C. P., Martín, G. A., and Bergoc, R. M. (2000). Histamine as an Autocrine Growth Factor: an Unusual Role for a Widespread Mediator. *Semin. Cancer Biol.* 10 (1), 15–23. doi:10.1006/scbi.2000.0303

Romano, A., and Martel, F. (2021). The Role of EGCG in Breast Cancer Prevention and Therapy. *Mini Rev. Med. Chem.* 21 (7), 883–898. doi:10.2174/1389557520999201211194445

Russell-Jones, G., McTavish, K., McEwan, J., Rice, J., and Nowotnik, D. (2004). Vitamin-mediated Targeting as a Potential Mechanism to Increase Drug Uptake by Tumours. *J. Inorg. Biochem.* 98 (10), 1625–1633. doi:10.1016/j.jinorgbio.2004.07.009

Sano, M., Tabata, M., Suzuki, M., Degawa, M., Miyase, T., and Maeda-Yamamoto, M. (2001). Simultaneous Determination of Twelve tea Catechins by High-Performance Liquid Chromatography with Electrochemical Detection. *Analyst* 126 (6), 816–820. doi:10.1039/b102541b

Schmidt, D. R., Patel, R., Kirsch, D. G., Lewis, C. A., Vander Heiden, M. G., and Locasale, J. W. (2021). Metabolomics in Cancer Research and Emerging Applications in Clinical Oncology. *CA A. Cancer J. Clin.* 71 (4), 333–358. doi:10.3322/caac.21670

Seijo, L. M., Peled, N., Ajona, D., Boeri, M., Field, J. K., Sozzi, G., et al. (2019). Biomarkers in Lung Cancer Screening: Achievements, Promises, and Challenges. *J. Thorac. Oncol.* 14 (3), 343–357. doi:10.1016/j.jtho.2018.11.023

Shi, J., Liu, F., Zhang, W., Liu, X., Lin, B., and Tang, X. (2015). Epigallocatechin-3-gallate Inhibits Nicotine-Induced Migration and Invasion by the Suppression of Angiogenesis and Epithelial-Mesenchymal Transition in Non-small Cell Lung Cancer Cells. *Oncol. Rep.* 33 (6), 2972–2980. doi:10.3892/or.2015.3889

Shi, J. F., Wu, P., Jiang, Z. H., and Wei, X. Y. (2014). Synthesis and Tumor Cell Growth Inhibitory Activity of Biotinylated Annonaceous Acetogenins. *Eur. J. Med. Chem.* 71, 219–228. doi:10.1016/j.ejmech.2013.11.012

Shi, X., Wang, S., Jasbi, P., Turner, C., Hrovat, J., Wei, Y., et al. (2019). Database-Assisted Globally Optimized Targeted Mass Spectrometry (dGOT-MS): Broad and Reliable Metabolomics Analysis with Enhanced Identification. *Anal. Chem.* 91 (21), 13737–13745. doi:10.1021/acs.analchem.9b03107

Siegel, R. L., Miller, K. D., Fuchs, H. E., and Jemal, A. (2021). Cancer Statistics, 2021. *CA A. Cancer J. Clin.* 71 (1), 7–33. doi:10.3322/caac.21654

Sonoda, J. I., Ikeda, R., Baba, Y., Narumi, K., Kawachi, A., Tomishige, E., et al. (2014). Green tea Catechin, Epigallocatechin-3-Gallate, Attenuates the Cell Viability of Human Non-small-cell Lung Cancer A549 Cells via Reducing Bcl-xL Expression. *Exp. Ther. Med.* 8 (1), 59–63. doi:10.3892/etm.2014.1719

Sperber, H., Mathieu, J., Wang, Y., Ferreccio, A., Hesson, J., Xu, Z., et al. (2015). The Metabolome Regulates the Epigenetic Landscape during Naive-To-Primed Human Embryonic Stem Cell Transition. *Nat. Cell Biol* 17 (12), 1523–1535. doi:10.1038/ncb3264

Sullivan, L. B., Gui, D. Y., Hosios, A. M., Bush, L. N., Freinkman, E., and Vander Heiden, M. G. (2015). Supporting Aspartate Biosynthesis Is an Essential Function of Respiration in Proliferating Cells. *Cell* 162 (3), 552–563. doi:10.1016/j.cell.2015.07.017

Sung, H., Ferlay, J., Siegel, R. L., Laversanne, M., Soerjomataram, I., Jemal, A., et al. (2021). Global Cancer Statistics 2020: GLOBOCAN Estimates of Incidence and Mortality Worldwide for 36 Cancers in 185 Countries. *CA A. Cancer J. Clin.* 71, 209–249. doi:10.3322/caac.21660

Tan, E. M., Ryhänen, L., and Uitto, J. (1983). Proline Analogues Inhibit Human Skin Fibroblast Growth and Collagen Production in Culture. *J. Invest. Dermatol.* 80 (4), 261–267. doi:10.1111/1523-1747.ep12534593

Tang, G. Y., Meng, X., Gan, R. Y., Zhao, C. N., Liu, Q., Feng, Y. B., et al. (2019). Health Functions and Related Molecular Mechanisms of Tea Components: An Update Review. *Int. J. Mol. Sci.* 20 (24). doi:10.3390/ijms20246196

Ullmann, U., Haller, J., Decourt, J. D., Girault, J., Spitzer, V., and Weber, P. (2004). Plasma-kinetic Characteristics of Purified and Isolated green tea Catechin Epigallocatechin Gallate (EGCG) after 10 Days Repeated Dosing in Healthy Volunteers. *Int. J. Vitam Nutr. Res.* 74 (4), 269–278. doi:10.1024/0300-9831.74.4.269

Warburg, O., Wind, F., and Negelein, E. (1927). The Metabolism of Tumors in the Body. *J. Gen. Physiol.* 8 (6), 519–530. doi:10.1085/jgp.8.6.519

Wei, L. H., Wu, G., Morris, S. M., Jr., and Ignarro, L. J. (2001). Elevated Arginase I Expression in Rat Aortic Smooth Muscle Cells Increases Cell Proliferation. *Proc. Natl. Acad. Sci. U S A.* 98 (16), 9260–9264. doi:10.1073/pnas.161294898

Wei, R., Penso, N. E. C., Hackman, R. M., Wang, Y., and Mackenzie, G. G. (2019). Epigallocatechin-3-Gallate (EGCG) Suppresses Pancreatic Cancer Cell Growth, Invasion, and Migration Partly through the Inhibition of Akt Pathway and Epithelial-Mesenchymal Transition: Enhanced Efficacy when Combined with Gemcitabine. *Nutrients* 11 (8), 1856. doi:10.3390/nu11081856

Wei, Y., Jasbi, P., Shi, X., Turner, C., Hrovat, J., Liu, L., et al. (2021). Early Breast Cancer Detection Using Untargeted and Targeted Metabolomics. *J. Proteome Res.* 20 (6), 3124–3133. doi:10.1021/acs.jproteome.1c00019

Wells, L., Vosseller, K., and Hart, G. W. (2003). A Role for N-Acetylglucosamine as a Nutrient Sensor and Mediator of Insulin Resistance. *Cell Mol Life Sci* 60 (2), 222–228. doi:10.1007/s000180300017

Wu, D., Liu, Z., Li, J., Zhang, Q., Zhong, P., Teng, T., et al. (2019). Epigallocatechin-3-gallate Inhibits the Growth and Increases the Apoptosis of Human Thyroid Carcinoma Cells through Suppression of EGFR/RAS/RAF/MEK/ERK Signaling Pathway. *Cancer Cell Int* 19, 43. doi:10.1186/s12935-019-0762-9

Wu, J., Li, G., Li, L., Li, D., Dong, Z., and Jiang, P. (2021). Asparagine Enhances LCK Signalling to Potentiate CD8+ T-Cell Activation and Anti-tumour Responses. *Nat. Cell Biol* 23 (1), 75–86. doi:10.1038/s41556-020-00615-4

Wu, M., Ye, H., Shao, C., Zheng, X., Li, Q., Wang, L., et al. (2017). Metabolomics-Proteomics Combined Approach Identifies Differential Metabolism-Associated Molecular Events between Senescence and Apoptosis. *J. Proteome Res.* 16 (6), 2250–2261. doi:10.1021/acs.jproteome.7b00111

Yan, M., and Xu, G. (2018). Current and Future Perspectives of Functional Metabolomics in Disease Studies-A Review. *Anal. Chim. Acta* 1037, 41–54. doi:10.1016/j.aca.2018.04.006

Yang, C., Du, W., and Yang, D. (2016). Inhibition of green tea Polyphenol EGCG((-)-epigallocatechin-3-gallate) on the Proliferation of Gastric Cancer Cells by Suppressing Canonical Wnt/β-Catenin Signalling Pathway. *Int. J. Food Sci. Nutr.* 67 (7), 818–827. doi:10.1080/09637486.2016.1198892

Yang, D., Yaguchi, T., Yamamoto, H., and Nishizaki, T. (2007). Intracellularly Transported Adenosine Induces Apoptosis in HuH-7 Human Hepatoma Cells

by Downregulating C-FLIP Expression Causing Caspase-3/-8 Activation. *Biochem. Pharmacol.* 73 (10), 1665–1675. doi:10.1016/j.bcp.2007.01.020

Yeung, P. K. (2018). Metabolomics and Biomarkers for Drug Discovery. *Metabolites* 8 (1). doi:10.3390/metabo8010011

Yin, Z., Li, J., Kang, L., Liu, X., Luo, J., Zhang, L., et al. (2021). Epigallocatechin-3-gallate Induces Autophagy-related Apoptosis Associated with LC3B II and Beclin Expression of Bladder Cancer Cells. *J. Food Biochem.* 45 (6), e13758. doi:10.1111/jfbc.13758

Yoshimura, H., Yoshida, H., Matsuda, S., Ryoke, T., Ohta, K., Ohmori, M., et al. (2019). The Therapeutic Potential of Epigallocatechin-3-gallate against H-uman O-ral S-quamous C-ell C-arcinoma through I-nhibition of C-ell P-roliferation and I-nduction of A-poptosis: In vitro and I-n vivo M-urine X-enograft S-tudy. *Mol. Med. Rep.* 20 (2), 1139–1148. doi:10.3892/mmr.2019.10331

Yu, L., Wu, J., Zhai, Q., Tian, F., Zhao, J., Zhang, H., et al. (2019). Metabolomic Analysis Reveals the Mechanism of Aluminum Cytotoxicity in HT-29 Cells. *PeerJ* 7, e7524. doi:10.7717/peerj.7524

Zampieri, M., Sekar, K., Zamboni, N., and Sauer, U. (2017). Frontiers of High-Throughput Metabolomics. *Curr. Opin. Chem. Biol.* 36, 15–23. doi:10.1016/j.cbpa.2016.12.006

Zhang, L., Xie, J., Gan, R., Wu, Z., Luo, H., Chen, X., et al. (2019). Synergistic Inhibition of Lung Cancer Cells by EGCG and NF-Kb Inhibitor BAY11-7082. *J. Cancer* 10 (26), 6543–6556. doi:10.7150/jca.34285

Zhang, Y., Owusu, L., Duan, W., Jiang, T., Zang, S., Ahmed, A., et al. (2013). Anti-metastatic and Differential Effects on Protein Expression of Epigallocatechin-3-Gallate in HCCLM6 Hepatocellular Carcinoma Cells. *Int. J. Mol. Med.* 32 (4), 959–964. doi:10.3892/ijmm.2013.1446

Zhang, Z., Zhang, S., Yang, J., Yi, P., Xu, P., Yi, M., et al. (2020). Integrated Transcriptomic and Metabolomic Analyses to Characterize the Anti-cancer Effects of (-)-Epigallocatechin-3-Gallate in Human colon Cancer Cells. *Toxicol. Appl. Pharmacol.* 401, 115100. doi:10.1016/j.taap.2020.115100

Zhou, C. G., Hui, L. M., and Luo, J. M. (2018). Epigallocatechin Gallate Inhibits the Proliferation and Induces Apoptosis of Multiple Myeloma Cells via Inactivating EZH2. *Eur. Rev. Med. Pharmacol. Sci.* 22 (7), 2093–2098. doi:10.26355/eurrev_201804_14742

Conflict of Interest: The authors declare that the research was conducted in the absence of any commercial or financial relationships that could be construed as a potential conflict of interest.

Publisher's Note: All claims expressed in this article are solely those of the authors and do not necessarily represent those of their affiliated organizations, or those of the publisher, the editors and the reviewers. Any product that may be evaluated in this article, or claim that may be made by its manufacturer, is not guaranteed or endorsed by the publisher.

frontiers in Pharmacology

ORIGINAL RESEARCH
published: 27 October 2021
doi: 10.3389/fphar.2021.731734

Musk Tongxin Dripping Pills for treating Ticagrelor in Patients After Percutaneous Coronary Intervention: Echocardiography Combined with Untargeted Metabolomics

Lyu Nan[1], *Lai Peng*[1], *Zhao Jinxia*[1], *Guo Mengzhe*[2], *Liang Jun*[1]*, *Wang Haibo*[1]* and *Geng Houfa*[1]*

[1]Clinical College, Xuzhou Medical University, Xuzhou Central Hospital, Xuzhou, China, [2]Jiangsu Key Laboratory of New Drug Research and Clinical Pharmacy, Xuzhou Medical University, Xuzhou, China

OPEN ACCESS

Edited by:
Xionghao Lin,
Howard University, United States

Reviewed by:
Cheng Guo,
Zhejiang University, China
Yongfeng Song,
Shandong Provincial Hospital, China

***Correspondence:**
Liang Jun
mwlj@njmu.edu.cn
Wang Haibo
1157162960@qq.com
Geng Houfa
genghoufa@njmu.edu.cn

Specialty section:
This article was submitted to Ethnopharmacology, a section of the journal Frontiers in Pharmacology

Received: *28 June 2021*
Accepted: *24 August 2021*
Published: *27 October 2021*

Citation:
Nan L, Peng L, Jinxia Z, Mengzhe G, Jun L, Haibo W and Houfa G (2021) Musk Tongxin Dripping Pills for treating Ticagrelor in Patients After Percutaneous Coronary Intervention: Echocardiography Combined with Untargeted Metabolomics. Front. Pharmacol. 12:731734. doi: 10.3389/fphar.2021.731734

Objectives: As current clinical practice guidelines, ticagrelor is the suggested therapeutic scheme to prevent adverse cardiovascular events in acute myocardial infarction (AMI) patients undergoing percutaneous coronary intervention (PCI) treatment. However, this therapeutic strategy still fails, and around 30% patients display inadequate antiplatelet responses. Musk Tongxin Dripping Pill (MTDP) in Chinese hospital was usually considered as the combination with ticagrelor to improve the treatment effect. Unfortunately, the mechanism has not been elucidated.

Methods: The untargeted metabolomic method was introduced based on liquid chromatography–high-resolution mass spectrometry (HPLC-HRMS) coupled with STI for the research of the drug combination mechanism between ticagrelor and MTDP. 28 patients with a confirmed diagnosis of AMI were selectively collected, who were then divided into two different dosage regimen groups, and the serum samples were collected for the untargeted metabolomics assay. Then the differential metabolites were associated with blood biochemical indicators.

Results: The GLS values in both groups increased after treatment and those in the ticagrelor and MTDP combination group after treatment were higher than those in the ticagrelor group ($p < 0.05$), suggesting that the combination medication has better therapeutic effect on patients with myocardial infarction. From metabolomics analysis, the species of metabolites changed in two groups before and after treatment. Moreover, 93 differential metabolites changed in the drug combination group compared with the ticagrelor group after treatment ($p < 0.05$), which mainly related to changes in fatty acid metabolism pathways. Then the differential metabolites were found to be related with blood biochemical indicators, such as lipid, high-density lipoprotein (HDL), and low-density lipoprotein (LDL).

Conclusion: This work will provide a possible mechanism of the drug combination interaction between ticagrelor and MTDP from two angles of echocardiography and

metabonomics. Several potential metabolic pathways were also found to have a relationship with MTDP, which will provide a new perspective in clinical medication.

Keywords: Musk Tongxin Dripping Pill, ticagrelor, echocardiography, untargeted metabolomics, LC-MS

INTRODUCTION

Acute myocardial infarction (AMI) is myocardial necrosis caused by acute and persistent ischemia and hypoxia of the coronary artery (Liam et al., 2021). As the primary cardiovascular disease, AMI seriously affects health and life safety of human beings, which causes over 30% mortality of coronary heart disease patients (Blais et al., 2020; Thomas et al., 2020). Percutaneous coronary intervention (PCI) is the guideline-recommended treatment for patients undergoing ST-segment elevation AMI (Matthews and Frishman, 2017). As the development of this technique, the PCI is now considered safe with the decrease of periprocedural complications, including the rates of associated stent thrombosis, Q-wave myocardial infarction, stroke, and death (Stephen et al., 2014). However, frequent periprocedural myonecrosis can still be found through highly sensitive cardiac troponin assay (Reed et al., 2017). Although these periprocedural complications were often asymptomatic, they can delay hospital discharge and have been associated with an increased risk of future major cardiac adverse events, containing death (Warren-Gash et al., 2009). Therefore, the patients also need antiplatelet therapy after surgery, which related to the prognosis of the patients.

At present, clopidogrel and ticagrelor are the two most commonly used antiplatelet agents in clinic (Johanne et al., 2020; Georg et al., 2021). Dishearteningly, despite the greater preponderance of ticagrelor, this treatment is still not ideal, with around 30% of patients showing an inadequate antiplatelet response (Lee et al., 2020). Therefore, in modern clinical practice of China, several drugs were considered as the combination with ticagrelor for the therapy. In particular, traditional Chinese medicine (TCM) usually used to be a significant adjuvant therapy jointly with ticagrelor. Musk Tongxin Dropping Pill (MTDP) is one of the most commonly used compound Chinese patent medicines in combination with ticagrelor (Liu et al., 2021; Zhao et al., 2021). The ingredients of MTDP mainly contain *Salvia miltiorrhiza* Bunge (Lamiaceae; *Salviae miltiorrhizae radix et rhizoma*), Artificial *moschus*, *Panax ginseng* C.A.Mey (Araliaceae; *Panax quinquefolius Linnaeus* var. *ginseng*), *Venenum bufonis*, artificial *Bovis calculus*, and *Borneolum* (Dipterocarpaceae; *Dryobalanops aromatica* Gaertn.f.), which have the curative effect in the elimination of blood stasis, the promotion of blood circulation, and the dredging of collaterals. Additionally, MTDP has also been reported to increase coronary blood flow, and improve myocardial hypoxia and ischemia tolerance, which can help to reduce the scope of myocardial injury. So far, the combination of ticagrelor and MTDP was extensively used in the department of cardiology, Xuzhou central hospital, which achieved good therapeutic effects. Some other literatures also reported the positive clinical effects of this combination therapy in improving efficacy and reducing adverse reactions. However, there are few studies on the pharmacodynamic mechanism and drug–drug interaction mechanism. One of the main reasons is the lack of appropriate research methods. Therefore, new strategy must be progressed to study the synergistic effect between ticagrelor and MTDP.

Metabolomics is an emerging method, which is considered to be a comprehensive and synchronous analytical method for the identification and quantification of small-molecule metabolites, and their amount changes under different circumstances (Chen et al., 2010; Basak et al., 2015a). In this way, the characteristics of biological systems can be objectively measured and evaluated, and can be used as indicators to be effective in the reciprocity between biological systems and intervention. Therefore, it will provide possibilities for the integral analysis of drug combination to explore the pharmacodynamic mechanisms. In addition, the un-targeted metabolomic strategy provides fast and high-flux assay of abundant possible metabolites in a given sample without the knowledge of metabolites in advance, which is appropriate for the study of drug combination mechanisms (Hua et al., 2011; Duranton et al., 2014). For un-targeted metabonomic applications, a variety of detecting platforms can be used, such as high-performance liquid chromatography–mass spectrometry (HPLC-MS), gas chromatography–mass spectrometry (GC-MS), and nuclear magnetic resonance (NMR). Among all these platforms, mass spectrometry has high sensitivity, high accuracy, high flux, minimal sample preprocessing requirements, and high data quantitation and reproducibility. In particular, the high-resolution mass spectrometry (HRMS) techniques provide accurate molecular weights, which can be used for the investigation of molecular formulas and structures (Yang et al., 2014; Ju et al., 2015). In addition, an association of separation strategy, containing SPE, GC, or HPLC, can reduce the complexity of the mass spectrometer, helping the suggestion of additional information on the metabolites' chemical properties.

Accurately assessing the cardiac function changes can help to evaluate the therapeutic effect of patients, as well as investigating the mechanism of drug combination. The speckle-tracking imaging (STI) technique, based on echocardiography, can delineate the region of interest (ROI) on the two-dimensional image of the cardiac wall. It will track the movement of the echo spots frame by frame automatically as the cardiac cycle in this ROI, which can calculate the strain of myocardial tissue by measuring the displacement and evaluate the systolic and diastolic functions of the myocardium. The strain of myocardial tissue, representing the various stages of myocardial deformation, contains longitudinal deformation, radial deformation, circumferential deformation, and rotational deformation. In particular, longitudinal deformation myocardium accounts for 70% of the total myocardium, which is more susceptible to ischemic damage when coronary artery stenosis is experienced. Therefore, longitudinal deformation would reflect the myocardial systolic function more sensitively.

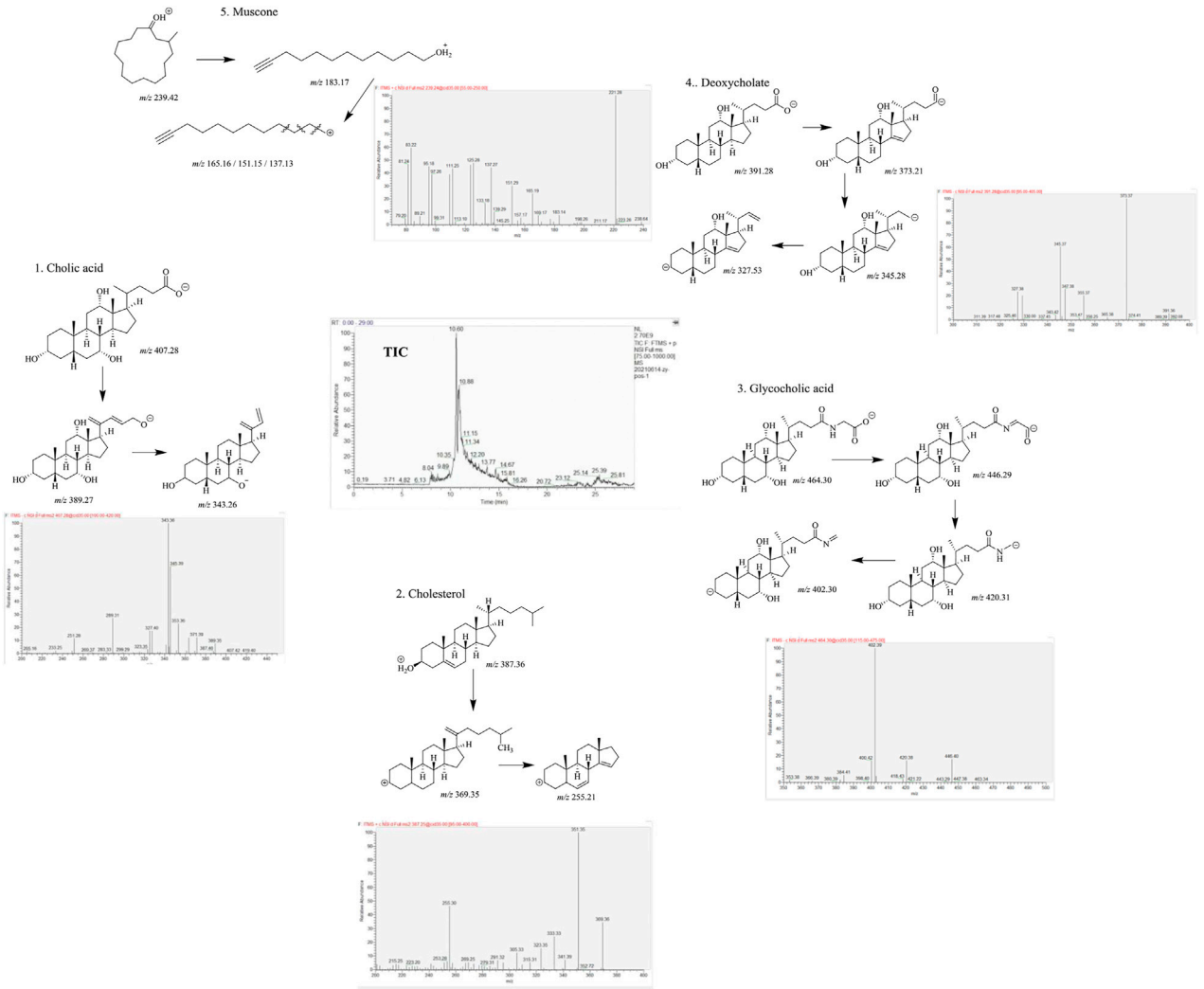

FIGURE 1 | Five main components of MTDP by liquid chromatography–high-resolution mass spectrometry analysis.

Herein, the mechanism of ticagrelor and MTDP combination was studied by un-targeted metabonomics based on HPLC-HRMS combined with STI. Serum analysis was performed before and after treatment in two groups, including the ticagrelor group and the ticagrelor and MTDP combination group. The STI technique was used to evaluate the myocardial function. The metabolite content changes were accurately detected to elucidate the combination mechanism between ticagrelor and MTDP. This study will make a basis for the clinical drug combination between TCM and western medicines.

MATERIALS AND METHODS

Pharmaceutical Composition Analysis

The composition of MTDP has been analyzed by using liquid chromatography–high-resolution mass spectrometry. First, the paraffin shell of the pill was stripped. Then the drug components were extracted by two solvents, methanol and dichloromethane. Next, the extractive was dried at low temperature and redissolved by methanol. Then the solution was analyzed by liquid chromatography–high-resolution mass spectrometry.

LC-MS conditions: LC separation was carried out by Waters e2695 Ultra-HPLC (Waters, United States) with a Fortis type of C18 column (4.6 × 150 mm, 3.5 μm). The temperature of the column was setup at 40°C. Solvent A of the mobile phase was water/acetic acid (99.9/0.1, *v/v*), and solvent B was methanol. The gradient was 0 min, 5% (B) to 20 min, and 95% (B). The flow rate was 0.3 ml min^{-1}, and the injection volume was 5 μl. Positive and negative modes of mass spectrometric assay were performed on Thermo Velos mass spectrometer (Thermo, CA, United States). A full scan mode was used for detection.

Study Subjects

Patients with cancer, bleeding, gastrointestinal hemorrhage, severe heart exhaustion, significantly abnormal clinical test

TABLE 1 | Basic patient enrollment information.

Group	Drug combination group	Ticagrelor group	*p* value
Gender (M/F)	4/10	4/10	0.0000
Age (years)	58.88 ± 2.401, *n* = 8	65.7 ± 2.765, *n* = 10	0.0891
Present smoker, n (%)	2 (14)	2 (14)	0.0000
Hypertension, n (%)	7 (58)	10 (71)	0.6828
β-Blocker, n (%)	1 (7)	0 (0)	0.0000
Calcium channel blocker, n (%)	0 (0)	5 (36)	0.0407
ACE inhibitors, n (%)	7 (50)	3 (21)	0.2365
Statins, n (%)	4 (29)	5 (36)	0.0000
ALT (U/L)	21.29 ± 2.57	18.83 ± 1.74	0.4527
AST (U/L)	19.43 ± 6.39	19.57 ± 5.39	0.9514
GLU (mmol/L)	5.44 ± 0.11	5.70 ± 0.31	0.0398
GGT (U/L)	28.71 ± 6.46	24.83 ± 5.38	0.0655
TG (mmol/L)	1.50 ± 0.19	1.99 ± 0.18	0.0736
HDL-C (mmol/L)	1.12 ± 0.03	1.15 ± 0.08	0.0005
LDL-C (mmol/L)	2.31 ± 0.14	2.84 ± 0.51	0.3071
CREA (mmol/L)	51.83 ± 2.57	52.28 ± 3.31	0.0001
CK-MB (U/L)	9.71 ± 0.38	9.67 ± 0.67	0.0001
APOA (g/L)	1.24 ± 0.03	1.16 ± 0.03	0.0639
APOB (g/L)	0.75 ± 0.04	0.85 ± 0.10	0.3634
LDH (U/L)	175.70 ± 6.33	178.00 ± 5.60	0.0792

indicators, and high sensitivity to ticagrelor or MTDP were excluded. 28 patients with a confirmed AMI were enrolled, ranging in age from 45 to 80 years. The clinical indicators of patients included the elevation of the ST segment and serum troponin levels. The patients with atrial fibrillation after the PCI were also excluded.

All subjects were informed with the benefits and risks of participating in the study by experienced physicians and voluntarily submitted in-person signed informed consents prior to participating in the clinical trial. The design and implementation of the study protocol were approved and supervised by the Ethics Review Committee of Xuzhou Central Hospital in accordance with the Declaration of Helsinki.

Study Design

28 patients were randomly divided into two groups: 1) ticagrelor group (n = 14), and 2) ticagrelor and MTDP combination group (n = 14). All of them were given the PCI as the initial treatment. The dose of ticagrelor was 90 mg bid and that of MTDP was 70 mg tid. Aspirin and atorvastatin were used as basic treatment, and the dosages were 100 mg qd and 40 mg qd, respectively. Serum samples were collected according to the group before and 30 days after medication. All serum samples were frozen at -80°C.

STI Detection

In this work, global longitudinal strain (GLS) was used to evaluate the drug therapeutic effect after 30-day treatment. The ultrasonograph was Philips EPIQ 7c (Philips, Germany) coupled with S5-1 ultrasonic probe. Three views were detected, including the apical four-chamber view, apical three-chamber view, and apical two-chamber view in four cardiac cycles. A boundary between inner and outer membranes of the left ventricle was drawn by the system and divided into 17 segments. GLS values were obtained by longitudinal deformation curves corresponding to these 17 segments, which is negative at myocardium contraction and positive at myocardium diastole.

Sample Detection

Sample pretreatment: The serum samples were prepared before being detected by high-performance liquid chromatography–high resolution mass spectrometry (HPLC-Thermo HFX MS). In this preparation, 1,200 μl of precooled methanol and acetonitrile (50/50, *v/v*) was added into 200 μl of the serum sample for the albumen precipitation. Then the mixture was centrifuged after standing at −20 C for 10 min, and the centrifugal condition was 12,000 g for 10 min. Finally, volatile drying was performed to the supernate by rotary evaporation. Then dry powder was redissolved by 50 μl of acetonitrile.

LC-MS conditions: LC separation was carried out on Waters e2695 Ultra-HPLC (Waters, the United States) with a Fortis type of C18 column (2.1 × 100 mm, 1.7 μm). The temperature of column was setup at 40 C. Solvent A of the mobile phase was water/acetic acid (99.9/0.1, *v/v*) and solvent B was methanol. The gradient was 0 min, 95% (A); 1 min, 75% (A); 3 min, 55% (A); 6 min, 5% (A); 12 min, 5% (A). The post time was 2 min. The flow rate was 0.3 ml min^{-1}, and the injection volume was 5 μl. Positive and negative modes of mass spectrometric assay were performed on Thermo HFX mass spectrometer (Thermo, CA, United States). A full scan mode were used for detection. Solutions were indoctrinated into the ESI source at 0.3 ml min^{-1} with the following parameters: 4000 V of capillary, 12 L min^{-1} of drying gas, and 350°C of drying gas temperature. Nitrogen was used as atomizing and drying gas. In order to obtain the highest detection sensitivity, all MS conditions were optimized.

Quality control (QC) samples were made by mixing all patients' serum. The QC samples were detected for 6 times to check system stability prior to sample analysis, and every 10 samples were injected during sample analysis.

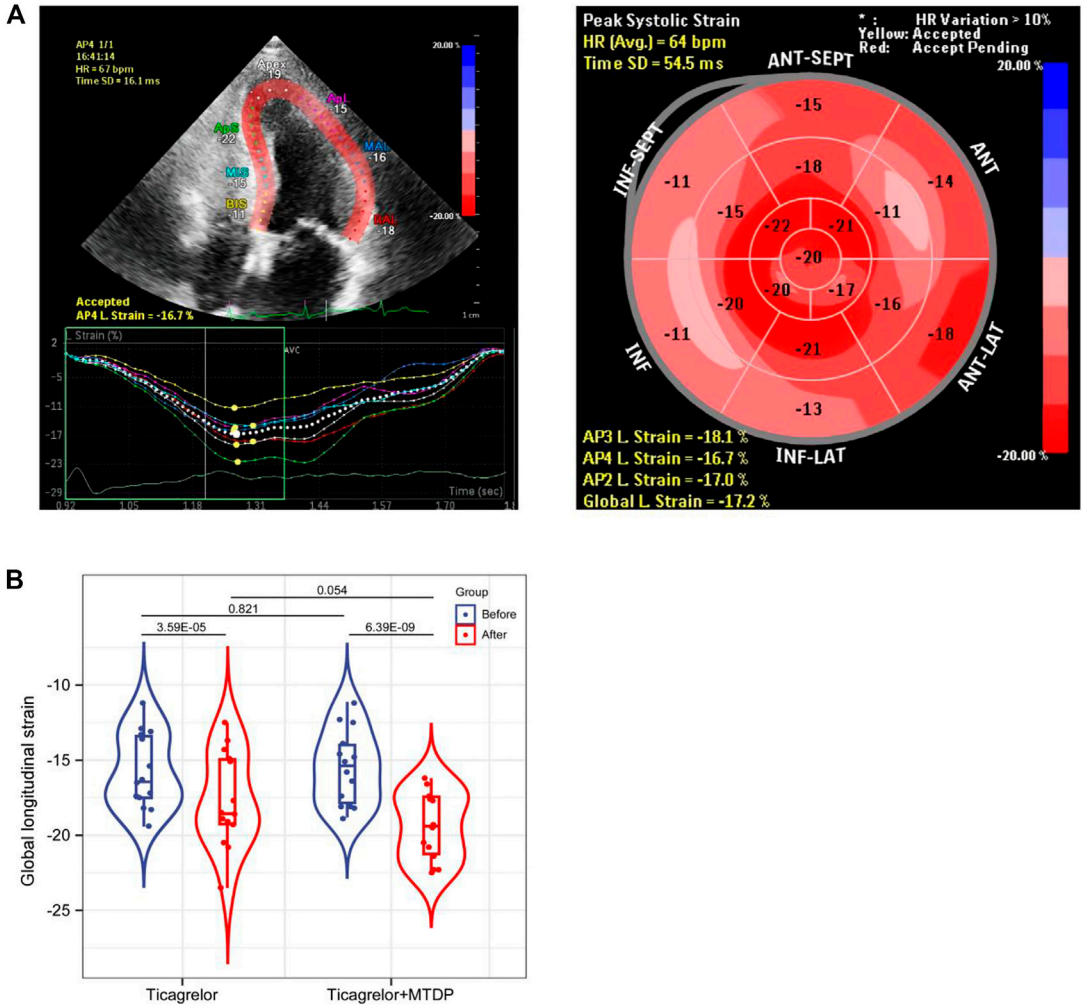

FIGURE 2 | Comparison of GLS values between the ticagrelor group and the MTDP ticagrelor combination group by STI based on echocardiography.

Safety

Adverse events were identified through relevant physical examinations and health-related questions asked throughout the study. Physical examination and clinical laboratory examination (hematology, blood biochemistry, urinalysis, and blood aggregation tests) are performed on the day before experimental drug therapy and within 48 h of the last dose.

Data and Statistical Analysis

Thermo Data Analysis software was used for the deconvolution of the LC-MS spectrum, including baseline correction, processing noise, and peak alignment. Then the compound detection (CD) was used for a matrix formed by retention time, m/z, and strength was then normalized by compound detection (CD). Then the matrix was analyzed by partial least squares discriminant analysis (PLS-DA), principal component analysis (PCA), and orthogonal PLS-DA (OPLS-DA) to obtain the differential metabolites among each group. SPSS16.0 software was used to further compare the differential metabolites data by one-way ANOVA, and an independent sample t test was conducted ($p < 0.05$). In addition, mass spectrometry data for different metabolites were traced to metabolite pathways through the Genomes (KEGG) and Kyoto Encyclopedia of Genes.

RESULTS

From the high-resolution mass spectrometry analysis, five main compounds have been identified according to tandem mass spectrum, including cholic acid (parent ion *m/z* 407.28, sub-ion *m/z* 389.27, 343.26), cholesterol (parent ion *m/z* 387.36, sub-ion *m/z* 369.35, 255.21), glycocholic acid (parent ion *m/z* 464.30, sub-ion *m/z* 446.29, 420.31, 402.30), deoxycholate (parent ion *m/z* 391.28, sub-ion *m/z* 373.21, 345.28, 327.53), and muscone (parent *ion* m/z 239.42, sub-ion *m/z* 183.17, 165.16, 151.15, 137.13). We considered that these five compounds can act as the main pharmacodynamics components (as shown in **Figure 1**).

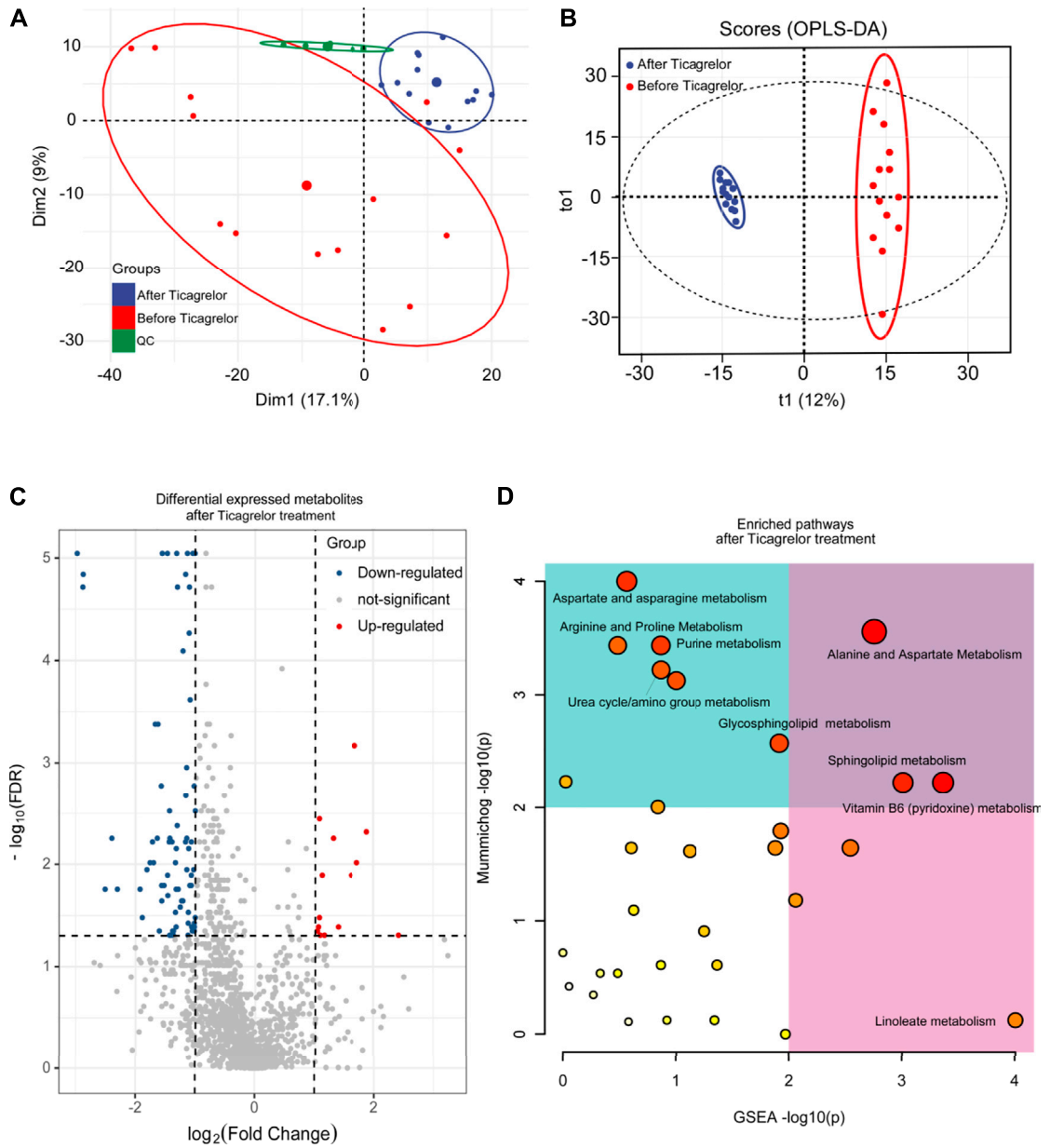

FIGURE 3 | PCA **(A)**, OPLS-DA **(B)**, differential metabolites **(C)**, and differential metabolic pathway **(D)** analysis in the ticagrelor group between before and after treatment.

28 patients were collected and divided into two groups: 1. ticagrelor group and 2. MTDP and ticagrelor combination group. The basic information of these patients can be found in **Table 1**. From the results, gender, age, and smoking status have no statistical differences between two groups. All these patients were treated with the same basic medication after the PCI. Moreover, the blood biochemical indicators of cardiac function, including CK-MB and LDH, have no statistical differences between two groups. After the drug treatment, the GLS values of patients were evaluated by STI. As shown in **Figure 2**, the GLS value in both groups increased after treatment, indicating that the medication can improve the prognosis of patients. In addition, the GLS values in the drug combination group after treatment were higher than those in the ticagrelor group, suggesting that the combination medication has better therapeutic effect on patients with myocardial infarction. The metabolomic results will elaborate the specific mechanism of the drug combination improving the therapeutic effect.

From the perspective of un-targeted metabolomics, the analysis of human serum samples by LC-HRMS includes two kinds of ions' (positive and negative) full scan modes. As shown in **Figure 3**, the total ion chromatograms of the six QC samples were completely overlapped, which indicated that

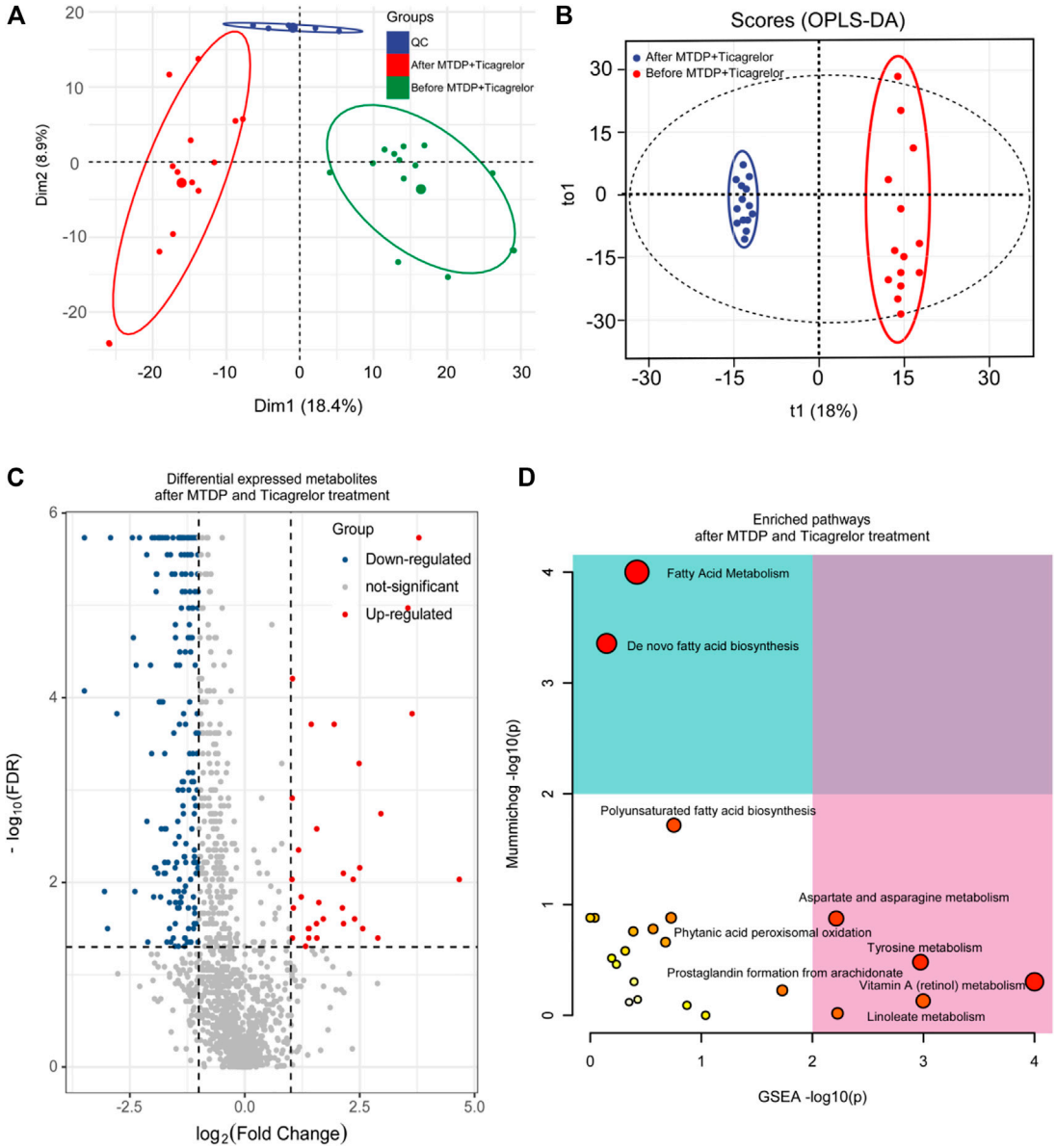

FIGURE 4 | PCA **(A)**, OPLS-DA **(B)**, differential metabolites **(C)**, and differential metabolic pathway **(D)** analysis in the ticagrelor MTDP combination group between before and after treatment.

the method had good reproducibility. Based on PCA and OPLS-DA model analysis, LC-MS results were performed to determine the metabolites in the ticagrelor group before and after treatment. From PCA (**Figure 3A**) and OPLS-DA (**Figure 3B**) results, the metabolites in the ticagrelor group changed after treatment crucially in contrast to those before treatment. Aggregate fitting parameters, that is, R^2X and R^2Y, were 0.271 and 0.981, respectively. And the forecasting parameter, Q^2, was 0.92. Moreover, about 208 differential metabolites from 1,454 total detected metabolites were screened out according to the loading diagram and VIP value greater than 1 (**Figure 3C**). The *t*-test for these differential metabolites showed that some of them had significant double-tailed differences ($p < 0.05$). In addition, these compounds were screened by Metline database to obtain the endogenous differential metabolites with exact molecular structure. Finally, these differential metabolites were used to search for corresponding differential metabolic pathways. Alanine and aspartate metabolism, sphingo lipid metabolism, and vitamin B6 metabolism were found as the related metabolic pathway.

In addition, based on principal component analysis and OPLS-DA model analysis, differences in metabolites in MTDP and ticagrelor combination between before and after treatment from LC-MS have been identified. From PCA (**Figure 4A**) and OPLS-DA (**Figure 4B**) results, the metabolites in the drug

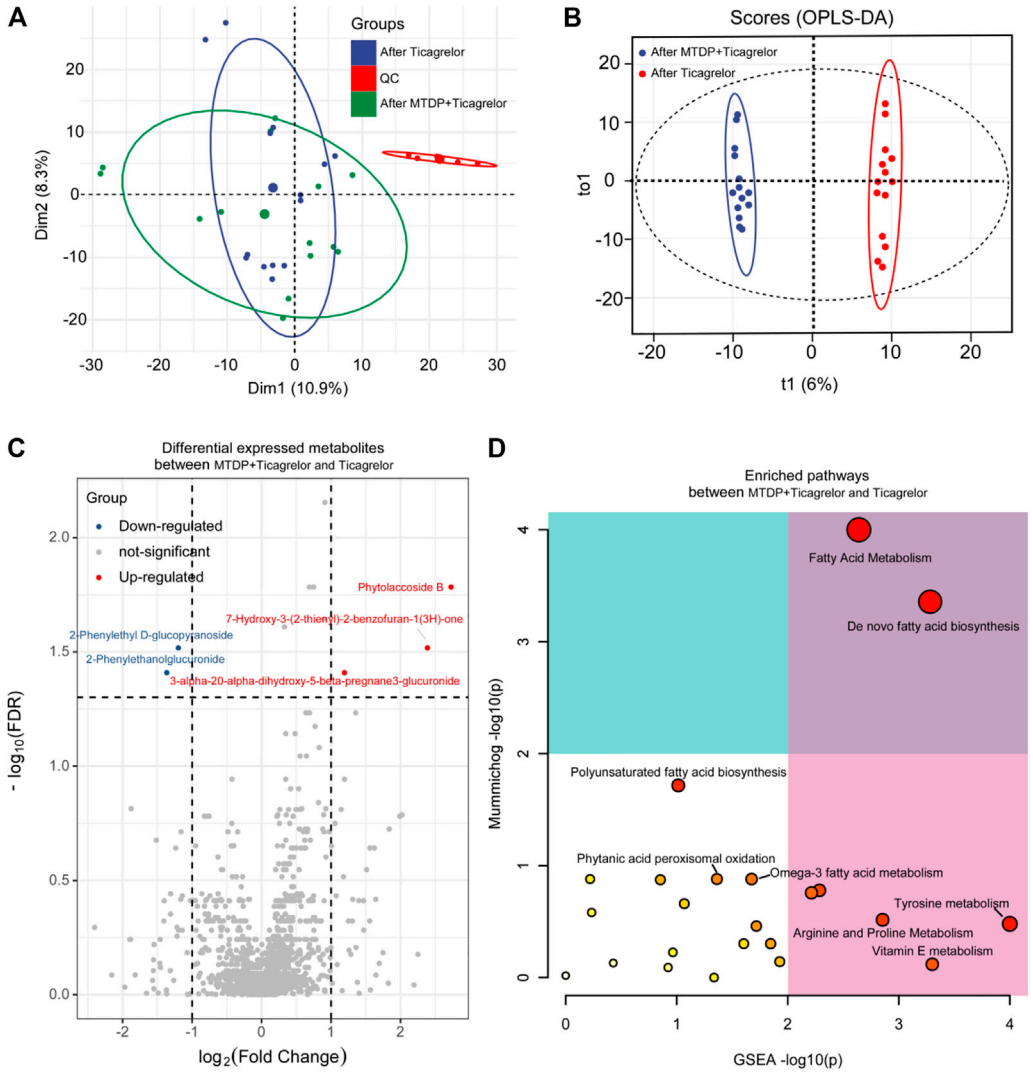

FIGURE 5 | PCA **(A)**, OPLS-DA **(B)**, differential metabolites **(C)**, and differential metabolic pathway **(D)** analysis between the ticagrelor group and the ticagrelor MTDP combination group after treatment.

TABLE 2 | Changes of blood biochemical indexes after treatment in two groups.

Group	Ticagrelor group	Drug combination group	*p* value
ALT (U/L)	28.86 ± 2.27	21.29 ± 2.57	0.0370
AST (U/L)	35.79 ± 16.56	14.33 ± 5.84	0.0004
GLU (mmol/L)	5.44 ± 0.11	5.86 ± 0.24	0.1755
GGT (U/L)	28.71 ± 6.46	34.86 ± 5.50	0.4756
TCH (mmol/L)	3.94 ± 0.22	3.47 ± 0.15	0.0878
TG (mmol/L)	1.50 ± 0.19	1.15 ± 0.08	0.1168
HDL-C (mmol/L)	1.12 ± 0.03	1.27 ± 0.05	0.0222
LDL-C (mmol/L)	2.31 ± 0.14	1.78 ± 0.11	0.0074
CREA (mmol/L)	51.83 ± 2.57	53.29 ± 4.07	0.7643
CK-MB (U/L)	13.29 ± 0.92	9.71 ± 0.38	0.0014
APOA (g/L)	1.24 ± 0.03	1.436 ± 0.04	0.0005
APOB (g/L)	0.75 ± 0.04	0.69 ± 0.02	0.2580
LDH (U/L)	218.60 ± 10.97	175.70 ± 6.33	0.0023

combination group changed after treatment crucially in contrast to those before treatment. Aggregate fitting parameters, that is, R^2X and R^2Y, were 0.271 and 0.985, respectively. Predictive parameter Q^2 was 0.876. In addition, according to the load diagram and VIP value greater than 1 (**Figure 4C**), about 93 differential metabolites were screened out from 1,454 detected metabolites. The *t*-test for these differential metabolites showed that some of them had significant double-tailed differences ($p < 0.05$). In addition, these compounds were screened by Metline database to obtain the endogenous differential metabolites with an exact molecular structure. Finally, these differential metabolites were used to search for corresponding differential metabolic pathways. Aspartate and asparagine metabolism, tyrosine metabolism, linoleate metabolism, and vitamin A metabolism were found as related metabolic pathway.

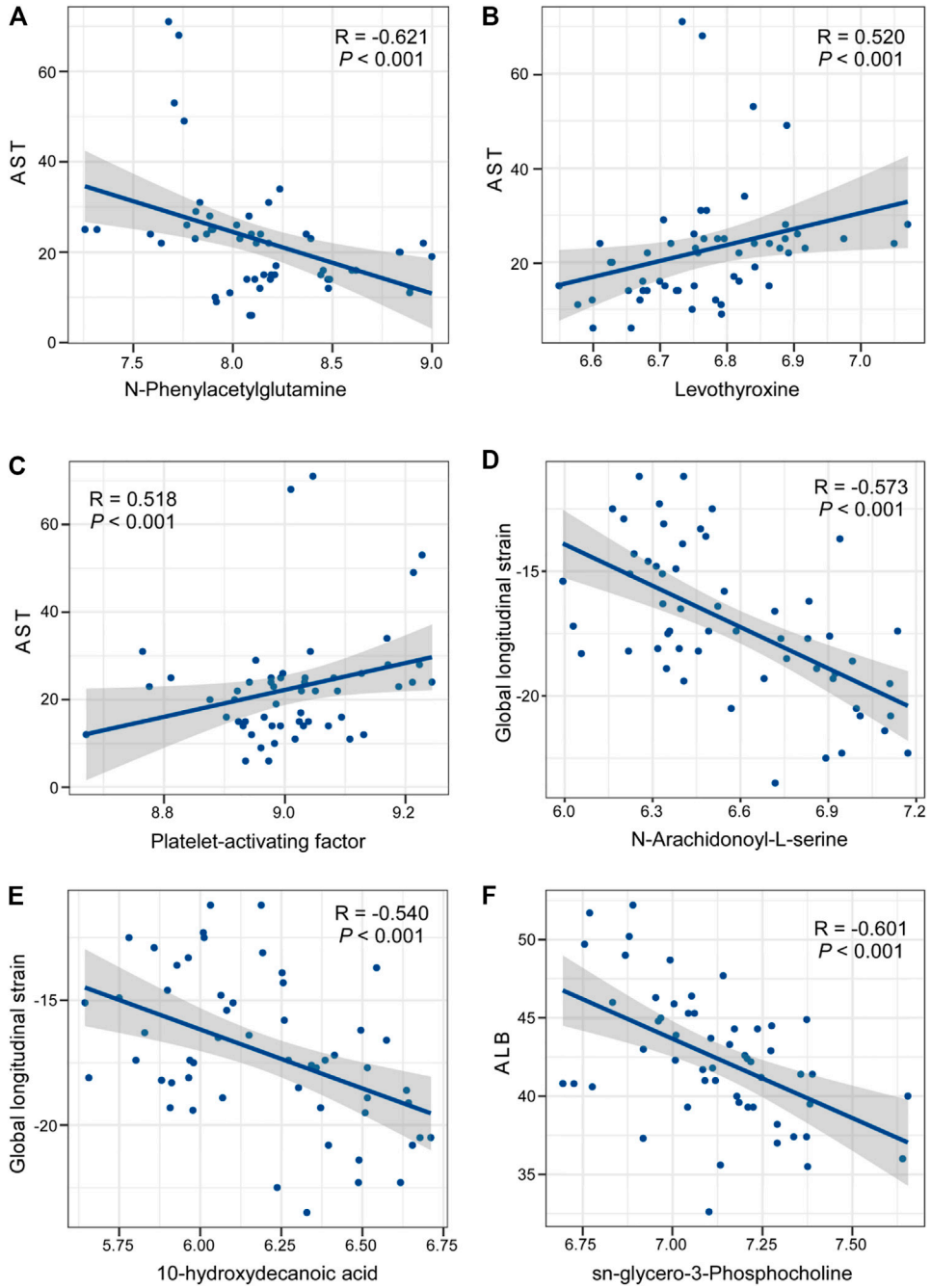

FIGURE 6 | Correlation analysis between differential metabolites in the ticagrelor MTDP combination group and blood biochemical indexes after treatment.

Moreover, we also did the OPLS-DA analysis between the drug combination group and ticagrelor group after treatment. R^2Y and Q^2 were 0.993 and 0.87, respectively. In **Figure 5**, the two groups were in different quadrants, with significant differences between the combination group and the ticagrelor group. In addition, according to the load diagram and VIP value greater than 1 (**Figure 5C**), about 93 differential metabolites were screened out from 1,454 detected metabolites. These results indicate that MTDP can significantly enhance the effect of ticagrelor on metabolites *in vivo*. Finally, the metabolic pathways of differential metabolites were analyzed by the MetaboAnalyst web. Fatty acid metabolism was found as the most probable related metabolic pathway.

Finally, we compared the blood biochemical indexes in two groups after treatment. From the results (**Table 2**), several prognostic indicators, such as CK-MB and LDH, in the drug combination group were outstanding lower than those in the ticagrelor group. We also found serum lipid parameters, such as

HDL and LDL, in the drug combination group were also much better than those in the ticagrelor group. Then we combined the differential metabolites with these blood biochemical indexes. As shown in **Figure 6**, N-phenylacetylglutamine, levothyroxine, platelet-activating factor, N-arachidonoyl-L-serine, 10-hydroxydecanoic acid, and sn-glycero-3-phosphocholine had significant correlations with these blood biochemical indexes.

DISCUSSION

In this study, the mechanism of drug combination therapy was analyzed by using STI combined with the un-targeted metabolism. The pharmacodynamics was evaluated by STI. In addition, the mass spectrometric data were divided satisfactorily between the two groups by PCA and OPLS-DA analysis. In data analysis, we found that 1,454 metabolites differed after treatment between the combination group and the ticagrelor group. These metabolites had dramatical changes, especially in the drug combination group. Finally, we analyzed the metabolic pathways involved according to different metabolites. Fatty acid metabolism had been found as the potential pathway which reflects the drug combination.

Aliphatic acids are the primary components of low-density lipoprotein (Gao et al., 2017). They have relationships with indirectly accumulate monocytes, leading to macrophage proliferation, overexpression of endothelial adhesion factors, and endothelial dysfunction, thereby promoting atherosclerosis (Cui et al., 2017; Paavola et al., 2017). Therefore, lipid metabolism is an independent factor for the evaluation of the prognosis and identification of the mechanism. In our experiment, about six kinds of aliphatic acid, containing FA(20:4), FA(22:5), FA-hydroxy(18:0), palmitic acid, stearic acid, and arachidonic acid, were detected to be lower in the drug combination group, indicating that the MTDP may have the function of lowering blood lipids.

The ingredients of MTDP mainly contain *Salvia miltiorrhiza* Bunge, artificial *moschus*, *Panax ginseng* C.A.Mey, *Venenum bufonis*, artificial *Bovis calculus*, and *Borneolum*, which can reduce the triglyceride and cholesterol in the blood, and inhibit the synthesis of low-density lipoprotein, but also act on a variety of thrombin to inhibit coagulation. Therefore, MTDP can cooperate with ticagrelor in regulating multiple metabolic pathways for the improvement of drug efficacy.

CONCLUSION

In this study, we have used the non-targeted metabolomic method based on HPLC-HRMS coupled with STI for the investigation the drug combination mechanism of ticagrelor and MTDP. From the STI analysis, the GLS values increased in the drug combination group, indicating that drug combination can provide better prognosis. The LC-MS results found 93 differential metabolites from 1,454 total detected metabolites in the drug combination group when compared with the ticagrelor group. And the MTDP can affect the lipid metabolism, which have relationship with the blood biochemical indexes after drug treatment. This work has explained the mechanism of the enhancement to ticagrelor by MTDP from the point of view of metabolic product change, and revealed the potential metabolic pathways it affects, which provided the new ideas for clinical medication.

DATA AVAILABILITY STATEMENT

The original contributions presented in the study are included in the article/**Supplementary Material**; further inquiries can be directed to the corresponding authors.

ETHICS STATEMENT

The studies involving human participants were reviewed and approved by Xuzhou Central Hospital. The patients/participants provided their written informed consent to participate in this study. Written informed consent was obtained from the individual(s) for the publication of any potentially identifiable images or data included in this article.

AUTHOR CONTRIBUTIONS

LN is the first author and performed all the experiments and drafted the manuscript. LP contributed toward study design and revised the article. ZJ, GM, and LJ helped the first author prepare the materials of this paper. WH and GH provided fund support.

FUNDING

We appreciate the support of Xuzhou Science and Technology Project (No. KC19033). The work was also supported by Science and Education Project for Young medical talents, Jiangsu Province (No. QNRC2016338).

SUPPLEMENTARY MATERIAL

The Supplementary Material for this article can be found online at: https://www.frontiersin.org/articles/10.3389/fphar.2021.731734/full#supplementary-material

REFERENCES

Basak, T., Varshney, S., Hamid, Z., Ghosh, S., Seth, S., and Sengupta, S. (2015a). Identification of Metabolic Markers in Coronary Artery Disease Using an Untargeted LC-MS Based Metabolomic Approach. *J. Proteomics* 127, 169–177. doi:10.1016/j.jprot.2015.03.011

Basak, T., Varshney, S., Akhtar, S., and Sengupta, S. (2015b). Understanding Different Facets of Cardiovascular Diseases Based on Model Systems to Human Studies: A Proteomic and Metabolomic Perspective. *J. Proteomics* 127, 50–60. doi:10.1016/j.jprot.2015.04.027

Blais, C., Rochette, L., Ouellet, S., and Huynh, T. (2020). Complex Evolution of Epidemiology of Vascular Diseases, Including Increased Disease Burden: From 2000 to 2015. *Can. J. Cardiol.* 36, 740–746. doi:10.1016/j.cjca.2019.10.021

Chen, X., Liu, L., Palacios, G., Gao, J., Zhang, N., Li, G., et al. (2010). Plasma Metabolomics Reveals Biomarkers of the Atherosclerosis. *J. Sep. Sci.* 33, 2776–2783. doi:10.1002/jssc.201000395

Cui, S., Li, K., Ang, L., Liu, J., Cui, L., Song, X., et al. (2017). Plasma Phospholipids and Sphingolipids Identify Stent Restenosis after Percutaneous Coronary Intervention. *JACC Cardiovasc. Interv.* 10, 1307–1316. doi:10.1016/j.jcin.2017.04.007

Duranton, F., Lundin, U., Gayrard, N., Mischak, H., Aparicio, M., Mourad, G., et al. (2014). Plasma and Urinary Amino Acid Metabolomic Profiling in Patients with Different Levels of Kidney Function. *Clin. J. Am. Soc. Nephrol.* 9, 37–45. doi:10.2215/CJN.06000613

Gao, X., Ke, C., Liu, H., Liu, W., Li, K., Yu, B., et al. (2017). Large-scale Metabolomic Analysis Reveals Potential Biomarkers for Early Stage Coronary Atherosclerosis. *Sci. Rep.* 7, 11817. doi:10.1038/s41598-017-12254-1

Gelbenegger, G., Schoergenhofer, C., Jilma, B., Gager, G. M., Dizdarevic, A. M., Mamas, M. A., et al. (2021). Efficacy and Safety of Ticagrelor Monotherapy in Patients Undergoing Percutaneous Coronary Intervention: A Meta-Analysis. *Clin. Pharmacol. Ther.* 110, 424–431. doi:10.1002/cpt.2226

Hua, Y., Qiu, Y., Zhao, A., Wang, X., Chen, T., Zhang, Z., et al. (2011). Dynamic Metabolic Transformation in Tumor Invasion and Metastasis in Mice with LM-8 Osteosarcoma Cell Transplantation. *J. Proteome Res.* 10, 3513–3521. doi:10.1021/pr200147g

Johanne, S., Benoit, L., Farzin, B., Grégoire, R., Zuzana, M., Jean-Guillaume, D., et al. (2020). Ticagrelor versus Clopidogrel in Elective Percutaneous Coronary Intervention (ALPHEUS): a Randomised, Open-Label, Phase 3b Trial. *Lancet* 396, 1737–1744. doi:10.1016/S0140-6736(20)32236-4

Park, J. Y., Lee, S. H., Shin, M. J., and Hwang, G. S. (2015). Alteration in Metabolic Signature and Lipid Metabolism in Patients with Angina Pectoris and Myocardial Infarction. *Plos One* 10, e0135228. doi:10.1371/journal.pone.0135228

Lee, S.-J., Cho, J. Y., Kim, B.-K., Yun, K. H., Suh, Y., Cho, Y.-H., et al. (2021). Ticagrelor Monotherapy versus Ticagrelor with Aspirin in Patients with ST-Segment Elevation Myocardial Infarction. *JACC: Cardiovasc. Interventions* 14, 431–440. doi:10.1016/j.jcin.2020.11.036

Mullen, L., Meah, M. N., Elamin, A., Aggarwal, S., Shahzad, A., Shaw, M., et al. (2021). Risk of Major Bleeding with Potent Antiplatelet Agents after an Acute Coronary Event: A Comparison of Ticagrelor and Clopidogrel in 5116 Consecutive Patients in Clinical Practice. *Jaha* 10, e019467. doi:10.1161/JAHA.120.019467

Liu, H., Zhao, J., Pan, S., Zhu, Y., Fu, G., Tang, W., et al. (2021). Shexiang Tongxin Dropping Pill Protects against Sodium Laurate-Induced Coronary Microcirculatory Dysfunction in Rats. *J. Tradit. Chin. Med.* 41, 89–97. doi:10.19852/j.cnki.jtcm.2021.01.011

Matthews, S. D., and Frishman, W. H. (2017). A Review of the Clinical Utility of Intravascular Ultrasound and Optical Coherence Tomography in the Assessment and Treatment of Coronary Artery Disease. *Cardiol. Rev.* 25, 68–76. doi:10.1097/CRD.0000000000000128

Paavola, T., Kuusisto, S., Jauhiainen, M., Kakko, S., Kangas-Kontio, T., Metso, J., et al. (2017). Impaired HDL2-Mediated Cholesterol Efflux Is Associated with Metabolic Syndrome in Families with Early Onset Coronary Heart Disease and Low HDL-Cholesterol Level. *Plos One* 12, e0171993. doi:10.1371/journal.pone.0171993

Reed, G. W., Rossi, J. E., and Cannon, C. P. (2017). Acute Myocardial Infarction. *Lancet* 389, 197–210. doi:10.1016/S0140-6736(16)30677-8

Kaptoge, S., Seshasai, S. R., Gao, P., Freitag, D. F., Butterworth, A. S., Borglykke, A., et al. (2014). Inflammatory Cytokines and Risk of Coronary Heart Disease: New Prospective Study and Updated Meta-Analysis. *Eur. Heart J.* 35, 578–589. doi:10.1093/eurheartj/eht367

Johnson, T. W., Baos, S., Collett, L., Hutchinson, J. L., Nkau, M., Molina, M., et al. (2020). Pharmacodynamic Comparison of Ticagrelor Monotherapy versus Ticagrelor and Aspirin in Patients after Percutaneous Coronary Intervention: The TEMPLATE (Ticagrelor Monotherapy and Platelet Reactivity) Randomized Controlled Trial. *Jaha* 9, e016495. doi:10.1161/JAHA.120.016495

Warren-Gash, C., Smeeth, L., and Hayward, A. C. (2009). Influenza as a Trigger for Acute Myocardial Infarction or Death from Cardiovascular Disease: a Systematic Review. *Lancet Infect. Dis.* 9, 601–610. doi:10.1016/S1473-3099(09)70233-6

Yang, J., Chun, J. Y., Qi, A., Liu, X., and Guo, L. (2014). The Effects of Compound Danshen Dripping Pills and Human Umbilical Cord Blood Mononuclear Cell Transplant after Acute Myocardial Infarction. *Exp. Clin. Transpl.* 12, 123–128. doi:10.6002/ect.2013.0204

Zhao, J., Zhou, Y., Liu, H., Zheng, Z., Liu, S., Peng, J., et al. (2021). Effect of Musk Tongxin Dropping Pill on Myocardial Remodeling and Microcirculation Dysfunction in Diabetic Cardiomyopathy. *Evidence-Based Complement. Altern. Med.* 2021, 1–10. doi:10.1155/2021/6620564

Conflict of Interest: The authors declare that the research was conducted in the absence of any commercial or financial relationships that could be construed as a potential conflict of interest.

frontiers in Pharmacology

ORIGINAL RESEARCH
published: 24 November 2021
doi: 10.3389/fphar.2021.772635

Geniposide Ameliorates Liver Fibrosis Through Reducing Oxidative Stress and Inflammatory Respose, Inhibiting Apoptosis and Modulating Overall Metabolism

Lu Yang[1,2†], Liping Bi[2†], Lulu Jin[1], Yuming Wang[1], Yuting Li[1,3], Zixuan Li[4], Wenju He[5], Huantian Cui[6], Jing Miao[2]* and Li Wang[2]**

[1]Tianjin University of Traditional Chinese Medicine, Tianjin, China, [2]Tianjin Second People's Hospital, Tianjin, China, [3]First Teaching Hospital of Tianjin University of Traditional Chinese Medicine, Tianjin, China, [4]Yunnan Provincial Hospital of Traditional Chinese Medicine, Kunming, China, [5]Tianjin First Central Hospital, Tianjin, China, [6]Shandong Provincial Key Laboratory of Animal Cell and Developmental Biology, School of Life Sciences, Shandong University, Qingdao, China

OPEN ACCESS

Edited by:
Marcello Locatelli,
University of Studies G. d'Annunzio Chieti and Pescara, Italy

Reviewed by:
Haci Ahmet Deveci,
University of Gaziantep, Turkey
Sanmoy Karmakar,
Jadavpur University, India
Hongrui Guo,
Sichuan Agricultural University, China

***Correspondence:**
Huantian Cui
1762316411@qq.com
Jing Miao
stinajing@163.com
Li Wang
554104751@qq.com

†These authors share first authorship

Specialty section:
This article was submitted to Ethnopharmacology, a section of the journal Frontiers in Pharmacology

Received: 08 September 2021
Accepted: 05 November 2021
Published: 24 November 2021

Citation:
Yang L, Bi L, Jin L, Wang Y, Li Y, Li Z, He W, Cui H, Miao J and Wang L (2021) Geniposide Ameliorates Liver Fibrosis Through Reducing Oxidative Stress and Inflammatory Respose, Inhibiting Apoptosis and Modulating Overall Metabolism. Front. Pharmacol. 12:772635. doi: 10.3389/fphar.2021.772635

Liver fibrosis is a progressive liver damage condition caused by various factors and may progress toward liver cirrhosis, and even hepatocellular carcinoma. Many studies have found that the disfunction in metabolism could contribute to the development of liver fibrosis. Geniposide, derived from *Gardenia jasminoides* J. Ellis, has been demonstrated with therapeutic effects on liver fibrosis. However, the exact molecular mechanisms of such liver-protection remain largely unknown. The aim of this study was to explored the effect of geniposide on metabolic regulations in liver fibrosis. We used carbon tetrachloride (CCl_4) to construct a mouse model of liver fibrosis and subsequently administered geniposide treatment. Therapeutic effects of geniposide on liver fibrosis were accessed through measuring the levels of hepatic enzymes in serum and the pathological changes in liver. We also investigated the effects of geniposide on inflammatory response, oxidative stress and apoptosis in liver. Furthermore, serum untargeted metabolomics were used to explore the metabolic regulatory mechanisms behind geniposide on liver fibrosis. Our results demonstrated that geniposide could reduce the levels of hepatic enzymes in serum and ameliorate the pathological changes in liver fibrosis mice. Geniposide enhanced the activities of superoxide dismutase (SOD) and glutathione peroxidase (GSH-Px) and decreased methane dicarboxylic aldehyde (MDA) levels in liver. Geniposide treatment also decreased the levels of interleukin (IL)-6, IL-1β, and tumor necrosis factor-alpha (TNF-a) in liver tissue homogenate. Terminal deoxynucleotidyl transferase-mediated dUTP-biotin nick end labeling assay (TUNEL) staining demonstrated that geniposide could reduce the apoptosis of hepatocytes. Geniposide increased the protein expression of B-cell lymphoma-2 (Bcl-2) and downregulated the protein expression of Bcl-2 Associated X (Bax), cleaved-Caspase 3, and cleaved-Caspase 9. Serum untargeted metabolomics analysis demonstrated that geniposide treatment improved the metabolic disorders including glycerophospholipid metabolism, arginine and proline metabolism, and arachidonic acid (AA) metabolism. In conclusion, our study demonstrated the

protective effects of geniposide on liver fibrosis. We found that geniposide could treat liver fibrosis by inhibiting oxidative stress, reducing inflammatory response and apoptosis in the liver, and modulating glycerophospholipid, and arginine, proline, and AA metabolism processes.

Keywords: liver fibrosis, geniposide, untargeted metabolomic analysis, oxidative stress, inflammation, apoptosis

INTRODUCTION

Liver fibrosis can be caused by infection (hepatitis virus, parasites), hepatotoxic factors (drugs, industrial factors, alcohol), and environmental factors. It is a progressive disease characterized by the activation and regeneration of inflammatory cells and fibroblasts and the accumulation of extracellular matrices in the liver (Liang et al., 2021). In recent years, changes in dietary habits have increased the incidence of liver fibrosis. The World Health Organization (WHO) estimates that there are approximately 100 million patients with liver fibrosis and liver cirrhosis worldwide, resulting in more than one million deaths annually (Qiao et al., 2020). Over the long term, liver fibrosis can develop into liver cirrhosis and liver cancer, both of which can seriously threaten human health. Therefore, preventing the progression of liver fibrosis is important to reduce the incidence of both liver fibrosis and liver cancer.

Previous researches have demonstrated that etiologic treatment, such as long-term anti-virus therapy (entecavir and tenofovir), can inhibit and even reverse liver fibrosis (Liaw, 2013; Choi et al., 2021; Yang et al., 2021). However, etiologic treatment is still limited in its ability to treat liver fibrosis, since once the mechanism behind liver fibrosis has been activated, the disease continues to progress (Liaw, 2013). Therefore, it is important to develop novel anti-fibrotic drug candidates.

Metabolomics is an important tool for studying changes in endogenous metabolites and can elucidate the pathogenesis of diseases on a metabolic level (Cui et al., 2021). Many studies have identified changes in host metabolism during the progression of liver fibrosis (Zhang et al., 2018). Compared to healthy controls, serum carbohydrate, lipid metabolism, and amino acid metabolism all dramatically changed in liver fibrosis and liver cirrhosis patients due to decreased levels of leucine, isoleucine, valine, and myristic acid and increased concentrations of phenylalanine, tyrosine, tryptophan, and palmitic acid (Yoo et al., 2019) The serum of carbon tetrachloride (CCl_4)-induced liver fibrosis mice exhibited higher levels of amino acids such as phenylalanine, tyrosine, glutamate, and lower levels of niacinamide and 3-hydroxyphenylacetate compared to mice without CCl_4 treatment (Liang et al., 2016). Modulating host metabolism is one potential method of alleviating liver fibrosis. Amino acid metabolism, including lysine and tryptophan degradation, was altered in liver fibrosis patients who had their spleen removed (Yang et al., 2018). Geniposide could prevent CCl_4-induced liver fibrosis by modulating glycolysis, fructose and mannose, glutathione, and sulfur metabolism (Song et al., 2017). Amarogentin has been found to have hepatoprotective effects by regulating the metabolism of amino acids and fatty acids (Zhang et al., 2018). Aqueous extracted from *Corydalis saxicola* Bunting could ameliorate the effects of liver fibrosis in rats by regulating amino acid metabolism, lipid metabolism, and pyruvate metabolism pathways (Liu et al., 2018).

Geniposide is an active ingredient extracted from *Gardenia jasminoides* J. Ellis and has multiple pharmacological effects, including anti-oxidative stress, anti-inflammatory properties, and anti-apoptotic effects (Yuan et al., 2020). It has been demonstrated that geniposide could downregulate the protein levels of alpha-smooth muscle actin (α-SMA), type I collagen alpha-1, Sonic hedgehog and Gli family zincfinger 1 in CCl_4-induced liver fibrosis model mice (Lin et al., 2019). In addition, geniposide could reduce inflammatory response and increase bile acids secretion in a 3,5-diethoxycarbonyl-1,4-dihydrocollidine-induced sclerosing cholangitis model mice (Wen et al., 2021). *In vitro* study showed that geniposide could suppress TGF-β1-induced epithelial-mesenchymal transition in hepatocytes through inhibiting the activation of mitogen-activated protein kinase signaling pathway (Park et al., 2015). However, there are few studies assessing the metabolic changes in liver fibrosis model treated with geniposide. In this study, we constructed a liver fibrosis mouse model using CCl_4, orally administered geniposide to these mice, and studied the effects of geniposide on oxidative stress, inflammation and apoptosis. We studied changes in serum metabolites following geniposide treatment using untargeted metabolomics (**Figure 1**).

MATERIALS AND METHODS

Reagents

Geniposide ($C_{17}H_{24}O_{10}$; molecular weight, 388.37 Da; virtue ≥98%) was obtained from Sichuan Weikeqi Biological Technology Co., Ltd. We obtained aspartate aminotransferase (AST), alanine aminotransferase (ALT), a bicinchoninic acid (BCA) protein quantitative kit, and superoxide dismutase (SOD), methane dicarboxylic aldehyde (MDA), and glutathione peroxidase (GSH-Px) assay kits from Nanjing Jiancheng Biological Engineering Institute. Mouse interleukin (IL)-6, IL-1β, and tumor necrosis factor-alpha (TNF-α) enzyme-linked immunosorbent assay (ELISA) kits were purchased from Shanghai BlueGene Biotech Co., Ltd. High-sig Enhanced chemiluminescence assay (ECL) western blotting substrates were obtained from Tanon Science and Technology Co., Ltd. Primary antibodies against mouse β-actin (20536-1-AP) were obtained from Proteintech Group, Inc. Terminal deoxynucleotidyl transferase-mediated dUTP-biotin nick end labeling assay (TUNEL) apoptosis detection kit, B-cell lymphoma-2 (Bcl-2, ab59348), Bcl-2 Associated X (Bax, ab32503), Caspase 3 (ab13847), and Caspase 9 (ab2786) were

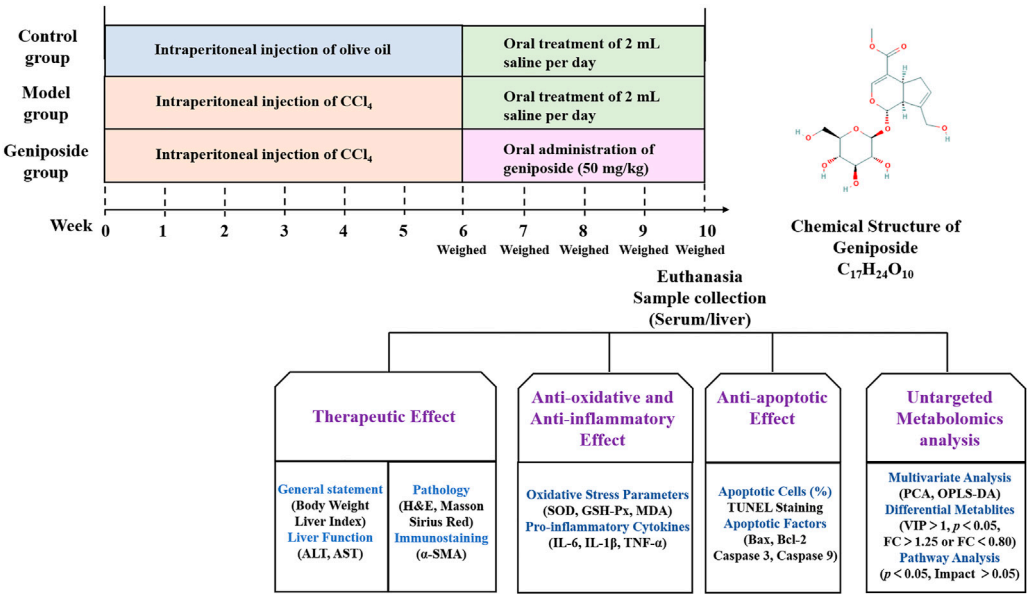

FIGURE 1 | Overview of the experimental design for all groups.

obtained from Abcam, Inc. The corresponding secondary antibodies were obtained from Abcam, Inc.

Animals

C57BL/6 male mice were obtained from Beijing Huafukang Biotechnology Co. Ltd. The experimental animals were fed for 1 week prior to the experiment. All mice were kept in an environment at a constant temperature (20–25°C with 60 ± 5% humidity) with a light cycle of 12 h light/12 h dark and provided with food and water. This study was performed according to the guidelines set by the National Institutes of Health and Institutional Guidelines and was approved by the Ethics Committee of Nankai University (Approval No. 2021-SYDWLL-000038).

Induction of Liver Fibrosis Mouse Model

We established a liver fibrosis mouse model via intraperitoneal injection of CCl_4, which was consistent with previous study (Wang et al., 2020). Briefly, CCl_4 was diluted with olive oil at a concentration of 2 ml/kg body weight and administered via intraperitoneal infusion twice per week over a six-week period.

Animal Grouping and Dosing Regimen

Thirty mice were used to induce liver fibrosis model. Seven mice died in the first 2 weeks after CCl_4 injection. After 6 weeks of CCl_4 injection, three mice were selected randomly and sacrificed. HE staining of liver was used to validate that the liver fibrosis model has been successfully induced. 20 mice were randomly divided into model group and geniposide group. The mice in the control group were intraperitoneally injected with olive oil (2 ml/kg body weight) twice per week for 6 weeks. Mice in the geniposide group were administered geniposide (50 mg/kg daily) via gavage for 4 weeks (Ma et al., 2018; Lin et al., 2019). The mice in the control and model groups were administered an equal amount of saline instead of geniposide. The mice were euthanized after 4 weeks of geniposide treatment, after which their livers were removed and weighed to obtain the liver index. The liver index (%) was calculated according to the following formula: liver weight (g)/body weight (g) × 100%.

TABLE 1 | Liver pathology score.

Feature score	Score	Description
Ballooning degeneration	0	None
	1	Minimal
	2	Mild
	3	Moderate
	4	Severe
Inflammation	0	None
	1	1 inflammatory per field of view
	2	2–4 inflammatory per field of view
	3	>4 inflammatory per field of view
Apoptotic cells	0	None
	1	Few
Fibrosis	0	None
	1	Portal/sinusoidal minimal fibrosis
	2	Portal/sinusoidal mild fibrosis
	3	Bridging fibrosis
	4	Cirrhosis

Scores ranged from 0 to 12 (total score), which represents the sum of scores from 0 to 4 for severity of swelling, inflammation, apoptotic cells and fibrosis.

Biochemistry Determination

Once the mice were euthanized, their blood was collected and centrifuged at 3,000 rpm for 15 min to obtain the serum. Liver function was evaluated by assessing the activities of hepatic enzymes in the serum, including ALT and AST. The AST and

ALT activities were measured by commercial assay kits according to the manufacturer's instructions.

Histopathology

After they were euthanized, the livers of three groups were isolated and immersed in 10% formalin. Liver tissues were dehydrated and paraffin-embedded. The tissues were cut into 5 μm thick strips, stained with hematoxylin and eosin (H&E), and subjected to Masson and Sirius Red staining. The severity of pathological changes in H&E staining were determined through a histological liver fibrosis score based on a previous studies (Klopfleisch, 2013; Aldahmash and El Nagar, 2016). Scores ranged from 0 to 12 (total score), which represents the sum of scores from 0 to 4 for severity of swelling, inflammation, apoptotic cells and fibrosis (**Table 1**). The relative collagenous fiber areas in Masson and Sirius Red staining were quantified using integrated optical density (IOD) with the Image-Pro Plus 6.0 software. The positive area (%) was calculated according to the following formula: IOD/sum area × 100%.

Immunostaining

Immunohistochemistry detection of α-SMA in livers was performed on the paraffin for each group. The positive expressed area (%) of α-SMA in liver was analyzed using Image-Pro Plus 6.0 software.

Assessment of the Oxidative Stress Parameters

Homogenates with 900 μL normal saline for every 0.1 g liver tissue were homogenized via ultrasonic trituration on ice. The protein concentration in liver homogenates was quantified by BCA. The homogenates were centrifuged (3,000 rpm, 15 min) and the supernatant was collected to detect SOD, GSH-Px activities and MDA level using relative commercial kits.

Determination of Inflammatory Factors in Liver Tissue by Enzyme-Linked Immunosorbent Assay

After 4 weeks of geniposide treatment, the levels of IL-6, IL-1β, and TNF-α in liver tissue homogenates were analyzed using ELISA kits according to the manufacturer's instructions. The total protein concentration in the liver tissue homogenate was quantified by a BCA protein quantitative kit assay, according to the manufacturer's instructions. Cytokine concentrations in liver homogenates were assessed according to the following formula: concentration of cytokines in the homogenate/total protein (pg/mg).

TUNEL Staining

The paraffin sections of the liver tissue were stained using the TUNEL assay kit according to the manufacturer's instructions. The apoptosis was observed under fluorescence microscope after rinsed with PBS. The ratio of apoptotic cells to the total cells was quantified by Image-pro Plus 6.0 software based on IOD.

Western Blot

The liver tissues were homogenized and lysed using RIPA lysis buffer to extract the proteins. A BCA Protein Assay Kit was used to measure the total protein concentration. The proteins were separated on an 8–12% sodium dodecyl sulfate polyacrylamide gel electrophoresis and transferred to a polyvinylidene difluoride (PVDF) membrane (Bio-Rad) via electroblotting. The membranes were blocked for 2 h with 5% non-fat milk powder in 1 × TBST at room temperature, after which they were incubated with the primary antibodies (rabbit anti-Bcl-2, 1: 800; rabbit anti-Bax, 1:10,000; rabbit anti-Caspase 3, 1:500; rabbit anti- Caspase 9, 1:1,000; and rabbit anti-β-Actin, 1:4,000) overnight at 4°C. After three TBST washes, the membranes were incubated with Goat anti-rabbit IgG (1:10,000) secondary antibodies at room temperature for 2 h. Blotting was observed using ECL. The gray value was quantitatively analyzed using ImageJ software.

Serum Untargeted Metabolomics Study

We obtained serum samples from the control, model, and geniposide groups to analyze the metabolomics at the end of 4 weeks of geniposide treatment. Differential metabolite screening in the three groups was performed using liquid chromatography-mass spectrometry (LC-MS). Details of the sample preparation and data analysis are described below (Cui et al., 2020).

Sample Preparation

We added 10 μL of 2-chloro-l-phenylalanine and 10 μL of Lyso PC 17:0 (concentrations were 0.3 and 0.01 mg/ml, dissolved with methanol) to 100 μL of the serum samples.

The serum samples were mixed with 300 μL of methanol: chloroform (2:1, v/v) and centrifuged for 1 min. The mixture was then treated in an ice-water bath for subsequent ultrasonic extraction, after which they were incubated at −20°C for 1 h to precipitate the proteins. They were centrifuged at 12,000 rpm for 10 min at 4°C, after which 300 μL of the upper solution dried and redissolved with 100 μL [acetonitrile water (1:1)]. The samples were then placed in a 200 μL lined tube for LC-MS analysis. In order to evaluate the stability and repeatability of the system during the sample collection process, all samples were mixed with the same volume to ensure quality control (QC).

Liquid Chromatography-Mass Spectrometry

Chromatographic separation was performed on a U3000 Ultra Performance Liquid Mass Spectrometer from Thermo Scientific, after which the metabolic profile of each serum sample was analyzed. ACQUITY UPLC HSS T3 columns (2.1*100 mm, 1.8 μm) were used for analysis, in positive and negative modes. The mobile phase was comprised of mobile phase A (0.1% formic acid) and mobile phase B (acetonitrile). The flow rate was constant at 0.3 ml/min, the injection volume was 1.0 μL, and the column temperature was 45°C. Separation was conducted as follows: 0 min, 80% A, 20%B; 2 min, 70% A, 30%B; 5 min, 55% A, 45%B; 6.5 min, 40% A, 60%B; 12 min, 20% A, 80%B; 14 min, 0%

A, 100%B; 16 min, 0% A, 100%B; 16.1 min, 80% A, 20%B; 18 min, 80% A, 20%B.

Mass spectrometry (MS) was performed using positive and negative ion mode electrospray ionization (ESI) techniques for MS scanning, with a scanning range from 50 m/z to 1,500 m/z and a resolution of 70,000. The positive and negative ion source voltages were 3.7 and 3.5 kV. The capillary heating temperature of both ions was set to 320°C. The sheath gas pressure and auxiliary gas pressure were 30 and 10 psi, respectively (temperature: 300°C; automatic gain control target: 1×10^6; maximum isolation time: 50 ms). During the analysis, every six samples was tested for quality control to ensure the accuracy of the data.

Data Processing and Analysis

Progenesis QI software (2.1, Nonlinear Dynamics, Newcastle, United Kingdom) was used for data analysis. Metabolites were identified using the Human Metabolome Database (HMDB, www.hmdb.ca) and local databases. Metabolites with coefficients of variation (CV) less than 30% in the QC samples were kept for the following analysis. Due to large differences in the concentrations of different metabolites, datasets were normalized to avoid masking the signals of metabolites with concentrations that were too high or too low. The principal component analysis (PCA) and orthogonal partial least squares discriminant analysis (OPLS-DA) were performed using SIMCA software (14.1, Umetrics) to visualize the results of the metabolite data results. The quality of the models was evaluated according to their respective R^2 and Q^2 values. PCA was used to represent between-group differences and within-group variation. Variable Importance in the Projection (VIP) with a threshold >1 from the OPLS-DA model and *p*-values ($p < 0.05$) from the t-test were used to search differentially expressed metabolites. The normalized peak areas of all metabolites were expressed as mean ± standard (mean ± SD) deviation and analyzed using a two-tailed Student's t-test.

Metabolites with fold changes higher than 1.25 or less than 0.80 were selected for metabolic pathway analysis. The MetaboAnalyst 5.0 software (www.metaboanalyst.ca) was used to analyze the metabolic pathways of the differential metabolites between two groups of samples (control and model; model and geniposide). The KEGG (www.kegg.jp) database was used for pathway analysis.

Statistical Analysis

All experimental data were expressed as the mean ± SD, and statistical differences between the experimental groups were evaluated using one-way ANOVA via SPSS software (version 20.0, United States). *p*-values were generated by the log-rank test, and $p < 0.05$ was considered statistically significant.

RESULTS

Effects of Geniposide on CCl_4-Induced Liver Fibrosis Model Mice

After 4 weeks of geniposide administration, the efficacy of the treatment was evaluated by measuring the body weight, liver index, hepatic enzyme activities of ALT and AST, and pathological changes in liver. As shown in **Figure 2A**, the body weight in the model group was significantly lower than that in the control group ($p < 0.01$). After 4 weeks of geniposide treatment, body weight increased in liver fibrosis model mice ($p < 0.01$). CCl_4 treatment resulted in significant ($p < 0.01$) increases in the liver index compared to the control group. Geniposide treatment decreased the liver index in the model group ($p < 0.05$, **Figure 2B**). Compared to the control group, AST and ALT activities in the model group significantly increased. Geniposide treatment reduced them ($p < 0.01$, **Table 2**) of liver fibrosis model mice.

Pathological changes in the liver following geniposide treatment were measured by H&E, Masson and Sirius Red staining, and immunostaining. H&E staining and liver pathology score showed that the hepatocytes in the control group were arranged radially along the central vein, while the liver structure was clearly visible. The model group's livers exhibited hepatic cord disorder, hepatocellular swelled and necrosis, nuclear shrinkage and disappearance, inflammatory cell infiltration and fibrosis appeared, while geniposide treatment improves morphological damage in hepatic tissues (**Figures 3A,E**).

Masson staining showed an increased overall collagen deposition and fibrotic lesions in liver fibrosis model mice. Sirius Red staining showed that type Ⅰ collagen significantly increased in liver fibrosis model mice. Following geniposide treatment, we observed significant reductions in collagen deposition and fibrotic lesions; the only area with visible collagen deposition was the portal area ($p < 0.01$, **Figures 2B,C,F,G**).

Immunostaining demonstrated that the expression of α-SMA in the model group was higher than that in the control group ($p < 0.01$, **Figures 2D,H**). Geniposide treatment could reduce α-SMA levels compared to the model group ($p < 0.01$, **Figures 2H**, **3D**).

Effects of Geniposide on Inflammation and Oxidative Stress in Liver Fibrosis Model Mice

We analyzed the impacts of geniposide on oxidative stress by detecting MDA levels and the activities of SOD and GSH-Px in liver tissue homogenate. Our results demonstrated that SOD ($p < 0.01$) and GSH-Px activities ($p < 0.01$) decreased and that MDA levels ($p < 0.05$) increased in the model group compared to the control group, while SOD ($p < 0.05$) and GSH-Px activities ($p < 0.05$) increased and MDA levels ($p < 0.05$) decreased in the geniposide group compared to the model group (**Table 3**). The anti-inflammatory effect was evaluated by detecting IL-6, IL-1β, and TNF-α levels in liver tissue homogenate using ELISA. Our results demonstrated that IL-6, IL-1β, and TNF-α levels increased in the model group compared to the control group ($p < 0.01$), and that geniposide treatment decreased IL-6, IL-1β ($p < 0.01$), and TNF-α ($p < 0.05$) levels in the liver tissue homogenate compared to the model group (**Figure 4**).

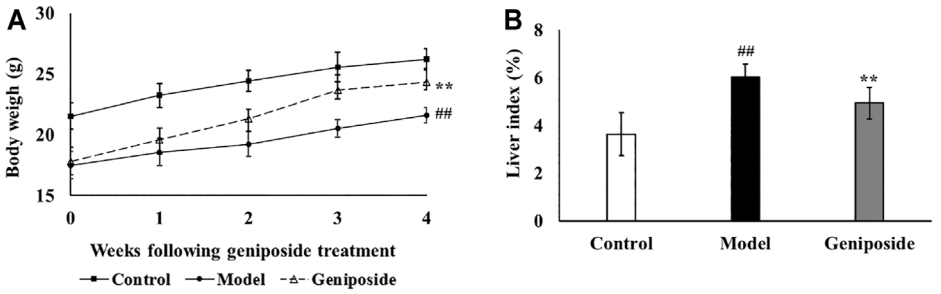

FIGURE 2 | Geniposide treatment increases body weight and liver index. **(A)** Body weight of 3 groups. **(B)** Liver index of 3 groups. Control, model, and geniposide groups (n = 10 per group). $^{\#\#}p < 0.01$, Model group *vs.* Control group; $^{*}p < 0.05$ and $^{**}p < 0.01$, Geniposide group *vs.* Model group.

TABLE 2 | Effects of geniposide ALT and AST levels in serum.

Group	AST (U/L)	ALT (U/L)
Control	102.79 ± 16.34	33.41 ± 8.57
Model	203.13 ± 36.75$^{\#\#}$	82.26 ± 12.48$^{\#\#}$
Geniposide	149.15 ± 22.96**	51.95 ± 10.81**

*Control, model, and geniposide treated groups (*n *= 10 per group). Data are presented as mean ± SD.* $^{\#\#}$p *< 0.01, Model group* vs. *Control group;* **p *< 0.01, Geniposide group* vs. *Model group.*

Effects of Geniposide on the Apoptosis of Cells in Liver Fibrosis Model Mice

TUNEL staining showed that there were almost no apoptotic cells in the liver tissue of the control group, while the numbers of apoptotic cells in the model group increased. The apoptotic cells decreased more after geniposide treatment compared to the model group. Image analysis of the apoptosis index of liver tissue with fibrosis in different groups is displayed in **Figure 5**.

Effects of Geniposid on Apoptosis-Related Factors in Liver Fibrosis Model Mice

We measured the expressions of Bax, Bcl-2, Caspase 3, and Caspase 9, which are all involved in apoptosis, to determine the anti-apoptotic activities of geniposide in CCl_4-induced liver fibrosis. We found that the expressions of Bax, Caspase 3, and Caspase 9 were all elevated and that the expression of Bcl-2 decreased in the model group compared with the control group (for Caspase 3, $p < 0.05$; for Bax, Bcl-2 and Caspase 9, $p < 0.01$; **Figure 4**). Geniposide treatment decreased the expressions of Bax, Caspase 3, and Caspase 9 and increased the expression of Bcl-2 compared with the model group (for Caspase 3 and Caspase 9, $p < 0.05$; for Bax and Bcl-2, $p < 0.01$; **Figure 6**).

Multivariate Analysis of Serum Metabolomics

Using untargeted metabolomics, we compared the changes of metabolites in the serum of all three groups. The metabolite profiles were analyzed via PCA and OPLS-DA. Our results demonstrated that there were significant differences between the control, model, and geniposide groups. The PCA model had an R^2 value of 0.641 and a Q^2 value of 0.366 (**Figures 7A,B**) and the OPLS-DA model had an R^2 value of 0.999 and a Q^2 value of 0.970 (**Figures 7C–F**).

Identification and Pathway Analysis of Differential Metabolites

A total of 24 differential metabolites were considered to be differential metabolites with a VIP >1 and $p < 0.05$ (fold change (FC) greater than 1.2 or less than 0.8) in the model group *vs.* control group or geniposide group *vs.* model group. These differential metabolites are listed in **Table 4**. Compared with the control group, levels of Decanoylcarnitine, Hexacosanoic acid, L-Palmitoylc, LysoPC(18:0), PE [18:0/18:1 (9Z)], PE (P-16:0e/0:0), Myristic acid, Arachidonic acid (AA), Oleic acid, Eicosadienoic acid, and Adrenic acid all increased in the model group, while levels of Hexanoylcarnitine, L-Octanoylcarnitine, Pentacosanoic acid, Creatine, L-Carnitine, Taurine, PC [18:0/18:2 (9Z,12Z)], Docosahexaenoic acid, L-Proline, Alpha-Linolenic acid, Linoleic acid, Nervonic acid, and PC (16:1 (9Z)/14:0) all decreased in the model group. When the geniposide group was compared with the model group, the levels of Decanoylcarnitine, L-Palmitoylcarnitine, LysoPC(18:0), PE [18:0/18:1 (9Z)], PE (P-16:0e/0:0), AA, Oleic acid, and Eicosadienoic acid all decreased, while levels of Hexanoylcarnitine, Creatine, Taurine, PC [18:0/18:2 (9Z,12Z)], Docosahexaenoic acid, L-Proline, Alpha-Linolenic acid, Linoleic acid, Nervonic acid and PC (16:1 (9Z)/14:0) increased (**Table 4**). Differential metabolites were used for pathway analysis. These products were then used to select pathways with impact values greater than 0.05 and p-values less than 0.05. Four pathways were screened out that varied between the control and model groups: Taurine and hypotaurine metabolism, Glycerophospholipid metabolism, Arginine and proline metabolism, and AA metabolism (**Figure 7G**). Five pathways were screened out that varied between the model and geniposide groups: Glycerophospholipid metabolism, Arginine and proline metabolism, AA metabolism, alpha-Linolenic acid

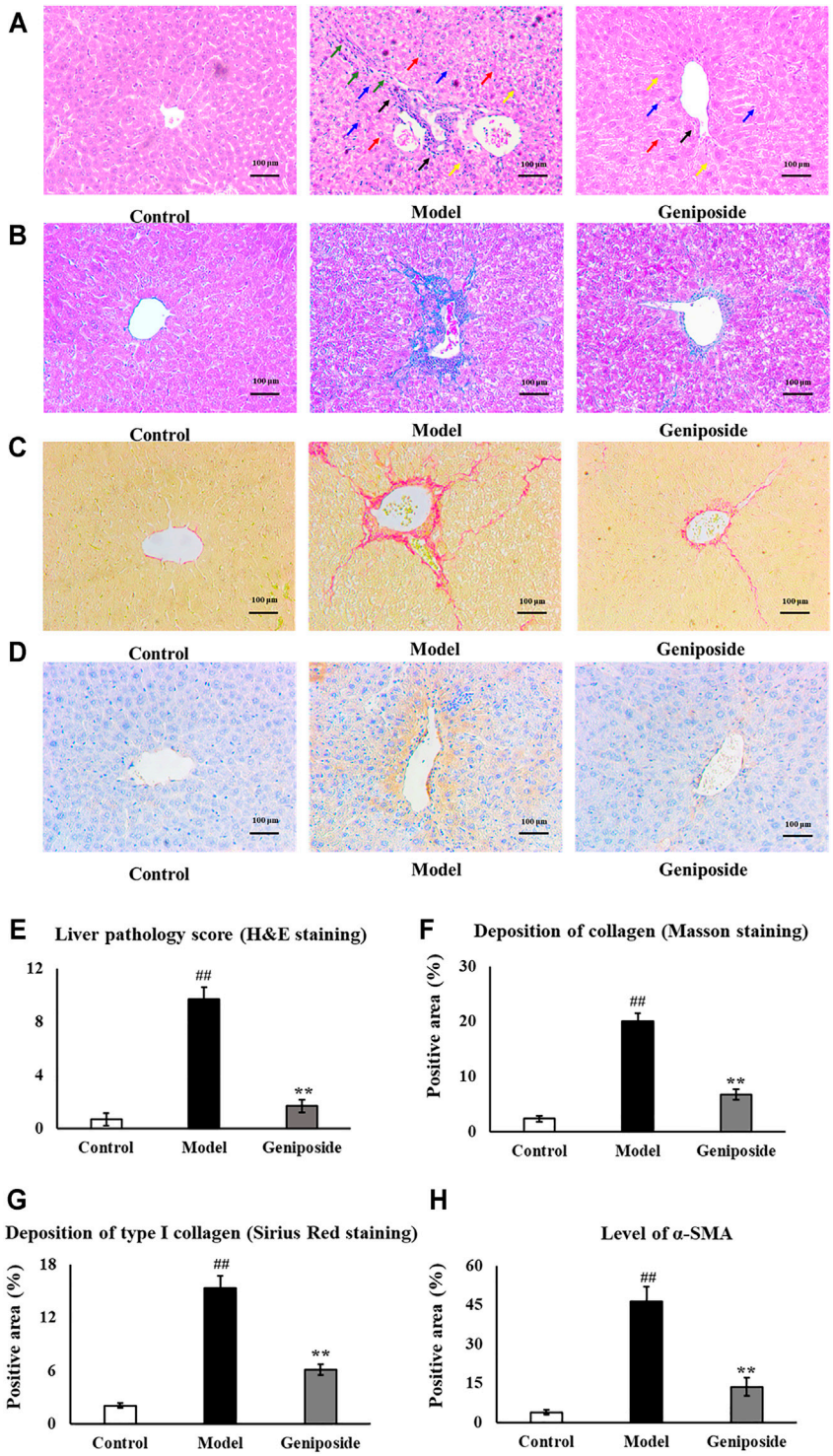

FIGURE 3 | Evaluation of liver histopathology. **(A,E)** H&E staining and liver pathology score showed that geniposide treatment improved pathological changes in the liver. Black arrows indicate infiltration of inflammatory cells. Yellow arrows indicate structural disorder of the hepatic cord. Red arrows indicate swelling of the liver cells. Blue arrows indicate necrosis of the liver cells. Green arrows indicate fibrosis. **(B,F)** Masson staining showed that geniposide treatment could reduce collagen deposition in the liver. **(C,G)** Sirius Red staining showed that geniposide treatment reduced liver type I collagen deposition. **(D H)** Immunostaining showed that geniposide treatment could decrease α-SMA levels in the liver (100×). Control, model, and geniposide groups ($n = 10$ per group). Data are presented as mean ± SD. $^{\#\#}p <$ 0.01, Model group *vs.* Control group; $^{**}p < 0.01$, Geniposide group *vs.* Model group.

TABLE 3 | SOD, GSH-Px activities, and MDA levels in liver homogenates after geniposide treatment.

Group	SOD (U/mg prot)	GSH-Px (U/mg prot)	MDA (nmol/mg prot)
Control	30.44 ± 3.29	265.76 ± 36.78	2.44 ± 0.64
Model	23.90 ± 1.24$^{\#\#}$	139.41 ± 45.49$^{\#\#}$	4.55 ± 1.26$^{\#\#}$
Geniposide	29.15 ± 4.75**	225.29 ± 43.09**	2.76 ± 0.47**

*Control, model, and geniposide groups (*n *= 10 per group). Data are presented as mean ± SD. #*p *< 0.05 and ##*p *< 0.01, Model group* vs. *Control group; *p < 0.05, Geniposide group* vs. *Model group.*

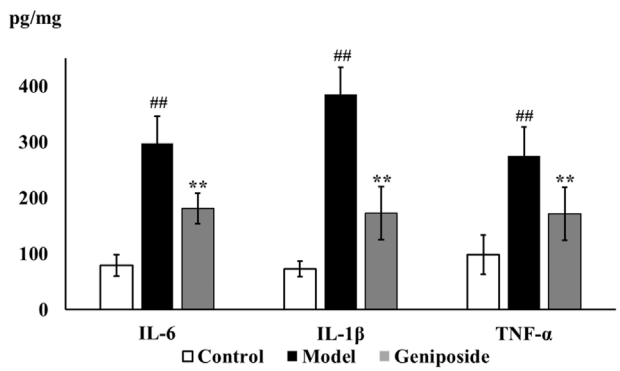

FIGURE 4 | Geniposide treatment improved inflammatory response in liver fibrosis model mice. ELISA test showed that geniposide treatment decreased the levels of IL-6, IL-1β, and TNF-α in liver tissue homogenate. Control, model, and geniposide groups (n = 10 per group). $^{\#\#}p < 0.01$, Model group *vs.* Control group; $^{*}p < 0.05$ and $^{**}p < 0.01$, Geniposide group *vs.* Model group.

(**Figure 7H**). The relationships between these pathways are displayed in **Figure 7I**.

DISCUSSION

CCl_4 is a commonly used to induce liver injury and liver fibrosis models (Zhu et al., 2019; Chen et al., 2021). Previous study showed that Swiss albino mice developed chronic liver injury after receiving oral treatment of CCl_4 (1.5 ml/kg) once daily for 8 weeks (Zhang et al., 2020). Intraperitoneal injection of CCl_4 (1 ml/kg) three times per week for 8 weeks could induce severe oxidative stress in Wistar rats (Goodla et al., 2019). Based on our previous study, we treated mice with intraperitoneal injection of CCl_4 (2 ml/kg) twice per week over a six-week period (Wang et al., 2020). Compared with the control group, the liver index, serum ALT, and AST levels of the model mice all increased. Additionally, pathological analysis of the liver tissue found hepatocyte degeneration, inflammatory infiltration, fibrous

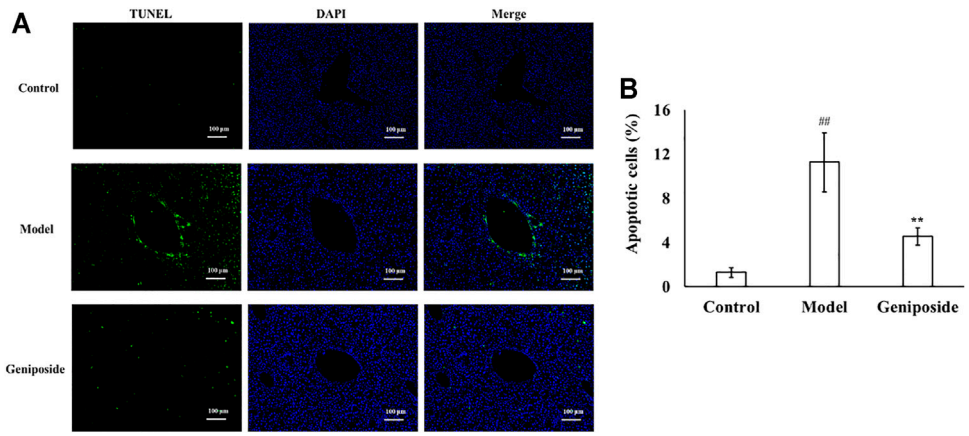

FIGURE 5 | Geniposide treatment improved apoptosis in liver fibrosis model mice. **(A)** Changes of TUNEL staining. **(B)** Changes of quantitative analysis of apoptotic cells. **(A,B)** TUNEL staining indicated that geniposide treatment reduced the number of apoptotic cells in a liver section. Control, model, and geniposide groups (n = 10 per group). Data are presented as mean ± SD. $^{\#\#}p < 0.01$, Model group *vs.* Control group; $^{**}p < 0.01$, Geniposide group *vs.* Model group.

metabolism, and Linoleic acid metabolism. Therefore, the common pathways between the control and model groups and the model and geniposide groups were considered significant pathways: Glycerophospholipid metabolism, Arginine and proline metabolism, and AA metabolism

connective tissue hyperplasia, damaged liver lobule structure, and the generation of a fibrous septum. This indicates that the model was successful. After being treated with geniposide, the ALT and AST values in the serum and the liver index decreased, resulting in improved pathological changes in the liver. This

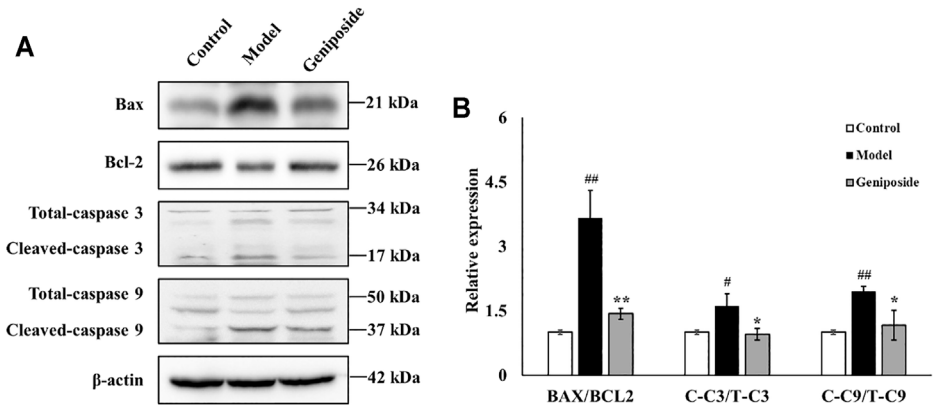

FIGURE 6 | Geniposide treatment regulated BAX, Bcl-2, Caspase 3, and Caspase 9 in liver fibrosis model mice. **(A,B)** Changes of the protein expression of BAX, Bcl-2, Caspase 3, Caspase 9, and β-actin in liver tissue. Geniposide treatment reversed the relative expression of the BAX, Bcl-2, Caspase 3, and Caspase 9 in model mice liver tissue. Control, model, and geniposide groups ($n = 3$ per group). #$p < 0.05$, Model group *vs.* Control group; ##$p < 0.01$, Model group *vs.* Control group; *$p <$ 0.05 and **$p < 0.01$, Geniposide group *vs.* Model group.

suggests that geniposide can ameliorate liver fibrosis induced by CCl_4.

Oxidative stress, inflammatory response and apoptosis are the major pathological characteristics during the progression of liver fibrosis (Zhu et al., 2020). We further evaluated the effects of geniposide on oxidative stress, inflammatory response and apoptosis in liver fibrosis mice. Our results found that geniposide could increase SOD and GSH-Px activities and decrease MDA content in the liver, indicating that geniposide could alleviate the oxidative stress reaction in model mice with liver fibrosis. Increased oxidative stress levels are a sign of the presence and development of liver fibrosis. In hepatocytes, CCl_4 could be transformed into active trichloromethylradical (CCl_3) under the catalyzation of cytochrome oxidase P450. Subsequently, CCl_3 could react with O_2 and generate more free radicals, resulting in lipid peroxidation and further damage to hepatocytes (Hermenean et al., 2012). MDA is an intermediate product of lipid peroxidation degradation and can seriously impair the composition, structure, and function of cells. MDA content can reflect the rate of lipid peroxidation in the body, and is an indicator of free radical content, indirectly indicating levels of cell damage (Shi et al., 2020). SOD and GSH-Px are anti-oxidative enzymes that demonstrate anti-oxidative strength and can protect liver cells from oxygen free radicals (El-Din et al., 2014). SOD is a vital scavenger of oxygen free radicals in the enzyme defense system, and can specifically scavenge superoxide anions and protect cells from damage (Forbes-Hernández et al., 2017). GSH-Px is a significant peroxide decomposing enzyme found throughout the body that eliminates free radicals such as hydrogen peroxide and prevents the formation of lipid peroxide. GSH-Px can catalyze the reaction between lipid peroxide and reduced glutathione to form oxidized glutathione, and plays a role in preserving the integrity of the structure and function of cell membranes (Lin et al., 2015).

ELISA experiments demonstrated that geniposide could reduce the contents of IL-6, IL-1β, and TNF-α in model mice and alleviate inflammatory reactions. CCl_4 could cause hepatocellular damage and subsequently activate Kupffer cells (Han et al., 2016). Activated Kupffer cells could produce inflammatory cytokines such as IL-6, IL1β and TNF-α. (Wang et al., 2019). These inflammatory factors contribute to the progression of liver fibrosis, while TNF-α can stimulate collagen synthesis and IL-6 and IL-1β can activate hepatic stellate cells and directly stimulate collagen secretion (Lee et al., 2014; Sun et al., 2018).

TUNEL staining and Western blot analysis were used to assess the apoptosis of liver tissues. TUNEL results demonstrated that geniposide could improve hepatocyte apoptosis in model mice. Western blot analysis demonstrated that the expressions of Bax, Caspase 3 and Caspase 9 all decreased and that the expression of Bcl-2 increased following geniposide treatment. During the development of liver fibrosis, the liver tissue is subjected to apoptosis (Jaeschke, 2006).

Excessive free radicals induced by CCl_4 could lead to the released of Cytc and then trigger the apoptosis of hepatocytes in liver (Ki et al., 2013; Mekky et al., 2016). Apoptosis is a process regulated by multiple factors, including Bax, Bcl-2, and the Caspase family (Tian et al., 2015). Bax and Bcl-2 are a pair of homologous regulatory factors with antagonistic effects. After forming a dimer, they induce apoptosis by changing the permeability of the outer membrane of the mitochondria (Moldoveanu et al., 2014; Hwang-Bo et al., 2019). Bax is a significant pro-apoptotic factor and participates in the mitochondrial apoptosis pathway. Bax forms holes in the outer membrane of the mitochondrial after activation, resulting in the loss of membrane integrity (Tait and Green, 2010). The anti-apoptotic factor Bcl-2 can inhibit Bax function, while the ratio between Bax and Bcl-2 determines the strength of their apoptosis-inducing effect. The Caspase family is another key regulator of the apoptosis pathway, and can also promote apoptosis (Zhao et al., 2018). In this family, Caspase-9 is upstream of the cascade reaction and belongs to the subclass of apoptosis initiation. Caspase-9 participates in the downstream initiation of Caspase-3 protease, which can directly induce apoptosis (Häcker and Paschen, 2007; Huang et al., 2021). As Bax

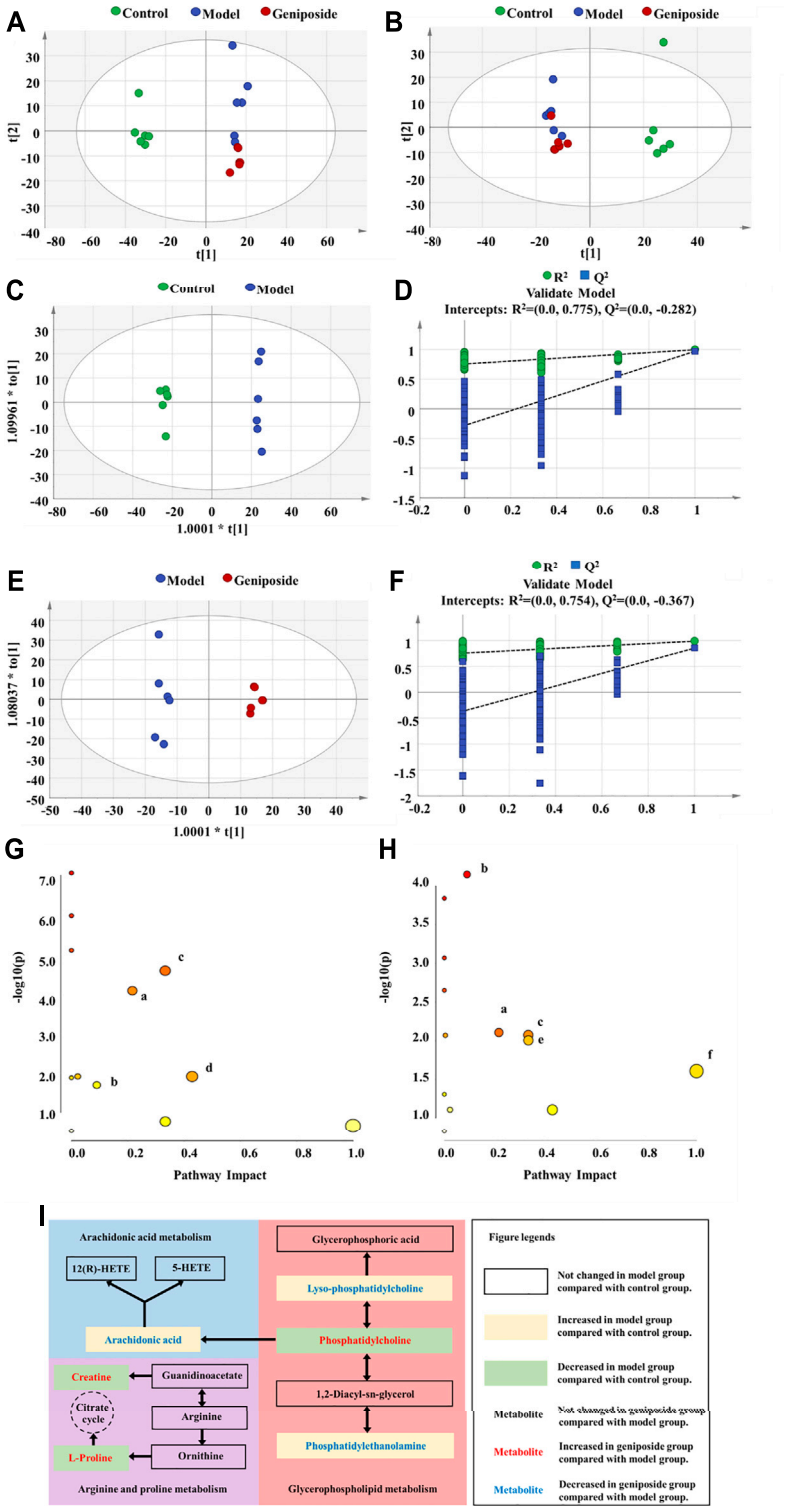

FIGURE 7 | Serum metabolism analysis of geniposide in liver fibrosis. **(A)** PCA score plot among control, model, and geniposide groups in positive mode. **(B)** PCA score plot among control, model, and geniposide groups in negative mode. **(C,D)** OPLS-DA score plot among control and model groups and the corresponding coefficient of loading plots. **(E,F)** OPLS-DA score plot among model and geniposide groups and the corresponding coefficient of loading plots. **(G)** Pathway analysis between control and model groups. **(H)** Pathway analysis between model and geniposide groups. (a) Glycerophospholipid metabolism, (b) Arginine and proline metabolism, (c) AA metabolism, (d) Taurine and hypotaurine metabolism, (e) alpha-Linolenic acid metabolism, and (f) Linoleic acid metabolism. Control, model, and geniposide treated groups (n = 6 per group). #: $p < 0.05$ and ##$p < 0.01$, Model group vs. Control group; *$p < 0.05$ and **$p < 0.01$, Geniposide group vs. Model group.

TABLE 4 | Summary of the differential metabolites identified in the serum of three Groups.

No.	Rt (min)	m/z	Formula	Metabolites	VIP	FC		Trend		Pathway
						M vs. C	G vs. M	M vs. C	G vs. M	
1	5.42	260.19	C13H25NO4	Hexanoylcarnitine	1.68	0.21	3.28	↓##	↑**	—
2	6.29	288.22	C15H29NO4	L-Octanoylcarnitine	1.63	0.22	1.27	↓##	↑	—
3	6.83	316.25	C17H33NO4	Decanoylcarnitine	1.60	2.16	0.70	↑##	↓**	—
4	13.95	395.39	C26H52O2	Hexacosanoic acid	1.08	5.53	0.79	↑##	↓	—
5	13.17	381.37	C25H50O2	Pentacosanoic acid	1.07	0.53	0.79	↓##	↓	—
6	7.70	400.34	C23H45NO4	L-Palmitoylcarnitine	1.07	2.09	0.76	↑##	↓*	—
7	0.90	132.08	C4H9N3O2	Creatine	1.07	0.68	1.32	↓##	↑**	b
8	0.86	162.11	C7H15NO3	L-Carnitine	1.06	0.70	1.27	↓##	↑	—
9	0.86	126.02	C2H7NO3S	Taurine	1.06	0.66	1.29	↓##	↑	d
10	9.10	524.37	C26H54NO7P	LysoPC(18:0)	1.03	1.26	0.79	↑##	↓**	a
11	13.08	786.60	C44H84NO8P	PC (18:0/18:2 (9Z,12Z))	1.04	0.72	1.33	↓#	↑*	a, c, e, f
12	9.03	327.23	C22H32O2	Docosahexaenoic acid	1.06	0.66	1.34	↓##	↑**	—
13	12.24	746.57	C41H80NO8P	PE (18:0/18:1 (9Z))	1.05	1.68	0.69	↑##	↓**	a
14	0.90	116.07	C5H9NO2	L-Proline	1.06	0.57	1.40	↓##	↑**	b
15	8.88	277.22	C18H30O2	Alpha-Linolenic acid	1.07	0.60	1.57	↓#	↑**	—
16	9.13	279.23	C18H32O2	Linoleic acid	1.08	0.76	1.29	↓#	↑*	f
17	8.80	438.30	C21H44NO6P	PE (P-16:0e/0:0)	1.09	1.73	0.73	↑##	↓**	—
18	11.58	365.34	C24H46O2	Nervonic acid	1.08	0.78	1.55	↓##	↑**	—
19	8.85	227.20	C14H28O2	Myristic acid	1.09	1.91	0.79	↑##	↓	—
20	9.09	303.23	C20H32O2	Arachidonic acid	1.11	2.09	0.77	↑##	↓**	c
21	9.45	281.25	C18H34O2	Oleic acid	1.44	1.44	0.73	↑##	↓**	e
22	11.03	704.52	C38H74NO8P	PC (16:1 (9Z)/14:0)	1.43	0.58	1.29	↓#	↑*	—
23	9.62	307.26	C20H36O2	Eicosadienoic acid	1.65	4.27	0.54	↑##	↓**	—
24	9.47	331.26	C22H36O2	Adrenic acid	1.65	4.58	0.74	↑##	↓	—

Control, model, and geniposide groups (n = 6 per group). $^{\#}p < 0.05$ *and* $^{\#\#}p < 0.01$, *Model group* vs. *Control group;* $^{*}p < 0.05$ *and* $^{**}p < 0.01$, *Geniposide group* vs. *Model group. (a) Glycerophospholipid metabolism, (b) Arginine and proline metabolism, (c) AA metabolism, (d) Taurine and hypotaurine metabolism, (e) alpha-Linolenic acid metabolism, and (f) Linoleic acid metabolism.*

expression in the Bax/Bcl-2 dimer increases, it will activate Caspase-9, and Caspase-9 will activate Caspase-3 *via* enzyme digestion. This will promote the cleavage of Caspase-3, beginning the apoptosis cascade reaction and resulting in apoptosis (Zhu et al., 2012; Perumal et al., 2018).

According to untargeted metabolomics, the metabolic profiles of the control group, the model group, and the geniposide group all differed, suggesting that geniposide affects the metabolic profiles of model mice with liver fibrosis induced by CCl_4. Recently, the metabolic regulatory effect of geniposide on liver disease models is becoming a hot spot. *In vivo* study showed that geniposide could regulate the interconversion of pentose and glucuronate and the biosynthesis of primary bile acid in jaundice model mice (Fang et al., 2020). Moreover, integrated miRNAomics, proteomics and metabolomics analysis found that geniposide could upregulate the protein levels of isocitrate dehydrogenase (IDH) 1 and 2 through downregulating the expression of miR-144-5p and then modulate energy metabolism in ethanol-induced apoptosis hepatocyte model *in vitro* (Qiu et al., 2017). Lipid peroxidation induced by CCl_4 treatment can alter the permeability of the cell membrane, resulting in damage to the intracellular organelle membrane structures, such as mitochondria, endoplasmic reticulum, and Golgi apparatus, etc., which further triggers the metabolic disorders in hepatocytes (Abdou et al., 2019). Untargeted metabolomics were used to analyze the metabolic regulatory effects of geniposide on CCl_4-induced liver fibrosis model. Our study found that glycerophospholipid metabolism, arginine and proline metabolism, and AA metabolism all changed between the control and model groups and between the model and geniposide groups. These results suggest that geniposide could improve liver fibrosis by regulating glycerophospholipid metabolism, arginine and proline metabolism, and AA metabolism.

Glycerophospholipid Metabolism

Glycerophospholipid is an important component of biofilm. Its metabolism is involved in many biological processes, such as membrane fusion, endocytosis, and membrane transport. Metabolism disorders related to glycerophospholipid can adversely affect the metabolism of the liver (Xue et al., 2020). The results of our metabolomic analysis indicated that PC decreased and Lyso PC and PE both increased in model mice with liver fibrosis, and that PC levels increased and Lyso PC and PE decreased following geniposide treatment. PC accounts for 40–50% of total glycerophospholipids, is the most abundant glycerophospholipids found in mammalian cells (Zhang et al., 2016). PC can promote collagenase activity, hydrolyze collagenated fibers, and alleviate liver fibrosis (Chen et al., 2016). PC has also demonstrated an anti-oxidative effect. PC can stop active free radicals from attacking the liver cell membrane and decrease stellate cell activity in the liver (Shmarakov et al., 2019). PE accounts for 40% of total glycerophospholipids, and primarily exists in the mitochondrial membrane (Rashid et al., 2020). PE is closely associated with cell proliferation and differentiation, and could

trigger apoptosis (Xue et al., 2014). A decrease in the PC/PE ratio can destroy the integrity of the hepatocyte and mitochondrial membrane and affect cell growth and induce apoptosis (Li, et al., 2006). Lyso PC could bind to the G protein-coupled receptor and the Toll-like receptor, promoting macrophage migration, stimulating the production of inflammatory factors, and inducing oxidative stress and apoptosis (Kabarowski et al., 2001; Chang et al., 2008; Kim et al., 2009; Bach et al., 2010; Song et al., 2010; Carneiro et al., 2013). Lyso PC exacerbated inflammation and promoted the development of liver fibrosis (Liu et al., 2020).

AA Metabolism

AA metabolism is a significant factor in inflammation (Gai et al., 2018; Sonnweber et al., 2018; Melgar-Lesmes et al., 2019). The results of our experiment demonstrated that AA content in the model group increased compared with the control group, a trend that decreased following geniposide treatment. AA metabolites include a series of prostaglandins and leukotrienes, which are highly active inflammatory mediators and can promote the infiltration and activation of inflammatory cells in the liver tissue, leading to the degeneration and necrosis of hepatocytes (Cardoso et al., 2003). AA not only plays a key role in inflammation, but also mediates the production of oxygen free radicals and membrane lipid peroxidation as a lipid medium. AA significantly increases the production of reactive oxygen species, which results in the oxidation of a large number of fatty acids and the formation of lipid peroxides in mitochondria, peroxisomes, endoplasmic reticulum, and other parts of hepatocytes. This can lead to oxidative stress and hepatocyte injury, hepatic stellate cells activation, and collagen deposition in liver (Moreno, 2003; Koek et al., 2011; Fujii and Kawada, 2012). Therefore, the effects of geniposide on inflammation and oxidative stress may be associated with modulating AA metabolism.

Arginine and Proline Metabolism

The arginine and proline metabolism pathway was closely linked to the progression of liver fibrosis. In model mice with liver fibrosis, we found that L-Proline and creatine in the arginine and proline metabolism pathway significantly increased, but decreased following geniposide treatment. Arginine is the largest nitrogen-supplying amino acid in the human body and is the precursor of proline and creatine (Ge et al., 2020). Proline plays a central role in metabolism, which is closely associated with oxidative stress and apoptosis (Pandhare et al., 2006). Proline can metabolize and produce electrons, and generate reactive oxygen species, leading to a variety of downstream effects, including blocking cell cycles, autophagy, and apoptosis (Selen et al., 2015). Creatine can alleviate liver injuries by inhibiting liver inflammation, oxidative stress, and cell senescence (Deminice et al., 2016; Aljobaily et al., 2020). Creatine can also reduce the consumption of adenosylmethionine and the production of homocysteine in the liver, lowering the damage to homocysteine metabolism in the liver and the accumulation of lipids (Barcelos et al., 2016).

CONCLUSION AND FUTURE PROSPECTIVE

In conclusion, our study demonstrated that geniposide could exhibit protective effects on liver fibrosis. This study is the first to screen the differential metabolites of geniposide on CCl4-induced liver fibrosis model. Our results further refine the metabolic regulatory effects of geniposide on liver diseases. The mechanism behind these protective effects could be related to inhibiting oxidative stress, inflammatory response, and apoptosis in the liver and modulating glycophorophospholipid, arginine and proline, and AA metabolism possesses.

DATA AVAILABILITY STATEMENT

The original contributions presented in the study are included in the article/**Supplementary Material**, further inquiries can be directed to the corresponding authors.

ETHICS STATEMENT

The animal study was reviewed and approved by the animal study was reviewed and approved by Animal Ethics Committee at Nankai University (2021-SYDWLL-000038).

AUTHOR CONTRIBUTIONS

LY carried out the experiments and manuscript writing. LY, LB, LJ, YW, and YL provided experimental help, and performed data analysis and result interpretation. ZL and WH finished molecular bioassays. HC, JM, and LW provided ideas and technical guidance for the whole work. All authors contributed to the article and approved the submitted version.

FUNDING

This work was supported by the National Natural Science Foundation of China (Nos 81703921 and 81973800), Science and Technology Projects in Key Fields of Traditional Chinese Medicine of Tianjin Municipal Health Commission (No. 2020006), Chunmiao Project of Tianjin First Central Hospital (No. 2019CM15), Tianjin Medical Key Construction Discipline Fund Project (No. 2021-492), the Key Research Project of Traditional Chinese Medicine of Tianjin Municipal Health Commission (202006).

SUPPLEMENTARY MATERIAL

The Supplementary Material for this article can be found online at: https://www.frontiersin.org/articles/10.3389/fphar.2021.772635/full#supplementary-material

REFERENCES

Abdou, E. M., Fayed, M. A. A., Helal, D., and Ahmed, K. A. (2019). Assessment of the Hepatoprotective Effect of Developed Lipid-Polymer Hybrid Nanoparticles (LPHNPs) Encapsulating Naturally Extracted β-Sitosterol against CCl4 Induced Hepatotoxicity in Rats. *Sci. Rep.* 9, 19779. doi:10.1038/s41598-019-56320-2

Aldahmash, B. A., and El-Nagar, D. M. (2016). Antioxidant Effects of Captopril against lead Acetate-Induced Hepatic and Splenic Tissue Toxicity in Swiss Albino Mice. *Saudi J. Biol. Sci.* 23, 667–673. doi:10.1016/j.sjbs.2016.05.005

Aljobaily, N., Viereckl, M. J., Hydock, D. S., Aljobaily, H., Wu, T.-Y., Busekrus, R., et al. (2020). Creatine Alleviates Doxorubicin-Induced Liver Damage by Inhibiting Liver Fibrosis, Inflammation, Oxidative Stress, and Cellular Senescence. *Nutrients* 13, 41. doi:10.3390/nu13010041

Bach, G., Perrin-Cocon, L., Gerossier, E., Guironnet-Paquet, A., Lotteau, V., Inchauspé, G., et al. (2010). Single Lysophosphatidylcholine Components Exhibit Adjuvant Activities *In Vitro* and *In Vivo*. *Clin. Vaccin. Immunol.* 17, 429–438. doi:10.1128/CVI.00420-09

Barcelos, R. P., Stefanello, S. T., Mauriz, J. L., Gonzalez-Gallego, J., and Soares, F. A. (2016). Creatine and the Liver: Metabolism and Possible Interactions. *Mini Rev. Med. Chem.* 16, 12–18. doi:10.2174/1389557515666150722102613

Cardoso, C. C., Paviani, E. R., Cruz, L. A., Guma, F. C., Borojevic, R., and Guaragna, R. M. (2003). Effect of Pentoxifylline on Arachidonic Acid Metabolism, Neutral Lipid Synthesis and Accumulation during Induction of the Lipocyte Phenotype by Retinol in Murine Hepatic Stellate Cell. *Mol. Cel Biochem.* 254, 37–46. doi:10.1023/a:1027356412399

Carneiro, A. B., Iaciura, B. M., Nohara, L. L., Lopes, C. D., Veas, E. M., Mariano, V. S., et al. (2013). Lysophosphatidylcholine Triggers TLR2- and TLR4-Mediated Signaling Pathways but Counteracts LPS-Induced NO Synthesis in Peritoneal Macrophages by Inhibiting NF-κB Translocation and MAPK/ERK Phosphorylation. *PLoS One* 8, e76233. doi:10.1371/journal.pone.0076233

Chang, D. H., Deng, H., Matthews, P., Krasovsky, J., Ragupathi, G., Spisek, R., et al. (2008). Inflammation-associated Lysophospholipids as Ligands for CD1d-Restricted T Cells in Human Cancer. *Blood* 112, 1308–1316. doi:10.1182/blood-2008-04-149831

Chen, P., Chen, Y., Wang, Y., Cai, S., Deng, L., Liu, J., et al. (2016). Comparative Evaluation of Hepatoprotective Activities of Geniposide, Crocins and Crocetin by CCl4-Induced Liver Injury in Mice. *Biomol. Ther. (Seoul)* 24, 156–162. doi:10.4062/biomolther.2015.094

Chen, X., Liu, A. Q., Wang, Y. M., Yang, L., Jin, L. L., Cui, H. T., et al. (2021). Liver Fibrosis in Mice Treated with Yue-Ju-Bao-He Pills. *TMR Pharmacol. Res.* 1, 2. doi:10.12032/TMRPR20210217002

Choi, W.-M., Choi, J., and Lim, Y.-S. (2021). Effects of Tenofovir vs Entecavir on Risk of Hepatocellular Carcinoma in Patients with Chronic HBV Infection: A Systematic Review and Meta-Analysis. *Clin. Gastroenterol. Hepatol.* 19, 246–258. doi:10.1016/j.cgh.2020.05.008

Cui, H., Li, Y., Cao, M., Liao, J., Liu, X., Miao, J., et al. (2020). Untargeted Metabolomic Analysis of the Effects and Mechanism of Nuciferine Treatment on Rats with Nonalcoholic Fatty Liver Disease. *Front. Pharmacol.* 11, 858. doi:10.3389/fphar.2020.00858

Cui, H., Yang, L., Li, Y., and Wang, H. (2021). Omics Technology: an Important Tool in Mechanism Studies of Chinese Herbal Formulas. *Tradit. Med. Res.* 6, 2. doi:10.53388/tmr20200920199

Deminice, R., Cella, P. S., Padilha, C. S., Borges, F. H., da Silva, L. E., Campos-Ferraz, P. L., et al. (2016). Creatine Supplementation Prevents Hyperhomocysteinemia, Oxidative Stress and Cancer-Induced Cachexia Progression in Walker-256 Tumor-Bearing Rats. *Amino Acids* 48, 2015–2024. doi:10.1007/s00726-016-2172-9

El-Din, S. H., Sabra, A. N., Hammam, O. A., Ebeid, F. A., and El-Lakkany, N. M. (2014). Pharmacological and Antioxidant Actions of Garlic and.or Onion in Non-alcoholic Fatty Liver Disease (NAFLD) in Rats. *J. Egypt. Soc. Parasitol.* 44, 295–308. doi:10.12816/0006468

Fang, H., Zhang, A., Zhou, X., Yu, J., Song, Q., and Wang, X. (2020). High-throughput Metabolomics Reveals the Perturbed Metabolic Pathways and Biomarkers of Yang Huang Syndrome as Potential Targets for Evaluating the Therapeutic Effects and Mechanism of Geniposide. *Front. Med.* 14, 651–663. doi:10.1007/s11684-019-0709-5

Forbes-Hernández, T. Y., Gasparrini, M., Afrin, S., Cianciosi, D., González-Paramás, A. M., Santos-Buelga, C., et al. (2017). Strawberry (Cv. Romina) Methanolic Extract and Anthocyanin-Enriched Fraction Improve Lipid Profile and Antioxidant Status in HepG2 Cells. *Int. J. Mol. Sci.* 18, 1149. doi:10.3390/ijms18061149

Fujii, H., and Kawada, N. (2012). Inflammation and Fibrogenesis in Steatohepatitis. *J. Gastroenterol.* 47, 215–225. doi:10.1007/s00535-012-0527-x

Gai, Z., Visentin, M., Gui, T., Zhao, L., Thasler, W. E., Häusler, S., et al. (2018). Effects of Farnesoid X Receptor Activation on Arachidonic Acid Metabolism, NF-kB Signaling, and Hepatic Inflammation. *Mol. Pharmacol.* 94, 802–811. doi:10.1124/mol.117.111047

Ge, S., Zhang, Q., Tian, Y., Hao, L., Duan, J., and Zhang, B. (2020). Cell Metabolic Profiling of Colorectal Cancer via 1H NMR. *Clin. Chim. Acta* 510, 291–297. doi:10.1016/j.cca.2020.07.039

Goodla, L., Manubolu, M., Pathakoti, K., Jayakumar, T., Sheu, J. R., Fraker, M., et al. (2019). Protective Effects of Ammannia Baccifera against CCl4-Induced Oxidative Stress in Rats. *Int. J. Environ. Res. Public Health* 16, 1440. doi:10.3390/ijerph16081440

Häcker, G., and Paschen, S. A. (2007). Therapeutic Targets in the Mitochondrial Apoptotic Pathway. *Expert Opin. Ther. Targets* 11, 515–526. doi:10.1517/14728222.11.4.515

Han, J., Bae, J., Choi, C. Y., Choi, S. P., Kang, H. S., Jo, E. K., et al. (2016). Autophagy Induced by AXL Receptor Tyrosine Kinase Alleviates Acute Liver Injury via Inhibition of NLRP3 Inflammasome Activation in Mice. *Autophagy* 12, 2326–2343. doi:10.1080/15548627.2016.1235124

Hermenean, A., Popescu, C., Ardelean, A., Stan, M., Hadaruga, N., Mihali, C. V., et al. (2012). Hepatoprotective Effects of Berberis Vulgaris L. Extract/β Cyclodextrin on Carbon Tetrachloride-Induced Acute Toxicity in Mice. *Int. J. Mol. Sci.* 13, 9014–9034. doi:10.3390/ijms13079014

Huang, Y. L., Zhang, F. L., Tang, X. L., and Yang, X. J. (2021). Telocytes Enhances M1 Differentiation and Phagocytosis while Inhibits Mitochondria-Mediated Apoptosis via Activation of NF-κB in Macrophages. *Cel Transpl.* 30, 9636897211002762. doi:10.1177/09636897211002762

Hwang-Bo, H., Lee, W. S., Nagappan, A., Kim, H. J., Panchanathan, R., Park, C., et al. (2019). Morin Enhances Auranofin Anticancer Activity by Up-Regulation of DR4 and DR5 and Modulation of Bcl-2 through Reactive Oxygen Species Generation in Hep3B Human Hepatocellular Carcinoma Cells. *Phytother. Res.* 33, 1384–1393. doi:10.1002/ptr.6329

Jaeschke, H. (2006). Mechanisms of Liver Injury. II. Mechanisms of Neutrophil-Induced Liver Cell Injury during Hepatic Ischemia-Reperfusion and Other Acute Inflammatory Conditions. *Am. J. Physiol. Gastrointest. Liver Physiol.* 290, G1083–G1088. doi:10.1152/ajpgi.00568.2005

Kabarowski, J. H., Zhu, K., Le, L. Q., Witte, O. N., and Xu, Y. (2001). Lysophosphatidylcholine as a Ligand for the Immunoregulatory Receptor G2A. *Science* 293, 702–705. doi:10.1126/science.1061781

Ki, S. H., Yang, J. H., Ku, S. K., Kim, S. C., Kim, Y. W., and Cho, I. J. (2013). Red Ginseng Extract Protects against Carbon Tetrachloride-Induced Liver Fibrosis. *J. Ginseng Res.* 37, 45–53. doi:10.5142/jgr.2013.37.45

Kim, E. A., Kim, J. A., Park, M. H., Jung, S. C., Suh, S. H., Pang, M. G., et al. (2009). Lysophosphatidylcholine Induces Endothelial Cell Injury by Nitric Oxide Production through Oxidative Stress. *J. Matern. Fetal. Neonatal. Med.* 22, 325–331. doi:10.1080/14767050802556075

Klopfleisch, R. (2013). Multiparametric and Semiquantitative Scoring Systems for the Evaluation of Mouse Model Histopathology-Aa Systematic Review. *BMC Vet. Res.* 9, 123. doi:10.1186/1746-6148-9-123

Koek, G. H., Liedorp, P. R., and Bast, A. (2011). The Role of Oxidative Stress in Non-Alcoholic Steatohepatitis. *Clin Chim Acta.* 412, 1297–1305. doi:10.1016/j.cca.2011.04.013

Lee, H. S., Son, W. C., Ryu, J. E., Koo, B. A., and Kim, Y. S. (2014). Standardized Salvia Miltiorrhiza Extract Suppresses Hepatic Stellate Cell Activation and Attenuates Steatohepatitis Induced by a Methionine-Choline Deficient Diet in Mice. *Molecules* 19, 8189–8211. doi:10.3390/molecules19068189

Li, Z., Agellon, L. B., Allen, T. M., Umeda, M., Jewell, L., Mason, A., et al. (2006). The Ratio of Phosphatidylcholine to Phosphatidylethanolamine Influences Membrane Integrity and Steatohepatitis. *Cell Metab.* 3, 321–331. doi:10.1016/j.cmet.2006.03.007

Liang, Y. H., Tang, C. L., Lu, S. Y., Cheng, B., Wu, F., Chen, Z. N., et al. (2016). Serum Metabonomics Study of the Hepatoprotective Effect of Corydalis Saxicola Bunting on Carbon Tetrachloride-Induced Acute Hepatotoxicity in Rats by (1)H NMR Analysis. *J. Pharm. Biomed. Anal.* 129, 70–79. doi:10.1016/j.jpba.2016.06.033

Liang, Y., Niu, Q., and Zhao, Y. (2021). Pharmacological Research Progress of Ursolic Acid for the Treatment of Liver Diseases. *Tradit. Med. Res.* 6, 38. doi:10.12032/TMR20210331227

Liaw, Y. F. (2013). Reversal of Cirrhosis: an Achievable Goal of Hepatitis B Antiviral Therapy. *J. Hepatol.* 59, 880–881. doi:10.1016/j.jhep.2013.05.007

Lin, W., Wang, W., Liao, D., Chen, D., Zhu, P., Cai, G., et al. (2015). Polysaccharides from Enteromorpha Prolifera Improve Glucose Metabolism in Diabetic Rats. *J. Diabetes Res.* 2015, 675201. doi:10.1155/2015/675201

Lin, X., Li, J., and Xing, Y. Q. (2019). Geniposide, a Sonic Hedgehog Signaling Inhibitor, Inhibits the Activation of Hepatic Stellate Cell. *Int. Immunopharmacol.* 72, 330–338. doi:10.1016/j.intimp.2019.04.016

Liu, X. W., Tang, C. L., Zheng, H., Wu, J. X., Wu, F., Mo, Y. Y., et al. (2018). Investigation of the Hepatoprotective Effect of Corydalis Saxicola Bunting on Carbon Tetrachloride-Induced Liver Fibrosis in Rats by 1H-NMR-Based Metabonomics and Network Pharmacology Approaches. *J. Pharm. Biomed. Anal.* 159, 252–261. doi:10.1016/j.jpba.2018.06.065

Liu, P., Zhu, W., Chen, C., Yan, B., Zhu, L., Chen, X., et al. (2020). The Mechanisms of Lysophosphatidylcholine in the Development of Diseases. *Life Sci.* 247, 117443. doi:10.1016/j.lfs.2020.117443

Ma, Z. G., Kong, C. Y., Song, P., Zhang, X., Yuan, Y. P., and Tang, Q. Z. (2018). Geniposide Protects against Obesity-Related Cardiac Injury through AMPKα- and Sirt1-dependent Mechanisms. *Oxid. Med. Cel Longev.* 2018, 6053727. doi:10.1155/2018/6053727

Mekky, R. H., Fayed, M. R., El-Gindi, M. R., Abdel-Monem, A. R., Contreras, M. D., Segura-Carretero, A., et al. (2016). Hepatoprotective Effect and Chemical Assessment of a Selected Egyptian Chickpea Cultivar. *Front. Pharmacol.* 7, 344. doi:10.3389/fphar.2016.00344

Melgar-Lesmes, P., Perramon, M., and Jiménez, W. (2019). Roles of the Hepatic Endocannabinoid and Apelin Systems in the Pathogenesis of Liver Fibrosis. *Cells* 8, 1311. doi:10.3390/cells8111311

Moldoveanu, T., Follis, A. V., Kriwacki, R. W., and Green, D. R. (2014). Many Players in BCL-2 Family Affairs. *Trends Biochem. Sci.* 39, 101–111. doi:10.1016/j.tibs.2013.12.006

Moreno, J. J. (2003). Effect of Olive Oil Minor Components on Oxidative Stress and Arachidonic Acid Mobilization and Metabolism by Macrophages RAW 264.7. *Free Radic. Biol. Med.* 35, 1073–1081. doi:10.1016/s0891-5849(03)00465-9

Pandhare, J., Cooper, S. K., and Phang, J. M. (2006). Proline Oxidase, a Proapoptotic Gene, Is Induced by Troglitazone: Evidence for Both Peroxisome Proliferator-Activated Receptor Gamma-dependent and -independent Mechanisms. *J. Biol. Chem.* 281, 2044–2052. doi:10.1074/jbc.M507867200

Park, J. H., Yoon, J., Lee, K. Y., and Park, B. (2015). Effects of Geniposide on Hepatocytes Undergoing Epithelial-Mesenchymal Transition in Hepatic Fibrosis by Targeting TGFβ/Smad and ERK-MAPK Signaling Pathways. *Biochimie* 113, 26–34. doi:10.1016/j.biochi.2015.03.015

Perumal, S., Langeshwaran, K., Selvaraj, J., Ponnulakshmi, R., Shyamaladevi, B., and Balasubramanian, M. P. (2018). Effect of Diosmin on Apoptotic Signaling Molecules in N-Nitrosodiethylamine-Induced Hepatocellular Carcinoma in Experimental Rats. *Mol. Cel Biochem.* 449, 27–37. doi:10.1007/s11010-018-3339-3

Qiao, J. B., Fan, Q. Q., Zhang, C. L., Lee, J., Byun, J., Xing, L., et al. (2020). Hyperbranched Lipoid-Based Lipid Nanoparticles for Bidirectional Regulation of Collagen Accumulation in Liver Fibrosis. *J. Control. Release* 321, 629–640. doi:10.1016/j.jconrel.2020.02.049

Qiu, S., Zhang, A., Zhang, T., Sun, H., Guan, Y., Yan, G., et al. (2017). Dissect New Mechanistic Insights for Geniposide Efficacy on the Hepatoprotection Using Multiomics Approach. *Oncotarget* 8, 108760–108770. doi:10.18632/oncotarget.21897

Rashid, M. M., Lee, H., and Jung, B. H. (2020). Evaluation of the Antitumor Effects of PP242 in a colon Cancer Xenograft Mouse Model Using Comprehensive Metabolomics and Lipidomics. *Sci. Rep.* 10, 17523. doi:10.1038/s41598-020-73721-w

Selen, E. S., Bolandnazar, Z., Tonelli, M., Bütz, D. E., Haviland, J. A., Porter, W. P., et al. (2015). NMR Metabolomics Show Evidence for Mitochondrial Oxidative Stress in a Mouse Model of Polycystic Ovary Syndrome. *J. Proteome Res.* 14, 3284–3291. doi:10.1021/acs.jproteome.5b00307

Shi, Z., Li, T., Liu, Y., Cai, T., Yao, W., Jiang, J., et al. (2020). Hepatoprotective and Anti-Oxidative Effects of Total Flavonoids from Qu Zhi Qiao (Fruit of Citrus Paradisi cv.Changshanhuyou) on Nonalcoholic Steatohepatitis *In Vivo* and *In Vitro* through Nrf2-ARE Signaling Pathway. *Front. Pharmacol.* 11, 483. doi:10.3389/fphar.2020.00483

Shmarakov, I. O., Jiang, H., Liu, J., Fernandez, E. J., and Blaner, W. S. (2019). Hepatic Stellate Cell Activation: A Source for Bioactive Lipids. *Biochim. Biophys. Acta Mol. Cel Biol. Lipids* 1864, 629–642. doi:10.1016/j.bbalip.2019.02.004

Song, J., Liu, K., Yi, J., Zhu, D., Liu, G., and Liu, B. (2010). Luteolin Inhibits Lysophosphatidylcholine-Induced Apoptosis in Endothelial Cells by a Calcium/mitocondrion/caspases-dependent Pathway. *Planta Med.* 76, 433–438. doi:10.1055/s-0029-1186197

Song, Y. N., Dong, S., Wei, B., Liu, P., Zhang, Y. Y., and Su, S. B. (2017). Metabolomic Mechanisms of Gypenoside against Liver Fibrosis in Rats: An Integrative Analysis of Proteomics and Metabolomics Data. *PLoS One* 12, e0173598. doi:10.1371/journal.pone.0173598

Sonnweber, T., Pizzini, A., Nairz, M., Weiss, G., and Tancevski, I. (2018). Arachidonic Acid Metabolites in Cardiovascular and Metabolic Diseases. *Int. J. Mol. Sci.* 19, 3285. doi:10.3390/ijms19113285

Sun, J., Wu, Y., Long, C., He, P., Gu, J., Yang, L., et al. (2018). Anthocyanins Isolated from Blueberry Ameliorates CCl4 Induced Liver Fibrosis by Modulation of Oxidative Stress, Inflammation and Stellate Cell Activation in Mice. *Food Chem. Toxicol.* 120, 491–499. doi:10.1016/j.fct.2018.07.048

Tait, S. W., and Green, D. R. (2010). Mitochondria and Cell Death: Outer Membrane Permeabilization and beyond. *Nat. Rev. Mol. Cel Biol.* 11, 621–632. doi:10.1038/nrm2952

Tian, X., Zeng, G., Li, X., Wu, Z., and Wang, L. (2015). Cantharidin Inhibits Cell Proliferation and Promotes Apoptosis in Tongue Squamous Cell Carcinoma through Suppression of miR-214 and Regulation of P53 and Bcl-2/Bax. *Oncol. Rep.* 33, 3061–3068. doi:10.3892/or.2015.3942

Wang, M., Niu, J., Ou, L., Deng, B., Wang, Y., and Li, S. (2019). Zerumbone Protects against Carbon Tetrachloride (CCl4)-Induced Acute Liver Injury in Mice via Inhibiting Oxidative Stress and the Inflammatory Response: Involving the TLR4/NF-κB/COX-2 Pathway. *Molecules* 24, 1964. doi:10.3390/molecules24101964

Wang, L., Cui, H., Li, Y., Cao, M., Man, S., Guo, L., et al. (2020). Kang-Xian Pills Inhibit Inflammatory Response and Decrease Gut Permeability to Treat Carbon Tetrachloride-Induced Chronic Hepatic Injury through Modulating Gut Microbiota. *Evid. Based Complement. Alternat. Med.* 2020, 8890182. doi:10.1155/2020/8890182

Wen, M., Liu, Y., Chen, R., He, P., Wu, F., Li, R., et al. (2021). Geniposide Suppresses Liver Injury in a Mouse Model of DDC-Induced Sclerosing Cholangitis. *Phytother. Res.* 35, 3799–3811. doi:10.1002/ptr.7086

Xue, L., Li, M., Chen, T., Sun, H., Zhu, J., Li, X., et al. (2014). PE-induced A-poptosis in SMMC-7721 C-ells: I-nvolvement of Erk and Stat S-ignalling P-athways. *Int. J. Mol. Med.* 34, 119–129. doi:10.3892/ijmm.2014.1777

Xue, L. J., Han, J. Q., Zhou, Y. C., Peng, H. Y., Yin, T. F., Li, K. M., et al. (2020). Untargeted Metabolomics Characteristics of Nonobese Nonalcoholic Fatty Liver Disease Induced by High-Temperature-Processed Feed in Sprague-Dawley Rats. *World J. Gastroenterol.* 26, 7299–7311. doi:10.3748/wjg.v26.i46.7299

Liu, Y., Li, J., Jin, Y., Zhao, L., Zhao, F., Feng, J., et al. (2018). Splenectomy Leads to Amelioration of Altered Gut Microbiota and Metabolome in Liver Cirrhosis Patients. *Front. Microbiol.* 9, 963. doi:10.3389/fmicb.2018.00963

Yang, L., Liao, J., Liu, A., Chen, X., Qu, F., Cui, H., et al. (2021). Advances in Traditional Chinese Medicine for Liver Disease Therapy in 2020. *Tradit. Med. Res.* 6, 30. doi:10.53388/tmr20210316225

Yoo, H. J., Jung, K. J., Kim, M., Kim, M., Kang, M., Jee, S. H., et al. (2019). Liver Cirrhosis Patients Who Had Normal Liver Function before Liver Cirrhosis Development Have the Altered Metabolic Profiles before the Disease Occurrence Compared to Healthy Controls. *Front. Physiol.* 10, 1421. doi:10.3389/fphys.2019.01421

Yuan, J., Zhang, J., Cao, J., Wang, G., and Bai, H. (2020). Geniposide Alleviates Traumatic Brain Injury in Rats via Anti-inflammatory Effect and MAPK/NF-

kB Inhibition. *Cell Mol. Neurobiol.* 40, 511–520. doi:10.1007/s10571-019-00749-6

Zhang, Z., Gao, W., Wang, X., Zhang, D., and Li, L. (2020). Geniposide Effectively Reverses Cognitive Impairment and Inhibits Pathological Cerebral Damage by Regulating the mTOR Signal Pathway in APP/PS1 Mice. *Neurosci. Lett.* 720, 134749. doi:10.1016/j.neulet.2020.134749

Zhang, M., Zheng, J., Nussinov, R., and Ma, B. (2016). Oncogenic Mutations Differentially Affect Bax Monomer, Dimer, and Oligomeric Pore Formation in the Membrane. *Sci. Rep.* 6, 33340. doi:10.1038/srep33340

Zhang, Y., Zhang, M., Li, H., Zhao, H., Wang, F., He, Q., et al. (2018). Serum Metabonomics Study of the Hepatoprotective Effect of Amarogentin on CCl4-Induced Liver Fibrosis in Mice by GC-TOF-MS Analysis. *J. Pharm. Biomed. Anal.* 149, 120–127. doi:10.1016/j.jpba.2017.10.029

Zhao, T., Fu, Y., Sun, H., and Liu, X. (2018). Ligustrazine Suppresses Neuron Apoptosis via the Bax/Bcl-2 and Caspase-3 Pathway in PC12 Cells and in Rats with Vascular Dementia. *IUBMB Life* 70, 60–70. doi:10.1002/iub.1704

Zhu, L., Yuan, H., Guo, C., Lu, Y., Deng, S., Yang, Y., et al. (2012). Zearalenone Induces Apoptosis and Necrosis in Porcine Granulosa Cells via a Caspase-3- and Caspase-9-dependent Mitochondrial Signaling Pathway. *J. Cel Physiol.* 227, 1814–1820. doi:10.1002/jcp.22906

Zhu, B., Li, Y., Hu, T., and Zhang, Y. (2019). The Hepatoprotective Effect of Polysaccharides from Pleurotus Ostreatus on Carbon Tetrachloride-Induced Acute Liver Injury Rats. *Int. J. Biol. Macromol.* 131, 1–9. doi:10.1016/j.ijbiomac.2019.03.043

Zhu, Y., Liu, C., Chen, X., Lu, S., and Chen, J. (2020). Hepatoprotective Effects and Mechanisms of Ixeris Denticulate Water Extract on Liver Cirrhosis in Experimental Rat. *BMC Complement. Med. Ther.* 20, 175. doi:10.1186/s12906-020-02957-w

Conflict of Interest: The authors declare that the research was conducted in the absence of any commercial or financial relationships that could be construed as a potential conflict of interest.

Publisher's Note: All claims expressed in this article are solely those of the authors and do not necessarily represent those of their affiliated organizations, or those of the publisher, the editors and the reviewers. Any product that may be evaluated in this article, or claim that may be made by its manufacturer, is not guaranteed or endorsed by the publisher.

frontiers in Pharmacology

ORIGINAL RESEARCH
published: 15 December 2021
doi: 10.3389/fphar.2021.766120

Rheum tanguticum Alleviates Cognitive Impairment in APP/PS1 Mice by Regulating Drug-Responsive Bacteria and Their Corresponding Microbial Metabolites

*Demin Gao†, Huizhen Zhao†, Zhihui Yin, Chen Han, Ying Wang, Gan Luo and Xiaoyan Gao**

School of Chinese Materia Medica, Beijing University of Chinese Medicine, Beijing, China

Drugs targeting intestinal bacteria have shown great efficacy for alleviating symptoms of Alzheimer's disease (AD), and microbial metabolites are important messengers. Our previous work indicated that *Rheum tanguticum* effectively improved cognitive function and reshaped the gut microbial homeostasis in AD rats. However, its therapeutic mechanisms remain unclear. Herein, this study aimed to elaborate the mechanisms of rhubarb for the treatment of AD by identifying effective metabolites associated with rhubarb-responsive bacteria. The results found that rhubarb reduced hippocampal inflammation and neuronal damage in APP/PS1 transgenic (Tg) mice. 16S rRNA sequencing and metabolomic analysis revealed that gut microbiota and their metabolism in Tg mice were disturbed in an age-dependent manner. Rhubarb-responsive bacteria were further identified by real-time polymerase chain reaction (RT-PCR) sequencing. Four different metabolites reversed by rhubarb were found in the position of the important nodes on rhubarb-responsive bacteria and their corresponding metabolites combined with pathological indicators co-network. Furthermore, *in vitro* experiments demonstrated *o*-tyrosine not only inhibited the viabilities of primary neurons as well as BV-2 cells, but also increased the levels of intracellular reactive oxygen species and nitric oxide. In the end, the results suggest that rhubarb ameliorates cognitive impairment in Tg mice through decreasing the abundance of *o*-tyrosine in the gut owing to the regulation of rhubarb-responsive bacteria. Our study provides a promising strategy for elaborating therapeutic mechanisms of bacteria-targeted drugs for AD.

Keywords: Alzheimer's disease, rhubarb, gut microbiota, drug-responsive bacteria, *o*-tyrosine

OPEN ACCESS

Edited by:
Wenzhi Yang,
Tianjin University of Traditional Chinese Medicine, China

Reviewed by:
Qiao Wang,
Hebei Medical University, China
Feng-Qing Yang,
Chongqing University, China

****Correspondence:***
Xiaoyan Gao
gaoxiaoyan@bucm.edu.cn

†These authors have contributed equally to this work

Specialty section:
This article was submitted to Ethnopharmacology, a section of the journal Frontiers in Pharmacology

Received: *28 August 2021*
Accepted: *24 November 2021*
Published: *15 December 2021*

Citation:
Gao D, Zhao H, Yin Z, Han C, Wang Y, Luo G and Gao X (2021) Rheum tanguticum *Alleviates Cognitive Impairment in APP/PS1 Mice by Regulating Drug-Responsive Bacteria and Their Corresponding Microbial Metabolites. Front. Pharmacol. 12:766120. doi: 10.3389/fphar.2021.766120*

INTRODUCTION

Alzheimer's disease (AD) is a progressive neurodegenerative disease with high incidence, disability and death rates (Sierksma et al., 2020). Clinically, AD patients are characterized by age-dependent memory loss, cognitive dysfunction and behavior abnormality (Jack et al., 2018). It is widely believed that the pathological changes in the brains of AD patients belong to the accumulated amyloid-β (Aβ) induced oxidative stress and inflammatory responses in brain, causing oxidative damage and release

of pro-inflammatory mediators, finally neuronal apoptosis (Stepanichev et al., 2004; Pistollato et al., 2016; Wu Y. et al., 2019). Emerging evidence has shown that gut microbial dysbiosis may mediate the pathogenesis of AD (Minter et al., 2016; Liu P. et al., 2019; Wang et al., 2019). Therefore, remodeling gut microbial homeostasis may represent a more effective therapeutic strategy for the treatment of AD.

Traditional Chinese medicine (TCM) has aroused increasing attention on account of its therapeutic effects in the prevention and treatment of AD (Xu et al., 2017). Among them, rhubarb exhibits excellent therapeutic effect for AD by "tonify the body by removing stasis" and "relaxing bowels and puzzle" according to "brain collateral damage due to toxin" raised by theoretical system of TCM (Li et al., 2019). Our previous studies have suggested that *Rheum tanguticum* effectively improves cognitive function and reshapes the gut microbial homeostasis in AD animal models (Zhao et al., 2019). However, its therapeutic mechanisms remain unclear. Herein, considering the fact that a relatively low content of chemical ingredients in rhubarb permeated into the brain (Sun et al., 2012; Dong et al., 2016), we hypothesized that therapeutic effects of rhubarb may attribute to remodeling gut microbiota. Thus, it is of great significance to the elaborating therapeutic mechanism of rhubarb for AD from the view of gut microbiota (Mancuso and Santangelo, 2018).

Among the researches involved in interaction between gut and brain, a growing body of evidence suggests that microbial metabolites are important messengers of intestinal bacteria responsible for regulation of physiological state in brain, although the mechanisms of gut-brain transmission have so far remained elusive (Nicholson et al., 2012; Rothhammer et al., 2018). It has been found that harmful microbial metabolites, such as lipopolysaccharides (LPS) and Trimethylamine-*N*-oxide (Vogt et al., 2018), are easy to enter the brain and destroy its homeostasis, because intestinal leakage and permeability of BBB are significantly increased in AD patients (Kim et al., 2020). Accordingly, the regulation of gut microbiota-derived microbial metabolites is beneficial to alleviating symptoms of AD. Therefore, accurate identification of microbial metabolites associated with drug-responsive bacteria is crucial to elucidate the mechanisms of bacteria-targeted drugs for the treatment of AD.

In terms of the progression in a disease as well as drug intervention, metabolomics is a powerful tool for comprehensive discovery of the disturbed metabolites in a biological system (Matysik et al., 2016; Shaffer et al., 2017; Luan et al., 2019). However, it fails to distinguish the metabolites derived from drug-responsive bacteria. Because of the lack of direct identification methods, the alternative methods are diverse bacteria-based correlation analysis and co-network analysis combined with pathophysiological indicators (Feng et al., 2019; Zheng et al., 2020). Over the last decade, microbiome research based on amplicon sequencing, such as 16S rRNA, offers the global relative abundance of bacteria in different taxonomies (Gohl et al., 2016). However, comprehensive yet redundant data hinder accurate quantification of the drug-responsive bacteria. Given that relative abundance of bacteria could not reflect actual content of gut microbiota by 16S rRNA sequencing (Eisenstein, 2018; Tkacz et al., 2018), meanwhile, uncertainty exists in peak area of the fragment ions and their real content in biological samples by metabolomics analysis (Luan et al., 2019), there would be many false positives in identified microbial metabolites by 16S rRNA sequencing-based co-network analysis (Peisl et al., 2018). Thus, it always gives obscure explanation of the therapeutic mechanisms of bacteria-targeted drugs. Therefore, it is urgent to improve the accuracy of identification for microbial metabolites associated with drug-responsive bacteria.

In recent years, real-time polymerase chain reaction (RT-PCR) has been adopted for quantifying microbiota significantly disturbed between the health individuals and patients (Tettamanti Boshier et al., 2020). Based on the filtered specific intestinal bacteria in disease by 16S rRNA, RT-PCR as a complementary technology can obtain more precise drug-responsive bacteria by semi-quantitative comparative analysis between the treatment group and the disease group (Neyrinck et al., 2017; Xu et al., 2021). To some extent, the above-mentioned method can eliminate false positive bacteria and contribute to unravel therapeutic mechanisms of bacteria-targeted drugs in a more accurate way. Hence, a co-network analysis proposed here, which consists of RT-PCR and different metabolites combined with measurable pathological indicators, can immensely improve the accuracy of identification for microbial metabolites associated with drug-responsive bacteria.

Based on the proposed strategy, the present study aimed to elaborate the mechanism of rhubarb for AD by identifying effective metabolites associated with rhubarb-responsive bacteria. First of all, the influence of long-term rhubarb treatment on the pathological indicator-related microbiota and corresponding metabolites was evaluated. And then, gut microbiota and metabolomic profiling based on a time series analysis were performed to filter the disturbed microbiota and metabolites with the progression of AD. Moreover, the rhubarb-responsive bacteria and their corresponding metabolites were discovered by the co-network analysis based on RT-PCR and different metabolites combined with pathological indicators. Finally, the effects of key metabolite on primary neurons and BV-2 cells were evaluated *in vitro* to validate the bidirectional cross-talk between the gut and brain. Together, a more accurate co-network analysis employed in our study demonstrates that rhubarb ameliorates cognitive impairment by influencing effective metabolites in the gut through the regulation of rhubarb-responsive bacteria.

MATERIALS AND METHODS

Animals

Eight-month-old male APP/PS1 Tg mice and littermate wild type (WT) mice were obtained from the Nanjing Biochemical Research Institute of Nanjing University and housed in environmentally controlled conditions (room temperature at 22 ± 1°C, 12-h light/dark cycle) with access to standard food and water ad libitum. All experiments were approved and conducted in accordance with the guidelines of the Care and

Use of Laboratory Animals approved by the Ethics Committee for Animal Care and Treatment at Beijing University of Chinese Medicine (BUCM-4-2018080101-3007).

Preparation of Drug Solutions

Preparation of Rhubarb Decoction

Small pieces of rhubarb (*Rheum tanguticum*; 171202 ZISUN MEDICINE HEALTH CO.LTD. GuangZhou, China) herbal medicine (~30 g) were weighed and soaked in 300 ml distilled water for 1 h and decocted twice in boiling water for 30 min on each occasion. The combined products from this water decoction were filtered and dried in a 60°C water bath, then topped up to 50 ml with ultrapure water to yield a 0.6 g mL^{-1} solution (Zhao et al., 2019).

Preparation of Donepezil Hydrochloride Solution

Donepezil hydrochloride solution was prepared by crushing one tablet containing 5 mg donepezil hydrochloride and dissolving it in 100 ml of normal saline by ultrasonication for 30 min to obtain a 0.05 mg ml^{-1} solution.

Experimental Design

All the 8-month-old Tg mice were randomly divided into three groups (n = 9 per group): Tg model group, rhubarb administration group (TgR), and positive drug group (TgP). Littermate wild type mice (n = 9) were used as the wild type control group (WT). Mice in the TgR group were given a rhubarb decoction by gavage at 0.91 g kg^{-1} every day for 60 consecutive days. Mice in the TgP group were given donepezil solution at 1.5 mg kg^{-1} daily for 60 days. The Tg model group and the WT control group were given 1 ml normal saline every day. The fecal samples of all mice were collected from 8-month-old mice after 3 days of acclimation. After 30-day-treatment, fecal samples of all mice were collected as 9-month-old samples. And after feeding for 60 days, fecal were collected as 10-month-old samples.

Behavioral Test

Morris Water Maze Test

The Morris water maze test was performed as described by Vorhees and Williams (Vorhees and Williams, 2006). The escape latency during the spatial learning phase and the number of platform crossings and the time spent in the target quadrant were recorded. The detailed experiments were provided in the **Supplementary Material**.

Step-down test

The step-down test was performed as described by Ruan et al. (2016). The error times during training, step-down delay and error times during experiments were recorded. The detailed experiments were provided in the **Supplementary Material**.

Tissue Collection

Brain Tissue Collection

After the behavioral tests, mice were deeply anesthetized with 10% chloral hydrate and euthanized by cervical dislocation. After craniotomy on ice, the whole brain was removed and the hippocampus was quickly separated, weighed, and frozen at −80°C for subsequent enzyme-linked immunosorbent assay (ELISA) and neurotransmitter analyses. Brain tissue samples from mice in each group were also collected, fixed, paraffin-embedded, and sectioned at 5 μm for pathological staining.

Fecal Sample Collection

Fecal samples were collected from 8-month-old mice after 3 days of acclimation. After feeding for 30 days, fecal samples were collected from the mice at 9 months of age. Finally, samples were collected at the age of 10 months after feeding for 60 days. Fecal samples of the same mice in the corresponding groups were collected at each time point and six samples from the WT, Tg and TgR groups were used for 16S rRNA gene sequencing and metabolomics analysis.

Congo Red Staining

The brain tissues of mice in various treatment groups were subjected to Congo Red staining to visualize amyloid plaques. Paraffin-embedded tissue sections were routinely dewaxed into water. The slices were immersed in alkaline solution for 20 min and washed with water. Alkaline Congo Red solution was soaked for 20 min and washed with water. The sections were immersed in alkaline solution for differentiation, observed under a microscope until the tissue staining contrast was clear, then washed with water to stop staining. Harris hematoxylin was applied for 5 min and washed off. Afterward, 1% hydrochloric acid ethanol solution was added for differentiation for a few seconds and the sections were washed with water for 15 min. The sections were dehydrated with gradient ethanol, hyalinized with xylene, and sealed with neutral gum.

Hematoxylin and Eosin Staining

The brain tissues of mice were fixed with neutral formalin, dehydrated with ethanol, and removed with xylene. The brain tissues were embedded in paraffin and sectioned at 5 μm. The paraffin sections were immersed in 100% xylene twice for 10 min each time and soaked in 95, 80, and 70% alcohol for 3 min in turn. Finally, phosphate-buffered saline (PBS) and distilled water were used to rinse the sections three times, for 2 min each time. The sections were soaked in hematoxylin solution, stained for 10 min, and washed with running water until the water was clear with no purple color. The cells were differentiated with 75% hydrochloric acid ethanol for 3 s (three times) and washed with running water. The nuclei were confirmed to have turned blue under the microscope. Eosin staining was performed for 5 min. The stained sections were dehydrated with pure alcohol and washed with xylene until the cut was transparent and sealed with neutral gum.

Iba-1 Immunohistochemical Staining

Tissue sections of the whole brain were embedded with paraffin and prepared for immunohistochemical staining. After deparaffinization and rehydration in graded alcohols, antigen retrieval was performed with citrate buffer for 10 min at 90°C. Next, the sections were gradually cooled at room temperature to block endogenous peroxidase activity. The sections were then washed thrice with PBS and blocked with goat serum for 10 min at room temperature. After the goat serum was removed, the

sections were incubated with mouse-anti Iba-1 at 4°C overnight, followed by intubation with biotin-labelled goat anti-mouse secondary antibody for 10 min and streptomycin anti-biotin peroxidase for 10 min at room temperature. Then, the sections were labelled with 3,3′-diaminobenzidine, followed by hematoxylin counterstaining. Lastly, after washing, the sections were dehydrated through gradients of ethanol and xylene. PBS displacement of the primary antibody was used as the negative criterion.

Analysis of Aβ, $Aβ_{42}$, Interleukin-1β, IL-18, and Tumor Necrosis Factor-α Levels with Enzyme-Linked Immunosorbent Assay

Hippocampus samples from the brain were homogenized and the concentrations of Aβ, $Aβ_{42}$, IL-1β, IL-18, and TNF-α were measured using an ELISA kit (BlueGene Biotech, Shanghai, China) according to the instructions. The standard curve was established and used to calculate the levels of Aβ, $Aβ_{42}$, IL-1β, IL-18, or TNF-α in the tissues. The obtained values were corrected for the wet weight of the brain sample and expressed as μg/mg.

Quantification of Neurotransmitters in Brain Tissue

Brain Tissue Sample Processing

The brain tissue was cut into pieces and mixed evenly. Afterward, 0.5 ml of water-methanol (8:2, v/v) was added to every 0.25 g brain tissue to remove protein and tissue homogenate was prepared in a homogenizer. The prepared homogenate was centrifuged twice at 4°C 13709 × g for 10 min. After centrifugation, 200 μl of homogenate supernatant solution was removed and added to 0.8 ml 0.1% formic acid acetonitrile (40–60%) followed by vortexing for 2 min. The prepared solution was centrifuged at 4°C, 13709 × g for 10 min and placed in an injection vial.

Liquid Chromatography–Mass Spectrometry Method

Ultra-Performance Liquid Chromatography (UPLC) analysis was performed on a Waters Acquity UPLC system (Waters Corporation, Milford, MA, United States) consisting of a binary solvent system, an autosampler, and a column temperature controller. Chromatographic separation was carried out on an ACQUITY BEH C18 column (2.1 mm × 100 mm, 1.7 μm, Waters, United Kingdom). The mobile phase was composed of eluent A (0.3% formic acid in water) and eluent B (acetonitrile). The line gradient program was optimized as follows: 0–2 min, maintained at 2% B; 2–3 min, increased from 2% B to 30% B; 3–3.5 min, increased from 30% B to 90% B; 3.5–5 min, maintained at 90% B; 5–5.1 min decreased from 90% B to 2% B; 5.1–7 min maintained at 2% B for column equilibrium. The column temperature was set at 30°C and the sample chamber temperature was set at 4°C. The mobile phase flow rate was set at 0.3 ml/min, and the injection volume was 2 μl for each run.

MS data were recorded using the Waters XEVO TQ-S system (Waters Corporation, Manchester, United Kingdom) equipped with an electrospray ionization source in positive ion mode with multiple reaction monitoring (MRM) of the transition of *m/z* 176.9360 → 160.1180 for serotonin (5-HT); *m/z* 146.0780 → 87.0840 for acetylcholine (Ach); *m/z* 154.3020 → 137.1390 for dopamine (DA); *m/z* 103.9040 → 86.9900 for γ-aminobutyric acid (GABA); *m/z* 148.2130 → 84.1240 for glutamate (Glu), and *m/z* 169.9140 → 152.1190 for norepinephrine (NE). The MS parameters were optimized as follows: the ion spray voltage was 4000 V; capillary voltage was 3.0 kV; cone voltage was 30 V; nitrogen was used as the desolvation gas and the cone gas with flow rates of 800 and 150 L/h, respectively; the source and desolvation temperatures were set at 150 and 400°C, respectively; the sheath and auxiliary gas pressures were 20 psi and 10 psi, respectively. Thereafter, the MS/MS conditions were optimized for the internal standard by infusing the individual solution into the electro-spray source. The optimized cone voltage and collision energy were 2 V and 10 eV for 5-HT, 32 V and 12 eV for Ach, 2 V and 8 eV for DA, 22 V and 8 eV for GABA, 2 V and 14 eV for Glu, and 72 V and 6 eV for NE, respectively.

16S rRNA Microbial Community Analysis

Illumina MiSeq Sequencing

The 16S rRNA sequencing was performed by Majorbio Bio-Pharm Technology Co. Ltd. (Shanghai, China). Purified amplicons were pooled in equimolar and paired-end sequences (2 × 300) on an Illumina MiSeq platform (Illumina, San Diego, United States) according to the standard protocols provided by Majorbio Bio-Pharm Technology Co. Ltd. (Shanghai, China). The detailed method of RNA extraction, PCR amplification and data processing is provided in the **Supplementary Material**.

Data Analysis

Association network analysis was performed using the Co-Net v1.1.1. beta tool (Faust and Raes, 2016) on Cytoscape v3.7.2. (Shannon et al., 2003). Taxa below a sum of 120 and 12 occurrences per condition were discarded and the relative abundances were calculated. Networks were inferred based on the 1000 top and bottom edges for each of the Pearson, Spearman, Bray, and Kullback-Leibler correlation methods with 1000 iterations. The final *p*-values were computed during bootstrapping and adjusted with Benjamini-Hochberg correction for multiple testing.

Metabolomics Analysis

Hundred-milligram fecal samples from each mouse were weighed and placed in a 2 ml centrifuge tube. Three times the volume of 50% methanol aqueous solution was added for 5 min, and centrifuged at 13709 × g for 10 min. The supernatant was dried with nitrogen and 100 μl of 50% methanol aqueous solution was added for re-dissolution. After shaking for 30 s and standing for 10 min, the supernatant was centrifuged at 13709 × g at 4°C for 10 min and the supernatant was placed in an injection vial.

UPLC analysis was carried out on a Waters Acquity™ UPLC system (Waters Corporation, Milford, MA, United States) consisting of a binary solvent system, an autosampler, and a column temperature controller. Chromatographic separation was

carried out on an ACQUITY UPLC® HSS T3 column (2.1 mm × 100 mm, 1.8 μm, Waters, United Kingdom). The mobile phase was composed of eluent A (0.1% formic acid in water) and eluent B (acetonitrile). The line gradient program was optimized as follows: 0–0.5 min, 1% B; 0.5–4 min, 1–20% B; 4–8 min, 20–100% B; 8–9 min, 100% B; 9–9.5 min, 100–1% B; 9.5–11 min 1% B. The column temperature was set at 45°C and the sample chamber temperature was set at 4°C. The mobile phase flow rate was set at 0.3 ml/min and the injection volume was 3 μl for each run.

MS analysis was carried out with a Waters SYNAPT G2-SI MS system (Waters, United States) equipped with an electrospray ionization source. The analysis was performed in the positive and negative ion electrospray modes. The source parameters were set as follows: capillary voltage, 3.0 kV; cone voltage, 28 V; source temperature, 100°C; desolvation temperature, 400°C; the cone gas flow, 35 L/h; desolvation gas flow, 800 L/h. The low collision energy was 6 eV and the high collision energy was 10–65 eV. Mass spectra were recorded across the *m/z* range of 50–1200 and 3D data were collected in the continuum mode. The mass spectrometry data were acquired and processed with Waters MassLynx V4.1 software.

Data Processing and Multivariate Data Analysis

The UPLC-quadrupole time-of-flight mass spectrometry (UPLC-Q-TOF/MS) data for the fecal samples were imported into Progenesis QI v1.0 (Nolinear Dynamics, Newcastle, United Kingdom) for peak selection and alignment. After normalizing the data using the total ion intensity, a data matrix of interesting features containing the retention time, *m/z* value, and normalized peak intensity was imported into Metaboanalysis 4.0 for principal component analysis (PCA) and partial least-squares discriminant analysis (PLS-DA) and further confirmed using analysis of variance (ANOVA). The differences in the trends were processed with an unsupervised PCA method. Supervised PLS-DA was used to search for interesting biomarkers. Then, the peak height intensities of the differential metabolites were compared with t-tests using statistical software to confirm the biomarker alterations between the WT and Tg groups at the age of 8, 9, and 10 months. A p value < 0.05 was set as the threshold. As a small sample set, a pooled quality control (QC) sample containing equal aliquots of all the samples was run at the beginning of the sample queue for column conditions and injected at regular intervals and the end of the run (Want et al., 2010). Mass data acquisition was performed for the evaluation of the sensitivity and stability of instrument performance with regard to mass accuracy, retention time stability, and the coefficient of variation (CV). All samples were kept at 4°C during the analysis.

Analysis of Fecal Metabolites and Their Metabolic Pathways

Metabolite peaks were assigned based on MS/MS analysis using the MassFragment™ application manager (Waters Corp., Milford, United States). After applying chemically intelligent peak-matching algorithms, the molecular composition of each metabolite and its fragments were structure-matched using available biochemical databases such as HMDB (http://www.hmdb.ca/), Kyoto Encyclopedia of Genes and Genomes (KEGG; http://www.genome.jp/kegg/), LIPIDMAPS (http://www.lipidmaps.org/), and Chemspider (http://www.chemspider.com). The identified metabolites were subjected to KEGG pathway mapping for metabolic pathway analysis. The KEGG database contains a collection of manually curated pathway maps from genomics, transcriptomics, proteomics, and metabolomics and provides molecular interactions and reaction networks.

HPLC Fingerprinting of Rhubarb Extraction

Chromatographic Conditions

Chromatographic analysis was performed on a Thermo UltiMate 3000 HPLC system (Thermo Scientific, United States). The separations were achieved on an Agilent SB-C18 column (250 mm × 4.6 mm, 5 μm) with the column temperature at 40°C. The mobile phases consisted of acetonitrile (A) and an aqueous solution containing 0.05% phosphoric acid (B) using a gradient elution as follows: 0–10 min 96–89% B, 10–25 min 89–87% B, 25–50 min 87–85% B, 50–70 min 85–80% B, 70–100 min 80–67% B, 100–115 min 67–40% B, and 115–140 min 40% B with a flow rate of 1.0 ml/min. The injection volume was 10 μl and the detection wavelength was at 268 nm.

Preparation of Reference Compound Solution

Stock solutions were prepared by dissolving seven substances (emodin (BP0532), 1.95 mg; rhein (BP1208), 1.95 mg; chrysophanol (BP0348), 1.51 mg; physcion (BP1092), 1.61 mg; aloe-emodin (BP0146), 1.75 mg; sennoside A (BP1292), 1.50 mg; sennoside B (BP1293), 2.36 mg) in 200 μl dimethyl sulfoxide (DMSO) as described in our previous paper (Gao et al., 2009) and distilled water was added to a constant volume of 5 ml. All the compounds were obtained from Chengdu Biopurify Phytochemicals Ltd. and the purity of these compound is over 98.0%. Subsequently, each reference compound solution was diluted to 100 times with distilled water and the diluent was filtered through a 0.22 μm microporous membrane and placed in an injection vial.

Method Validation

The precision was determined by successively analyzing the same sample solution six times. The repeatability was assessed by analyzing six independently prepared sample solutions. The stability was evaluated with the same sample solution at different periods in 1 day (0, 2, 4, 8, 16, 24 h). Each sample solution was tested twice in parallel.

Data Analysis

The data analysis was performed on a "TCM chromatographic fingerprint similarity evaluation system (version 2012, Chinese Pharmacopoeia Commission)".

TABLE 1 | Primer sets used in this study.

Target Bacteria	Sense primer	Anti-sense primer
Bacteroides	5′-CATGTGGTTTAATTCGATGAT-3′	5′-AGCTGACGACAACCATGCAG-3′
Erysipelatoclostridium	5′-GACACTGCATGGTGACC-3′	5′-GGTTTCTATGGCTTACTG-3′
Marvinbryantia	5′-CAGGGATTTTACGTGCTTTATTTTAGTTAT-3′	5′-AGTTCGGATTCGCTCGTATTTTCT-3′
norank_f_Ruminococcaceae	5′-TGTTAACAGAGGGAAGCAAAGCA-3′	5′-TGCAGCCTACAATCCGAACTAA-3′

RT-PCR

The total bacterial DNA was extracted from the fecal samples of mice in each group with the E.Z.N.A ™. Stool DNA kit (D4015, Omega Biotek, United States), and the procedures were carried out according to the manufacturer's instructions. First, fecal samples were removed from a −80°C refrigerator, 200 mg of feces from each sample was measured into a 1.5 ml sterile centrifuge tube, and genomic DNA was detected with 2% agarose gel electrophoresis. For detection of the bacteria *Marvinbryantia* (Desai et al., 2016) and *Erysipelatoclostridium* (Zakham et al., 2019), extracted bacterial DNA was subjected to RT-PCR using the CFX Connect real-time PCR system (Bio-rad Laboratories, Hercules California, United States). PCR was performed with a 10 μl sample containing 5 μl SG Green qPCR Mix (with ROX Q1002, SinoGene), 0.2 μl 20 μm upstream and downstream primers, 1 μl bacterial genomic DNA template, and 3.6 μl deionized water. In the blank control, the template DNA was replaced with deionized water. After the PCR reaction, the melting curve temperature was set at 60–95°C and increased by 0.5°C/s. For detection of the bacteria *Bacteroides* (Haugland et al., 2010) and *norank_f_Ruminococcaceae* (Jiang et al., 2017), extracted bacterial DNA was subjected to RT-PCR using the LineGene 9600 Plus real-time PCR system (Bioer Technology, Hangzhou, China). PCR was performed with a 20 μl sample containing 10 μl ChamQ SYBR Color qPCR Master MiX (Vazyme Biotech Co., Ltd, Nanjing China), 0.4 μl 5 μm upstream and downstream primers, 2 μl bacterial genomic DNA template, and 7.2 μl deionized water. In the blank control, the template DNA was replaced with deionized water. After PCR reaction, the melting curve temperature was set at 60–95°C and increased by 0.5°C/s. **Table 1** shows the sequences for each primer set, which targeted the 16S rRNA genes for each bacteria group. Each standard curve was prepared based on the cell numbers measured using a bacterial counting chamber with each strain indicated. DNA from each standard strain was extracted as described above and used for RT-PCR. All RT-PCR experiments were performed with duplicates for each sample. The detailed PCR reaction information is listed in the **Supplementary Material**.

Cell Culture

Primary Culture of Rat Neurons

Twenty specific-pathogen-free Sprague-Dawley (SD) neonatal rats were purchased from SPF Biotechnology Co., Ltd (Beijing). The healthy SD neonatal rats were sterilized with 75% alcohol within 24 h after birth and decapitated under sterile conditions. The scalp and skull were cut. Brain tissue was taken out and placed in a dish containing cold D-Hank's solution with pH 7.2 free of calcium and magnesium. The brain tissue was peeled under sterile conditions and the cerebellum, hippocampus, and medulla were removed. The cortex was isolated and the meninges and blood vessels were carefully peeled off. The tissue was cut into blocks of about 1 mm^3 using iris scissors, digested in 0.125% trypsin for 20 min at 37°C and shaken two to three times. The supernatant was discarded and complete media was added to terminate digestion. The tissues were rinsed twice and gently pipetted 20 times using a Pasteur pipette. The cell suspension was allowed to stand for 2 min. The cell suspension was collected in a new centrifuge tube and centrifuged at 95 × g at 4°C for 10 min. The supernatant was discarded. The cells were resuspended in complete media and filtered with a 200 mesh stainless steel filter. The filtrate was stained using trypan blue and the cells were counted using a hemocytometer under a microscope. The cells were inoculated at an intensity of 8.0×10^4 to 1.0×10^5 ml with 100 μl/well into a 96-well plate pre-coated with poly-L-lysine. The cells were cultured for 4–6 h in an incubator at 37°C with 5% CO_2 and the medium was replaced with serum-free media. After culturing for 3 days, Ara-C working solution was added to inhibit over-proliferation of non-neuronal cells and aspirated after 24 h. Thereafter, half of the medium was replaced every 3 days. Cells collected from days 7–21 of culture were used for the experiment.

Cell Culture of Rat Microglial Cells

The murine microglial cell line BV-2 was cultured in high-glucose Dulbecco's modified Eagle's medium (DMEM) supplemented with 10% fetal bovine serum (FBS) and 1% penicillin/streptomycin (P/S) in a humidified incubator with 5% CO_2 at 37°C. BV-2 cells were plated into 96-well plates (1.0×10^5 cells/well) and incubated overnight for subsequent experiments.

MTT Analysis

The 3-(4,5-dimethylthiazol-2-yl)-2,5-diphenyltetrazolium bromide (MTT) assay is based on the protocol described by Mosmann (1983). The assay was optimized for the cells used in the experiments. Briefly, after the cells were incubated with different concentrations of *o*-tyrosine (*o*-tyr) (0.5, 1, and 2 mM) for 48 h at 37°C (Pennathur et al., 1999), the culture medium was removed, then the cells were incubated for 4 h with 0.5 mg ml^{-1} of MTT and dissolved in serum free medium. Washing with PBS was followed by the addition of 100 μl DMSO and gentle shaking for 10 min to facilitate complete dissolution. After the formazan crystals had dissolved, the absorbance was determined spectrophotometrically at 490 nm on an ELX800 UV universal microplate reader. The results were analyzed with the Soft max pro software (version 2.2.2) and are presented as a percentage of the control values.

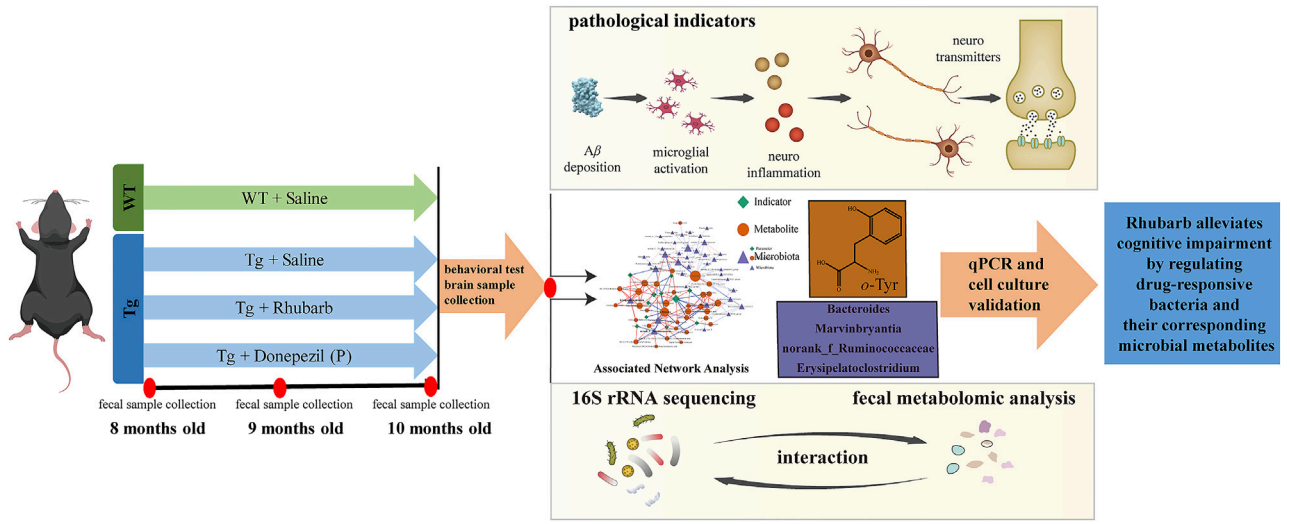

FIGURE 1 | The main content of this study.

Active Oxygen Detection

Reactive oxygen species (ROS) production in neuronal and BV-2 cells was assessed with a 2′,7′-dichlorodihydrofluorescein diacetate (DCFH-DA) probe. Different concentrations of *o*-tyr (0.5, 1, and 2 mM) were incubated with the cells for 48 h at 37°C. After the culture medium was removed, the cells were treated with 5 μM DCFH-DA at 37°C for 30 min. Washing with PBS three times was followed by the addition of 100 μl PBS and the intracellular ROS levels in the cells were viewed with a fluorescence microscope (Nikon Eclipse).

Measurement of Nitric Oxide

Nitric oxide (NO) production in neuronal and BV-2 cells was performed using 2′,7′-dichlorodihydrofluorescein diacetate (DAF-FM DA). Different concentrations of *o*-tyr (0.5, 1, and 2 mM) were incubated with the cells for 48 h at 37°C. After the culture medium was removed, DAF-FM DA (5 μM) was added to the wells. After incubating at 37°C for 20 min, the chemical was removed and the cells were washed three times with PBS followed by measurement with a fluorescence microscope.

Statistical Analysis

Statistical analyses were performed using R 2.15.0 and GraphPad Prism software v 8.0. All the data were presented as the mean ± SEM. The significance of the differences between two groups was analyzed using the Student's unpaired *t*-test and multiple comparisons were analyzed using one-way ANOVA followed by Dunnett's post hoc test. The differential abundances of genera and metabolites were determined using non-parametric tests including the Wilcoxon rank sum test and Mann–Whitney U test. The correlations among fecal metabolites, 16S levels, and physiological and biochemical indexes were tested with both the Pearson Correlation Coefficient and Spearman rank correlation. *p* values were corrected for multiple comparisons using the Benjamini–Hochberg false discovery rate (FDR) and $p < 0.05$ was statistically significant.

RESULTS

Rhubarb Alleviates Cognitive Impairment in APP/PS1 Transgenic Mice

Our previous study revealed that *Rheum tanguticum* ameliorated cognitive impairment in AD rat model, possibly due to the regulation of the gut microbiota (Zhao et al., 2019). In this study, to further verify the therapeutic effects for the treatment of AD, rhubarb extraction with a uniform and stable quality (**Supplementary Figure S1A**) and donepezil as positive drug were administrated to APP/PS1 transgenic mice for 2 months, named the TgR and TgP group, respectively. The main content of this study was shown in **Figure 1**. The effect of rhubarb on the learning and memory abilities of the Tg mice was tested by the Morris water maze. During the training period, the escape latencies of the mice in each group were similar on the first day, and gradually decreased in the next 5 days (**Figure 2A**). On the sixth day, the escape latency of Tg mice was significantly longer than that of wild-type (WT) mice. After the treatment of rhubarb or donepezil, the escape latency of Tg mice was significantly shortened and there was no significant difference between them. In the probe trial, Tg mice exhibited a lower platform passing times (**Figure 2B**) and shorter swimming time in target zone (**Figure 2C**). However, rhubarb or donepezil treatment significantly reversed these defects in Tg mice. These results indicated that rhubarb could attenuate spatial learning and memory deficits in APP/PS1 mice (**Figure 2D**).

The step-down test was performed to investigate the passive avoidance ability of Tg mice. Compared with the WT mice, Tg mice showed more errors times during the training period (**Figure 2E**) and shorter step-down delay (**Figure 2F**)

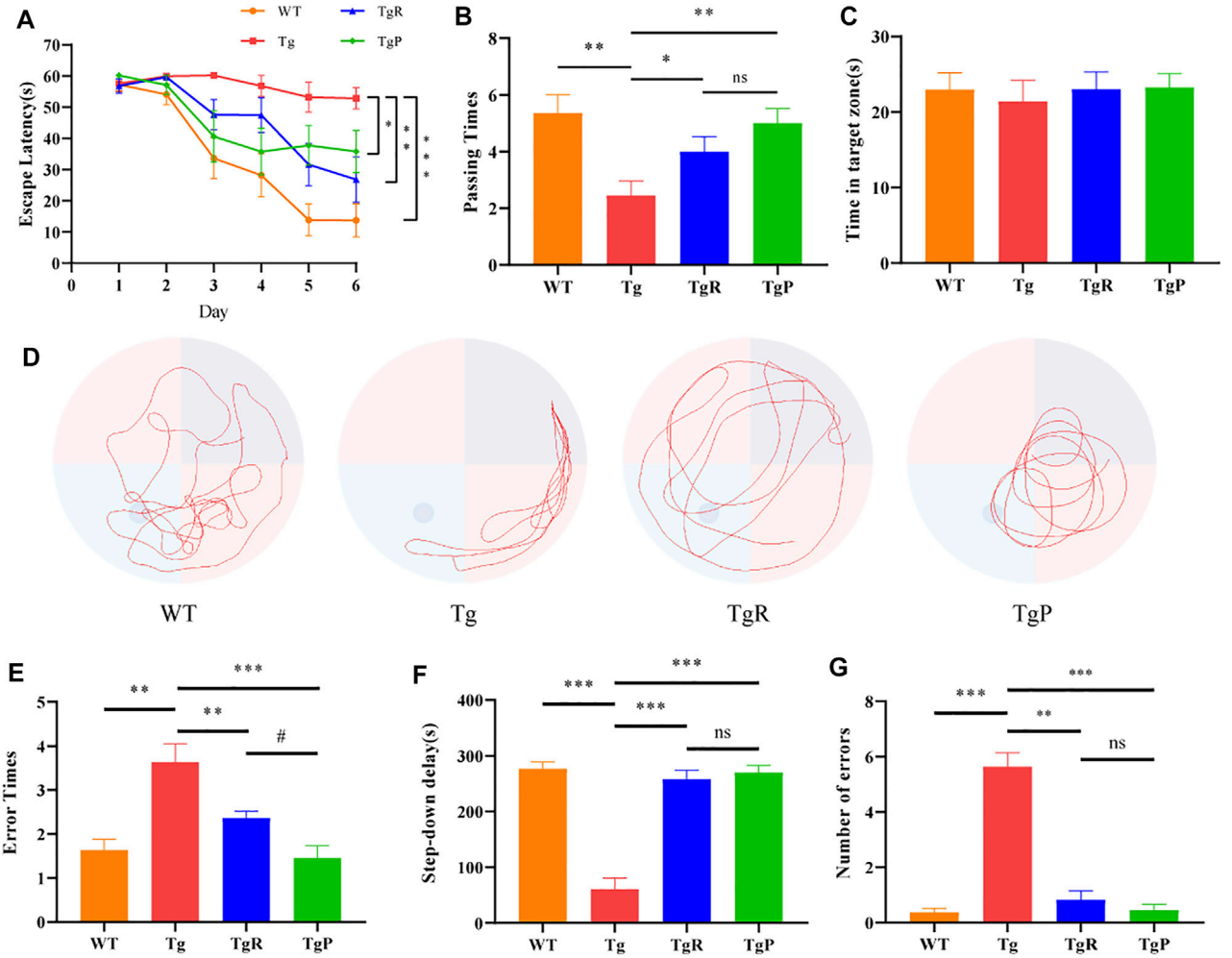

FIGURE 2 | Effects of rhubarb on memory and cognitive function of APP/PS1 mice. **(A–D)** Morris water maze test, including assessments of escape latency **(A)**, platform crossing times **(B)**, swimming time in the target quadrant **(C)**, representative swimming path **(D)**. **(E–G)** Step-down test, including assessments of error times during training **(E)**, step-down delay **(F)**, error times during experiments **(G)**. Values are expressed as the mean ± S.E.M.; $n = 9$, $^{*}p < 0.05$ versus Tg, $\#p < 0.05$ versus TgP, by Student's unpaired *t*-test.

accompanied by a greater number of errors (**Figure 2G**) during the experimental period. Fortunately, rhubarb or donepezil treatment reduced the errors times during the training period, increased the step-down delay, and reduced the number of errors during the experimental period in Tg mice with no significant difference. These results suggested that rhubarb extract could alleviate the stimulation avoidance response and cognitive impairment in APP/PS1 mice.

Rhubarb Reverses the Pathological Changes in Tg Mice

After the behavioral tests, the mice were sacrificed to further investigate the effect of rhubarb on the pathological changes in the brain of Tg mice, including Aβ deposition, activated microglia, neuronal damage and neurotransmitter disorders. The main pathological feature of AD is senile plaques composed of extracellular Aβ, which mainly deposited in the brain parenchyma and cerebral vessels (Pistollato et al., 2016; Friedland and Chapman, 2017). Here, Aβ deposition in the brain of Tg mice was stained by Congo Red, and the amount of total Aβ and $A\beta_{42}$ were quantified by ELISA. As expected, cerebral Aβ deposition (**Figure 3A**), and the levels of hippocampal Aβ and $A\beta_{42}$ (**Figures 3B,C**) in Tg mice was significantly higher than that of WT mice. After the treatment of rhubarb or donepezil, Aβ deposition in the brain of Tg mice was significantly reduced (**Figure 3A**). Moreover, although there was no significant difference in the level of total Aβ between the TgR and Tg group, the level of $A\beta_{42}$ was markedly reduced in the TgR group (**Figures 3B,C**). Donepezil treatment significantly reduced both the levels of total Aβ and $A\beta_{42}$.

Recent studies have shown that Aβ deposition in the brain can activate microglia and release inflammatory factors (Wu Y. et al., 2019). Therefore, the activation of microglia in the brain and the

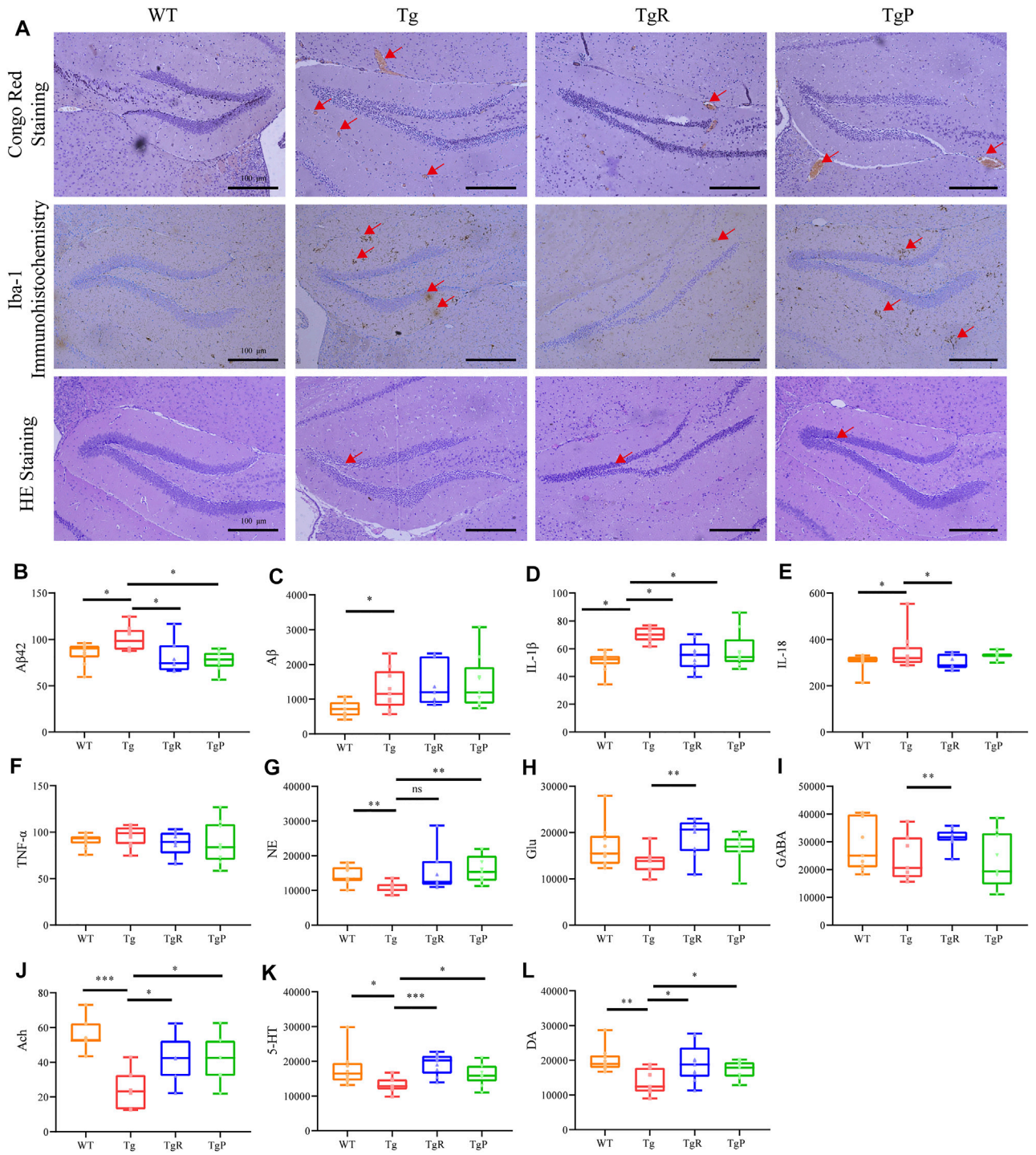

FIGURE 3 | Rhubarb alleviates the pathological changes in APP/PS1 mice. **(A)** Histopathology examination of the hippocampus in the brain. (Scale bar: 100 μm). **(B–L)** Levels of β-amyloids, pro-inflammatory cytokines, and neurotransmitters in the brain. $A\beta_{42}$ (B), Aβ **(C)**, IL-1β **(D)**, IL-18 **(E)**, TNF-α **(F)**, norepinephrine (NE) **(G)**, glutamate (Glu) **(H)**, γ-aminobutyric acid (GABA) **(I)**, Acetylcholine (Ach) **(J)**, serotonin (5-HT) **(K)**, dopamine (DA) **(L)**. Values are expressed as the mean ± S.E.M.; $n = 9$; $^{*}p < 0.05$ versus Tg; $^{**}p < 0.01$ versus Tg; $^{**}p < 0.001$ versus Tg, by Student's unpaired *t*-test.

content of inflammatory factors in the hippocampus were evaluated by Iba-1 immunohistochemistry and ELISA, respectively. Compared with the WT mice, both the density and the number of activated microglia in the hippocampus of Tg mice were larger (**Figure 3A**). In addition, the levels of IL-1β and IL-18 in Tg mice were significantly higher than that of WT

mice, and the level of and TNF-α was slightly higher (**Figures 3D–F**). As shown in **Figure 3**, rhubarb treatment exhibited a significant decrease in the number of activated microglia, and the levels of IL-18 and IL-1β (**Figure 3**) alone with a slight decrease of TNF-α similar to the donepezil treatment.

Activated microglia release inflammatory factors and induce neuroinflammation reaction, and eventually lead to neuronal apoptosis, resulting in the decline of learning and memory abilities (Rothhammer et al., 2018; Wu Y. et al., 2019). Therefore, the morphology of neurons in the brain tissue of mice was observed by HE staining. The results showed the disordered arrangement of neurons, condensed cytoplasm and karyopyknosis, and decreased number of neurons were observed in Tg mice (**Figure 3A**). Rhubarb or donepezil treatment reversed the above histopathological changes.

Neuronal injury can lead to the neurotransmitter disorders in the brain. Different kinds of neurotransmitters participate in neural activities in multiple brain regions. Therefore, the levels of 5-HT, DA, NE, Ach, Glu, and GABA in the brain of mice were detected by UPLC-TQ/MS. Compared with the WT mice, the levels of NE, Ach, 5-HT, and DA in the brain of Tg mice were significantly decreased, and the levels of Glu and GABA were slightly reduced (**Figures 3G–L**). As illustrated in **Figure 3A**, rhubarb and donepezil showed a favourable regulation in neurotransmitters in brain of Tg mice. Altogether, these results provided evidence that rhubarb could alleviate the pathological changes in Tg mice. Moreover, after 60 days treatment with rhubarb, there were no obvious abnormalities in body weight (**Supplementary Figure S2A**) and also no tissue damage or any other adverse effect in brain tissues (**Supplementary Figure S2B**).

Screening Drug-Responsive Bacteria in Rhubarb Treated Tg Mice in an Age-dependent Alteration by RT-PCR Analysis

In order to explore the changes in intestinal microbiota during the progression of AD, gut microbial dysbiosis in Tg mice in an age-dependent alteration (six samples per time point, $n = 36$) was evaluated, and distributed intestinal microbiota was identified by 16S rRNA gene sequencing. As a result, a total of 1237622 valid sequences were obtained from 36 samples (average 34378 ± 9394 reads per sample). These sequences were classified into 521 OTUs with a 97% similarity level. The α-diversity index includes the Chao1, Shannon, and Simpson indexes, which were used to determine the ecological diversity of the microbial community. The results showed that the α-diversity of gut microbiota in Tg mice decreased to a certain extent compared with the value of WT mice (**Figures 4A–D**). The dominant microbiota at the phylum level in the WT mice changed regularly with age (**Figure 4E**).

The β diversity of all bacteria in the six groups was calculated by the unweighted UniFrac metric and visualized by principal coordinate analysis, respectively. We found that the gut microbiota composition between WT and Tg mice changed similarly with time, but the variation in Tg mice was more significant (**Figure 4F**).

To further explore the microbiota that was related to the aggravation of the disease, the gut microbiota in WT and Tg mice was compared based on a PLS-DA model. According to the VIP > 0.7, 72 differential bacterial genera were screened at 8 months of age (**Figure 5A**), 76 at 9 months of age (**Figure 5B**), and 69 at 10 months of age (**Figure 5C**), respectively. However, only nine genera exhibited the same trends at the three time points. In the Tg group, the relative abundances of *Tyzzerella*, *Ruminococcaceae_UCG_009*, *Bacteroides*, *Escherichia-Shigella,* and *Marvinbryantia*, *norank_f_Ruminococcaceae* and *Erysipelatoclostridium* increased gradually, while *Odoribacter* and *Akkermansia* decreased gradually (**Figure 5D**).

After that, drug-responsive bacteria between the Tg and TgR group were identified by RT-PCR analysis. As shown in **Figures 5E–H**, rhubarb treatment increased the number of *norank_f_Ruminococcaceae*, *Erysipelatoclostridium* and *Bacteroides* and reduced the number of *Marvinbryantia* compared with the Tg group. To confirm the changes in the gut microbiota in Tg mice with age, co-network analysis was conducted on all OTUs detected in fecal samples from Tg mice at three time points (**Figure 5I**, **Supplementary Figure S3**). The results showed that there were close interactions between the intestinal microbiota, which increased or decreased together.

Screening Microbial Metabolites in Rhubarb Treated Tg Mice in an Age-dependent Alteration by Metabolomics Analysis

To clarify the effects of gut microbiota changes on AD-related pathological changes in mice, the metabolic profiles of fecal metabolites from the Tg and WT groups at 8, 9, and 10 months of age were analysed by UPLC-Q-TOF/MS in positive and negative ion modes. BPIs of the metabolomic profiles of Tg sample in the negative ion modes is shown in **Figure 6A**. A total of 9941 features in the positive ion mode and 5139 features in the negative ion mode were detected in all samples from the WT and Tg groups.

The fecal metabolic profiles of the WT and Tg mice were analysed with PCA. Different metabolites were observed among the groups at 8, 9, and 10 months of age. The PCA scores for the WT and Tg at three time points are shown in **Figure 6B** (positive ion mode) and **Figure 6C** (negative ion mode). It can be observed that the profile for the fecal metabolites showed age-dependent changes. The obvious difference between the WT and Tg groups indicated that the fecal metabolites of Tg mice had changed significantly. To explore potential biomarkers related to the pathogenesis of AD, the fecal metabolomics data for WT and Tg mice was compared by a PLS-DA model (**Supplementary Figure S4**). According to PLS-DA model with a VIP value greater than 1 and a p value less than 0.05 for the ANOVA t-test, differential metabolites were identified based on the fragment

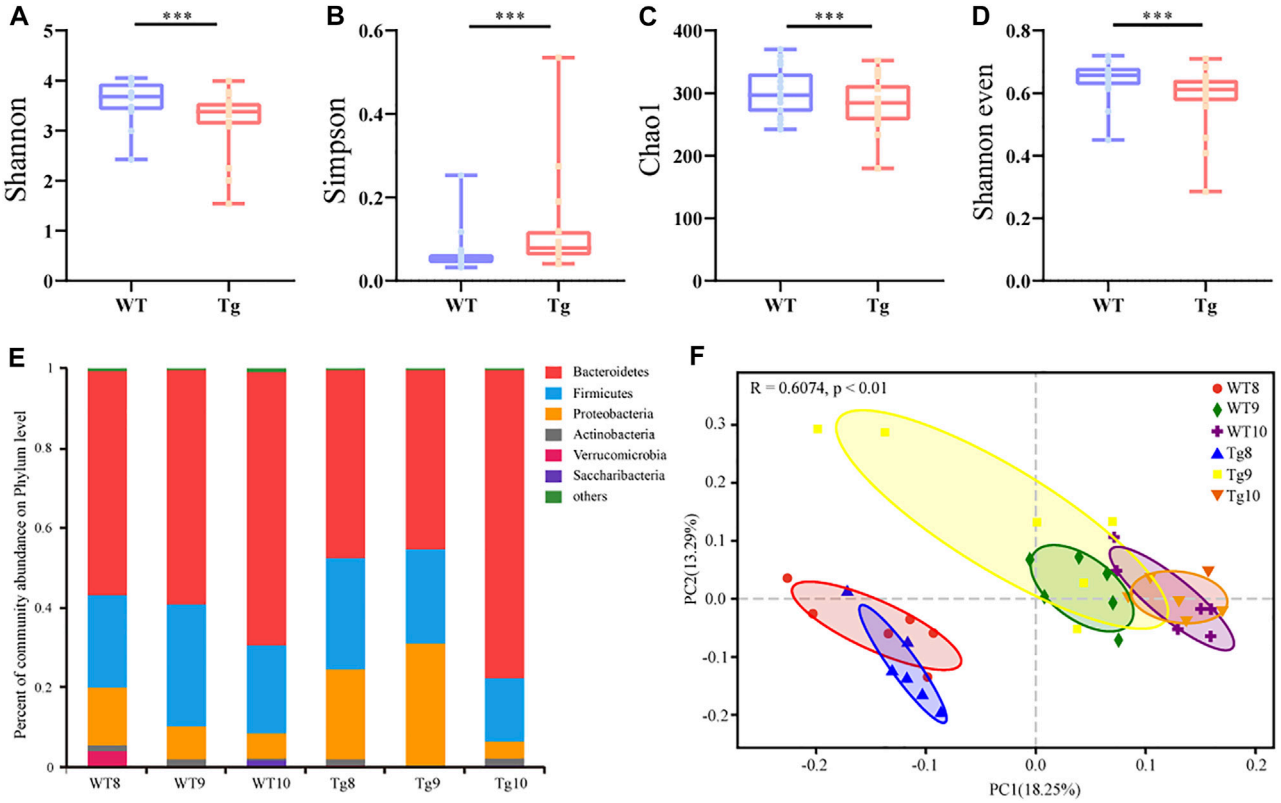

FIGURE 4 | Alteration of gut microbiota profile in AD model **(A–D)** α diversity of WT (n = 6) and Tg mice (n = 6) evaluated by Shannon **(A)**, Simpson **(B)**, Chao1 **(C)**, and Shannon even indices **(D)**. Error bars represent mean ± S.E.M. *p < 0.05 versus Tg; **p < 0.01 versus Tg; **p < 0.001 versus Tg, ***p < 0.0001 versus Tg, by Wilcoxon rank-sum test. **(E)** Bacterial taxonomic profiling at phylum level. Number in the group name represents months of age. **(F)** Principal component analysis (PCoA) based on unweighted UniFrac distances.

information and accurate mass number. Through a search and comparison of the HMDB, Metlin, and Chemspider databases, 50 differential metabolites with similar trends were found in the feces of Tg mice at three time points (**Figure 6D**). We speculate that some of these 50 differential metabolites were directly related to the pathological process in AD.

Drug-specific responsive microbial metabolites in the TgR group were screened by metabolomics analysis. After the administration of rhubarb extract for 30 and 60 days, the fecal metabolic profile for Tg mice showed a gradual recovery to a profile similar to that of WT mice (**Figures 6E,F**, **Supplementary Figures S1B,C**). Further, 27 of the 50 metabolites (**Figure 6D**) present at both time points in the TgR group showed a rhubarb intervention-dependent trend.

To gain insight into the mechanism underlying the rhubarb-induced improvement of cognitive impairment in AD mice, the metabolic pathways for 50 age-dependent metabolites with differences between the WT and Tg groups and 27 biomarkers for the long-term effects of rhubarb on AD cognitive impairment were evaluated. The results showed that the main metabolic pathways for rhubarb were histidine metabolism, D-glutamine, and D-glutamic acid metabolism, aminoacyl tRNA biosynthesis, alanine, aspartic acid, and glutamic acid metabolism (**Figure 6G**).

Screening Microbial Metabolites Associated With Rhubarb-Responsive Bacteria by Co-network Analysis

To further screen the microbial metabolites associated with bacteria in response to rhubarb, an improved co-network analysis was conducted based on the gut microbiota data at the OTU level and 50 differential metabolites detected in mouse fecal samples, with five pathological indicators and six neurotransmitters. As shown in **Figure 7**, *Bacteroides*, *Marvinbryantia*, *norank_f_Ruminococcaceae,* and *Erysipelatoclostridium* were significantly correlated with several biomarkers and pathological indicators. Phosphatidylcholine (PC; 15:0/18:2(9Z,12Z)), *o*-tyr, 3-hydroxyundecanoyl carnitine, L-glutamic acid, LysoPE (14:0/0:0), 3-hydroxytetradecanedioic acid, and pyroglutamic acid showed strong correlations with both the microbiota and indicator nodes. Interestingly, *o*-tyr showed a significant correlation with both the microbiota and indicator nodes (**Supplementary Table S6**), suggesting that *o*-tyr may lay on an important node in this network. We speculated that these

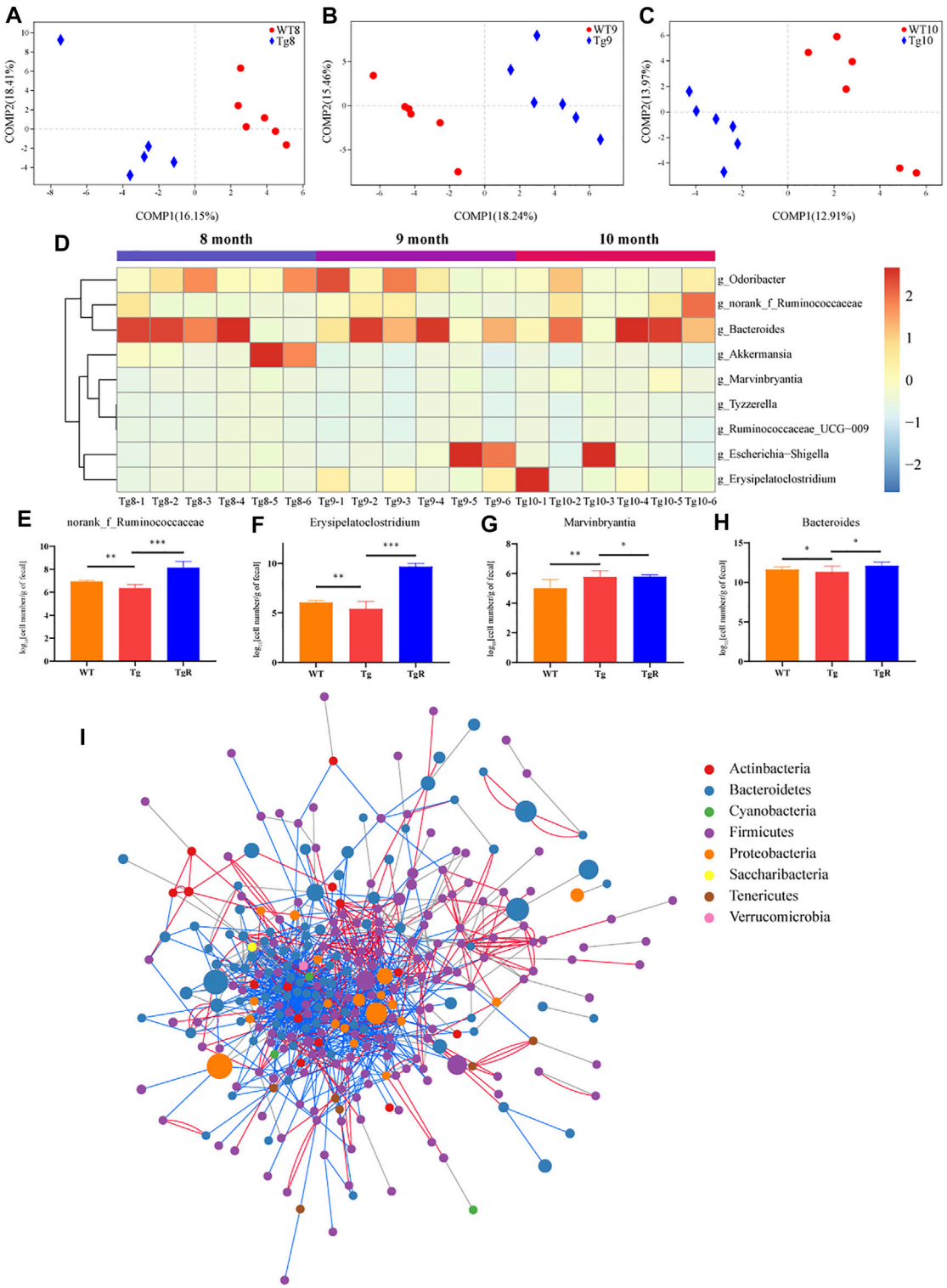

FIGURE 5 | The gut microbiota of Tg mice exhibited a common trend with age. **(A–C)** PLS-DA score plots of WT and Tg groups. Number in the group name represents months of age. **(D)** Heatmap formed by the abundance of genera. **(E–H)** Abundance of the key bacteria in the network, quantified by species-specific quantitative PCR. *$p < 0.05$ versus Tg; **$p < 0.01$ versus Tg; **$p < 0.001$ versus Tg, ***$p < 0.0001$ versus Tg, by Wilcoxon rank-sum test. **(I)** Co-network constructed by all OTUs in the fecal samples of Tg mice at three time points. The size of the node indicates the relative OTU abundance; the color of the node indicates different phyla; the lines between the nodes indicate co-abundance (red) or co-exclusion (blue) between the nodes.

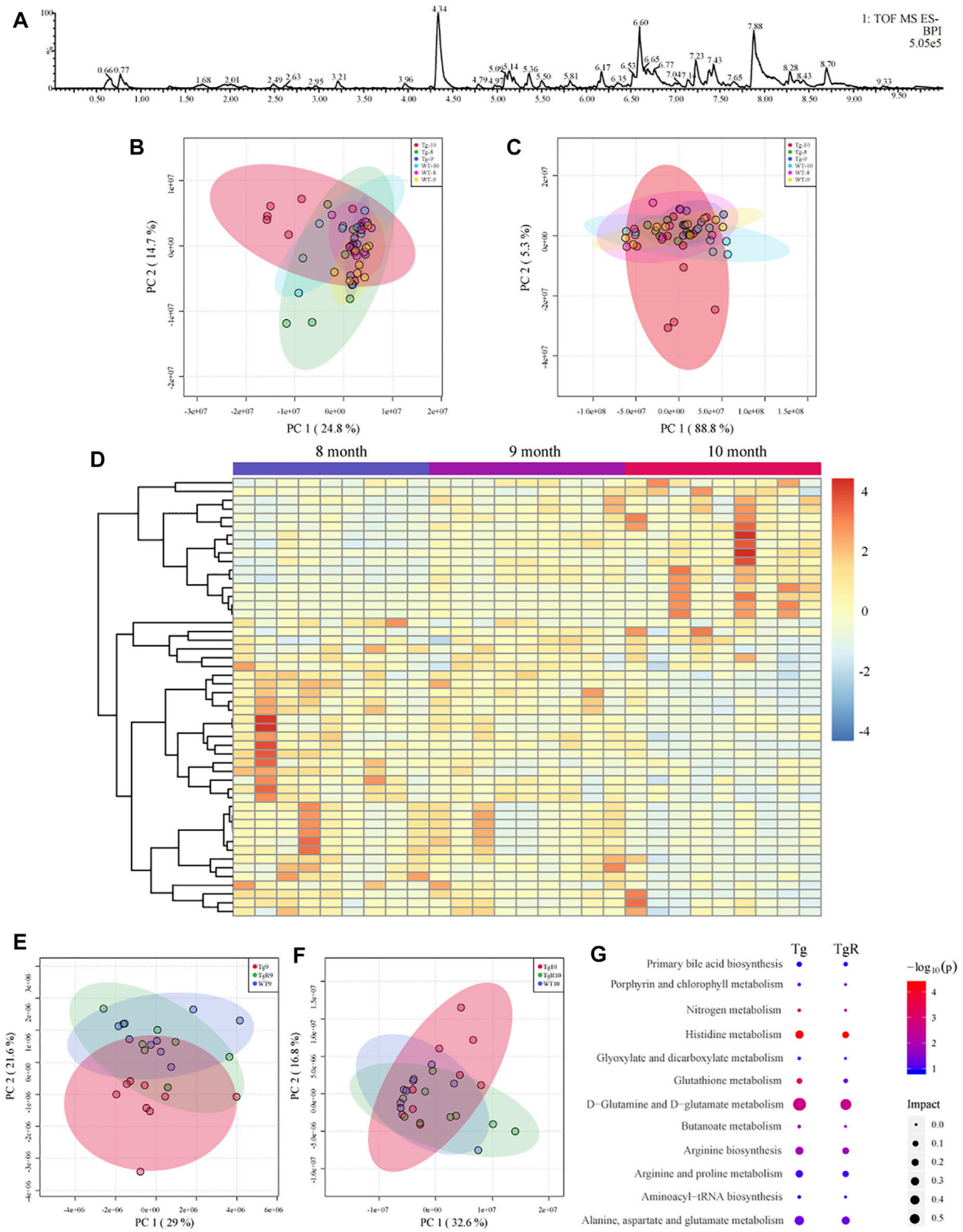

FIGURE 6 | Fecal metabolomics profile of Tg mice **(A–D)**. **(A)** Representative base peak ion chromatogram (BPI) of fecal metabolites from Tg sample. PCA score plots in positive **(B)** and negative **(C)** ion mode. **(D)** Heatmap showing the trend of metabolomic profiling in all the Tg groups. Effects of rhubarb on the fecal metabolomics of AD model **(E,F)**. PCA score plots based on fecal metabolic profiles under the negative ion mode. TgR mice received rhubarb intervention 30 days **(E)** and 60 days **(F)**. **(G)** Pathway enrichment of different metabolites in WT and Tg mice and the metabolites recovered after rhubarb administration. The size of the node represents the path impact value and the colour represents the $-\log_{10}(p)$ value of the pathway.

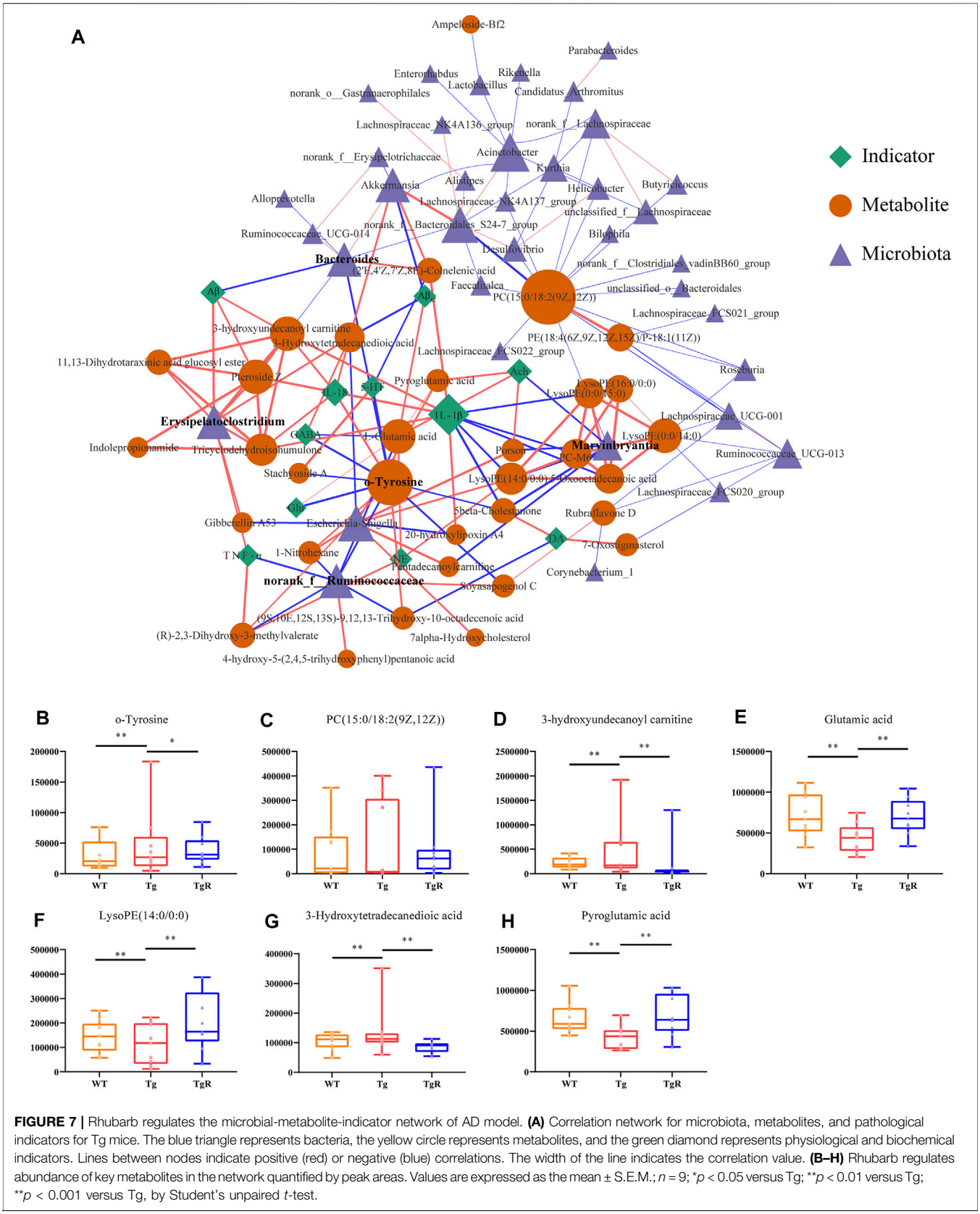

FIGURE 7 | Rhubarb regulates the microbial-metabolite-indicator network of AD model. **(A)** Correlation network for microbiota, metabolites, and pathological indicators for Tg mice. The blue triangle represents bacteria, the yellow circle represents metabolites, and the green diamond represents physiological and biochemical indicators. Lines between nodes indicate positive (red) or negative (blue) correlations. The width of the line indicates the correlation value. **(B–H)** Rhubarb regulates abundance of key metabolites in the network quantified by peak areas. Values are expressed as the mean ± S.E.M.; $n = 9$; $^{*}p < 0.05$ versus Tg; $^{**}p < 0.01$ versus Tg; $^{**}p < 0.001$ versus Tg, by Student's unpaired *t*-test.

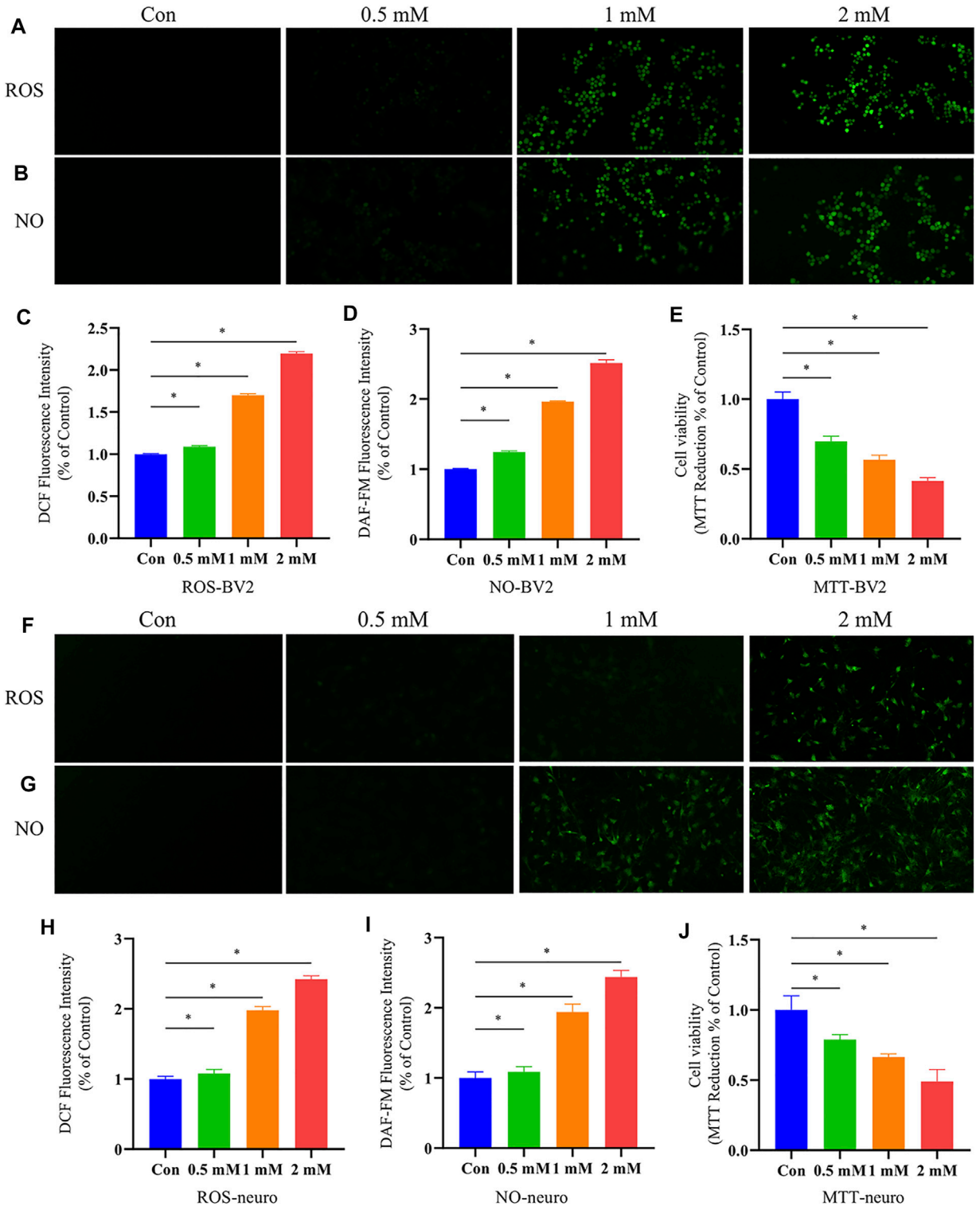

FIGURE 8 | Effects of *o*-tyr on oxidative stress and cell viability of BV-2 and neurons. **(A,B)** Fluorescent images of ROS **(A)** and NO **(B)** in BV-2 cells, with *in situ* signals quantified in **(C)** and **(D)**. **(E)** Effect of *o*-tyr on the viability of BV-2 cells. **(F,G)** Fluorescent images of ROS **(F)** and NO **(G)** in BV-2 cells, with *in situ* signals quantified in **(H)** and **(I)**. **(J)** Effect of *o*-tyr on the viability of neuronal cells. Values are expressed as the mean ± S.E.M.; $n = 6$; $^*p < 0.05$ versus Con, by Student's unpaired *t*-test.

four genera and their related metabolites and pathways may influence AD-related pathological indicators and play an important role in the progression of AD. A variety of pathological indicators for AD are related to intestinal microbiota disorders and metabolic disorders (**Supplementary Figure S5**). It suggested that the decline of cognitive function in AD was related to the microbiota composition and metabolites and further aggravates cognitive impairment.

As shown in **Figure 7**, some bacteria and metabolites play pivotal roles in the microbiota-metabolite-indicator network and may react specifically to rhubarb. To understand the potential effect of rhubarb on the microbiota-metabolite-indicator network, metabolite nodes with higher node degrees were analysed. Interestingly, the abundance of *o*-tyr, 3-hydroxyundecanoyl carnitine, L-glutamic acid, LysoPE (14:0/0:0), 3-Hydroxytetradecanedioic acid, and pyroglutamic acid, which connected the microbiota and indicator nodes in the network, were recovered after rhubarb treatment (**Figures 7B–H**).

Validation of *o*-tyr as Key Microbial Metabolites Mediating the Pathological Changes in Alzheimer's disease

As mentioned above, the relative peak area of *o*-tyr in the feces of the Tg group continued to increase with age. The level of *o*-tyr was significantly reduced by rhubarb intervention (**Figure 7B**). In the microbiota-metabolites-indicators network, *o*-tyr was significantly correlated with two types of bacteria, four pathological indicators, and seven metabolites, suggesting it may play a pivotal role in connecting the microbiota to the pathological indicators in the microbiota-metabolites-indicators network.

It has been reported that *o*-tyrosine could not only produce intracellular hydroxyl radicals, but other reactive oxygen species (ROS), such as hydrogen peroxide and superoxide radical anion (Ipson and Fisher, 2016). We speculated that in the process of aging, *o*-tyr from bacteria could enter the brain due to the increased permeability of the blood-brain barrier, induced neuronal oxidative stress and apoptosis. In this study, *in vitro* experiments on primary neurons and BV-2 cells were performed to validate whether *o*-tyr could promote the pathology of AD. ROS is considered to participate in the pathogenesis of AD, which can cause oxidative stress and trigger damages to cells in the brain. The intracellular ROS levels in neuronal and BV-2 cells were determined with DCFH-DA and the fluorescence intensity was further monitored by fluorescence microscope. As shown in **Figures 8A,C,F,H**, as the increase of *o*-tyr concentration, the fluorescence intensity of both cells significantly enhanced.

NO, as an inflammatory factor, plays an important role in neuronal death. To investigate the effect of *o*-tyr on the inflammatory response in neuronal and BV-2 cells, DAF-FM DA was used as a probe for NO. As shown in **Figure 8**, the fluorescence intensity in both neuronal and BV-2 cells significantly enhanced with the increase of the *o*-tyr concentration.

Studies have shown the potential of *o*-tyr to induce apoptosis. Therefore, the impact of *o*-tyr on the viability of neuronal and BV-2 cells was evaluated by the MTT assay. As shown in **Figure 8**, both of the two cells treated with 2 mM *o*-tyr reduced the cell viability to approximately 50%. These results demonstrated that *o*-tyr adversely affected the function and viability of the neuronal and BV-2 cells.

DISCUSSION

In this study, we found that there were age-dependent alterations in both gut microbiota and fecal metabolites in Tg mice, indicating a dynamic change in microbial community and related metabolites during the development of AD. Through a more accurate co-network analysis based on indicator and multi-omics correlation analyses, we found a significant correlation between the metabolites and microbiota with the development of AD disease. *In vitro* experiments were conducted to confirm the toxicity of the microbial metabolite *o*-tyr, which was closely related to the microbiota and pathological indicators in response to rhubarb intervention. The therapeutic mechanisms by which rhubarb acts on key gut microbiota, affects the related metabolites, and improves pathological indicators and finally cognitive impairment in Tg mice were further examined.

It has been reported that APP/PS1 mice show amyloid deposition at 2 months of age, amyloid plaques at 5 months of age, synaptic loss after 7–9 months, and severe cognitive impairment (Want et al., 2010). In addition, age-dependent alterations in the microbiome of APP/PS1 Tg mice have been reported (Shen et al., 2017; Bauerl et al., 2018). These reports indicate that pathological changes in AD are a dynamic process; hence, disturbed intestinal bacteria based on a single time point are not enough to reflect the pathological process of AD. Accordingly, our study confirmed that the gut microbiota community structure changed with the age of the Tg mice by 16S rRNA analysis. The abundance of *Akkermansia* in the Tg group decreased significantly with the increase of age and was negatively correlated with the $A\beta_{42}$ content in the hippocampus. As a next generation probiotic (Zhang T. et al., 2019), *Akkermansia muciniphila* is considered the most abundant mucolytic bacteria in a healthy gut (Belzer and de Vos, 2012). The continuous decrease of *Akkermansia* in the gut during aging may lead to the thinning of intestinal mucosa and the weakening of the intestinal barrier function, and subsequently the translocation of endotoxins and other proinflammatory bacterial products (Bodogai et al., 2018). The abundance of *Escherichia-Shigella* in the Tg group also increased with age. A clinical study showed that the abundance of *Escherichia-Shigella* involved in inflammatory response increased in the feces of AD patients and there was a significant positive correlation between the expression of IL-6, cxcl2, and NLRP3 (Cattaneo et al., 2017). Interestingly, both *Ruminococcaceae_UCG_09* and *norank_f_Ruminococcaceae* belong to the Ruminococcaceae family, although the two species are similar at the taxonomic level, they may perform distinct functions *in vivo* to influence disease progression (Liu H. et al., 2019). One study reported that

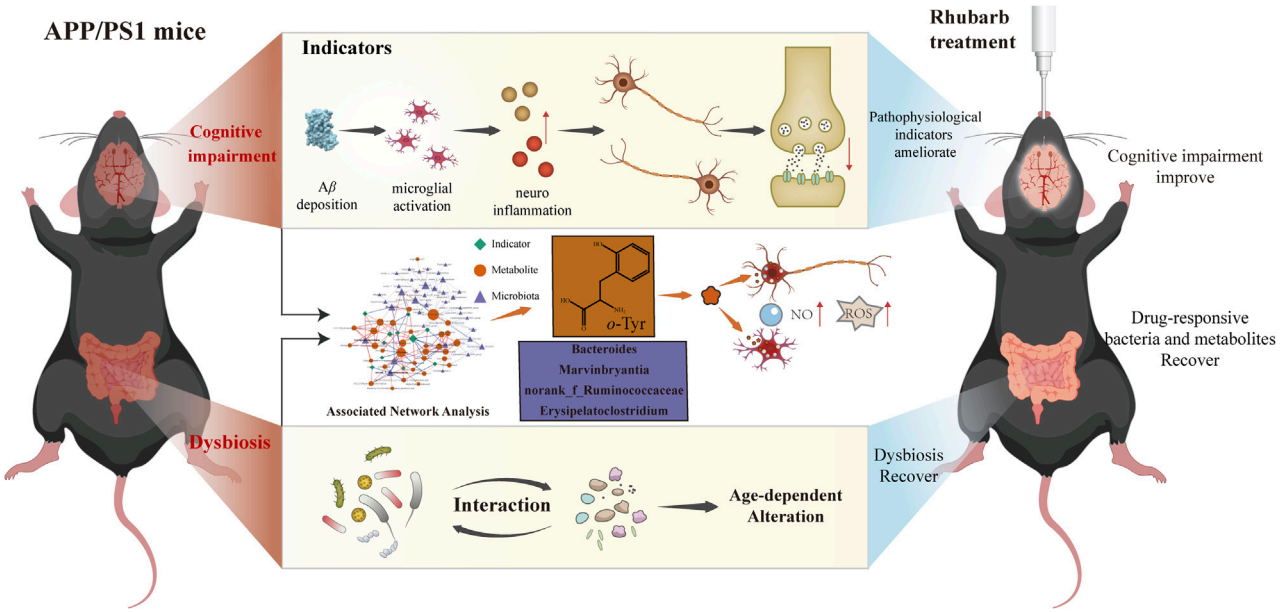

FIGURE 9 | Rhubarb alleviates cognitive impairment in APP/PS1 mice by regulating drug-responsive bacteria and their corresponding microbial metabolites.

high salt diet induced an increase in the abundance of *Ruminococcaceae_UCG_09* in hypertensive mice, accompanied by increased intestinal permeability and inflammation in the small intestine and periphery (Zhang Z. et al., 2019). The increased intestinal permeability led to intestinal bacterial translocation, and the Aβ peptides and LPS secreted by harmful bacteria further induced peripheral and neuronal inflammation, exacerbating cognitive impairment in AD (Friedland and Chapman, 2017). Taken together, our results suggested that there were highly dynamic changes and extensive interactions between the gut microbiota of Tg mice that exacerbated the disease phenotype over time.

Changes in the composition and function of the gut microbiota can affect the overall effectiveness of the drug (Wu TR. et al., 2019; Zeng et al., 2020). Meng Yu et al. (Yu et al., 2017) reported a reduced abundance of *Marvinbryantia* in the gut microbiota and fecal metabolites of rats in a depression model and a significant association existed in bile acid and tryptophan metabolism as well as 5-HT, DA, and NE in the brain. An observational study of AD patients indicated that bile acids may be a biomarker for the early diagnosis of AD (MahmoudianDehkordi et al., 2019). Gut microbiota and the host co-regulate tryptophan metabolic pathways associated with several neurodegenerative diseases (Platten et al., 2019; Dong et al., 2020). Gut microbiota has a regulatory effect on 5-HT production by intestinal enterochromaffin cells and affect the overall tryptophan metabolism and 5-HT levels in the colon and blood, which in turn affects the central concentration of the precursor substance of 5-HT, 5-HTP, and regulates neurotransmitter levels in the brain (Kwon et al., 2019). Herein, rhubarb-responsive bacteria were screened by RT-PCR analysis. We found that the abundance of *Marvinbryantia* gradually decreased with increasing age in Tg mice and was correlated with various metabolites in feces as well as the 5-HT, DA, Glu, and GABA neurotransmitters in the brain. We also found that long-term intervention with rhubarb elevated the abundance of *Marvinbryantia*. Therefore, we hypothesized that *Marvinbryantia* might be an important microbiome target for rhubarb to alleviate AD cognitive impairment.

Studies have indicated that microbial metabolites derived from intestinal bacteria may be important messengers for bidirectional cross-talk between the gut and brain. In food and the human body, choline mainly exists in the form of phosphatidylcholine (PC) (Wang et al., 2011). Many intestinal bacteria that can utilize choline to convert PC into free choline, which is metabolized to trimethylamine (TMA) (Chittim et al., 2019). Some studies have identified the involvement of phospholipase D in PC metabolism from gut microbiota, indicating that intestinal microorganisms are potential targets for phospholipid metabolism and TMA inhibition (Chittim et al., 2019; Orman et al., 2019). Herein, drug-responsive microbial metabolites in Tg mice after rhubarb intervention for 30 and 60 days with consistent trends were further screened by metabolomic analysis. Our study showed that PC (15:0/18:2(9Z,12Z)) was broadly correlated with gut microbiota. Rhubarb reversed the abnormal increase of PC (15:0/18:2(9Z,12Z)) in Tg mice, which suggested that choline metabolism disorders in gut microbiota were alleviated. Patients with inflammatory bowel disease (IBD) harbour a variety of clinically pathogenic bacteria that damaged the integrity of the intestinal barrier by reducing the level of intestinal lysophosphatide, leading to the destruction of the intestinal epithelial barrier and immune activation (Zou et al., 2020). Our results showed that the lysophospholipid LysoPE (14:0/0:0) was associated with *Escherichia-Shigella*, *Marvinbryantia,* and IL-1β. Rhubarb significantly increased the LysoPE (14:0/0:0) level and decreased *Marvinbryantia* abundance in Tg mice. This suggested

that rhubarb could affect the metabolism of lysophosphatidylcholine by regulating gut microbiota, thereby playing an important role in reducing inflammation, improving the intestinal barrier. 3-hydroxyundecanoyl carnitine belongs to the acyl carnitine family and structurally contains *O*-acyl carnitine. Our study showed that rhubarb reduced 3-hydroxyundecanoyl carnitine, which was positively correlated with IL-1β, IL-18, Aβ, and *Erysipelatoclostridium*, but negatively correlated with *Bacteroides*. A multi-omic study in the human microbiome program found that the imbalance of acyl carnitine compounds in the feces of patients with IBD with microbiome transcriptome and serum antibodies was accompanied by the reduction of obligatory anaerobes and the overgrowth of facultative anaerobes (Integrative, 2019). These results suggest that 3-hydroxyundecanoyl carnitine may be a key metabolic marker for rhubarb to improve the flora and indicators of AD. Pyroglutamic acid is a cyclized derivative of lactam formed from free amino cyclization of L-glutamic acid (Ponnusamy et al., 2011). Our results showed that rhubarb could significantly increase the levels of glutamate and pyroglutamate in the feces of Tg mice, regulate the metabolism of neurotransmitters related to intestinal microbiota positively, and thus increase the content of neurotransmitters in the brain.

As a biomarker for oxidative stress (Ipson and Fisher, 2016), *o*-tyr is affected by a variety of microorganisms and can bind abnormally to phenylalanine tRNA in cells, producing oxidative proteins that lead to intracellular protein degradation (Bertin et al., 2007; Klipcan et al., 2009), further reducing cellular activity and inhibiting cellular proliferation (Aronson and Wermus, 1965). In this study, we found that *o*-tyr, which continued to increase in the progression of AD, was significantly negatively correlated with a number of neurotransmitters and positively correlated with IL-18. In further *in vitro* experiments, *o*-tyr was proved to increase ROS and NO in neuronal and BV-2 cells as well as to inhibit cellular activity. These results suggested that gut microbiota-derived *o*-tyr might contribute to oxidative stress and neuroinflammation, exacerbating pathological damage in AD.

As the largest endocrine organ in the body, the gut microbial system can produce a wide range of small biologically active metabolites that enter the circulation and affect the brain (Vogt et al., 2017). As AD is a progressive neurodegenerative disease, the gut microbiota and their metabolites accumulate over time as the disease progresses and may exacerbate the process. However, the identified gut microbiota by 16S rRNA sequencing can be highly variable across studies, even yielding completely opposite results regarding a single genus in different studies with the same disease model [6]. Thus, there would be many false positives in screened microbial metabolites by 16S rRNA sequencing-based co-network analysis and presents difficulties for the development of bacteria-targeted drugs for AD. In this study, an improved co-network analysis consisting of RT-PCR and different metabolites combined with pathological indicators provided a more accurate view to uncover the therapeutic mechanisms of rhubarb for AD from the point of gut microbiota. At the very beginning, we explored the microbiota and metabolites that changed with age and correlated with disease indicators. Four bacterial genera were discovered as the drug-responsive bacteria in the process of rhubarb treatment for AD, which were validated using RT-PCR. Then, based on the above identification results, the accuracy of identification for microbial metabolites associated with drug-responsive bacteria was immensely improved by co-network analysis. After that, *o*-tyr was identified and validated its role in promotion of AD pathology by gut-brain transmission. Finally, it demonstrated that rhubarb ameliorated cognitive impairment in Tg mice through decreasing the abundance of *o*-tyr in the gut owing to the regulation of rhubarb-responsive bacteria.

In conclusion (**Figure 9**), our results demonstrated that with the progression of AD, dynamic changes occur in gut microbiota and their corresponding metabolites. Most importantly, a more accurate co-network analysis employed here demonstrated that the therapeutic effects of rhubarb for AD relies on certain bacteria and metabolites correlated with pathological indicators. Reducing the accumulation of metabolites produced by microbiota *in vivo* would help to intervene the progression of AD. The current findings provide a novel perspective on the accurate identification of drug-responsive gut microbes and metabolites to elaborate therapeutic mechanisms of bacteria-targeted drugs for AD.

DATA AVAILABILITY STATEMENT

The original contributions presented in the study are publicly available. This data can be found here: https://www.ncbi.nlm.nih.gov/bioproject/, PRJNA779704. 210917.

ETHICS STATEMENT

The animal study was reviewed and approved by the Ethics Committee for Animal Care and Treatment at Beijing University of Chinese Medicine.

AUTHOR CONTRIBUTIONS

GL, YW, and XG contributed to study conception and design; DG and HZ conducted the experiments, analyzed and interpreted the data, and wrote the manuscript. ZY and CH collected the samples and performed the analysis of samples. All authors critically reviewed the manuscript and approved the final version for submission.

FUNDING

This work was supported by the National Natural Science Foundation of China (81973467/H2803) and the Fundamental Research Funds for the Central Universities (2020-JYB-ZDGG-033).

SUPPLEMENTARY MATERIAL

The Supplementary Material for this article can be found online at: https://www.frontiersin.org/articles/10.3389/fphar.2021.766120/full#supplementary-material

REFERENCES

Aronson, J. N., and Wermus, G. R. (1965). Effects of M-Tyrosine on Growth and Sporulation of Bacillus Species. *J. Bacteriol.* 90 (1), 38–46. doi:10.1128/JB.90.1.38-46.1965

Bäuerl, C., Collado, M. C., Diaz Cuevas, A., Viña, J., and Pérez Martínez, G. (2018). Shifts in Gut Microbiota Composition in an APP/PSS1 Transgenic Mouse Model of Alzheimer's Disease during Lifespan. *Lett. Appl. Microbiol.* 66 (6), 464–471. doi:10.1111/lam.12882

Belzer, C., and de Vos, W. M. (2012). Microbes Inside-Ffrom Diversity to Function: the Case of Akkermansia. *ISME J.* 6 (8), 1449–1458. doi:10.1038/ismej.2012.6

Bertin, C., Weston, L. A., Huang, T., Jander, G., Owens, T., Meinwald, J., et al. (2007). Grass Roots Chemistry: Meta-Tyrosine, an Herbicidal Nonprotein Amino Acid. *Proc. Natl. Acad. Sci. U. S. A.* 104 (43), 16964–16969. doi:10.1073/pnas.0707198104

Bodogai, M., O'Connell, J., Kim, K., Kim, Y., Moritoh, K., Chen, C., et al. (2018). Commensal Bacteria Contribute to Insulin Resistance in Aging by Activating Innate B1a Cells. *Sci. Transl. Med.* 10 (467), eaat4271. doi:10.1126/scitranslmed.aat4271

Cattaneo, A., Cattane, N., Galluzzi, S., Provasi, S., Lopizzo, N., Festari, C., et al. (2017). Association of Brain Amyloidosis with Pro-inflammatory Gut Bacterial Taxa and Peripheral Inflammation Markers in Cognitively Impaired Elderly. *Neurobiol. Aging* 49, 60–68. doi:10.1016/j.neurobiolaging.2016.08.019

Chittim, C. L., Martínez Del Campo, A., and Balskus, E. P. (2019). Gut Bacterial Phospholipase Ds Support Disease-Associated Metabolism by Generating Choline. *Nat. Microbiol.* 4 (1), 155–163. doi:10.1038/s41564-018-0294-4

Desai, M. S., Seekatz, A. M., Koropatkin, N. M., Kamada, N., Hickey, C. A., Wolter, M., et al. (2016). A Dietary Fiber-Deprived Gut Microbiota Degrades the Colonic Mucus Barrier and Enhances Pathogen Susceptibility. *Cell* 167 (5), 1339–1353.e21. doi:10.1016/j.cell.2016.10.043

Dong, F., Hao, F., Murray, I. A., Smith, P. B., Koo, I., Tindall, A. M., et al. (2020). Intestinal Microbiota-Derived Tryptophan Metabolites Are Predictive of Ah Receptor Activity. *Gut Microbes* 12 (1), 1–24. doi:10.1080/19490976.2020.1788899

Dong, X., Fu, J., Yin, X., Cao, S., Li, X., Lin, L., et al. (2016). Emodin: A Review of its Pharmacology, Toxicity and Pharmacokinetics. *Phytother. Res.* 30 (8), 1207–1218. doi:10.1002/ptr.5631

Eisenstein, M. (2018). Microbiology: Making the Best of PCR Bias. *Nat. Methods* 15 (5), 317–320. doi:10.1038/nmeth.4683

Faust, K., and Raes, J. (2016). CoNet App: Inference of Biological Association Networks Using Cytoscape. *F1000Res* 5, 1519. doi:10.12688/f1000research.9050.2

Feng, Y. L., Cao, G., Chen, D. Q., Vaziri, N. D., Chen, L., Zhang, J., et al. (2019). Microbiome-metabolomics Reveals Gut Microbiota Associated with Glycine-Conjugated Metabolites and Polyamine Metabolism in Chronic Kidney Disease. *Cell. Mol. Life Sci.* 76 (24), 4961–4978. doi:10.1007/s00018-019-03155-9

Friedland, R. P., and Chapman, M. R. (2017). The Role of Microbial Amyloid in Neurodegeneration. *Plos Pathog.* 13 (12), e1006654. doi:10.1371/journal.ppat.1006654

Gao, X. Y., Jiang, Y., Lu, J. Q., and Tu, P. F. (2009). One Single Standard Substance for the Determination of Multiple Anthraquinone Derivatives in Rhubarb Using High-Performance Liquid Chromatography-Diode Array Detection. *J. Chromatogr. A.* 1216 (11), 2118–2123. doi:10.1016/j.chroma.2008.11.104

Gohl, D. M., Vangay, P., Garbe, J., MacLean, A., Hauge, A., Becker, A., et al. (2016). Systematic Improvement of Amplicon Marker Gene Methods for Increased Accuracy in Microbiome Studies. *Nat. Biotechnol.* 34 (9), 942–949. doi:10.1038/nbt.3601

Haugland, R. A., Varma, M., Sivaganesan, M., Kelty, C., Peed, L., and Shanks, O. C. (2010). Evaluation of Genetic Markers from the 16S rRNA Gene V2 Region for Use in Quantitative Detection of Selected Bacteroidales Species and Human Fecal Waste by qPCR. *Syst. Appl. Microbiol.* 33 (6), 348–357. doi:10.1016/j.syapm.2010.06.001

Integrative, H. M. P. R. N. C. (2019). The Integrative Human Microbiome Project. *Nature* 569 (7758), 641–648. doi:10.1038/s41586-019-1238-8

Ipson, B. R., and Fisher, A. L. (2016). Roles of the Tyrosine Isomers Meta-Tyrosine and Ortho-Tyrosine in Oxidative Stress. *Ageing Res. Rev.* 27, 93–107. doi:10.1016/j.arr.2016.03.005

Jack, C. R., Jr., Bennett, D. A., Blennow, K., Carrillo, M. C., Dunn, B., Haeberlein, S. B., et al. (2018). NIA-AA Research Framework: Toward a Biological Definition of Alzheimer's Disease. *Alzheimers Dement* 14 (4), 535–562. doi:10.1016/j.jalz.2018.02.018

Jiang, Y., Ogunade, I. M., Qi, S., Hackmann, T. J., Staples, C. R., and Adesogan, A. T. (2017). Effects of the Dose and Viability of *Saccharomyces cerevisiae*. 1. Diversity of Ruminal Microbes as Analyzed by Illumina MiSeq Sequencing and Quantitative PCR. *J. Dairy Sci.* 100 (1), 325–342. doi:10.3168/jds.2016-11263

Kim, M. S., Kim, Y., Choi, H., Kim, W., Park, S., Lee, D., et al. (2020). Transfer of a Healthy Microbiota Reduces Amyloid and Tau Pathology in an Alzheimer's Disease Animal Model. *Gut* 69 (2), 283–294. doi:10.1136/gutjnl-2018-317431

Klipcan, L., Moor, N., Kessler, N., and Safro, M. G. (2009). Eukaryotic Cytosolic and Mitochondrial Phenylalanyl-tRNA Synthetases Catalyze the Charging of tRNA with the Meta-Tyrosine. *Proc. Natl. Acad. Sci. U. S. A.* 106 (27), 11045–11048. doi:10.1073/pnas.0905212106

Kwon, Y. H., Wang, H., Denou, E., Ghia, J. E., Rossi, L., Fontes, M. E., et al. (2019). Modulation of Gut Microbiota Composition by Serotonin Signaling Influences Intestinal Immune Response and Susceptibility to Colitis. *Cell Mol. Gastroenterol. Hepatol.* 7 (4), 709–728. doi:10.1016/j.jcmgh.2019.01.004

Li, X., Chu, S., Liu, Y., and Chen, N. (2019). Neuroprotective Effects of Anthraquinones from Rhubarb in Central Nervous System Diseases. *Evid. Based Complement. Alternat Med.* 2019, 3790728. doi:10.1155/2019/3790728

Liu, H., Chen, X., Hu, X., Niu, H., Tian, R., Wang, H., et al. (2019a). Alterations in the Gut Microbiome and Metabolism with Coronary Artery Disease Severity. *Microbiome* 7 (1), 68. doi:10.1186/s40168-019-0683-9

Liu, P., Wu, L., Peng, G., Han, Y., Tang, R., Ge, J., et al. (2019b). Altered Microbiomes Distinguish Alzheimer's Disease from Amnestic Mild Cognitive Impairment and Health in a Chinese Cohort. *Brain Behav. Immun.* 80, 633–643. doi:10.1016/j.bbi.2019.05.008

Luan, H., Wang, X., and Cai, Z. (2019). Mass Spectrometry-Based Metabolomics: Targeting the Crosstalk between Gut Microbiota and Brain in Neurodegenerative Disorders. *Mass. Spectrom. Rev.* 38 (1), 22–33. doi:10.1002/mas.21553

MahmoudianDehkordi, S., Arnold, M., Nho, K., Ahmad, S., Jia, W., Xie, G., et al. (2019). Altered Bile Acid Profile Associates with Cognitive Impairment in Alzheimer's Disease-An Emerging Role for Gut Microbiome. *Alzheimers Dement* 15 (1), 76–92. doi:10.1016/j.jalz.2018.07.217

Mancuso, C., and Santangelo, R. (2018). Alzheimer's Disease and Gut Microbiota Modifications: The Long Way between Preclinical Studies and Clinical Evidence. *Pharmacol. Res.* 129, 329–336. doi:10.1016/j.phrs.2017.12.009

Matysik, S., Le Roy, C. I., Liebisch, G., and Claus, S. P. (2016). Metabolomics of Fecal Samples: A Practical Consideration. *Trends Food Sci. Technology* 57, 244–255. doi:10.1016/j.tifs.2016.05.011

Minter, M. R., Zhang, C., Leone, V., Ringus, D. L., Zhang, X., Oyler-Castrillo, P., et al. (2016). Antibiotic-induced Perturbations in Gut Microbial Diversity Influences Neuro-Inflammation and Amyloidosis in a Murine Model of Alzheimer's Disease. *Sci. Rep.* 6 (1), 30028. doi:10.1038/srep30028

Mosmann, T. (1983). Rapid Colorimetric Assay for Cellular Growth and Survival: Application to Proliferation and Cytotoxicity Assays. *J. Immunol. Methods* 65 (1-2), 55–63. doi:10.1016/0022-1759(83)90303-4

Neyrinck, A. M., Etxeberria, U., Taminiau, B., Daube, G., Van Hul, M., Everard, A., et al. (2017). Rhubarb Extract Prevents Hepatic Inflammation Induced by Acute Alcohol Intake, an Effect Related to the Modulation of the Gut Microbiota. *Mol. Nutr. Food Res.* 61 (1), 1500899. doi:10.1002/mnfr.201500899

Nicholson, J. K., Holmes, E., Kinross, J., Burcelin, R., Gibson, G., Jia, W., et al. (2012). Host-gut Microbiota Metabolic Interactions. *Science* 336 (6086), 1262–1267. doi:10.1126/science.1223813

Orman, M., Bodea, S., Funk, M. A., Campo, A. M., Bollenbach, M., Drennan, C. L., et al. (2019). Structure-Guided Identification of a Small Molecule that Inhibits Anaerobic Choline Metabolism by Human Gut Bacteria. *J. Am. Chem. Soc.* 141 (1), 33–37. doi:10.1021/jacs.8b04883

Peisl, B. Y. L., Schymanski, E. L., and Wilmes, P. (2018). Dark Matter in Host-Microbiome Metabolomics: Tackling the Unknowns-A Review. *Anal. Chim. Acta* 1037, 13–27. doi:10.1016/j.aca.2017.12.034

Pennathur, S., Jackson-Lewis, V., Przedborski, S., and Heinecke, J. W. (1999). Mass Spectrometric Quantification of 3-nitrotyrosine, Ortho-Tyrosine, and O,o'-Dityrosine in Brain Tissue of 1-Methyl-4-Phenyl-1,2,3, 6-Tetrahydropyridine-

Treated Mice, a Model of Oxidative Stress in Parkinson's Disease. *J. Biol. Chem.* 274 (49), 34621–34628. doi:10.1074/jbc.274.49.34621

Pistollato, F., Sumalla Cano, S., Elio, I., Masias Vergara, M., Giampieri, F., and Battino, M. (2016). Role of Gut Microbiota and Nutrients in Amyloid Formation and Pathogenesis of Alzheimer Disease. *Nutr. Rev.* 74 (10), 624–634. doi:10.1093/nutrit/nuw023

Platten, M., Nollen, E. A. A., Röhrig, U. F., Fallarino, F., and Opitz, C. A. (2019). Tryptophan Metabolism as a Common Therapeutic Target in Cancer, Neurodegeneration and beyond. *Nat. Rev. Drug Discov.* 18 (5), 379–401. doi:10.1038/s41573-019-0016-5

Ponnusamy, K., Choi, J. N., Kim, J., Lee, S. Y., and Lee, C. H. (2011). Microbial Community and Metabolomic Comparison of Irritable Bowel Syndrome Faeces. *J. Med. Microbiol.* 60 (Pt 6), 817–827. doi:10.1099/jmm.0.028126-0

Rothhammer, V., Borucki, D. M., Tjon, E. C., Takenaka, M. C., Chao, C. C., Ardura-Fabregat, A., et al. (2018). Microglial Control of Astrocytes in Response to Microbial Metabolites. *Nature* 557 (7707), 724–728. doi:10.1038/s41586-018-0119-x

Ruan, Y. Y., Zhai, W., Shi, X. M., Zhang, L., and Hu, Y. L. (2016). Safflower Yellow Ameliorates Cognition Deficits and Reduces Tau Phosphorylation in APP/PS1 Transgenic Mice. *Metab. Brain Dis.* 31 (5), 1133–1142. doi:10.1007/s11011-016-9857-3

Shaffer, M., Armstrong, A. J. S., Phelan, V. V., Reisdorph, N., and Lozupone, C. A. (2017). Microbiome and Metabolome Data Integration Provides Insight into Health and Disease. *Transl. Res.* 189, 51–64. doi:10.1016/j.trsl.2017.07.001

Shannon, P., Markiel, A., Ozier, O., Baliga, N. S., Wang, J. T., Ramage, D., et al. (2003). Cytoscape: a Software Environment for Integrated Models of Biomolecular Interaction Networks. *Genome Res.* 13 (11), 2498–2504. doi:10.1101/gr.1239303

Shen, L., Liu, L., and Ji, H. F. (2017). Alzheimer's Disease Histological and Behavioral Manifestations in Transgenic Mice Correlate with Specific Gut Microbiome State. *J. Alzheimers Dis.* 56 (1), 385–390. doi:10.3233/jad-160884

Sierksma, A., Escott-Price, V., and De Strooper, B. (2020). Translating Genetic Risk of Alzheimer's Disease into Mechanistic Insight and Drug Targets. *Science* 370 (6512), 61–66. doi:10.1126/science.abb8575

Stepanichev, M. Y., Zdobnova, I. M., Zarubenko, I. I., Moiseeva, Y. V., Lazareva, N. A., Onufriev, M. V., et al. (2004). Amyloid-beta(25-35)-induced Memory Impairments Correlate with Cell Loss in Rat hippocampus. *Physiol. Behav.* 80 (5), 647–655. doi:10.1016/j.physbeh.2003.11.003

Sun, H., Yin, Q., Zhang, A., and Wang, X. (2012). UPLC-MS/MS Performing Pharmacokinetic and Biodistribution Studies of Rhein. *J. Sep. Sci.* 35 (16), 2063–2068. doi:10.1002/jssc.201200378

Tettamanti Boshier, F. A., Srinivasan, S., Lopez, A., Hoffman, N. G., Proll, S., Fredricks, D. N., et al. (2020). Complementing 16S rRNA Gene Amplicon Sequencing with Total Bacterial Load to Infer Absolute Species Concentrations in the Vaginal Microbiome. *mSystems* 5 (2), e00777–19. doi:10.1128/mSystems.00777-19

Tkacz, A., Hortala, M., and Poole, P. S. (2018). Absolute Quantitation of Microbiota Abundance in Environmental Samples. *Microbiome* 6 (1), 110. doi:10.1186/s40168-018-0491-7

Vogt, N. M., Kerby, R. L., Dill-McFarland, K. A., Harding, S. J., Merluzzi, A. P., Johnson, S. C., et al. (2017). Gut Microbiome Alterations in Alzheimer's Disease. *Sci. Rep.* 7 (1), 13537. doi:10.1038/s41598-017-13601-y

Vogt, N. M., Romano, K. A., Darst, B. F., Engelman, C. D., Johnson, S. C., Carlsson, C. M., et al. (2018). The Gut Microbiota-Derived Metabolite Trimethylamine N-Oxide Is Elevated in Alzheimer's Disease. *Alzheimers Res. Ther.* 10 (1), 124. doi:10.1186/s13195-018-0451-2

Vorhees, C. V., and Williams, M. T. (2006). Morris Water Maze: Procedures for Assessing Spatial and Related Forms of Learning and Memory. *Nat. Protoc.* 1 (2), 848–858. doi:10.1038/nprot.2006.116

Wang, X., Sun, G., Feng, T., Zhang, J., Huang, X., Wang, T., et al. (2019). Sodium Oligomannate Therapeutically Remodels Gut Microbiota and Suppresses Gut Bacterial Amino Acids-Shaped Neuroinflammation to Inhibit Alzheimer's Disease Progression. *Cell Res* 29 (10), 787–803. doi:10.1038/s41422-019-0216-x

Wang, Z., Klipfell, E., Bennett, B. J., Koeth, R., Levison, B. S., Dugar, B., et al. (2011). Gut flora Metabolism of Phosphatidylcholine Promotes Cardiovascular Disease. *Nature* 472 (7341), 57–63. doi:10.1038/nature09922

Want, E. J., Wilson, I. D., Gika, H., Theodoridis, G., Plumb, R. S., Shockcor, J., et al. (2010). Global Metabolic Profiling Procedures for Urine Using UPLC-MS. *Nat. Protoc.* 5 (6), 1005–1018. doi:10.1038/nprot.2010.50

Wu, T. R., Lin, C. S., Chang, C. J., Lin, T. L., Martel, J., Ko, Y. F., et al. (2019a). Gut Commensal Parabacteroides Goldsteinii Plays a Predominant Role in the Anti-obesity Effects of Polysaccharides Isolated from Hirsutella Sinensis. *Gut* 68 (2), 248–262. doi:10.1136/gutjnl-2017-315458

Wu, Y., Du, S., Johnson, J. L., Tung, H. Y., Landers, C. T., Liu, Y., et al. (2019b). Microglia and Amyloid Precursor Protein Coordinate Control of Transient Candida Cerebritis with Memory Deficits. *Nat. Commun.* 10 (1), 58. doi:10.1038/s41467-018-07991-4

Xu, J., Chen, H. B., and Li, S. L. (2017). Understanding the Molecular Mechanisms of the Interplay between Herbal Medicines and Gut Microbiota. *Med. Res. Rev.* 37 (5), 1140–1185. doi:10.1002/med.21431

Xu, K., Gao, X., Xia, G., Chen, M., Zeng, N., Wang, S., et al. (2021). Rapid Gut Dysbiosis Induced by Stroke Exacerbates Brain Infarction in Turn. *Gut* 70 (8), 1486–1494. doi:10.1136/gutjnl-2020-323263

Yu, M., Jia, H., Zhou, C., Yang, Y., Zhao, Y., Yang, M., et al. (2017). Variations in Gut Microbiota and Fecal Metabolic Phenotype Associated with Depression by 16S rRNA Gene Sequencing and LC/MS-based Metabolomics. *J. Pharm. Biomed. Anal.* 138, 231–239. doi:10.1016/j.jpba.2017.02.008

Zakham, F., Pillonel, T., Brunel, A. S., Zambelli, P. Y., Greub, G., Croxatto, A., et al. (2019). Molecular Diagnosis and Enrichment Culture Identified a Septic Pseudoarthrosis Due to an Infection with Erysipelatoclostridium Ramosum. *Int. J. Infect. Dis.* 81, 167–169. doi:10.1016/j.ijid.2019.02.001

Zeng, S. L., Li, S. Z., Xiao, P. T., Cai, Y. Y., Chu, C., Chen, B. Z., et al. (2020). Citrus Polymethoxyflavones Attenuate Metabolic Syndrome by Regulating Gut Microbiome and Amino Acid Metabolism. *Sci. Adv.* 6 (1), eaax6208. doi:10.1126/sciadv.aax6208

Zhang, T., Li, Q., Cheng, L., Buch, H., and Zhang, F. (2019a). Akkermansia Muciniphila Is a Promising Probiotic. *Microb. Biotechnol.* 12 (6), 1109–1125. doi:10.1111/1751-7915.13410

Zhang, Z., Zhao, J., Tian, C., Chen, X., Li, H., Wei, X., et al. (2019b). Targeting the Gut Microbiota to Investigate the Mechanism of Lactulose in Negating the Effects of a High-Salt Diet on Hypertension. *Mol. Nutr. Food Res.* 63 (11), e1800941. doi:10.1002/mnfr.201800941

Zhao, H., Gao, D., and Gao, X. (2019). Rhubarb Ameliorates Cognitive Dysfunction in a Rat Model of Alzheimer's Disease through Regulation of the Intestinal Microbiome. *J. Traditional Chin. Med. Sci.* 6 (3), 234–243. doi:10.1016/j.jtcms.2019.08.004

Zheng, P., Wu, J., Zhang, H., Perry, S. W., Yin, B., Tan, X., et al. (2020). The Gut Microbiome Modulates Gut-Brain axis Glycerophospholipid Metabolism in a Region-specific Manner in a Nonhuman Primate Model of Depression. *Mol. Psychiatry* 26 (6), 2380–2392. doi:10.1038/s41380-020-0744-2

Zou, D., Pei, J., Lan, J., Sang, H., Chen, H., Yuan, H., et al. (2020). A SNP of Bacterial Blc Disturbs Gut Lysophospholipid Homeostasis and Induces Inflammation through Epithelial Barrier Disruption. *EBioMedicine* 52, 102652. doi:10.1016/j.ebiom.2020.102652

Conflict of Interest: The authors declare that the research was conducted in the absence of any commercial or financial relationships that could be construed as a potential conflict of interest.

Publisher's Note: All claims expressed in this article are solely those of the authors and do not necessarily represent those of their affiliated organizations, or those of the publisher, the editors and the reviewers. Any product that may be evaluated in this article, or claim that may be made by its manufacturer, is not guaranteed or endorsed by the publisher.

GLOSSARY

5-HT serotonin

Aβ amyloid-β

Ach acetylcholine

AD Alzheimer's disease

ANOVA the analysis of variance

BBB blood brain barrier

BPIs Representative base peak ion chromatograms

CV coefficient of variation

DA dopamine

DAF-FM DA 3-amino,4-aminomethyl-2′,7′-difluorofluorescein diacetate

DCFH-DA 2′,7′-dichlorodihydrofluorescein diacetate

DMEM Dulbecco's modified Eagle's medium

DMSO dimethyl sulfoxide

dNTP deoxynucleoside triphosphate

ELISA enzyme-linked immunosorbent assay

FBS fetal bovine serum

FDR false discovery rate

GABA γ-aminobutyric acid

Glu glutamate

HE hematoxylin and eosin

IBD inflammatory bowel disease

IL interleukin

LC-MS Liquid chromatography–mass spectrometry

LPS lipopolysaccharides

MRM multiple reaction monitoring

MS mass spectrometry

NE norepinephrine

NO Nitric oxide

***o*-tyr** *o*-tyrosine

OTUs operational taxonomic units

PBS phosphate-buffered saline

PC phosphatidylcholine

PCA principal component analysis

PLS-DA partial least-squares discriminant analysis

QC quality control

RT-PCR real-time polymerase chain reaction

ROS reactive oxygen species

SD Sprague-Dawley

TCM Traditional Chinese medicine

Tg transgenic

TgP positive drug group

TgR rhubarb administration group

TMA trimethylamine

TNF tumour necrosis factor

UPLC ultra-performance liquid chromatography

UPLC-Q-TOF/MS Ultra-Performance Liquid Chromatography-quadrupole time-of-flight mass spectrometry

UPLC-TQ/MS Ultra-Performance Liquid Chromatography-Triple Quadruple Mass Spectrometry

VIP variable importance of projection

WT wild type control group

frontiers in Pharmacology

ORIGINAL RESEARCH
published: 04 January 2022
doi: 10.3389/fphar.2021.808867

San-Huang-Yi-Shen Capsule Ameliorates Diabetic Nephropathy in Rats Through Modulating the Gut Microbiota and Overall Metabolism

*Xiuhai Su, Wenxia Yu, Airu Liu, Congxiang Wang, Xiuzhen Li, Juanjuan Gao, Xiaofei Liu, Wenhui Jiang, Yue Yang and Shuquan Lv**

Cangzhou Hospital of Integrated TCM and Western Medicine of Hebei Province, Cangzhou, China

San-Huang-Yi-Shen capsule (SHYS) has been used in the treatment of diabetic nephropathy (DN) in clinic. However, the mechanisms of SHYS on DN remain unknown. In this study, we used a high-fat diet (HFD) combined with streptozotocin (STZ) injection to establish a DN rat model. Next, we used 16S rRNA sequencing and untargeted metabolomics to study the potential mechanisms of SHYS on DN. Our results showed that SHYS treatment alleviated the body weight loss, hyperglycemia, proteinuria, pathological changes in kidney in DN rats. SHYS could also inhibite the oxidative stress and inflammatory response in kidney. 16S rRNA sequencing analysis showed that SHYS affected the beta diversity of gut microbiota community in DN model rats. SHYX could also decrease the *Firmicutes* to *Bacteroidetes* (*F* to *B*) ratio in phylum level. In genus level, SHYX treatment affected the relative abundances of *Lactobacillus*, *Ruminococcaceae UCG-005*, *Allobaculum*, *Anaerovibrio*, *Bacteroides* and *Candidatus_Saccharimonas.* Untargeted metabolomics analysis showed that SHYX treatment altered the serum metabolic profile in DN model rats through affecting the levels of guanidineacetic acid, L-kynurenine, prostaglandin F1α, threonine, creatine, acetylcholine and other 21 kind of metabolites. These metabolites are mainly involved in glycerophospholipid metabolism, tryptophan metabolism, alanine, aspartate and glutamate metabolism, arginine biosynthesis, tricarboxylic acid (TCA) cycle, tyrosine metabolism, arginine and proline metabolism, arginine and proline metabolism, phenylalanine, tyrosine and tryptophan biosynthesis, phenylalanine metabolism, and D-glutamine and D-glutamate metabolism pathways. Spearman correlation analysis showed that *Lactobacillus, Candidatus_Saccharimonas, Ruminococcaceae UCG-005, Anaerovibrio, Bacteroides,* and *Christensenellaceae_R-7_group* were closely correlated with most of physiological data and the differential metabolites following SHYS treatment. In conclusion, our study revealed multiple ameliorative effects of SHYS on DN including the alleviation of hyperglycemia and the improvement of renal function, pathological changes in kidney, oxidative stress, and the inflammatory response. The mechanism of SHYS on DN may be related to the improvement of gut microbiota which regulates arginine biosynthesis, TCA cycle, tyrosine metabolism, and arginine and proline metabolism.

Keywords: San-Huang-Yi-Shen capsule, diabetic nephropathy, gut microbiota, arginine biosynthesis, tricarboxylic acid cycle, tyrosine metabolism, arginine and proline metabolism

OPEN ACCESS

Edited by:
Shuai Ji,
Xuzhou Medical University, China

Reviewed by:
Meng Xianglong,
Shanxi University of Traditional Chinese Medicine, China
Di Zhao,
Nanjing Agricultural University, China
Muhammad Ishfaq,
Northeast Agricultural University, China

****Correspondence:***
Shuquan Lv
czlvshuquan@163.com

Specialty section:
This article was submitted to Ethnopharmacology, a section of the journal Frontiers in Pharmacology

Received: *04 November 2021*
Accepted: *10 December 2021*
Published: *04 January 2022*

Citation:
Su X, Yu W, Liu A, Wang C, Li X, Gao J, Liu X, Jiang W, Yang Y and Lv S (2022) San-Huang-Yi-Shen Capsule Ameliorates Diabetic Nephropathy in Rats Through Modulating the Gut Microbiota and Overall Metabolism. Front. Pharmacol. 12:808867. doi: 10.3389/fphar.2021.808867

1 INTRODUCTION

Diabetic nephropathy (DN), major complications of diabetes, is a contributing factor in late-stage renal failure (Wang et al., 2016). The current treatment for DN includes blood glucose control and regulation of lipid metabolism using anti-hypertension medicines (Mann et al., 2010; Pazdro and Burgess, 2010; Tone et al., 2005; Jin et al., 2014). However, these conventional treatments do not completely prevent the progression of DN (Tuttle et al., 2018). The development of new therapeutic agents to improve renal function and halt the progression of DN has become an active area of investigation.

Traditional Chinese medicine (TCM) has contributed significantly to the treatment of DN. Numerous studies have shown that TCM has significant advantages for improving renal function, controlling blood glucose levels, and inhibiting the inflammatory response on DN (Zhong et al., 2015). A multicenter randomized controlled study showed that Liu-Wei-Di-Huang pill significantly reduces erythrocyte aldose reductase activity, β2-microglobulin expression, and urinary protein levels in diabetic patients (Song et al., 2004). Qi-Zhi-Jiang-Tang decoction also delays the progression of DN (Guo et al., 2014). Wu-Ling powder ameliorates the inflammatory response in a rat model of DN by inhibiting the NF-κB signaling pathway (Liu et al., 2009). Tong-Shen-Luo (TSL) significantly reduces the extracellular matrix in renal tissues in a rat model of DN (Wu et al., 2007). Finally, Xian-Zhen decoction decreases the accumulation of glycosylated products in renal tissues of rats with DN (Tang et al., 2005).

The human intestine contains a plethora of microorganisms that interact with each other and together maintain the metabolic-immune nervous system homeostasis of the body (Li et al., 2020). Disorders in gut microbiota contribute to the development of various diseases (Guarner, 2006). Patients with DN have an increased ratio of *Firmicutes* to *Bacteroides* in the gut compared with healthy individuals (Gong et al., 2021). These alterations in the microbiota are associated with various pathological changes associated with DN, abnormal hemodynamic inflammatory responses, and metabolic abnormalities (Grigor'eva, 2020; Magne et al., 2020; Macho-González et al., 2021; Zhang et al., 2021). Transplantation of germ-free mice with microbiota from mice with DN resulted in elevated levels of 24-h urine proteins (Cai et al., 2020). Furthermore, gut microbiota may be involved in the progression of DN by modulating metabolism (Li et al., 2020). The pathogenesis of DN may be elucidated by analyzing microbiota metabolism using 16S rRNA sequencing technology combined with untargeted metabolomics, This may lead to the development of new treatments for DN that regulate gut microbiota and host metabolism.

San-Huang-Yi-Shen capsule (SHYS) consists of *Astragalus mongholicus* Bunge, *Panax quinquefolius* L., *Dioscorea oppositifolia* L., *Cornus officinalis* Siebold and Zucc., *Cuscuta chinensis* Lam., *Polygonatum sibiricum* Redouté, *Rehmannia glutinosa* (Gaertn.) DC., *Euryale ferox* Salisb., *Rosa laevigata* Michx., *Leonurus japonicus* Houtt., *Salvia miltiorrhiza* Bunge, *Conioselinum anthriscoides* 'Chuanxiong', *Atractylodes lancea* (Thunb.) DC., *Paeonia lactiflora* Pall., and *Gypsophila vaccaria* (L.) Sm. And has been used in the treatment of many chronic renal diseases including DN, IgA nephropathy and chronic renal failure (Bian et al., 2011; Su et al., 2015b; Zhong et al., 2016). Clinical studies showed that SHYS could alleviate the proteinuria in DN patients (Su et al., 2015a). Animal study has also demonstrated the protective effects of SHYS on DN model rats (Chi et al., 2013). However, the mechanisms of SHYS on DN remain unknown. In this study, we used a high-fat diet (HFD) combined with streptozotocin (STZ) injection to establish a DN rat model. Next, we used 16S rRNA sequencing and untargeted metabolomics to study the potential mechanisms of SHYS on DN.

2 MATERIALS AND METHODS

2.1 Reagents

HFD (65.75% basal chow, 20% sucrose, 10% lard, 3% egg yolk powder, 1% cholesterol, 0.25% pig bile salt) was purchased from Beijing Sibeifu Bioscience Co., Ltd. (Beijing, China). Irbesartan was obtained from Sanofi Winthrop Industrie (France). STZ was purchased from Solarbio Biotechnology Co., Ltd. (Beijing, China). Creatinine (Cr), blood urea nitrogen (BUN), urine protein, superoxide dismutase (SOD), methane dicarboxylic aldehyde (MDA), and glutathione peroxidase (GSH-Px) assay kits test kits were obtained from Nanjing Jiancheng Biological Engineering Institute (Nanjing, China). Rat interleukin (IL)-1β, IL-6, tumor necrosis factor alpha (TNF-α) enzyme-linked immunosorbent assay (ELISA) kit was obtained from Multi Science Biotechnology Co., Ltd. (Hangzhou, China). Reference standards of ferulic acid, atractylodin, tanshinone, astragaloside, hyperoside, loganin, gallic acid, morroniside, allantoin, oleanic acid, ginsenoside Rb1, ginsenoside Re, ginsenoside Rg1, paeoniflorin, vaccarin, pyrrolidinium, leonurine, and catalpol were obtained from Sichuan Weikeqi Biological Technology Co., Ltd. (Sichuan, China).

2.2 Quality Control and Analysis of Main Compounds in SHYS

SHYS was prepared from the pharmacy department of Cangzhou Hospital of Integrated Traditional Chinese and Western Medicine. Briefly, 15 g of *Astragalus mongholicus* Bunge (Batch number: 201126), 12 g of *Panax quinquefolius* L., 12 g of *Dioscorea oppositifolia* L. (Batch number: 201008), 12 g of *Cornus officinalis* Siebold and Zucc. (Batch number: 201126), 12 g of *Cuscuta chinensis* Lam. (Batch number: 200815), 12 g of *Polygonatum sibiricum* Redouté (Batch number: 200912), 15 g of *Rehmannia glutinosa* (Gaertn.) DC. (Batch number: 201126), 12 g of *Euryale ferox* Salisb. (Batch number: 201012), 12 g of *Rosa laevigata* Michx. (Batch number: 201126), 10 g of *Leonurus japonicus* Houtt. (Batch number: 200817), 12 g of *Salvia*

miltiorrhiza Bunge (Batch number: 201102), 12 g of *Conioselinum anthriscoides* 'Chuanxiong' (Batch number: 200817), 10 g of *Atractylodes lancea* (Thunb.) DC. (Batch number: 201014), 10 g of *Paeonia lactiflora* Pall. (Batch number: 201012), and 6 g of *Gypsophila vaccaria* (L.) Sm. (Batch number: 201106) were weighed. All herbs were authenticated by pharmacist in the pharmacy department of Cangzhou Hospital of Integrated Traditional Chinese and Western Medicine. Then, these crude herbs were decocted, evaporated and made into capsuled prepapation according to the medical institution preparation standard in Hebei (approval number: Z20050795). The specification of SHYS was 0.45 g per capsule. The production licence of SHYS was shown in **Supplementary Figure S1**.

Quality control of SHYS was performed using Ultra performance liquid chromatography (UPLC; ACQUITY UPLC®, United States) coupled with Xevo G2 quadrupole-time of-flight (Q-TOF) mass spectrometer (MS; Waters Corp., Milford, MA, United States) systems. Briefly, the test solution was injected onto an ACQUITY UPLC BEH C18 Column (2.1 mm × 100 mm, 1.7 μm) held at 50°C. The flow rate was 0.3 ml/min and the injection volumn was 2 μl. Mobile phase A was 0.1% formic acid aqueous solution and mobile phase B was acetonitrile contained 0.1% formic acid. The mobile phase conditions were: 0 min, 5% B; 1 min, 10% B; 6 min 60% B; 6.5 min 100% B; 10 min 100% B; 10.1 min 5% B; 13 min 5% B.

A Q-TOF MS equipped with an electrospray ionization (ESI) source was used for both positive and negative ionization scan modes (m/z ranges from 50 to 1,200 Da). The scan time was 0.2 s. The capillary voltages were 3,000 V (positive mode) and 2,200 V (negative mode), respectively. The desolvation temperature was 350°C and the source temperature was 100°C. The sample cone voltage was 40 V and the extraction cone voltage was 4 V. The cone gas flow was 40 L/h and the desolvation gas flow was 800 L/h (both positive and negative modes).

2.3 Animals

Sixty male Sprague-Dawley (SD) rats (speciic pathogen free grade, 6–8 weeks old) weighing 200 ± 20 g, were obtained from the Beijing Huafukang Biotechnology Co., Ltd. [Production License No.: SCXK (Beijing) 2020-0016]. The animal were housed at 25 ± 2°C, a 12 h light-dark cycle, with free access to food and water. The study was approved by the Ethics Committee of Cangzhou Hospital of Integrated Traditional Chinese and Western Medicine.

2.4 Induction of DN Rat Model

DN model was induced using HFD and STZ injection as described previously (Shen et al., 2020). Briefly, rats were fed with HFD for 8 weeks. Subsequently, rats were injected intraperitoneally with 30 mg/kg of STZ (dissolved in 0.1 mol/L citric acid buffer, pH = 4.5). After STZ injection, rats were continued to be fed with HFD and blood glucose and 24-h urine protein levels after fasted for 12 h were investigated weekly. FBG levels of ≥12 mmol/L and urine protein levels of ≥20 mg/24 h were used as criteria for establishing the animal model of DN (Zhang et al., 2014), this occurred 2 weeks after STZ injection.

2.5 Animal Grouping

After 1 week of acclimatization, 10 rats were randomly selected as the Control group and provided a standard diet, whereas the remaining 50 rats received HFD and STZ injection to induce DN. After the animal model had been established, DN rats were randomly divided into the Model, Irbesartan, SHYS low-dose, SHYS middle-dose, and SHYS high-dose groups, with 10 rats in each group. Rats in Control and Model groups were gavaged with 2 ml of distilled water; Rats in Irbesartan were gavaged with 11.51 mg/kg irbesartan (Wang et al., 2018); while rats in SHYS low-dose, SHYS middle-dose and SHYS high-dose groups were gavaged with SHYS capsule doses of 0.41, 0.81, and 1.62 g/kg, respectively, once daily for 4 consecutive weeks. The dosage in SHYS middle-dose group in our study was based on a conversion of human to rat body surface area, while the low dose was half the middle dose and high dose was double the middle dose. Body weight and FBG were measured every 2 weeks after SHYS treatment (**Figure 1**).

2.6 Measurement of Biochemical Indicators

After 4 weeks of SHYS intervention, 24 h urine samples were collected from all rats using metabolic cages. Then, rats were anesthetized with an intraperitoneal injection of 50 mg/kg pentobarbital sodium. Blood was collected from the inner canthus, and centrifuged at 3,000 rpm for 15 min to collect the serum. The levels of 24-h urine protein and serum creatine (Cr) and blood urea nitrogen (BUN) in each group of rats were determined using the test kits according to the manufacturer's instructions (Nanjing Jiancheng Biological Engineering Institute).

The rats were sacrificed by cervical dislocation after blood sampling. The kidneys were quickly removed. 0.1 g of kidney tissues were weighed and immersed in 900 μl of normal saline and homogenized at 4°C. The supernatants were collected after centrifugation at 3,000 rpm for 15 min to obtain the renal tissue homogenate. Level of the total protein content in renal tissue homogenate was detected by BCA assay according to the manufacturer's instructions (Nanjing Jiancheng Biological Engineering Institute). Besides, SOD and GSH-Px activities and MDA levels representing oxidative stress were measured according to the instructions described in the kit (Nanjing Jiancheng Biological Engineering Institute).

2.7 ELISA

After 4 weeks of SHYS intervention, IL-6, IL-1β, and TNF-α levels in renal tissue homogenates from each group were measured by ELISA, which was performed based on the manufacturer's instructions (Multi Science Biotechnology Co., Ltd.).

2.8 Histopathology Staining of Renal Tissues

After 4 weeks of SHYS intervention, the renal tissues from each group were fixed in 10% formalin, washed with water for 20 min, dehydrated in gradient alcohol, cleared with xylene, embedded in paraffin. The tissues were cut into 5 μm thick strips, stained with hematoxylin and eosin (H and E), and subjected to Masson and Sirius Red staining. The relative collagenous fiber area was quantified using integrated optical density (IOD) with the Image-Pro Plus 6.0

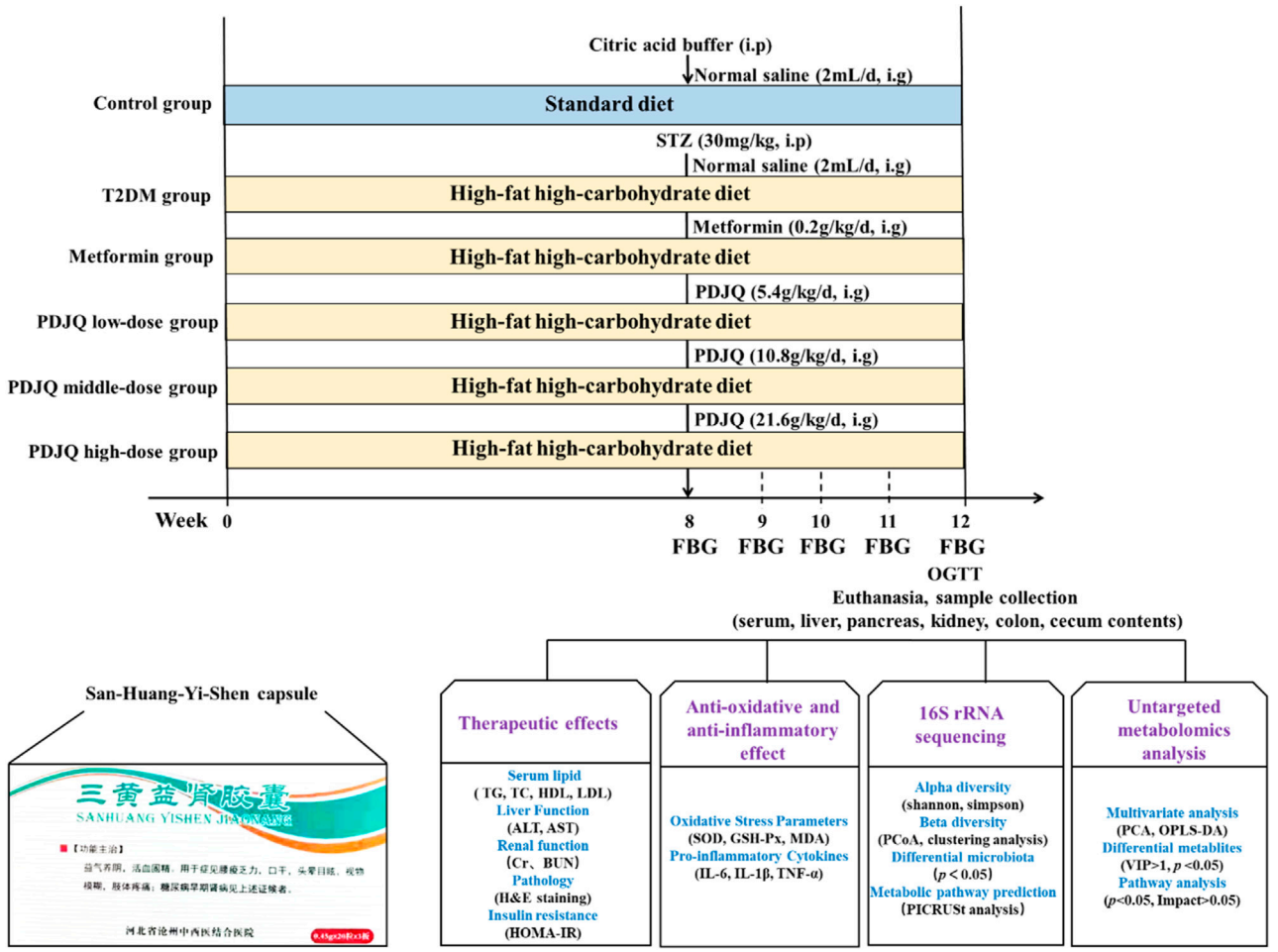

FIGURE 1 | Overview of the experimental design for all groups.

software. The positive area (%) was calculated according to the following formula: IOD/sum area × 100%.

2.9 16S rRNA Sequencing

2.9.1 Extraction of Fecal Genomic DNA

After 4 weeks of SHYS intervention, cecum contents were collected and weighed. Total genomic DNA was extracted using the CTAB/SDS method. The purity and concentration of DNA samples were assessed on a 1% agarose gel. The DNA was diluted to 1 ng/μl with sterile water.

2.9.2 Polymerase Chain Reaction Amplification and Sequencing of 16S rRNA Gene

The V3-V4 region of the 16S rRNA gene was amplified using 338 F (5'-ACTCCTACGGGAGGCAGCAG-3') and 806R (5'-GGACTACHVGGGTWTCTAAT-3') primers. PCR amplification included 10 ng of template DNA, 0.2 μm of forward and reverse primers, and 15 μl of Phusion® High-Fidelity PCR Master Mix (New England Biolabs). The reaction conditions were as follows: pre-denaturation at 98°C for 1 min, 15 cycles of denaturation at 95°C for 10 s, annealing at 50°C for 30 s and extension at 72°C for 30 s, and then holding at 72°C for 5 min and storage at 4°C. The PCR products were purified using the Qiagen Gel Extraction Kit (Qiagen, Germany). A 2% agarose gel was used for detection. Sequencing libraries were generated using the TruSeq® DNA PCR-Free Sample Preparation Kit (Illumina, United States) and library quality was assessed on a Qubit@ 2.0 Fluorometer (Thermo Scientific) and an Agilent Bioanalyzer 5400 system (Agilent, United States). The analysis of peak-heights in agarose gel electropherogram was shown in **Supplementary Figure S2**. Finally, the libraries were sequenced on the Illumina NovaSeq platform to obtain 250 bp of paired-end sequences.

2.9.3 Sequencing Data Analysis

The raw sequencing data were spliced using FLASH (Version 1.2.7, http://ccb.jhu.edu/software/FLASH/). After quality control, the effective tags were obtained. The tags were clustered using Uparse software (Version 7.0.1001, http://drive5.com/uparse/) at 97% similarity to obtain operational taxonomic units (OTUs) (Edgar, 2013). The SILVA reference database (Version 138, http://www.arb-silva.de/) based on the Mothur the algorithm,

was used to annotate the OTUs with taxonomic information (Quast et al., 2012). Multiple sequence comparisons were conducted using MUSCLE software (Version 3.8.31, http://www.drive5.com/muscle/) (Edgar, 2004). The abundance of OTUs was normalized using the sequence number corresponding to the sample with the smallest sequence. Alpha-diversity indicator and beta-diversity analysis were subsequently performed. The Wilcoxon Rank-Sum test was used for statistical difference analysis between groups of diversity indicators. The Kruskal–Wallis rank-sum test was used (Games–Howell test was chosen as the post-hoc test) in conjunction with the multiple testing method of false discovery rate to screen for different bacteria. $p < 0.05$ after false discovery rate (FDR) correction was considered to be statistically significant. Finally, data analysis using Phylogenetic Investigation of Communities by Reconstruction of Unobserved States database (PICRUSt) was performed to predict the relevant biological pathways that may be affected by each group exhibiting different microbiota.

2.10 Metabolomics Analysis

2.10.1 Serum Sample Processing

A 100 μl of serum sample was added to 400 μl of 80% methanol. The mixture was vortexed, shaken, and centrifuged at 15,000 g for 20 min at 4°C in an ice bath. After centrifugation, the supernatant was diluted with ultrapure water to 53% methanol and centrifuged again at 15,000 g for 20 min at 4°C. The supernatant was collected and used as the test sample. All samples were mixed in equal amounts as a quality control (QC) sample and analyzed periodically throughout the analysis process to ensure the stability and accuracy of the measurement throughout the analysis.

2.10.2 Conditions of Chromatography and Mass Spectrometry

Chromatography was performed on a Hypesil Gold column (C_{18}) column (2.1 mm × 100 mm, 1.9 μm) with a mobile phase consisting of (A) 0.1% formic acid and (B) methanol, using a gradient elution of 0 min, 98% A, 2% B; 1.5 min, 98% A, 2% B; 12 min, 0% A, 100% B; 14 min, 0% A, 100% B; 14.1 min, 98% A, 2% B; 17 min, and 98% A, 2% B. The column temperature was set to 40°C with a flow rate of 0.2 ml/min and an injection volume of 2 μl. MS conditions were simultaneous detected in positive- and negative-ion modes using electrospray ionization (ESI). The settings of the ESI were as follows: Spray Voltage: 3.2 kV; Sheath gas flow rate: 40 arb; Aux Gas flow rate: 10 arb; Capillary Temp: 320°C. QC samples were injected every six samples throughout the analytical run, and the data obtained were used to evaluate stability.

2.10.3 Data Processing and Analysis

Molecular signature peaks in the samples were detected based on the results of high-resolution mass spectrometry. The molecular peaks were matched and identified by combining the high-quality mzCloud (https://www.mzcloud.org/), mzVault, and MassList databases constructed from the standards. The raw files (.raw) obtained by MS were imported into Compound Discoverer 3.1 (CD3.1, Thermo Fisher) software for data preprocessing. First, the data were briefly screened by the parameters of retention time and mass-to-charge ratio, and then the peaks from different samples were aligned according to the retention time deviation of 0.2 min and the mass deviation (Part per million, ppm) of 5 ppm to make identification accurate. Subsequently, the data were aligned according to the settings of 5 ppm, signal intensity deviation of 30%, signal-to-noise ratio (S/N) of 3, minimum signal intensity of 1,00,000. Adduct ions for peak extraction and peak area were also quantified. The metabolites were identified by the molecular formula prediction using molecular ion peaks and fragment ions, and were compared with the mzCloud and mzVault and MassList databases. Metabolites with a coefficient of variation of less than 30% in the QC samples were then retained as the final identification results for subsequent analysis. The peaks detected in the samples were integrated using CD3.1 software, where the peak area of each characteristic peak represented the relative quantitative values of a metabolite, and the quantitative results were normalized using the total peak area to obtain the final quantitative results for the metabolites. The data were then subjected to QC to ensure the accuracy and reliability of the results.

Next, the metabolites were subjected to a multivariate statistical analysis, including principal component analysis (PCA) and orthogonal partial least squares discriminant analysis (OPLS-DA), to identify differences in the metabolic patterns among groups. PCA and OPLS-DA were performed using SIMCA software (version 14.1, Umetrics, Sweden). Furthermore, two-tailed Student's *t*-test was used to analyze the normalized peak areas for each metabolite. Differential metabolites between Control and Model groups and between Model and SHYS high-dose groups were screened based on $p < 0.05$ and variable importance of projection (VIP) > 1. Finally, the biological significance of metabolite correlations was explained by functional analysis including metabolic pathways. Metabolic pathway enrichment analysis was performed for differential metabolites with a fold-change (FC) > 1.20 or FC < 0.80 based on MetaboAnalyst software (https://www.metaboanalyst.ca/) and Kyoto Encyclopedia of Genes and Genomes (KEGG) database (https://www.kegg.jp/).

2.10.4 Statistical Methods

The experimental data were analyzed using SPSS 20.0 statistical software. Data were expressed as the mean ± standard deviation (SD). *t*-test was used for comparison between two groups. One-way analysis of variance and post-hoc analysis was used for comparison among multiple groups. Differences were considered statistically significant at $p < 0.05$.

3 RESULTS

3.1 Identification of Main Compounds in SHYS by UPLC-MS Analysis

Ferulic acid, atractylodin, tanshinone, astragaloside, hyperoside, loganin, gallic acid, morroniside, allantoin, oleanic acid, ginsenoside Rb1, ginsenoside Re, ginsenoside Rg1, paeoniflorin, vaccarin, pyrrolidinium, leonurine, and catalpol were used as the reference standards to validate the main compounds in SHYS. The detailed information of these compounds were shown in **Supplementary Figure S3**. The typical based peak intensity (BPI)

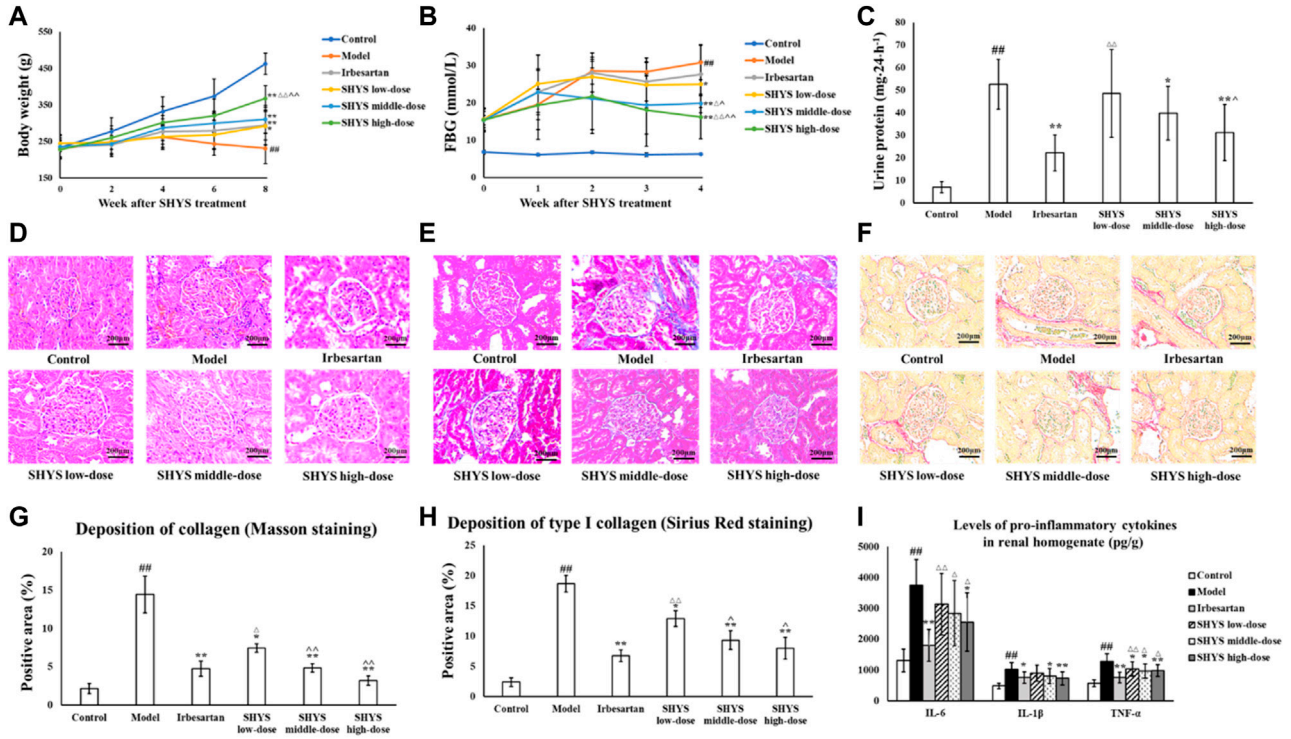

FIGURE 2 | SHYS treatment alleviated the body weight loss, hyperglycemia, proteinuria, pathological changes in kidney and inflammatory response in DN rats. **(A)** SHYS treatment alleviated the body weight loss in DN model rats. **(B)** SHYS treatment decreased the FBG in DN rats. **(C)** SHYS treatment decreased the level of 24-h urine protein. **(D)** H and E staining indicated that SHYS treatment significantly improved the pathological changes of kidney in DN rats (200 ×) **(E–H)** Masson **(E,G)** and Sirius red **(F,H)** staining indicated that SHYS treatment significantly decreased collagen depositions in kidney (200 ×). **(I)** SHYS treatment decreased the levels of pro-inflammatory cytokines in renal tissue homogenates. Control, Model, Irbesartan, SHYS low-dose, SHYS middle-dose and SHYS high-dose (n = 10 per group) groups. Data are presented as the mean ± SD. $^{\#\#}$: $p < 0.01$ as compared to the Control group; *: $p < 0.05$ as compared to the Model group; **: $p < 0.01$ as compared to the Model group; $^{\triangle}$: $p < 0.05$ as compared to the Irbesartan group; $^{\triangle\triangle}$: $p < 0.01$ as compared to the Irbesartan group; $^{\wedge}$: $p < 0.05$ as compared to the SHYS low-dose group; $^{\wedge\wedge}$: $p < 0.01$ as compared to the SHYS low-dose group

chromatograms of SHYS and these reference standards were shown in **Supplementary Figure S4**. The characteristic fragment ions of these compounds were shown in **Supplementary Table S1**. Astragaloside in *Astragalus mongholicus* Bunge, ginsenoside Rb1, ginsenoside Re, and ginsenoside Rg1 in *Panax quinquefolius* L., allantoin in *Dioscorea oppositifolia* L., loganin and morroniside in *Cornus officinalis* Siebold and Zucc., hyperoside in *Cuscuta chinensis* Lam., Pyrrolidinium in *Polygonatum sibiricum* Redouté, Catalpol in *Rehmannia glutinosa* (Gaertn.) DC., gallic acid in *Euryale ferox* Salisb., oleanic acid in *Rosa laevigata* Michx., leonurine in *Leonurus japonicus* Houtt., tanshinone in *Salvia miltiorrhiza* Bunge, ferulic acid in *Conioselinum anthriscoides* 'Chuanxiong', atractylodin in *Atractylodes lancea* (Thunb.) DC., paeoniflorin in *Paeonia lactiflora* Pall., and vaccarin in *Gypsophila vaccaria* (L.) Sm. were identified as the preeminent compounds in SHYS.

3.2 Effect of SHYS on Body Weight, FBG, Renal Function, and Pathological Changes in DN Rats

At the end of drug administration, the body weight in the Model group decreased significantly compared with that of the Control group ($p < 0.01$). The body weight of the rats in the Irbesartan, SHYS low-, middle-, and high-dose groups increased significantly compared with that of the Model group ($p < 0.01$, $p < 0.05$, $p < 0.01$, $p < 0.01$, respectively, **Figure 2A**). FBG levels were ≥12 mmol/L in all rats 2 weeks after STZ injection. After 8 weeks of SHYS intervention, FBG levels were significantly higher in Model group compared with the Control group ($p < 0.01$) and were lower in the SHYS low-, middle-, and high-dose groups compared with that of the Model group ($p < 0.05$, $p < 0.01$, $p < 0.01$, **Figure 2B**). The results of renal function tests showed that the serum levels of Cr and BUN as well as 24-h urine protein levels were significantly higher in the Model group compared with that of the Control group ($p < 0.01$, respectively). The intervention with irbesartan and high-dose SHYS significantly reduced the serum levels of Cr ($p < 0.05$, $p < 0.01$, respectively), BUN ($p < 0.05$, $p < 0.01$, respectively), and 24-h urine protein in the DN rats ($p < 0.01$, respectively). The middle-dose SHYS resulted in significantly reduced 24-h urine protein ($p < 0.05$) and serum BUN levels in DN rats ($p < 0.01$, **Table 1** and **Figure 2C**).

H and E staining results of the kidneys showed that the glomeruli and tubules of the animals in the Control group had normal structure. No mesentery or mesangial stromal

TABLE 1 | Changes of serum Cr and BUN levels in DN rats after SHYS treatment.

Group	Cr (μmol/L)	BUN (mmol/L)
Control	37.39 ± 17.17	3.49 ± 0.2
Model	80.41 ± 32.13[a]	6.82 ± 0.81[a]
Irbesartan	40.73 ± 24.01[b]	5.31 ± 1.48[b]
SHYS low-dose	65.41 ± 32.01[c]	5.55 ± 1.78
SHYS middle-dose	53.83 ± 15.07	3.76 ± 0.84[d,c]
SHYS high-dose	39.04 ± 18.19[d]	3.61 ± 0.40[d,e]

Control, Model, Irbesartan, SHYS low-dose, SHYS middle-dose and SHYS high-dose (n = 10 per group) groups. Data are presented as the mean ± SD.
[a]p < 0.01 as compared to the Control group.
[b]p < 0.05 as compared to the Model group.
[c]p < 0.05 as compared to the Irbesartan group.
[d]p < 0.01 as compared to the Model group.
[e]p < 0.01 as compared to the Irbesartan group.

hyperplasia was observed and no inflammatory cell infiltration was evident. The Model group showed focal tubular degeneration and atrophy, slight thickening of the glomerular basement membrane and mesangial hyperplasia. Compared with the Model group, the lesions were reduced in each drug-treated group and the improvement was more significant in the irbesartan group as well as the SHYS middle- and high-dose groups (**Figure 2D**). Masson staining revealed that the collagen appeared as a blue color by light microscopy. As shown in **Figures 2E,G**, the glomeruli and tubules of animals in the Control group had normal structures and collagen expression was unchanged. In the Model group, however, the collagen areas in the glomerular mesangial region and basement membrane were showed significantly increased compared with the Control group ($p < 0.01$). The glomerular and tubulointerstitial collagen deposition was lower in Irbesartan, SHYS low-dose, SHYS middle-dose, and SHYS high-dose groups compared with those in the Model group ($p < 0.01$, $p < 0.05$, $p < 0.01$, $p < 0.01$, respectively). The results of Sirius red staining was shown in **Figures 2F,H** and indicated that the Model group had significant increase of renal interstitial and vascular wall collagen depositions and thickened glomerular arterioles compared with the Control group, whereas the collagen deposition was lower in Irbesartan, SHYS low-dose, SHYS middle-dose, and SHYS high-dose groups compared with those in the Model group ($p < 0.01$, $p < 0.05$, $p < 0.01$, $p < 0.01$, respectively).

3.3 Effect of SHYS on Oxidative Stress and Inflammatory Factor Levels in DN Rats

We further evaluated the effects of SHYS on oxidative stress in DN rats by measuring SOD, MDA, and GSH-Px in renal tissue homogenates from each group. Compared with the Control group, the activities of SOD and GSH-Px ($p < 0.01$, respectively) in the renal tissue homogenates of animals in Model group were significantly decreased, whereas the level of MDA ($p < 0.01$) was significantly increased. Irbesartan, SHYS middle-dose, and SHYS high-dose treated animals exhibited a significant increase in SOD ($p < 0.01$, $p < 0.05$, $p < 0.01$, respectively) and GSH- Px ($p < 0.01$, $p < 0.05$, $p < 0.01$, respectively) activities and decreased MDA ($p < 0.01$, $p < 0.05$, $p < 0.01$, respectively) levels in renal tissue homogenates (**Table 2**). The effects of SHYS on the inflammatory response of DN rats was also determined by measuring the levels of pro-inflammatory factors, IL-6, IL-1β, and TNF-α, in renal tissue homogenates from each group by ELISA. The levels of proinflammatory factors, IL-6, IL-1β, and TNF-α ($p < 0.01$, respectively) in renal tissue homogenates were significantly increased in rats of the Model group compared with that of the Control group. The levels of IL-6 in the renal tissue homogenates of DN rats were significantly decreased following treatment with irbesartan and high-dose of SHYS ($p < 0.01$ and $p < 0.05$, respectively). The levels of IL-1β were significantly decreased in Irbesartan, SHYS middle-dose and SHYS high-dose groups compared with the Model group ($p < 0.05$, $p < 0.05$ and $p < 0.01$, respectively). The levels of TNF-α were lower in Irbesartan, SHYS low-dose, SHYS middle-dose and SHYS high-dose groups compared with that in the Model group ($p < 0.01$, $p < 0.05$, $p < 0.05$, $p < 0.01$, respectively, **Figure 2I**). These results indicated that SHYS exhibits therapeutic effects on DN rats and the efficacy is most significant at high doses. Therefore, high-dose SHYS was selected for subsequent gut microbiota and metabolomics studies.

3.4 Effects of SHYS on Gut Microbiota in DN Rats

We used 16S rRNA high-throughput sequencing to determine the changes in gut microbiota of DN rats after SHYS treatment. The abundance and diversity of the microbial communities within the samples were analyzed using alpha diversity (i.e., Shannon index and Simpson index). The results indicated that the Shannon and Simpson indexes did not reveal significant differences in the Model group compared with the Control group. Similarly, there was no significant difference in the Shannon and Simpson indexes in the SHYS high-dose group compared with the Model group (**Figures 3A,B**). Next, we analyzed the composition of microbial communities of different samples using beta diversity and evaluated them by principal coordinate analysis (PCoA) and cluster analysis. The PCoA analysis was performed based on unweighted distance, in which the higher the similarity of species composition structure between samples, the more clustered in the diagram. Conversely, the lower the similarity between samples, the more distant the linear distance. The PCoA results indicated that sample points in the Model group could be completely separated from those in the Control group, and sample points in the SHYS high-dose group were very close to that of the Control group (**Figure 3C**). The clustering analysis also showed similar results (**Figure 3D**). The results indicated that the distance from the Control group to the SHYS high-dose group was closer than that between the Control group and the Model group. The above results indicated that the overall structure and composition of the gut microbiota of DN rats changed significantly and high-dose SHYS effectively reversed this change.

The composition of the gut microbiota in each group of samples at the phylum level indicated that *Firmicutes* and

TABLE 2 | Changes of SOD, GSH-Px activities and MDA level in renal tissue homogenates after SHYS treatment.

Group	SOD (U/mgprot)	MDA (nmol/mgprot)	GSH-px (U/ mgprot)
Control	184.65 ± 32.81	3.56 ± 0.82	82.07 ± 11.3
Model	115.8 ± 37.01[a]	15.29 ± 3.27[a]	36.65 ± 18.52[a]
Irbesartan	163.2 ± 31.64[b]	5.11 ± 1.87[b]	74.85 ± 11.98[b]
SHYS low-dose	117.61 ± 37.42[c]	14.06 ± 5.78[d]	49.76 ± 15.39[d]
SHYS middle-dose	148.55 ± 27.43[e]	11.09 ± 2.81[d,e]	56.63 ± 21.64[c,e]
SHYS high-dose	167.89 ± 26.99[b,f]	8.25 ± 2.05[b,d,g]	61.62 ± 14.15[b,c]

Control, Model, Irbesartan, SHYS low-dose, SHYS middle-dose and SHYS high-dose (n = *10 per group*) *groups. Data are presented as the mean ± SD.*

[a]p < *0.01 as compared to the Control group.*

[b]p < *0.01 as compared to the Model group.*

[c]p < *0.05 as compared to the Irbesartan group.*

[d]p < *0.01 as compared to the Irbesartan group.*

[e]p < *0.05 as compared to the Model group.*

[f]p < *0.01 as compared to the SHYS low-dose group.*

[g]p < *0.05 as compared to the SHYS low-dose group.*

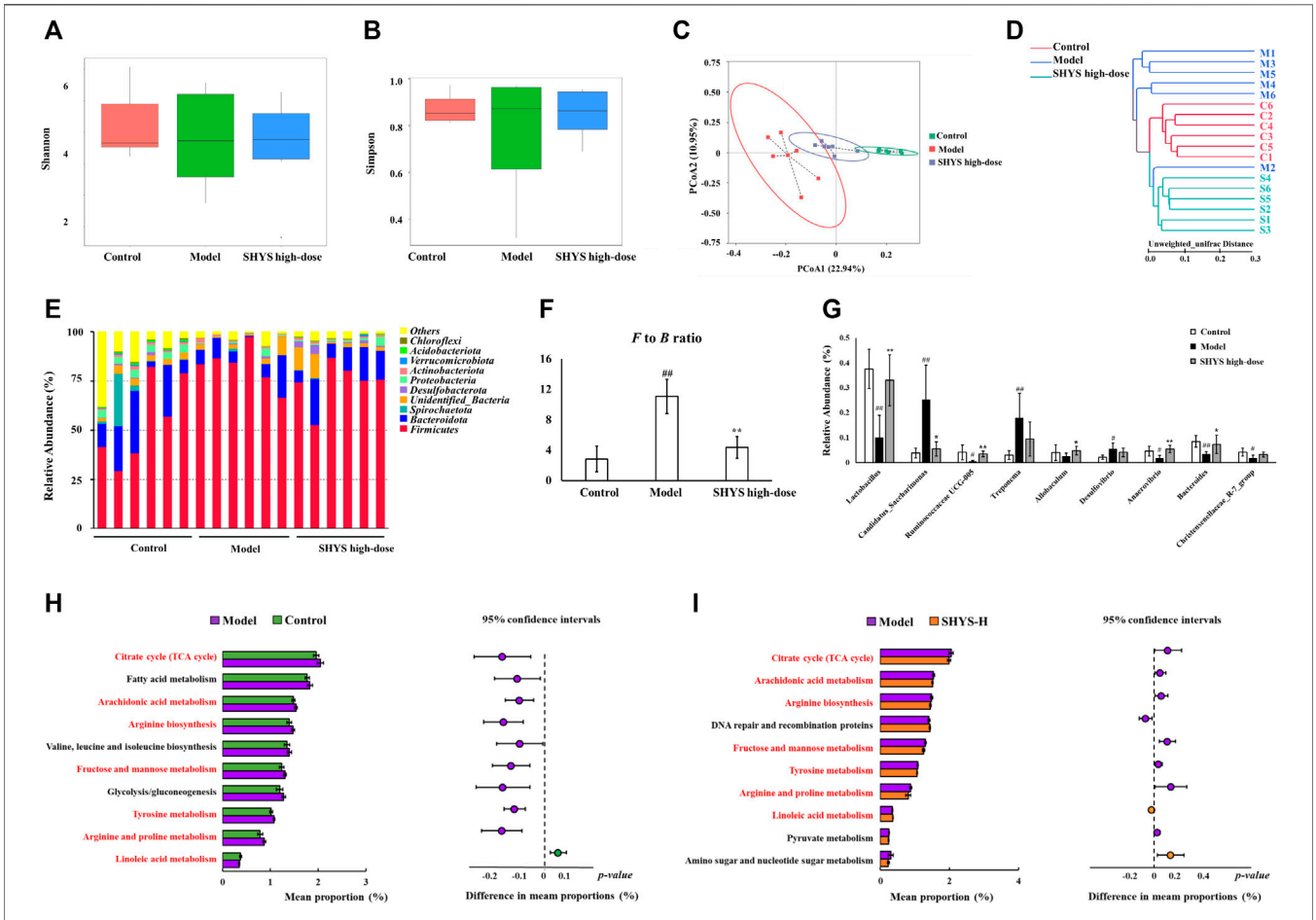

FIGURE 3 | SHYS treatment affected the diversity and abundances of gut microbiota in DN rats **(A,B)** No significant differences were observed among the Control, Model and SHYS high-dose groups. **(C,D)** PCoA and system clustering tree indicated more similar beta diversity between SHYS high-dose and Control groups than that between the Model and Control groups (C: Control group; M: Model group; S: SHYS high-dose group). **(E,F)** At the phylum level, SHYS treatment decreased the *F* to *B* ratio in DN rats. **(G)** At the genus level, SHYS treatment affected the relative abundances of *Lactobacillus*, *Ruminococcaceae UCG-005*, *Allobaculum*, *Anaerovibrio*, *Bacteroides* and *Candidatus_Saccharimonas* in DN rats **(H,I)** The differential metabolic pathways (written in red) of SHYS on DN were predicted using PICRUSt analysis based on the 16S rRNA sequencing data. Control, Model and SHYS high-dose (*n* = 6 per group) groups. Data are presented as the mean ± SD. $^{\#}$: $p < 0.05$ as compared to the Control group; $^{\#\#}$: $p < 0.01$ as compared to the Control group; *: $p < 0.05$ as compared to the Model group; **: $p < 0.01$ as compared to the Model group

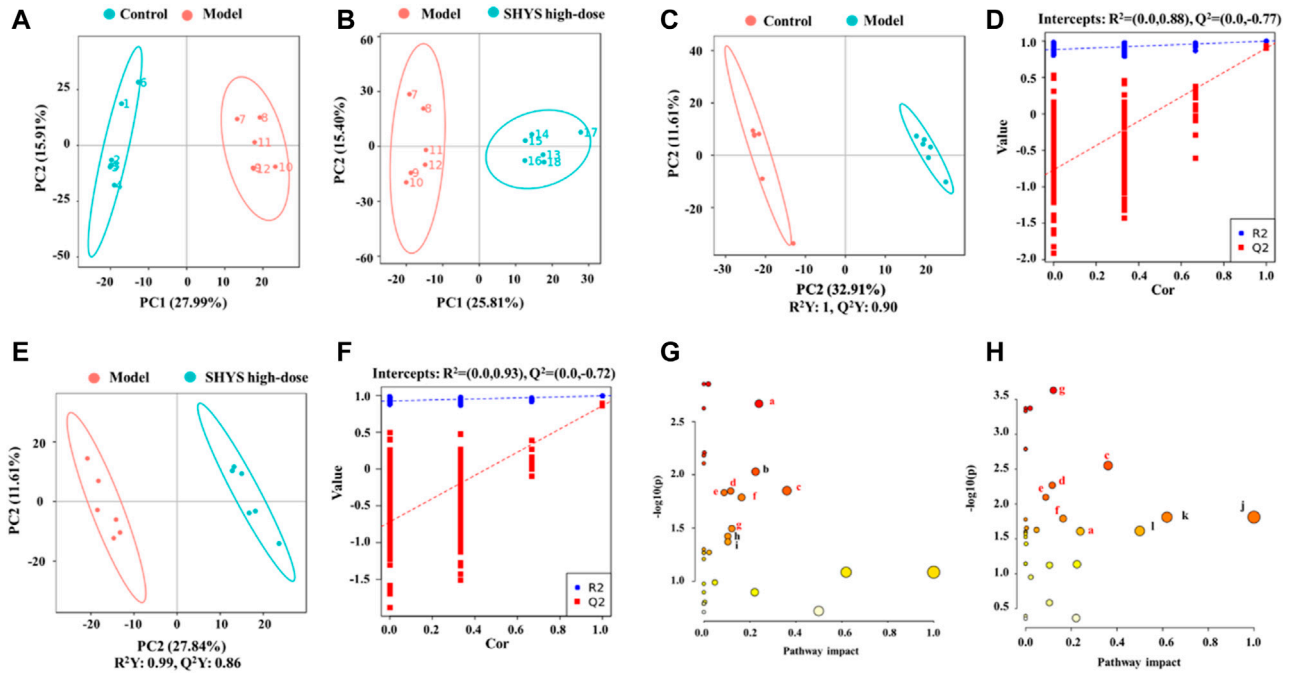

FIGURE 4 | SHYS treatment modulated the serum metabolites in DN rats **(A,B)** Scores plots of PCA between the Control and Model groups **(A)** and between the Model and SHYS high-dose groups **(B–D)** Scores plots of OPLS-DA between the Control and Model groups and the corresponding coefficient of loading plots. **(E,F)** Scores plots of OPLS-DA between the Model and SHYS high-dose groups and the corresponding coefficient of loading plots **(G,H)** Summary of pathway analysis of serum samples between Control and Model groups **(G)** and between Model and SHYS high-dose groups **(H)**, the sames pathways were written in red. a: Glycerophospholipid metabolism; b: Tryptophan metabolism; c: Alanine, aspartate and glutamate metabolism; d: Arginine biosynthesis; e: TCA cycle; f: Tyrosine metabolism; g: Arginine and proline metabolism; h: Cysteine and methionine metabolism; i: Glycerolipid metabolism; j: Phenylalanine, tyrosine and tryptophan biosynthesis; k: Phenylalanine metabolism. Control, Model and SHYS high-dose (n = 6 per group) groups.

Bacteroidetes were the dominant species (**Figure 3E**). The *Firmicutes* to *Bacteroidetes* (*F* to *B*) ratio was significantly higher in the Model group compared with that in the Control group ($p < 0.01$), whereas the *F* to *B* ratio was significantly lower in the SHYS high-dose group compared with that in the Model group ($p < 0.01$, **Figure 3F**). At the genus level, *Candidatus_Saccharimonas*, *Treponema* and *Desulfovibrio* ($p < 0.01$, $p < 0.01$, $p < 0.05$, respectively) were at relatively higher abundances in Model group compared with the Control group, whereas *Lactobacillus*, *Ruminococcaceae UCG-005*, *Anaerovibrio*, *Bacteroides* and *Christensenellaceae_R-7_group* ($p < 0.01$, $p < 0.05$, $p < 0.05$, $p < 0.01$, $p < 0.05$, respectively) were relatively lower in abundance in Model group compared with the Control group. *Lactobacillus*, *Ruminococcaceae UCG-005*, *Allobaculum*, *Anaerovibrio* and *Bacteroides* ($p < 0.01$, $p < 0.01$, $p < 0.05$, $p < 0.01$, $p < 0.05$) were relatively more abundant and *Candidatus_Saccharimonas* ($p < 0.05$) was relatively less abundant in the SHYS high-dose group compared with the Model group (**Figure 3G**).

To determine the effect of high-dose SHYS treatment on the function of the gut microbiota in DN rats, bacterial function prediction was performed using PICRUSt analysis. The top 10 metabolic pathways with the highest proportions and with a p value less than 0.05 were listed in **Figure 3H** (Control group vs Model group) and **Figure 3I** (Model group vs SHYS high-dose group). Proportions of metabolic pathways that were increased in the Model group compared with Control group but decreased in SHYS high-dose group compared with Model group, or vice versa, were considered as differential pathways, including arachidonic acid metabolism, fructose and mannose metabolism, tricarboxylic acid (TCA) cycle, arginine and proline metabolism tyrosine metabolism, linoleic acid metabolism, and arginine biosynthesis pathways.

3.5 Effect of SHYS on Serum Metabolite Levels in DN Rats

Liquid chromatography–mass spectrometry (LC-MS) was used to detect and analyze the sera of animals in each group in both positive- and negative-ion conditions to obtain the total ion current of the metabolites. PCA generates new characteristic variables by linearly combining metabolite variables with certain weights and categorizes the data for each group by new principal variables (principal components). The PCA model reflects the original state of the metabolome data, and the degree of aggregation and dispersion of the samples were observed from the PCA model, where the PCA plots showed that the Control group

TABLE 3 | The differential metabolites in serum after SHYS treatment.

No	Formula	Rt (min)	m/z	Metabolites	VIP		FC		Trend		Pathway
					M vs C	S vs M	M vs C	S vs M	M vs C	S vs M	
1	$C_{45}H_{82}NO_8P$	15.42	854.59	PC (17:0/20:4)	1.68	1.51	0.48	1.68	$\downarrow^{\#\#}$	$\uparrow^{*}$	a
2	$C_8H_8N_2O_3$	6.91	181.06	Nicotinuric acid	1.39	2.05	1.67	0.57	$\uparrow^{\#}$	$\downarrow^{*}$	—
3	$C_3H_7N_3O_2$	1.31	118.06	Guanidineacetic acid	1.35	2.16	1.90	0.56	$\uparrow^{\#\#}$	$\downarrow^{**}$	g
4	$C_{10}H_{12}N_2O_3$	8.39	209.09	L-Kynurenine	1.56	2.02	1.80	0.62	$\uparrow^{\#\#}$	$\downarrow^{**}$	b
5	$C_{20}H_{36}O_5$	11.24	355.25	Prostaglandin F1α	1.06	1.73	0.61	1.70	$\downarrow^{\#\#}$	$\uparrow^{*}$	—
6	$C_4H_4O_4$	1.20	115.00	Fumaric acid	1.29	1.45	1.90	0.54	$\uparrow^{\#\#}$	$\downarrow^{**}$	c,d,e,f
7	$C_4H_9NO_3$	1.30	118.05	Threonine	1.09	1.22	0.48	1.90	$\downarrow^{\#\#}$	$\uparrow^{**}$	—
8	$C_4H_9N_3O_2$	1.35	132.08	Creatine	1.36	1.82	0.61	1.66	$\downarrow^{\#\#}$	$\uparrow^{*}$	g
9	$C_4H_6O_5$	1.20	133.01	D-(+)-Malic acid	1.30	1.50	1.62	0.66	$\uparrow^{\#\#}$	$\downarrow^{**}$	—
10	$C_7H_{15}NO_2$	1.36	146.12	Acetylcholine	1.65	1.94	0.52	1.91	$\downarrow^{\#\#}$	$\uparrow^{**}$	a
11	$C_5H_{11}NO_2S$	1.43	150.06	Methionine	1.57	1.99	1.36	0.65	$\uparrow^{\#\#}$	$\downarrow^{*}$	h
12	$C_5H_9NO_2$	1.54	116.07	D-Proline	1.31	1.85	0.55	2.00	$\downarrow^{\#\#}$	$\uparrow^{**}$	g
13	$C_5H_9NO_4$	1.21	146.05	L-Glutamic acid	1.18	1.75	1.82	0.56	$\uparrow^{\#\#}$	$\downarrow^{*}$	c,d,g,i
14	$C_5H_6O_5$	1.25	145.01	α-Ketoglutaric acid	1.13	2.02	0.45	1.84	$\downarrow^{\#\#}$	$\uparrow^{**}$	c,d,e,i
15	$C_4H_8N_2O_3$	1.24	131.05	Asparagine	1.90	2.41	0.49	2.05	$\downarrow^{\#\#}$	$\uparrow^{**}$	c
16	$C_9H_{17}NO_4$	9.45	204.12	Acetylcarnitine	1.81	2.00	0.66	3.96	$\downarrow^{\#}$	$\uparrow^{**}$	—
17	$C_{19}H_{39}O_7P$	13.04	409.24	Lysopa 16:0	1.38	1.22	1.78	0.67	$\uparrow^{\#}$	$\downarrow^{*}$	a,i
18	$C_{45}H_{80}NO_7P$	15.84	776.56	PE (18:2e/22:4)	1.07	1.35	1.52	0.55	$\uparrow^{\#}$	$\downarrow^{**}$	a
19	$C_9H_{11}NO_3$	1.98	180.07	L-Tyrosine	1.51	1.44	1.81	0.47	$\uparrow^{\#\#}$	$\downarrow^{**}$	f,j,k
20	$C_9H_{11}NO_2$	4.54	166.09	L-Phenylalanine	1.82	1.36	1.92	0.43	$\uparrow^{\#\#}$	$\downarrow^{**}$	j,k
21	$C_{27}H_{44}O3$	14.08	415.32	Calcitriol	1.58	1.45	0.44	1.98	$\downarrow^{\#}$	$\uparrow^{**}$	—
22	$C_{26}H_{43}NO_6$	11.15	464.30	Glycocholic acid	1.26	1.49	2.44	0.53	$\uparrow^{\#}$	$\downarrow^{*}$	—
23	$C_6H_9N_3O_2$	1.65	154.06	L-Histidine	1.63	1.76	0.47	1.98	$\downarrow^{\#\#}$	$\uparrow^{*}$	—
24	$C_{11}H_{12}N_2O_3$	6.55	221.09	5-Hydroxytryptophan	1.17	1.78	1.65	0.61	$\uparrow^{\#}$	$\downarrow^{*}$	b
25	$C_{26}H_{52}NO_7P$	14.77	566.35	LPC 18:1	1.24	1.58	1.73	0.65	$\uparrow^{\#\#}$	$\downarrow^{*}$	a
26	$C_5H_{10}N_2O_3$	1.32	147.08	L-Glutamine	1.22	1.76	0.76	1.29	$\downarrow^{\#}$	$\uparrow^{*}$	c,d,i
27	$C_9H_8O_3$	1.98	163.04	Phenylpyruvic acid	1.64	1.29	1.52	0.57	$\uparrow^{\#}$	$\downarrow^{**}$	j,k
28	$C_8H_{16}O_2$	10.41	143.11	Caprylic acid	1.37	1.32	0.44	1.71	$\downarrow^{\#\#}$	↑	—
29	$C_{10}H_{19}NO_4$	10.36	218.14	Propionyl-L-carnitine	1.48	2.26	0.59	1.28	$\downarrow^{\#\#}$	↑	—

Control, Model and SHYS high-dose (n = 6 per group) groups.

$^{\#}p < 0.05$ as compared to the Control group; $^{\#\#}p < 0.01$ as compared to the Control group; $^{*}p < 0.05$ as compared to the Model group; $^{**}p < 0.01$ as compared to the Model group; ↑: content increased; ↓: content decreased; vs: versus; C: control group; M: Model group; S: SHYS high-dose group; Rt: retention time; VIP: variable importance of projection; FC: fold change. a: Glycerophospholipid metabolism; b: Tryptophan metabolism; c: Alanine, aspartate and glutamate metabolism; d: Arginine biosynthesis; e: TCA cycle; f: Tyrosine metabolism; g: Arginine and proline metabolism; h: Cysteine and methionine metabolism; i: Glycerolipid metabolism; j: Phenylalanine, tyrosine and tryptophan biosynthesis; k: Phenylalanine metabolism.

and the Model group were well-differentiated and the Model group and SHYS high-dose group were also well-differentiated (**Figures 4A,B**). For the identification of differential metabolites, the model of OPLS-DA was employed, and the explanatory rate (R^2) and predictive power (Q^2) of the model were evaluated under the established OPLS-DA model. Compared with the Control group, the Model group yielded an $R^2 = 0.88$ and a $Q^2 = -0.77$ (**Figures 4C,D**). Compared with the Model group, the SHYS high-dose group had an $R^2 = 0.93$ and a $Q^2 = -0.72$ (**Figures 4E,F**). These results indicate that the model is stable and shows good predictive ability.

The $p < 0.05$ and VIP > 1.0 were used on differential metabolites for screening, in which a total of 29 differential metabolites with 13 down-regulated and 16 up-regulated metabolites were screened in the Model group compared with the Control group. A total of 27 differential metabolites including 11 down-regulated and 16 up-regulated metabolites were screened in the SHYS high-dose group compared with the Model group (**Table 3**). Next, we used MetaboAnalyst software to analyze the metabolic pathways of the identified differential metabolites. Differential pathways were considered with a p-value < 0.05 and pathway impact > 0.1. Metabolic pathways that were altered between Control and Model groups included glycerophospholipid metabolism, tryptophan metabolism, alanine, aspartate and glutamate metabolism, arginine biosynthesis, TCA cycle, tyrosine metabolism, arginine and proline metabolism, cysteine and methionine metabolism, and glycerophospholipid metabolism metabolism pathways (**Figure 4G**). The metabolic pathways altered between SHYS high-dose and Model groups included glycerophospholipid metabolism, tryptophan metabolism, alanine, aspartate and glutamate metabolism, arginine biosynthesis, TCA cycle, tyrosine metabolism, arginine and proline metabolism, arginine and proline metabolism, phenylalanine, tyrosine and tryptophan biosynthesis, phenylalanine metabolism, and D-glutamine and D-glutamate metabolism pathways (**Figure 4H**). The same metabolic pathway of PICRUSt analysis that had done 16S rRNA sequencing and untargeted metabolomics pathway analysis included arginine biosynthesis, TCA cycle, tyrosine metabolism, and arginine and proline metabolism and were discussed in detail.

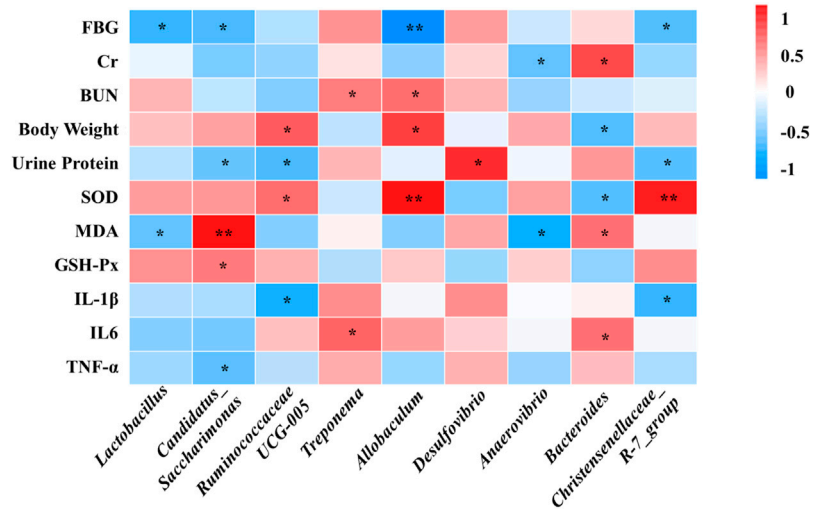

FIGURE 5 | Correlations between between physiological data, oxidative stress and inflammatory factors and gut microbiota were analyzed using spearman's analysis (heatmap). *X*-axis represents the gut microbiota with differential abundance. *Y*-axis represents the physiological data, oxidative stress and inflammatory factors. The colors of grids represent the correlation analysis value of spearman's correlation analysis. Grids in red indicate positive correlations (correlation analysis value more than 0.1), while grids in blue indicate negative correlations (correlation analysis value less than –0.1). Color coding scale indicates the correlation analysis value from heatmap, the deeper red or blue indicates higher correlation values. *: $p < 0.05$ between physiological data, oxidative stress and inflammatory factors and gut microbiota. **: $p < 0.01$ between physiological data, oxidative stress and inflammatory factors and gut microbiota.

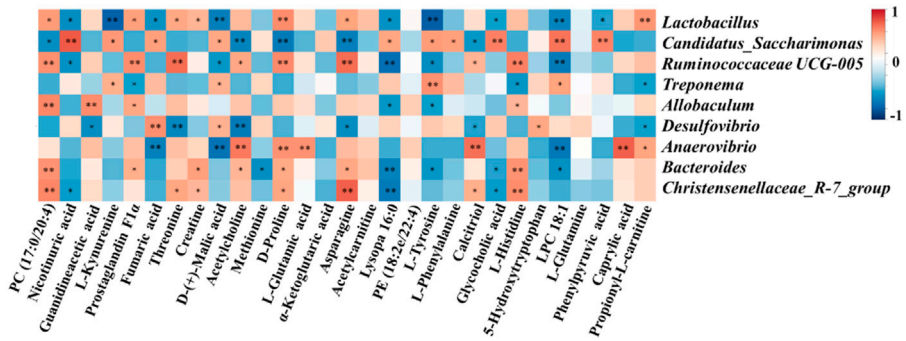

FIGURE 6 | Correlation analysis of untargeted metabolomics and 16S rRNA sequencing. Correlations between between untargeted metabolomics and gut microbiota were analyzed using spearman's analysis (heatmap). *X*-axis represents the differential metabolites in the serum. *Y*-axis represents the gut microbiota with differential abundance. The colors of grids represent the correlation analysis value of spearman's correlation analysis. Grids in red indicate positive correlations (correlation analysis value more than 0.1), while grids in blue indicate negative correlations (correlation analysis value less than –0.1). Color coding scale indicates the correlation analysis value from heatmap, the deeper red or blue indicates higher correlation values. *: $p < 0.05$ between differential serum metabolites and gut microbiota. **: $p < 0.01$ between differential serum metabolites and gut microbiota.

3.6 Correlation Analysis of Physiological Data, Oxidative Stress and Inflammatory

3.6.1 Factors, Untargeted Metabolomics and Gut Microbiota

Spearman's correlation analysis was conducted to analyze the relationship between physiological data, oxidative stress and inflammatory factors, differential serum metabolites and gut microbiota at genus level in the Control, Model and SHYS high-dose groups. As shown in **Figure 5**, *Candidatus_Saccharimona, Ruminococcaceae UCG-005,* and *Christensenellaceae_R-7_group* showed negative correlations and *Treponema and Bacteroides* showed positive correlations with some of the pro-inflamatory cytokines. *Lactobacillus, Candidatus_Saccharimonas, Ruminococcaceae UCG-005, Allobaculum, Anaerovibrio, Bacteroides,* and *Christensenellaceae_R-7_group* showed correlations with some of the oxidative stress factors. In addition, *Lactobacillus, Candidatus_Saccharimonas, Ruminococcaceae UCG-005, Anaerovibrio, Bacteroides,* and *Christensenellaceae_R-7_group* were correlated with most of the metabolites (**Figure 6**).

4 DISCUSSION

In the present study, we used a HFD combined with STZ injection to establish a rat model of DN. Compared with the Control group, the rats in the Model group exhibited a significant increase in FBG levels and there were abnormal biochemical indicators related to renal function, as manifested in increased serum Cr and BUN as well as a significant increase in 24-h urine protein levels. In addition, the pathology results revealed that the renal tissues of the DN model rats showed significant tubular atrophy and glomerular hyperplasia along with a certain degree of inflammatory cell infiltration. This is consistent with the pathological manifestations of DN. The SHYS-treated groups exhibited reduced FBG, improved biochemical indicators of renal function, and alleviated renal histopathological changes to varying degrees in rats with DN. This suggests that SHYS exhibits a therapeutic effect on DN, particularly in the high-dose group. In addition, we selected irbesartan as a positive control drug. The results showed that irbesartan had no significant improvement on blood glucose in rats with DN and there was no significant difference in the improvement of renal function and pathological changes between animals in the positive control group and the high-dose SHYS-treated group. These results suggest that SHYS can be used as an alternative therapy to irbesartan for the treatment of DN.

We further examined the effect of SHYS on inflammation in rats with DN. The hyperglycemic state induces chronic inflammation in the body, which contributes to the infiltration of inflammatory cells in renal tissue and the production of large amounts of pro-inflammatory factors including IL-1β, IL6, and TNF-α (Casqueiro et al., 2012). Our results indicated that the level of pro-inflammatory factors in the renal tissues of rats in the Model group were decreased after SHYS treatment suggesting that SHYS exhibits some anti-inflammatory effects.

We investigated the effect of high-dose SHYS on the gut microbiota of rats in DN model using 16S RNA sequencing technology. There were no significant differences in the Shannon and Simpson indexes between the groups, suggesting that the alpha diversity of gut microbiota in the rat model of DN was unchanged. SHYS did not affect the alpha diversity of gut microbiota in rats with DN. However, in the beta diversity analysis, we found significant differences between animals in the Model group and the Control group in the PCoA plot. The beta diversity of gut microbiota in rats from the high-dose SHYS-treated group was significantly different from that of the Model group. Interestingly, the PCoA plot showed that the beta diversity of gut microbiota in rats from the SHYS-treated groups was more similar to that of the Control group compared with the Model group. These results suggest that SHYS restores the beta diversity of gut microbiota in this DN rat model to a level similar to the Control group. Further analysis of the abundance of microbiota revealed that at the phylum level, the primary species of gut microbiota in the rats from each group were *Firmicutes* and *Bacteroides*. The rats in the DN model showed an increase in the ratio of *F* to *B*, whereas SHYS significantly reduced the *F* to *B* ratio. The elevated *F* to *B* ratio is closely associated with the inflammatory response, metabolic disorders, and other pathological states in DN (Lee et al., 2019). Further analysis at the genus level revealed that SHYS could increase the abundance of *Lactobacillus*, *Ruminococcaceae UCG-005*, *Allobaculum*, *Anaerovibrio* and *Bacteroides* in DN model rats. *Lactobacillus* is a major probiotic with an important role in the regulation of metabolism and immunity (Zhang et al., 2020). A reduced abundance of *Lactobacillus* was found in models of diabetes, fatty liver, and obesity (Mishra et al., 2016; Nova et al., 2016). The metabolic and inflammatory responses of the organism can be improved by the transplantation of *Lactobacillus*. *Ruminococcaceae UCG-005*, *Allobaculum*, and *Bacteroides* produce short-chain fatty acids (SCFAs) by degrading cellulose in food (Zhang et al., 2015; Wu et al., 2020; Xue et al., 2020). SCFAs are important metabolites of the gut microbiota and studies have shown that increasing the SCFA-producing microbiota can significantly improve a number of metabolic diseases, including diabetes and obesity (Yang et al., 2019; Zhang et al., 2019; Birkeland et al., 2020; Tian et al., 2021). In addition, recent studies have shown that SCFAs inhibit the inflammatory responses of renal tissue in DN through G protein-coupled receptors (GPR43 and GPR109A) (Li et al., 2020a). *Anaerovibrio* is capable of catabolizing lipids. Studies have shown that polyphenols in green tea can alleviate chronic inflammation caused by translocation of gut microbiota in an obesity model, while increasing the amount of *Anaerovibrio* in the gut. However, the specific relationship of *Anaerovibrio* to DN remains unknown (Li et al., 2020b). SHYS treatment also caused a decrease of *Candidatus_Saccharimonas* in gut. *Candidatus_Saccharimonas* is a conditional pathogenic bacterium that is significantly elevated in the gut of gout patients (Shao et al., 2017). In addition, green tea leaf powder ameliorates the abnormal lipid metabolism induced by a HFD, while reducing the abundance of *Candidatus_Saccharimonas* in the gut (Li et al., 2020b). Likewise, our correlation analysis also showed negative correlations of *Lactobacillus*, *Candidatus_Saccharimonas*, *Ruminococcaceae UCG-005*, *Allobaculum*, *Anaerovibrio*, *Bacteroides,* and *Christensenellaceae_R-7_grou* with some of the physiological indicies (FBG, Cr, BUN, body weight and Urine Protein), oxidative stress factor (MDA) and pro-inflammatory cytokines (IL-1β, IL-6, TNF-α). Correlation analysis also showed positive correlations of *Treponema* and *Desulfovibrio* with physiological indicies (BUN, Urine Protein) and pro-inflammatory cytokine (IL-6). Further studies should also be carried out using fecal transplantation or gut microbiota depletion models to verify whether SHYS can ameliorate hyperglycemia, hyperlipidemia, IR, oxidative stress and inflammatory responses to treat DN through regulating these gut microbiota.

PCA and OPLS-DA of serum untargeted metabolomics revealed that the metabolites of DN in the rat model were significantly different from those of normal rats. In addition, the serum metabolite levels of rats after SHYS treatment were also significantly different from those of DN rats. Metabolic pathway analysis for differential metabolites using MetaboAnalyst showed that SHYS had an impact on several metabolic pathways including arginine and proline metabolism, alanine, aspartate and glutamate metabolism, arginine biosynthesis, TCA cycle,

tyrosine metabolism, and glycerophospholipid metabolism. After correlating the differential metabolic pathways obtained from metabolomics with those deduced from 16s rRNA sequencing, the pathways of arginine biosynthesis, TCA cycle, tyrosine metabolism, and arginine and proline metabolism were the most common, suggesting that SHYS may play a role in the treatment of DN by regulating gut microbiota, which in turn affects arginine biosynthesis, the TCA cycle, tyrosine metabolism, and arginine and proline metabolism.

4.1 Arginine Biosynthesis and Arginine and Proline Metabolism

Amino acid metabolism is closely related to metabolic disorders during DN. In the present study, we found that the level of guanidineacetic acid and L-glutamic acid were elevated in DN model rats and significantly decreased after treatment with SHYS. The level of creatine, D-proline, and L-glutamine were decreased and significantly increased after treated with SHYS. Arginine is the largest nitrogen-donating amino acid and is a precursor to proline and creatine (Ge et al., 2020). Proline metabolizes and generates electrons as well as reactive oxygen species, leading to a variety of downstream effects including blocking the cell cycle, autophagy, and apoptosis (Selen et al., 2015). Creatine is a naturally produced nitrogen-containing molecule that promotes the ATP cycle and provides energy to muscles and cells (Arlin et al., 2014). Creatine may reduce damage by inhibiting inflammation, oxidative stress, and aging (Deminice et al., 2016; Aljobaily et al., 2020). Studies have found that supplementation of creatine to diabetic patients results in hypoglycemic effects (Gualano et al., 2011). Guanidineacetic acid is an immediate precursor of creatine biosynthesis, however, this reaction causes elevated levels of homocysteine in the blood. This can result in vasculopathy, which is one of the causes of diabetic macrovascular and microvascular complications in diabetic patients (De Luis et al., 2005; Zhao et al., 2018; Ma et al., 2020). L-glutamic acid and L-glutamine are interconvertible. L-glutamine is an abundant free amino acid inside and outside of human cells that plays an essential role in protein and energy metabolism. It is a precursor substance for the synthesis of amino acids, proteins, and nucleic acids (Tanaka et al., 2015; Kou et al., 2016). Paul et al. found that L-glutamine is effective at resisting obesity and insulin tolerance (Petrus et al., 2020). L-glutamine provides energy to immune cells, such as lymphocytes and macrophages, ensuring immune cell proliferation, and enhancing immunity (Csibi et al., 2014). Also, L-glutamine has anti-inflammatory and antioxidant effects. L-glutamine is a precursor substance for glutathione synthesis and reduces the inflammatory response by increasing glutathione synthesis, inhibiting the NF-κB pathway, and decreasing the levels of IL-8 and TNF-α (Pusapati et al., 2016). Interestingly, the ratio of glutamine to glutamic acid is strongly associated with diabetes and insulin resistance. An elevated ratio is significantly associated with a low risk of developing diabetes (Cheng et al., 2012; Rhee et al., 2018), which primarily occurs through various cell related metabolic events, such as protein synthesis, muscle growth, uropoiesis in the liver, insulin secretion, hepatic and renal gluconeogenesis, neurotransmitter synthesis and glutathione production (Newsholme et al., 2003). A Spearman analysis revealed that guanidineacetic acid was positively correlated with *Allobaculum* and negatively correlated with *Desulfovibrio*; D-Proline was positively correlated with *Lactobacillus, Ruminococcaceae UCG-005, Anaerovibrio, Bacteroides* and *Christensenellaceae*_R-7_group and negatively correlated with *Candidatus_Saccharimona*; creatine was positively correlated with *Lactobacillus, Bacteroides* and *Christensenellaceae_R-7_group*; and L-glutamic acid was positively correlated with *Anaerovibrio*. Therefore, we hypothesize that the effect of SHYS on arginine biosynthesis and arginine and proline metabolism may be related to the regulation of the abundance of *Allobaculum, Desulfovibrio*, *Lactobacillus*, *Ruminococcaceae UCG- 005*, *Anaerovibrio*, *Bacteroides*, *Candidatus_Saccharimona*, and *Christensenellaceae*_R-7_group abundance.

4.2 TCA Cycle

The TCA cycle is the final metabolic pathway for carbohydrates, lipids, and amino acids (Chen et al., 2014). It also affects the immune system and is closely associated with various metabolic diseases, including diabetes (Choi et al., 2021). In the present study, we found that fumaric acid was significantly elevated in the DN rat model and decreased after SHYS administration, whereas alpha-ketoglutaric acid was increased after SHYS administration. Fumaric acid is a dicarboxylic acid that is produced by succinic dehydrogenase from precursor adenosine in the TCA cycle and is converted to malic acid by fumarate hydratase (You et al., 2015). The metabolic disorder of fumaric acid may be associated with renal impairment in diabetes, in which its accumulation leads to oxidative stress and prolonged oxidative stress leads to kidney injury in DN (Zheng et al., 2015). Studies have found that the accumulation of fumaric acid is positively associated with progression toward DN in patients (Liu, et al., 2018). Elevated levels of fumaric acid in DN causes endoplasmic reticulum stress and HIF-1α expression, steering metabolism to the glycolytic pathways and leading to pathological renal injury (Isaacs et al., 2005; Tong et al., 2011; Linehan and Rouault, 2013). Alpha-ketoglutaric acid is a key intermediate in the TCA cycle located between succinyl-coenzyme A and isocitric acid. As a key member of the anaplerotic reactions, alpha-ketoglutaric acid regulates ATP production and reduces NAD+/NADH production in the TCA cycle, thereby affecting ROS levels and immune system homeostasis (B Zdzisińska et al., 2017). In addition, alpha-ketoglutaric acid is an important source of glutamine and glutamate, which are required for the synthesis of amino acids and collagen (Xiao et al., 2016). It was found that alpha-ketoglutaric acid supplementation protects mice from myocardial ischemia reperfusion injury (Olenchock et al., 2016). A Spearman analysis showed that fumaric acid was positively correlated with *Candidatus_ Saccharimonas* and *Desulfovibrio*, and negatively correlated with *Lactobacillus and Anaerovibrio.* No bacterial was found significantly corrected with alpha-ketoglutaric acid. Therefore, we hypothesized that the effect of SHYS on the TCA cycle may be associated with the regulating the abundance of *Candidatus_Saccharimonas*, *Desulfovibri, Lactobacillus,* and *Anaerovibrio.*

4.3 Tyrosine Metabolism

Tyrosine metabolism is associated with a variety of diseases including fatty liver, insulin resistance, and obesity (Gaggini et al., 2018; Gitto et al., 2018). In the present study, we found that L-tyrosine was significantly elevated in rats of the model group and decreased after the administration of SHYS. Therefore, high levels of tyrosine may promote fatty acid synthesis, which further promotes fat deposition in the liver (Jin et al., 2016). Meanwhile, the characteristic nitrification of tyrosine residues in proteins using peroxynitrite (ONOO-) produces nitrotyrosine (NT). NT is involved in the development of diabetes and its complications and elevated levels of NT can disrupt renal pathology and cause renal dysfunction in diabetic rats (Chew et al., 2010). Increased levels of NT have also been observed in patients with DN (Julius et al., 2008; Castro et al., 2011). NT induces glomerular mesangial cells to express NF-κB, MCP-1, and TGF-β1, causing inflammatory injury and further aggravating nephropathy (Jing et al., 2018). In addition, NT is also a marker of oxidative stress in diabetic patients and NT activates the ERK pathway to increase iNOS and produce excess ROS to mediate oxidative stress damage in the body (Inoguchi and Takayanagi, 2008). A Spearman analysis showed that L-tyrosine was positively correlated with *Candidatus_Saccharimonas* and *Treponema*, and negatively correlated with *Lactobacillus, Ruminococcaceae UCG-005, Allobaculum,* and *Bacteroides*. Therefore, we speculated that the effect of SHYS on the tyrosine metabolism may be with the regulation of the abundance of *Candidatus_Saccharimonas*, *Treponema*, *Lactobacillus, Ruminococcaceae UCG-005, Allobaculum,* and *Bacteroides*.

In conclusion, our study revealed multiple ameliorative effects of SHYS on DN including the alleviation of hyperglycemia and the improvement of renal function, pathological changes in kidney, oxidative stress, and the inflammatory response. The mechanism of SHYS on DN may be related to the improvement of gut microbiota which regulates arginine biosynthesis, TCA cycle, tyrosine metabolism, and arginine and proline metabolism.

DATA AVAILABILITY STATEMENT

The datasets presented in this study can be found in online repositories. The names of the repository/repositories and accession number(s) can be found below: NCBI (accession: PRJNA778921).

ETHICS STATEMENT

The animal study was reviewed and approved by the study was approved by the Ethics Committee of Cangzhou Hospital of Integrated Traditional Chinese and Western Medicine.

AUTHOR CONTRIBUTIONS

XS carried out the experiments and manuscript writing. WY, AL, and CW provided experimental help, and performed data analysis and result interpretation. XLi, JG, and XLiu finished molecular bioassays. WJ, YY, and SL provided ideas and technical guidance for the whole work. All authors contributed to the article and approved the submitted version.

FUNDING

This work was supported by the Scientific Program Project of Administration of Traditional Chinese Medicine in Hebei Province (No. 2021311).

SUPPLEMENTARY MATERIAL

The Supplementary Material for this article can be found online at: https://www.frontiersin.org/articles/10.3389/fphar.2021.808867/full#supplementary-material

REFERENCES

Aljobaily, N., Viereckl, M. J., Hydock, D. S., Aljobaily, H., Wu, T.-Y., Busekrus, R., et al. (2020). Creatine Alleviates Doxorubicin-Induced Liver Damage by Inhibiting Liver Fibrosis, Inflammation, Oxidative Stress, and Cellular Senescence. *Nutrients* 13, 41. doi:10.3390/nu13010041

Arlin, J.-B., Bhardwaj, R. M., Johnston, A., Miller, G. J., Bardin, J., Macdougall, F., et al. (2014). Structure and Stability of Two Polymorphs of Creatine and its Monohydrate. *Crystengcomm* 16, 8197–8204. doi:10.1039/C4CE00508B

Bian, S. S., Zhuang, K. S., Zhang, F. G., Wang, F., Li, L. Z., Jiang, X., et al. (2011). Effect of Sanhuang Yishen Capsule on Microinflammatory State in Patients with Maintenance Hemodialysis. *Chin. Arch. Tradit. Chin. Med.* 12, 57–58. doi:10.13457/j.cnki.jncm.2011.12.025

Birkeland, E., Gharagozlian, S., Birkeland, K. I., Valeur, J., Måge, I., Rud, I., et al. (2020). Correction to: Prebiotic Effect of Inulin-type Fructans on Faecal Microbiota and Short-chain Fatty Acids in Type 2 Diabetes: a Randomised Controlled Trial. *Eur. J. Nutr.* 59, 3339–3340. doi:10.1007/s00394-020-02282-5

Cai, T. T., Ye, X. L., Li, R. R., Chen, H., Wang, Y. Y., Yong, H. J., et al. (2020). Resveratrol Modulates the Gut Microbiota and Inflammation to Protect against Diabetic Nephropathy in Mice. *Front. Pharmacol.* 11, 1249. doi:10.3389/fphar.2020.01249

Casqueiro, J., Casqueiro, J., and Alves, C. (2012). Infections in Patients with Diabetes Mellitus: A Review of Pathogenesis. *Indian J. Endocrinol. Metab.* 16 (Suppl. 1), S27–S36. doi:10.4103/2230-8210.94253

Castro, L., Demicheli, V., Tórtora, V., and Radi, R. (2011). Mitochondrial Protein Tyrosine Nitration. *Free Radic. Res.* 45, 37–52. doi:10.3109/10715762.2010.516254

Chen, L., Liu, T., Zhou, J., Wang, Y., Wang, X., Di, W., et al. (2014). Citrate Synthase Expression Affects Tumor Phenotype and Drug Resistance in Human Ovarian Carcinoma. *PLoS One* 9, e115708. doi:10.1371/journal.pone.0115708

Cheng, S., Rhee, E. P., Larson, M. G., Lewis, G. D., Mccabe, E. L., Shen, D., et al. (2012). Metabolite Profiling Identifies Pathways Associated with Metabolic Risk in Humans. *Circulation* 125, 2222–2231. doi:10.1161/CIRCULATIONAHA.111.067827

Chew, P., Yuen, D. Y., Stefanovic, N., Pete, J., Coughlan, M. T., Jandeleit-Dahm, K. A., et al. (2010). Antiatherosclerotic and Renoprotective Effects of Ebselen in the Diabetic Apolipoprotein E/GPx1-double Knockout Mouse. *Diabetes* 59, 3198–3207. doi:10.2337/db10-0195

Chi, X. E., Lv, S. Q., Wang, Y. S., Wang, X., Su, X., Jia, C., et al. (2013). Protective Effect on Kidney and Mechanism of Sanhuang Yishen Capsule in Rats with Diabetes. *J. Liaoning Univ. Tradit Chin. Med.* 15, 41–43.

Choi, I., Son, H., and Baek, J.-H. (2021). Tricarboxylic Acid (TCA) Cycle Intermediates: Regulators of Immune Responses. *Life* 11, 69. doi:10.3390/life11010069

Csibi, A., Lee, G., Yoon, S. O., Tong, H., Ilter, D., Elia, I., et al. (2014). The mTORC1/S6K1 Pathway Regulates Glutamine Metabolism through the eIF4B-dependent Control of C-Myc Translation. *Curr. Biol.* 24, 2274–2280. doi:10.1016/j.cub.2014.08.007

De Luis, D. A., Fernandez, N., Arranz, M. L., Aller, R., Izaola, O., and Romero, E. (2005). Total Homocysteine Levels Relation with Chronic Complications of Diabetes, Body Composition, and Other Cardiovascular Risk Factors in a Population of Patients with Diabetes Mellitus Type 2. *J. Diabetes Complications* 19, 42–46. doi:10.1016/j.jdiacomp.2003.12.003

Deminice, R., Cella, P. S., Padilha, C. S., Borges, F. H., da Silva, L. E., Campos-Ferraz, P. L., et al. (2016). Creatine Supplementation Prevents Hyperhomocysteinemia, Oxidative Stress and Cancer-Induced Cachexia Progression in Walker-256 Tumor-Bearing Rats. *Amino Acids* 48, 2015–2024. doi:10.1007/s00726-016-2172-9

Edgar, R. C. (2004). MUSCLE: Multiple Sequence Alignment with High Accuracy and High Throughput. *Nucleic Acids Res.* 32, 1792–1797. doi:10.1093/nar/gkh340

Edgar, R. C. (2013). UPARSE: Highly Accurate OTU Sequences from Microbial Amplicon Reads. *Nat. Methods* 10, 996–998. doi:10.1038/nmeth.2604

Gaggini, M., Carli, F., Rosso, C., Buzzigoli, E., Marietti, M., Della Latta, V., et al. (2018). Altered Amino Acid Concentrations in NAFLD: Impact of Obesity and Insulin Resistance. *Hepatology* 67, 145–158. doi:10.1002/hep.29465

Ge, S., Zhang, Q., Tian, Y., Hao, L., Duan, J., and Zhang, B. (2020). Cell Metabolic Profiling of Colorectal Cancer via 1H NMR. *Clin. Chim. Acta* 510, 291–297. doi:10.1016/j.cca.2020.07.039

Gitto, S., Schepis, F., Andreone, P., and Villa, E. (2018). Study of the Serum Metabolomic Profile in Nonalcoholic Fatty Liver Disease: Research and Clinical Perspectives. *Metabolites* 8, 17. doi:10.3390/metabo8010017

Gong, X., Xiong, L., Bi, C., and Zhang, B. (2021). Diosmetin Ameliorate Type 2 Diabetic Mellitus by Up-Regulating Corynebacterium Glutamicum to Regulate IRS/PI3K/AKT-mediated Glucose Metabolism Disorder in KK-Ay Mice. *Phytomedicine* 87, 153582. doi:10.1016/j.phymed.2021.153582

Grigor'eva, I. N. (2020). Gallstone Disease, Obesity and the Firmicutes/Bacteroidetes Ratio as a Possible Biomarker of Gut Dysbiosis. *Jpm* 11, 13. doi:10.3390/jpm11010013

Gualano, B., De Salles Painneli, V., Roschel, H., Artioli, G. G., Neves, M., De Sá Pinto, A. L., et al. (2011). Creatine in Type 2 Diabetes: a Randomized, Double-Blind, Placebo-Controlled Trial. *Med. Sci. Sports Exerc.* 43, 770–778. doi:10.1249/mss.0b013e3181fcee7d

Guarner, F. (2006). Enteric flora in Health and Disease. *Digestion* 73 (Suppl. 1), 5–12. doi:10.1159/000089775

Guo, Z. A., Yu, C. J., Liu, G., Meng, F. C., Li, Y., and Peng, S. L. (2014). Treatment of Stage 3b Diabetic Kidney Disease Patients with Macroalbuminuria by Qizhi Jiangtang Capsule: a Multicenter Randomized Control Clinical Study. *Zhongguo Zhong Xi Yi Jie He Za Zhi* 34, 1047–1052. doi:10.1016/s0254-6272(15)30043-1

Inoguchi, T., and Takayanagi, R. (2008). Role of Oxidative Stress in Diabetic Vascular Complications. *Fukuoka Igaku Zasshi* 99, 47–55. doi:10.2337/diacare.19.3.257

Isaacs, J. S., Jung, Y. J., Mole, D. R., Lee, S., Torres-Cabala, C., Chung, Y. L., et al. (2005). HIF Overexpression Correlates with Biallelic Loss of Fumarate Hydratase in Renal Cancer: Novel Role of Fumarate in Regulation of HIF Stability. *Cancer Cell* 8, 143–153. doi:10.1016/j.ccr.2005.06.017

Jin, H., Piao, S. G., Jin, J. Z., Jin, Y. S., Cui, Z. H., Jin, H. F., et al. (2014). Synergistic Effects of Leflunomide and Benazepril in Streptozotocin-Induced Diabetic Nephropathy. *Nephron Exp. Nephrol.* 126, 148–156. doi:10.1159/000362556

Jin, R., Banton, S., Tran, V. T., Konomi, J. V., Li, S., Jones, D. P., et al. (2016). Amino Acid Metabolism Is Altered in Adolescents with Nonalcoholic Fatty Liver Disease-An Untargeted, High Resolution Metabolomics Study. *J. Pediatr.* 172, 14–19. doi:10.1016/j.jpeds.2016.01.026

Jing, W., Jabbari, B., and Vaziri, N. D. (2018). Uremia Induces Upregulation of Cerebral Tissue Oxidative/inflammatory cascade, Down-Regulation of Nrf2 Pathway and Disruption of Blood Brain Barrier. *Am. J. Transl Res.* 10, 2137–2147. Available at https://escholarship.org/uc/item/9qv048rm.

Julius, U., Drel, V., Gräßler, J., Obrosova, I., Schmidt, W. E., and Meier, J. J. (2008). Nitrosylated Proteins in Monocytes as a New Marker of Oxidative-Nitrosative Stress in Diabetic Subjects with Macroangiopathy. *Exp. Clin. Endocrinol. Diabetes* 117, 72–77. doi:10.1055/s-2008-1078710

Kou, Y., Zheng, W. T., and Zhang, Y. R. (2016). Inhibition of miR-23 Protects Myocardial Function from Ischemia-Reperfusion Injury through Restoration of Glutamine Metabolism. *Eur. Rev. Med. Pharmacol. Sci.* 20, 4286–4293. Available at https://www.europeanreview.org/article/11599.

Lee, H. C., Yu, S. C., Lo, Y. C., Lin, I. H., Tung, T. H., and Huang, S. Y. (2019). A High Linoleic Acid Diet Exacerbates Metabolic Responses and Gut Microbiota Dysbiosis in Obese Rats with Diabetes Mellitus. *Food Funct.* 10, 786–798. doi:10.1039/C8fo02423e

Li, S., He, Y., Zhang, H., Zheng, R., Xu, R., Liu, Q., et al. (2020). Formulation of Traditional Chinese Medicine and its Application on Intestinal flora of Constipated Rats. *Microb. Cel Fact* 19, 212. doi:10.1186/s12934-020-01473-3

Li, Y., Chen, X., Kwan, T., Loh, Y., Singer, J., Liu, Y., et al. (2020a). Sat-160 Dietary Fibre and Bacterial Scfa Modulate Renal Inflammation in Diabetic Nephropathy through Activation of G-Protein Coupled Receptors Gpr43 and Gpr109a. *Kidney Int. Rep.* 5, S68–S69. doi:10.1016/j.ekir.2020.02.170

Li, Y., Rahman, S. U., Huang, Y., Zhang, Y., Ming, P., Zhu, L., et al. (2020b). Green tea Polyphenols Decrease Weight Gain, Ameliorate Alteration of Gut Microbiota, and Mitigate Intestinal Inflammation in Canines with High-Fat-Diet-Induced Obesity. *J. Nutr. Biochem.* 78, 108324. doi:10.1016/j.jnutbio.2019.108324

Li, Y. J., Chen, X., Kwan, T. K., Loh, Y. W., Singer, J., Liu, Y., et al. (2020). Dietary Fiber Protects Against Diabetic Nephropathy Through Short-Chain Fatty Acid-Mediated Activation of G Protein-Coupled Receptors GPR43 and GPR109A. *J. Am. Soc. Nephrol.* 31, 1267–1281. doi:10.1681/ASN.2019101029

Linehan, W. M., and Rouault, T. A. (2013). Molecular Pathways: Fumarate Hydratase-Deficient Kidney Cancer-Ttargeting the Warburg Effect in Cancer. *Clin. Cancer Res.* 19, 3345–3352. doi:10.1158/1078-0432.CCR-13-0304

Liu, I. M., Tzeng, T. F., Liou, S. S., and Chang, C. J. (2009). The Amelioration of Streptozotocin Diabetes-Induced Renal Damage by Wu-Ling-San (Hoelen Five Herb Formula), a Traditional Chinese Prescription. *J. Ethnopharmacol.* 124, 211–218. doi:10.1016/j.jep.2009.04.021

Liu, J. J., Liu, S., Gurung, R. L., Ching, J., Kovalik, J. P., Tan, T. Y., et al. (2018). Urine Tricarboxylic Acid Cycle Metabolites Predict Progressive Chronic Kidney Disease in Type 2 Diabetes. *J. Clin. Endocrinol. Metab.* 103, 4357–4364. doi:10.1210/jc.2018-00947

Ma, Y., Zhou, H., Li, C., Zou, X., Luo, X., Wu, L., et al. (2020). Differential Metabolites in Chinese Autistic Children: A Multi-Center Study Based on Urinary 1H-NMR Metabolomics Analysis. *Front. Psychiatry* 12, 624767. doi:10.3389/fpsyt.2021.624767

Macho-González, A., Garcimartín, A., Redondo, N., Cofrades, S., Bastida, S., Nova, E., et al. (2021). Carob Fruit Extract-Enriched Meat, as Preventive and Curative Treatments, Improves Gut Microbiota and Colonic Barrier Integrity in a Late-Stage T2DM Model. *Food Res. Int.* 141, 110124. doi:10.1016/j.foodres.2021.110124

Magne, F., Gotteland, M., Gauthier, L., Zazueta, A., Pesoa, S., Navarrete, P., et al. (2020). The Firmicutes/Bacteroidetes Ratio: A Relevant Marker of Gut Dysbiosis in Obese Patients? *Nutrients* 12, E1474. doi:10.3390/nu12051474

Mann, J. F., Green, D., Jamerson, K., Ruilope, L. M., Kuranoff, S. J., Littke, T., et al. (2010). Avosentan for Overt Diabetic Nephropathy. *J. Am. Soc. Nephrol.* 21, 527–535. doi:10.1681/ASN.2009060593

Mishra, A. K., Dubey, V., and Ghosh, A. R. (2016). Obesity: An Overview of Possible Role(s) of Gut Hormones, Lipid Sensing and Gut Microbiota. *Metabolism* 65, 48–65. doi:10.1016/j.metabol.2015.10.008

Newsholme, P., Procopio, J., Lima, M. M., Pithon-Curi, T. C., and Curi, R. (2003). Glutamine and Glutamate-Ttheir central Role in Cell Metabolism and Function. *Cell Biochem. Funct.* 21, 1–9. doi:10.1002/cbf.1003

Nova, E., Pérez de Heredia, F., Gómez-Martínez, S., and Marcos, A. (2016). The Role of Probiotics on the Microbiota: Effect on Obesity. *Nutr. Clin. Pract.* 31, 387–400. doi:10.1177/0884533615620350

Olenchock, B. A., Moslehi, J., Baik, A. H., Davidson, S. M., Williams, J., Gibson, W. J., et al. (2016). EGLN1 Inhibition and Rerouting of α-Ketoglutarate Suffice for Remote Ischemic Protection. *Cell* 165, 497–895. doi:10.1016/j.cell.2016.02.006

Pazdro, R., and Burgess, J. R. (2010). The Role of Vitamin E and Oxidative Stress in Diabetes Complications. *Mech. Ageing Dev.* 131, 276–286. doi:10.1016/j.mad.2010.03.005

Petrus, P., Lecoutre, S., Dollet, L., Wiel, C., Sulen, A., Gao, H., et al. (2020). Glutamine Links Obesity to Inflammation in Human White Adipose Tissue. *Cell Metab* 31, 375–e11. doi:10.1016/j.cmet.2019.11.019

Pusapati, R. V., Daemen, A., Wilson, C., Sandoval, W., Gao, M., Haley, B., et al. (2016). mTORC1-Dependent Metabolic Reprogramming Underlies Escape from Glycolysis Addiction in Cancer Cells. *Cancer Cell* 29, 548–562. doi:10.1016/j.ccell.2016.02.018

Quast, C., Pruesse, E., Yilmaz, P., Gerken, J., Schweer, T., Yarza, P., et al. (2012). The SILVA Ribosomal RNA Gene Database Project: Improved Data Processing and Web-Based Tools. *Nucleic Acids Res.* 41, D590–D596. doi:10.1093/nar/gks1219

Rhee, S. Y., Jung, E. S., Park, H. M., Jeong, S. J., Kim, K., Chon, S., et al. (2018). Plasma Glutamine and Glutamic Acid Are Potential Biomarkers for Predicting Diabetic Retinopathy. *Metabolomics* 14, 89. doi:10.1007/s11306-018-1383-3

Selen, E. S., Bolandnazar, Z., Tonelli, M., Bütz, D. E., Haviland, J. A., Porter, W. P., et al. (2015). NMR Metabolomics Show Evidence for Mitochondrial Oxidative Stress in a Mouse Model of Polycystic Ovary Syndrome. *J. Proteome Res.* 14, 3284–3291. doi:10.1021/acs.jproteome.5b00307

Shao, T., Shao, L., Li, H., Xie, Z., He, Z., and Wen, C. (2017). Combined Signature of the Fecal Microbiome and Metabolome in Patients with Gout. *Front. Microbiol.* 8, 268. doi:10.3389/fmicb.2017.00268

Shen, Y. L., Jiang, Y. P., Li, X. Q., Wang, S. J., Ma, M. H., Zhang, C. Y., et al. (2020). ErHuang Formula Improves Renal Fibrosis in Diabetic Nephropathy Rats by Inhibiting CXCL6/JAK/STAT3 Signaling Pathway. *Front. Pharmacol.* 10, 1596. doi:10.3389/fphar.2019.01596

Song, X. Y., Chen, Q., and Qi, X. Y. (2004). Effect of Liuwei Dihuang Pill on Erythrocyte Aldose Reductase Activity in Early Diabetic Nephropathy Patients. *Zhongguo Zhong Xi Yi Jie He Za Zhi* 24, 1087–1090. Available at https://pubmed.ncbi.nlm.nih.gov/15658651/.

Su, X. H., Lv, S. Q., Wang, X. Y., and Tian, F. S. (2015a). Clinical Observation of Sanhuang Yishen Capsule to Early Diabetic Nephropathy. *J. Liaoning Univer TCM* 13, 18–19. Available at http://en.cnki.com.cn/Article_en/CJFDTOTAL-LZXB201101008.htm.

Su, X. H., Lv, S. Q., Zhang, S. F., Li, S. L., Yu, W. X., Guo, R. Q., et al. (2015b). Sanhuang Yishen Capsule Combined with Epalrestat in the Treatment of Early Diabetes Clinical Observation of Nephropathy. *J. Basic Chin. Med.* 21, 1169–1170. doi:10.3969/j.issn.1674-7860.2013.19.003

Tanaka, K., Sasayama, T., Irino, Y., Takata, K., Nagashima, H., Satoh, N., et al. (2015). Compensatory Glutamine Metabolism Promotes Glioblastoma Resistance to mTOR Inhibitor Treatment. *J. Clin. Invest.* 125, 1591–1602. doi:10.1172/jci78239

Tang, D. Y., Guo, S. S., and Sun, R. Y. (2005). Effect of Xianzhen Tablet on Content of Advanced Glycosylation End Products (AGEs) and mRNA Expression of AGE-specific Cellular Receptor in Renal Cortex of Diabetic Rats. *Zhongguo Zhong Xi Yi Jie He Za Zhi* 25, 60–63. Available at https://pubmed.ncbi.nlm.nih.gov/15719755/.

Tian, B., Zhao, J., Zhang, M., Chen, Z., Ma, Q., Liu, H., et al. (2021). Lycium Ruthenicum Anthocyanins Attenuate High-Fat Diet-Induced Colonic Barrier Dysfunction and Inflammation in Mice by Modulating the Gut Microbiota. *Mol. Nutr. Food Res.* 65, e2000745. doi:10.1002/mnfr.202000745

Tone, A., Shikata, K., Sasaki, M., Ohga, S., Yozai, K., Nishishita, S., et al. (2005). Erythromycin Ameliorates Renal Injury via Anti-inflammatory Effects in Experimental Diabetic Rats. *Diabetologia* 48, 2402–2411. doi:10.1007/s00125-005-1945-6

Tong, W. H., Sourbier, C., Kovtunovych, G., Jeong, S. Y., Vira, M., Ghosh, M., et al. (2011). The Glycolytic Shift in Fumarate-Hydratase-Deficient Kidney Cancer Lowers AMPK Levels, Increases Anabolic Propensities and Lowers Cellular Iron Levels. *Cancer Cell* 20, 315–327. doi:10.1016/j.ccr.2011.07.018

Tuttle, K. R., Brosius, F. C., Adler, S. G., Kretzler, M., Mehta, R. L., Tumlin, J. A., et al. (2018). JAK1/JAK2 Inhibition by Baricitinib in Diabetic Kidney Disease: Results from a Phase 2 Randomized Controlled Clinical Trial. *Nephrol. Dial. Transpl.* 33, 1950–1959. doi:10.1093/ndt/gfx377

Wang, D., Guan, M. P., Zheng, Z. J., Li, W. Q., Lyv, F. P., Pang, R. Y., et al. (2015). Transcription Factor Egr1 Is Involved in High Glucose-Induced Proliferation and Fibrosis in Rat Glomerular Mesangial Cells. *Cell. Physiol. Biochem.* 36, 2093–2107. doi:10.1159/000430177

Wang, F. L., Wang, Y. H., Han, L., An, H. Y., Zhang, J. H., Zhang, X. Y., et al. (2018). Renoprotective Effect of Yiqi Yangyin Huayu Tongluo Formula against Diabetic Nephropathy in Diabetic Rats. *Evid. Based Complement. Alternat Med.* 2018, 4276052. doi:10.1155/2018/4276052

Wang, H., Zhang, H., Chen, X., Zhao, T., Kong, Q., Yan, M., et al. (2016). The Decreased Expression of Electron Transfer Flavoprotein β Is Associated with Tubular Cell Apoptosis in Diabetic Nephropathy. *Int. J. Mol. Med.* 37, 1290–1298. doi:10.3892/ijmm.2016.2533

Wu, G., Shi, Y., Han, L., Feng, C., Ge, Y., Yu, Y., et al. (2020). Dietary Methionine Restriction Ameliorated Fat Accumulation, Systemic Inflammation, and Increased Energy Metabolism by Altering Gut Microbiota in Middle-Aged Mice Administered Different Fat Diets. *J. Agric. Food Chem.* 68, 7745–7756. doi:10.1021/acs.jafc.0c02965

Wu, Y. L., Wei, C., and Wang, H. T. (2007). Effect of Tongshenluo Capsule on the Components of Extracellular Matrix and Their Metabolism in Kidney of Rats with Diabetic Nephropathy. *Zhongguo Zhong Xi Yi Jie He Za Zhi* 27, 326–330. Available at https://pubmed.ncbi.nlm.nih.gov/17526172/.

Xiao, D., Zeng, L., Yao, K., Kong, X., Wu, G., and Yin, Y. (2016). The Glutamine-Alpha-Ketoglutarate (AKG) Metabolism and its Nutritional Implications. *Amino Acids* 48, 2067–2080. doi:10.1007/s00726-016-2254-8

Xue, H., Zhang, M., Ma, J., Chen, T., Wang, F., and Tang, X. (2020). Lactose-Induced Chronic Diarrhea Results from Abnormal Luminal Microbial Fermentation and Disorder of Ion Transport in the Colon. *Front. Physiol.* 11, 877. doi:10.3389/fphys.2020.00877

Yang, Y., Zhang, Y., Xu, Y., Luo, T., Ge, Y., Jiang, Y., et al. (2019). Dietary Methionine Restriction Improves the Gut Microbiota and Reduces Intestinal Permeability and Inflammation in High-Fat-Fed Mice. *Food Funct.* 10, 5952–5968. doi:10.1039/c9fo00766k

You, Y. H., Quach, T., Saito, R., Pham, J., and Sharma, K. (2015). Metabolomics Reveals a Key Role for Fumarate in Mediating the Effects of NADPH Oxidase 4 in Diabetic Kidney Disease. *J. Am. Soc. Nephrol.* 27, 466–481. doi:10.1681/ASN.2015030302

Zdzisińska, B., Żurek, A., and Kandefer-Szerszeń, M. (2017). Alpha-Ketoglutarate as a Molecule with Pleiotropic Activity: Well-Known and Novel Possibilities of Therapeutic Use. *Arch. Immunol. Ther. Exp. (Warsz)* 65, 21–36. doi:10.1007/s00005-016-0406-x

Zhang, B., Li, G., Shahid, M. S., Gan, L., Fan, H., Lv, Z., et al. (2020). Dietary L-Arginine Supplementation Ameliorates Inflammatory Response and Alters Gut Microbiota Composition in Broiler Chickens Infected with *Salmonella enterica* Serovar Typhimurium. *Poult. Sci.* 99, 1862–1874. doi:10.1016/j.psj.2019.10.049

Zhang, L., Shi, M., Ji, J., Hu, X., and Chen, F. (2019). Gut Microbiota Determines the Prevention Effects of Luffa Cylindrica (L.) Roem Supplementation against Obesity and Associated Metabolic Disorders Induced by High-Fat Diet. *FASEB J.* 33, 10339–10352. doi:10.1096/fj.201900488R

Zhang, M. H., Feng, L., Zhu, M. M., Gu, J. F., Jiang, J., Cheng, X. D., et al. (2014). The Anti-inflammation Effect of Moutan Cortex on Advanced Glycation End Products-Induced Rat Mesangial Cells Dysfunction and High-Glucose-Fat Diet and Streptozotocin-Induced Diabetic Nephropathy Rats. *J. Ethnopharmacol.* 151, 591–600. doi:10.1016/j.jep.2013.11.015

Zhang, X., Zhao, Y., Xu, J., Xue, Z., Zhang, M., Pang, X., et al. (2015). Modulation of Gut Microbiota by Berberine and Metformin during the Treatment of High-Fat Diet-Induced Obesity in Rats. *Sci. Rep.* 5, 14405. doi:10.1038/srep14405

Zhang, Y., Peng, Y., Zhao, L., Zhou, G., and Li, X. (2021). Regulating the Gut Microbiota and SCFAs in the Faeces of T2DM Rats Should Be One of Antidiabetic Mechanisms of Mogrosides in the Fruits of Siraitia Grosvenorii. *J. Ethnopharmacol.* 274, 114033. doi:10.1016/j.jep.2021.114033

Zhao, M., Yuan, M. M., Yuan, L., Huang, L. L., Liao, J. H., Yu, X. L., et al. (2018). Chronic Folate Deficiency Induces Glucose and Lipid Metabolism Disorders and Subsequent Cognitive Dysfunction in Mice. *PLoS One* 13, e0202910. doi:10.1371/journal.pone.0202910

Zheng, L., Cardaci, S., Jerby, L., MacKenzie, E. D., Sciacovelli, M., Johnson, T. I., et al. (2015). Fumarate Induces Redox-dependent Senescence by

Modifying Glutathione Metabolism. *Nat. Commun.* 6, 6001. doi:10.1038/ncomms7001

Zhong, Y., Menon, M. C., Deng, Y., Chen, Y., and He, J. C. (2015). Recent Advances in Traditional Chinese Medicine for Kidney Disease. *Am. J. Kidney Dis.* 66, 513–522. doi:10.1053/j.ajkd.2015.04.013

Zhong, Y. F., Zhou, Y. H., Liu, S. X., Guo, J. L., and Zuo, D. Y. (2016). Clinical Observation on Curative Effect of IgA Nephropathy Treated with Sanhuang Yishen Capsule Combining with Corticosteroids and Impact on Serum VEGF. *Chin. J. Tradit Med. Sci. Tech.* 5, 3, 2016 . Available at http://en.cnki.com.cn/Article_en/CJFDTOTAL-TJYY201605008.htm.

Conflict of Interest: The authors declare that the research was conducted in the absence of any commercial or financial relationships that could be construed as a potential conflict of interest.

Publisher's Note: All claims expressed in this article are solely those of the authors and do not necessarily represent those of their affiliated organizations, or those of the publisher, the editors and the reviewers. Any product that may be evaluated in this article, or claim that may be made by its manufacturer, is not guaranteed or endorsed by the publisher.

frontiers in Pharmacology

ORIGINAL RESEARCH
published: 24 January 2022
doi: 10.3389/fphar.2022.823341

Spectrum-Effect Relationship Between Antioxidant and Anti-inflammatory Effects of Banxia Baizhu Tianma Decoction: An Identification Method of Active Substances With Endothelial Cell Protective Effect

Nan Xu[1], *Mingchen Li*[2], *Ping Wang*[1], *Shuling Wang*[3] *and Haiyan Shi*[2]*

[1]*Laboratory of Chinese Medicine Preparation, Shandong Research Academy of Traditional Chinese Medicine, Jinan, China,* [2]*Department of Clinical Pharmacy, The First Affiliated Hospital of Shandong First Medical University & Shandong Provincial Qianfoshan Hospital, Shandong Engineering and Technology Research Center for Pediatric Drug Development, Shandong Medicine and Health Key Laboratory of Clinical Pharmacy, Jinan, China,* [3]*School of Pharmacy, Hangzhou Normal University, Hangzhou, China*

OPEN ACCESS

Edited by:
Shuai Ji,
Xuzhou Medical University, China

Reviewed by:
Yean Chun Loh,
Universiti Sains Malaysia (USM), Malaysia
Chunyu Li,
Chinese Academy of Medical Sciences and Peking Union Medical College, China
Dan-dan Zhang,
Shanghai University of Traditional Chinese Medicine, China

***Correspondence:**
Haiyan Shi
shihaiyan123@163.com

Specialty section:
This article was submitted to Ethnopharmacology, a section of the journal Frontiers in Pharmacology

Received: *27 November 2021*
Accepted: *07 January 2022*
Published: *24 January 2022*

Citation:
Xu N, Li M, Wang P, Wang S and Shi H (2022) Spectrum-Effect Relationship Between Antioxidant and Anti-inflammatory Effects of Banxia Baizhu Tianma Decoction: An Identification Method of Active Substances With Endothelial Cell Protective Effect. Front. Pharmacol. 13:823341. doi: 10.3389/fphar.2022.823341

Banxia Baizhu Tianma decoction (BBTD), a six-herb Chinese medicine formula first described approximately 1732 AD, is commonly prescribed for Hypertension with Phlegm-dampness Stagnation (HPDS) as an adjuvant therapy in China. Obesity is an important risk factor for the increasing prevalence of hypertension year by year in China. In Traditional Chinese medicine, obesity is often differentiated as the syndrome of excessive phlegm-dampness.Vascular endothelial cell injury plays an important role in the development and occurrence of HPDS. In this study, the protective effects of 18 batches of BBTD samples from different origins on HUVEC cells were evaluated, including antioxidant and anti-inflammatory activities. Ultrahigh performance liquid chromatography (UPLC) was used to establish fingerprints, and combined with pharmacodynamic indexes, the protective components of BBTD on endothelial cells were analyzed. Antioxidant and anti-inflammatory activities were evaluated by ROS and Hs-CRP models, respectively. Hierarchical cluster analysis (HCA) and Bivariate correlation analysis (BCA) were used to investigate the potential correlation between chemical components and endothelial cell protection. The results indicated that BBTD could reduce ROS and hs-CRP levels in HUVEC cells, and the pharmacological activities in 18 batches of BBTD samples were significantly different. The results of BCA indicated that Gastrodin, Liquiritin, Hesperidin, Isoliquiritin, Hesperetin, and Isoliquiritigenin might be the active constituents to activate ROS and suppress hs-CRP as determined by spectrum-effect relationships. The antioxidant and anti-inflammatory activities of the 6 components at different concentration were verified, and the results showed that all of them had good antioxidant and anti-inflammatory activities in a concentration-dependent manner. This study showed that activity determination and spectral correlation can be used to search for active substances

in Chinese medicine formula and provide data support for quality control of Traditional Chinese medicine (TCM).

Keywords: banxia baizhu tianma decoction, spectrum-effect relationship, antioxidant—phytochemical studies, anti-inflammatory, active substances from natural resource

1 INTRODUCTION

Banxia Baizhu Tianma decoction (BBTD), as a classical representative prescription, has the effects of expectorating phlegm, dispelling wind, invigorating the spleen and dispersing overflow. Based on TCM theory and clinical practice for many years, BBTD is especially suitable for the lack of exercise, abdominal obesity, and hypertension (Jiang et al., 2021). Recent studies have shown that BBTD has the potential to lower blood pressure *in vivo* and *in vitro* (Jiang J. et al., 2019). As reactive derivatives of oxygen metabolism, the activity of Reactive Oxygen Species (ROS) changes due to various stimuli, including G-protein coupled receptor agonists, growth factors, perfusion pressure, flow, and oxygen in vascular smooth muscle and endothelial cells. ROS are involved in smooth muscle contraction, endothelium-dependent relaxation, smooth muscle growth, proliferation, and migration, thereby contributing to fine-tuning of blood flow, arterial wall thickness, and vascular resistance (Knock, 2019). Oxidative stress will occur when the equilibrium state of ROS in the body is broken, which plays a key role in the development of vascular dysfunction under special conditions such as hypertension. It is characterized by NO loss bioavailability, vascular inflammation and endothelial dysfunction. Given that oxidative stress is a key regulating factor of vascular dysfunction, the application of classical antioxidant oxidation treatment seems to be a promising treatment for vascular disease, such as angiotensin converting enzyme (ACE) inhibitors or angiotensin AT1 receptor antagonist. It is confirmed that angiotensin II plays a key role in the reaction (Do Vale and Tirapelli, 2020). High sensitivity C-reactive protein (Hs-CRP) is a common biomarker of cardiovascular disease. Studies have shown that CRP directly involved in endothelial dysfunction in patients with high blood pressure, the development of vascular sclerosis and blood pressure, and CRP indicators can serve as a biomarker associated with atherosclerosis, vascular stiffness, end-organ injury, and the development of cardiovascular events (Hage, 2014; Zhang J. et al., 2019). CRP is an acute inflammatory protein that increases up to 1,000-fold at sites of infection or inflammation. There is now growing evidence that CRP plays an important role in inflammatory processes, and CRP is used as a classic marker of inflammation and cardiovascular events. Therefore, endothelial proliferation rate, ROS and Hs-CRP can be used as potential targets of antihypertensive effect of BBTD.

UPLC fingerprint is an effective tool to evaluate the quality of TCM, and identify the authenticity of traditional Chinese medicine as well as its components (Sun et al., 2019). It is a scientific method to clarify the substance basis of TCM pharmacological action and establish the quality control method of TCM to determine the correlation between fingerprint and biological activity by using spectrum-effect relationship (Farrag et al., 2019; Zhang J. et al., 2019; Liao et al., 2021). In this study, 18 BBTD samples were fingerprinted for component analysis, and the antioxidant and anti-inflammatory activities of endothelial cells were determined. Statistical methods were used to determine the relationship between spectrum and activity, identify possible active components, and further verify the activity.

2 MATERIALS AND METHODS

2.1 Chemicals, Reagents and Materials

18 batches of BBTD comprising of Pinelliae Rhizoma (PR), Gastrodiae Rhizoma (GR), Rhizoma Atractylodis Macrocephalae (RAM), Citri Exocarpium Rubrum (CER), Poria (PO) and *Glycyrrhiza uralensis* Fisch (GUF) were included in this study. PR is the dry rhizome of Pinellia ternata (Thunb.) Makino [Araceae]. GR is the dry rhizome of Gastrodia elata Blume [Orchidaceae]. RAM is the dry rhizome of Atractylodes macrocephala Koidz [Compositae]. CER is the dry ripe peel of Citrus reticulata Blanco [Rutaceae]. PO is the dry sclerotia of Poria cocos (Schw.)Wolf [Polyporaceae]. GUF is the dried rhizome of *Glycyrrhiza* uralensis Fisch [Leguminosae]. The 18 batches of herbs came from Chinese herbal medicine markets in Anhui, Hebei, Shandong, Jilin, Guangxi, Beijing, Hunan, Sichuan and other places. All herbs were identified by Professor Jin Guangqian, TCM identification expert of Shandong Academy of Traditional Chinese Medicine. Each herb came from 3 different producing areas. L_{18} (3^7) random number table method was used to randomly combine and sequence these 6 herbs, and 18 batches of BBTD samples (S1-S18) were obtained.

Acetonitrile (HPLC grade) and Methanol (HPLC grade) were purchased from Fisher Scientific Co. (FairLawn, NJ, United States). Ultrapure water was acquired from a Millipore Milli-Q-Plus system (Millipore, Bedford, MA, United States). The Gastrodin (a), Liquiritin (b), Narirutin (c), Naringin (d), Hesperidin (e), Neohesperidin (f), Isoliquiritin (g), Liquiritigenin (h), Hesperetin (i), Isoliquiritigenin (j), Nobiletin (k), Protopine (l), Atractylenolide III (m), Poricoic acid A (n) and Glycyrrhetinic acid (o) were purchased from Chengdu Skoqi-Biotechnology Co. Ltd. (Chengdu, China).

ROS kit was acquired from Solarbio Technology Co., Ltd. (Beijing, China). Hs-CRP enzyme-linked immunosorbent assay kit was purchased from Yubo Biotechnology Co., Ltd. (Shanghai, China). DMEM medium RPMI - 1640, fetal bovine serum, penicillin and streptomycin were purchased from biological sharp, from Shanghai, China. HUVEC cell line was purchased

from Wuxi Bohe Biomedical Technology Co., LTD. (Jiangsu, China).

2.2 Instruments

Thermo Acquity UPLC system (Thermo, Waltham, MA, United States) consisted of a photodiode array (PDA)detector, autosampler manager, column compartment, and a binary solvent delivery pump and was connected to Thermo chromeleon software. Inverted photographic microscope was purchased from Tokyo, Japan. Enzyme label detector was purchased from Thermo (United States). palmitic acid was from MedChemExpress (United States). ELISA kits were purchased from BosterBio (United States). Dimethyl sulfoxide (DMSO) was acquired from Invitrogen (United States).

2.3 Ultra high Performance Liquid Chromatography Fingerprints

2.3.1 Plant Sample Preparation

PR, GR, RAM, CER, PO and GUF was ground into powder using a mill. 4.6 g BBTD powder consisted of PR, GR, RAM, CER, PO and GUF powder (ratio 9:6:6:6:15:4) were dissolved in 50 ml water. The proportion of medicinal materials is mainly determined according to the ancient Chinese medicine book "Yi Xue Xin Wu". The mixture was heated to boil and simmered for 1.0 h. After the sample was cooled, it was centrifuged at 3,000 rpm for 10min and then concentrated with a rotary evaporator.

2.3.2 Preparation of Standard Compounds

All standard compounds were weighed accurately and dissolved in methanol to form reserve solution, which was stored at 4°C. All reserve fluids are diluted to the desired concentration and then mixed immediately prior to analysis. The final concentrations were 56.8 μg/ml(a), 38.9 μg/ml(b), 59.4 μg/ml(c), 59.9 μg/ml(d), 56.8 μg/ml(e), 40.5 μg/ml(f), 38.9 μg/ml(g), 15.7 μg/ml(h), 53.9 μg/ml(i), 31.8 μg/ml(j), 17.8 μg/ml (k), 18.6 μg/ml(l), 19.3 μg/ml(m), 71.8 μg/ml (n) and 59.2 μg/ml (o), respectively.

2.3.3 Chromatographic Conditions

The solution was filtered by 0.22 μm microporous membrane and injected into UPLC for analysis. An Acclaim TM RSLC Lot Validation-120 C18 column (2.1 mm × 100 mm i. d., 2.2 μm particle size) (Thermo, Sunnyvale, CA, United States) was used for chromatographic separation. The temperature of the column temperature oven was set as 30°C. The mobile phase was a mixture of acetonitrile (solvent A) and water (solvent B) with a flow rate at 0.30 $mlmin^{-1}$. Gradient elution condition: 0–5 min, 5–12% A; 5–20 min, 12%-26%A; 20–30 min, 26–80% A; 30–35 min, 80%–100% A. The absorption wavelength was set at 235 nm and the injection volume was 5.0 μL.

2.3.4 Methodology Validation

The standard curve and linear range were established in the method validation part, and the precision, stability and repeatability were investigated. Precision was calculated by 6 consecutive injections of the same sample solution, and repeatability was evaluated by six samples from the same source. A sample solution was stored in a volumetric flask at room temperature and repeated injection analysis was performed within 1 day (0, 4, 8, 12, 16 and 24 h) to investigate the stability of the sample at room temperature.

2.3.5 Peak Identification

The standard solution was injected into the UPLC system for qualitative analysis, and the retention time of the standard was recorded. The retention time of a-o was determined by comparing the retention time of reference substance.

2.3.6 Fingerprint Established and Evaluated

For 18 batches of samples, each sample solution was injected three times according to the determined UPLC conditions, and fingerprint analysis was carried out. UPLC fingerprint data was saved in CDF format. Traditional Chinese medicine chromatographic fingerprint system (Version 2012A) was used to automatically match the chromatographic peak fingerprints, and then the chromatogram of different extracts was generally compared by using the median method to form reference chromatogram. The similarity between chromatogram and reference chromatogram of different extracts in 18 samples was calculated by using this software.

2.4 Cell Experiments

2.4.1 Cell Viability Assay

HUVEC cells were cultured in the RPMI-1640 DMEM supplemented with 10% fetal bovine serum, penicillin (100 U/mL), and streptomycin (100 μg/ml) at 37°C under a humidified atmosphere containing 5% CO2. The mother liquor of 200 mM was obtained by dissolving 0.1024 g Palmitic acid in 20 ml DMSO, diluted to 200 umol/L with RPMI-1640 complete medium.All Eighteen water extracts of BBTD (1 mg/ml) were dissolved in the RPMI-1640. After incubation at 37°C with 5% CO2 for 24 h, HUVEC cells were inoculated on a 96-well plate for 24 h.

2.4.2 Antioxidant Activity Test

Briefly, 200 μL of each extract solution under "2.4.1" was mixed with DCFH-DA (10 $\mu mol\ L^{-1}$), then diluted to 1 ml. After stayed and reacted in dark for 20 min at 37°C, Using fluorescence inversion microscope to observe the fluorescence intensity of cells and take pictures. and converted to radical scavenging activity by the following equation:

$$\text{Scavenging activity}\,(\%) = (\text{Amodel} - \text{Asample}) \times / (\text{Amodel} - \text{Ablank}) \times 100\%$$

Serum-free medium (supplement to the total volume of 6 ml) plus sample solution (200 μL)/DCFH-DA solution (4 ml) was used as a blank/control. Each sample was run in triplicate and averaged.

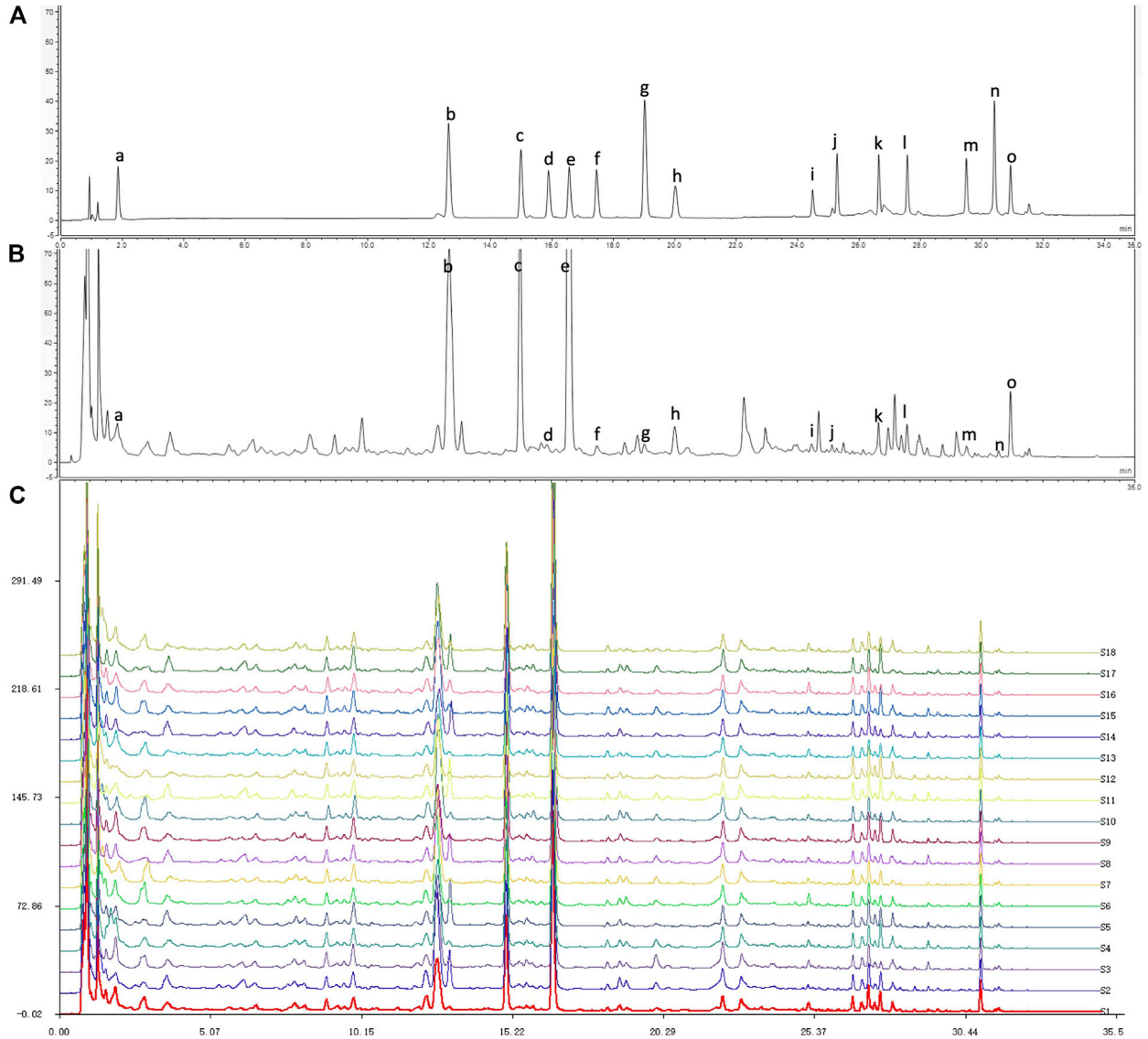

FIGURE 1 | UPLC-PDA chromatogram of reference substances **(A)**, test sample **(B)** and 18 batches of BBTD **(C)**. 15 peaks were identified by comparison with standard substances: Gastrodin (a), Liquiritin (b), Narirutin (c), Naringin (d), Hesperidin (e), Neohesperidin (f), Isoliquiritin (g), Liquiritigenin (h), Hesperetin (i), Isoliquiritigenin (j), Nobiletin (k), Protopine (l), Atractylenolide III (m), Poricoic acid A (n) and Glycyrrhetinic acid (o).

2.4.3 High Sensitivity C-Reactive Protein Inhibition Rate Test

Hs-CRP value was assessed by absorbance determination using an enzyme-linked immunosorbent assay (ELISA) kit. The hs-CRP concentration in Cell supernatant was determined by ELISA kit, then the absorbance was measured at 450 nm using a microplate reader. The inhibition of hs-CRP release was calculated according to the following:

$$\text{hs} - \text{CRP inhibition rate}\,(\%) = (\text{Cmodel} - \text{Csample}) \times / (\text{Cmodel} - \text{Cblank}) \times 100\%$$

The experiments were performed in triplicates, the data were presented as the mean ± SD.

2.5 Hierarchical Cluster Analysis

As a multivariate analysis method, Hierarchical Cluster Analysis (HCA) sorted specimens into clusters. This analysis method could maximize each cluster in homogeneity, maximized the heterogeneity between cluster at the same time, the objects were divided into specific cluster (Song et al., 2019; Jia et al., 2021). This study applied HCA to assess the correlation of 18 samples of BBTD UPLC fingerprint, and used Heatmapper (http://www.heatmapper.ca/) for testing.

TABLE 1 | The relative peak area of 15 common peaks measured by UPLC-PDA.

Sample	Peak area of each compound														
	a	b	c	d	e	F	g	h	i	j	k	l	m	n	o
S1	2.9705	6.7800	6.9694	0.4316	19.4671	0.1729	0.2999	0.3552	0.1285	0.1413	0.7508	1.0291	0.1982	0.0848	1.4926
S2	3.4193	13.9931	7.9431	0.3181	23.5922	0.2120	0.7751	0.7416	0.1383	0.1564	0.7503	0.9441	0.2109	0.0978	1.0891
S3	3.4786	10.4605	9.5405	0.4705	25.6195	0.1619	0.5068	1.6416	0.1558	0.1739	0.7108	0.3911	0.1061	0.0793	1.4765
S4	1.2530	6.4111	9.2160	0.6422	14.9526	0.4228	0.5212	1.8039	0.1612	0.0809	0.7050	1.3536	0.1961	0.1335	1.4787
S5	2.9468	6.0807	9.3892	0.7715	16.6287	0.1772	0.3497	1.4001	0.1154	0.1202	0.7718	1.0118	0.2129	0.0962	1.5332
S6	4.0820	12.0234	8.1739	0.3407	18.3150	0.2274	0.6982	0.6319	0.1200	0.1141	0.6238	0.5591	0.1495	0.1675	1.4383
S7	3.6789	11.8086	7.9348	0.3843	17.7325	0.2395	0.5949	0.6166	0.1702	0.1542	0.6610	0.7323	0.1205	0.0843	1.3763
S8	2.0217	7.3211	8.1127	0.6066	18.4095	0.1055	0.3298	0.8529	0.0955	0.1492	0.6376	0.4799	0.1260	0.0771	1.3693
S9	1.8181	11.0485	9.5243	0.9790	25.2465	0.1254	0.3457	0.4269	0.1126	0.1531	0.9428	1.3085	0.2763	0.0939	1.0119
S10	3.0666	13.5824	9.7096	0.8454	24.4846	0.0748	0.5487	1.4372	0.1011	0.1663	0.6429	0.4886	0.1301	0.1070	1.3618
S11	3.5990	8.2719	7.7308	0.5255	16.9096	0.2513	0.3704	0.8104	0.1525	0.1340	0.8455	1.1785	0.2422	0.0961	1.3550
S12	1.1075	5.6802	9.5294	0.2282	19.5106	0.1747	0.3094	0.4383	0.0857	0.1281	1.0632	1.1950	0.1856	0.1488	1.3598
S13	3.9153	6.9918	8.4033	0.5787	22.2395	0.1761	0.3595	0.7494	0.1256	0.2233	0.5665	0.7138	0.1363	0.0913	1.3832
S14	1.4633	5.1123	7.8654	0.2456	19.2884	0.2443	0.2840	1.3744	0.2460	0.1398	0.7797	0.4300	0.1348	0.1302	1.4210
S15	3.8311	10.4729	10.0549	0.5285	21.2086	0.3013	0.5395	1.0647	0.1683	0.1490	0.7798	1.3745	0.2739	0.0901	1.4228
S16	3.5314	6.4247	9.5296	0.3500	19.2174	0.1608	0.3582	0.4160	0.1672	0.1042	0.8654	0.5053	0.1157	0.1203	1.0202
S17	2.4918	11.8817	9.4389	0.4328	25.6747	0.1411	0.5792	0.7563	0.2447	0.1280	0.7337	1.4214	0.2626	0.0977	1.4113
S18	1.9341	5.1496	8.0547	0.5038	19.5670	0.1564	0.2901	0.4407	0.1086	0.1158	0.6136	0.7767	0.1513	0.1297	1.4159
RSD%	34.85	34.03	10.32	39.86	16.80	40.63	33.59	51.65	31.31	22.03	16.68	41.07	31.90	23.91	11.39

2.6 Bivariate Correlation Analysis

Pearson's correlation coefficient was used to quantify the degree of co-location between paired data. In this study, the Bivariate correlation analysis function of SPSS statistical software (SPSS for Windows 20.0, SPSS Inc., United States) was used to analyze the correlation between the peak area value of UPLC fingerprint and the antioxidant/anti-inflammatory effect of HUVEC cells.

3 RESULTS

3.1 Method Validation for Fingerprint

The relative standard deviations (RSD) of precision and reproducibility were both less than 2.60%, and samples for UPLC determination were stable at room temperature for 24 h.

3.2 Ultrahigh Performance Liquid Chromatography Fingerprints

18 bathes of BBTD samples were analyzed with UPLC. was shown in **Figure 1**. Mixed reference substances (**Figure 1A**), BBTD test sample (**Figure 1B**) and Chromatograms of all batches of BBTD (**Figure 1C**), were generated under the determined chromatographic condition. The similarity between reference fingerprints and chromatograms among 18 batches of BBTD samples was evaluated by calculating correlation coefficients. Similar chemical signatures were found across batches, and 15 common peaks were found over intervals of 1–30 min by comparing the UV spectra and UPLC retention times of 18 chromatograms. 15 common peaks were identified as Gastrodin (a), Liquiritin (b), Narirutin (c), Naringin (d), Hesperidin (e), Neohesperidin (f), Isoliquiritin (g), Liquiritigenin (h), Hesperetin (i), Isoliquiritigenin (j), Nobiletin (k), Protopine (l), Atractylenolide III (m), Poricoic acid A (n) and Glycyrrhetinic acid (o) by comparison. Peak a has the largest peak area in the fingerprint. As shown in **Table 1**, the peak areas of common peaks of different samples were different to some extent, and the RSD% of all common peaks were greater than 10%, indicating that the content of chemical components in different batches of BBTD samples from different producing areas were different.

TABLE 2 | Similarities of different batches BBTD samples from various regions.

Sample	Similarities	Sample	Similarities	Sample	Similarities
S1	0.989	S7	0.964	S13	0.992
S2	0.897	S8	0.992	S14	0.967
S3	0.988	S9	0.991	S15	0.986
S4	0.982	S10	0.974	S16	0.989
S5	0.987	S11	0.984	S17	0.983
S6	0.920	S12	0.990	S18	0.984

3.3 Fingerprint Similarity

In order to assess the similarity between these samples, fingerprints of 18 BBTD samples were compared and analyzed with reference fingerprints. The similarity between the fingerprint of each sample of different samples and the reference fingerprint ranges from 0.897 to 0.992, as shown in **Table 2**.

3.4 Antioxidant Activity Test

The ROS inhibition rates of 18 BBTD samples was analyzed by ANOVA and further multiple comparisons were performed. All the model results showed $p = 0.000 < 0.01$, indicating that there were significant differences in ROS scavenging ability of different extracts. ROS fluorescence intensity and inhibition rates of 18 batches of BBTD extracts were shown in **Figure 2** and **Table 3**.

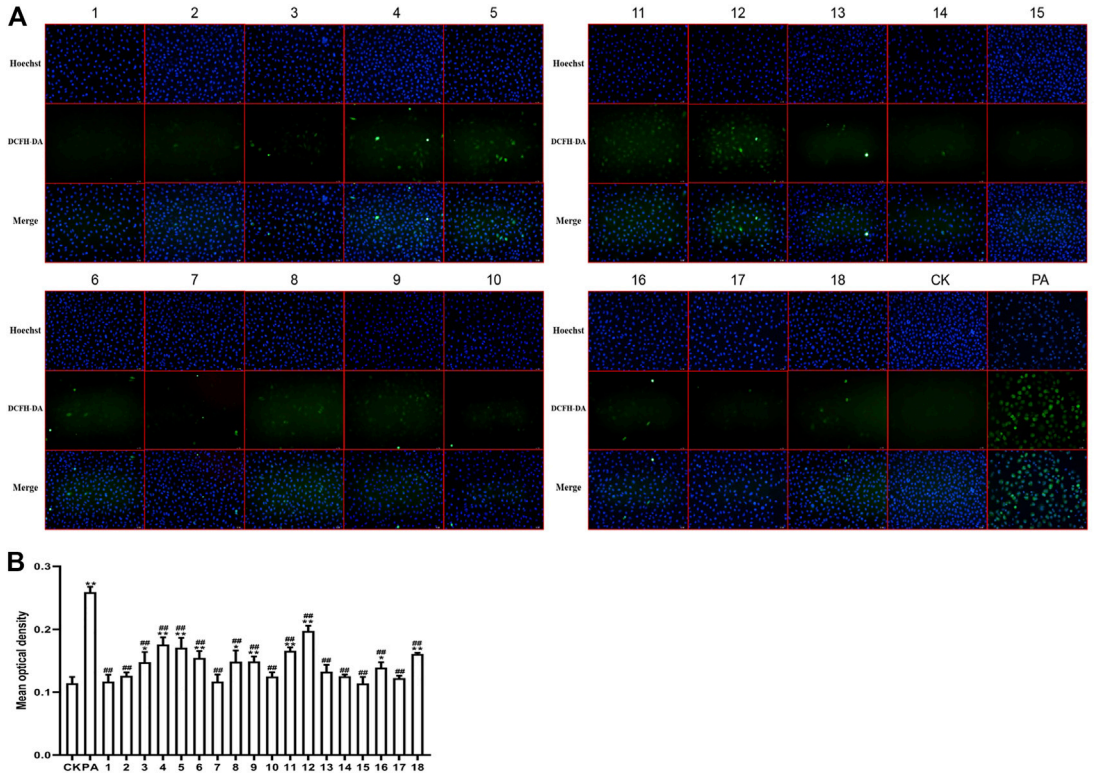

FIGURE 2 | ROS fluorescence intensity **(A)** and scavenging activity **(B)** of Eighteen batches BBTD samples.

TABLE 3 | ROS inhibition rates of 18 batches of BBTD extracts (mean ± SD, n = 3).

Sample	Mean optical density	Scavenging rate %	Sample	Mean optical density	Scavenging rate %
CK	0.1141 ± 0.0102	—	S9	0.1489 ± 0.0080	196.77
PA	0.2539 ± 0.0084	—	S10	0.1250 ± 0.0065	217.68
S1	0.1166 ± 0.0110	225.03	S11	0.1656 ± 0.0057	182.11
S2	0.1258 ± 0.0056	217.03	S12	0.1975 ± 0.0083	154.17
S3	0.1476 ± 0.0163	197.87	S13	0.1323 ± 0.0110	211.29
S4	0.1758 ± 0.0115	173.17	S14	0.1253 ± 0.0027	217.41
S5	0.1711 ± 0.0153	177.33	S15	0.1136 ± 0.0106	227.68
S6	0.1543 ± 0.0112	192.00	S16	0.1392 ± 0.0085	205.29
S7	0.1168 ± 0.0111	224.90	S17	0.1222 ± 0.0041	220.12
S8	0.1485 ± 0.0179	197.14	S18	0.1609 ± 0.0018	186.21

3.5 High Sensitivity C-Reactive Protein Inhibition Rate Test

Then the hs-CRP inhibition rate in 18 BBTD samples was analyzed by ANOVA model and multiple-comparison model, and the resulted demonstrated that all has significant difference (p = 0.001 < 0.05). The hs-CRP concentration and inhibition rate of BBTD extracted from 18 batches were shown in **Figure 3** and **Table 4**.

3.6 Results of Hierarchical Cluster Analysis

Heat map is a graphical representation of data, each color unit corresponding to the matrix contains a single value. In the vicinity of HCA, 15 common peaks of 18 BBTD samples are shown by heat maps, and three clusters can be detected from **Figure 4**. Cluster 1 was composed of S3, S10 and S17, cluster 2 consisted of S2, S4, S6, S7, and S15, and cluster 3 consisted of S1, S5, S8, S9, S11, S12, S13, S14, S16, and S18. The results showed that the different sources of BBTD samples with similar chemical fingerprint, but the peak area of the ingredients are different. HCA can achieve preliminary separation of the samples at the chemical level. The different contents of chemical components in the cluster samples indicate that the chemical components may be different according to different places of origin.

3.7 Spectrum-Effect Relationship Analysis

As shown in **Figure 5** and **Table 5**, the correlation coefficient showed that 6 peaks a, b, e, g, i, and j were positively correlated with activity. a, b, e, g, i and j were identified as Gastrodin,

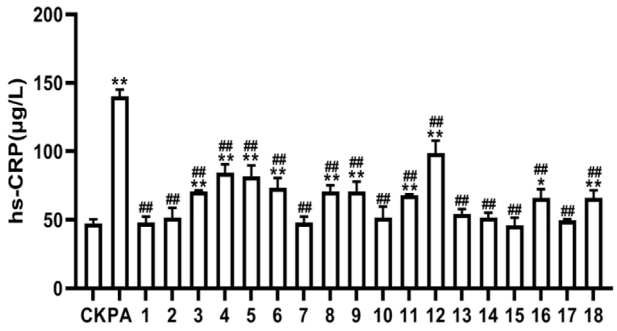

FIGURE 3 | Hs-CRP concentration of 18 batches among BBTD samples.

them in the process of practice to accumulate experience. Therefore, the prescription varies with the person, the disease and the progress of disease, and the prescription is adjusted and modified at any time, which fully embodies the characteristics of personalized treatment (Jiang L. et al., 2019). TCM and western medicine come from different cultural backgrounds, theoretical systems and medical models are greatly different. Under the guidance of modern medical theory, Western medicine is researched and developed for some pathological process of diseases or symptoms. Most of them are single chemical components, with clear targets and mechanisms of action and clear adverse reactions. Traditional Chinese medicine has become a hot spot in the research field of traditional Chinese medicine decoction because of its many

TABLE 4 | The hs-CRP inhibition rate of BBTD extracted from 18 batches (mean ± SD, *n* = 3).

Sample	Mean optical density	Scavenging rate %	Sample	Mean optical density	Scavenging rate %
CK	47.3030 ± 3.1926	—	S9	70.6364 ± 7.2727	31.83
PA	140.0303 ± 5.0069	—	S10	51.5455 ± 8.1818	46.54
S1	47.9091 ± 4.5455	48.65	S11	67.9091 ± 0.9091	34.41
S2	51.5455 ± 7.2727	46.54	S12	98.8182 ± 9.0909	22.72
S3	70.6364 ± 0.9091	31.83	S13	54.2727 ± 3.6364	44.84
S4	84.2727 ± 6.3636	15.16	S14	51.5455 ± 3.6364	46.54
S5	81.5455 ± 8.1818	19.12	S15	46.0909 ± 5.4545	49.65
S6	73.3636 ± 7.2727	29.05	S16	66.0909 ± 6.3636	36.02
S7	47.9091 ± 4.5455	48.65	S17	49.7273 ± 0.9091	47.62
S8	70.6364 ± 4.5455	31.83	S18	66.0909 ± 5.4545	36.02

Liquiritin, Hesperidin, Isoliquiritin, Hesperetin and Isoliquiritigenin, respectively.

3.8 Experimental Validation

6 correlated peaks, Gastrodin (a), Liquiritin (b), Hesperidin (e), Isoliquiritin (g), Hesperetin (i) and Isoliquiritigenin (j) were positively correlated with antioxidant and anti-Inflammatory activity of HUVEC cells. In order to verify the protective effect of the 6 components on HUVEC cells, the antioxidant and anti-inflammatory effects of the 6 components on HUVEC cells were measured at different concentrations. The results showed that all samples could promote the proliferation of HUVEC cells in a concentration-dependent manner (**Figures 6**, **7**).

4 DISCUSSION

Traditional Chinese medicine decoction is a kind of oral liquid preparation made by decocting several Chinese herbs in proper dosage proportion according to the theory of "Jun-Chen-Zuo-Shi" (Li et al., 2021a). Based on accurate diagnosis of "looking, listening, asking and feeling the pulse" of patients, TCM often selects prescriptions according to the physical signs of patient and changes in the course of disease. Combined with the "taste and meridian return" of drugs, constantly adjusts producing areas and difficult quality control (Kang et al., 2019).

Many studies have shown that the study of spectrum-effect relationshipship is an effective method to control the quality of traditional Chinese medicine, because it can be used as a chromatographic fingerprint with biological activity and explore the quality of markers related to clinical efficacy (Fan et al., 2020). Traditional Chinese medicine is the product of multi-component and multi-target synergy. It is impossible to control the quality of traditional Chinese medicine only by the content of one characteristic ingredient. Fingerprint has integrity and fuzziness, which is well adapted to the complexity and diversity of TCM components and can evaluate and control the quality of TCM and its compounds (Zhang H. et al., 2019; Liu et al., 2020). Therefore, in this study, we constructed fingerprints of 18 batches of medicinal materials, and searched for common peaks as potential active ingredients.

This study found that BBTD can protect vascular endothelial cells, promote endothelial cell proliferation, reduce ROS and Hs-CRP levels, and indicated that Gastrodin (a), Liquiritin (b), Hesperidin (e), Isoliquiritin (g), Hesperetin 1) and Isoliquiritigenin (j) may be the main active components for promoting the proliferation of HUVEC cells. These results suggest that BBTD may reduce oxidative stress and inflammatory expression of endothelial cells

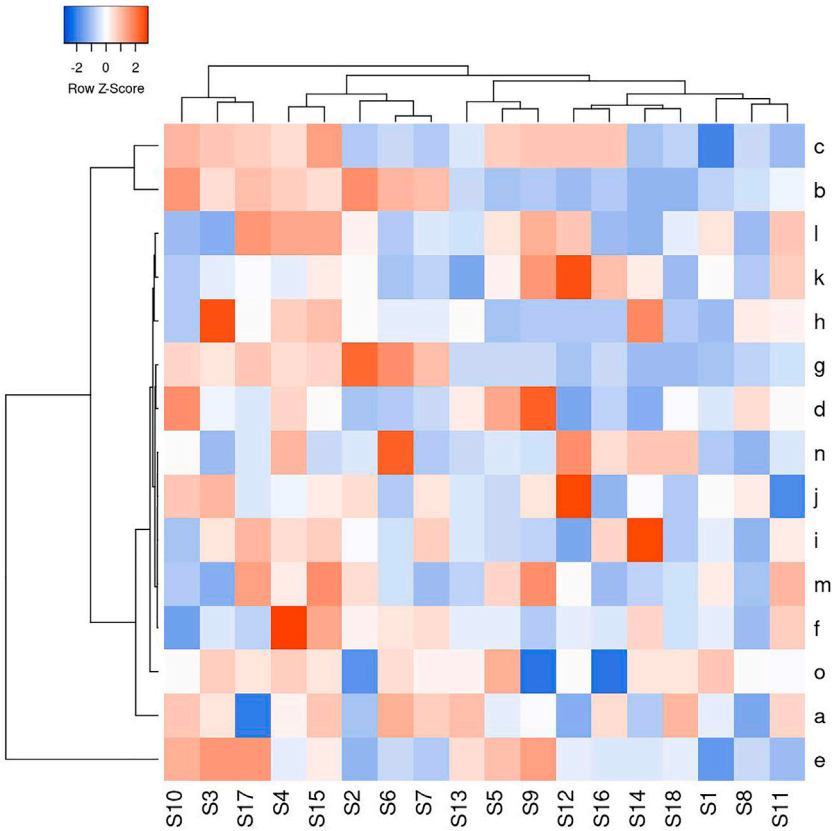

FIGURE 4 | HCA heat map for 18 BBTD samples and 15 chemical compounds.

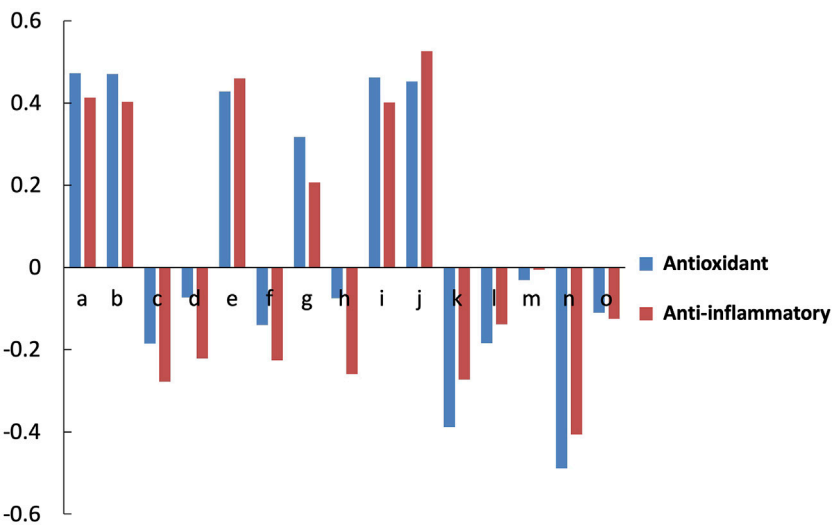

FIGURE 5 | Analysis of the spectrum-effect relationship: the correlation coefficient between the content of chemical compounds and bioactivity.

through these 6 components, and play a protective role in endothelial cells, thus achieving the effect of reducing hypertension.

6 correlated peaks, Gastrodin (a), Liquiritin (b), Hesperidin (e), Isoliquiritin (g), Hesperetin (i) and Isoliquiritigenin (j) were positively correlated with

TABLE 5 | The correlations coefficient of Multivariate Statistical Analysis.

	Correlations and grade between peak and antioxidant	Correlations and grade between peak and anti-inflammatory
A	0.472*	0.413
B	0.471*	0.403
C	−0.185	−0.278
D	−0.073	−0.221
E	0.428	0.460
F	−0.140	−0.226
G	0.317	0.207
H	−0.075	−0.259
I	0.462	0.401
J	0.452	0.526*
K	−0.388	−0.273
L	−0.184	−0.138
M	−0.031	−0.005
N	−0.489*	−0.406
O	−0.110	−0.125

antioxidant and anti-Inflammatory activity of HUVEC cells. In order to verify the protective effect of the 6 components on HUVEC cells, the antioxidant and anti-inflammatory effects of the 6 components on HUVEC cells were measured at different concentrations.

It can be seen from the results that all the six potential active ingredients (Gastrodin, Liquiritin, Hesperidin, Isoliquiritin, Hesperetin and Isoliquiritigenin) have antioxidant and anti-inflammatory activities to varying degrees, which is consistent with the results of literature studies. Zhang H et al. found that Gastrodin induced HO-1 and Nrf2 up-regulation to alleviate H_2O_2-induced oxidative stress in mouse liver sinusoidal endothelial cells through p38 MAPK phosphorylation (Zhang et al., 2018). Ye T et al. discovered that Gastrodin attenuates the diabetic encephalopathy by inhibiting ER stress and NLRP3 inflammasome activation (Ye et al., 2018). Application of Liquiritin to exposed skin of rats can reduce the increase in ROS, pro-inflammatory factors, and MMPs caused by UVB

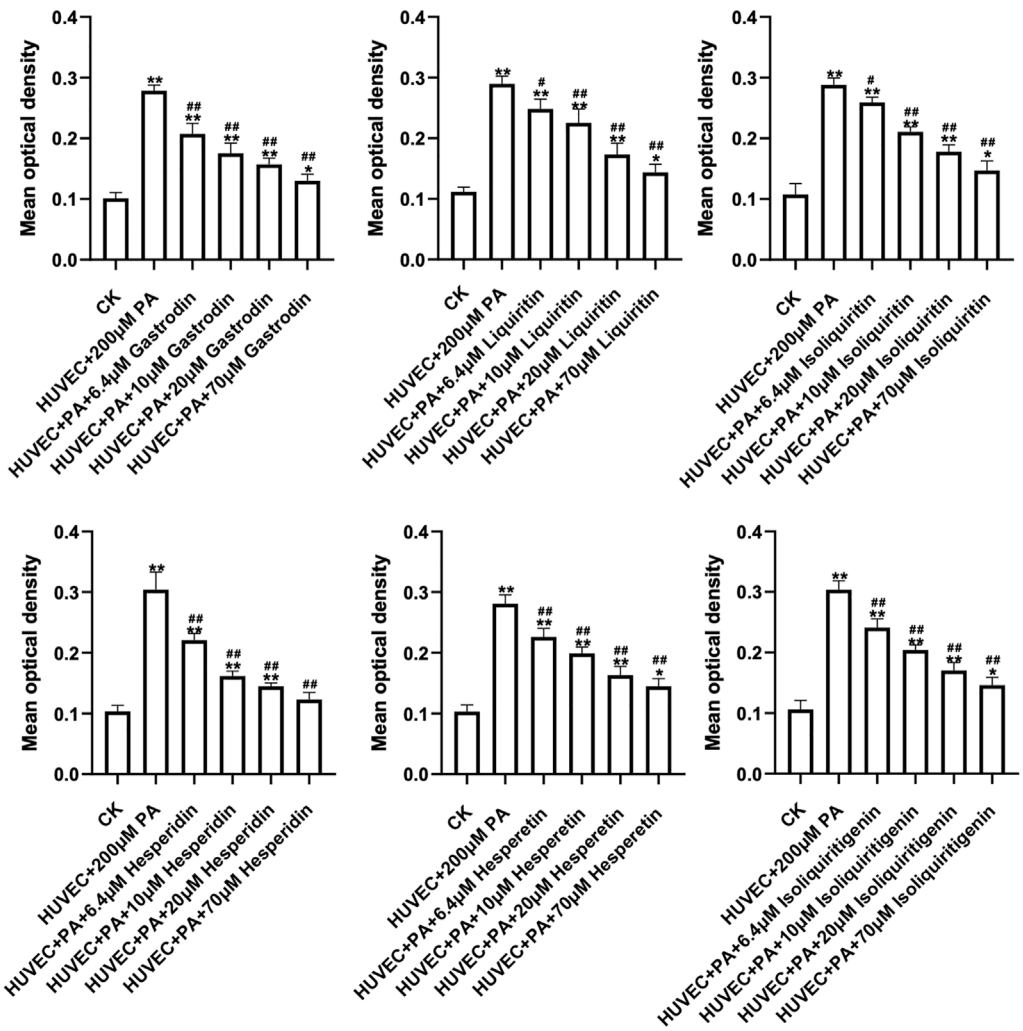

FIGURE 6 | Concentration-response curves of 6 constituents Antioxidant effects.

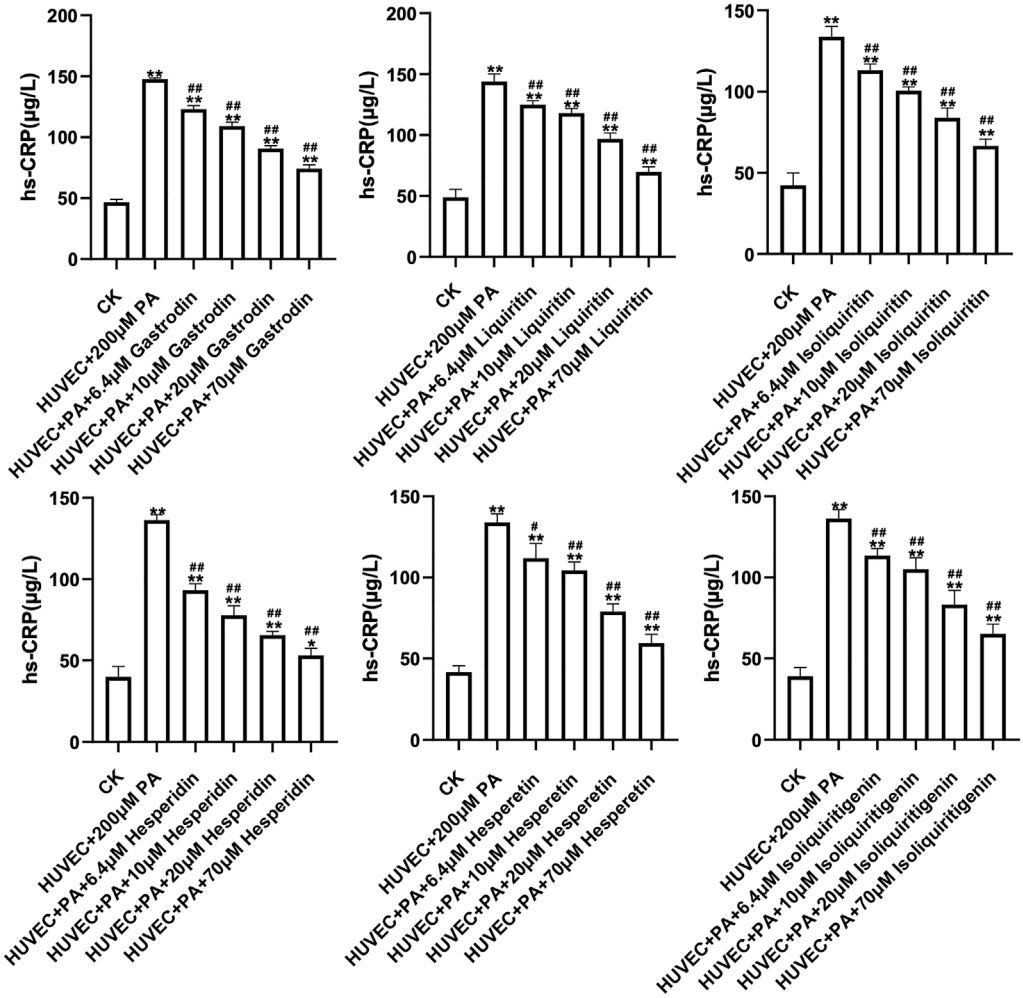

FIGURE 7 | Concentration-response curves of 6 constituents Anti-Inflammatory effects.

irradiation and increased the levels of Sirtuin3 (SIRT3) and Collagen α1 (Li et al., 2021b). Hesperidin and Hesperetin can decreased inflammatory mediators and exerted significant antioxidant effects (Tejada et al., 2018; Muhammad et al., 2019). Isoliquiritin can protect the kidney of membranous glomerulonephritis model rats through antioxidant and anti-inflammatory effects, and these effects were found to be related to the activation of Nrf2 and the down-regulation of NF-κB pathway (Liu et al., 2019). Isoliquiritigenin is also used in the prevention and treatment of a variety of diseases because of its anti-inflammatory and antioxidant properties (Peng et al., 2015). Therefore, we hypothesized that these six chemical components could serve as potential quality markers for BBTD protection of endothelial cells.

The results of this study suggest that the spectrum-effect relationship can provide an effective tool for the correlation between the quality indexes of TCM decoction and clinical efficacy, and also provide an example for the quality control of other TCM decoction. However, these 6 compounds cannot be used as an indicator of overall quality control of BBTD because antioxidant and anti-inflammatory effects are only two of its many clinical effects. In addition, due to instrument limitations, we mainly focused on compounds with strong UV signals (PDA detector). Some of the components may play an important role in antioxidant and anti-inflammatory effects. However, they were not detected in this study due to their low levels. Therefore, further studies are needed to determine whether Gastrodin, Liquiritin, Hesperidin, Isoliquiritin, Hesperetin and Isoliquiritigenin can be used as a quality control indicator for the treatment of other diseases, as well as a quality control indicator for whether there are other potential active ingredients in BBTD. Next, this study will consider mass spectrometry analysis, so as to explore more active ingredients or metabolites.

5 CONCLUSION

UPLC fingerprints of 18 different BBTD extracts are established by UPLC-PDA technique. The results show that

the extracts of BBTD has antioxidant and anti-inflammatory activities, significantly increases the proliferation of endothelial cells and protected endothelial cells. The spectrum-effect relationship between fingerprint and activity value (ROS inhibition rate and Hs-CRP inhibition rate) is established by multivariate statistics. The results shows that Gastrodin, Liquiritin, Hesperidin, Isoliquiritin, Hesperetin, and Isoliquiritigenin have antioxidant and anti-inflammatory activities to different degrees. These six ingredients can be used as potential pharmacodynamic substances of BBTD to protect endothelial cells.

DATA AVAILABILITY STATEMENT

The original contributions presented in the study are included in the article/Supplementary Material, further inquiries can be directed to the corresponding author.

AUTHOR CONTRIBUTIONS

NX: Data analysis and article writing; ML: Medicinal herbs extract; PW: Design and implementation of pharmacological experiments; SW: Chromatographic analysis; HS: Experimental design and article writing guidance.

FUNDING

This study was supported by the following grants: Natural Science Foundation of Shandong Province, No. ZR2020KH017; Shandong Traditional Chinese Medicine Science and Technology Development Program, No. 2019-0368, 2017-136; National Natural Science Foundation of China, No.82074052; Collaborative Innovation Center Project of TCM Quality Control and Whole Industry Chain Construction in Universities of Shandong Province (CYLXTCX2020-03, CYLXTCX2021-02).

REFERENCES

Do Vale, G. T., and Tirapelli, C. R. (2020). Are Reactive Oxygen Species Important Mediators of Vascular Dysfunction. *Curr. Hypertens. Rev.* 16 (3), 163–165. doi:10.2174/1573402115666190416153638

Fan, Q., Yang, R., Yang, F., Xia, P., and Zhao, L. (2020). Spectrum-effect Relationship between HPLC Fingerprints and Antioxidant Activity of Angelica Sinensis. *Biomed. Chromatogr.* 34 (2), e4707. doi:10.1002/bmc.4707

Farrag, A. R. H., Abdallah, H. M. I., Khattab, A. R., Elshamy, A. I., Gendy, A. E. G. E., Mohamed, T. A., et al. (2019). Antiulcer Activity of Cyperus Alternifolius in Relation to its UPLC-MS Metabolite Fingerprint: A Mechanistic Study. *Phytomedicine* 62, 152970. doi:10.1016/j.phymed.2019.152970

Hage, F. G. (2014). C-reactive Protein and Hypertension. *J. Hum. Hypertens.* 28 (7), 410–415. doi:10.1038/jhh.2013.111

Jia, S., Sun, Y., Li, L., Wang, R., Xiang, Y., Li, S., et al. (2021). Discrimination of Turmeric from Different Origins in China by MRM-Based Curcuminoid Profiling and Multivariate Analysis. *Food Chem.* 338, 127794. doi:10.1016/j.foodchem.2020.127794

Jiang, J., Huang, D., Li, Y., Gan, Z., Li, H., Li, X., et al. (2019). Heart Protection by Herb Formula BanXia BaiZhu TianMa Decoction in Spontaneously Hypertensive Rats. *Evid. Based Complement. Alternat Med.* 2019, 5612929. doi:10.1155/2019/5612929

Jiang, L., Xiong, Y., Yu, L., Chen, Y., Zhang, Q., Ding, X., et al. (2019). Simultaneous Determination of Seven Active Components in Rat Plasma by UHPLC-MS/MS and Application to a Quantitative Study after Oral Administration of Huang-Lian Jie-Du Decoction in High Fat-Induced Atherosclerosis Rats. *Int. J. Anal. Chem.* 2019, 5628160. doi:10.1155/2019/5628160

Jiang, Y. H., Zhang, P., Tao, Y., Liu, Y., Cao, G., Zhou, L., et al. (2021). Banxia Baizhu Tianma Decoction Attenuates Obesity-Related Hypertension. *J. Ethnopharmacol* 266, 113453. doi:10.1016/j.jep.2020.113453

Kang, T., Dou, D., and Xu, L. (2019). Establishment of a Quality Marker (Q-Marker) System for Chinese Herbal Medicines Using Burdock as an Example. *Phytomedicine* 54, 339–346. doi:10.1016/j.phymed.2018.04.005

Knock, G. A. (2019). NADPH Oxidase in the Vasculature: Expression, Regulation and Signalling Pathways; Role in normal Cardiovascular Physiology and its Dysregulation in Hypertension. *Free Radic. Biol. Med.* 145, 385–427. doi:10.1016/j.freeradbiomed.2019.09.029

Li, Y., Liu, S. S., Guo, Z. Y., Yi, H., Li, C., Chen, L. M., et al. (2021a). Discovery of Potential Pharmacodynamic Ingredients of Dang-Gui-Si-Ni Decoction Based on Absorbed Ingredients and Molecular Docking. *J. Ethnopharmacol* 275, 114045. doi:10.1016/j.jep.2021.114045

Li, Y., Xia, C., Yao, G., Zhang, X., Zhao, J., Gao, X., et al. (2021b). Protective Effects of Liquiritin on UVB-Induced Skin Damage in SD Rats. *Int. Immunopharmacol* 97, 107614. doi:10.1016/j.intimp.2021.107614

Liao, J. C., Wu, Y. S., Xu, F. F., Chen, W. Y., Zheng, Z. L., Han, X. D., et al. (2021). Comprehensive Evaluation of NAODESHENG by Combining UPLC Quantitative Fingerprint and Antioxidant Activity. *J. Pharm. Biomed. Anal.* 193, 113636. doi:10.1016/j.jpba.2020.113636

Liu, X., Jiang, W., Su, M., Sun, Y., Liu, H., Nie, L., et al. (2020). Quality Evaluation of Traditional Chinese Medicines Based on Fingerprinting. *J. Sep. Sci.* 43 (1), 6–17. doi:10.1002/jssc.201900365

Liu, Y., Xu, X., Xu, R., and Zhang, S. (2019). Renoprotective Effects of Isoliquiritin against Cationic Bovine Serum Albumin-Induced Membranous Glomerulonephritis in Experimental Rat Model through its Anti-oxidative and Anti-inflammatory Properties. *Drug Des. Devel Ther.* 13, 3735–3751. doi:10.2147/DDDT.S213088

Muhammad, T., Ikram, M., Ullah, R., Rehman, S. U., and Kim, M. O. (2019). Hesperetin, a Citrus Flavonoid, Attenuates LPS-Induced Neuroinflammation, Apoptosis and Memory Impairments by Modulating TLR4/NF-Kb Signaling. *Nutrients* 11 (3), 648. doi:10.3390/nu11030648

Peng, F., Du, Q., Peng, C., Wang, N., Tang, H., Xie, X., et al. (2015). A Review: The Pharmacology of Isoliquiritigenin. *Phytother Res.* 29 (7), 969–977. doi:10.1002/ptr.5348

Song, L., Zheng, J., Zhang, L., Yan, S., Huang, W., He, J., et al. (2019). Phytochemical Profiling and Fingerprint Analysis of Chinese Jujube (Ziziphus Jujuba Mill.) Leaves of 66 Cultivars from Xinjiang Province. *Molecules* 24 (24), 4528. doi:10.3390/molecules24244528

Sun, J., Tian, F., Zhang, Y., Wu, M., Mao, R., Le, Z., et al. (2019). Chromatographic Fingerprint and Quantitative Analysis of Commercial Pheretima Aspergillum (Guang Dilong) and its Adulterants by UPLC-DAD. *Int. J. Anal. Chem.* 2019, 4531092. doi:10.1155/2019/4531092

Tejada, S., Pinya, S., Martorell, M., Capó, X., Tur, J. A., Pons, A., et al. (2018). Potential Anti-inflammatory Effects of Hesperidin from the Genus Citrus. *Curr. Med. Chem.* 25 (37), 4929–4945. doi:10.2174/0929867324666170718104412

Ye, T., Meng, X., Wang, R., Zhang, C., He, S., Sun, G., et al. (2018). Gastrodin Alleviates Cognitive Dysfunction and Depressive-like Behaviors by Inhibiting ER Stress and NLRP3 Inflammasome Activation in Db/db Mice. *Int. J. Mol. Sci.* 19 (12), 3977. doi:10.3390/ijms19123977

Zhang, H., Yuan, B., Huang, H., Qu, S., Yang, S., and Zeng, Z. (2018). Gastrodin Induced HO-1 and Nrf2 Up-Regulation to Alleviate H2O2-Induced Oxidative Stress in Mouse Liver Sinusoidal Endothelial Cells through P38 MAPK Phosphorylation. *Braz. J. Med. Biol. Res.* 51 (10), e7439. doi:10.1590/1414-431X20187439

Zhang, J., Wu, Y., and Gao, Z. (2019). Correlations of C-Reactive Protein (CRP), Interleukin-6 (IL-6), and Insulin Resistance with Cerebral Infarction in Hypertensive Patients. *Med. Sci. Monit.* 25, 1506–1511. doi:10.12659/MSM.912898

Zhang, J., Chen, T., Li, K., Xu, H., Liang, R., Wang, W., et al. (2019). Screening Active Ingredients of Rosemary Based on Spectrum-Effect Relationships between UPLC Fingerprint and Vasorelaxant Activity Using Three Chemometrics. *J. Chromatogr. B Analyt Technol. Biomed. Life Sci.* 1134-1135, 121854. doi:10.1016/j.jchromb.2019.121854

Zhang, H., Wang, J., Chen, Y., Shen, X., Jiang, H., Gong, X., et al. (2019). Establishing the Chromatographic Fingerprint of Traditional Chinese Medicine Standard Decoction Based on Quality by Design Approach: A Case Study of Licorice. *J. Sep. Sci.* 42 (6), 1144–1154. doi:10.1002/jssc.201800989

Conflict of Interest: The authors declare that the research was conducted in the absence of any commercial or financial relationships that could be construed as a potential conflict of interest.

Publisher's Note: All claims expressed in this article are solely those of the authors and do not necessarily represent those of their affiliated organizations, or those of the publisher, the editors and the reviewers. Any product that may be evaluated in this article, or claim that may be made by its manufacturer, is not guaranteed or endorsed by the publisher.

frontiers in Pharmacology

ORIGINAL RESEARCH
published: 28 January 2022
doi: 10.3389/fphar.2021.824180

Liu Shen Capsule Alters Airway Microbiota Composition and Metabolite Profiles in Healthy Humans

Xuerui Wang[1,2,3†], *Xiaolong Xu*[1,2,3†], *Yishan Chen*[1], *Zhenxuan Li*[1], *Mina Zhang*[1], *Chunxia Zhao*[1], *Bo Lian*[1], *Jingxia Zhao*[1,3], *Yuhong Guo*[1] *and Qingquan Liu*[1,2,3*]

[1]*Beijing Hospital of Traditional Chinese Medicine, Capital Medical University, Beijing, China,* [2]*Beijing Key Laboratory of Basic Research with Traditional Chinese Medicine on Infectious Diseases, Beijing, China,* [3]*Beijing Institute of Chinese Medicine, Beijing, China*

Alteration in airway microbiota composition and perturbations in microbe-metabolites interactions have been proposed as markers of many diseases. Liu Shen (LS) capsule, a traditional Chinese medicine, was proved as favorable in treating respiratory diseases. However, the effects of the LS capsule in terms of regulating human microorganisms and metabolite profiles are not well known. This study aimed to define and compare the respiratory microbiota composition and circulating and fecal metabolite profiles before and after LS capsule administration. A total of 30 healthy volunteers were recruited. The pharyngeal swab samples were collected for 16S rRNA gene sequencing. The serum and fecal samples were collected to analyze the non-targeted ultra-performance liquid chromatography–tandem mass spectrometry metabolomics. The airway microbial compositions were profoundly altered after LS capsule administration, as evidenced by increased microbial diversity and altered microbial taxa distribution. The increasing abundance of bacterial *Bifidobacteria*, and *Lactobacillus* characterized the after-administration groups, and the increasing of abundance bacterial Proteobacteria, *Veillonella*, *Prevotella*, *Neisseria*, and *Actinomyces* characterized the before-administration groups. Significant discriminations were observed in both serum and fecal metabolic profiles between the before- and after-administration groups. A total number of 134 and 71 significant HMDB taxonomic metabolites including glycerophospholipids, fatty acyls, and prenol lipids in the serum and fecal samples were identified respectively between the before- and after-administration groups. The integrated analysis showed that some altered airway microbiota phylum, such as Bacteroidetes and Proteobacteria, significantly correlated with metabolites in serum and fecal. Hence, our study reported the alternations in the composition and functions of the airway microbial community and the changes in circulating and fecal metabolite profiles after LS capsule administration in healthy humans, thus providing a novel insight into the mechanisms underlying the role of LS capsule treating and preventing related diseases.

Keywords: airway microbiota, circulating metabolite, fecal metabolite, Liu Shen capsule, traditional Chinese medicine

OPEN ACCESS

Edited by:
Wenzhi Yang,
Tianjin University of Traditional Chinese Medicine, China

Reviewed by:
Xin Zhao,
Tianjin University of Traditional Chinese Medicine, China
Eugenia Bezirtzoglou,
Democritus University of Thrace, Greece

***Correspondence:**
Qingquan Liu
liuqingquan_2003@126.com

†These authors have contributed equally to this work

Specialty section:
This article was submitted to Ethnopharmacology, a section of the journal Frontiers in Pharmacology

Received: *29 November 2021*
Accepted: *31 December 2021*
Published: *28 January 2022*

Citation:
Wang X, Xu X, Chen Y, Li Z, Zhang M, Zhao C, Lian B, Zhao J, Guo Y and Liu Q (2022) Liu Shen Capsule Alters Airway Microbiota Composition and Metabolite Profiles in Healthy Humans. Front. Pharmacol. 12:824180. doi: 10.3389/fphar.2021.824180

INTRODUCTION

The respiratory microbiota plays an essential role in the development, education of the immune system, and maintenance of the homeostasis. Antimicrobial defense is impaired in germ-free and microbiota-depleted animals, leading to a high possibility of respiratory infections (Maschirow et al., 2019). Previous studies also found shrunk lungs and less mature alveoli development in germ-free rodents (Yun et al., 2014). Microbes and their products tune the immune system toward healthy homeostasis and provide local and systemic signals to the immune system to support the protective responses against diverse pathogens. The pivotal role of airway microbiota has been pointed out by clinical and basic studies in various diseases, for example pulmonary hypertension, influenza, 30445563 and chronic obstructive pulmonary disease (COPD) (Ramos-Sevillano et al., 2019; Zhang et al., 2020a; Wang et al., 2021). Linked by a key mediator, the immune system, the microbiome-host interaction influences the clinical outcomes. The respiratory tract microbiome in asthma patients is associated with T-helper-17 (Th17) cell regulated inflammatory responses and disease severity (Huang et al., 2015). In sepsis and the acute respiratory distress syndrome patients, ltered lung microbiota was significantly correlated with alveolar TNF-α amd systemic inflammatory response (Dickson et al., 2016). The gene expression profile analysis in lung transplant recipients also distinguishes a neutrophilic activation profile pattern (Firmicutes or Proteobacteria colonization dominant) from a macrophage-dominant remodeling profile pattern (Bacteroidetes colonization dominant) (Bernasconi et al., 2016). In mice, lung bacterial composition are correlated with lung concentrations of interleukin (IL)-1α and IL-4, which does not alter after the usage of IL-1 receptor blockade; supporting the concept that microbiota drives the immune phenotype (Dickson et al., 2018).

Over the years, accumulating evidence has identified metabolites produced by respiratory microbiota that can influence host immunity (Man et al., 2017; Budden et al., 2019). The metabolic by-products derived from bacterial fermentation have been reported as the key local and systemic signaling molecules in sustaining immune and tissue homeostasis (Buck et al., 2017). For instance, oral microbiomes produce vasoactive and anti-inflammatory nitrite, nitric oxide, and other bioactive nitrogen oxides (Koch et al., 2017; Pignatelli et al., 2020). Moreover, specific microbiota-associated metabolites, such as short-chain fatty acids (SCFAs), have been shown to affect the progression of varied diseases, including respiratory diseases (Hecker et al., 2021; Zhang et al., 2021). Lung microbiota comprise nitrate reducers and SCFAs producers, such as *Pseudomonas* species and *Staphylococcus* species, which are linked to protection against respiratory diseases by inhibiting histone deacetylases or binding GPR41, GPR43, and GPR109A to alter chemotaxis and phagocytosis, change cell proliferation, and regulate inflammatory responses (McKenzie et al., 2017).

Liu Shen (LS) capsule is a traditional Chinese medicine first prescribed in Qing dynasty. It is widely used in China for treating influenza, tonsillitis, pharyngitis, and mumps (Liu et al., 2018; Wang et al., 2020). The composition of LS capsule includes bezoar (the gallstone of *Bos taurus domesticus* Gmelin), musk (the excretion of *Moschus*), cinobufagin venom toad (the excretion of Venenum Bufonis), pearl (the shell of Pernulo), realgar, and borneol. A number of studies have shown that LS displayed an anti-inflammatory, anti-cancer, anti-viral, analgesic, and anti-bacterial activities in a variety of diseases. In treating influenza, LS capsule inhibited the virus replication and proliferation *in vitro* and ameliorated pneumonia damage *in vivo* via suppressing the TLR4/NF-κB signaling pathway (Ma et al., 2020a; Zhao et al., 2021). LS capsule also inhibited SARS-CoV-2 virus infection via regulating the activity of the NF-κB/MAPK signaling pathway *in vitro* (Ma et al., 2020b). These studies suggested the potential effect of LS capsule on respiratory diseases. However, little is known about the effect of LS capsule on microbiota and metabolite profiles. Therefore, in this study, we used 16S ribosomal RNA (16S rRNA) gene sequencing and metabolomics to systematically characterize altered airway microbial communities and circulating and fecal metabolism, and to further analyze their potential interactions in healthy individuals after LS capsule administration.

MATERIALS AND METHODS

Study Design and Intervention

Thirty healthy volunteers were recruited through advertisements online at Beijing Hospital of Traditional Chinese Medicine, China, between November 2 and 20, 2020. The inclusion criteria were as follows: age 18–45 years; male body weight ≥50 kg, female body weight ≥45 kg, and body mass index (BMI) in the range of 19.0–26.0 kg/m^2. The participants had no history of chronic or serious diseases in cardiovascular, liver, kidney, respiratory, blood and lymph, endocrine, immune, mental, neurological, gastrointestinal, and other systems. They were able to communicate well with the researchers and agreed to sign the informed consent form. The exclusion criteria were as follows: antibiotics used in the recent 2 months, a history of gastrointestinal diseases within 3 years (including existing ones), diseases with abnormal clinical manifestations excluded; pregnant or lactating women, constitution allergy or Chinese medicine allergy, and participants in other trials in the recent 3 months.

Healthy participants were given one oral LS capsule three times a day for 7 days. LS capsule was provided by Lei Yun Shang Pharmaceutical Group Co., Ltd (Suzhou; batch number ra18029a).

The study was conducted according to the Declaration of Helsinki and approved by the Ethics Committee of Beijing Hospital of Traditional Chinese Medicine Affiliated to Capital Medical University (No. 2019BL02-047-02). The registration number is ChiCTR2000032794 on chictr.org.cn. All participants gave written informed consent.

Sample Collection

The pharyngeal swab, morning fasting blood, mid-morning urine, and fecal samples were collected on the first and eighth days of the trial (before and after oral LS capsule administration). The pharyngeal swabs were tested for 16S ribosomal RNA Gene (16S rRNA) sequencing. The samples were collected strictly following the process. All participants were forbidden to brush their teeth, gargle, or eat breakfast before collecting morning swabs. The swab should not touch the teeth, oral cavity, and tongue mucosa. Afterward, the swab head was cut off and inserted into a sterilized cryopreservation tube. The samples were stored at −80°C for further processing. The serum and fecal samples were tested for metabolites using a non-targeted metabolomics ultra-performance liquid chromatography–tandem mass spectrometry (UPLC-MS/MS). The blood samples were kept at room temperature for 30 min for clotting. The clotted blood samples were centrifuged at 3000 *g* at 4°C for 20 min to remove the supernatant serum and quickly stored at −80°C for further processing. The fecal samples were collected in a sterile conical tube and immediately frozen at −80°C until further analysis. The morning fasting blood and mid-morning urine samples were tested for blood routine, urine routine, liver function, and renal function to evaluate drug safety.

DNA Extraction and High-Throughput 16S rRNA Sequencing

DNA from pharyngeal swabs was isolated using an E. Z.N.A. soil DNA Kit (Omega Bio-Tek, GA, United States) following the manufacturer's protocols. Total DNA quality was measured using a spectrophotometer (NanoDrop 2000 UV; Thermo Fisher Scientific, MA, United States) with 1% agarose gel electrophoresis. 16S sequencing was detected by Biomarker Technologies. The V3–V4 hypervariable regions of the bacterial 16S rRNA gene were amplified with the following primer pairs: 338F (5′-ACTCCTACGGGAGGC AGCAG-3′) and 806R (5′-GGACTACHVGGGTWTCTAAT-3′) using a thermocycler polymerase chain reaction system (ABI GeneAmp 9700, ABI, United States). The polymerase chain reactions were conducted using the following program: 3 min of denaturation at 95°C, 27 cycles of 30 s at 95°C, 30 s for annealing at 55°C, and 45 s for elongation at 72°C, and a final extension at 72°C for 10 min. Polymerase chain reactions were performed in triplicate using a 20-μl mixture containing 4 μl of 5× FastPfu Buffer, 2 μl of 2.5 mmol/L dNTPs, 0.8 μl of each primer (5 μmol/L), 0.4 μl of FastPfu polymerase, 0.2 μl of bovine serum albumin, and 10 ng of template DNA. The yielding polymerase chain reaction products were extracted from a 2% agarose gel and further purified using an AxyPrep DNA Gel Extraction Kit (Axygen Biosciences, CA, United States) and quantified using QuantiFluor (Promega, United States) following the manufacturer's protocol.

Sample Preparation and Ultra-performance Liquid Chromatography–Tandem Mass Spectrometry Analysis for Metabolomics

For the serum samples, 100 μl of the samples were mixed with 400 μl of ice-cold methanol/water solution. For the fecal samples, 50 mg samples were weighed and mixed with 400 μl of ice-cold methanol/water solution. The samples were homogenized at 60 Hz for 6 min using a mechanical disruptor. They were vortexed for 15 min, sonicated for 10 min three times, then placed at −20°C for 30 min to precipitate proteins. After centrifugation at 13,000 *g* at 4°C for 15 min, the supernatant was prepared for ultra-performance liquid chromatography–tandem mass spectrometry (UPLC-MS/MS)/MS analysis. UPLC-MS/MS analyses were performed using a ultra-high performance liquid chromatograph system (1290, Agilent Technologies). The mobile phase consisted of 25 mM NH_4OAc and 25 mM NH_4OH in water (pH = 9.75) and acetonitrile. The Triple TOF mass spectrometer was used to acquire MS/MS spectra on an information-dependent acquisition basis during an LC/MS experiment. In this mode, the acquisition software (Analyst TF 1.7, AB Sciex) continuously evaluated the full-scan survey MS data as it collected and triggered the acquisition of MS/MS spectra depending on the preselected criteria. In each cycle, 12 precursor ions with intensity greater than 100 were chosen for fragmentation at collision energy (CE) of 30 V (15 MS/MS events with product ion accumulation time of 50 ms each). Mass data were collected in both positive and negative modes. Quality control samples were injected at regular intervals (every 10 samples). All raw data were imported into the Progenesis QI 2.3 (Nonlinear Dynamics, Waters, United States) and SIMCA-P C 14.0 software package for further data analysis.

Safety and Adverse Event Monitoring

Adverse events were assessed according to the Common Terminology Criteria for Adverse Events version 4.03 on days 1 and 8 of the trial. The laboratory examinations were standardized in the laboratory department of the hospital. On days 1 and 8 of the trial, routine blood examinations for complete blood cell count and serum biochemical tests for renal and liver functions were conducted for the safety evaluation.

Statistical Analysis

Ace, Chao, and Shannon indices were calculated to assess *a*-diversity. The *ß*-diversity was estimated by computing the Bray-Curtis dissimilarity and visualized using principal coordinate analysis, and the results were plotted using the R software. The nonparametric Wilcoxon test was used to analyze the different taxonomies at the phylum and genus levels. Statistically significant differences in genera between groups were determined using a linear discriminant analysis (LDA) effect size (LEfSe) algorithm. LDA >3.5 with a $p < 0.05$ was considered significantly enriched. For metabolomics analysis, data obtained in the positive ion mode were used for orthogonal partial least squares discriminant analysis (OPLS-DA) algorithms to visually compare metabolite profiles. Through multivariate and univariate analyses, the significant remaining features were identified by database searches, including the Human Metabolome Database (http://www.hmdb.ca) and Kyoto Encyclopedia of Genes and Genomes (KEGG) (http://www.kegg.com). Spearman correlation analysis was used to evaluate the correlations between metabolites and the microbiota. All the data were presented as mean ± standard

TABLE 1 | Characteristics and laboratory tests of the healthy volunteers.

Characteristic	Before	After	*p* Value
Female sex, n (%)	17 (56.6%)	17 (56.6%)	-
Age, y	24.4 ± 0.42	24.4 ± 0.42	-
Body Mass Index, kg/m^2	20.98 ± 0.82	20.98 ± 0.82	-
Smoking status			
Current	2 (0.06%)	2 (0.06%)	-
Former	2 (0.06%)	2 (0.06%)	-
Never	28 (93.3%)	28 (93.3%)	-
Laboratory tests			
White blood cell count,×10^9/L	6.57 ± 0.50	7.16 ± 0.86	0.57
Red blood cell count,×10^9/L	4.62 ± 0.15	4.57 ± 0.16	0.84
Neutrophil count,×10^9/L	4.18 ± 0.38	4.44 ± 0.59	0.72
Lymphocyte count,×10^9/L	1.87 ± 0.16	2.08 ± 0.26	0.52
Platelet count,×10^9/L	252.60 ± 11.57	246.90 ± 11.22	0.78
Hemoglobin, g/L	139.8 ± 4.67	138.3 ± 4.87	0.83
Alanine aminotransferase, U/L	22.33 ± 5.61	20.64 ± 4.37	0.81
Aspartate aminotransferase, U/L	19.55 ± 1.84	20.55 ± 1.81	0.47
Blood urea nitrogen, mmol/L	4.57 ± 0.27	4.34 ± 0.21	0.52
Creatinine, mmol/L	65.34 ± 3.67	64.17 ± 3.44	0.82

error of the mean. The significance of the difference between the two groups was analyzed using the Student unpaired-sample *t* test, and multiple comparisons were analyzed using one-way analysis of variance followed by Dunnett's post hoc test. *p* values were corrected for multiple comparisons using the Benjamini–Hochberg false discovery rate, and $p < 0.05$ indicated a statistically significant difference.

RESULTS

Characteristics and Laboratory Tests of the Healthy Volunteers

According to the inclusive and exclusive criteria, samples of 30 healthy volunteers were collected. The characteristic of sex, gender distribution, BMI and smoking status, as well as the laboratory test results before and after LS capsule administration of the healthy volunteers are shown in **Table 1**. No significant difference were observed in laboratory tests between the before- and after-administration groups. No adverse events were observed before and after administration.

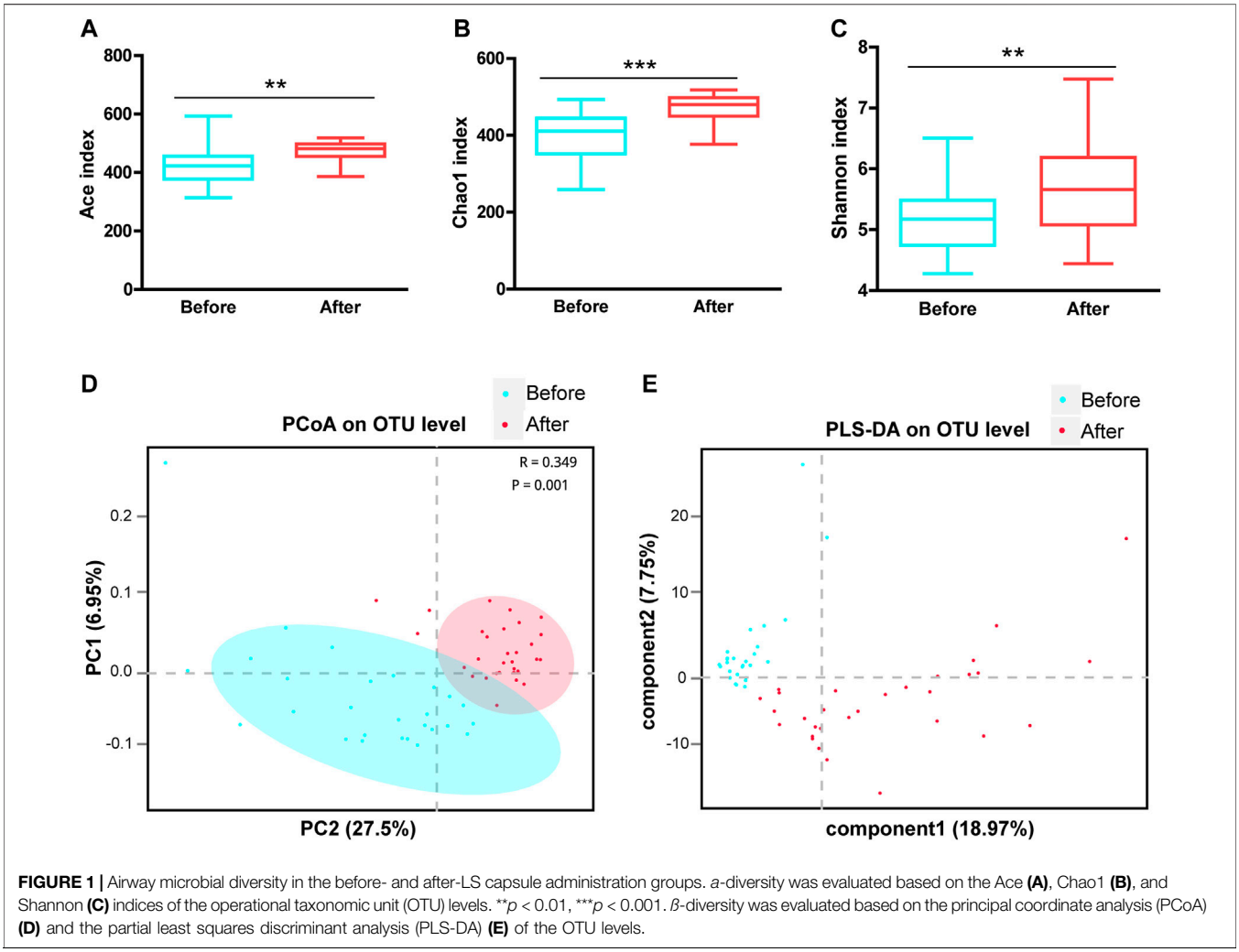

FIGURE 1 | Airway microbial diversity in the before- and after-LS capsule administration groups. *a*-diversity was evaluated based on the Ace **(A)**, Chao1 **(B)**, and Shannon **(C)** indices of the operational taxonomic unit (OTU) levels. $^{**}p < 0.01$, $^{***}p < 0.001$. *β*-diversity was evaluated based on the principal coordinate analysis (PCoA) **(D)** and the partial least squares discriminant analysis (PLS-DA) **(E)** of the OTU levels.

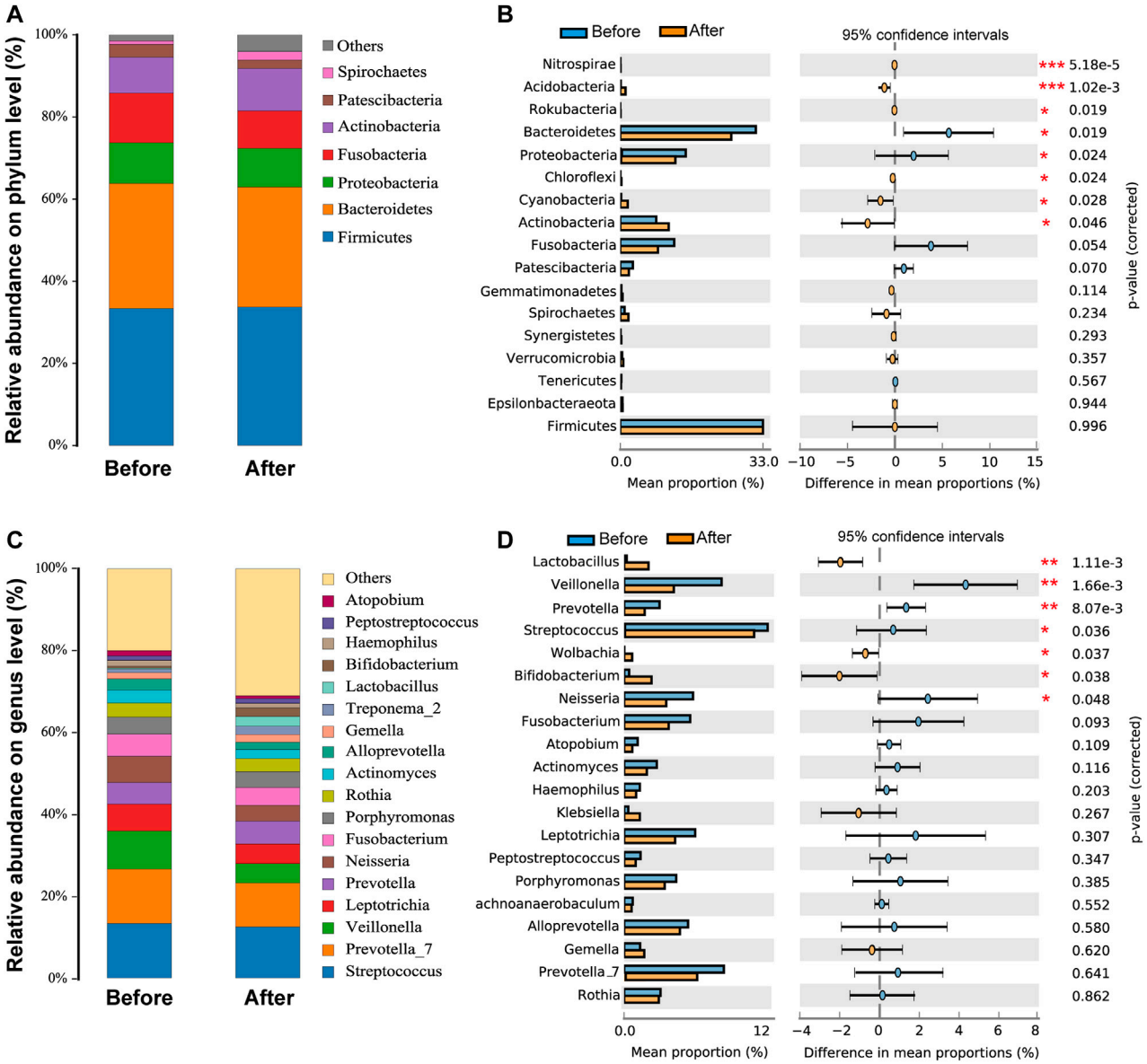

FIGURE 2 | Airway microbiota composition in the before- and after-LS capsule administration groups. The percentage of community abundance at the phylum **(A)** and genus **(C)** levels. Phylum-level **(B)** and genus-level **(D)** bacteria that were significantly different between the before- and after-administration groups. Data were shown as relative abundance (%) of the top 20 most abundant taxa in each group. Statistical analysis was performed using the Wilcoxon rank-sum test. *$p < 0.05$, **$p < 0.01$, ***$p < 0.001$.

LS Capsule Altered Airway Microbiota Structural Diversity

The *a*-diversity indexes, including Ace, Chao1, and Shannon, were used to determine the ecological diversity within a microbial community. These indexes reflected the species richness and evenness, which were significantly higher after LS capsule administration than before administration (**Figures 1A–C**).

The *ß*-diversity was measured by the principal coordinate analysis (PCoA) (**Figure 1D**) and the partial least squares discriminant analysis (PLS-DA) (**Figure 1E**). PCoA based on the Bray-Curtis dissimilarity index showed a significant difference between before- and after-administration groups (**Figure 1D**, ANOSIM $R = 0.349$, $p = 0.001$). Moreover, PLS-DA represented distinct microbiome profiles before and after LS capsule administration (**Figure 1E**). Overall, LS capsule administration significantly altered the structural microbial diversity of airways in healthy humans.

LS Capsule Altered Airway Microbiota Composition

As shown in **Figure 2C**, Firmicutes, Bacteroidetes, Proteobacteria, Fusobacteria, Actinobacteria, Patescibacteria, and Spirochaetes were

the seven dominant phyla microbiota (relative abundance >1%) in the upper respiratory tract in the before- and after-administration groups (**Figure 2A**). The proportions of Bacteroidetes, Fusobacteria, and Patescibacteria were smaller after LS capsule administration than those before administration. Mann–Whitney *U* tests were further performed to compare the differences in pharynx bacterial communities between the two groups. At the phylum level, among the top 20 abundant bacterial species, the abundance of Bacteroidetes and Patescibacteria was statistically significantly lower, while the abundance of Nitrospirae, Acidobacteria, Rokubacteria, Chloroflexi, Cyanobacteria, and Actinobacteria was statistically significantly higher, after LS capsule administration than that before administration (**Figure 2B**).

As shown in **Figure 2C**, the taxonomic analysis indicated 20 dominant genera (relative abundance >1%) in the before- and after-administration groups. Before LS capsule administration, *Streptococcus* and *Prevotella_7* were the predominant genera (13.3%), followed by *Veillonella* (9.3%). The prevalent genera were *Streptococcus* (12.4%), *Prevotella_7* (10.7%), and *Prevotella* (5.5%) after LS capsule administration. *Prevotella_7*, *Prevotella*, *Leptotrichia*, *Veillonella Fusobacterium*, *Neisseria*, *Actinomyces*, *Alloprevotella*, *Gemella*, *Haemophilus*, *Streptococcus*, and *Atopobium* had a smaller proportion after LS capsule administration than that before administration. At the phylum level, among the top 20 abundant bacterial species, the abundance of *Veillonella*, *Prevotella*, *Streptococcus*, and *Neisseria* was statistically significantly lower after LS capsule administration than that before administration (**Figure 2D**). In contrast, the abundance of *Lactobacillus*, *Wolbachia*, and *Bifidobacterium* was statistically significantly higher after LS capsule administration than that before administration (**Figure 2D**).

Moreover, the differences in microbiota structures from the phylum to the genus level were analyzed. Using a logarithmic LDA score cutoff of 3.5, we identified 40 discriminatory genera as key discriminants (**Figure 3A**). The abundance of several bacterial including Fusobacteria, *Fusobacteriales*, and *Veillonella* were significantly down-regulated after LS capsule administration, whereas bacterial including Clostridiales, Clostridia, and *Lactobacillus* were significantly enriched after LS capsule administration than that before administration. The LDA scoring at the genus level was performed to further dissect the potential roles of the pharynx microbiome in discriminating the before-from after-administration groups (**Figure 3B**). A higher proportion of *Klebsiella*, *Bifidobacterium*, and *Lactobacillus* was identified in the after-administration group, while a higher proportion of *Veillonella*, *Neisseria*, *Leptotrichia*, *Fusobacterium*, *Prevotella*, and *Actinomyces* was identified in the before-administration group (LDA score [log10] > 3.5).

LS Capsule Changed the Potential Function of the Airway Microbiome

PICRUSt analysis was carried out to predict the possible impact of the altered airway microbiome by LS capsule administration. The pharynx microbiome with relative abundance greater than 1% was used for analysis. The significantly different abundance compositions of the KEGG pathway (level 2) (**Supplementary Table 1**) and Cluster of Orthologous Groups of proteins (COG) (level 2) (**Supplementary Table 2**) between the two groups were listed ($p < 0.05$). As shown in **Figure 3C**, 12 KEGG pathways, including lipid metabolism and metabolism of terpenoids and polyketides, were significantly enriched after LS capsule administration, while three KEGG pathways, including glycan biosynthesis and metabolism, metabolism of cofactors and vitamins, and drug (antimicrobial) resistance were significantly lower after LS capsule administration. As shown in **Figure 3D** six functional COG categories were highly enriched after LS capsule administration, including carbohydrate transport and metabolism, lipid transport and metabolism, and secondary metabolite biosynthesis/transport and catabolism. In contrast, seven COG categories, including coenzyme transport and metabolism, inorganic ion transport and metabolism, and nucleotide transport and metabolism, were significantly lower after LS capsule administration. Notably, the dominant COG categories and KEGG pathways associated with LS capsule administration were in the metabolism cluster.

Alteration of Circulating Metabolome After LS Capsule Administration

A non-targeted UPLC-MS/MS metabolomics approach was used to analyze serum samples in the two groups. We successfully quantified 1749 metabolites in the positive ion mode, of which 449 had variable importance in projection (VIP) scores >1 and were significantly different ($p < 0.05$) between the two groups (**Supplementary Table 3**). The OPLS-DA score plot showed clear discrimination between the two groups with R2X = 0.417, R2Y = 0.996, and Q2Y = 0.974, suggesting that the model was predictive and reliable (**Figure 4A**). Permutation plots of the correlation coefficients of the two OPLS-DA models verified the validation of the models (**Figure 4B**). Among the metabolites with significant differences between the two groups, 271 were upregulated and 170 were downregulated. The top five metabolites with the most significant differences included the downregulation of PC(20:5 (5Z,8Z,11Z,14Z,17Z)/20:5 (5Z,8Z,11Z,14Z,17Z)), PC(18:0/22:6 (4Z,7Z,10Z,13Z,16Z,19Z)), sirolimus, methoxybrassinin, and flutamide (**Figure 4C**). A total of 134 metabolites with HMDB taxonomy are listed in **Supplementary Table 4** (**Figure 7C**). A heat map was constructed to visualize 36 significantly differentially abundant metabolites among them (**Figure 5**). Carboxylic acids and derivatives, including glutamyl-asparagine, prolyl-serine, threoninyl-methionine, and 6-hydroxysandoricin; fatty acyls, including tricosanoic acid, *cis*-4-decenoic acid, and nonadeca-10(Z)-enoic acid; organonitrogen compounds, including histidinal and azacitidine, showed higher abundance in the after-administration group than in the before-administration group. Glycerophospholipids, including PC(20:5 (5Z,8Z,11Z,14Z,17Z)/20:5 (5Z,8Z,11Z,14Z,17Z)), PS(14:0/18:1 (9Z)), and PS(18:0/20:4 (8Z,11Z,14Z,17Z)), showed lower abundances in the after-administration group than in the before-administration group.

Alteration of Fecal Metabolome After LS Capsule Administration

Moreover, UPLC-MS/MS metabolomics analysis was used on the fecal samples in the two groups. A total of 1749 metabolites in the

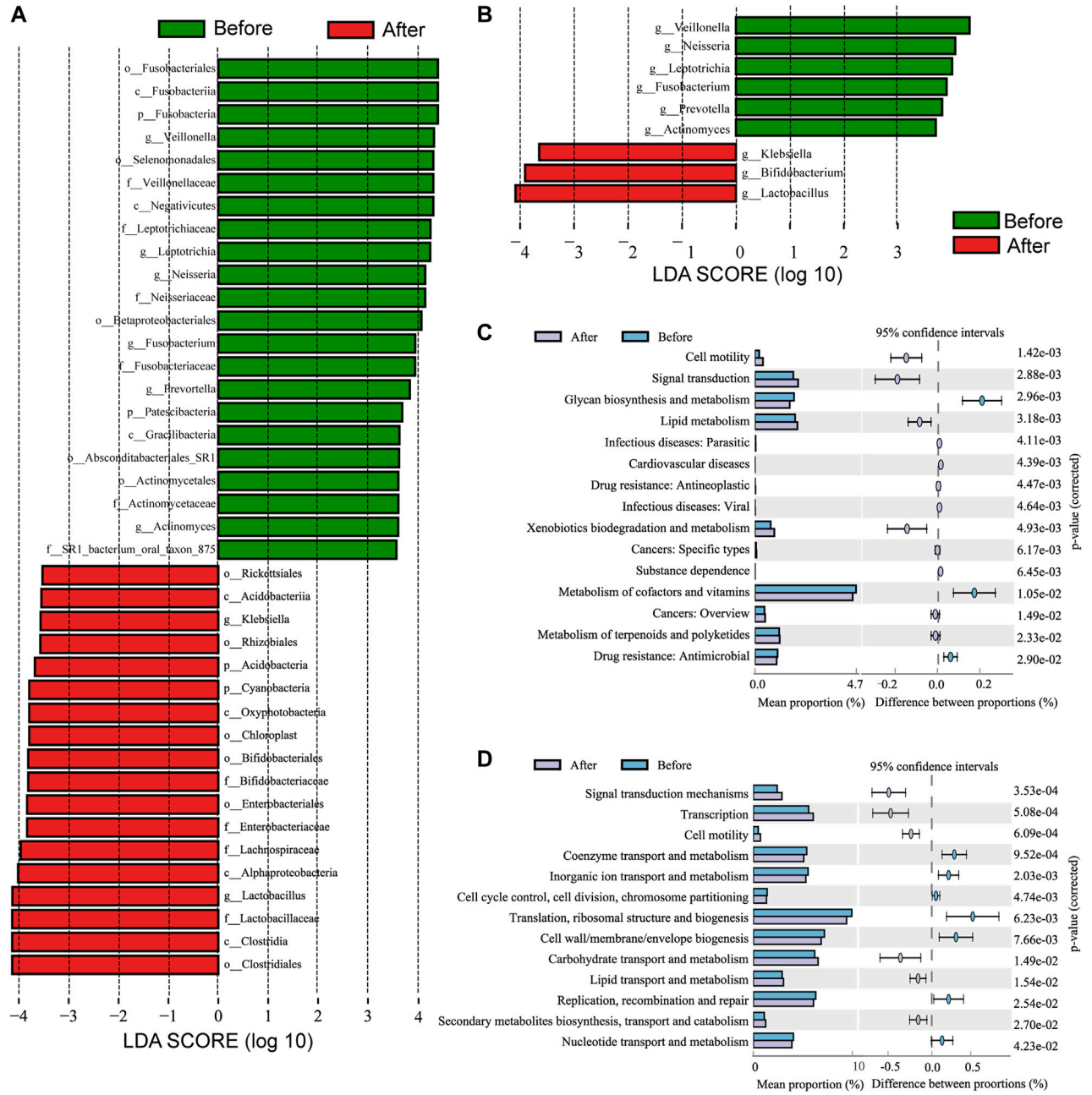

FIGURE 3 | Linear discriminant analysis effect size (LefSe) and linear discriminant analysis (LDA) analysis characterized microbiomes between the before- and after-LS capsule administration groups. **(A)** LDA scores showing the significant bacterial difference between the before- and after-administration groups. Only taxa with LDA scores of >3.5 are presented. Prefix p_ phyla, c_ class, o_ order, f_ family, and g_ genus. **(B)** LDA scores showed a significant bacterial difference between the before- and after-administration groups at the genus level. **(C)** Significant Kyoto Encyclopedia of Genes and Genomes (KEGG) pathway at level 2 and **(D)** Cluster of Orthologous Groups of proteins (COG) at level 2 for the pharynx microbiome in the before- and after-administration groups identified using STAMP software. In STAMP, the differences in abundance between the PH and control groups were analyzed using the White *t* test. Multiple test correction: Benjamini–Hochberg false discovery rate ($p < 0.05$).

positive ion mode were acquired, of which 195 were with VIP scores>1 and were significantly different ($p < 0.05$) between the two groups (**Supplementary Table 5**). The OPLS-DA score plot showed clear discrimination between two groups with R2X = 0.265, R2Y = 0.987, and Q2Y = 0.816, and the correlation coefficient verified the validation of the models (**Figures 6A,B**). Among the metabolites with significant differences between the before- and after-administration groups, 53 were upregulated and 143 were downregulated. The top five metabolites with the most significant differences included the

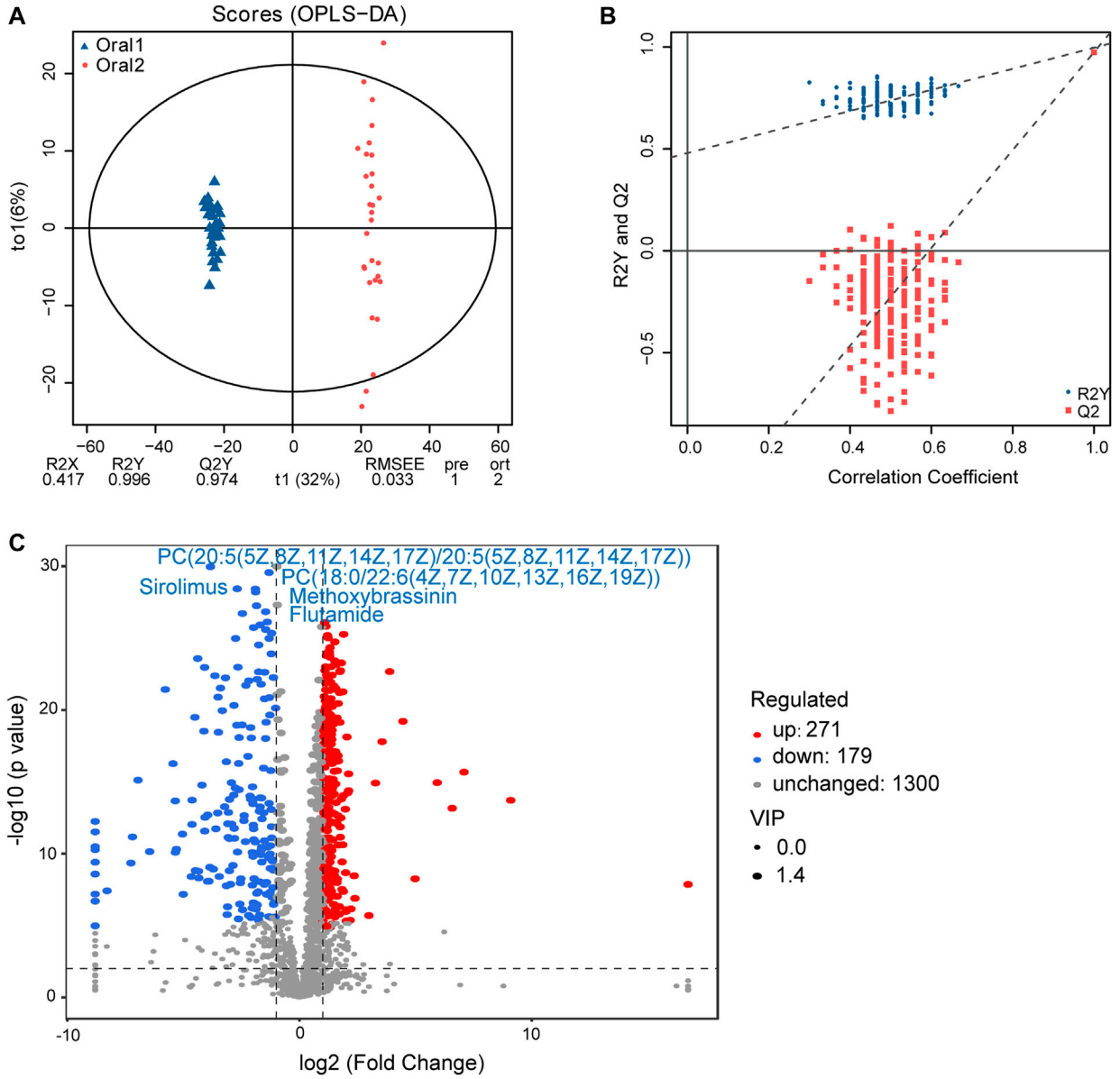

FIGURE 4 | Circulating metabolomics for the quantification of metabolites in the before- and after-administration groups. **(A)** OPLS-DA plots showing the spatial division between the before- and after-LS capsule administration groups. **(B)** Permutation plots of OPLS-DA models correlation coefficient. **(C)** Volcano plot showing the differentially accumulated [log2 (fold-change) on *x*-axis] and significantly changed [–log10 (*p* value) on *y*-axis] metabolites in the before- and after-administration groups.

downregulation of PIP(16:0/20:2 (11Z,14Z)) and indapamide and the upregulation of lyciumoside IV, L-acetylcarnitine, and CDP-DG (16:0/18:1 (11Z)). A total of 74 metabolites with HMDB taxonomy are listed in **Supplementary Table 6** (**Figure 7C**). A heat map was constructed to visualize 34 significantly differentially abundant metabolites among them (**Figure 7**). Glycerolipids, including TG (22:0/i-12:0/8:0), DG (24:0/0:0/18:2n6), and DG (16:1 (9Z)/22:2 (13Z,16Z)/0:0), showed higher abundance in the after-administration group than in the before-administration group. Glycerophospholipids, prenol lipids, carboxylic acids and derivatives, and steroids and steroid derivatives showed lower abundance in the after-administration group than in the before-administration group.

134 differential metabolites with HMDB taxonomy in serum samples before and after treatment were compared with 74 differential metabolites with HMDB taxonomy in fecal samples, and three metabolites were overlapped including colistin, gamma-tocopherol, and tetradecanoylcarnitine (**Figure 7C**). Compared with before administration, the contents of these three metabolites in serum and fecal samples decreased after administration.

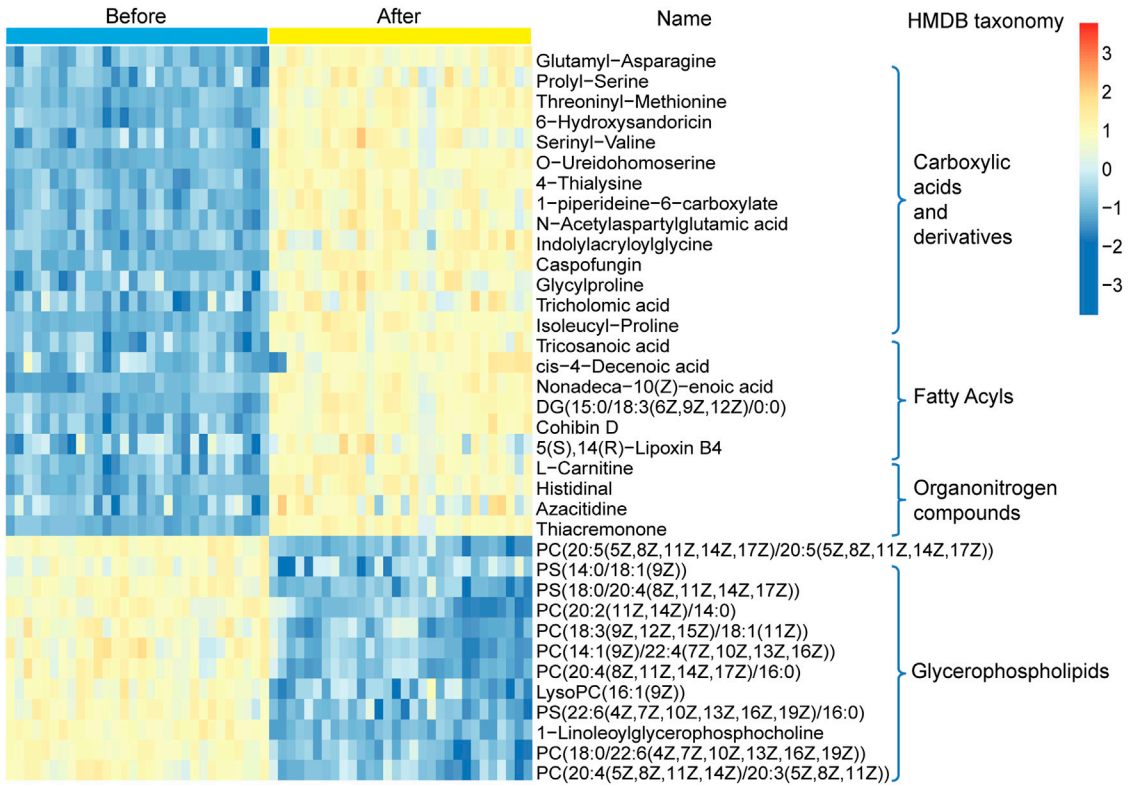

FIGURE 5 | Hierarchical clustering analysis for the circulating metabolites in the before- and after-administration groups based on their z-normalized abundance. The name and HMDB taxonomy clusters of the metabolites were listed.

Correlation Analysis of Airway Microbiota and Circulating Metabolic Phenotype

Spearman correlation analysis was performed between microbial communities at the phylum level and the 20 top fold-change metabolites in serum and fecal samples to explore the functional correlation between pharyngeal microbiota dysbiosis and altered circulating metabolites. In serum samples, as shown in **Figure 8A**, the abundance of Bacteroidetes and Proteobacteria was positively correlated with the contents of alpha-carboxy-delta-decalactone, 18-oxocortisol, and bufotenin, and negatively correlated with the contents of metabolites including cryptocapsone, ganglioside GM3 (d18:0/18:0), and (25 R)-4beta,26-dihydroxycholesterol in the serum samples. The abundance of Actinobacteria was positively correlated with the contents of metabolites including cryptocapsone, ganglioside GM3 (d18:0/18:0) (25 R)-4beta,26-dihydroxycholesterol, ganglioside GM3 (d18:1/18:1 (11Z)), and 1-undecanol, but negatively correlated with the content of alpha-carboxy-delta-decalactone. The abundance of microbiota Acidobacteria, Chloroflexi, Nitrospirae, Cyanobacteria, and Rokubacteria showed a strong positive correlation with the contents of most of the metabolites including cryptocapsone, ganglioside GM3 (d18:0/18:0), and (25R)-4beta,26-dihydroxycholesterol, and a negative correlation with the contents including 18-oxocortisol and bufotenin.

In fecal samples, as shown in **Figure 8B**, the abundance of Bacteroidetes and Proteobacteria was positively correlated with the contents of most metabolites including CE (17:1), oleamide, and DG (16:1n7/0:0/18:2n6), and negatively correlated with the content of serotinose. The abundance of Acidobacteria, Chloroflexi, Nitrospirae, Cyanobacteria, and Rokubacteria was positively correlated with the contents of 6alpha,9alpha-difluoroprednisolone-17-butyrate, serotinose, and schidigerasaponin F1, but negatively correlated with the contents of most metabolites including DG (20:1 (11Z)/24:1 (15Z)/0:0) and CE (17:1).

DISCUSSION

In this study, 16S rRNA sequencing was performed in pharyngeal swab samples, and UPLC-MS/MS-based metabolomics was performed in serum and fecal samples collected from 30 healthy participants before and after LS capsule administration. Our results showed that the respiratory microbiota composition and function and serum/fecal metabolic phenotype were significantly different after LS capsule administration. The potential regulatory mechanism of LS capsule on bacterial microbiota and metabolites might be involved in its prevention or treatment effects on diseases.

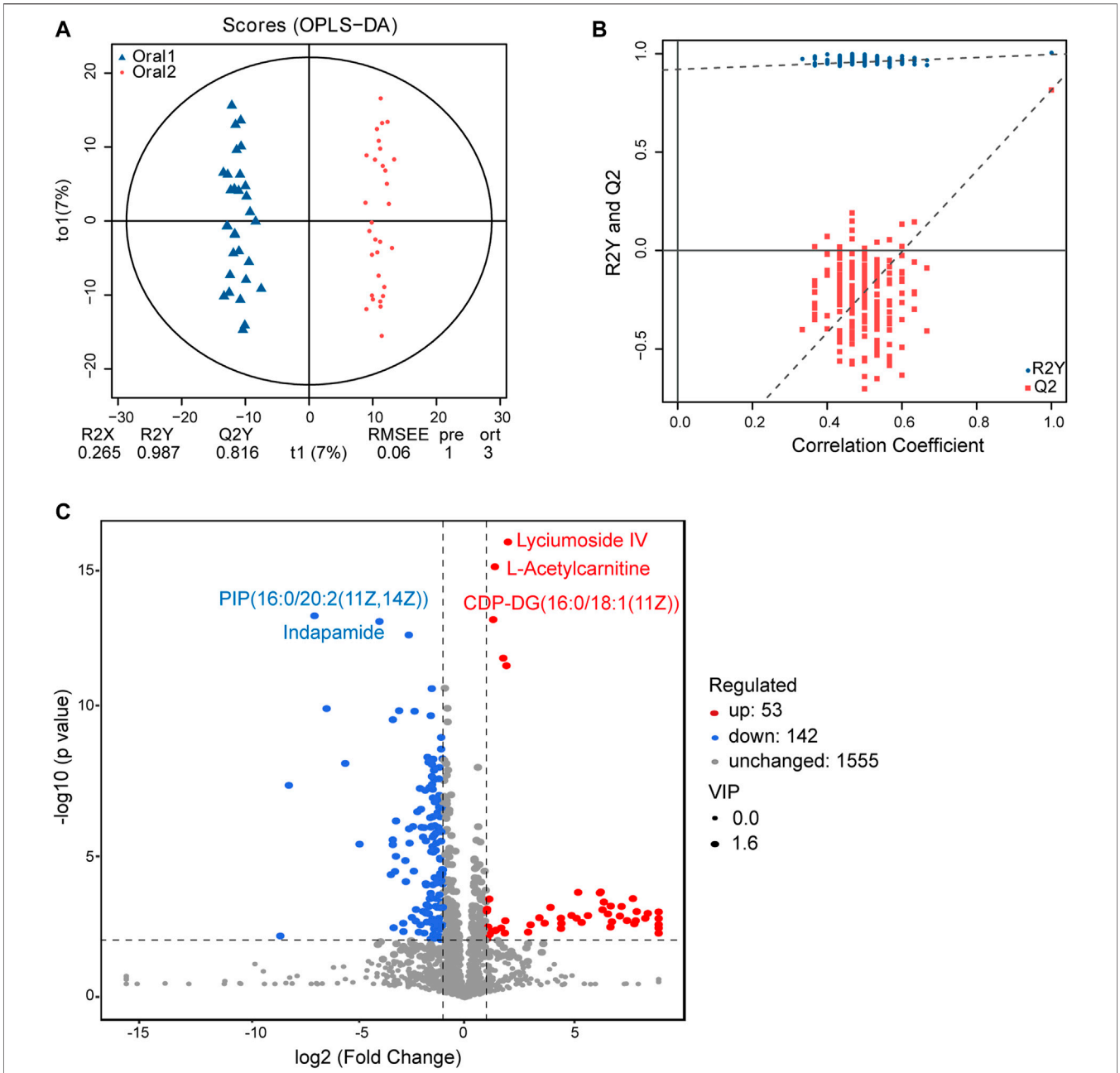

FIGURE 6 | Fecal metabolomics for the quantification of metabolites in the before- and after-administration groups. **(A)** OPLS-DA plots showing the spatial division between the before- and after-LS capsule administration groups. **(B)** Permutation plots of the correlation coefficient of OPLS-DA models. **(C)** Volcano plot showing the differentially accumulated [log2 (fold-change) on *x*-axis] and significantly changed [–log10 (*p* value) on *y*-axis] metabolites in the before- and after-administration groups.

The surface area of the human respiratory tract is approximately 40 times larger than that of the skin inhabited by microbiota. For most respiratory pathogens, the colonization of the upper respiratory tract is the first step before causing the infection on the mucosal surface and spreading to the lower respiratory tract (Bogaert et al., 2004). Hence, the microbiota in the upper respiratory tract acts as a "gatekeeper" that provides resistance to pathogen colonization. Clinical studies suggested that the lower respiratory tract microbiota shared considerable similarity to that of the oropharynx in both healthy individuals and patients with chronic lung diseases (Botero et al., 2014). The predominant phyla of healthy individuals are Bacteroidetes and Firmicutes in the lungs and Firmicutes, Proteobacteria, and Actinobacteria in the oropharynx (Pulvirenti et al., 2019; Maleki et al., 2020). The most common genera in the lung and oral cavity are similar, including *Streptococcus*, *Prevotella*, and *Veillonella*, which is consistent with our results. Since the isolation of lower respiratory tract microbiota samples is usually

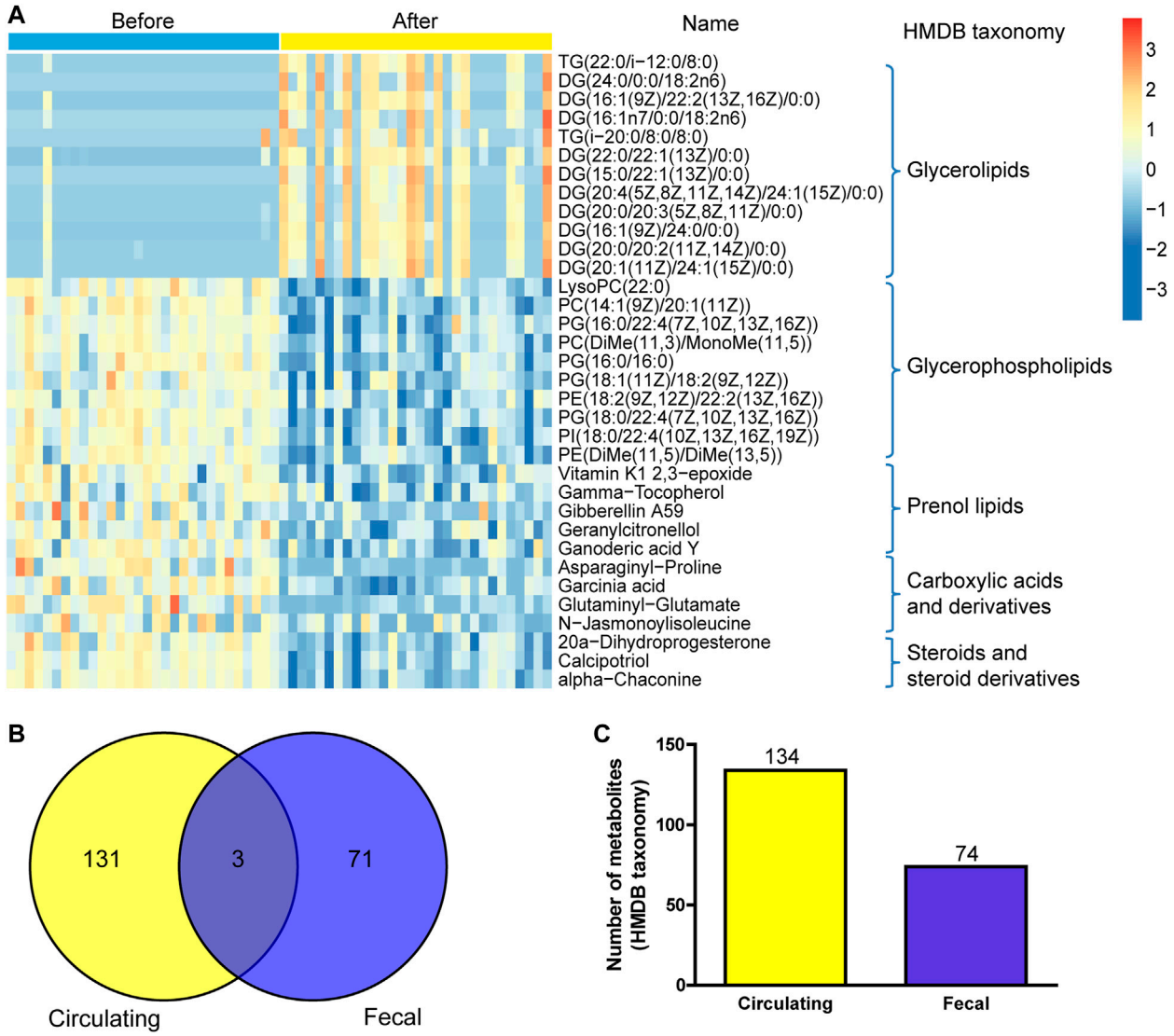

FIGURE 7 | Correlation analysis of fecal metabolites and circulating metabolites. **(A)** Hierarchical clustering analysis for the fecal metabolites in the before- and after-administration groups based on their z-normalized abundances. The name and HMDB taxonomy clusters of the metabolites were listed. **(B)** Venn and number **(C)** of HMDB taxonomy metabolite with differences in serum and fecal samples before and after administration.

completed by fiberoptic bronchoscopy, which is a risky invasive operation. We selected pharyngeal swab samples and analyzed the effect of LS capsule on the upper respiratory tract microbiota.

The decreased diversity of local bacterial communities is associated with many lung diseases. For example, in patients with cystic fibrosis, a significant ecological pattern with decreasing airway microbiota diversity and a reducing lung function was found (Cuthbertson et al., 2020). In patients and an animal model of pulmonary fibrosis, decreased lung bacterial diversity was significantly associated with increased alveolar concentrations of pro-inflammatory cytokines and growth factors (O'Dwyer et al., 2019). Compared with reference subjects, Zhang et al. also reported decreased community diversity in patients with pulmonary hypertension (Zhang et al., 2020a). Although the causal relationship between microbial diversity and disease occurrence is not clear, these studies demonstrated a certain link between decreased diversity of specific microecological environment and unhealthy outcomes. The traditional Chinese medicine prescription of LS capsule has a history of thousands of years. It is widely used in clinic in China and is effective in treating influenza, acute bronchitis, and other respiratory diseases. The present study found that the diversity of the airway microbiota was significantly increased after LS capsule administration compared with that of before administration. The regulatory effect on microbiota diversity might be one of the potential mechanisms of LS capsule in treating diseases.

LS capsule administration significantly decreased the abundance of several airway bacterial. Among them, Proteobacteria, *Veillonella*, *Streptococcus*, *Prevotella*, *Neisseria*

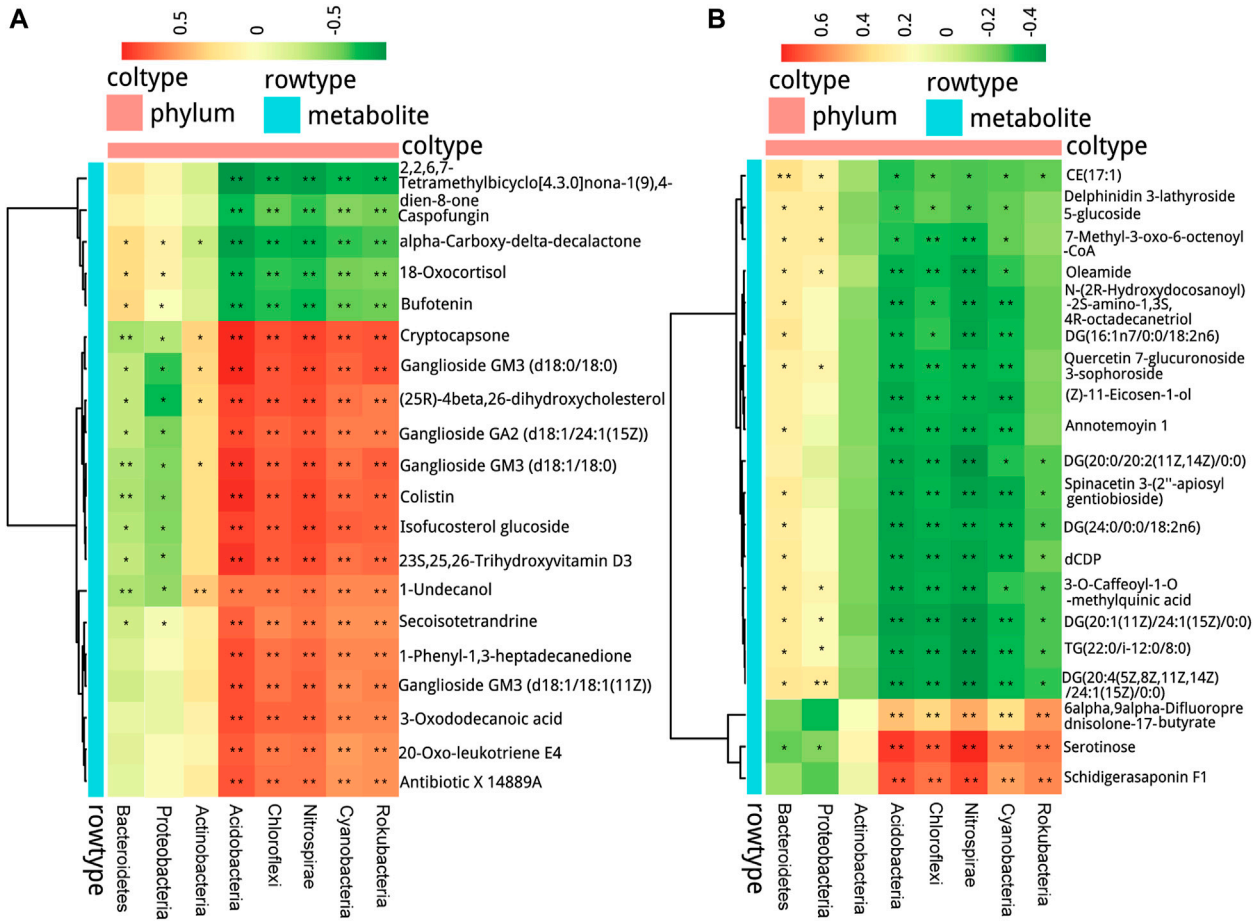

FIGURE 8 | Interrelationship between airway microbiota composition and host metabolic profile. The positive and negative correlations are shown as red and green, respectively, in the heat map according to Spearman correlation analysis between the airway significant microbiota at the phylum level with **(A)** the serum metabolites and **(B)** the fecal metabolites. Significant microbiota–metabolite correlations were presented with $^{*}p < 0.05$, $^{**}p < 0.01$, and $^{***}p < 0.001$.

and *Actinomyces* were reported to be highly associated with the development of respiratory diseases. In both upper airway and acellular bronchoalveolar lavage samples from participants without known pulmonary diseases, Segal et al. observed that enriched *Veillonella* and *Prevotella* were associated with the enhanced expression of Th-17 lymphocyte–derived inflammatory cytokines, and conversely, a blunted alveolar macrophage TLR4 response (Segal et al., 2016). Tsay et al. reported enriched airway *Veillonella*, *Prevotella*, and *Streptococcus* in patients with lung cancer, which were associated with the upregulation of the ERK and PI3K signaling pathways and tested in both patients and *in vitro* epithelial cell experiments (Tsay et al., 2018). In patients with asthma, Proteobacteria dominance is associated with hyper-responsiveness and neutrophil-derived excessive airway inflammation (Huang et al., 2011; Yang et al., 2018). In patients with COPD, Proteobacteria dominance was also reported to be associated with increased mortality and neutrophil activation (Dicker et al., 2021). Proteobacteria and Actinobacteria are associated with infiltrating immune cells in lung tissue, including neutrophils, eosinophils, and B cells (Sze et al., 2015). Moreover, increased *Prevotella* abundance was associated with augmented T-helper type 17 (Th17)-mediated mucosal inflammation, which was in line with the marked capacity of *Prevotella* in driving Th17 immune responses *in vitro* (Huang et al., 2020). *Neisseria*, such as *Neisseria meningitidis*, is a colonizing bacterium in the respiratory tract, which can cause diseases under certain conditions. The respiratory mucosa is the site of *Neisseria* colonization and the barrier to protect its invasion (Audry et al., 2019). In our study, we also observed higher taxa of *Bifidobacteria* and *Lactobacillus* after LC capsule administration than before. *Bifidobacteria* and *Lactobacillus* are common probiotics. *Bifidobacterium* was reported to play a protective role on the respiratory mucosa (Flemer et al., 2018). In our study, no pathogenic bacteria (e.g., *S pneumonia*, *H influenzae*) were detected since the participants in both groups were healthy people. Unlike the above bacteria, some altered bacteria, such as *wolbachia*, were barely report related to diseases. Based on the aforementioned findings, we speculated that the mechanism of LS capsule is related to the alternation of

the microbiota structure in the upper respiratory tract and the downregulation of certain microbiota closely related to the development of respiratory diseases.

The alternation of respiratory microbiota after LS capsule administration might impact the metabolites, since COG and KEGG pathway analysis of airway microbiota showed several metabolic pathways with signature alternation. Indeed, we confirmed that the serum and fecal samples had completely different metabolomics before and after LS capsule administration. In the serum and the fecal samples of the two groups, the numbers of lipid metabolites were changed the most (50% in the serum and 77% in feces). Lipid is the basic component of the cell membrane and plays an important role in energy storage, signal transduction, and formation of membrane bilayer and cellular barriers. Lipid metabolisms are indicated in numerous human diseases, such as Alzheimer's disease, respiratory diseases, obesity, and atherosclerosis (Hannun and Obeid, 2018; Zhang et al., 2020b). In our study, we identified several categories of lipid types, including fatty acids, sphingolipids, prenol lipids, and glycerophospholipids. Fatty acyls are a source of energy in cells to produce ATP. We identified the alternation of 16 fatty acyl metabolites between the before- and after-administration groups, of which 5 were downregulated and 11 were upregulated. A growing number of studies proposed fatty acyls as the biomarkers of some diseases. For example, in patients with idiopathic pulmonary fibrosis, 20 fatty acyls have been listed with significant compared with the controls (Yan et al., 2017). A previous study also found that chiral ibuprofen treatment caused disorders in the metabolism of the brain lipids, including glycerophospholipid and fatty acid metabolism, which affected the composition of biological membranes, inflammatory responses, and cardiovascular and cerebrovascular disease development in zebrafish (Zhang et al., 2020c). Sphingolipids are ubiquitous cellular membrane components implicated in multiple cellular processes including autophagy, apoptosis, differentiation, and cell division. We found that two sphingolipids were downregulated after LS capsule administration in serum samples. Previous studies found that four out of 46 sphingolipids could distinguish the patients with idiopathic pulmonary fibrosis from control subjects (Yan et al., 2017). Glycerophospholipids are important biomolecules that constitute the cytoskeleton of the cell membrane, and also a repository of a large number of bioactive media produced by the reaction of phospholipase (Frisardi et al., 2011). We identified the alternation of 26 glycerophospholipid metabolites between the before- and after-administration groups, of which 18 were downregulated and eight were upregulated. Previous studies demonstrated decreased plasma glycerophospholipid levels in patients with cystic fibrosis (Grothe et al., 2015) and those with pulmonary fibrosis (Yan et al., 2017), implying that glycerophospholipid metabolites could be used as potential biomarkers for the aforementioned lung diseases.

The pharmacodynamic components of LS capsule include bufonidine lactones, cholic acid compounds of bezoar, androgen of musk, volatile components in borneol, and minerals in realgar and pearl, among which the former three are the major ones. We detected that the metabolites including bufotenin and shoyuflavone b were upregulated in serum samples after administration, which was due to the metabolism of LS capsule in the body. The levels of benzene compounds, which are usually produced and degraded by bacterial species, were significantly different before and after administration, suggesting that the bacterial–metabolite interaction was involved in the mechanism of LS capsule (Nguyen and Kim, 2019). After oral administration of LS capsule, some drug active components could be directly absorb, while some other components were with low bioavailability or cannot be absorbed, which need to be reused through the transformation of intestinal flora. Blood metabolites (serum metabolomics) and metabolites transformed via intestinal flora (fecal metabolomics) reach the respiratory tract with circulation and regulate the local microbiota. As supported by our results, we observed a significant correlation between airway microbiota with serum and fecal metabolites, indicating that the perturbations of microbiota were associated with metabolic phenotype alterations. We found three metabolites that were significant altered in both feces and serum samples before and after administration. These metabolites could be used as a marker for taking LS capsule. However, since both groups of metabolites were from healthy participants, the abnormalities in main synthetic or catabolic pathways were not detected, nor were the main classes of microorganism-dependent metabolites, such as SCFAs.

In conclusion, our study demonstrated that *Bifidobacteria* and *Lactobacillus* were significantly enriched in the oropharynx respiratory tract samples after LS capsule administration; on the contrary, the bacterial Proteobacteria, *Veillonella*, *Prevotella*, *Neisseria*, and *Actinomyces* were relatively more abundant before administration. These divergent patterns of microbiota composition before and after administration might provide potential novel insights into the mechanisms of LS capsule. Furthermore, we found significant differences in circulating and fecal metabolic profiles before and after administration, especially the changes in lipid-type categories. Our results hinted that LS capsule might play a preventive role in respiratory diseases by regulating microbiota and metabolites. Although the basic characteristics and laboratory tests between the two groups showed no difference, a few samples in PCoA analysis were still discreted. These individual differences are inevitable, since many factors including diet habits, environmental influence, and genetic backgrounds could affect the microbiome composition. The sensitivity and accuracy of non-targeted metabonomics in detecting lipid contents are limited compared to lipid metabolomics. Most importantly, since the participants in both groups were healthy volunteers, whether LS capsule could play similar regulatory effect on respiratory microbiota under respiratory diseases conditions needs to be further investigated in the future.

DATA AVAILABILITY STATEMENT

The original contributions presented in the study are included in the article/**Supplementary Material**, further inquiries can be directed to the corresponding author.

ETHICS STATEMENT

The studies involving human participants were reviewed and approved by Ethics Committee of Beijing Hospital of Traditional Chinese Medicine Affiliated to Capital Medical University (No. 2019BL02-047-02). The registration number is ChiCTR2000032794 on chictr.org.cn. The patients/participants provided their written informed consent to participate in this study. Written informed consent was obtained from the individual(s) for the publication of any potentially identifiable images or data included in this article.

AUTHOR CONTRIBUTIONS

QL initiated and designed the project; XW and XX wrote and edited the manuscript. YC and ZL collected the samples; MZ, CZ, and BL analyzed the data; JZ and YG provided consultation and advice on the project.

FUNDING

This work was supported by National key R and D projects of the Ministry of science and technology (No. 2020YFC0841600) and financial project of Beijing Municipal Health Commission (No. PXM2020026273000001).

ACKNOWLEDGMENTS

We thank Lei Yun Shang Pharmaceutical Group Co., Ltd. (Suzhou, China) for providing LS capsule (batch number ra18029a) in this study.

SUPPLEMENTARY MATERIAL

The Supplementary Material for this article can be found online at: https://www.frontiersin.org/articles/10.3389/fphar.2021.824180/full#supplementary-material

REFERENCES

Audry, M., Robbe-Masselot, C., Barnier, J. P., Gachet, B., Saubaméa, B., Schmitt, A., et al. (2019). Airway Mucus Restricts neisseria Meningitidis Away from Nasopharyngeal Epithelial Cells and Protects the Mucosa from Inflammation. *mSphere* 4, e00494–19. doi:10.1128/mSphere.00494-19

Bernasconi, E., Pattaroni, C., Koutsokera, A., Pison, C., Kessler, R., Benden, C., et al. (2016). Airway Microbiota Determines Innate Cell Inflammatory or Tissue Remodeling Profiles in Lung Transplantation. *Am. J. Respir. Crit. Care Med.* 194, 1252–1263. doi:10.1164/rccm.201512-2424OC

Bogaert, D., De Groot, R., and Hermans, P. W. (2004). Streptococcus Pneumoniae Colonisation: The Key to Pneumococcal Disease. *Lancet Infect. Dis.* 4, 144–154. doi:10.1016/S1473-3099(04)00938-7

Botero, L. E., Delgado-Serrano, L., Cepeda, M. L., Bustos, J. R., Anzola, J. M., Del Portillo, P., et al. (2014). Respiratory Tract Clinical Sample Selection for Microbiota Analysis in Patients with Pulmonary Tuberculosis. *Microbiome* 2, 29. doi:10.1186/2049-2618-2-29

Buck, M. D., Sowell, R. T., Kaech, S. M., and Pearce, E. L. (2017). Metabolic Instruction of Immunity. *Cell* 169, 570–586. doi:10.1016/j.cell.2017.04.004

Budden, K. F., Shukla, S. D., Rehman, S. F., Bowerman, K. L., Keely, S., Hugenholtz, P., et al. (2019). Functional Effects of the Microbiota in Chronic Respiratory Disease. *Lancet Respir. Med.* 7, 907–920. doi:10.1016/S2213-2600(18)30510-1

Cuthbertson, L., Walker, A. W., Oliver, A. E., Rogers, G. B., Rivett, D. W., Hampton, T. H., et al. (2020). Lung Function and Microbiota Diversity in Cystic Fibrosis. *Microbiome* 8, 45. doi:10.1186/s40168-020-00810-3

Dicker, A. J., Huang, J. T. J., Lonergan, M., Keir, H. R., Fong, C. J., Tan, B., et al. (2021). The Sputum Microbiome, Airway Inflammation, and Mortality in Chronic Obstructive Pulmonary Disease. *J. Allergy Clin. Immunol.* 147, 158–167. doi:10.1016/j.jaci.2020.02.040

Dickson, R. P., Erb-Downward, J. R., Falkowski, N. R., Hunter, E. M., Ashley, S. L., and Huffnagle, G. B. (2018). The Lung Microbiota of Healthy Mice Are Highly Variable, Cluster by Environment, and Reflect Variation in Baseline Lung Innate Immunity. *Am. J. Respir. Crit. Care Med.* 198, 497–508. doi:10.1164/rccm.201711-2180OC

Dickson, R. P., Singer, B. H., Newstead, M. W., Falkowski, N. R., Erb-Downward, J. R., Standiford, T. J., et al. (2016). Enrichment of the Lung Microbiome with Gut Bacteria in Sepsis and the Acute Respiratory Distress Syndrome. *Nat. Microbiol.* 1, 16113. doi:10.1038/nmicrobiol.2016.113

Flemer, B., Warren, R. D., Barrett, M. P., Cisek, K., Das, A., Jeffery, I. B., et al. (2018). The Oral Microbiota in Colorectal Cancer Is Distinctive and Predictive. *Gut* 67, 1454–1463. doi:10.1136/gutjnl-2017-314814

Frisardi, V., Panza, F., Seripa, D., Farooqui, T., and Farooqui, A. A. (2011). Glycerophospholipids and Glycerophospholipid-Derived Lipid Mediators: A Complex Meshwork in Alzheimer's Disease Pathology. *Prog. Lipid Res.* 50, 313–330. doi:10.1016/j.plipres.2011.06.001

Grothe, J., Riethmüller, J., Tschürtz, S. M., Raith, M., Pynn, C. J., Stoll, D., et al. (2015). Plasma Phosphatidylcholine Alterations in Cystic Fibrosis Patients: Impaired Metabolism and Correlation with Lung Function and Inflammation. *Cell Physiol Biochem* 35, 1437–1453. doi:10.1159/000373964

Hannun, Y. A., and Obeid, L. M. (2018). Sphingolipids and Their Metabolism in Physiology and Disease. *Nat. Rev. Mol. Cel Biol* 19, 175–191. doi:10.1038/nrm.2017.107

Hecker, M., Sommer, N., and Mayer, K. (2021). Assessment of Short- and Medium-Chain Fatty Acids on Mitochondrial Function in Severe Inflammation. *Methods Mol. Biol.* 2277, 125–132. doi:10.1007/978-1-0716-1270-5_8

Huang, Y. J., Nariya, S., Harris, J. M., Lynch, S. V., Choy, D. F., Arron, J. R., et al. (2015). The Airway Microbiome in Patients with Severe Asthma: Associations with Disease Features and Severity. *J. Allergy Clin. Immunol.* 136, 874–884. doi:10.1016/j.jaci.2015.05.044

Huang, Y. J., Nelson, C. E., Brodie, E. L., Desantis, T. Z., Baek, M. S., Liu, J., et al. (2011). Airway Microbiota and Bronchial Hyperresponsiveness in Patients with Suboptimally Controlled Asthma. *J. Allergy Clin. Immunol.* 127, 372–373. doi:10.1016/j.jaci.2010.10.048

Huang, Y., Tang, J., Cai, Z., Zhou, K., Chang, L., Bai, Y., et al. (2020). Prevotella Induces the Production of Th17 Cells in the colon of Mice. *J. Immunol. Res.* 2020, 9607328. doi:10.1155/2020/9607328

Koch, C. D., Gladwin, M. T., Freeman, B. A., Lundberg, J. O., Weitzberg, E., and Morris, A. (2017). Enterosalivary Nitrate Metabolism and the Microbiome: Intersection of Microbial Metabolism, Nitric Oxide and Diet in Cardiac and Pulmonary Vascular Health. *Free Radic. Biol. Med.* 105, 48–67. doi:10.1016/j.freeradbiomed.2016.12.015

Liu, J., Wei, L. X., Wang, Q., Lu, Y. F., Zhang, F., Shi, J. Z., et al. (2018). A Review of Cinnabar (Hgs) And/or Realgar (As4s4)-containing Traditional Medicines. *J. Ethnopharmacol* 210, 340–350. doi:10.1016/j.jep.2017.08.037

Ma, Q., Huang, W., Zhao, J., and Yang, Z. (2020). Liu Shen Wan Inhibits Influenza a Virus and Excessive Virus-Induced Inflammatory Response via Suppression of TLR4/NF-Kb Signaling Pathway *In Vitro* and *In Vivo*. *J. Ethnopharmacol* 252, 112584. doi:10.1016/j.jep.2020.112584

Ma, Q., Pan, W., Li, R., Liu, B., Li, C., Xie, Y., et al. (2020). Liu Shen Capsule Shows Antiviral and Anti-inflammatory Abilities against Novel Coronavirus SARS-CoV-2 via Suppression of NF-Kb Signaling Pathway. *Pharmacol. Res.* 158, 104850. doi:10.1016/j.phrs.2020.104850

Maleki, A., Zamirnasta, M., Taherikalani, M., Pakzad, I., Mohammadi, J., Krutova, M., et al. (2020). The Characterization of Bacterial Communities of Oropharynx

Microbiota in Healthy Children by Combining Culture Techniques and Sequencing of the 16s Rrna Gene. *Microb. Pathog.* 143, 104115. doi:10.1016/j.micpath.2020.104115

Man, W. H., de Steenhuijsen Piters, W. A., and Bogaert, D. (2017). The Microbiota of the Respiratory Tract: Gatekeeper to Respiratory Health. *Nat. Rev. Microbiol.* 15, 259–270. doi:10.1038/nrmicro.2017.14

Maschirow, L., Suttorp, N., and Opitz, B. (2019). Microbiota-dependent Regulation of Antimicrobial Immunity in the Lung. *Am. J. Respir. Cel Mol Biol* 61, 284–289. doi:10.1165/rcmb.2019-0101TR

McKenzie, C., Tan, J., Macia, L., and Mackay, C. R. (2017). The Nutrition-Gut Microbiome-Physiology axis and Allergic Diseases. *Immunol. Rev.* 278, 277–295. doi:10.1111/imr.12556

Nguyen, T. M., and Kim, J. (2019). Sphingobium Aromaticivastans Sp. Nov., a Novel Aniline- and Benzene-Degrading, and Antimicrobial Compound Producing Bacterium. *Arch. Microbiol.* 201, 155–161. doi:10.1007/s00203-018-1611-2

O'Dwyer, D. N., Ashley, S. L., Gurczynski, S. J., Xia, M., Wilke, C., Falkowski, N. R., et al. (2019). Lung Microbiota Contribute to Pulmonary Inflammation and Disease Progression in Pulmonary Fibrosis. *Am. J. Respir. Crit. Care Med.* 199, 1127–1138. doi:10.1164/rccm.201809-1650OC

Pignatelli, P., Fabietti, G., Ricci, A., Piattelli, A., and Curia, M. C. (2020). How Periodontal Disease and Presence of Nitric Oxide Reducing Oral Bacteria Can Affect Blood Pressure. *Int. J. Mol. Sci.* 21, 21. doi:10.3390/ijms21207538

Pulvirenti, G., Parisi, G. F., Giallongo, A., Papale, M., Manti, S., Savasta, S., et al. (2019). Lower Airway Microbiota. *Front. Pediatr.* 7, 393. doi:10.3389/fped.2019.00393

Ramos-Sevillano, E., Wade, W. G., Mann, A., Gilbert, A., Lambkin-Williams, R., Killingley, B., et al. (2019). The Effect of Influenza Virus on the Human Oropharyngeal Microbiome. *Clin. Infect. Dis.* 68, 1993–2002. doi:10.1093/cid/ciy821

Segal, L. N., Clemente, J. C., Tsay, J. C., Koralov, S. B., Keller, B. C., Wu, B. G., et al. (2016). Enrichment of the Lung Microbiome with Oral Taxa Is Associated with Lung Inflammation of a Th17 Phenotype. *Nat. Microbiol.* 1, 16031. doi:10.1038/nmicrobiol.2016.31

Sze, M. A., Dimitriu, P. A., Suzuki, M., McDonough, J. E., Campbell, J. D., Brothers, J. F., et al. (2015). Host Response to the Lung Microbiome in Chronic Obstructive Pulmonary Disease. *Am. J. Respir. Crit. Care Med.* 192, 438–445. doi:10.1164/rccm.201502-0223OC

Tsay, J. J., Wu, B. G., Badri, M. H., Clemente, J. C., Shen, N., Meyn, P., et al. (2018). Airway Microbiota Is Associated with Upregulation of the Pi3k Pathway in Lung Cancer. *Am. J. Respir. Crit. Care Med.* 198, 1188–1198. doi:10.1164/rccm.201710-2118OC

Wang, J., Ding, L., Zhou, J., Ma, H., Wu, Y., Wang, J., et al. (2020). Target Lipidomics Approach to Reveal the Resolution of Inflammation Induced by Chinese Medicine Combination in Liu-Shen-Wan against Realgar Overexposure to Rats. *J. Ethnopharmacol* 249, 112171. doi:10.1016/j.jep.2019.112171

Wang, Z., Locantore, N., Haldar, K., Ramsheh, M. Y., Beech, A. S., Ma, W., et al. (2021). Inflammatory Endotype-Associated Airway Microbiome in Chronic Obstructive Pulmonary Disease Clinical Stability and Exacerbations: A Multicohort Longitudinal Analysis. *Am. J. Respir. Crit. Care Med.* 203, 1488–1502. doi:10.1164/rccm.202009-3448OC

Yan, F., Wen, Z., Wang, R., Luo, W., Du, Y., Wang, W., et al. (2017). Identification of the Lipid Biomarkers from Plasma in Idiopathic Pulmonary Fibrosis by Lipidomics. *BMC Pulm. Med.* 17, 174. doi:10.1186/s12890-017-0513-4

Yang, X., Li, H., Ma, Q., Zhang, Q., and Wang, C. (2018). Neutrophilic Asthma Is Associated with Increased Airway Bacterial burden and Disordered Community Composition. *Biomed. Res. Int.* 2018, 9230234. doi:10.1155/2018/9230234

Yun, Y., Srinivas, G., Kuenzel, S., Linnenbrink, M., Alnahas, S., Bruce, K. D., et al. (2014). Environmentally Determined Differences in the Murine Lung Microbiota and Their Relation to Alveolar Architecture. *PLoS One* 9, e113466. doi:10.1371/journal.pone.0113466

Zhang, C., Zhang, T., Lu, W., Duan, X., Luo, X., Liu, S., et al. (2020). Altered Airway Microbiota Composition in Patients with Pulmonary Hypertension. *Hypertension* 76, 1589–1599. doi:10.1161/HYPERTENSIONAHA.120.15025

Zhang, L., Zhu, B., Zeng, Y., Shen, H., Zhang, J., and Wang, X. (2020). Clinical Lipidomics in Understanding of Lung Cancer: Opportunity and challenge. *Cancer Lett.* 470, 75–83. doi:10.1016/j.canlet.2019.08.014

Zhang, W., Song, Y., Chai, T., Liao, G., Zhang, L., Jia, Q., et al. (2020). Lipidomics Perturbations in the Brain of Adult Zebrafish (danio Rerio) after Exposure to Chiral Ibuprofen. *Sci. Total Environ.* 713, 136565. doi:10.1016/j.scitotenv.2020.136565

Zhang, F., Wan, Y., Zuo, T., Yeoh, Y. K., Liu, Q., Zhang, L., et al. (2021). Prolonged Impairment of Short-Chain Fatty Acid and L-Isoleucine Biosynthesis in Gut Microbiome in Patients with Covid-19. *Gastroenterology* 277, 1–10. doi:10.1053/j.gastro.2021.10.013

Zhao, J., Wang, Y., Huang, X., Ma, Q., Song, J., Wu, X., et al. (2021). Liu Shen Wan Inhibits Influenza Virus-Induced Secondary staphylococcus Aureus Infection *In Vivo* and *In Vitro*. *J. Ethnopharmacol* 277, 114066. doi:10.1016/j.jep.2021.114066

Conflict of Interest: The authors declare that the research was conducted in the absence of any commercial or financial relationships that could be construed as a potential conflict of interest.

Publisher's Note: All claims expressed in this article are solely those of the authors and do not necessarily represent those of their affiliated organizations, or those of the publisher, the editors and the reviewers. Any product that may be evaluated in this article, or claim that may be made by its manufacturer, is not guaranteed or endorsed by the publisher.

frontiers in Pharmacology

ORIGINAL RESEARCH
published: 10 February 2022
doi: 10.3389/fphar.2022.828920

Traditional Tibetan Medicine Twenty-Five Wei'er Tea Pills Ameliorate Rheumatoid Arthritis Based on Chemical Crosstalk Between Gut Microbiota and the Host

Zixuan Li[1†], Lijuan Nie[2†], Yong Li[3], Lu Yang[4], Lulu Jin[4], Baozhong Du[1], Juan Yang[1], Xulin Zhang[5], Huantian Cui[6] and Ouzhu Luobu[7,8]**

[1]Department of Basic Medicine, Medical College of Tibet University, Lhasa, China, [2]Department of Pharmacy, Medical College of Tibet University, Lhasa, China, [3]Institute of Oxygen Supply, Center of Tibetan Studies (Everest Research Institute), Tibet University, Lhasa, China, [4]Tianjin University of Traditional Chinese Medicine, Tianjin, China, [5]Second Affiliated Hospital of University of South China, Hengyang, China, [6]Shandong Provincial Key Laboratory of Animal Cell and Developmental Biology, School of Life Sciences, Shandong University, Qingdao, China, [7]Medical College of Tibet University, Lhasa, China, [8]Affiliated Fukang Hospital of Tibet University, Lhasa, China

Twenty-Five Wei'er Tea Pills (TFP), a traditional Tibetan medicine, has shown to have a promising therapeutic effect in patients with Rheumatoid arthritis (RA), as well as being safe. Nonetheless, there have been limited pharmacological studies that have explored this therapeutic option. As gut microbiota has been proven to have a critical role in the pathogenesis of RA, this study aims to explore and reveal relevant ways by which TFP interacts with the chemical crosstalk between the gut microbiome and its host. 16S rRNA sequencing, combined with un-targeted metabolomics, were conducted on collagen-induced arthritis (CIA) rats. CIA model rats treated with TFP showed significant improvement in weight gain, pathological phenomena in joints, as well as decreased serum levels of TNF-α, IL-6 and increased level of IL-4 and IL-10. Significant dysfunction in the gut microbiome and alteration in serum metabolites were observed in CIA model rats, which were restored by TFP treatment. Coherence analysis indicated that TFP modulated the pathways of histidine metabolism, phenylalanine metabolism, alanine, aspartate, glutamate metabolism, amino sugar and nucleotide sugar metabolism owing to the abundances of *Lactobacillus*, *Bacteroides*, Prevotellaceae_*UCG-001* and Christensenellaceae_*R-7_group* in the gut microflora. The corresponding metabolites involved L-histidine, histamine, phenylethylamine, asparagine, L-aspartic acid, D-fructose 1-phosphate, D-Mannose 6-phosphate, D-Glucose 6-phosphate, and Glucose 1-phosphate. In conclusion, this study reveals the ameliorative effects of TFP on RA through the chemical crosstalk that exists between the gut microbiota and its host, and also further enriches our understandings of the pathogenesis of RA.

Keywords: Tibetan medicine, twenty-five Wei'er tea pills, rheumatoid arthritis, gut microbiota, metabolomics

OPEN ACCESS

Edited by:
Shuai Ji,
Xuzhou Medical University, China

Reviewed by:
Wuwen Feng,
Chengdu University of Traditional Chinese Medicine, China
Bo Yang,
Jiangnan University, China

****Correspondence:***
Ouzhu Luobu
tbciyang@163.com
Huantian Cui
1762316411@qq.com

[†]These authors have contributed equally to this work and share first authorship

Specialty section:
This article was submitted to Ethnopharmacology, a section of the journal Frontiers in Pharmacology

Received: *04 December 2021*
Accepted: *17 January 2022*
Published: *10 February 2022*

Citation:
Li Z, Nie L, Li Y, Yang L, Jin L, Du B, Yang J, Zhang X, Cui H and Luobu O (2022) Traditional Tibetan Medicine Twenty-Five Wei'er Tea Pills Ameliorate Rheumatoid Arthritis Based on Chemical Crosstalk Between Gut Microbiota and the Host. Front. Pharmacol. 13:828920. doi: 10.3389/fphar.2022.828920

INTRODUCTION

Rheumatoid arthritis (RA) is a chronic immune disease, which involves multiple systems. The hallmark pathological features of RA include the proliferation of synovial lining cells, significant inflammatory cell infiltration into the interstitium, regeneration of microvessels, pannus formation, damage of both cartilage and bone tissue, as well as reported metabolic disorders (Liu et al., 2021; Jiang et al., 2021). Globally, the prevalence of RA is relatively high, about 0.5–1.0% (Tobon et al., 2010; Ardalan and Vahed, 2017). This autoimmune disease is primarily diagnosed in patients aged between 40 and 60 years, and is approximately three times more prevalent in women compared with in men(Tobon et al., 2010). Its clinical manifestations are joint stiffness, deformity, rigidity, and even joint dislocation; furthermore, RA has an exceptionally high disability rate. The predominantly prescribed medications to treat RA include nonsteroidal anti-inflammatory drugs (NSAIDs), glucocorticoids (GCs), disease-modifying antirheumatic drugs, and targeted biological agents. However, due to the complex pathogenesis of RA, these drugs have failed to produce satisfactory pharmacological effects while also being known create severe side effects, including immunodeficiency, gastrointestinal disorders, and bodily fluid disorders.

An increasing number of studies have shown the effect of gut microbiota on the immune system (de Oliveira et al., 2017; Castro Rocha et al., 2020), metabolic homeostasis (Wu et al., 2020; Tsai et al., 2021), and gastrointestinal integrity (Owen and Mohamadzadeh, 2013; Guerreiro et al., 2018). Studies conducted in recent years have suggested that the abnormal immune response of RA may be associated with the imbalance of gut microbiota (Xu et al., 2020; Brandl et al., 2021; Li and Wang, 2021). Changes in the normal gut microbiota impact mucosal immunity, affecting extraintestinal diseases, such as RA (Owen and Mohamadzadeh, 2013; Jiao et al., 2020). Patients with RA and other rheumatoid diseases have shown differences in the abundance of specific common gut microbiota compared to healthy controls (Maeda et al., 2016; Bodkhe et al., 2019). In an animal study, arthritis was alleviated in K/BxN mice under aseptic conditions (Teng et al., 2017). However, the germ-free mice developed more severe arthritis after being transplanted with the gut microbiota from collagen-induced arthritis (CIA) susceptible mice (Wu et al., 2010).

The imbalance of gut microbiota may lead to changes in metabolomic profiling in the human body which accounts for etiology of autoimmune diseases (Kim et al., 2017; Tsai et al., 2021; Yang and Cong, 2021). Metabolomics, the systematic study of the sets of metabolites in an organism, is an excellent tool to provide further insight or scientific basis into specific pathogeneses as well as the mechanism of actions of botanical medicines (Marchev et al., 2021; Oyenihi et al., 2021). In addition, ethnomedicine such as berberine can modulate the composition and metabolites of gut microbiota, and thus ameliorate the diseases (Cheng et al., 2021). Combined application of 16S rRNA sequencing and metabolomics, therefore, can help explain the mechanism of ethnic Medications through the metabolic interaction between the gut microbiota and the host (Cui et al., 2020a).

Twenty-five Wei'er tea pills (TFP), made of 25 Tibetan natural drugs (mostly botanical drugs), such as stem of *Senegalia catechu* (L.f.) P.J.H.Hurter and Mabb. (100 g), fruits of *Terminalia chebula* Retz. (100 g), fruits of *Terminalia billerica* (Gaertn.) Roxb. (125 g), fruits of *Phyllanthus emblica* L. (100 g), *Hymenidium hookeri* (C.B.Clarke) Pimenov and Kljuykov (50 g), rhizome of *Polygonatum sibiricum* Redouté (40 g), root of *Asparagus cochinchinensis* (Lour.) Merr. (40 g), root of *Oxybaphus himalaicus* Edgew. (25 g), fruits of *Tribulus terrestris* L. (30 g), resin of *Boswellia sacra* Flück. (*Boswellia carterii* Birdw.) (50 g), seeds of *Senna tora* (L.) Roxb. (50 g), seeds of *Abelmoschus manihot* (L.). Medik. (35 g), stem of *Tinospora sinensis* (Lour.) Merr. (100 g), fruits cluster of *Piper longum* L. (30 g), rhizome of *Acorus calamus* L. (acori calami rhizoma) (50 g), root of *Dolomiaea costus* (Falc.) Kasana and A.K.Pandey (aucklandiae radix) (50 g), *Oxytropis kansuensis* Bunge (40 g), fruits of *Rosa sweginzowii* Hemsl. and E.H.Wilson (50 g), flower of *Gentiana macrophylla* Pall. (30 g), root of *Aconitum pendulum* N.Busch (*Aconitum pendulum* Busch) (40 g), musk of *Moschus chrysogaster sifanicus* (30 g), shell of *Hyriopsis cumingii* (Lea) (25 g), horn of *Bubalus arnee f. bubalis* (25 g), is a traditional Tibetan medicine used to treat RA by relieving pain and inflammation and dispelling wind and numbness in clinical practice (Li, 2014). A recent case-control study revealed TFP's remarkable curative effect and safety compared with conventional antirheumatic drugs (Zha, 2017). However, the mechanism of TFP relating to the treatment of RA has not been reported yet. In this study, we used the CIA rat model to evaluate the therapeutic effect of TFP on RA rats and explored the potential mechanism by a combination of 16S rRNA sequencing of gut microbiota and investigation on serum metabolites.

MATERIALS AND METHODS

Materials

TFP was purchased from Tibet Ganlu Tibetan Medicine Co., Ltd. (Lhasa, China. Batch number: 20200502). Dexamethasone tablets, produced by South Land Pharmaceutical Co., Ltd., were obtained from Lhasa Jiming Pharmacy (Lhasa, China). The IL-1β, IL-4, IL-6, IL-10, IFN enzyme-linked immunosorbent assay (ELISA) kits were purchased from Wuhan Saipei Biotechnology Co., Ltd. (Wuhan, China). The immunohistochemistry kits were purchased from Solarbio Biotechnology Co., Ltd. (Beijing, China). The Bovine Type II Collagen-Solution was purchased from Amyjet Scientific Inc. (Wuhan, China).

Animals

Male Sprague Dawley rats, aged 6–8 weeks and weighing 190–210 g, were selected and purchased from Beijing Huafukang Animal Co., Ltd. (Beijing, China) (Certificate No. SYXK (Jing) 2019–0022). They were conventionally raised for one week in a controlled environment (12-h light/dark cycle,

temperature 21 ± 2°C, relative humidity of 45 ± 10%) and were given free access to food and water. All animal experiments were conducted under guidelines approved by the Animal Ethics Committee of Tibet University.

Animal Experiment Procedures

CIA Rat Modeling

The collagen emulsion was prepared on a sterile table: first, the 0.05 M glacial acetic acid solution was prepared. Then, the Bovine Type II Collagen was weighed (protected from light) with an electronic balance and added into the glacial acetic acid solution to form a mixed solution with a concentration of 2 mg/ml. Next, the above-mixed solution was shaken using a laboratory shaker for 12 h at 4°C under dark conditions. Finally, an equal volume of complete Freund's adjuvant was added into the shaken solution to form a water-insoluble mixture. The mixture was stored in an ice bath and kept away from light for later use.

After 1 week of acclimation, six rats were randomly selected to be used in the Control group, while the remaining 24 rats were used for modeling. Primary immunization of the models took place on day 0 as follows: after skin disinfection, the collagen emulsion was given at a dose of 0.2 ml/rat *via* subcutaneous injection at 2 cm from the base of the tail. Pressure was kept on the base of the tail for 30 s after administering the injection to prevent extravasation of the emulsion. Booster immunization of the models took place on day 7 as follows: the collagen emulsion was given at a dose of 0.1 ml/rat *via* subcutaneous injection at 2 cm from the base of the tail. Rats in the control group were injected with an equal volume of normal saline using an identical method.

Grouping and Drug Administration

On day 21 post-modeling, the twenty-four rat models were randomly divided into four groups evenly:

The Model group: each rat was given saline.
The Positive group: each rat was given dexamethasone for four consecutive weeks through intragastric administration, firstly with a dosage of 0.15 mg/kg/day for three consecutive days, then changed to 0.075 mg/kg/day.
The TFP low-dose (TFP-L) group: each rat was intragastrically administered 150 mg/kg/day of TFP for four consecutive weeks.
The TFP high-dose (TFP-H) group: each rat was given with 450 mg/kg/day of TFP for four consecutive weeks.

Another six normally fed rats were classified as the Control group.

The TFP (pills) were crushed and weighed, then the ground TFP was dispersed into water with a concentration of 150 mg/ml (stock suspension). The stock suspension was further diluted to concentrations that were needed for administration. The dexamethasone (tablets) was treated the same way as TFP to get a suspension of 150 mg/ml.

Sample Collection

Rats from all groups were anesthetized by pentobarbital sodium 24 h after the last TFP intervention. Then blood and fecal samples were collected. Blood was collected from the abdominal aorta and centrifuged at 3,000 r/min for 15 min at 4°C, then the supernatant was obtained and aliquoted for inflammatory factors assay and metabolomic test. Feces were collected under sterile conditions for 16S rRNA analysis. Both serum and stool samples were stored in a freezer at −80°C until analysis. In addition, the portion of the left hind foot at 1.5 cm above the ankle joints were removed for histopathological observation after all rats were euthanized.

Pharmacodynamics Indexes Assay

Measurement of Basic Physiological Indices

The total duration of the animal experiment lasted 49 days. Rats were weighed every 5–7 days from the first day of the experiment. The bodyweight (in g) of the rats was recorded.

After the initial dose of the drug was administered, the anteroposterior diameter of the left ankle joint, as well as the thickness of the left sole, were measured and recorded (in cm) every 5–8 days using a vernier caliper.

Detection of Serum Inflammatory Factors

All rats were anesthetized on day 49 and serum was collected to measure the inflammatory factors in the ELISA kit to detect inflammatory factors, such as TNF-α, IL-1β, IL-4, IL-6, and IL-10.

Histopathological Observation

The abovementioned left ankle joints (see 2.3.3) were immediately fixed in the 10% formalin, and decalcified with 15% ethylenediaminetetraacetic acid (EDTA) for 30 days. After which, the same tissue was dehydrated with different concentrations of ethanol step-by-step, embedded in paraffin, sliced (using a Leica RM2125, Buffalo Grove, United States), and stained with hematoxylin and eosin (HE). Pathological features of the synovial tissue were observed under an optical microscope, especially tissue involving inflammatory cell infiltration and hyperplasia of the synovial tissue, pannus, and cartilage erosion.

Data Analysis

Measurement data of basic physiological indices and inflammatory factors were reported as mean ± standard deviation (SD). Statistical differences were tested between the experimental groups using SPSS 21.0 with one way Analysis of Variance, or a nonparametric test (Kruskal–Wallis test). $p < 0.05$ was considered statistically significant.

Fecal 16S rRNA Sequencing, Data Processing and Analysis

After 4 weeks of medication, feces were collected under sterile conditions from the control, model, and TFP groups. The DNA in the feces was extracted and determined through agarose gel electrophoresis. Then, the DNA samples were diluted to 1 ng/μL. The 16S rRNA V4 region of the DNA samples were amplified by polymerase chain reaction (PCR) using specific primers (forward: GTGCCAGCMGCCGCGGTAA; reverse: GGACTACHVGGGTWTCTAAT). Four deoxynucleoside triphosphates (dNTP) were mixed 0.2 μL primers and 10 ng of template DNA to make up the amplification mixture of each

sample. Subsequently, PCR products were quantified through 2% agarose gel electrophoresis and purified using the Qiagen Gel Extraction Kit (Qiagen, Germany). The sequencing library was completed using TruSeqRDNA PCR Sequencing Preparation Kit (Illumina, United States) and then sequenced on the NovaSeq6000 platform to generate paired-end reads.

Barcode and primer sequences were removed from the raw reads obtained from the above 16S rRNA sequencing, and reads from the same sample were merged using the flashv1.2.7 analysis tool (http://ccb.jhu.edu/software/FLASH/) to obtain the raw marks. Then the raw marks were filtered using the software Qiime (V1.9.1, http://qiime.org/scripts/split_libraries_fastq.html) quality Control process to obtain clean tags. Furthermore, chimeric sequences were detected and removed from the clean data using the UCHIME algorithm to obtain valid data. Afterwards, the software Uparse (Uparse v7.0.1001, http://www.drive5.com/uparse/) was used to assign valid sequences with a similarity of ≥97% to the same OTU (Operational Taxonomic Units) and the representative sequence with the highest frequency was filtered for each OUT. Subsequently, species annotation analysis was carried out through the Silva database (http://www.arb-silva.de/). As a result, the taxonomic information was obtained and the community composition of each sample was counted at each taxonomic level, such as phylum, genus and species. After that, the indexes reflecting alpha or beta diversity were calculated by the software Qiime V1.9.1, such as Observed-species, Chao1, Shannon, Unifrac distance, et al. Moreover, the gene family abundance was predicted using a phylogenetic investigation of communities by reconstruction of unobserved states (PICRUSt).

The quantitative data of alpha diversity, such as the observed_species, chao1 index and Shannon, were analyzed and visualized using SPSS 21.0. Data of beta diversity was analyzed and visualized in the statistical software R (Version 3.4.3). Results with $p < 0.05$ were considered statistically significant.

Untargeted Metabolomics Test

Sample Preparation for Metabolomics Analysis

The samples (100 μL) were placed in the EP tubes and resuspended with prechilled 80% methanol by well vortex. The mixtures were then incubated on ice for 5 min and centrifuged at 15,000 rpm, 4°C for 20 min. Afterwards, the supernatant was diluted to final concentration containing 53% methanol by LC-MS grade water. Subsequently, the treated samples were transferred to a fresh Eppendorf tube and centrifuged at 15,000 rpm, 4°C for 20 min. Finally, the supernatant was injected into the LC-MS/MS system. Meanwhile, quality control (QC) sample was prepared for analysis by mixing equal amount of the final supernatant of each sample.

LC-MS Conditions

Metabolomic profiling was analyzed using UHPLC-MS/MS. The UPLC was conducted on Dionex U3000 UPLC system (ThermoFisher, Germany) coupled with ACQUITY UPLC BEH C18 column (100 × 2.1 mm, 1.7 μm, Waters Corporation) at 45°C. The mobile phase was comprised of eluent A (0.1% formic acid in water, v/v) and eluent B (methanol) and the gradient program was: 2% B, 1.5 min; 2–85% B, 3 min; 100% B, 10 min; 100–2% B, 10.1 min; 2% B, 12 min.The MS was carried out on an Orbitrap Q ExactiveTM HF mass spectrometer (Thermo Fisher, Germany). The electrospray ionization source (ESI) in both positive and negative ion modes was used with spray voltage of 3.5 kV, capillary temperature of 320°C, sheath gas flow rate of 35 arb and aux gas flow rate of 10 arb, S-lens RF level of 60, Aux gas heater temperature of 350°C.

Data Processing and Analysis

The raw data files generated by UHPLC-MS/MS were processed using the Compound Discoverer 3.1 software (CD3.1, ThermoFisher) to perform peak alignment, peak picking, and quantitation for each metabolite. The main parameters were set as follows: retention time tolerance, 0.2 min; actual mass tolerance, 5 ppm; signal intensity tolerance, 30%; signal/noise ratio, three; and minimum intensity, et al. After that, peak intensities were normalized to the total spectral intensity. The normalized data was used to predict the molecular formula based on additive ions, molecular ion peaks and fragment ions. And then peaks were matched with the mzCloud (https://www.mzcloud.org/), mzVault and MassList database to obtain the accurate qualitative and relative quantitative results. Statistical analyses were performed using the statistical software R (R version R-3.4.3), Python (Python 2.7.6 version) and CentOS (CentOS release 6.6).

The processed data were analyzed using the method described by Cui et al. (2020b). Principal components analysis (PCA) and Partial least squares discriminant analysis (PLS-DA) were performed at metaX (a flexible and comprehensive software for processing metabolomics data) (Wen et al., 2017). Univariate analysis (*t*-test) was used to calculate the statistical significance (*p*-value). Metabolites with variable importance in projection (VIP) > 1, fold change (FC) value > 1.2 or <0.8 and $p < 0.05$ between the Control and Model groups or between the TFP and model groups are considered as differential metabolites. The False Discovery Rate (FDR) was also calculated using the statistical software R and the differential metabolites with the reported values of FDR less than 0.05 were supposed to be statistically significant. In addition, pathway analysis was conducted using the MetaboAnalyst 5.0 software (https://www.metaboanalyst.ca/).

Correlation Analysis of the Gut Microbiota and Metabolites

The spearman correlations were analyzed between significant differential metabolites and altered species of gut bacteria and visualized using the software R. P-value < 0.05 was considered as statistically significant. Furthermore, pathways were intersected between differential metabolites and altered species of gut bacteria.

Chemical Composition Characterization

Sample Preparation

TFP was weighed accurately and extracted using ultrasonic assisted extraction with methanol. The extract was then

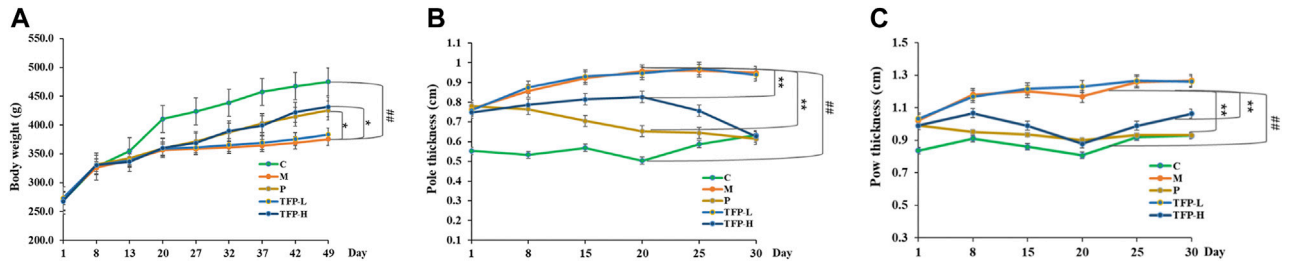

FIGURE 1 | (A): Effect of TFP on the bodyweight; **(B)**: Effect of TFP on the ankle joint diameter; **(C)**: Effect of TFP on the sole thickness. ##: Significantly different compared with the Control group ($p < 0.01$); *: Significantly different compared with the Model group, **: ($p < 0.01$), *: ($p < 0.05$).

concentrated and re-dissolved by methanol to prepare a sample solution of 0.7 g/ml. The sample solution was filtered with 0.22 μM microporous membrane for high performance liquid chromatograph (HPLC) analysis.

Standard substances were dissolved in methanol separately to prepare standard solutions, which were also filtered with 0.22 μM microporous membrane for HPLC test.

HPLC Conditions

The HPLC was performed on Agilent 1200 HPLC system (Agilent Technologies Inc., United States) coupled with Agilent HC-C_{18} column (250 × 4.6 mm, 5 μm) at 35°C. The mobile phase was composed of eluent A (0.03% acetic acid in water, v/v) and eluent B (methanol: acetonitrile, 11:9, v/v), with a gradient set as following: 5–15% B, 20 min; 15–18% B, 35 min; 18–55% B, 60 min; 55–78% B, 80 min. The flow rate was 0.9 ml/min.

Data Analysis

Retention time of a sample peak was compared with peaks of standard substances and the retention time tolerance was set at 0.3 min. Spectral characteristics of the sample peaks were also compared with those of standard substances for further confirmation. Then the Chromatograms of samples and standard substances were imported into the Similarity evaluation system A of chromatographic fingerprint of traditional Chinese medicine (version Year-2012) (Zou and Yan, 2018) for visualization.

RESULTS

Effect of TFP on the Body Weight, Sole Thickness, and Joint Diameter of CIA Models Rats

After 1 week of modeling, we observed the following changes in the studied rats (with the exception of the control group): slowed weight gain, loss of appetite, dried hair, and joint redness/swellin. After drug administration, body weight was reduced in the model group compared with the control group ($p < 0.01$); weight gain became significantly faster in the Positive and TFP-H groups compared with the Model group ($p < 0.05$). No significant difference was noted in the bodyweight changes when comparing the TFP-L group and the Model group (**Figure 1A**).

The ankle joint diameter of the left foot and the thickness of the left sole varied significantly between the Model group and Control group ($p < 0.01$). The two indicators were improved significantly in the Positive and TFP-H groups ($p < 0.01$), but did not show distinct differences in the TFP-L group compared with the Model group (**Figures 1B,C**).

TFP Therapy Improved the Inflammatory Response of CIA Rats and the Pathological Phenomena of Their Ankle Joints

Compared with the Control group, the expression level of TNF-α, IL-1β, and IL-6 increased significantly ($p < 0.05$, 0.01, and 0.01, respectively), and the expression level of IL-4 and IL-10 decreased significantly (both $p < 0.01$) in the Model group and TFP-L group. Compared with the Model group, the expression level of TNF-α and IL-6 decreased ($p < 0.05$ and 0.01, respectively), and the expression level of IL-4 and IL-10 increased (both $p < 0.01$) in the Positive and TFP-H groups. No significant difference was noted between the TFP-L group and Model group (**Table 1**).

Compared with the Model group, no significant improvement was found in the bodyweight, joint swelling, or expression levels of inflammatory factors in the TFP-L group. Therefore, the TFP-L group was excluded, and the TFP-H group was named as TFP group in subsequent tests.

HE staining was then performed to the ankle joint slice of the left hind foot. The results are shown in **Figure 2**. Rats in the Control group were observed to have structurally complete articular cartilage, evenly distributed chondrocytes, and no pathological changes in the joints (see **Figure 2A**). Massive inflammatory cell infiltration, synovial hyperplasia, fibrous hyperplasia, and other pathological changes were found in the Model group rats (see **Figure 2B**). Compared with the Model group, the inflammatory response of the ankle joint in the TFP group was significantly improved (see **Figure 2C**).

Regulation of TFP on the Gut Microbiota of CIA Rats

A total of 1,068,736 Effective Tags and 1,763 OTUs were obtained from 18 samples. The 16S rRNA sequencing of gut

TABLE 1 | Changes of inflammatory factors after TFP therapy.

Group	TNF-α	IL-1β	IL-4	IL-6	IL-10
Control	1063.34 ± 27.48	30.59 ± 5.48	674.4 ± 67,72	44.4 ± 1.93	555.42 ± 60.23
Model	1220.97 ± 75.85$^{\#}$	72.36 ± 25.65$^{\#\#}$	351.31 ± 24.22$^{\#\#}$	100.29 ± 14.12$^{\#\#}$	365.52 ± 34.27$^{\#\#}$
Positive	1056.03 ± 45.35*	33.88 ± 3.27 *	598.53 ± 50.27 **	55.42 ± 7.26 **	513.74 ± 38.38**
TFP-L	1182.79 ± 98.5$^{\#}$	65.34 ± 14.29$^{\#\#}$	378.36 ± 20.12$^{\#\#}$	92.89 ± 9.69$^{\#\#}$	390.94 ± 22.94$^{\#\#}$
TFP-H	1061.07 ± 27.67*	41.3 ± 7.88	625.64 ± 89.19 **	60.74 ± 8.66 **	495.38 ± 60.21**

*Note: Data were reported as mean ± SD (pg/ml). #: compared with the Control group (p < 0.01 as ##, p < 0.05 as #); *: compared with the Model group (p < 0.01 as **, p < 0.05 as *).*

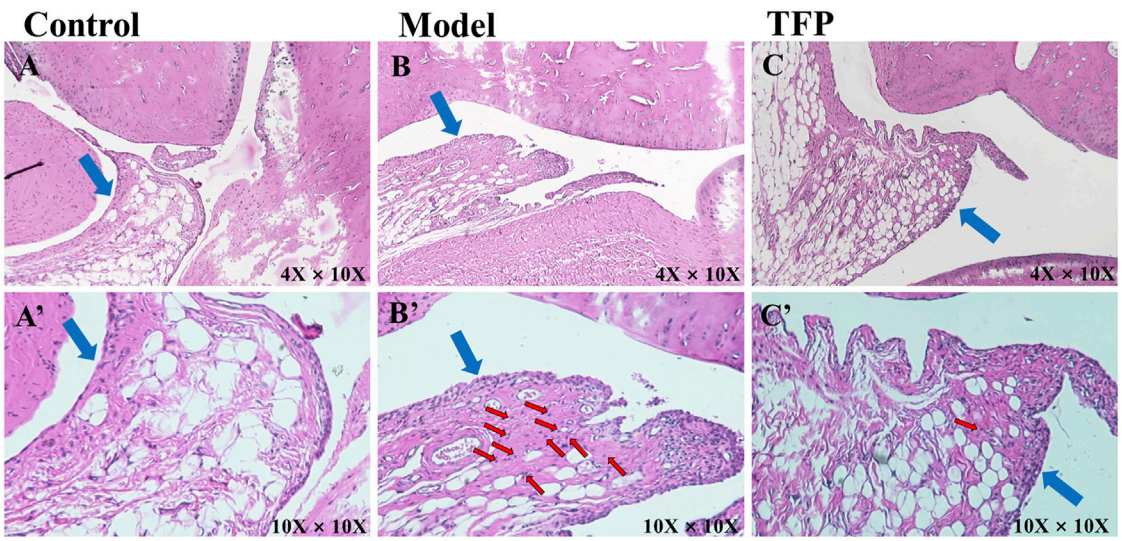

FIGURE 2 | H and E staining of ankle joint tissue (×10 objective lens on a microscope); the blue arrows point at synovium and the red arrows point at inflammatory cell infiltration. **(A)/(A')**: Joint tissue slice of rats in Control group (4X/10X eyepiece); **(B)/(B')**: Joint tissue slice of rats in Model group (4X/10X eyepiece); **(C)/(C')**: Joint tissue slice of rats in TFP group (4X/10X eyepiece).

microbiota from the rat cecum of the three groups showed gut microbiota changes in RA rat models before and after TFP therapy. Both the observed_species and Chao1 indexes demonstrated no significant difference in the number of gut microbial species between the Model and Control groups. In contrast, the number of gut microbial species increased significantly in rats receiving the TFP therapy ($p < 0.01$ *vs*. Control and Model group) (**Figures 3A,B**). The Shannon index showed that the evenness of gut microbiota in the Model group was significantly changed compared with that of the Control group ($p < 0.01$), and it returned to a normal level after TFP therapy ($p < 0.05$ *vs*. Model group) (**Figure 3C**).

The principal co-ordinates analysis (PCoA) based on the Weighted UniFrac algorithm suggested that the control, model, and TFP groups differed significantly in the gut microbiota/microbial colony. The gut microbiota of RA rats mainly aggregated on the left of axis 0 before treatment but on the right of axis 0 after treatment. The distance between the TFP and control groups was closer than the distance between the TFP and Model groups (**Figure 3D**). The hierarchical cluster tree also revealed a closer distance between the TFP and Control groups (**Figure 3E**).

We obtained 1,763 OTUs by analyzing 16s rRNA of the gut microbiota. The Venn diagram showed 899 overlapping OTUs in all groups, and there were 103 specific OTUs in the Model group, 93 in the Control group, and 265 in the TFP group (**Figure 3F**).

At the phylum level, Firmicutes and Bacteroidetes were the most abundant phyla in all microbial colonies (**Figure 3G**). The Model group had a significantly higher abundance of Firmicutes ($p < 0.01$) but a significantly lower abundance of Bacteroidetes ($p < 0.01$) than the control. No statistical difference was found between the TFP and control groups in the abundance of Firmicutes and Bacteroidetes. The differences in *the Firmicutes to Bacteroidetes* (F to B) ratio between the groups are shown in **Figure 3H**. In addition, abundance of Desulfobacterota in the Model group ($p < 0.05$) was significantly reduced compared to that in the control group, and was increased in the TFP group compared with the model group ($p < 0.05$).

At the genus level, the relative abundance of *Bacteroides*, Eubacterium, *Prevotellaceae_UCG-001*, *Helicobacter*, Blautia, and Faecalibacterium was significantly reduced ($p < 0.01$, 0.05, 0.01, 0.01, 0.01, and 0.05, respectively, **Figure 3I**), and the relative abundance of *Lactobacillus*, Romboutsia, and Christensenellace_R-7_group was significantly increased ($p < 0.01$, 0.01, and 0.05, respectively, **Figure 3I**) in the Model

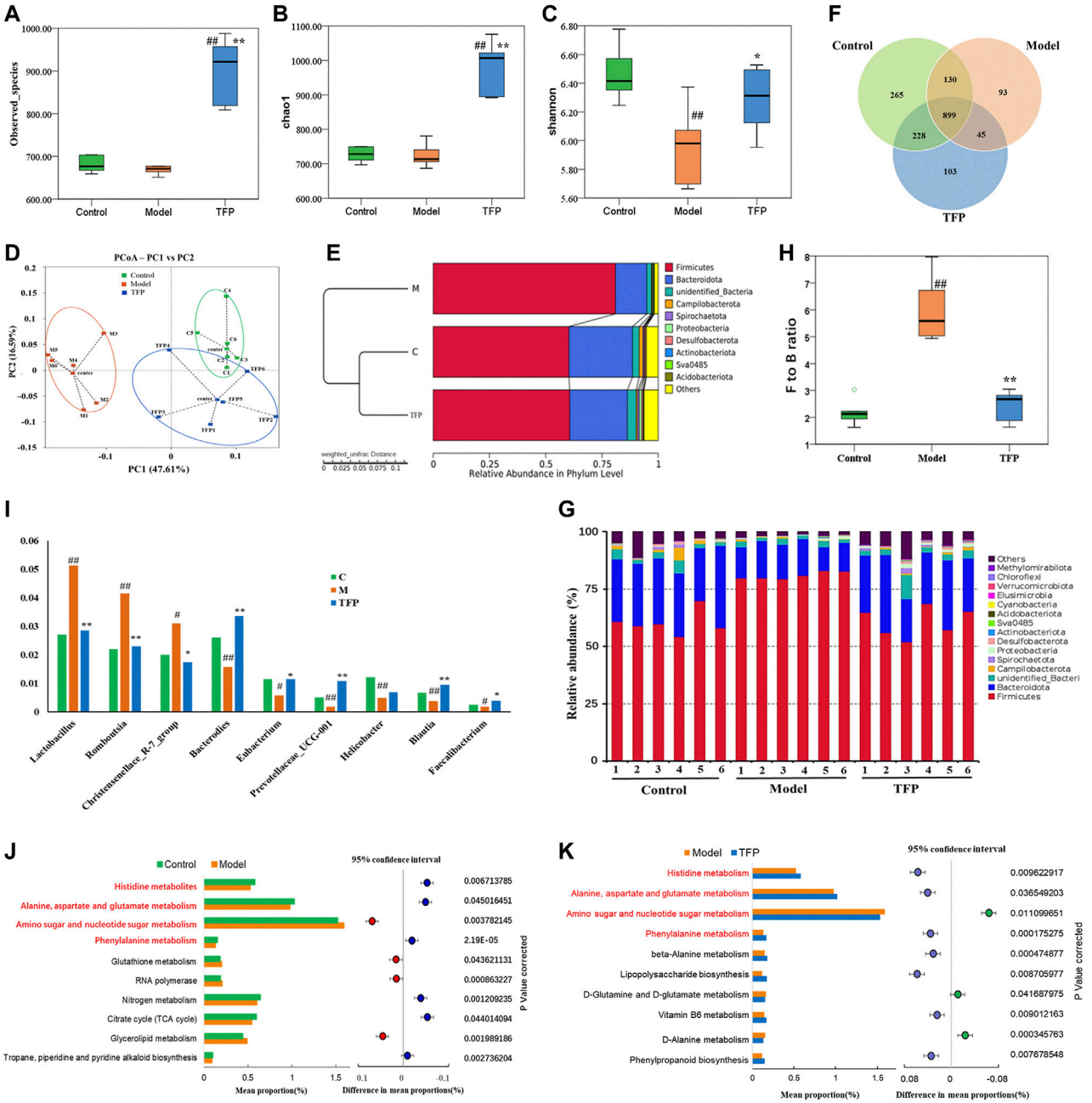

FIGURE 3 | TFP therapy affected the gut microbiota of RA model rats. **(A,B)** Chao1 index and Observed_species for each group, where TFP group significantly increased. No significant difference was noted between the Model group and the Control group. **(C)** The Shannon index was significantly lower in the Model group than in the Control group. No significant difference was noted between the TFP group and the Control group. **(D)** In terms of PCoA, the TFP group was closer to the Control group. **(E)** The hierarchical cluster tree showed that the TFP group had a more similar Beta diversity with the Control group. **(F)** Different numbers of OTUs are shown in the Venn diagram. **(G,H)** At the phylum level, TFP lowered the Firmicutes to Bacteroidetes (F to B) ratio of RA model rats. **(I)** TFP affected the relative abundance of Bacteroides, Eubacterium, Prevotellaceae_UCG-001, Blautia, Faecalibacterium, Lactobacillus, Romboutsia, and Christensenellace_R-7_group at the genus level in RA model rats. **(J,K)** Based on 16S rRNA sequencing data, the PICRUSt analysis was used to predict different metabolic pathways of TFP in RA. Control, Model, and TFP groups (n = 6 per group).

group when compared with the control group. The relative abundance *of Bacteroides, Eubacterium, Prevotellaceae_UCG-001, Blautia and Faecalibacterium was* increased (p < 0.01, 0.01, and 0.05, respectively, Figure 2I) and the relative abundance of *Lactobacillus*, Romboutsia, Christensenellace_R-7_group was reduced (p < 0.01, 0.01, and 0.05, respectively, **Figure 3I**) in the TFP group when compared with the model group.

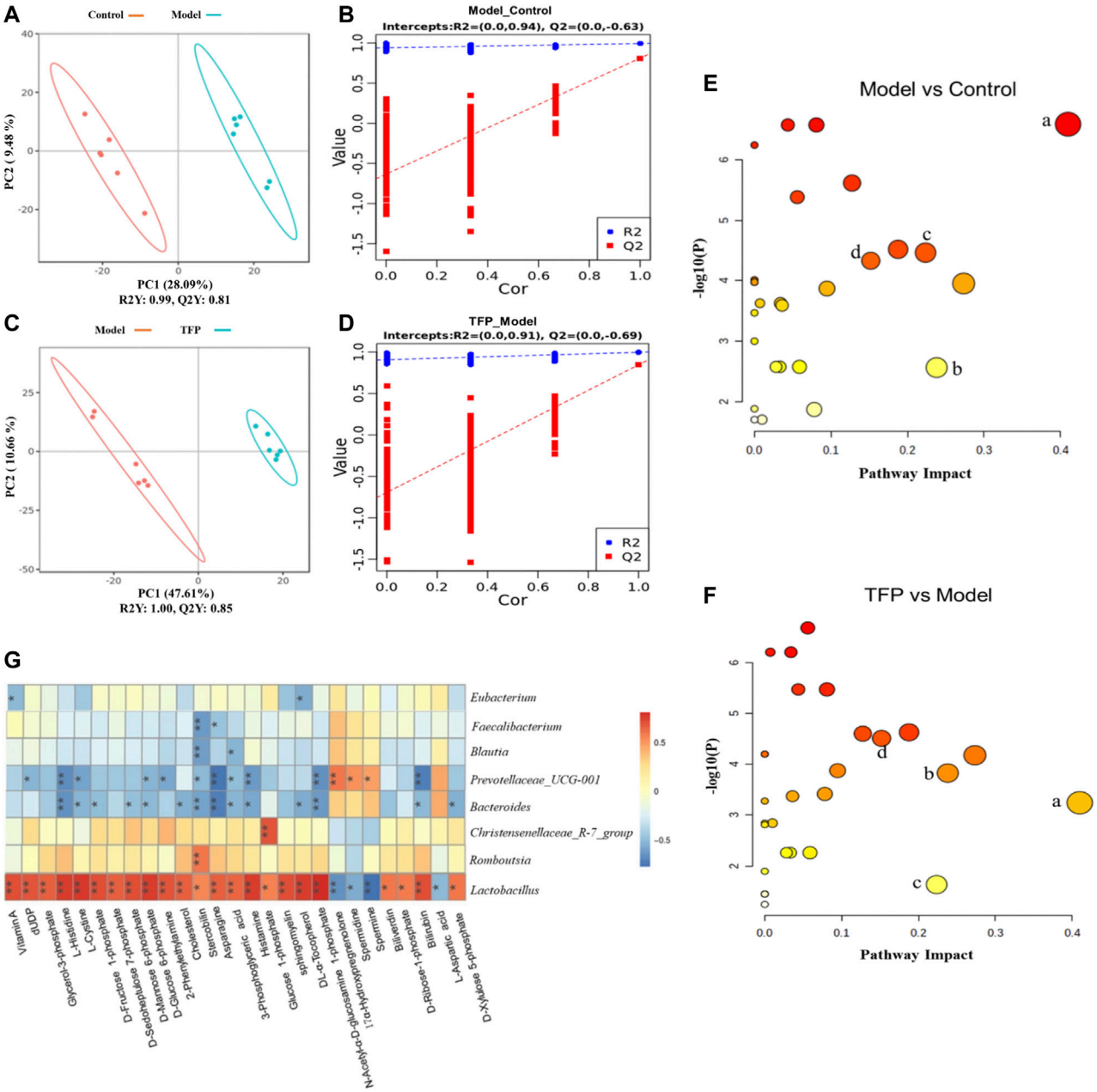

FIGURE 4 | TFP therapy regulated the metabolites in serum of CIA rats and the correlations with gut microbiota. **(A, C)**: PCoA scores of OPLS-DA between Control/Model groups and between Model/TFP groups. **(B,D)**: OPLS-DA loading coefficients between Control/Model groups and between Model/TFP groups. **(E,F)**: Analysis on pathways of the 27 differential metabolites. Commo pathways between those obtained from PICRUSt of 16S rRNA sequencing and those related to untargeted metabolomics ($p < 0.05$, Impact >0.1) were remarked as a: Histidine metabolism; b: Phenylalanine metabolism; c: Alanine, aspartate and glutamate metabolism; d: Amino sugar and nucleotide sugar metabolism **(G)**: Spearman's analysis between the 27 differential metabolites and the gut microbiota modulated by TFP at genus level.

The functions of different gut microbiota at the genus level were predicted using the PICRUSt. The top 10 metabolic pathways with the highest proportion and $p < 0.05$ are shown in **Figure 3J** (comparison between the control group and the model group) and **Figure 3K** (comparison between the model and TFP group). Compared with the control group, the abundances of amino sugar and nucleotide sugar metabolism, glycerolipid metabolism, RNA polymerase and glutathione metabolism, increased, while abundances of others decreased; such as histidine metabolism, phenylalanine metabolism, as well as alanine, aspartate and glutamate metabolism (**Figure 3J**). Compared with the model group, the TFP group had a lower abundance of amino sugar and nucleotide sugar metabolism and a higher abundance of histidine metabolism, phenylalanine metabolism, and alanine, aspartate and glutamate metabolism (**Figure 3K**).

TABLE 2 | The differential metabolites in serum after TFP therapy.

NO	RT [min]	m/z	Formula	Name	VIP			FC		Trend	Pathway
					M vs C	TFP vs M	M vs C	TFP vs M	M vs C	TFP vs M	
1	15.623	285.222	$C_{20}H_{30}O$	Vitamin A	1.67	1.10	2.59	0.57	↑##	↓*	–
2	1.162	387.001	$C_9H_{14}N_2O_{11}P_2$	dUDP	2.03	1.83	4.59	0.27	↑##	↓**	–
3	1.194	171.006	$C_3H_9O_6P$	Glycerol-3-phosphate	2.46	1.43	5.53	0.36	↑##	↓**	–
4	1.934	154.062	$C_6H_9N_3O_2$	L-Histidine	1.96	1.94	1.79	0.58	↑##	↓**	a
5	1.204	239.017	$C_6H_{12}N_2O_4S_2$	L-Cystine	1.74	1.30	3.08	0.49	↑##	↓*	–
6	1.185	221.067	$C_6H_{13}O_9P$	D-Fructose 1-phosphate	2.16	1.81	2.84	0.40	↑##	↓**	d
7	1.192	253.057	$C_7H_{15}O_{10}P$	D-Sedoheptulose 7-phosphate	1.98	1.67	4.01	0.31	↑##	↓**	–
8	1.184	259.022	$C_6H_{13}O_9P$	D-Mannose 6-phosphate	2.09	1.80	3.04	0.36	↑##	↓**	d
9	1.182	223.046	$C_6H_{13}O_9P$	D-Glucose 6-phosphate	2.10	1.96	2.60	0.40	↑##	↓**	d
10	5.933	122.097	$C_8H_{11}N$	2-Phenylethylamine	1.33	2.14	3.33	0.11	↑##	↓**	b
11	15.175	387.362	$C_{27}H_{46}O$	Cholesterol	1.63	1.22	1.83	0.60	↑##	↓*	–
12	10.184	595.350	$C_{33}H_{46}N_4O_6$	Stercobilin	1.20	1.58	1.99	0.45	↑#	↓*	–
13	1.225	131.046	$C_4H_8N_2O_3$	Asparagine	1.67	1.70	1.69	0.60	↑##	↓**	a,c
14	1.216	192.988	$C_3H_8NaO_6P$	3-Phosphoglyceric acid	1.75	1.82	3.28	0.30	↑##	↓**	–
15	1.069	112.087	$C_5H_9N_3$	Histamine	1.78	1.49	2.15	0.52	↑##	↓**	a
16	1.489	261.037	$C_6H_{13}O_9P$	Glucose 1-phosphate	1.09	1.84	2.38	0.20	↑#	↓**	d
17	15.452	759.567	$C_{39}H_{77}N_2O_6P$	Sphingomyelin	1.92	1.22	2.01	0.64	↑##	↓*	–
18	15.111	429.374	$C_{29}H_{50}O_2$	DL-α-Tocopherol	1.99	1.25	2.25	0.59	↑##	↓**	–
19	1.19	262.093	$C_8H_{16}NO_9P$	N-Acety-D-glucosamine1-phosphate	2.08	1.67	2.48	0.50	↑##	↓**	–
20	13.163	331.228	$C_{21}H_{32}O_3$	17-Hydroxypregnenolone	1.53	1.54	0.39	2.31	↓##	↑**	–
21	1.092	129.139	$C_7H_{19}N_3$	Spermidine	1.90	1.77	0.40	2.28	↓##	↑**	–
22	1.109	203.223	$C_{10}H_{26}N_4$	Spermine	1.82	1.06	0.61	1.63	↓#	↑*	–
23	15.612	583.255	$C_{33}H_{34}N_4O_6$	Biliverdin	1.34	0.47	2.30	0.69	↑#	↓	–
24	1.207	191.056	$C_5H_{11}O_8P$	D-Ribose-1-phosphate	1.71	1.48	2.39	0.54	↑##	↓**	–
25	12.596	583.257	$C_{33}H_{36}N_4O_6$	Bilirubin	1.54	1.15	1.57	0.71	↑##	↓**	–
26	1.195	132.030	$C_4H_7NO_4$	L-Aspartic acid	1.19	1.53	0.68	1.43	↓#	↑*	c
27	1.192	229.012	$C_5H_{11}O_8P$	D-Xylulose 5-phosphate	1.62	1.70	1.45	0.49	↑##	↓**	–

*Note: Control, Model, and TFP, groups (n = 6 per group). #, p < 0.05 compared with the Control group; ##, p < 0.01 compared with the Control group; *, p < 0.05 compared with the Model group; **, p < 0.01 compared with the Model group; ↑content increased; ↓, content decreased; vs, versus; C: control group; M: model group; TFP: TFP, group. (a) Histidine metabolism. (b) Phenylalanine metabolism (c) Alanine, aspartate and glutamate metabolism. (d) Amino sugar and nucleotide sugar metabolism.*

Effect of TFP on Serum Metabolism in CIA Rats

Changes of metabolites in serum were investigated using untargeted metabolomics. The Principal Component Analysis (PCA) model showed the significant group separation between the Control and Model groups and between the Model and TFP groups (**Figures 4A,C**). The orthogonal projections to latent structures (OPLS-DA) model also showed a significant difference in metabolomics data between the control and model groups and between the model and TFP groups. Overfitting in the OPLS-DA model was controlled by seven rounds of cross-validation and 200 repetitions (RPT) based on R2 and Q2 values (**Figures 4B,D**). 27 common differential metabolites between control/model and model/TFP groups were identified and FDR calculation confirmed the statistical significances. The significant differential metabolites are: Vitamin A, dUDP, Glycerol-3-phosphate, L-Histidine, L-Cystine, D-Fructose 1-phosphate, D-Sedoheptulose 7-phosphate, D-Mannose 6-phosphate, D-Glucose 6-phosphate, 2-Phenylethylamine, Cholesterol, Stercobilin, Asparagine, 3-Phosphoglyceric acid, Histamine, Glucose 1-phosphate, sphingomyelin, DL-α-Tocopherol, N-Acetyl-α-D-glucosamine 1-phosphate, Biliverdin, D-Ribose-1-phosphate, Bilirubin, and D-Xylulose 5-phosphate (**Table 2**). Pathway analysis resulted in a total of 29 metabolic pathways as shown in **Figures 4E,F**, and they were further analyzed below.

Correlation Analysis Between Untargeted Metabolomics and Gut Microbiota

Common pathways were investigated between those obtained from PICRUSt of 16S rRNA sequencing and those related to the differential metabolomics ($p < 0.05$, Impact >0.1), which resulted in four pathways: Histidine metabolism, Phenylalanine metabolism, Alanine, aspartate and glutamate metabolism, as well as amino sugar and nucleotide sugar metabolism (remarked in red in **Figures 3J,K** and noted with 'a', 'b', 'c', 'd' in **Figures 4E,F**).

Spearman's analysis was conducted between the 27 differential metabolites and the gut microbiota modulated by TFP at genus level (**Figure 4G**). *Lactobacillus* and Christensenellaceae_R-7_group had significant positive correlations with the abnormal changes of serum metabolites in RA rat models. In contrast, *Bacteroides* and *Prevotellaceae_UCG-001* showed negative correlations with those changes in CIA rat models. Notably, *Lactobacillus* exhibited correlations with all the metabolites.

Chemical Composition of TFP

Supplementary Figure S1 and **Figure 2** exhibited chemical composition profile of TFP methanol extract obtained through

HPLC. Seven major ingredients were identified: ferulic acid, gallic acid, catechin hydrate, gentiopicroside, ellagic acid, piperine, and dehydrocostus lactone. Their respective structures are showed in **Supplementary Material S3**.

DISCUSSION

The complexity of RA calls for multi-target therapeutics (He et al., 2016). Studies have shown that ethnomedicine has a unique effect on the treatment of RA (Rather et al., 2013; Xiao et al., 2018; Li et al., 2021). The traditional Tibetan medicine, TFP, has a significant clinical effect in the treatment of RA, but its mechanism of action has not yet been studied.

The collagen-induced RA model is a well established and widely used animal model used to explore the mechanism of RA as well as the pharmacological effects of relevant trial drugs; this is because the comprising tissue the model is made up of produces similar features to human clinical RA in histopathological and immunological terms (Bessis et al., 2017; Lu et al., 2018). In this study, RA models were established in CIA rats to evaluate the therapeutic effect of TFP on RA. CIA model rats treated with TFP showed significant improvement in weight gain, pathological phenomena in joints, as well as decreased serum levels of TNF-α, IL-6 and increased level of IL-4 and IL-10.

Both TNF-α and IL-6 are important pro-inflammatory cytokines in the progression of RA (Tanaka et al., 2014; McInnes et al., 2016; Mateen et al., 2016). For example, TNF-α can mediate the activation of the NF-kB pathway, promote RA synovitis, and promote pannus formation (Medoff et al., 2009; Piga et al., 2014). IL-6 promotes the differentiation of Th17 cells and inhibits the differentiation of Treg cells (Tanaka et al., 2014); while IL-6 receptor antagonist reduces the inflammatory disease activity of RA (McInnes et al., 2015). IL-4 and IL-10, as anti-inflammatory cytokines, can limit the inflammatory process of RA (Leung et al., 2002; Finnegan et al., 2003; Henningsson et al., 2012; Lin et al., 2015). Studies have indicated arthritis is aggravated in CIA rats receiving anti-IL-10 antibodies (Finnegan et al., 2003), and the use of IL-10 significantly eased the collagen-induced joint swelling, infiltration, cytokine synthesis, cartilage deformity, and necrosis (Henningsson et al., 2012). IL-4 are used to treat various autoimmune models *in vivo*(Haikal et al., 2019); itregulates the polarization and activity of macrophages by inhibiting the Th1-mediated pro-inflammatory effect, thereby enhancing the Th2-mediated anti-inflammatory effect (Lin et al., 2015).

As a chronic autoimmune disease, the inflammation of RA cannot resolve spontaneously; therefore, the homeostasis of inflammation regulation, namely inhibiting the development of inflammation and promoting the inflammation resolution, may be a new strategy for the treatment of RA (Chen Z. et al., 2019). This study showed that TFP blocked the development of inflammation in RA rats not only by inhibiting the expression of inflammatory cytokines (TNF-α, IL-6), but also by increasing the expression of anti-inflammatory cytokines (IL-4 and IL-10). Such two-way regulation may be an advantage of TFP in treating RA, although the mechanism behind it needs further investigation.

Furthermore, we found that CIA model rats that had reduced diversities of gut microbiota were restored by TFP therapy. This is consistent with findings from other researchers, which showed that decreased diversity of gut microbiota in RA patients or RA model animals can be restored to their normal levels after treatment (Xiao et al., 2018; Li et al., 2021; Nayak et al., 2021). It should be noted that we observed a remarkable increase in gut microbiota organism abundance in TFP groups, which might be an indicator of improving pathologies. A recent cohort study based on meta-genome shotgun sequencing showed that the species richness of intestinal flora in RA patients with clinical improvement was higher than those without improvement in disease activity within 6 ~ 12 months (Gupta et al., 2021).

We found RA rats had an increased abundance of Firmicutes and a decreased abundance of Bacteroidetes compared with normal rats, which is in line with findings from a previously published report (Rogier et al., 2017). Moreover, such changes were reversed and restored to the levels in normal rats after TFP therapy. Firmicutes and Bacteroidetes are the main phyla of gut microbiota in humans and rats (Jandhyala et al., 2015; Li et al., 2021). Many of their subordinate microorganisms participate in digesting the complex polysaccharide in their host's food and produce short-chain fatty acids (SCFAs), the primary energy source of colonic mucosa, as well as essential regulators in host cell gene expression, inflammation, differentiation, and apoptosis (Hamer et al., 2008; Rosser et al., 2020).

At the genus level, TFP up-regulates the decreased abundance of *Bacteroides*, Eubacterium, *Prevotellaceae_UCG-001*, Blautia and Faecalibacterium, and downregulates the increased relative abundance of *Lactobacillus*, Romboutsia, Christensenellaceae_R-7_group in RA rats. In addition, 27 differential metabolites were identified and their relationship with the above eight genera of gut microbiota were analyzed. Four common metabolic pathways were found to be related to TFPs' therapeutic effects by regulating metabolic pathways and mediating gut microbiota, including the metabolism of: Histidine, Phenylalanine, Alanine/Aspartate/Glutamate, as well as Amino- and nucleotide sugars.

According to our findings, the KEGG pathway map and numerous literatures, we propose TFP's working mechanisms by illustrating relationships of metabolites, pathways and gut microbiota as shown in **Figure 5**. TFP affects the abundances *of Lactobacillus, Christensenellace_R-7_group, Bacteroides, and* Prevotellaceae*_UCG-001,* and then influences metabolic pathways in CIA rats; the two processes are mediated by several key metabolites bound up with the above intestinal bacteria.

Lactobacillus are the most abundant flora genus in our study, in line with a previous research (Li et al., 2021). Numerous researches have reported significant increased gut *Lactobacillus* in RA patients (Picchianti-Diamanti et al., 2018), especially in active RA patients (Zhang et al., 2015; Qiao et al., 2020). This was as also noted in animals susceptible to collagen-induced arthritis (Liu et al., 2016; Qiao et al., 2020). On the other hand, some species of *Lactobacillus* such as *Lactobacillus casei* is widely accepted as probiotic and has potential to be used to ameliorate RA (Cannarella et al., 2021). Different species of *Lactobacillus* may play divergent roles. An increased

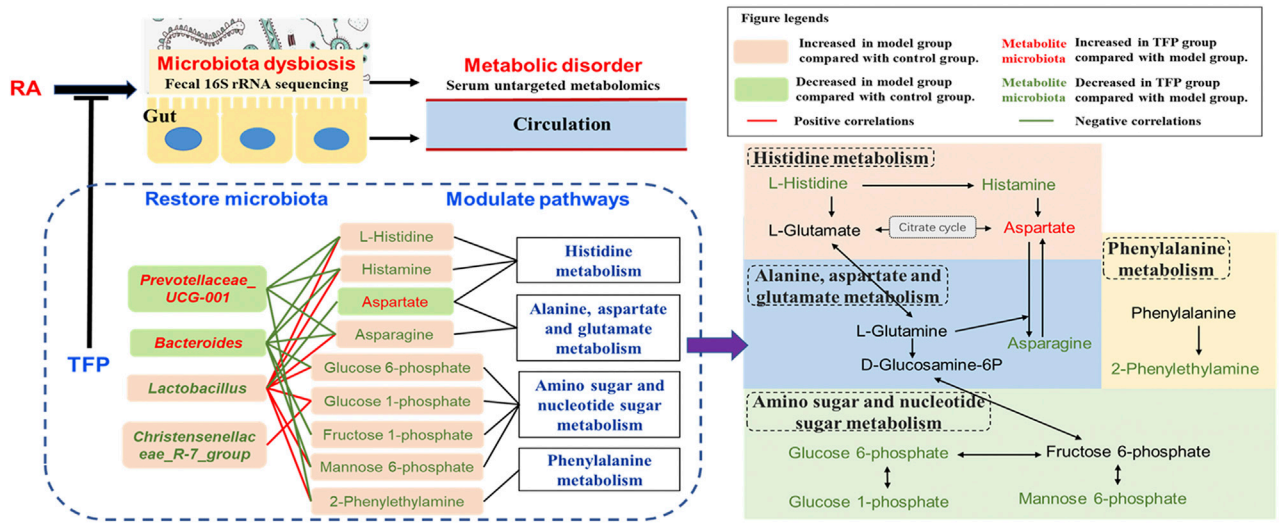

FIGURE 5 | Schematic diagram of TFP's mechanism based on modulation of gut Microbiota and metabolic pathways.

abundance of *Christensenellaceae_R-7_group* was reported in mice feaces of mice treated with high fat, but it dropped after administering medication (Gong et al., 2020).

Bacteroides, members of Bacteroidetes, are SCFAs producing bacteria. Kaori Kitamura er al revealed a protective effect of *Bacteroides* on the inflammatory changes of RA mice (Kitamura et al., 2021). Jin ZL et al. reported a significant decline of *Bacteroides* in the gut of RA rats, but the abundance of *Bacteroides* were elevated after treating with probiotics (Jin and Chen, 2020). Prevotellaceae_*UCG-001* has been found significantly decreased in colitis model mice and could have a protective effect on the intestinal mucosal barrier function (Hu et al., 2020).

Histidine Metabolism

Histamine, mediated by the activation of its four receptors (H1R–H4R), exhibits extensive effects related to visceral fat mass. It is known to function as a human neurotransmitter, a modulator of inflammatory and immune responses, and a key mediator of several allergic pathways and autoimmune pathogeneses (Mohammad et al., 2009). Innate and adaptive immune cells throughout the body can produce histamine by decarboxylation of the amino acid L-histidine by the enzyme histidine decarboxylase (HDC) (Jutel et al., 2009). Many bacteria are able to synthesize and secrete histamine as well and histamine has been considered as another central signal molecule that mediates bacteria–host interactions (Krell et al., 2021). For example, the administration of the histamine-secreting *Lactobacillus rhamnosus* had an anti-inflammatory effect by reducing the secretion of various interleukines and tumor necrosis factor *α* (Frei et al., 2013). However, another *Lactobacillus* species, L. saerimneri, which is able to secrete approximately 100-fold more histamine than L. rhamnosus, resulted in animal weight loss and signs of deteriorating health (Ferstl et al., 2014). Chen H et al. reported that *M. morganii* and L. reuteri strains generate histamine *in vitro* as well as *in vivo*, and that L-histidine significantly increases histamine production (Chen H. et al., 2019).

In our study, L-histidine and histamine was seen to have a positive correlation with *Lactobacillus* and a negative correlation with *Bacteroides* and *Prevotellaceae_UCG-001*. *Lactobacillus* revealed an unfavorable association with TFP's regulation of the pathway, whereas *Bacteroides* and *Prevotellaceae_UCG-001* had beneficial effects. It is likely that these bacteria have an impact on the utilization of exogenous L-histidine/histamine and (or) production of histamine by the host.

Phenylalanine Metabolism

Phenylalanine metabolism disorder with altered level of Phenylethylamine (PEA) has been suggested in RA models and RA patients by numerous studies (Xu et al., 2017; Liu et al., 2019; Tang et al., 2021). PEA is produced *via* decarboxylation of phenylalanine by the aromatic L-amino acid decarboxylase. Some gut bacteria such as *B. theta* could produce phenylalanine, a substrate for other intestinal bacteria stains to generate PEA; this metabolic exchange among gut bacteria has contributed to *in vivo* production of PEA and resulted in its increased level in host serum. (Chen H. et al., 2019). In addition, decreased PEA level in blood has been reported to be associated with improvement of osteoarthritis in patients (Smith-Ryan et al., 2020). Our study suggests that the elevated level of 2-Phenylethylamine (PEA) in RA rat serum was restored to normal by TFP through phenylalanine metabolism with the participation of *Lactobacillus* and *Prevotellaceae_UCG-001*. *Lactobacillus* upregulates serum level of PEA while *Prevotellaceae_UCG-001* down-regulates it.

Alanine, Aspartate and Glutamate Metabolism

L-asparagine (ASN) is synthesized by asparagine synthetase (ASNsynt, EC 6.3.5.4) from aspartic acid (also named aspartate) and L-glutamine (Gln) in nature, and it is the

substrate of ASNase (EC 3.5.1.1), which catalyzes its deamidation giving L-aspartic acid and ammonia as reaction products (Covini et al., 2012). Various microorganisms, including commensal intestinal bacteria have the capacity to secrete ASNase; ASNase has been used as an anti-tumor medicine for acute lymphoblastic leukemia and lymphosarcoma, which blocks exogenous ASN supply of tumor cells (Paul et al., 2019). In addition to reports related to antitumor, altered level of L-asparagine/L-aspartic acid has been linked to other diseases (Chen et al., 2020). Alanine, aspartate and glutamate metabolism disorder has also been reported with distinctly changed serum levels of L-aspartic acid and synovial tissue level of L-asparagine in CIA rats (Pang et al., 2021).

We observed a lower serum level of L-aspartic acid and a higher level of L-asparagine in RA rats compared with the control group; the concentration of the two compounds recovered after TFP treatment. Moreover, the abundance of *Lactobacillus* shows positive relation to serum L-asparagine concentration and negative relation to L-aspartic acid concentration, while *Bacteroides* and *Prevotellaceae_UCG-001* showed a negative correlation with serum L-asparagine level. Similar to modulation effects on histamine metabolism, it indicated that Lactobacillus has an adverse correlation with TFP's regulation of Alanine, aspartate and glutamate metabolism, while *Bacteroides* and *Prevotellaceae_UCG-001* show a beneficial correlation. Notably, Gln, a precursor for the synthesis of asparagine, can be produce from L-glutamate in histamine metabolism. Hence, we infer *Bacteroides* and *Prevotellaceae_UCG-001* mainly affects the generation of L-asparagine *via* L-glutamate/L-glutamine through histamine metabolism.

Amino Sugar and Nucleotide Sugar Metabolism

While the dysfunction of Amino sugar and nucleotide sugar metabolism has been reported in numerous metabolic abnormalities such as oxidative damage (Salau et al., 2020), dyslipidemia (Huang et al., 2020), and type 2 diabetes (Zhang et al., 2020), we have not found any significant association of this pathway relating to RA in previous researches. In our study, several key metabolites in Amino sugar and nucleotide sugar metabolism are modulated by TFP, which is mediated by *Lactobacillus*, Christensenellace_R-7_group, *Bacteroides*, and *Prevotellaceae_UCG-001*.

As shown in **Figure 5**, Histidine, Alanine, aspartate and glutamate metabolism, as well as Amino- and nucleotide sugar metabolism, influence each other through L-Glutamate, L-Glutamine, D-Glucosamine-6P, and Fructose 6-phosphate. Considering the aforementioned, we speculate that influences on serum L-histidine/histamine concentrations might be a major contributor to TFP's therapeutic effects in RA rats, mediated by gut microbiota.

CONCLUSION

In summary, our study revealed various ameliorative effects of TFP on RA, including promoting weight gain, improving pathological phenomena in joints, relieving inflammation, and favorably regulating cytokines. These effects most likely relates to the improvement of the dysbiosis that exists in the gut flora, as well as the modulation of Histidine metabolism, Phenylalanine metabolism, Alanine, aspartate and glutamate metabolism, in addition to Amino sugar and nucleotide sugar metabolism (**Figure 5**). As this is a preliminary in the field, there are a few limitations to it: 1) the dose planning is a little rough without giving an optimal range; 2) we only included pharmacodynamic indexes that were inflammation related, which is not comprehensive; and 3) sequencing and analytical techniques, as well as examination of gut microbiota did not get to the species level, which may result in non-precise conclusions and requires further exploration.

DATA AVAILABILITY STATEMENT

The datasets presented in this study can be found in online repositories. The names of the repository/repositories and accession number(s) can be found below: PRJNA786950.

ETHICS STATEMENT

The animal study was reviewed and approved by the Animal Ethics Committee of Tibet University.

AUTHOR CONTRIBUTIONS

ZL and LN: Conceive ideas, collect and analyse data, write the article. LY and LJ: Animal experiment implementation. BD and JY: Article revision. XZ: Supportive work. HC: Design experiments. YL and OL: Fund experiments.

FUNDING

This study was funded by National Natural Science Foundation of China (31660308), Natural Science Foundation of Tibet Autonomous Region (XZ 2018ZR G-05), Scientific research and cultivation fund of Tibet University (ZDCZJH21-07) and Central Government Funds for the Reform and Development of Local Colleges and Universities (Grant No: ZCKJ2020-11).

ACKNOWLEDGMENTS

Thanks to the Innovation Center for Traditional Tibetan Medicine Modernization and Quality Control for partially providing experimental platform.

SUPPLEMENTARY MATERIAL

The Supplementary Material for this article can be found online at: https://www.frontiersin.org/articles/10.3389/fphar.2022.828920/full#supplementary-material

REFERENCES

Ardalan, M., and Vahed, S. Z. (2017). Gut Microbiota and Renal Transplant Outcome. *Biomed. Pharmacother.* 90, 229–236. doi:10.1016/j.biopha.2017.02.114

Bessis, N., Decker, P., Assier, E., Semerano, L., and Boissier, M.-C. (2017). Arthritis Models: Usefulness and Interpretation. *Semin. Immunopathol.* 39 (4), 469–486. doi:10.1007/s00281-017-0622-4

Bodkhe, R., Balakrishnan, B., and Taneja, V. (2019). The Role of Microbiome in Rheumatoid Arthritis Treatment. *Ther. Adv. Musculoskelet.* 11, 1759720X1984463. doi:10.1177/1759720x19844632

Brandl, C., Bucci, L., Schett, G., and Zaiss, M. M. (2021). Crossing the Barriers: Revisiting the Gut Feeling in Rheumatoid Arthritis. *Eur. J. Immunol.* 51 (4), 798–810. doi:10.1002/eji.202048876

Cannarella, L. A. T., Mari, N. L., Alcântara, C. C., Iryioda, T. M. V., Costa, N. T., Oliveira, S. R., et al. (2021). Mixture of Probiotics Reduces Inflammatory Biomarkers and Improves the Oxidative/nitrosative Profile in People with Rheumatoid Arthritis. *Nutrition* 89, 111282. doi:10.1016/j.nut.2021.111282

Castro Rocha, F. A., Duarte-Monteiro, A. M., Henrique da Mota, L. M., Matias Dinelly Pinto, A. C., and Fonseca, J. E. (2020). Microbes, Helminths, and Rheumatic Diseases. *Best Pract. Res. Clin. Rheumatol.* 34 (4), 101528. doi:10.1016/j.berh.2020.101528

Chen, X., Xu, J., Tang, J., Dai, X., Huang, H., Cao, R., et al. (2020). Dysregulation of Amino Acids and Lipids Metabolism in Schizophrenia with Violence. *BMC Psychiatry* 20 (1), 97. doi:10.1186/s12888-020-02499-y

Chen, H., Nwe, P.-K., Yang, Y., Rosen, C. E., Bielecka, A. A., Kuchroo, M., et al. (2019). A Forward Chemical Genetic Screen Reveals Gut Microbiota Metabolites that Modulate Host Physiology. *Cell* 177 (5), 1217–1231. e1218. doi:10.1016/j.cell.2019.03.036

Chen, Z., Bozec, A., Ramming, A., and Schett, G. (2019). Anti-inflammatory and Immune-Regulatory Cytokines in Rheumatoid Arthritis. *Nat. Rev. Rheumatol.* 15 (1), 9–17. doi:10.1038/s41584-018-0109-2

Cheng, H., Liu, J., Tan, Y., Feng, W., and Peng, C. (2021). Interactions between Gut Microbiota and Berberine, a Necessary Procedure to Understand the Mechanisms of Berberine. *J. Pharm. Anal.* doi:10.1016/j.jpha.2021.10.003

Covini, D., Tardito, S., Bussolati, O., R. Chiarelli, L., V. Pasquetto, M., Digilio, R., et al. (2012). Expanding Targets for a Metabolic Therapy of Cancer: L-Asparaginase. *Recent Patents Anti-Cancer Drug Discov.* 7 (1), 4–13. doi:10.2174/157489212798358001

Cui, H., Li, Y., Cao, M., Liao, J., Liu, X., Miao, J., et al. (2020a). Untargeted Metabolomic Analysis of the Effects and Mechanism of Nuciferine Treatment on Rats with Nonalcoholic Fatty Liver Disease. *Front. Pharmacol.* 11, 858. doi:10.3389/fphar.2020.00858

Cui, H., Li, Y., Wang, Y., Jin, L., Yang, L., Wang, L., et al. (2020b). Da-Chai-Hu Decoction Ameliorates High Fat Diet-Induced Nonalcoholic Fatty Liver Disease through Remodeling the Gut Microbiota and Modulating the Serum Metabolism. *Front. Pharmacol.* 11, 584090. doi:10.3389/fphar.2020.584090

de Oliveira, G. L. V., Leite, A. Z., Higuchi, B. S., Gonzaga, M. I., and Mariano, V. S. (2017). Intestinal Dysbiosis and Probiotic Applications in Autoimmune Diseases. *Immunology* 152 (1), 1–12. doi:10.1111/imm.12765

Ferstl, R., Frei, R., Schiavi, E., Konieczna, P., Barcik, W., Ziegler, M., et al. (2014). Histamine Receptor 2 Is a Key Influence in Immune Responses to Intestinal Histamine-Secreting Microbes. *J. Allergy Clin. Immunol.* 134 (3), 744–746. doi:10.1016/j.jaci.2014.04.034

Finnegan, A., Kaplan, C. D., Cao, Y., Eibel, H., Glant, T. T., and Zhang, J. (2003). Collagen-induced Arthritis Is Exacerbated in IL-10-deficient Mice. *Arthritis Res. Ther.* 5 (1), R18–R24. doi:10.1186/ar601

Frei, R., Ferstl, R., Konieczna, P., Ziegler, M., Simon, T., Rugeles, T. M., et al. (2013). Histamine Receptor 2 Modifies Dendritic Cell Responses to Microbial Ligands. *J. Allergy Clin. Immunol.* 132 (1), 194–204. doi:10.1016/j.jaci.2013.01.013

Gong, S., Ye, T., Wang, M., Wang, M., Li, Y., Ma, L., et al. (2020). Traditional Chinese Medicine Formula Kang Shuai Lao Pian Improves Obesity, Gut Dysbiosis, and Fecal Metabolic Disorders in High-Fat Diet-Fed Mice. *Front. Pharmacol.* 11, 297. doi:10.3389/fphar.2020.00297

Guerreiro, C. S., Calado, Â., Sousa, J., and Fonseca, J. E. (2018). Diet, Microbiota, and Gut Permeability-The Unknown Triad in Rheumatoid Arthritis. *Front. Med.* 5, 349. doi:10.3389/fmed.2018.00349

Gupta, V. K., Cunningham, K. Y., Hur, B., Bakshi, U., Huang, H., Warrington, K. J., et al. (2021). Gut Microbial Determinants of Clinically Important Improvement in Patients with Rheumatoid Arthritis. *Genome Med.* 13 (1), 149. doi:10.1186/s13073-021-00957-0

Haikal, S. M., Abdeltawab, N. F., Rashed, L. A., Abd El-Galil, T. I., Elmalt, H. A., and Amin, M. A. (2019). Combination Therapy of Mesenchymal Stromal Cells and Interleukin-4 Attenuates Rheumatoid Arthritis in a Collagen-Induced Murine Model. *Cells* 8 (8), 823. doi:10.3390/cells8080823

Hamer, H. M., Jonkers, D., Venema, K., Vanhoutvin, S., Troost, F. J., and Brummer, R.-J. (2008). Review Article: the Role of Butyrate on Colonic Function. *Aliment. Pharmacol. Ther.* 27 (2), 104–119. doi:10.1111/j.1365-2036.2007.03562.x

He, B., Lu, C., Zheng, G., He, X., Wang, M., Chen, G., et al. (2016). Combination Therapeutics in Complex Diseases. *J. Cel. Mol. Med.* 20 (12), 2231–2240. doi:10.1111/jcmm.12930

Henningsson, L., Eneljung, T., Jirholt, P., Tengvall, S., Lidberg, U., van den Berg, W. B., et al. (2012). Disease-dependent Local IL-10 Production Ameliorates Collagen Induced Arthritis in Mice. *PLoS One* 7 (11), e49731. doi:10.1371/journal.pone.0049731

Hu, L., Jin, L., Xia, D., Zhang, Q., Ma, L., Zheng, H., et al. (2020). Nitrate Ameliorates Dextran Sodium Sulfate-Induced Colitis by Regulating the Homeostasis of the Intestinal Microbiota. *Free Radic. Biol. Med.* 152, 609–621. doi:10.1016/j.freeradbiomed.2019.12.002

Huang, Z.-R., Chen, M., Guo, W.-L., Li, T.-T., Liu, B., Bai, W.-D., et al. (2020). Monascus Purpureus-Fermented Common Buckwheat Protects against Dyslipidemia and Non-alcoholic Fatty Liver Disease through the Regulation of Liver Metabolome and Intestinal Microbiome. *Food Res. Int.* 136, 109511. doi:10.1016/j.foodres.2020.109511

Jandhyala, S. M., Talukdar, R., Subramanyam, C., Vuyyuru, H., Sasikala, M., and Nageshwar Reddy, D. (2015). Role of the normal Gut Microbiota. *World J. Gastroenterol.* 21 (29), 8787–8803. doi:10.3748/wjg.v21.i29.8787

Jiang, Y., Zheng, Y., Dong, Q., Liao, W., Pang, L., Chen, J., et al. (2022). Metabolomics Combined with Network Pharmacology to Study the Mechanism of Shentong Zhuyu Decoction in the Treatment of Rheumatoid Arthritis. *J. Ethnopharmacol.* 285, 114846. doi:10.1016/j.jep.2021.114846

Jiao, Y., Wu, L., Huntington, N. D., and Zhang, X. (2020). Crosstalk between Gut Microbiota and Innate Immunity and its Implication in Autoimmune Diseases. *Front. Immunol.* 11, 282. doi:10.3389/fimmu.2020.00282

Jin, Z. L., and Chen, X. C. (2020). Changes in Intestinal Florae and Serum Inflammation in Rheumatoid Arthritis Rats and the Effects of Probiotics. *Eur. Rev. Med. Pharmacol. Sci.* 24 (22), 11820–11826. doi:10.26355/eurrev_202011_23839

Jutel, M., Akdis, M., and Akdis, C. A. (2009). Histamine, Histamine Receptors and Their Role in Immune Pathology. *Clin. Exp. Allergy* 39 (12), 1786–1800. doi:10.1111/j.1365-2222.2009.03374.x

Kim, D., Zeng, M. Y., and Núñez, G. (2017). The Interplay between Host Immune Cells and Gut Microbiota in Chronic Inflammatory Diseases. *Exp. Mol. Med.* 49 (5), e339. doi:10.1038/emm.2017.24

Kitamura, K., Sasaki, M., Matsumoto, M., Shionoya, H., and Iida, K. (2021). Protective Effect of Bacteroides Fragilis LPS on Escherichia coli LPS-Induced Inflammatory Changes in Human Monocytic Cells and in a Rheumatoid Arthritis Mouse Model. *Immunol. Lett.* 233, 48–56. doi:10.1016/j.imlet.2021.03.008

Krell, T., Gavira, J. A., Velando, F., Fernández, M., Roca, A., Monteagudo-Cascales, E., et al. (2021). Histamine: A Bacterial Signal Molecule. *Int. J. Mol. Sci.* 22 (12), 6312. doi:10.3390/ijms22126312

Leung, B. P., Conacher, M., Hunter, D., McInnes, I. B., Liew, F. Y., and Brewer, J. M. (2002). A Novel Dendritic Cell-Induced Model of Erosive Inflammatory Arthritis: Distinct Roles for Dendritic Cells in T Cell Activation and Induction of Local Inflammation. *J. Immunol.* 169 (12), 7071–7077. doi:10.4049/jimmunol.169.12.7071

Li, M., and Wang, F. (2021). Role of Intestinal Microbiota on Gut Homeostasis and Rheumatoid Arthritis. *J. Immunol. Res.* 2021, 1–9. doi:10.1155/2021/8167283

Li, Y., Dai, M., Wang, L., and Wang, G. (2021). Polysaccharides and Glycosides from Aralia Echinocaulis Protect Rats from Arthritis by Modulating the Gut Microbiota Composition. *J. Ethnopharmacol.* 269, 113749. doi:10.1016/j.jep.2020.113749

Li, C. (2014). Clinical Observation of Tibetan Medicine in the Treatment of Rheumatoid Arthritis with Kidney Deficiency and Cold Excess Syndrome. *J. Med. Pharm. Chin. Minorities* 07 (20), 9–10. doi:10.3969/j.issn.1006-6810.2014.07.005

Lin, S., Qiu, M., and Chen, J. (2015). IL-4 Modulates Macrophage Polarization in Ankylosing Spondylitis. *Cell Physiol. Biochem.* 35 (6), 2213–2222. doi:10.1159/000374026

Liu, X., Zeng, B., Zhang, J., Li, W., Mou, F., Wang, H., et al. (2016). Role of the Gut Microbiome in Modulating Arthritis Progression in Mice. *Sci. Rep.* 6 (1), 30594. doi:10.1038/srep30594

Liu, Y., Wei, M., Yue, K., Wang, R., Ma, Y., Men, L., et al. (2019). Non-target Metabonomic Method provided New Insights on the Therapeutical Mechanism of Gancao Fuzi Decoction on Rheumatoid Arthritis Rats. *J. Chromatogr. B* 1105, 93–103. doi:10.1016/j.jchromb.2018.11.015

Liu, J., Wang, X., Wang, S., and Liu, F. (2021). Therapeutic Potential of Non-coding RNAs and TLR Signalling Pathways in Rheumatoid Arthritis. *Curr. Pharm. Biotechnol.* 22 (11), 1490–1500. doi:10.2174/1389201021666201001142829

Lu, D. R., McDavid, A. N., Kongpachith, S., Lingampalli, N., Glanville, J., Ju, C.-H., et al. (2018). T Cell-dependent Affinity Maturation and Innate Immune Pathways Differentially Drive Autoreactive B Cell Responses in Rheumatoid Arthritis. *Arthritis Rheumatol.* 70 (11), 1732–1744. doi:10.1002/art.40578

Maeda, Y., Kumanogoh, A., and Takeda, K. (2016). Altered Composition of Gut Microbiota in Rheumatoid Arthritis Patients. *Jpn. J. Clin. Immunol.* 39 (1), 59–63. doi:10.2177/jsci.39.59

Marchev, A. S., Vasileva, L. V., Amirova, K. M., Savova, M. S., Balcheva-Sivenova, Z. P., and Georgiev, M. I. (2021). Metabolomics and Health: from Nutritional Crops and Plant-Based Pharmaceuticals to Profiling of Human Biofluids. *Cell. Mol. Life Sci.* 78 (19-20), 6487–6503. doi:10.1007/s00018-021-03918-3

Mateen, S., Zafar, A., Moin, S., Khan, A. Q., and Zubair, S. (2016). Understanding the Role of Cytokines in the Pathogenesis of Rheumatoid Arthritis. *Clin. Chim. Acta* 455, 161–171. doi:10.1016/j.cca.2016.02.010

McInnes, I. B., Thompson, L., Giles, J. T., Bathon, J. M., Salmon, J. E., Beaulieu, A. D., et al. (2015). Effect of Interleukin-6 Receptor Blockade on Surrogates of Vascular Risk in Rheumatoid Arthritis: MEASURE, a Randomised, Placebo-Controlled Study. *Ann. Rheum. Dis.* 74 (4), 694–702. doi:10.1136/annrheumdis-2013-204345

McInnes, I. B., Buckley, C. D., and Isaacs, J. D. (2016). Cytokines in Rheumatoid Arthritis - Shaping the Immunological Landscape. *Nat. Rev. Rheumatol.* 12 (1), 63–68. doi:10.1038/nrrheum.2015.171

Medoff, B. D., Seung, E., Hong, S., Thomas, S. Y., Sandall, B. P., Duffield, J. S., et al. (2009). CD11b+Myeloid Cells Are the Key Mediators of Th2 Cell Homing into the Airway in Allergic Inflammation. *J. Immunol.* 182 (1), 623–635. doi:10.4049/jimmunol.182.1.623

Mohammad, S., Trivendra, T., Farrukh, S., Shagufta, M., Mashiatullah, S., and Ali, K. R. (2009). Histamine, Histamine Receptors, and Their Role in Immunomodulation: An Updated Systematic Review. *Open Immunol. J.* 2 (1), 9–41. doi:10.2174/1874226200902010009

Nayak, R. R., Alexander, M., Deshpande, I., Stapleton-Gray, K., Rimal, B., Patterson, A. D., et al. (2021). Methotrexate Impacts Conserved Pathways in Diverse Human Gut Bacteria Leading to Decreased Host Immune Activation. *Cell Host Microbe* 29 (3), 362–377. e311. doi:10.1016/j.chom.2020.12.008

Owen, J. L., and Mohamadzadeh, M. (2013). Microbial Activation of Gut Dendritic Cells and the Control of Mucosal Immunity. *J. Interferon Cytokine Res.* 33 (11), 619–631. doi:10.1089/jir.2013.0046

Oyenihi, O. R., Oyenihi, A. B., Erhabor, J. O., Matsabisa, M. G., and Oguntibeju, O. O. (2021). Unravelling the Anticancer Mechanisms of Traditional Herbal Medicines with Metabolomics. *Molecules* 26 (21), 6541. doi:10.3390/molecules26216541

Pang, X.-t., Zhang, Y.-y., Leng, Y.-f., Yao, Y., Zhang, R., Wang, D.-w., et al. (2021). Metabolomics Study of Biochemical Changes in the Serum and Articular Synovium Tissue of Moxibustion in Rats with Collagen-Induced Arthritis. *World J. Acupuncture - Moxibustion* 31 (1), 30–43. doi:10.1016/j.wjam.2020.09.004

Paul, T., Mondal, A., and Bandyopadhyay, T. K. (2019). Isolation, Purification, Characterisation and Application of L-ASNase: A Review. *Recent Patents Biotechnol.* 13 (1), 33–44. doi:10.2174/1872208312666181012150407

Picchianti-Diamanti, A., Panebianco, C., Salemi, S., Sorgi, M., Di Rosa, R., Tropea, A., et al. (2018). Analysis of Gut Microbiota in Rheumatoid Arthritis Patients: Disease-Related Dysbiosis and Modifications Induced by Etanercept. *Int. J. Mol. Sci.* 19 (10), 2938. doi:10.3390/ijms19102938

Piga, M., Chessa, E., Ibba, V., Mura, V., Floris, A., Cauli, A., et al. (2014). Biologics-induced Autoimmune Renal Disorders in Chronic Inflammatory Rheumatic Diseases: Systematic Literature Review and Analysis of a Monocentric Cohort. *Autoimmun. Rev.* 13 (8), 873–879. doi:10.1016/j.autrev.2014.05.005

Qiao, S., Lian, X., Yue, M., Zhang, Q., Wei, Z., Chen, L., et al. (2020). Regulation of Gut Microbiota Substantially Contributes to the Induction of Intestinal Treg Cells and Consequent Anti-arthritis Effect of Madecassoside. *Int. Immunopharmacol.* 89 (Pt A), 107047. doi:10.1016/j.intimp.2020.107047

Rather, M. A., Bhat, B. A., and Qurishi, M. A. (2013). Multicomponent Phytotherapeutic Approach Gaining Momentum: Is the "one Drug to Fit All" Model Breaking Down. *Phytomedicine* 21 (1), 1–14. doi:10.1016/j.phymed.2013.07.015

Rogier, R., Evans-Marin, H., Manasson, J., van der Kraan, P. M., Walgreen, B., Helsen, M. M., et al. (2017). Alteration of the Intestinal Microbiome Characterizes Preclinical Inflammatory Arthritis in Mice and its Modulation Attenuates Established Arthritis. *Sci. Rep.* 7 (1), 15613. doi:10.1038/s41598-017-15802-x

Rosser, E. C., Piper, C. J. M., Matei, D. E., Blair, P. A., Rendeiro, A. F., Orford, M., et al. (2020). Microbiota-Derived Metabolites Suppress Arthritis by Amplifying Aryl-Hydrocarbon Receptor Activation in Regulatory B Cells. *Cel Metab.* 31 (4), 837–851. e810. doi:10.1016/j.cmet.2020.03.003

Salau, V. F., Erukainure, O. L., Koorbanally, N. A., and Islam, M. S. (2020). Kolaviron Modulates Dysregulated Metabolism in Oxidative Pancreatic Injury and Inhibits Intestinal Glucose Absorption with Concomitant Stimulation of Muscle Glucose Uptake. *Arch. Physiol. Biochem.*, 1–11. doi:10.1080/13813455.2020.1806331

Smith-Ryan, A. E., Blue, M. N. M., Anderson, K. C., Hirsch, K. R., Allen, K. D., Huebner, J. L., et al. (2020). Metabolic and Physiological Effects of High Intensity Interval Training in Patients with Knee Osteoarthritis: A Pilot and Feasibility Study. *Osteoarthritis Cartilage Open* 2 (4), 100083. doi:10.1016/j.ocarto.2020.100083

Tanaka, T., Narazaki, M., and Kishimoto, T. (2014). IL-6 in Inflammation, Immunity, and Disease. *Cold Spring Harbor Perspect. Biol.* 6 (10), a016295. doi:10.1101/cshperspect.a016295

Tang, M., Gao, X., Geng, T., Chen, X., Wang, J., Shen, C., et al. (2021). Metabolomics Analysis of the Therapeutic Effects of Qiwei Tongbi Oral Liquid on Rheumatoid Arthritis in Rats. *J. Pharm. Biomed. Anal.* 202, 114166. doi:10.1016/j.jpba.2021.114166

Teng, F., Felix, K. M., Bradley, C. P., Naskar, D., Ma, H., Raslan, W. A., et al. (2017). The Impact of Age and Gut Microbiota on Th17 and Tfh Cells in K/BxN Autoimmune Arthritis. *Arthritis Res. Ther.* 19 (1), 188. doi:10.1186/s13075-017-1398-6

Tobón, G. J., Youinou, P., and Saraux, A. (2010). The Environment, Geo-Epidemiology, and Autoimmune Disease: Rheumatoid Arthritis. *Autoimmun. Rev.* 9 (5), A288–A292. doi:10.1016/j.autrev.2009.11.019

Tsai, Y.-W., Dong, J.-L., Jian, Y.-J., Fu, S.-H., Chien, M.-W., Liu, Y.-W., et al. (2021). Gut Microbiota-Modulated Metabolomic Profiling Shapes the Etiology and Pathogenesis of Autoimmune Diseases. *Microorganisms* 9 (9), 1930. doi:10.3390/microorganisms9091930

Wen, B., Mei, Z., Zeng, C., and Liu, S. (2017). metaX: a Flexible and Comprehensive Software for Processing Metabolomics Data. *BMC Bioinformatics* 18 (1), 183. doi:10.1186/s12859-017-1579-y

Wu, H.-J., Ivanov, I. I., Darce, J., Hattori, K., Shima, T., Umesaki, Y., et al. (2010). Ivanov, IIGut-Residing Segmented Filamentous Bacteria Drive Autoimmune Arthritis via T Helper 17 Cells. *Immunity* 32 (6), 815–827. doi:10.1016/j.immuni.2010.06.001

Wu, J., Wei, Z., Cheng, P., Qian, C., Xu, F., Yang, Y., et al. (2020). Rhein Modulates Host Purine Metabolism in Intestine through Gut Microbiota and Ameliorates Experimental Colitis. *Theranostics* 10 (23), 10665–10679. doi:10.7150/thno.43528

Xiao, M., Fu, X., Ni, Y., Chen, J., Jian, S., Wang, L., et al. (2018). Protective Effects of Paederia Scandens Extract on Rheumatoid Arthritis Mouse Model by Modulating Gut Microbiota. *J. Ethnopharmacol.* 226, 97–104. doi:10.1016/j.jep.2018.08.012

Xu, T., Feng, G., Zhao, B., Zhao, J., Pi, Z., Liu, S., et al. (2017). A Non-target Urinary and Serum Metabolomics Strategy Reveals Therapeutical Mechanism of Radix Astragali on Adjuvant-Induced Arthritis Rats. *J. Chromatogr. B* 1048, 94–101. doi:10.1016/j.jchromb.2017.01.040

Xu, H., Zhao, H., Fan, D., Liu, M., Cao, J., Xia, Y., et al. (2020). Interactions between Gut Microbiota and Immunomodulatory Cells in Rheumatoid Arthritis. *Mediators Inflamm.* 2020, 1–14. doi:10.1155/2020/1430605

Yang, W., and Cong, Y. (2021). Gut Microbiota-Derived Metabolites in the Regulation of Host Immune Responses and Immune-Related Inflammatory Diseases. *Cell Mol Immunol* 18 (4), 866–877. doi:10.1038/s41423-021-00661-4

Zha, S. (2017). Twenty Five Catechu Pill in the Treatment of Rheumatoid Arthritis Curative Effect Is Discussed in This Paper. *Smart Healthc.* 5 (3), 67–68. doi:10.19335/j.cnki.2096-1219.2017.05.28

Zhang, X., Zhang, D., Jia, H., Feng, Q., Wang, D., Liang, D., et al. (2015). The Oral and Gut Microbiomes Are Perturbed in Rheumatoid Arthritis and Partly Normalized after Treatment. *Nat. Med.* 21 (8), 895–905. doi:10.1038/nm.3914

Zhang, L., Luo, J., Li, X., Guo, S., and Shi, D. (2020). 16S rRNA Sequencing and Metagenomics Study of Gut Microbiota: Implications of BDB on Type 2 Diabetes Mellitus. *Mar. Drugs* 18 (9), 469. doi:10.3390/md18090469

Zou, C. C., and Yan, H. Y. (2018). Research Progress on Chromatographic Fingerprint Similar Evaluation Method for Traditional Chinese Medicine in Past Three Years (1988-2017) and its prospect. *China J. Chin. Materia Med.* 43 (10), 1969–1977. doi:10.19540/j.cnki.cjcmm.20180115.018

Conflict of Interest: The authors declare that the research was conducted in the absence of any commercial or financial relationships that could be construed as a potential conflict of interest.

frontiers in Pharmacology

ORIGINAL RESEARCH
published: 22 February 2022
doi: 10.3389/fphar.2022.827733

Therapeutic Effect and Mechanism of Si-Miao-Yong-An-Tang on Thromboangiitis Obliterans Based on the Urine Metabolomics Approach

Hui-Yu Li[1,2], Hui Sun[2], Ai-Hua Zhang[2], Lu-Wen He[2], Shi Qiu[2], Jun-Ru Xue[2], Fangfang Wu[1] and Xi-Jun Wang[1,2,3]**

[1]National Engineering Laboratory for the Development of Southwestern Endangered Medicinal Materials, Guangxi Botanical Garden of Medicinal Plant, Nanning, China, [2]National Chinmedomics Research Center, National TCM Key Laboratory of Serum Pharmacochemistry, Functional Metabolomics Laboratory, Heilongjiang University of Chinese Medicine, Harbin, China, [3]State Key Laboratory of Quality Research in Chinese Medicine, Macau University of Science and Technology, Macao SAR, China

Si-Miao-Yong-An-Tang (SMYAT) is a classic prescription for the treatment of thromboangiitis obliterans (TAO). However, the effect and mechanism are still unclear. This experiment aims to evaluate the therapeutic effect and mechanism of SMYAT on sodium laurate solution induced thromboangiitis obliterans model rats using urine metabolomics. The therapeutic effect of SMYAT was evaluated by histopathology, hemorheology and other indexes. The urine metabolomic method, principal component analysis (PCA) and orthogonal partial least squares discriminant analysis (OPLS-DA) were used for clustering group and discriminant analysis to screen urine differential metabolic biomarkers, and explore new insight into pathophysiological mechanisms of SMYAT in the treatment of TAO. SMYAT has significant antithrombotic and anti-inflammatory effects, according to the results of urine metabolomic analysis, and regulate the metabolic profile of TAO rats, and its return profile is close to the state of control group. Through metabolomics technology, a total of 35 urine biomarkers of TAO model were characterized. Among them, SMYAT treatment can regulate 22 core biomarkers, such as normetanephrine and 4-pyridoxic acid. It is found that the therapeutic effect of SMYAT is closely related to the tyrosine metabolism, vitamin B6 metabolism and cysteine and methionine metabolism. It preliminarily explored the therapeutic mechanism of SMYAT, and provided a scientific basis for the application of SMYAT.

Keywords: metabolomics, biomarker, therapeutic effect and mechanism, pathway, metabolites

OPEN ACCESS

Edited by:
Wenzhi Yang,
Tianjin University of Traditional Chinese Medicine, China

Reviewed by:
Wei Zhang,
Macau University of Science and Technology, Macao SAR, China
Zhi Yong Du,
Capital Medical University, China

****Correspondence:***
Ai-Hua Zhang
aihuatcm@163.com
Xi-Jun Wang
xijunw@sina.com

Specialty section:
This article was submitted to "Ethnopharmacology", a section of the journal Frontiers in Pharmacology

Received: *02 December 2021*
Accepted: *12 January 2022*
Published: *22 February 2022*

Citation:
Li H-Y, Sun H, Zhang A-H, He L-W, Qiu S, Xue J-R, Wu F and Wang X-J (2022) Therapeutic Effect and Mechanism of Si-Miao-Yong-An-Tang on Thromboangiitis Obliterans Based on the Urine Metabolomics Approach. Front. Pharmacol. 13:827733. doi: 10.3389/fphar.2022.827733

INTRODUCTION

Traditional Chinese medicine (TCM) is widely used in China, and its curative effect is remarkable (Wang et al., 2011; Zhang et al., 2013; Guo et al., 2020). However, due to the lack of modern scientific evidence to prove the use of TCM, the mechanism of action is unclear, leading to the therapeutic effect of TCM did not play an original potential. Metabolomics is an innovative method in modern research and it can find biomarkers and clarify biochemical pathways, thereby improving diagnosis and treatment (Zhang et al., 2012a; Liang et al., 2015a; Liang et al., 2016b). The analysis of key

biomarkers and the monitoring of metabolic pathways are, in analytical biology, an important means of physical state (Zhang et al., 2012b). Its purpose is to measure a wide range of small molecules under physiological stimulation or disease state (Roberts et al., 2012; Filla and Edwards, 2016). Due to the high sensitivity of metabolomics, it can detect subtle changes in metabolic pathways to explore the underlying mechanism of disease (Johnson et al., 2016). At present, metabolomics has been increasingly used to identify biomarkers in diseases (Liang et al., 2014; Liang et al., 2015b), and is considered a very powerful tool.

Metabolomics analysis based on mass spectrometry provides information on the metabolic pathways in the development of thromboangiitis obliterans disease, which has a certain reference value for studying the potential mechanisms of treatment strategies. Metabolomics can provide metabolic fingerprints of organisms, which can be used to study the mechanism of disease (Zhang et al., 2015; Zhang et al., 2019 A.-H.). It can explore metabolites and body pathology through high-throughput analysis of metabolites in organisms and explore the correlation between metabolites and the pathophysiological changes of the body (Li et al., 2018; Zhang et al., 2016; Zhang et al., 2019 AH.), and clarifies the interaction of complex systems in the body (Liang et al., 2016a; Liang et al., 2017; Zhang et al., 2018). It can btain corresponding biomarkers through metabolomics technology to characterize or reveal the functional state of a specific time or environment (Zhang et al., 2017; 2020). For example, by establishing a powerful metabolomics strategy to explain the pathological changes of Yanghuang syndrome and the therapeutic effect of TCM, and the Yin-Chen-Hao-Tang was used to achieve significant results (Liu X.-y. et al., 2018). Through metabolomics, the mechanism of Gancao Fuzi decoction achieved good results in the treatment of rheumatoid arthritis in rats by regulating various metabolic pathways (Liu Y. et al., 2018). Using the metabolomics method, the effect of *Angelica sinensis* on urinary metabolites in blood deficiency in mice was studied and the mechanism of blood tonifying was explored. It was found that *Angelica sinensis* could regulate a variety of metabolic pathways and exert a curative effect (Wang et al., 2016). In our research, the potential mechanism of SMYAT in the treatment of thromboangiitis obliterans through multi-component, multi-target, and multi-channel regulation of body function is explored by metabolomics. The study of metabolomics and related pathways will help us to increase our understanding of pathophysiology and mechanisms of disease (Laíns et al., 2019). Moreover, urine is one of the important samples for metabolome research (Zhang et al., 2012c; Harpole et al., 2016), which contains a variety of endogenous small molecule metabolites and can well reflect the changes of the body. As a very attractive sample in metabolomics research, it has several advantages, such as low protein content and simple pretreatment (Khamis et al., 2017).

Thromboangiitis obliterans (TAO) is a staged inflammatory disease and mainly occurs in the arteries, veins, and nerve parts of the limbs (Quintas and Albuquerque, 2008; Piazza and Creager, 2010; Highlander et al., 2011). The clinical symptoms are mainly manifested in the following conditions: limb ischemia; cold; severe pain limp, weakening or disappearance of arterial pulsation; gangrene, etc. Serious cases can endanger limbs and life and . the exact pathogenesis and etiology of the disease are not clear (Fazeli and Ravari, 2015; Li et al., 2020). In this experiment, a rat model of thromboangiitis obliterans was induced by an injection of sodium laurate solution. Sodium laurate has a strong endothelial damage effect and can cause the vascular endothelium to fall off. It is the most commonly used method of modeling (Munnix et al., 2009; Asada et al., 2018; Liu et al., 2019; Wang et al., 2021). Existing models mostly evaluate the success of model preparation by observing changes in apparent behavior and the degree of gangrene, hemorheology, and histopathology are the most commonly used detection indicators. In our research, hemorheology and histopathology test results support the successful model building. The SMYAT is included in《YAN-FANG-XIN-BIAN》 (Li et al., 2013; Yang et al., 2020), and is a famous classic prescription in ancient China, which is composed of four kinds of traditional Chinese medicines, namely Flos *Lonicerae Japonicae* [*Lonicera japonica* Thunb. (Jinyinhua), Caprifoliaceae], Radix *Scrophulariae Ningpoensis* [*Scrophularia ningpoensis* Hemsl. (Xuanshen) Scrophulariaceae], Radix *Scrophulariae Ningpoensis* [*Angelica sinensis* (Oliv.) Diels (Danggui) Apiaceae], and Radix *Glycyrrhizae Uralensis* [*Glycyrrhiza uralensis* Fisch. (Gancao) Leguminosae]. (Peng et al., 2012; Liu et al., 2017; Zhong et al., 2017), which contain terpenoids, flavonoids, phenylpropanoid, and organic acids, which can achieve anti-inflammatory, anti-oxidation stress, regulating blood lipid, inhibiting thrombosis and improving hemorheology, etc. (Zheng et al., 2019). It has the function of clearing heat and detoxifying poison. It is commonly used in the treatment of thromboangitis obliterans (Zhao et al., 2020). In our experiment, we analyzed the chemical components in the sample of Si-Miao-Yong-An-Tang, and a total of 79 chemical components were characterized. The relevant chromatograms and specific information tables of the compounds are shown in **Supplementary Material S1**. This study determined urine biomarkers of TAO model rats, which were used to distinguish between the control group and the TAO model groupThe biomarkers are expected to be used as therapeutic targets and to regulate relevant monitoring and treatment biomarkers when using SMYAT.

MATERIALS AND METHODS

Instrument

Acquity™ UPLC liquid chromatography (Waters, USA); Synapt™ G2-Si mass spectrometry (Waters, USA); Masslynx v4.1 workstation (Waters, USA); Ultrasonic cleaner (KQ-250 DB, Kunshan Ultrasonic Instrument Co., Ltd., China); Table centrifuge (sorvall ST 16R, Thermo Scientific, USA); Thermo Scientific 995 ultra low temperature refrigerator (Thermo Scientific, USA).

Reagents and Materials

All herbs were obtained from Harbin No.4 Chinese Medicine Factory Co., Ltd. Flos *Lonicerae Japonicae* (Lot number: JL030-180401), Radix *Scrophulariae Ningpoensis* (Lot number: JL031-180601), Radix *Angelicae Sinensis* (Lot number: JL048-180601) and Radix *Glycyrrhizae Uralensis* (Lot number: JL054-180501) were weighed out according to the ratio 3:3:2:1 and soaked in distilled water for 30 min and boiled for 1 h. The solution was filtered and freeze-dried under vacuum to obtain a loose powder and freeze-dried powder was dissolved in water and prepared in 8.2 g/kg solution for oral gavage administration to rats. In addition, we carried out quality control on the sample of Si-Miao-Yong-An-Tang. For details, please refer to the **Supplementary Material S2**.

Mai-Luo-Ning Granules (MLN) are provided by Jiangxi Yintao Pharmaceutical Co., Ltd. (Lot number:1808025). Sodium Laurate are provided by Sinopharm Chemical Reagent Co., Ltd. (Lot number:20171224). Methanol and acetonitrile (HPLC grade) were purchased from Fisher Scientific Corporation (Fisher, United States); leucine enkephalin was purchased from Sigma-Aldrich (SIGMA, United States); formic acid (HPLC grade) was purchased from Aladdin Industrial Corporation (Shanghai, China); sodium chloride injection was purchased from Kelun Pharmaceutical Co., Ltd., (Sichuan, China); all other reagents were HPLC grade.

Animal Models and Study Design

Sixty male SD rats with the weight of (280–320) g were purchased from the Liaoning Changsheng Biotechnology Co., Ltd. [Permit number: SCXK (Liao) 2015-0001]. Those rats were exposed to a temperature of 24 ± 2°C and the humidity of 40 ± 5%, the animals were reared in separate cages, all rats were adaptive fed for 7 days and then randomly divided into four groups: Control group (n = 20), Model group (n = 20), SMYAT group (n = 10), and MLN group (n = 10). Rats in model group, SMYAT group and MLN group were injected with a sodium laurate solution to induce thromboangiitis obliterans model, while rats in control group were injected with the same amount of normal saline. After 10 days, the rats in SMYAT group (rats were fed with SMYAT 8.2 g/kg per day for 15 days) and MLN group (rats were fed with MLN 2.7 g/kg per day for 15 days) were given medicine treatment. The rats in control group and thromboangiitis obliterans model group were given pure water. This research was approved by the Ethical Committee of Heilongjiang University of Chinese Medicine and was conducted according to the principles expressed in the Declaration of Helsinki.

Sample Preparation

Urine Sample Preparation

Control group and model group of urine samples were collected at 10th day of the experiment. Accompanying control group, accompanying model group, SMYAT group and MLN group of urine samples were collected at 25th day of experiment and then centrifuged with of 13,000 rpm/min in 4°C for 10 min to obtain urine samples. Before UPLC-MS analysis, the urine supernatant was stored at −80°C.

Before analysis, the urine samples were thawed in an ice bath, 500 μL of urine was taken and added to 500 μL of ultra-pure water, placed in a vortex mixer for 30 s, centrifuged at 13,000 rpm for 15 min at 4°C; and filtered over 0.22 μm, then the supernatant were injected into the UPLC-MS.

Pharmacodynamic Evaluation Sample Preparation

The accompanying control group, accompanying model group, SMYAT group and MLN group of blood samples were collected from the abdominal aorta of rats (on the 25th day of the experiment, 1 h after the last administration). Sodium citrate and EDTA-K2 were used for anticoagulation. The whole blood viscosity and plasma viscosity and other indexes of rats in each group were determined. In each group, the femoral artery tissues below 2–3 cm and around the artery were taken from the affected limb. After washing with normal saline, the femoral artery was fixed with 10% formalin solution for 24 h for histopathological observation.

Analysis of Samples by HPLC-MS

Chromatographic Conditions

Chromatograph condition: Acquity™ UPLC liquid chromatography (Waters, USA); chromatographic column used was an ACQUITY HSS T3 chromatographic column (100 mm × 2.1 mm i.d., 1.8 μm. Waters, USA); the column temperature is set at 40°C; the sample bin temperature is set at 4°C; meanwhile mobile phase for gradient elution consist of phase A (acetonitrile containing 0.1% formic acid) and phase B (water with 0.1% formic acid). The gradient was as follows: 0–1 min, 1% A; 1–6 min, 1–30%A; 6–8 min, 30–70%A; 8–9 min, 70–99%A; 9–10 min, 99%A; 10–10.1 min, 99–1%A; 10.1–14 min, 1%A. In addition, equal volume of each sample was mixed into a quality control sample (QC) for monitoring the stability of the instrument in the experiment, and one QC solution was run every ten samples, which were crucial for optimization during metabolomic analytical method development.

Mass Spectrometry Conditions

Synapt TM G2-Si mass spectrometer (Waters, USA). MS system using ESI as an ion source to operate in ESI+ and ESI-modes with a scanning range of 50–1,200 m/z. The desolvation temperature was 400°C, the source temperature was 110°C, desolvation gas flow was 800 L/h, and cone gas flow was 50 L/h. Sampling cone voltage was maintained at 20 V; Leucine enkaphalin was used as the reference compound {positive ion mode [$(M + H)^+$ = 556.2771] and $(M–H)^-$ = 554.2615}. All the above parameters are set using Masslynx v4.1 workstation (waters, United States).

Metabolomics Data Processing

In order to more accurately find the urine biomarkers in TAO model rats original urine files were imported into Progensis QI software for analysis and processing, andpeak matching and normalization for each peak was performed. Meanwhile, we used Ezinfo 3.0 software, including PCA and OPLS-DA. SPSS 22.0 for Windows was used for the statistical analysis. The variable importance for the projection (VIP) value >2 in

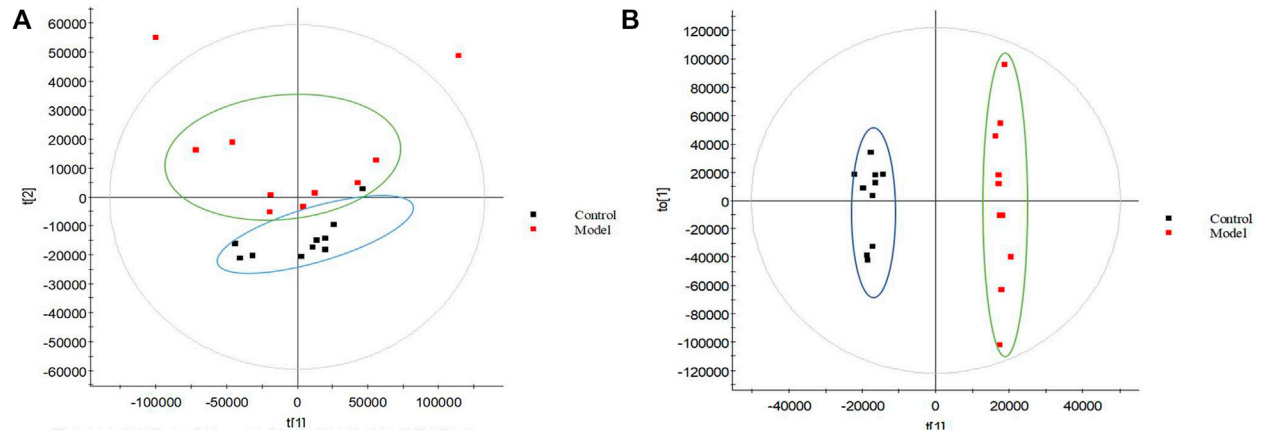

FIGURE 1 | Metabolomic profiling of TAO. PCA model results for TAO model group in positive mode **(A)**; OPLS-DA model results for TAO model group in positive mode **(B)**; Black spot represents the control group and red spot represents the model group.

OPLS-DA, and $p < 0.05$ for Students t-test were selected as potential urine biomarkers.

The identification of biomarkers is to lock the Rt_m/z of important metabolite ions to help confirm the molecular mass of metabolites and perform elemental composition analysis to determine possible chemical formulas. Based on the possible chemical formulas, accurate masses and secondary mass spectrometry data (MS/MS) of ions, the Human Metabolome Database (HMDB) and Metaboanalyst were used to match the mass spectrometry information. The MassFragment application manager was used to facilitate the chemically intelligent peak matching algorithms MS/MS fragment ion analysis process and to determine the final biomarker. The results of the secondary ion fragmentation information matching of these 35 compounds are shown in **Supplementary Material S3**.

RESULTS

Biomarkers Discovery of TAO Model

The urine datasets collected on the 10th day were further subjected to multivariate statistical analysis using EZinfo 3.0 software. The PCA score plots (**Figure 1A**) showed an obvious separation between the TAO model and control model. The OPLS-DA was employed to find the potential biomarkers (**Figure 1B**). The R2Y and Q2 values of the model [R2Y (cum) = 0.991607, Q2 (cum) = 0.905193 in positive mode and R2Y (cum) = 0.993259, Q2 (cum) = 0.942307] in negative mode indicated that the models have good quality and predictability. The OPLS-DA score plots showed that there was a significant difference between the TAO model groups and control groups, suggesting that the TAO model group had obvious urinary biochemical disorders and its metabolic profile had changed significantly. Screen out potential urine markers, and by using related databases, such as HMDB, KEGG, etc. Meanwhile, we combined the fragment information of the secondary mass spectrometer to obtain the chemical information of potential biomarkers, see **Supplementary Table S1** for details. The content of these potential biomarkers in the 10th day model group and the 10th day control group were statistically analyzed (**Figure 2**). We constructed a PLS-DA model with the obtained differential metabolic markers (**Figure 3A**). **Figure 3B** showed top significant features of the metabolite markers based the VIP projection. Correlation analysis of differential metabolites are marked on the hierarchical clustering plot (**Figure 3C**), and the obtained differential metabolic markers are analyzed by heat mapwith results shown in **Figure 3D**.

Metabolic Pathways of Thromboangiitis Obliterans

MetPA (Metabolomics Pathway Analysis) is used to analyze metabolic pathways in metabolomics data. MetPA analysis was performed on the characterized 35 biomarkers related to thromboangiitis obliterans model, and 17 related metabolic pathways were obtained including vitamin B6 metabolism, cysteine and methionine metabolism, tyrosine metabolism, phenylalanine metabolism, and so forth. The results show that these endogenous metabolites are closely related to the thromboangiitis obliterans model. The metabolic pathway is shown in **Figure 4**.

Efficacy Evaluation of SMYAT

SMYAT Improves the Animal Signs of TAO Model Rats

Rats in each group were in good condition, lively and active prior to the start of the experiment. After modeling, except for control group, the other groups of rats showed obvious ischemic symptoms, such as lower skin temperature, obvious swelling of foot and paw, weakened arterial pulsation, limping and dragging walking in varying degrees. On the 10th–25th day, the condition of the affected limbs of the rats in each treatment group was gradually improved, among them, the SMYAT group had a significant effect, the skin temperature returned to normal, the swelling of the paws subsided, and the arterial pulsation recovered, while the state of the rats in the following model group remained

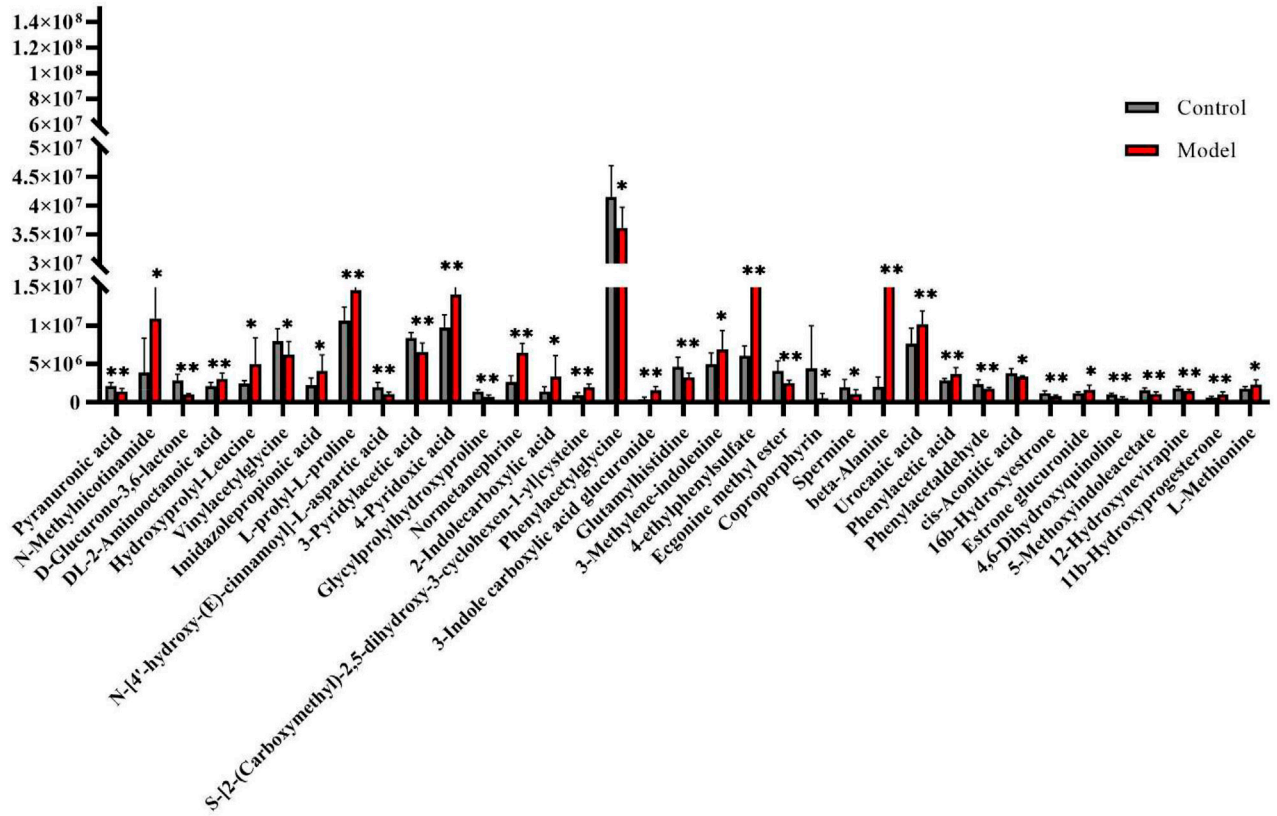

FIGURE 2 | Change trend of biomarker content in control group and model group. *Significant difference between the control group and model group ($p < 0.05$). **Very significant difference between the control group and model group ($p < 0.01$).

the same as that after modeling, and there was no improvement trend.

SMYAT Improves the Hemorheology of TAO Model Rats

The results in **Figure 5A**, show low shear whole blood viscosity and that the blood plasma viscosity of the thromboangiitis obliterans model rats had changed significantly compared with the control group. After treatment with SMYAT, all the indexes had a significant decrease, which showed that SMYAT had a good effect on regulating blood viscosity and treating thrombosis.

The results in **Figure 5B**, show the hematocrit, erythrocyte aggregation index and erythrocyte rigidity index of the thromboangiitis obliterans model rats changed significantly compared with the control group. After treatment with SMYAT, the erythrocyte rigidity index, erythrocyte aggregation index and erythrocyte deformation index have been significantly adjusted, indicating that SMYAT has a significant regulatory effect on red blood cells and other indicators, and can achieve good therapeutic effects.

SMYAT Improves Histopathology of TAO Model Rats

We evaluated the effect of SMYAT on the histopathology of TAO model rats (**Figure 6**), and observation of rat femoral artery sections showed that there were no pathological changes in the control group, the vascular endothelium was smooth and orderly, and the endothelial cells were neatly arranged (**Figure 6A**). The femoral artery sections in the TAO model group found obvious pathological changes, such as vascular thinning, endothelial cell deformation, vascular endothelial cells and smooth muscle cells disorderly arranged, and a large number of inflammatory cell infiltration (**Figure 6B**). In the SMYAT treatment group, the degree of femoral artery lesions was improved, the deformation of endothelial cells was improved, and the arrangement of vascular endothelial cells and smooth muscle cells was restored, and the injure condition was restored and maintained a stable state (**Figure 6C**). In MLN group, the femoral artery became slightly thinner, intimal peeling phenomenon relieved, and the inflammatory cell infiltration in the blood vessel wall and surrounding tissues gradually reduced (**Figure 6D**).

Effect of SMYAT on Biomarkers

The PCA was carried out on the urine data by collected on the 25th day from the four different groups, and the plots obtained (**Figure 7**), show that there are obvious clusters between each group of data, they are distributed in different positions, especially between the control group and the TAO model group which are far away and can be distinguished significantly. The position of the SMYAT treatment group gradually approached the control groupwhich shows that

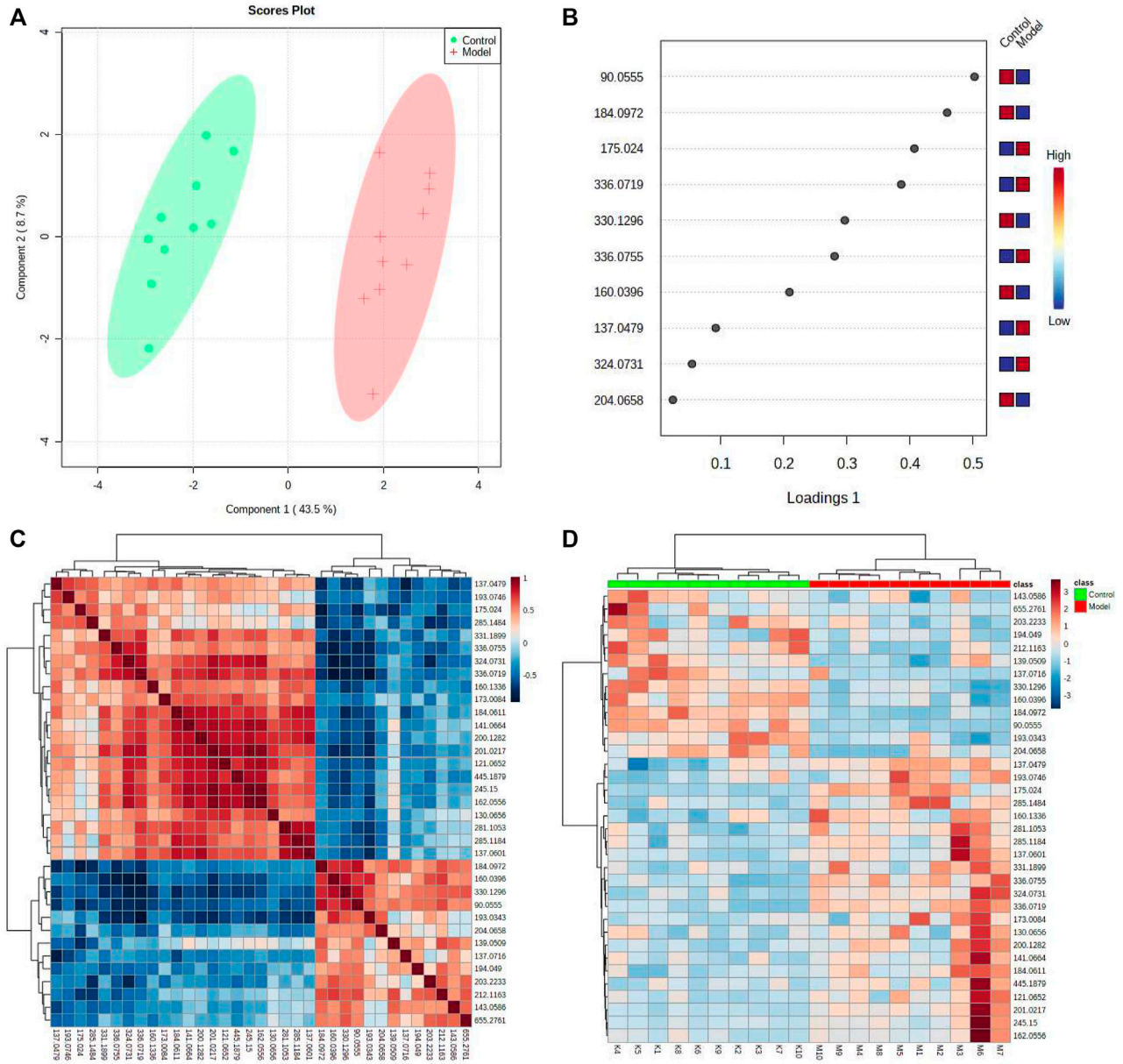

FIGURE 3 | Systems analysis of metabolomic alterations of the model and control samples with MetaboAnalyst's data annotation tools: **(A)** PLS-plot revealed differences between the two groups. **(B)** Correlation analysis of the 10 differential metabolites are marked on the plot. Three clusters were identified representing the different groups of metabolites. Top significant features of the metabolite markers based the VIP projection **(B)**. **(C)** Hierarchical clustering of the differential metabolites. **(D)** Heatmap visualization constructed based on the differential metabolites of importance for the urine of model. The heatmaps were constructed based on the potential candidates of importance, which were extracted with OPLS-DA analysis. Rows: metabolites; columns: samples; Variable differences are revealed between the control and model groups.

SMYAT could improve the abnormal metabolic network of TAO model rats.

On the 25th day of the experiment, the regulation of biomarkers in rats with thromboangiitis obliterans model by SMYAT was analyzed, among the 35 potential biomarkers that were characterized, SMYAT could be adjusted to 22 biomarkers; respectively including pyranuronic acid, DL-2-aminooctanoic acid, imidazolepropionic acid, L-prolyl-L-prolin, 4-pyridoxic acid, normetanephrine, 2-indolecarboxylic acid, S-[2-(carboxymethyl)-2, 5-dihydroxy-3-cyclohexen-1-yl]cysteine, 3-methylene-indolenine, 4-ethylphenylsulfate, coproporphyrin, hydroxyprolyl-leucine, N-methylnicotinamide, beta-alanine, 3-indole carboxylic acid glucuronide, urocanic acid, phenylacetaldehyde, cis-aconitic acid, estrone glucuronide, 5-methoxyindoleacetate, 11b-hydroxyprogesterone, and L-methionine (**Figure 8**).

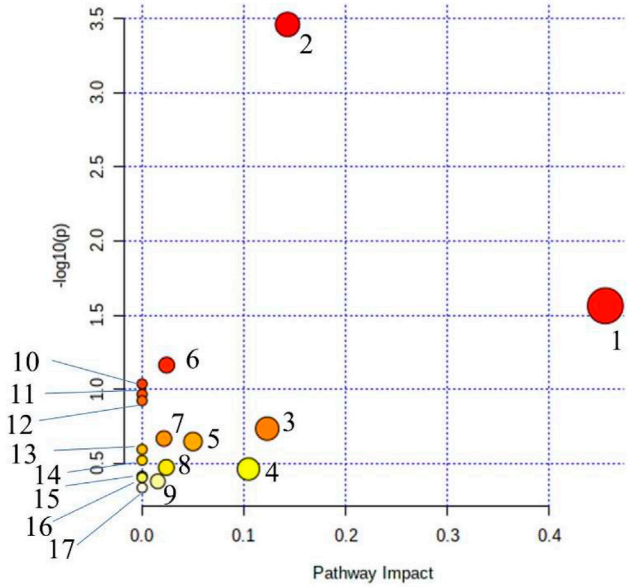

FIGURE 4 | Main metabolic pathways of potential biomarkers. (1) beta-Alanine metabolism; (2) Phenylalanine metabolism; (3) Histidine metabolism; (4) Cysteine and methionine metabolism; (5) Citrate cycle (TCA cycle); (6) Steroid hormone biosynthesis; (7) Pantothenate and CoA biosynthesis; (8) Glyoxylate and dicarboxylate metabolism; (9) Tyrosine metabolism; (10) Tryptophan metabolism; (11) Vitamin B6 metabolism; (12) Ascorbate and aldarate metabolism; (13) Propanoate metabolism; (14) Glutathione metabolism; (15) Arginine and proline metabolism; (16) Pyrimidine metabolism; (17) Aminoacyl-tRNA biosynthesis.

Metabolic Network Analysis

Based on the HMDB, KEGG and the metaboanalyst platform, the metabolic network of SMYAT on thromboangiitis obliterans rats was mapped to clarify its potential mechanism (**Figure 9**).

DISCUSSION

Thromboangiitis obliterans is a common vascular disease in clinics, which mainly affects small and medium-sized arteries and veins (Klein-Weigel et al., 2015). Amputation is needed in severe cases. Because its exact pathogenesis and etiology are not clear, there is no radical treatment, causing great pain to patients, but the research on it has not stopped. In this study, metabolomics provides a powerful approach to analyze the urine of TAO model rats and control group rats to study the difference of endogenous small molecule metabolic profiles. On this basis, we found the biomarkers and metabolic pathways regulated by SMYAT, so as to provide ideas for the research on the mechanism of SMYAT in the treatment of thromboangiitis obliterans. In this study, a total of 35 biomarkers of thromboangiitis obliterans model were characterized. In the visualized thermogram of the biomarkers of the thromboangiitis obliterans model, it can be clearly seen that these 35 urine biomarkers can clearly distinguish the control group from the TAO model group, suggesting that the biomarkers we found are significantly related to thromboangiitis obliterans. Among them, 22 biomarkers were adjusted by SMYAT. According to the results of treatment, the affected limbs of rats in the SMYAT treatment group were recovered in varying degrees, the hemorheology and other indicators significantly adjusted back, and the degree of femoral artery lesions improved. This study can show that the metabolomics method can accurately analyze the potential biomarkers and metabolic pathways, so as to achieve a specific, targeted, therapeutic effect. SMYAT can regulate multiple metabolic pathways such as cysteine and methionine metabolism, phenylalanine metabolism, tyrosine metabolism and vitamin B6 metabolism in rats with thromboangiitis obliterans, and achieve good therapeutic effects.

Methionine is an alpha-amino acid, and is found in all organisms ranging from bacteria to plants to animals. It is

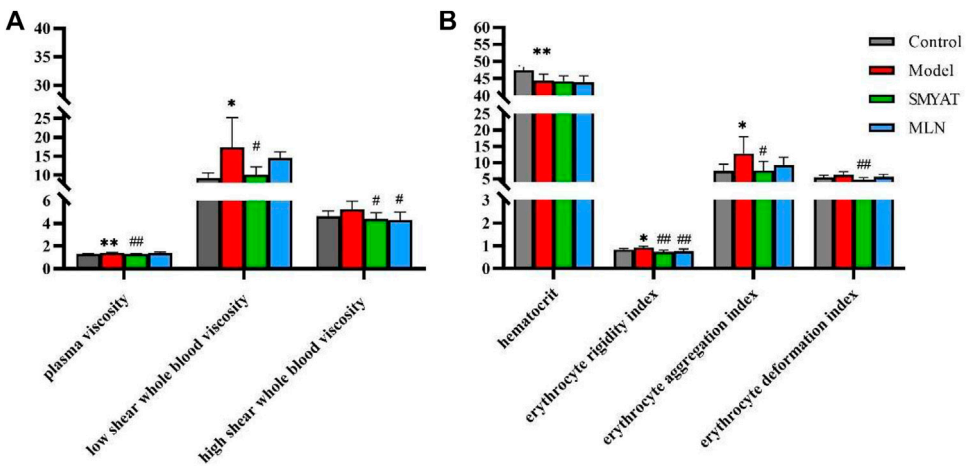

FIGURE 5 | (A) Effects of administration on plasma viscosity and whole blood viscosity of rats in each group; **(B)** Effects of administration on related indexes of red blood cells of rats in each group; $^{*}p < 0.05$, $^{**}p < 0.01$ compared with control group; $^{\#}p < 0.05$, $^{\#\#}p < 0.01$ compared with model group.

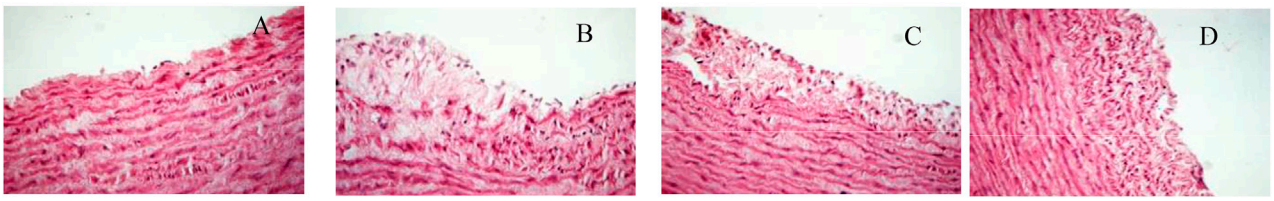

FIGURE 6 | Femoral artery sections of rats in each group on the 25th day of the experiment (×400); **(A)**: control group; **(B)**: model group; **(C)**: SMYAT group; **(D)**: MLN group.

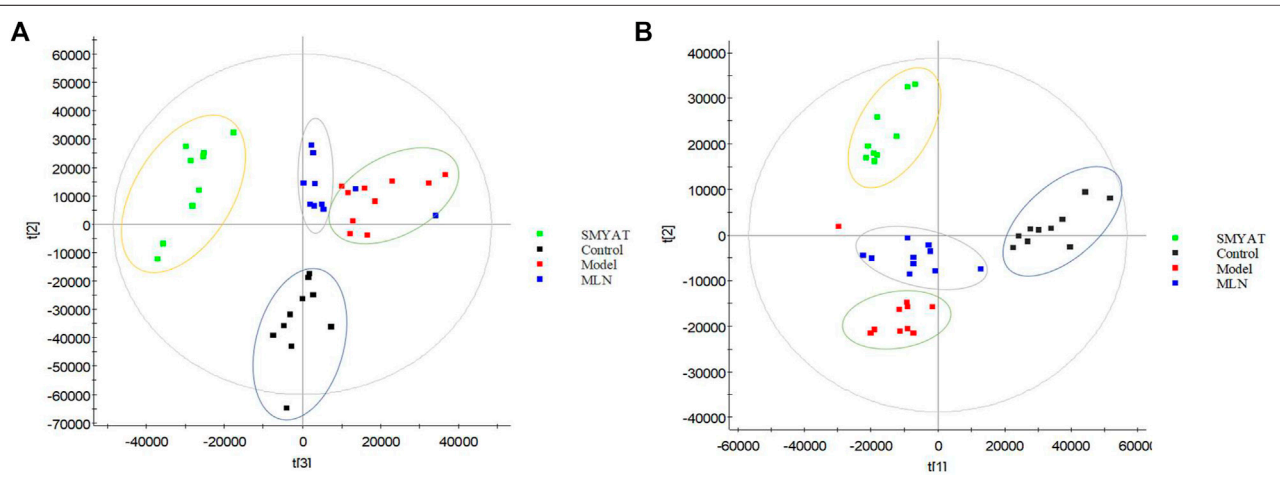

FIGURE 7 | The PCA score plot of control, model, SMYAT, and MLN groups in urine metabolism profile. **(A)** Positive ion mode and **(B)** negative ion mode. Black spot represents the control group, red spot represents the model group, green spot represents the SMYAT group and blue spot represents the MLN group.

classified as an aliphatic, non-polar amino acid. In addition to being a substrate for protein synthesis, methionine is an intermediate in transmethylation reactions, serving as the major methyl group donor *in vivo*, including the methyl groups for DNA and RNA intermediates. Acute doses of methionine can lead to acute increases in plasma homocysteine, which can be used as an index of the susceptibility to cardiovascular disease. When present in sufficiently high levels, methionine can act as an atherogen and a metabotoxin. An atherogen is a compound that, when present at chronically high levels, causes atherosclerosis and cardiovascular disease. Methionine oxidation metabolism has a promoting effect on vascular diseases such as atherosclerosis and thrombosis (Gu et al., 2015). Studies have shown that increased homocysteine levels are related to thrombosis. *In vivo*, cysteine is derived from the amino acid containing thiol group formed by methionine metabolism (Undas et al., 2005; Qureshi et al., 2019), and the methionine content is significantly increased in rats with thromboangiitis obliterans, resulting in the metabolic disorder of cysteine and the methionine metabolic pathway, thus promoting thrombosis. After treatment with SMYAT, the content of methionine was significantly reduced. It reminds us that maintaining a stable methionine content plays an important role in preventing thrombosis. The content of normetanephrine in TAO model rats was significantly increased, and normetanephrine was a metabolite produced by catechol-O-methyl transferase. Within humans, normetanephrine participates in a number of enzymatic reactions. It is also involved in the metabolic disorder called transient tyrosinemia. Phenylalanine and tyrosine are used as the precursor of catecholamine and participate in the synthesis of normetanephrine and other substances. In this TAO model, the tyrosine metabolism pathway is disordered, which led to the increase of normetanephrine content. Normetanephrine has a regulatory effect on the degree of vascular tension, which affects the model state (Desjars and Pinaud, 1989). High levels of norepinephrine can reduce blood supply, aggravate ischemia, expand the scope of infarction, and promote thrombosis. After treatment with SMYAT, normetanephrine content is significantly regulated, and the state of blood vessels is improved to prevent thrombosis. The content of hydroxyprolyl-leucine in TAO model rats significantly increased and hydroxyprolyl-leucine was a dipeptide composed of hydroxyproline and leucine. Most of these substances have cell signaling effects and are intermediate products of amino acid degradation pathways. The content of hydroxyprolyl-leucine significantly decreased after treatment with SMYAT, suggesting that the therapeutic effect of SMYAT might be related to the regulation of the hydroxyprolyl-

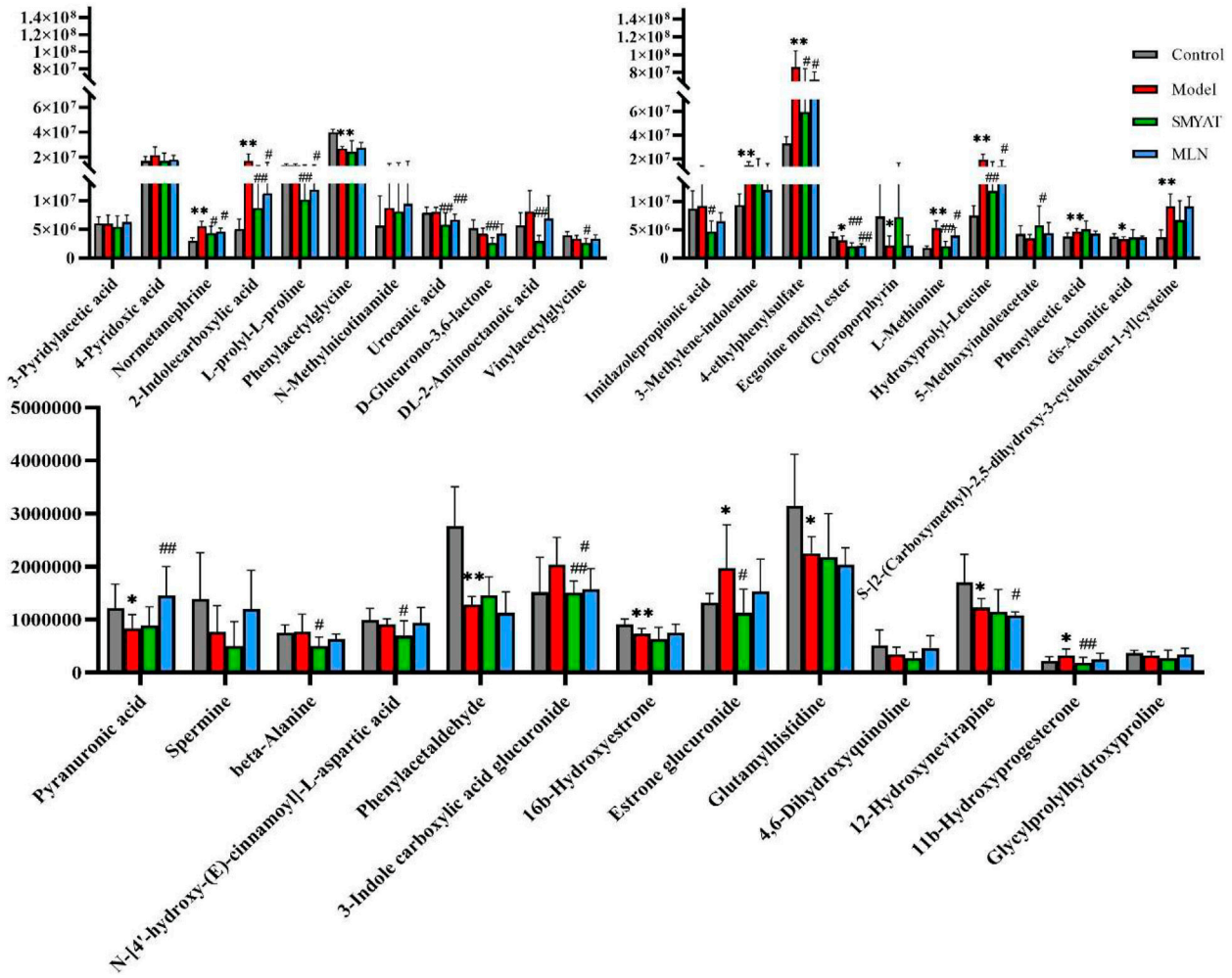

FIGURE 8 | *Significant difference between the control group and model group ($p < 0.05$). **Very significant difference between the control group and model group ($p < 0.01$). # Significant difference between SMYAT and model groups, $p < 0.05$. ## Very significant difference compared between SMYAT and model groups, $p < 0.01$.

leucine content. 4-ethylphenylsulfate is an organic compound, called phenylsulfate benzene sulfate is a compound containing sulfuric acid group which combines with phenyl. The component in TAO model group is significantly increased and it is significantly regulated after giving SMYAT. Vitamin B6 is a term for a group of interconvertible molecules containing pyridoxine, pyridoxal, pyridoxamine, and their phosphates (Kalle et al., 2016). Vitamin B6 is the main component of a coenzyme in the human body and participates in a variety of metabolic reactions. Vitamin B6 is finally metabolized into 4-pyridoxic through a series of processes in the body (Stanulović et al., 1976). The ratio of 4-pyridoxic acid to pyridoxine is related to cardiovascular disease. It is believed that vitamin B6 in plasma can be metabolized to 4-pyridoxic acid, which increases the risk factors of blood vessels (Obeid et al., 2019). In this research, the vitamin B6 metabolism in TAO model rats was disordered, and the content of 4-pyridoxic acid increased. 4-pyridoxic acid will accumulate in the body, thereby increasing the risk of thrombosis, and it is significantly regulated after giving SMYAT. Many of the biomarkers we have found are related to thrombosis and have been significantly adjusted. This also shows that SMYAT has a significant effect in the treatment of this disease and has the value of in-depth analysis.

Metabolomics technology is used to characterize the metabolic profile of syndromes and find biomarkers from the level of endogenous small molecule metabolism (Liang et al., 2015c; Qiu et al., 2017, 2020). Because of its high sensitivity, it is very effective in the identification of biomarkers, so it also reflects a new strategy for the diagnosis of thromboangiitis obliterans. This study is the first to apply the technology of urine metabolomics to the study of the mechanism of thromboangiitis obliterans, which provides an innovative idea for the study of the mechanism of thromboangiitis obliterans. SMYAT has a good regulatory effect on thromboangiitis obliterans. Based on UPLC-MS/MS technology, the metabolomics method was used to evaluate the overall therapeutic effect of SMYAT and study its potential molecular mechanism. This experiment provides strong evidence for the mechanism of SMYAT in treating thromboangiitis obliterans and a reliable method for exploring the mechanism of traditional Chinese medicine.

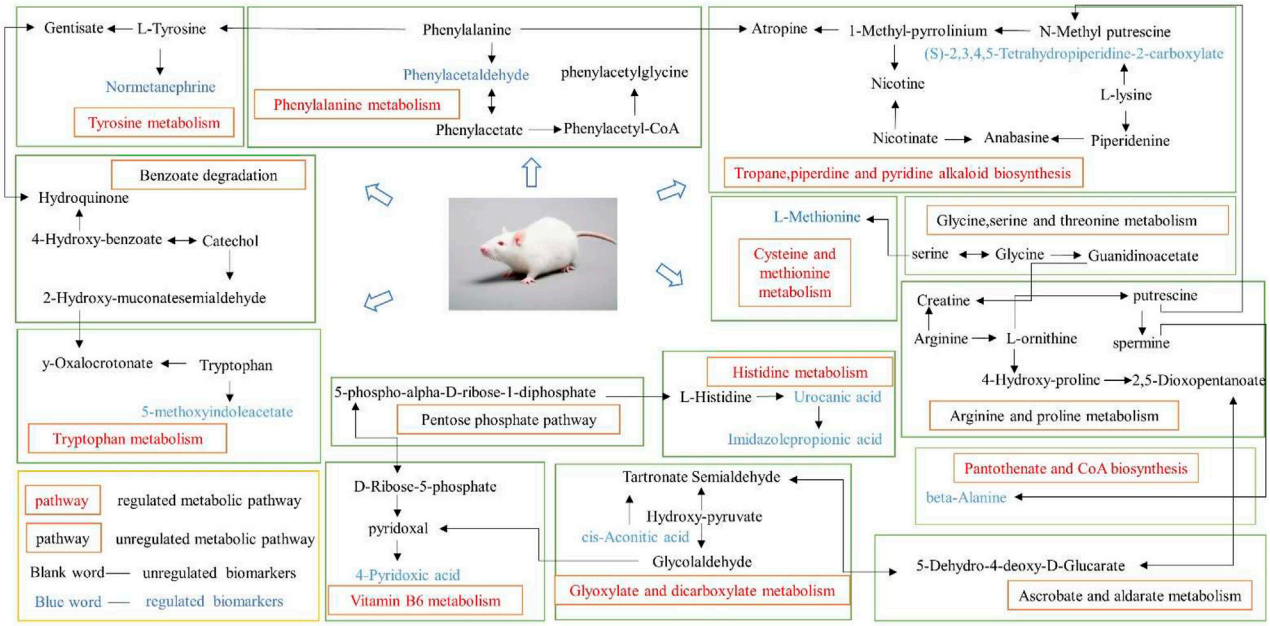

FIGURE 9 | Correlation networks of the potential biomarkers based on the KEGG.

CONCLUSION

In our research, the rat model of thromboangiitis obliterans was established by injection of sodium laurate, and the effect of SMYAT was evaluated by combining the evaluation indexes of hemorheology, histopathology, and metabolomic methods. In the rat model of thromboangiitis obliterans, there are 35 endogenous urinary metabolites as potential biomarkers. The metabolic pathways include vitamin B6 metabolism, phenylalanine metabolism, cysteine and methionine metabolism and tyrosine metabolism, and so forth. These findings add to our understanding of the pathogenesis of thromboangiitis obliterans and reveal the molecular basis of the efficacy of SMYAT in the treatment of thromboangiitis obliterans through metabolomic techniques. SMYAT can improve thromboangiitis obliterans and is a promising candidate drug for thromboangiitis obliterans.

DATA AVAILABILITY STATEMENT

The original contributions presented in the study are included in the article/**Supplementary Material**, further inquiries can be directed to the corresponding authors.

ETHICS STATEMENT

The animal study was reviewed and approved by the ethics committee of Heilongjiang University of Chinese Medicine.

AUTHOR CONTRIBUTIONS

X-JW and A-HZ designed the experiments; H-YL, L-WH, and J-RX, performed the experiment; H-YL, HS, L-WH, SQ, and FW analyzed the data; H-YL, wrote the paper. All the authors read and approved the final manuscript.

FUNDING

This work was supported by grants from the Key Program of Natural Science Foundation of State (Grant No. 81430093), Natural Science Foundation of Heilongjiang Province (YQ2019H030), Scientific and Technology Development Program of Guangxi (AD18126013), the Ba Gui Scholars program of Guangxi, the Central Government Guides Local Science and Technology Development Fund Projects (ZY21195044) and Heilongjiang Touyan Innovation Team Program.

SUPPLEMENTARY MATERIAL

The Supplementary Material for this article can be found online at: https://www.frontiersin.org/articles/10.3389/fphar.2022.827733/full#supplementary-material

REFERENCES

Asada, Y., Yamashita, A., Sato, Y., and Hatakeyama, K. (2018). Thrombus Formation and Propagation in the Onset of Cardiovascular Events. *J. Atheroscler. Thromb.* 25 (8), 653–664. doi:10.5551/jat.RV17022

Desjars, P., and Pinaud, M. (1989). Norepinephrine in Hyperkinetic Septic Shock: from a Misunderstood Process to Justified Rehabilitation. *Ann. Fr Anesth. Reanim* 8 (1), 1–3. doi:10.1016/s0750-7658(89)80134-0

Fazeli, B., and Ravari, H. (2015). Mechanisms of Thrombosis, Available Treatments and Management Challenges Presented by Thromboangiitis Obliterans. *Curr. Med. Chem.* 22 (16), 1992–2001. doi:10.2174/0929867322666150429112111

Filla, L. A., and Edwards, J. L. (2016). Metabolomics in Diabetic Complications. *Mol. Biosyst.* 12 (4), 1090–1105. doi:10.1039/c6mb00014b

Gu, S. X., Stevens, J. W., and Lentz, S. R. (2015). Regulation of Thrombosis and Vascular Function by Protein Methionine Oxidation. *Blood* 125 (25), 3851–3859. doi:10.1182/blood-2015-01-544676

Guo, R., Luo, X., Liu, J., Liu, L., Wang, X., and Lu, H. (2020). Omics Strategies Decipher Therapeutic Discoveries of Traditional Chinese Medicine against Different Diseases at Multiple Layers Molecular-Level. *Pharmacol. Res.* 152, 104627. doi:10.1016/j.phrs.2020.104627

Harpole, M., Davis, J., and Espina, V. (2016). Current State of the Art for Enhancing Urine Biomarker Discovery. *Expert Rev. Proteomics* 13 (6), 609–626. doi:10.1080/14789450.2016.1190651

Highlander, P., Southerland, C. C., VonHerbulis, E., and Gonzalez, A. (2011). Buerger Disease (Thromboangiitis Obliterans): a Clinical Diagnosis. *Adv. Skin Wound Care* 24 (1), 15–17. doi:10.1097/01.ASW.0000392923.37852.43

Johnson, C. H., Ivanisevic, J., and Siuzdak, G. (2016). Metabolomics: beyond Biomarkers and towards Mechanisms. *Nat. Rev. Mol. Cel Biol* 17 (7), 451–459. doi:10.1038/nrm.2016.25

Kalle, S., Tanner, R., Arund, J., Tomson, R., Luman, M., and Fridolin, I. (2016). 4-Pyridoxic Acid in the Spent Dialysate: Contribution to Fluorescence and Optical Monitoring. *PLoS One* 11 (119), e0162346. doi:10.1371/journal.pone.0162346

Khamis, M. M., Adamko, D. J., and El-Aneed, A. (2017). Mass Spectrometric Based Approaches in Urine Metabolomics and Biomarker Discovery. *Mass. Spectrom. Rev.* 36 (2), 115–134. doi:10.1002/mas.21455

Klein-Weigel, P., Volz, T. S., and Richter, J. (2015). Thromboangiitis Obliterans (Buerger's Disease): Update 2015. *Dtsch Med. Wochenschr* 140 (20), 1486–1489. doi:10.1055/s-0041-106246

Laíns, I., Gantner, M., Murinello, S., Lasky-Su, J. A., Miller, J. W., Friedlander, M., et al. (2019). Metabolomics in the Study of Retinal Health and Disease. *Prog. Retin. Eye Res.* 69, 57–79. doi:10.1016/j.preteyeres.2018.11.002

Li, M. D., Wang, Y. F., Yang, M. W., Hong, F. F., and Yang, S. L. (2020). Risk Factors, Mechanisms and Treatments of Thromboangiitis Obliterans: An Overview of Recent Research. *Curr. Med. Chem.* 27 (35), 6057–6072. doi:10.2174/0929867326666190816233042

Li, N., Qu, X. B., Lin, S., Li, H., Lin, H., Li, J., et al. (2013). Protective Effect of Simiao Yongan Decoction on Rats with Thromboangiitis Obliterans. *Chin. J. Exp. Traditional Med. Formulae* 19 (08), 225–227.

Li, Y.-F., Qiu, S., Gao, L.-J., and Zhang, A.-H. (2018). Metabolomic Estimation of the Diagnosis of Hepatocellular Carcinoma Based on Ultrahigh Performance Liquid Chromatography Coupled with Time-Of-Flight Mass Spectrometry. *RSC Adv.* 8 (17), 9375–9382. doi:10.1039/c7ra13616a

Liang, Q., Liu, H., Xie, L.-X., Li, X., and Zhang, A.-H. (2017). High-throughput Metabolomics Enables Biomarker Discovery in Prostate Cancer. *RSC Adv.* 7 (5), 2587–2593. doi:10.1039/c6ra25007f

Liang, Q., Liu, H., Zhang, T., Jiang, Y., Xing, H., and Zhang, A.-H. (2016b). Discovery of Serum Metabolites for Diagnosis of Progression of Mild Cognitive Impairment to Alzheimer's Disease Using an Optimized Metabolomics Method. *RSC Adv.* 6 (5), 3586–3591. doi:10.1039/c5ra19349d

Liang, Q., Liu, H., Zhang, T., Jiang, Y., Xing, H., and Zhang, A.-H. (2015b). Metabolomics-based Screening of Salivary Biomarkers for Early Diagnosis of Alzheimer's Disease. *RSC Adv.* 5 (116), 96074–96079. doi:10.1039/c5ra19094k

Liang, Q., Liu, H., Zhang, T., Jiang, Y., and Zhang, A.-H. (2016a). Untargeted Lipidomics Study of Coronary Artery Disease by FUPLC-Q-TOF-MS. *Anal. Methods* 8 (6), 1229–1234. doi:10.1039/c5ay02258d

Liang, Q., Wang, C., Li, B., and Zhang, A.-H. (2015a). Lipidomics Analysis Based on Liquid Chromatography Mass Spectrometry for Hepatocellular Carcinoma and Intrahepatic Cholangiocarcinoma. *RSC Adv.* 5 (78), 63711–63718. doi:10.1039/c5ra09589a

Liang, Q., Wang, C., Li, B., and Zhang, A.-H. (2015c). Metabolomics of Alcoholic Liver Disease: A Clinical Discovery Study. *RSC Adv.* 5 (98), 80381–80387. doi:10.1039/c5ra13417j

Liang, Q., Yu, Q., Wu, H., Zhu, Y.-Z., and Zhang, A.-H. (2014). Metabolite Fingerprint Analysis of Cervical Cancer Using LC-QTOF/MS and Multivariate Data Analysis. *Anal. Methods* 6 (12), 3937–3942. doi:10.1039/c4ay00399c

Liu, J., Tian, S., and Miao, M. S. (2019). Effect of Essential Oil of Sanshencao on Thromboangiitis Obliterans Model in Rats. *Chin. J. Exp. Traditional Med. Formulae* 25 (04), 18–22.

Liu, X.-y., Zhang, A.-h., Fang, H., Li, M.-x., Song, Q., Su, J., et al. (2018a). Serum Metabolomics Strategy for Understanding the Therapeutic Effects of Yin-Chen-Hao-Tang against Yanghuang Syndrome. *RSC Adv.* 8, 7403–7413. doi:10.1039/c7ra11048k

Liu, Y., Wei, M., Yue, K., Wang, R., Ma, Y., Men, L., et al. (2018b). Non-target Metabonomic Method provided New Insights on the Therapeutical Mechanism of Gancao Fuzi Decoction on Rheumatoid Arthritis Rats. *J. Chromatogr. B Analyt Technol. Biomed. Life Sci.* 1105, 93–103. doi:10.1016/j.jchromb.2018.11.015

Liu, Z., Zhang, Y., Zhang, R., Gu, L., and Chen, X. (2017). Promotion of Classic Neutral Bile Acids Synthesis Pathway Is Responsible for Cholesterol-Lowing Effect of Si-Miao-Yong-An Decoction: Application of LC-MS/MS Method to Determine 6 Major Bile Acids in Rat Liver and Plasma. *J. Pharm. Biomed. Anal.* 135, 167–175. doi:10.1016/j.jpba.2016.12.021

Munnix, I. C., Cosemans, J. M., Auger, J. M., and Heemskerk, J. W. (2009). Platelet Response Heterogeneity in Thrombus Formation. *Thromb. Haemost.* 102 (6), 1149–1156. doi:10.1160/TH09-05-0289

Obeid, R., Geisel, J., and Nix, W. A. (2019). 4-Pyridoxic Acid/Pyridoxine Ratio in Patients with Type 2 Diabetes Is Related to Global Cardiovascular Risk Scores. *Diagnostics (Basel)* 9 (1), 28. doi:10.3390/diagnostics9010028

Peng, L., Li, M., Xu, Y. Z., Zhang, G. Y., Yang, C., Zhou, Y. N., et al. (2012). Effect of Si-Miao-Yong-An on the Stability of Atherosclerotic Plaque in a Diet-Induced Rabbit Model. *J. Ethnopharmacol* 143 (1), 241–248. doi:10.1016/j.jep.2012.06.030

Piazza, G., and Creager, M. A. (2010). Thromboangiitis Obliterans. *Circulation* 121 (16), 1858–1861. doi:10.1161/CIRCULATIONAHA.110.942383

Qiu, S., Zhang, A., Zhang, T., Sun, H., Guan, Y., Yan, G., et al. (2017). Dissect New Mechanistic Insights for Geniposide Efficacy on the Hepatoprotection Using Multiomics Approach. *Oncotarget* 8 (65), 108760–108770. doi:10.18632/oncotarget.21897

Qiu, S., Zhang, A.-h., Guan, Y., Sun, H., Zhang, T.-l., Han, Y., et al. (2020). Functional Metabolomics Using UPLC-Q/TOF-MS Combined with Ingenuity Pathway Analysis as a Promising Strategy for Evaluating the Efficacy and Discovering Amino Acid Metabolism as a Potential Therapeutic Mechanism-Related Target for Geniposide against Alcoholic Liver Disease. *RSC Adv.* 10 (5), 2677–2690. doi:10.1039/c9ra09305b

Quintas, A., and Albuquerque, R. (2008). Buerger's Disease: Current Concepts. *Rev. Port Cir Cardiotorac Vasc.* 15 (1), 33–40.

Qureshi, S. S., Gupta, J. K., Goyal, A., and Narayan Yadav, H. (2019). A Novel Approach in the Management of Hyperhomocysteinemia. *Med. Hypotheses* 129, 109245. doi:10.1016/j.mehy.2019.109245

Roberts, L. D., Souza, A. L., Gerszten, R. E., and Clish, C. B. (2012). Targeted Metabolomics. *Curr. Protoc. Mol. Biol.* 30, Unit–24. doi:10.1002/0471142727.mb3002s98

Stanulović, M., Jeremić, V., Leskovac, V., and Chaykin, S. (1976). New Pathway of Conversion of Pyridoxal to 4-pyridoxic Acid. *Enzyme* 21 (4), 357–369. doi:10.1159/000458879

Undas, A., Brozek, J., and Szczeklik, A. (2005). Homocysteine and Thrombosis: from Basic Science to Clinical Evidence. *Thromb. Haemost.* 94 (5), 907–915. doi:10.1160/TH05-05-0313

Wang, S., Bai, M., and Miao, M. S. (2021). Analysis of Animal Models of Thromboangiitis Obliterans Based on the Characteristics of Clinical Symptoms in Chinese and Western Medicine. *Chin. J. Exp. Traditional Med. Formulae* 27 (08), 235–240.

Wang, T., Sun, H. G., Hua, Y. L., Li, P. L., and Wei, Y. M. (2016). Urine Metabonomic Study for Blood-Replenishing Mechanism of Angelica Sinensis in a Blood-Deficient Mouse Model. *Chin. J. Nat. Med.* 14 (3), 210–219. doi:10.1016/S1875-5364(16)30018-8

Wang, X., Sun, H., Zhang, A., Sun, W., Wang, P., and Wang, Z. (2011). Potential Role of Metabolomics Apporoaches in the Area of Traditional Chinese Medicine: as Pillars of the Bridge between Chinese and Western Medicine. *J. Pharm. Biomed. Anal.* 55 (5), 859–868. doi:10.1016/j.jpba.2011.01.042

Yang, Z. L., Liu, Z., Meng, Y. H., and Ma, H. Q. (2020). Application of Simiao Yongan Decoction in Cardiovascular Diseases and Research Progress of its Mechanism. *Chin. J. Integr. Med. Cardio-Cerebrovascular Dis.* 18 (01), 85–88.

Zhang, A., Sun, H., Han, Y., Yuan, Y., Wang, P., Song, G., et al. (2012a). Exploratory Urinary Metabolic Biomarkers and Pathways Using UPLC-Q-TOF-HDMS Coupled with Pattern Recognition Approach. *Analyst* 137 (13718), 4200–4208. doi:10.1039/c2an35780a

Zhang, A., Sun, H., and Wang, X. (2012b). Saliva Metabolomics Opens Door to Biomarker Discovery, Disease Diagnosis, and Treatment. *Appl. Biochem. Biotechnol.* 168 (6), 1718–1727. doi:10.1007/s12010-012-9891-5

Zhang, A., Sun, H., Wu, X., and Wang, X. (2012c). Urine Metabolomics. *Clin. Chim. Acta* 414, 65–69. doi:10.1016/j.cca.2012.08.016

Zhang, A., Sun, H., Yan, G., Wang, P., and Wang, X. (2016). Mass Spectrometry-Based Metabolomics: Applications to Biomarker and Metabolic Pathway Research. *Biomed. Chromatogr.* 30 (1), 7–12. doi:10.1002/bmc.3453

Zhang, A., Wang, H., Sun, H., Zhang, Y., An, N., Yan, G., et al. (2015). Metabolomics Strategy Reveals Therapeutical Assessment of Limonin on Nonbacterial Prostatitis. *Food Funct.* 6 (11), 3540–3549. doi:10.1039/c5fo00489f

Zhang, A.-H., Sun, H., Yan, G.-L., Han, Y., Zhao, Q.-Q., and Wang, X.-J. (2019a). Chinmedomics: A Powerful Approach Integrating Metabolomics with Serum Pharmacochemistry to Evaluate the Efficacy of Traditional Chinese Medicine. *Engineering* 5, 60–68. doi:10.1016/j.eng.2018.11.008

Zhang, A., Fang, H., Wang, Y., Yan, G., Sun, H., Zhou, X., et al. (2017). Discovery and Verification of the Potential Targets from Bioactive Molecules by Network Pharmacology-Based Target Prediction Combined with High-Throughput Metabolomics. *RSC Adv.* 7, 51069–51078. doi:10.1039/c7ra09522h

Zhang, A. H., Ma, Z. M., Kong, L., Gao, H. L., Sun, H., Wang, X. Q., et al. (2020). High-throughput Lipidomics Analysis to Discover Lipid Biomarkers and Profiles as Potential Targets for Evaluating Efficacy of Kai-Xin-San against APP/PS1 Transgenic Mice Based on UPLC-Q/TOF-MS. *Biomed. Chromatogr.* 34 (2), e4724. doi:10.1002/bmc.4724

Zhang, A. H., Ma, Z. M., Sun, H., Zhang, Y., Liu, J. H., Wu, F. F., et al. (2019b). High-Throughput Metabolomics Evaluate the Efficacy of Total Lignans from Acanthophanax Senticosus Stem against Ovariectomized Osteoporosis Rat. *Front. Pharmacol.* 10, 553. doi:10.3389/fphar.2019.00553

Zhang, A. H., Yu, J. B., Sun, H., Kong, L., Wang, X. Q., Zhang, Q. Y., et al. (2018). Identifying Quality-Markers from Shengmai San Protects against Transgenic Mouse Model of Alzheimer's Disease Using Chinmedomics Approach. *Phytomedicine* 45, 84–92. doi:10.1016/j.phymed.2018.04.004

Zhang, A., Sun, H., Qiu, S., and Wang, X. (2013). Advancing Drug Discovery and Development from Active Constituents of Yinchenhao Tang, a Famous Traditional Chinese Medicine Formula. *Evidence-Based Complement. Altern. Med.* 2013, 1–6. doi:10.1155/2013/257909

Zhao, Y., Jiang, Y., Chen, Y., Zhang, F., Zhang, X., Zhu, L., et al. (2020). Dissection of Mechanisms of Chinese Medicinal Formula Si-Miao-Yong-An Decoction Protects against Cardiac Hypertrophy and Fibrosis in Isoprenaline-Induced Heart Failure. *J. Ethnopharmacology* 248, 112050. doi:10.1016/j.jep.2019.112050

Zheng, L., Wang, M. Y., Chen, Z., and Li, X. B. (2019). Research Progress of Simiao Yongan Decoction. *Chin. Traditional Patent Med.* 41 (06), 1365–1370.

Zhong, J., Liu, J., and Liu, Y. Y. (2017). Research Progress on the Mechanism of Simiao Yongan Decoction. *World Latest Med. Inf.* 17 (32), 25–26+30.

Conflict of Interest: The authors declare that the research was conducted in the absence of any commercial or financial relationships that could be construed as a potential conflict of interest.

Publisher's Note: All claims expressed in this article are solely those of the authors and do not necessarily represent those of their affiliated organizations, or those of the publisher, the editors and the reviewers. Any product that may be evaluated in this article, or claim that may be made by its manufacturer, is not guaranteed or endorsed by the publisher.

Advantages of publishing in Frontiers

OPEN ACCESS
Articles are free to read for greatest visibility and readership

FAST PUBLICATION
Around 90 days from submission to decision

HIGH QUALITY PEER-REVIEW
Rigorous, collaborative, and constructive peer-review

TRANSPARENT PEER-REVIEW
Editors and reviewers acknowledged by name on published articles

Frontiers
Avenue du Tribunal-Fédéral 34
1005 Lausanne | Switzerland

Visit us: www.frontiersin.org
Contact us: frontiersin.org/about/contact

REPRODUCIBILITY OF RESEARCH
Support open data and methods to enhance research reproducibility

DIGITAL PUBLISHING
Articles designed for optimal readership across devices

FOLLOW US
@frontiersin

IMPACT METRICS
Advanced article metrics track visibility across digital media

EXTENSIVE PROMOTION
Marketing and promotion of impactful research

LOOP RESEARCH NETWORK
Our network increases your article's readership